Università
degli Studi
di Palermo

AREA QUALITÀ, PROGRAMMAZIONE E
SUPPORTO STRATEGICO SETTORE
STRATEGIA PER LA RICERCA
U. O. DOTTORATI

UNIVERSITÀ DEGLI STUDI DI PALERMO

Dottorato di Ricerca in Scienze Fisiche e Chimiche
Dipartimento di Fisica e Chimica-Emilio Segré
Settore Scientifico Disciplinare - FIS/05 - Astronomia e Astrofisica

Unveiling the nature of the Unassociated Gamma-ray Sources in the fourth Fermi catalog: a multi-wavelength approach

IL DOTTORE
ALBERTO ULGIATI
Alberto Ulgiati

IL COORDINATORE
PROF. MARCO CANNAS
Marco Cannas

IL TUTOR
DR. GIANCARLO CUSUMANO
Giancarlo Cusumano

CO TUTORS
DR. FABIO PINTORE
DR. SIMONA PAIANO
Fabio Pintore
Simona Paiano

CICLO XXXVII
ANNO CONSEGUIMENTO TITOLO 2024

Dedicato

a chi mi è stato più vicino in questo periodo

Contents

List of Figures

List of Tables

Abstract

Fifteen years have passed since the launch of the *Fermi Gamma-ray Space Telescope*, a space observatory designed to study celestial objects emitting in the γ-ray energy range. Equipped with two main instruments, the *Large Area Telescope* (LAT) and the *Gamma-ray Burst Monitor* (GBM), *Fermi* has transformed our understanding of the high-energy universe.

Fermi's all-sky monitoring capabilities have provided an unprecedented view of the universe in γ-rays, detecting a wide variety of sources such as active galactic nuclei (AGNs), pulsars, supernova remnants, and γ-ray bursts with exceptional precision. Its observations have unveiled the dynamic and energetic processes driving these objects, offering new insights into extreme astrophysical phenomena and shedding light on some of the most energetic events in the cosmos. By significantly improving sensitivity and spatial resolution compared to its predecessors, *Fermi* has uncovered thousands of previously unknown γ-ray sources, enriching our understanding of high-energy astrophysics.

One of the key achievements of the *Fermi* mission has been the development of comprehensive γ-ray source catalogs, essential resources for the high-energy astrophysics community. These catalogs list and characterize the γ-ray sources detected by the LAT, providing critical data on their locations, energy spectra, and variability. Over the years, several iterations of these catalogs have been released, each incorporating new data and refined analysis methods.

The most recent and extensive catalog is the *Fourth Fermi-LAT Gamma-ray Source Catalog* (4FGL), first released in 2019. In 2023, the *Fermi* collaboration published an incremental update to this catalog, referred to as 4FGL-DR4. This version reports sources detected over 14 years of LAT observations, cataloging a total of 7195 objects. Of these, 4765 have been associated or identified at other wavelengths through positional overlap, correlated variability, or multi-wavelength spectral properties. Among the associated and identified sources, the majority are blazars—a subclass of AGN with relativistic jets pointing at an angle of $\theta \leq 10^\circ$ with respect to the observer's line of sight.

However, a significant portion of the *Fermi* catalog, approximately 30% of sources, remains unclassified and unassociated with lower-energy counterparts, collectively referred to as unassociated gamma-ray sources (UGSs). UGSs play a key role in the high-energy sky, potentially hiding new blazars or other types of AGNs. Identifying and classifying these sources can enhance our understanding of the most extreme environments in the universe, such as those involving supermassive black holes, and may reveal missing components in our current models of the high-energy universe. UGSs are typically faint, with lower γ-ray fluxes. On average, UGSs have fluxes $\sim 5.3 \times 10^{-12}$ erg cm^{-2} s^{-1}, compared to $\sim 1.6 \times 10^{-11}$ erg cm^{-2} s^{-1} for associated AGN in the 100 MeV to 100 GeV range), suggesting that they may represent a higher redshift AGN population and/or lower luminosity sources. Identifying UGSs is crucial for population studies, developing physical models, understanding the cosmic evolution of γ-ray sources and estimating the very high-energy (VHE) cosmic background.

The goal of this thesis is to associate and classify extragalactic UGSs from the fourth *Fermi* catalog, with the aim of unveiling new blazars and, more broadly, new AGNs. To achieve this, the analysis focuses on the 1284 UGSs located outside the Galactic plane ($|b| \geq 10°$), searching for X-ray, optical, and radio counterparts that spatially coincide with the γ-ray positions. Given the large uncertainty regions in γ-rays, the search begins in the X-ray band, where the potential counterpart confusion is limited compared to lower energy bands such as optical and radio, and where positional uncertainties are more constrained relative to γ-rays. This strategy allows for a more focused search region.

In the past decade, the Swift X-ray satellite has been conducting a dedicated observational campaign targeting *Fermi*'s unassociated sources, providing real-time access to its data. This thesis begins by analyzing all the available *Swift* X-ray images, which cover the γ-ray positions of the UGSs. The number of UGSs with *Swift* observations is 714. From this analysis, I found that 274 of these γ-ray emitters have at least one X-ray source detected with a significance of $\geq 3\sigma$ within their *Fermi* error box. Among these, 193 UGSs have a single potential X-ray counterpart (referred to as UGS1), while 81 have multiple potential X-ray counterparts within the *Fermi* error box (referred to as UGS2). Of the UGS2, 54 have two X-ray counterparts, 11 have three, and the remaining 16 have more than three.

Starting from the X-ray positions and error boxes, optical and radio counterparts are searched within several catalogs or by dedicated observations. I found that each UGS1 has a potential optical counterpart, and 113 also could be associated to a radio counterpart. Regarding the UGS2 sub-sample, I found a large degeneracy of potential counterparts, which complicates the association process. I separated the sources in the sample in radio-loud and radio-quiet sources (accordingly to the historical threshold of the radio-loudness ratio, placed to R=10).

To assess the reliability of the associations, I compared the absolute and relative fluxes of the potential counterparts with those of blazars from the fourth *Fermi* catalog. The comparison revealed that radio-loud sources exhibit emission profiles similar to those of blazars, making them strong candidates for counterparts. In contrast, radio-quiet sources tend to deviate from typical blazar behavior. Given that only radio-loud AGNs are listed in the *Fermi* catalog, a more in-depth analysis is necessary to confirm these associations.

I found that 33 UGS1 have optical spectra already available in the literature. The analysis of optical spectra is a fundamental step in determining the extragalactic origin of UGSs, estimating their distance, and classifying them among the various AGN sub-classes. From the analysis of these 33 UGSs, I found that the X-ray emitter located within their *Fermi* error box is a BL Lac (a subclass of blazars with an optical spectrum described by a featureless power law or weak emission lines) for 21 of them, a Flat Spectrum Radio Quasar (FSRQ, a subclass of blazars distinguished from BL Lacs by its strong and broad optical emission lines) for one source, a radio galaxy (a subclass of AGN characterized by extended radio emission) for one source, and a Seyfert or Quasi Stellar Object (subclasses of AGN with strong emission lines in the optical but weak or absent radio emission) for 10 of them. The presence of radio-quiet AGNs in the *Fermi* catalog is unexpected and potentially interesting, as all AGNs listed in the fourth *Fermi* catalog so far are radio-loud.

The 33 UGSs associated and classified in this thesis, along with a sample of 44 UGSs from the second and third Fermi catalogs, which were associated and classified by Paiano et al. (2017a, 2019), are characterized through their multi-wavelength emission. Specifically, I analyzed the spectral energy distributions (SEDs) of these 77 γ-ray emitters to study their properties, while also examining the emission intensities of the BL Lacs in the sample to identify new masquerading BL Lacs (FSRQs with featureless optical spectra typical of BL Lacs, due to their strong continuum masking the spectral lines).

The SED analysis leads to the conclusion that radio-loud AGNs in the sample (64 objects on a total of 77) are well-associated, as they exhibit continuity between the emission of the counterpart and the γ-ray emitter. These objects are then classified into the blazar subclasses low synchrotron peak (LSP), intermediate synchrotron peak (ISP), and high synchrotron peak (HSP), based on the position of the synchrotron emission peak in their SEDs. The majority are classified as HSP (46 objects), with 11 as ISP and 7 as LSP.

Furthermore the multi-wavelength analysis led to the identification of 9 candidates masquerading BL Lacs, representing approximately 15% (possibly $\sim 30\%$) of the radio-loud sample, which is somewhat smaller than the value of $\gtrsim 34\%$ found in the previous studies.

Regarding the 13 radio-quiet sources in the sample, I found that they exhibit behavior that diverges from that of jetted-AGNs. Many of them do not show radio emission, and their SEDs deviate from the typical double peak trend, indicating the absence of a jet. This makes reconciling the γ-ray emission with lower-energy emissions challenging. Since γ-ray emission requires non-thermal processes, and having excluded the jet as the source of this emission, I wondered about the possibility of having a γ-ray emission from star formation processes. This analysis yields negative results. In the absence of a jet and star formation processes, linking the γ-ray emission to lower-energy emission is complicated.

For this reason I searched for alternative counterparts, looking for radio sources that are positionally coincident with the γ-ray emitters. From this search, I find a possible alternative counterpart for 7 out of 13 UGSs, which shows a jet and continuity across the entire SED, described by a typical double peak trend of jetted AGNs. These sources will be the subject of a future observational campaign, which will allow for a definitive classification and verification of the associations. No valid alternative counterparts are found for the remaining 6 sources. Therefore, these sources require a more in-depth analysis regarding the origin of the γ-ray emission.

Introduction

The project presented in this PhD thesis aims to find the lower-energy counterparts of unassociated γ-ray emitters detected by the *Fermi* satellite. In 2023, the *Fermi* collaboration released an incremental version of the fourth catalog (4FGL-DR4, Abdollahi et al. 2020; Ballet et al. 2023), which lists the sources detected over 14 years of observations by LAT, the satellite's main detector. This catalog includes 7195 γ-ray emitters, of which 4675 have already been associated and classified. The majority of the extragalactic population ($|b| > 10$ degrees) belongs to the blazar class, a type of active galactic nuclei (AGNs) with jets oriented along the line of sight, capable of emitting across the entire electromagnetic spectrum, from radio to very high-energy (VHE) γ-rays.

However, the catalog also includes a substantial population of sources, approximately 30%, that remains unclassified and unassociated with any lower-energy counterparts. These are known as unassociated gamma-ray sources (UGSs). UGSs represent a key component of the high-energy sky, as their association with lower-energy counterparts and subsequent classification are crucial for achieving a comprehensive understanding of the γ-ray population and for conducting statistical analyses. Moreover, UGSs may conceal new blazars or even new classes of AGN emitting at GeV energies, such as Narrow Line Seyfert 1 and Seyfert 2-like objects. Given their weaker γ-ray fluxes, these sources are likely to be located at greater distances and/or may be AGNs with a lower nucleus-to-host flux ratio. This has significant implications for understanding the cosmic evolution of γ-ray blazars. The effort dedicated to the project on the association of UGSs is focused on the search for new blazars and AGNs capable of emitting in the γ-ray band.

The primary challenge in associating UGS counterparts lies in the significant positional uncertainties of the *Fermi* detections. These uncertainties are due to the limited photon statistics and the angular resolution of the LAT detector (3.5° at E = 100 MeV, 0.6° at E = 1 GeV, and $> 0.15°$ at E $>$ 10 GeV). As a result, the *Fermi* error boxes often contain a large number of potential lower energy counterparts (e.g., in the optical and radio bands), making it challenging to determine the true origin of the γ-ray emission.

The approach adopted in this project focuses on searching for low-energy counterparts by starting with their X-ray emission. In the X-ray band, the number of sources is smaller compared to the radio and optical bands, and the positional uncertainties are smaller when compared to the

Fermi ones, which helps to narrow down the number of potential counterparts.

For over 10 years, the *Swift* satellite has been conducting an observational campaign dedicated to UGSs, using its main detector, the XRT. If a X-ray source is detected inside the γ-ray error box, the next step is to search for counterparts in radio, infrared and optical bands to determine a possible positional association. Given their orientation in the sky, the emission from blazars is dominated by the relativistic jet of particles, which exhibits its highest flux density in the radio band. Additionally, the radio emission is correlated with the γ-ray emission. Therefore, particular attention is given to identifying counterparts that emit in the radio band. However, the definitive classification of extra-galactic UGSs is achieved through the study of the optical spectra of their counterparts. Optical spectra serve as the "fingerprint" of these objects, allowing for their classification, the confirmation of their extragalactic nature and their distance (redshift).

Once the potential low-energy counterpart of the UGS is identified, the Spectral Energy Distribution (SED) of the object can be constructed by combining the available multi-wavelength flux measurements. This approach provides a broader perspective on the source, aiding in the verification of the proposed association and helping to determine the origin of the emission. The association's validity is assessed through SED analysis, with spectral consistency across different energy bands indicating a common source. In many cases, emissions in lower energy bands, such as radio, infrared, and X-rays, should align with γ-ray emissions, supporting the hypothesis of a shared physical origin, often through processes like synchrotron or inverse Compton scattering. However, distinct components within the same object may contribute to emissions in different bands, suggesting multiple origins. This requires careful interpretation of the SED to ensure an accurate association.

The study of UGSs in this project is, therefore, a multifaceted process that incorporates complementary approaches, including the search for multi-wavelength counterparts, optical spectroscopy, and SED construction and analysis. Together, these methods provide a comprehensive understanding of the sources, shedding light onto their nature and the mechanisms driving γ-ray emission.

This thesis is structured as follow:

Chapter 1 provides a theoretical introduction to the physics of AGNs. The chapter begins by describing the accretion processes and how accretion can be a source of energy. It then introduces the Eddington limit, a mechanism by which accretion is inhibited by the radiation pressure produced by the emitting object. Following this, the chapter discusses the emission spectrum of AGNs, which results from the contributions of various structures of matter that form around the supermassive black hole (SMBH). Each of these structures contributes to or dominates a specific energy range within the spectrum, and the different structures are detailed in dedicated subsections of the chapter. Finally, the chapter concludes with a discussion on γ-ray absorption processes.

Chapter 2 discusses the unified model of AGNs, which asserts that the various classes of AGNs arise from differences in observational perspective and the intrinsic characteristics of the system. This model suggests that the observed variations among different types of AGNs, such as quasars, radio galaxies, and blazars, are primarily due to the orientation of the relativistic jet with respect to the observer's line of sight, as well as the presence or absence of certain structures like the torus of dust and gas. The chapter then describes the different classes of AGNs, distinguishing between two main groups: radio-loud and and the radio-quiet sources. The radio-loudness parameter R is defined as the ratio of the radio flux density in the 2-4 GHz range to the optical flux density in the g-band. Sources with $R > 10$ are classified as radio-loud, while those with $R \leq 10$ are considered radio-quiet.

Chapter 3 introduces the *Fermi* γ-ray satellite and the most recent source catalog, 4FGL-DR4. The first part of the chapter provides a detailed description of the instruments on board the satellite and their performance. In the second part, the 4FGL-DR4 catalog is discussed, highlighting the types and number of sources detected, as well as the specific information provided for each. Special attention is given to the description of UGSs, which are the central focus of this thesis project.

Chapter 4 describes the multi-band observatories (X-ray, optical, and radio) and the surveys used to search for the lower-energy counterparts of UGSs. The first part of the chapter is dedicated to the X-ray band and the *Swift* satellite, which is central to the search for counterparts. The second part of the chapter focuses on optical telescopes and their surveys. It describes the PanSTARRS and SDSS surveys, which cover the northern sky, while DES and SSS cover the southern sky. The last part of the chapter describes the radio facilities and their surveys. The VLA survey (VLASS) covered the northern sky, while the southern sky was covered by the RACS survey of the ASKAP antennas. Additionally, the ATCA facility is discussed, which was used for dedicated observations of potential radio counterparts located in the southern sky.

Chapter 5 is dedicated to the procedures for X-ray and optical data analysis. The first part of the chapter describes the online data analysis tool provided by the *Swift* consortium. It details the tool's performance, which is crucial for the detection and analysis of X-ray counterparts, including source detection, source positioning, and the extraction and analysis of X-ray spectra. The second part of the chapter focuses on optical spectroscopy as an essential method for classifying extragalactic UGSs and estimating their distances. It outlines the key steps involved in analyzing the spectra of AGNs.

Chapter 6 details the search for counterparts for all extra-galactic UGSs ($|b| \geq 10°$) covered by *Swift* observations. It describes the procedures that led to the creation of a catalog of potential X-ray, radio, and optical counterparts. The chapter then outlines the analysis of the X-ray spectra. Finally, the identified potential counterparts are compared with those of *Fermi* blazars that have already been associated and classified, using the X-ray flux distribution and color-color diagrams.

Chapter 7 discusses the optical spectroscopy of a sample of 33 UGSs, among which only one X-ray source was found to be positionally coincident with a γ-ray emitter, and for which an optical spectrum is already available in the literature, though it has not been analyzed in detail. The spectroscopic analysis revealed that all counterparts are extragalactic objects: 22 sources classified as blazars, 1 radio galaxy, and 10 radio-quiet AGNs, including Seyfert galaxies and quasi-stellar objects (QSOs). Given that the *Fermi* catalog includes only radio-loud AGNs, this raises the question of whether radio-quiet sources may represent an emerging new population among *Fermi* sources.

Chapter 8 focuses on the multi-wavelength study of a sample of 77 UGSs, previously associated in this thesis and in other works from our research group. Specifically, the SEDs of these objects are constructed and qualitatively analyzed to identify emission processes that can simultaneously explain the spectrum of the counterpart (from radio to X-ray) and that of the γ-ray emitter. Regarding the radio-loud sources, it is found that they exhibit coherent emission across the entire spectrum, originating from the jet. In contrast, the radio-quiet sources show a behavior that diverges from that of jetted AGNs. In their SEDs, it is not possible to identify a jet or star formation processes, complicating the reconciliation between the γ-ray emission and that of the counterpart. For these sources, alternative counterparts are sought, a search that yields only partially satisfactory results, necessitating a more in-depth analysis. Finally, the chapter explores the possibility to identify new masquerading BL Lac objects [blazars belonging to the subclass of flat spectrum radio quasars (FSRQ) that exhibit an optical spectrum typical of BL Lacs] within this sample of 77 UGSs.

Finally, **Chapter 9** presents the conclusions of this thesis project, summarizing the key findings and their implications for the study of UGSs. It discusses the significance of the identified counterparts and their contribution to understanding the nature of γ-ray emitters. Additionally, the chapter highlights potential avenues for future research, suggesting how the methodologies developed can be applied to further explore unassociated sources and enhance our knowledge of the broader cosmic landscape.

1

Active Galactic Nuclei

According to the standard paradigm, at the center of each large galaxy resides a supermassive black hole (SMBH) (Kormendy & Richstone 1995; Kormendy & Ho 2013), an astronomical object with masses ranging from millions to tens of billions of solar masses. The Active Galactic Nuclei (AGNs) are very bright regions at the center of the galaxies, powered by the accretion of matter onto the SMBHs. Accretion involves the accumulation of gas and dust onto the central object under the influence of gravity.

The interaction between the gravitational force of the SMBH, its angular momentum, and that of the surrounding matter results in the formation of inflow and outflow structures around the compact object (Alloin 2006). As matter accumulates, it releases vast amounts of energy, producing intense radiation across the electromagnetic spectrum. These energetic emissions characterize AGNs, making them some of the brightest objects at high energies in the universe.

In many cases, the emission from AGNs exceeds that of the host galaxy at high energies [from the ultraviolet (UV) band] or in the radio band, and sometimes even over the entire electromagnetic spectrum, influencing its evolution and shaping the surrounding galactic environment(Kormendy & Ho 2013). Each structure within AGNs emits characteristic radiation, allowing us to identify and study these cosmic phenomena in detail.

1.1.0 Accretion as a source of energy

The accretion, the process by which material falls onto a gravitating body, has emerged as the primary mechanism that powers the most brilliant objects in the universe in UV and X-ray bands (Frank et al. 2002). It is known to be the principal source of power in several types of close binary systems, and is widely believed to provide the power supply in AGNs and quasars.

The understanding of the importance of accretion processes enhanced the observational techniques in astronomy. Particularly noteworthy is the exploitation of the full electromagnetic spectrum, from radio waves to X-rays and γ-rays. Simultaneously, the existence of compact objects has been unequivocally established, marked by the discovery of pulsars, and further supported by the detection of gravitational waves, while black holes have gained firm theoretical grounding.

This evolution underscores a paradigm shift in our understanding of gravity's role in the cosmos. Accretion onto compact objects emerges as a natural and powerful mechanism for generating high-energy radiation. Indeed, accretion onto compact objects forms the cornerstone of most high-energy astrophysical sources.

To get an idea of the orders of magnitude involved, let us make a simple estimate. For a body of mass M and radius R the gravitational potential energy released by the accretion of a mass m on to its surface is:

$$\Delta E_{acc} = GMm/R \tag{1.1}$$

where G is the gravitational constant. If the accreting body is a neutron star with radius R ~ 10 km, mass M ~ $M_\odot$, we obtain 10^{20} erg per accreted gram. We would expect this energy to be released eventually mainly in the form of electromagnetic radiation. For comparison, consider the energy that could be extracted from the mass m by nuclear fusion reactions. We know that in a nuclear fusion reaction the maximum is obtained from the conversion, of hydrogen to helium. This yields an energy release:

$$\Delta E_{nuc} = 0.007mc^2 \tag{1.2}$$

where c is the speed of light. In this case we obtain and energy of about 6×10^{18} erg g^{-1}, that is about 1/20 of the accretion yield in this case.

It is also clear from the equation 1.1 that the efficiency of accretion as an energy release mechanism is strongly dependent on the compactness, M/R, of the accreting object: the larger the compactness, the greater the efficiency. Considering therefore a black hole with M ~ $M_\odot$ e R ~ $2GM/c^2$ ~ $3(M/M_\odot)$ km, the energy released will be 3 times higher, while for a typical withe dwarf with M ~ $M_\odot$ and R ~ 10^9 cm, the energy released will be $1/10^3$ lower. For accretion on to a 'normal', less compact, star, such as the Sun, the accretion yield is smaller than the potential nuclear yield by a factor of several thousand. Even so, accretion on to such stars may be of observational importance. For example, a binary system containing an accreting main-sequence star has been proposed as a model for the so-called symbiotic stars (Frank et al. 2002).

For a fixed value of the compactness, the luminosity of an accreting system depends on the rate $\dot{m}$ at which matter is accreted. At high luminosities, the accretion rate may itself be controlled by the outward momentum transferred to the accreting material from the radiation pressure. Under certain circumstances, this can lead to the existence of a maximum luminosity for a given mass, usually referred to as the Eddington luminosity.

1.2.0 The Eddington limit

The Eddington limit is a fundamental concept in astrophysics that describes the maximum luminosity that an object, such as a star or a black hole, can achieve during accretion while still being in equilibrium (Rybicki & Lightman 1979). It arises from the balance between the radiation pressure generated by the object's luminosity and the gravitational force trying to pull matter inward. When the luminosity of an object exceeds the Eddington limit, the outward radiation pressure becomes so strong that it overcomes gravity, leading to instability.

Let us consider a hydrogen atom at a distance r and accreting onto a star of mass M. This atom is part of a matter flow that we assume to be steady and spherical. We define the flux of radiative energy emitted by the star as $\mathrm{F}_R = \mathrm{L}/4\pi\mathrm{R}^2$, which results in a photon flux at distance r equal to $\mathrm{L}/4\pi\mathrm{r}^2\mathrm{pc}$, where p in the average momentum of the photons. The cross-section for the interaction between photons and the hydrogen atom is the Thomson cross-section, therefore we would have a number of collisions between photons and electron (it is possible to neglet the interaction with proton since $\sigma_T \propto \mathrm{m}^{-4}$) equal to $\mathrm{N} = \mathrm{L}\sigma_T/4\pi\mathrm{r}^2\mathrm{pc}$. We then have that the radiative force is equal to $\mathrm{F}_{rad} = \mathrm{L}\sigma_T/4\pi\mathrm{r}^2\mathrm{c}$, while the gravitational attraction is equal to $\mathrm{F}_{grav} = \mathrm{GMm}_p/\mathrm{c}^2$, where m_p is the mass of the proton (it is possible to neglect the mass of the electron being $\mathrm{m}_e \sim \mathrm{m}_p/1800$). By equating the two quantities, we would have that:

$$L_{Edd} = \frac{4\pi c G M m_p}{\sigma_T} \cong 1.3 \times 10^{38} \frac{M}{M_\odot} erg/s \tag{1.3}$$

At greater luminosities the pressure of the radiation dominates, and the accretion is stopped. We must, however, point out that what we have said so far holds under the assumption of steady accretion and spherical symmetry. More complicated cases could lead to different results, as seen, for example, in the supernovae, where accretion is not steady, ultra-luminous X-ray sources (ULX), where accretion is non-spherical, and certain AGN, where both accretion is non-spherical and radiation efficiency can exceed the standard, managing to exceed the Eddington limit by several orders of magnitude (e.g. see Brightman et al. 2019).

Under our assumption, the Eddington limit imposes a constraint on the steady accretion rate, $\dot{m}$ (the mass accreted per unit time, measured in g s^{-1}), for accretion-powered objects. If all the kinetic energy of infalling matter is converted to radiation at the stellar surface, denoted as R, then the accretion luminosity is:

$$L_{acc} = GM\dot{m}/R \tag{1.4}$$

In the case of black holes, however, we do not have a rigid surface, but rather a region from which once crossed, nothing can escape. This results in a decrease in the potential radiation emitted. To account for this, we rewrite equation 1.4 as:

$$L_{acc} = 2\eta GM\dot{m}/R = \eta\dot{m}c^2 \tag{1.5}$$

where we have used $\mathrm{R}=2\mathrm{GM}/\mathrm{c}^2$ for the black hole radius. η measures the conversion efficiency of the accreted material into radiation. A reasonable guess for η in a solar mass neutron star is $\eta \sim 0.1$. This leads to typical accretion values of $\dot{m} \sim 10^{18}$ g s^{-1}. For a stellar mass black hole, despite its extra compactness, the conversion efficiency may be small than one for a neutron star of similar mass.

Now let us consider the case of AGNs. These systems can reach luminosities as high as of 10^{47} erg s^{-1}, which can vary by an order of 2 on a timescale of weeks or less. Assuming a nuclear burning efficiency, $\eta = 0.007$, the accretion rate should be $\dot{m} \sim 200$ $M_{\odot}$ yr^{-1}. Instead, the accretion rate required for an efficiency close to $\eta \sim 0.1$ should be $\dot{m} \sim 10$ $M_{\odot}$ yr^{-1}. If these systems are assumed to radiate at less than the Eddington limit, then in extreme cases where luminosity is $\sim 10^{47}$ erg s^{-1}, accreting masses of at least 10^{9} $M_{\odot}$ are required.

1.3.0 The emitted spectrum

The accretion process typically leads to emission in the ultraviolet range or higher energies (i.e., in the high-energy band). Let us understand the reason for this through a simple estimation that will give us an idea of the magnitudes involved. We are looking for the range of temperatures characterizing emission in compact objects. The minimum temperature will be found by assuming blackbody (BB) emission, as it is the most efficient thermal emission process. As seen in equation 1.1, the released energy scales as $\sim$ 1/R. If the accretion is onto an object with R $\simeq$ 2GM/c^2 = 3 km (M/$M_{\odot}$), the luminosity is the Eddington luminosity, and we consider the region where the most of the energy is released for example at r $\simeq$ 5R, we will have:

$$L = 4\pi r^2 \sigma T_{BB}^4 = L_{Edd} \tag{1.6}$$

where σ is the Stefan-Boltzmann constant. Substituting the values for the Eddington luminosity and simplifying, we would have:

$$kT_{min} = kT_{BB} \simeq 1.5 \left(\frac{M}{M_{\odot}}\right)^{-\frac{1}{4}} \left(\frac{L}{L_{Edd}}\right)^{\frac{1}{4}} keV \tag{1.7}$$

For the estimation of T_{max}, let us consider a flux of hydrogen atoms accreting at the same distance r $\simeq$ 5R, onto an object with a mass M, which, upon falling, releases its energy thermally. For each proton-electron pair we have:

$$\frac{GM(m_p + m_e)}{5R} = 3kT_{Th} = 3kT_{max} \tag{1.8}$$

where k is the Boltzmann constant and T_{Th} is the temperature for a thermal emission.

So $T_{min} \lesssim T_{Th} \lesssim T_{max}$. For M = $M_{\odot}$ and L = L_{Edd}: 1.5 keV $\lesssim kT_{Th} \lesssim$ 30 MeV.

The dependence between T and M is weak, kT $\propto M^{-\frac{1}{4}}$. However, in the case of SMBHs, where M $\sim 10^{8}$ $M_{\odot}$, the energy decreases significantly because $(M/M_{\odot})^{-\frac{1}{4}} \sim 10^{-2}$. This causes the emission energy band to move from keV to approximately 10 eV, transitioning from X-ray to UV.

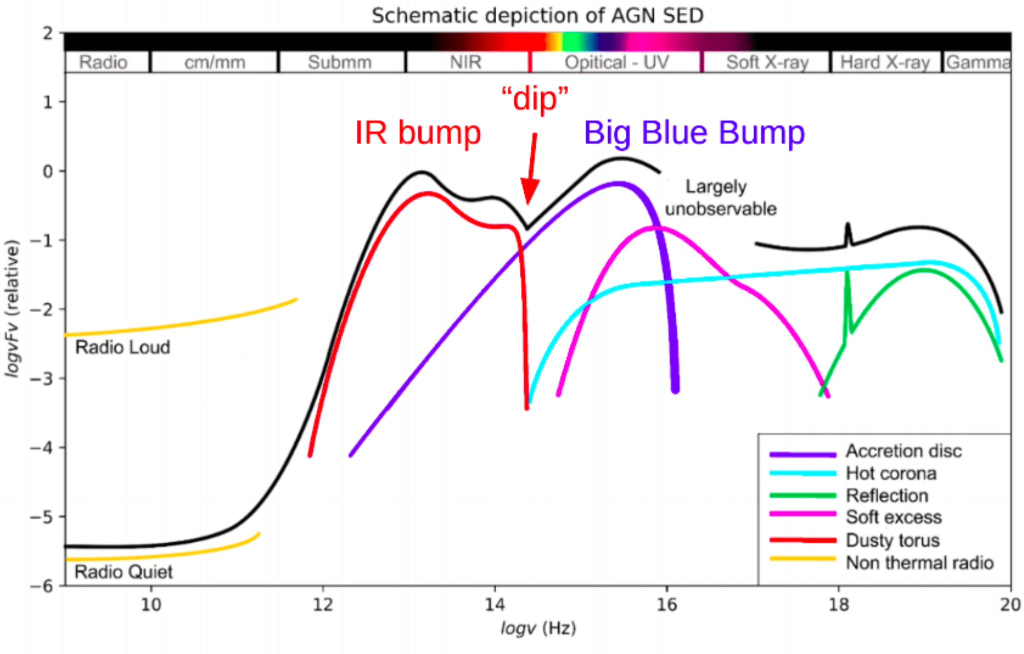

Figure 1.1: Schematic view of AGN emission. Image adapted from Elvis et al. (1994).

1.4.0 The structures around the supermassive black hole

In the previous sections, we have seen how accretion can be a source of energy. Now let us examine how accretion must occur in order to be consistent with what we observe.

Consider an atom of hydrogen, part of a matter flow, that falls onto an object with a mass M and a radius R, in free-fall (ff), from infinity. Each atom will acquire a kinetic energy approaching the minimum of the potential:

$$\frac{1}{2}(m_p + m_e)v_{ff}^2 = \frac{GMm_p}{r} \tag{1.9}$$

When this matter reaches the surface of the star at r = R, it is rapidly decelerated and, assuming all the matter accumulates on the surface of the object, the total kinetic energy of free-fall is radiated away as heat. However as said before a black hole do not have a solid surface onto which the matter can be accreted unlike for example in the case of a neutron star. If matter fell radially into the black hole, no heat would be released. The infalling matter must have some angular momentum, and its conservation prevents matter from falling directly into the black hole. This angular momentum contributes to the formation of structures around the black hole. Through these structures, which include both inflow and outflow, the central object exchanges matter with its surrounding environment. In the following paragraphs, we will explore these structures in detail, focusing on their geometry, emission models, and emission bands. We will begin our examination with the outermost structures and progress toward the center.

1.4.1 Dusty torus

The dusty torus is a geometrically thick structure of size 1-100 pc, located around the central BH, with a density of 10^4 - 10^6 cm^{-3} and an extremely large column density, 10^{25} or even larger (Alloin 2006). It is primarily composed of a mixture of dust and gas, that is flowing towards and/or away from the black hole. The dust consists mainly of materials such as silicates, graphite, and other complex organic molecules. These dust grains can vary in size, ranging from fractions of micrometers to several tens of micrometers. The gas within the torus may primarily consist of molecular hydrogen (H2), but it can also include other molecules such as carbon monoxide (CO), water (H2O), and other organic and inorganic compounds (Alloin 2006). There exists a significant debate within the literature regarding the distribution of dust within the torus. Some studies argue for a smooth distribution, while others suggest a clumpy structure consisting of optically and geometrically thick clouds, or propose a combination of both scenarios (see references in Padovani et al. 2017).

The inner part of such a structure is exposed to the central radiation field produced by the accretion disc. It has been measured (Peterson 1997) that the inner regions reach a temperature of:

$$T_{in} \simeq 1000 L_{46}^{1/5} r_{pc}^{-2/5} K \tag{1.10}$$

where L_{46} is the luminosity in unit of 10^{46} erg s^{-1}, and r_{pc} is the distance from the central object in unit of 1 pc (the distance from the SMBH to the disc is $\ll$ 1 pc, making it negligible for this estimate). Silicon and graphite grains sublime at temperatures $T_{sub} \sim 1500$ K. By setting T_{sub}=T_{in}, it is found that:

$$r_{sub} \simeq 0.36 L_{46}^{1/2} pc \tag{1.11}$$

that for a luminosity 10^{47} erg s^{-1}, it is consistent with an inner radius of 1 pc.

The emission from the dusty torus in AGNs plays a crucial role in shaping the observed spectral energy distribution (SED) of these objects across a wide range of wavelengths. The torus absorbs a significant fraction of the radiation emitted from the central engine, primarily in the ultraviolet (UV) and X-ray bands, and re-emits thermally mainly in the infrared (IR) and submillimeter bands (Padovani et al. 2017). The hallmark of the torus emission in the SED of AGNs is represented by what is referred to as the IR-bump (see Fig. 1.1). Finally, the fact that the temperature of the dust cannot exceed the sublimation temperature of 1500 K indicates that the hottest dust emits at $\lambda \sim 2$ μm, explaining the "dip" in the SED of AGNs (Peterson 1997).

1.4.2 Disc

In the main section (see Sec. 1.1), we have seen that the angular momentum of infalling matter prevents its direct fall into the black hole. However, in a situation of equilibrium, with only angular velocity present and in the absence of external forces, a single particle of matter remains at a distance r in a classical Keplerian motion. In order to move to smaller radii, viscous forces between the different particles that make up the flow must be present. Furthermore, since nothing can be emitted once the Schwarzschild radius of the black hole is crossed, emission must occur beforehand, during the accretion phase. The viscous forces will therefore have two effects: they will cause individual flow particles to lose angular momentum, and they will act as a frictional force resulting in heat dissipation.

Assuming an initial Gaussian distribution of particles accreting around a certain radius r_0, we find that particles at larger radii will have lower velocities, while those closer to the central attractor will have higher velocities. Through the interaction between particles, those closer to the center will be slowed down by those farther out, which in turn will acquire velocity. Each ring of accreting matter will tend to move mass towards the minimum of the potential and angular momentum outward. This leads to a widening of the individual Gaussian distributions, resulting in the formation of an accretion disc around the SMBH (Pringle 1981).

The fundamental parameters that govern the properties of the disc are the accretion rate, the BH mass, and the BH spin. These parameters determine the geometry of the disc, the plasma temperature in the disc, the overall luminosity, and the emitted spectrum. Usually, for convenience, the accretion rate and the luminosity are referred to the Eddington quantities, and L/L_{Edd} is defined as the *normalized accretion rate* (Alloin 2006).

The geometry of the disk is described through two parameters: its vertical scale height H and its radial distance r from the black hole. At sub-Eddington accretion rates ($L/L_{Edd} \ll 1$), the radiation pressure is relatively low, preventing significant inflation of the disk such that $H \ll r$. In this case, the disk is defined as thin. This geometrical configuration leads to a very narrow vertical extent, resulting in a high surface density. This high surface density means that there is a significant amount of material along the line of sight, increasing the probability that photons will interact with the disk material before escaping, making the disk optically thick.

In the standard model (Shakura & Sunyaev 1973) we consider the disc as an optically thick geometrically thin structure, rotating around the object (in our case around a SMBH) and following a Keplerian motion ($v_K(r) = \sqrt{\frac{GM}{r}}$). This model is considered adequate under the approximation that $10^{-4} \lesssim L/L_{Edd} \lesssim 0.3$ (Netzer 2013).

As the accretion rate increases beyond these limits, the disk geometry undergoes significant transformations. Approaching or exceeding the Eddington limit, the disk experiences heightened radiation pressure, causing it to expand or "puff up," thereby increasing its scale height H. This results in a transition from a thin disk to a thick disk or even an accretion torus, where H/R is no longer significantly less than one. These thicker disks exhibit lower optical thickness due to reduced surface density from vertical extension, leading to complex behaviors such as strong outflows and winds driven by radiation pressure (Netzer 2013).

In order to characterize the emission in the disc, we report the differential luminosities arising from the gravitational energy loss of the accreting matter and the work done by the torque, N, that results in outward loss of angular momentum (Netzer 2013). The first of these can be written as:

$$dL_g = -d\left(\frac{G\dot{M}M}{2r}\right) \tag{1.12}$$

and the second as:

$$dL_N = -d(N\Omega_K) = -d\left(\frac{G\dot{M}M}{2r}\right) \tag{1.13}$$

where Ω_K is the associated Keplerian angular velocity:

$$\Omega_K = \frac{v_K}{r} = \left[\frac{GM}{r^3}\right]^{1/2} \tag{1.14}$$

Combining the two values of luminosities and differentiating with respect to r we obtain an expression for the energy released at various radii:

$$\frac{dL}{dR} = \frac{3GM\dot{M}}{2R^2}\left[1-\left(\frac{r_{in}}{r}\right)^{1/2}\right] \tag{1.15}$$

where r_{in} is the innermost radius of the disc. During the process of friction causing angular momentum loss, the disc emits thermally (Frank et al. 2002). It is thus possible to express the luminosity of each ring of matter as:

$$dL = A\sigma T^4 = 2 \times 2\pi r dr \sigma T^4 \tag{1.16}$$

where A is the area of the annulus, T is its temperature and σ is the Stephan-Boltzmann constant. Combining the equations 1.15 and 1.16 we obtain the temperature at all radii:

$$T(r) = \left(\frac{3GM\dot{M}}{8\sigma\pi r^3}\left[1-\left(\frac{r_{in}}{r}\right)^{1/2}\right]\right)^{1/4} \tag{1.17}$$

The spectrum emitted by the disc will therefore be the superposition of many blackbodies (the so-called multicolor blackbody) with a temperature scaling with radius (Shakura & Sunyaev 1973; Longair 2011):

$$S_\nu \propto \int_{r_{min}}^{r_{max}} 2\pi r B(\nu,T) dr \tag{1.18}$$

where B(ν,T) is the Planck function (ν^3/(exp(hν/kT)-1)). The typical values for r_{min} and r_{max} in a AGN with M ~ 10^9 $M_\odot$ are $r_{min} \sim 10^{-4}$ pc and $r_{max} \sim 0.01$ pc (Alloin 2006). The disc's trace in the SED is called the Big Blue Bump, and it extends from IR to soft X-ray wavelengths (see Fig. 1.1).

1.4.3 Corona

The presence of a standard, optically thick, and geometrically thin disc alone cannot account for the entire observed SED (Netzer 2013). As we have seen in section 1.3, the emission peak of the disc falls in the UV band, implying a temperature of the inner disc of a few × 10^5 K. However, emissions implying temperatures well beyond this value are observed. It is therefore plausible that there is a hot medium, close to the disc (or perhaps constituted by the same disc, which near the BH decreases its density), where more energetic photons are emitted (Alloin 2006). This structure is called a corona or hot flow, and it is believed to be an optically thin and geometrically thick region populated by hot and relativistic electrons, with a temperature of T $\sim 10^8$ K. The disc and the corona interact with each other and influence one another. Photons emitted from the disc interact with the relativistic electrons in the corona, which transfer to the photons part of their kinetic energy in the so called inverse Compton processes[1]. The resulted energy of a photon, with initial energy ϵ, will be:

$$\epsilon_s = \frac{\epsilon}{1 - \frac{\epsilon}{m_e c^2 (1 - cos\theta)}} \tag{1.19}$$

While the energy loss of electron is given by:

$$\frac{dE}{dt} = \frac{4}{3} \sigma U_{rad} \beta^2 \gamma^2 \tag{1.20}$$

where U_{rad} is the energy density of the radiation field, σ is the scattering cross section, γ is the Lorentz factor, defined as $1/\sqrt{(1-\beta^2)}$, with β = v/c, where v is the plasma velocity.

Inverse Compton can occur in two distinct regimes: Thomson regime and Klein-Nishina regime (Rybicki & Lightman 1979). In the former case, the energy of the incident photon is much lower than the rest energy of the electron, $\epsilon = \frac{h\nu}{m_e c^2} \ll 1$, while in the latter case, the energy of the incident photon is comparable to the rest energy of the electron, $\epsilon = \frac{h\nu}{m_e c^2} \sim 1$. The emitted radiation is a continuum spectrum with a maximum at the energy E $\sim 4\gamma^2 E_0$. Considering a seed photon with an initial energy of 10 eV (UV), if $\gamma \sim 100$, we will have a resulted energy after the scatter of E $\sim$ 0.5 MeV (hard X-ray).

Considering a population of electrons distributed according to a power-law (N(E)dE $\propto E^{-p}$dE), we can see that the emitted spectrum will be described by a power-law (sky-blue track in Fig. 1.1):

$$S_\nu \propto \nu^{(1-p)/2} \tag{1.21}$$

On the contrary, the corona irradiate the disc, altering its structure, the local level of ionization, the local temperature, and consequently, the emitted local spectrum (Netzer 2013). As a result, a reflection spectrum emerge from the disc, which can be described by a superimposition of thermal (heated disc) and no-thermal (reflected corona) emissions (green trace in Fig. 1.1).

Moreover, since disc is much cooler than the surrounding X-ray emission, elements such as iron are not fully ionised and these ions still possess filled K- and L-shell electrons (Longair 2011). The X-ray photons from the corona thus cause the removal of one of the two K-shell electrons, whose vacancy is subsequently filled by one of L-shell electrons. This results in an emission line at the characteristic frequency of 6.4 keV (emission line within the reflection spectrum in the

---

[1] the process is called inverse because the electrons lose energy rather than the photons, the opposite of the standard Compton effect

SED). The emission of this line is very important for BH physics because it not only acts as a tracer of the velocity field in the accretion discs but also as a probe of general relativity. The line will appear broadened due to the rotation of the disk (redshifted and blueshifted by the Doppler effect). Additionally, it will be relativistically distorted because it is moving at speeds close to the speed of light (the blueshifted part is therefore also boosted). Since the disk extends into regions where the gravitational field is very strong, it will undergo an overall shift towards red wavelengths (gravitational redshift).

In addition to the spectral components of the disc and the corona, another component has been observed in an intermediate energy range between the two, called the "soft excess" (magenta track in Fig. 1.1) (Done et al. 2012). The origin of this component is not entirely clear; however, various theories agree on the presence of an additional Comptonization component responsible for this excess. One among the different models (Done et al. 2012) predicts that the disc only thermalizes at large radii (component described by the multi-color blackbody). At smaller radii, gravitational energy is divided between powering optically thick Comptonized disc emission (forming the soft X-ray excess) and an optically thin corona above the disc (forming the tail to higher energies).

Other models instead predict that the sole interaction between the disc and the corona can give rise to the excess (e.g. Boissay et al. 2016). Examples include the warm Comptonization model and the Blurred Ionized Reflection model: photons originating from the disc gain energy during interactions with hot gas, such as the corona, while photons from the corona are reflected by the disc. However, unlike purely reflective reflection, blurred ionized reflection takes into account the non-uniform distribution of ionized gas around the disc. This non-uniform distribution can lead to a softening and broadening of the emission lines in the disc, resulting in a "blurred" reflection spectrum.

1.4.4 Broad Line Regions

The broad line regions (BLR) are clouds of ionized gas located between the dusty torus and the accretion disc (Alloin 2006). They are characterized by large column densities (approximately 10^{23} cm^{-2}) and high densities (around 10^{10} cm^{-3}), situated at a distance where the incident luminosity per unit area, generated by the accretion disc, $L/4\pi r^2$, is approximately 10^9 erg s^{-1} cm^{-2}. Considering a range of luminosity for the disc equal to 10^{44} erg s^{-1} $\lesssim L_{disc} \lesssim 10^{47}$ erg s^{-1}, this corresponds to a distance of 0.02 pc $\lesssim r \lesssim 1$ pc, consistent with the fact that the BLR are located between the disc and the dusty torus.

There is also another way to calculate the distance of the BLR, through reverberation mapping (Alloin 2006). Variations in the emission of ionizing continuum radiation emitted by the accretion disc are followed by "echoes" in the broad lines which, however, have a delay τ. The delay is the "light travel time," which means, the time required for the propagation of the ionizing radiation and the photons of the line: $\Delta\tau \sim r / c$. Measuring the delay $\Delta\tau$ therefore provides an estimate of the size of the broad line region. However, this method requires a long time since in AGNs where this calculation has been done, it has been measured that $r_{BLR} = c\Delta\tau$ varies from a few light days to light years (Peterson 1997).

Knowing the distance of the BLR, it is also possible to estimate the mass of the SMBH using the virial theorem:

$$M_{BH} = f\frac{V^2 R_{BLR}}{G} \tag{1.22}$$

where the rotational velocity V can be calculated from the line broadening.

Thanks to their high column density, BLR can persist for many dynamical times ($t_{dyn} \sim 300$ years) in their location, being gravitationally bound to the SMBH. Indeed, at these distances, gravity dominates over radiation pressure (Alloin 2006). Moreover, assuming a global (4π) covering factor of order 0.1-0.3, the radiation from individual clouds does not perturb others. The clouds have typical velocities of 3000-5000 km s^{-1}, which is reflected in the observed widths of the emission lines.

In this region, the ionization parameter for hydrogen, U(hydrogen), define as the ratio between the number of ionized atoms and the total number of atoms of hydrogen in a given region is U(hydrogen) $\sim 10^{-2}$. Consequently, only the surface of the cloud that is exposed to illumination exhibits significant ionization. The ions predominantly present in this region include He III, O IV-VI, C III-IV, and others (Alloin 2006). The most prominent emission lines anticipated are Lyα, Hα (6563 $\AA$), Hβ (4861 $\AA$), C IV (1549 $\AA$), Mg II (2800 $\AA$), and O VI (1035 $\AA$) (Alloin 2006). While the density is relatively high, it is not excessively so as to completely suppress semi-forbidden[2] lines, indicated with a "]" parenthesis next to the line designation (while for forbidden lines, a double parenthesis, "[*]", is used). Notable examples of such lines are C III] (1909 $\AA$) and O III] (1661 $\AA$). These clouds, despite their considerable column density, are likely partially neutral since only X-ray photons can penetrate beyond a hydrogen column of approximately 10^{22} cm^{-2} (Alloin 2006). Consequently, these areas are expected to exhibit strong lines of H I, Mg II, and Fe II. The observed equivalent widths (EWs) of the most prominent lines are contingent upon the emissivity and covering factor and are typically in the range of 10 - 100 Å for the specified conditions. Conversely, the observed absorption lines are notably weak due to their limited covering factor.

1.4.5 Narrow Line Regions

Narrow Line Regions (NLR) are regions of ionized gas, located outside the BLR. They have a similar level of ionization as the BLR, although their physical conditions are significantly different (Alloin 2006).

---

[2] In physics, a forbidden line is a spectral line emitted by an atom where energy transitions occur that are not allowed by the selection rules of quantum mechanics (Bun 1998). In physics, this does not mean that the process violates the laws of nature but rather that it could not occur via the most efficient pathway (electric dipole). When an atom or molecule is in an excited state, there is a small probability for the transition to occur. By definition, this probability is much lower than that of transitions allowed by selection rules. Consequently, if an atom can emit radiation through an allowed transition, it will almost certainly follow this pathway rather than the forbidden one. However, forbidden transitions have a non-zero probability. States that can only decay in this manner (so-called metastable states) typically have durations of a few milliseconds, much longer than states decaying via allowed transitions, which have durations shorter than a microsecond.

In comparison with BLR, they present a smaller column density ($\sim 10^{20-21}$ cm^{-2}), a lower density ($\sim 10^4$ cm^{-3}), a smaller covering factor, of order 0.01-0.1, and they are located farther away, where the disc flux is $L/4\pi r^2 \simeq 10^2$ erg s^{-1} cm^{-2}. Considering the usual range of luminosity for the disc, 10^{44} erg s^{-1} $\lesssim L_{disc} \lesssim 10^{47}$ erg s^{-1}, this corresponds to a distance of 100 pc $\lesssim r \lesssim$ 3 kpc.

In this case as well, the system is bound, gravity dominates over radiation pressure, and the typical velocity is 500 km s^{-1}. Unlike the BLR, the NLR is optically thin, and the gas is on average more ionized, albeit with a similar ionization parameter. The observed spectrum of this component includes intense forbidden lines [such as [O ɪɪ] (3727 $\AA$), the [O ɪɪɪ] doublet (4959 $\AA$, 5007 $\AA$), the [N ɪɪ] doublet (6548 $\AA$, 6583 $\AA$) and the [S ɪɪ] doublet (6716 $\AA$ e 6731 $\AA$)] due to the low densities. This shifts the line cooling balance in such a way that the semi-forbidden and permitted lines [e.g. Hα and Hβ] are relatively weaker. Another group of lines predicted to be intense in the innermost part of this region are coronal lines [e.g., [Si ᴠɪ] (1.963 μm), [Fe xɪᴠ] (5303 $\AA$), and [Ca ᴠɪɪɪ] (2.321 μm)], produced by fine-structure transitions and observed mostly in the infrared (Peterson 1997).

1.4.6 Jet

The jets are highly energetic outflows of matter emitted in the central region of the AGN, perpendicular to the accretion plane (Netzer 2013). They can extend for thousands of parsecs into intergalactic space, carrying an enormous amount of matter and energy. They are generally composed of charged particles, such as electrons and protons, which are accelerated close to the speed of light by intense magnetic forces present near the black hole. It was calculated that plasma moves with a Lorentz factor Γ of the order of $\sim$ 10, and occasionally as high as $\sim$ 50 (Begelman et al. 2008).

There are three general categories of jet models proposed for explaining the formation and behavior of jets in AGNs (Netzer 2013): thermal pressure models, radiation pressure-driven models, and hydromagnetic jet models. Thermal pressure models postulate that jets are propelled by the thermal pressure of material near the black hole, expanding adiabatically from its vicinity. Radiation pressure-driven models suggest that intense AGN radiation can overcome gravity along certain directions, driving material outward to form jets. In the hydromagnetic models of jets, the spin of the black hole creates tension on the magnetic fields generated by a dynamo effect in the disc. This process allows for the extraction of energy from the rotating black hole, ejecting plasma in two opposite directions and producing electromagnetic radiation (Blandford & Payne 1982).

The emission in the jet occurs through synchrotron radiation of electrons that are part of the ejected matter flow, accelerated by magnetic fields (B) within the jet. Since we can consider synchrotron emission as cyclotron radiation in the relativistic regime, we can write the emission frequency of a single electron with energy E as (Rybicki & Lightman 1979):

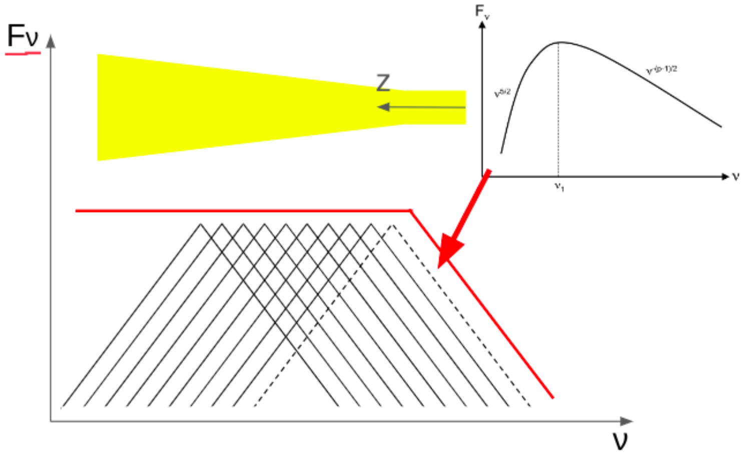

Figure 1.2: Schematic representation of the overall synchrotron emission of the jet. The close-up represents the flux of a single electron.

$$\nu_c \approx \gamma^2 \nu_g = \left(\frac{E}{m_e c}\right)^2 \nu_g \tag{1.23}$$

where ν_g = eB/2πm$_e$ is the gyrofrequency in the non-relativistic regime.

Now, considering a population of electrons distributed according to a power-law (N(E)dE $\propto$ E^{-p}dE), we see that the emitted flux turns out to be:

$$S_\nu \propto B^{(p+1)/2} \nu^{(1-p)/2} \tag{1.24}$$

Self-absorption also plays a key role in the overall spectral shape. In particular, at low frequencies it leads to a break in the spectrum, which starts to drop as:

$$S_\nu \propto B^{-1/2} \nu^{5/2} \tag{1.25}$$

Since jets are extended structures, the emission will result as the overlap of profiles described by equations 1.24 and 1.25, produced by individual electrons in different regions along the jet (see Fig. 1.2). Furthermore, considering that the magnetic field decreases as a function of distance from the SMBH, in accordance with equations 1.24 and 1.25, the peak frequency also decreases along the jet. In particular, assuming continuous re-acceleration of electrons along the jet, balancing radiative and adiabatic energy losses, results in a flat spectrum (Blandford & Königl 1979). The mechanism of re-acceleration is not yet fully understood. One proposed model involves shock shells of matter at different velocities within the jet.

Given the two regimes (self-absorbed and not) in the synchrotron emission profile, it is possible to identify two regions in the jet spectrum. At the base of the jet, where the first population of electrons are accelerated, the emission will be optically thin, with decreasing spectrum as a function of frequency (Rybicki & Lightman 1979). The rest of the flat spectrum, which is the result of different contributions from different regions of the jet, will be instead dominated by optically thick emission. The transition between these two regimes appears in the spectrum as a break, which corresponds also to the frequency where most of the energy is emitted.

It is possible to identify the jet component in the SED as a flat spectrum at low energies (yellow line in Fig. 1.1). In the SED, two sub-classes of AGN are shown: the radio loud and the radio quiet AGNs. The radio loudness parameter (R) is defined as the ratio between the radio flux in the energy range of 2-4 GHz and the radio flux in the g-band. According to the definition of (Kellermann et al. 1989), a source is defined as radio loud if R>10, or radio quiet if R<10. Furthermore, if an AGN shows no radio emission at all, it is defined as a no-jetted AGN, which is clearly distinguished from jetted AGN.

However, there are particular cases in radio loud AGNs where, depending on the ratio between the emission from the jet and that of the other components, the jet dominates over the other components, and the shape of the SED changes radically, leading to the so-called AGN jet-dominated (Urry & Padovani 1995). This typically occurs when the direction of the jet forms a small angle with the line of sight.

Due to the highly relativistic kinematic regime and the small viewing angle, the emission is affected by the Doppler effect (quantified by the factor $\delta = [\gamma(1\text{-}\beta\cos\theta)]^{-1}$), in addition to being highly variable (Netzer 2013). The Doppler aberration leads to a decrease in the observed timescale, a blue-shift of the observed spectrum, and an increase in luminosity across all wavelengths. Direct evidence for this interpretation comes from the detection of superluminal motion of plasma blobs along the jet, the apparent velocity of which, as measured with radio interferometry, can be up to 20c. When corrected for Doppler aberration, these velocities are obviously lower than the speed of light, and compatible with the Lorentz factors described above.

The SEDs of jetted AGNs appear with a double-peaked shape, as shown in Fig. 1.3, where both types of AGN, jetted and no-jetted AGN, have been overlaid in the same plot. In the case of jetted AGN, the emission from the jet covers the entire electromagnetic spectrum, from radio to the most energetic γ-ray bands. It has been observed that the maximum energy reached by the jet depends on the accretion rate (hence the distinction of the two double-peaked SEDs in the plot) (Costamante 2020).

The low energy peak in the jetted AGN SEDs, that extends from radio to X-ray, is described by a synchrotron emission of accelerated electrons (or positrons). Regarding the second bump, the origin is still under debate. According to leptonic models, it is possible to describe high-energy emission using the inverse Compton process (e.g. Costamante et al. 2018). When seed photons originate from external regions to the jet (e.g., from the disc, the BLR or the torus), this process is called External Inverse Compton (EC). Conversely, when seed photons come from the synchrotron radiation itself, it is referred to as Synchrotron Self-Compton (SSC).

Additionally, studies have proposed an alternative hadronic mechanism to describe the second peak, which predict synchrotron emission from relativistic protons or the decay of neutral pions resulting from p-p or p-γ interactions (e.g. Gao et al. 2019; Cerruti 2020).

Relativistic protons of sufficient energy can interact with nuclei of the interstellar medium or with a target field of photons emitted by the other structure of the AGN, or by the jet itself, producing charged and uncharged pions (Berezinskii et al. 1990; Gaisser 1990):

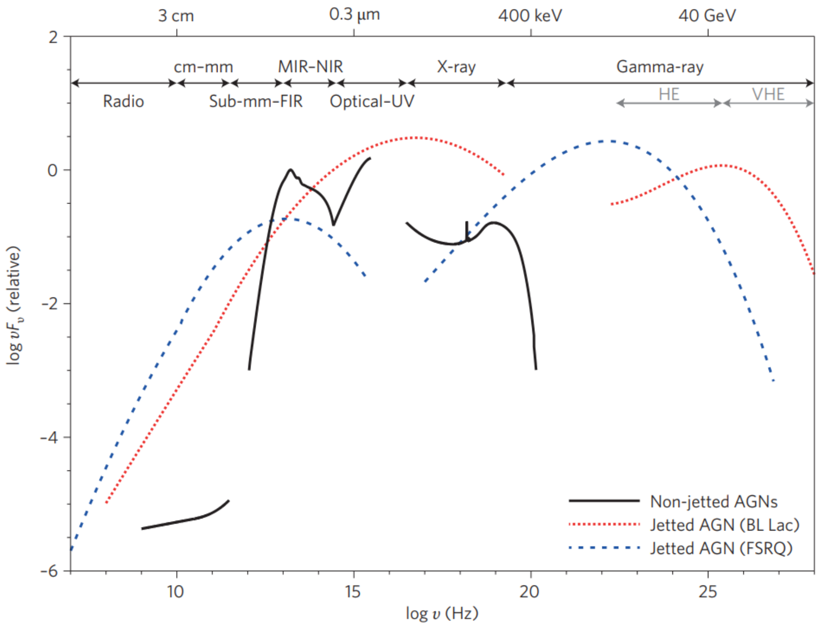

Figure 1.3: Typical SED of jetted (dotted red and dashed blue lines) and non-jetted AGNs (black solid curve). Image credit: Harrison (2016).

$$p + p \longrightarrow p + p + \pi^+ + \pi^- + \pi^0 \tag{1.26}$$

or

$$p + \gamma \longrightarrow p + \pi^0;\ p + \gamma \longrightarrow n + \pi^+;\ p + \gamma \longrightarrow p + \pi^+ + \pi^- \tag{1.27}$$

and they can subsequently decay according to the following decay channels:

$$\begin{aligned} \pi^+ &\longrightarrow \mu^+ + \nu_\mu;\ \mu^+ \longrightarrow e^+ + \nu_\mu + \bar{\nu}_e \\ \pi^- &\longrightarrow \mu^- + \bar{\nu}_\mu;\ \mu^- \longrightarrow e^- + \nu_e + \bar{\nu}_\mu \\ \pi^0 &\longrightarrow \gamma + \gamma \end{aligned} \tag{1.28}$$

where the charged pions decay into muons and neutrinos by weak interaction and with a life-time of $\sim 2.6 \times 10^{-8}$ s, whereas the neutral pions decay electromagnetically into two γ-rays within an average life-time of $\sim 8.4 \times 10^{-17}$ s. Given the energies involved, the photons produced by the decay of the neutral pion will be γ-ray photons. In particular, they will have an energy equal to $\mathrm{m}_\pi/2$. This will be reflected in the SED with a characteristic feature known as the *Pion bump*, that will be the smoking gun for the hadronic process.

If protons are distributed according to a power-law ($\mathrm{N(E)dE} \propto \mathrm{E}^{-p}\mathrm{dE}$), and γ-ray photons are produced in an hadronic process (e.g. $\mathrm{p} + \mathrm{p} \longrightarrow \pi^0 \longrightarrow \gamma + \gamma$), they will be emitted with the same spectrum of emitted protons:

$$S_\nu \propto \nu^{-p} \tag{1.29}$$

so, also from the index of the spectrum it is theoretically possible to distinguish the leptonic

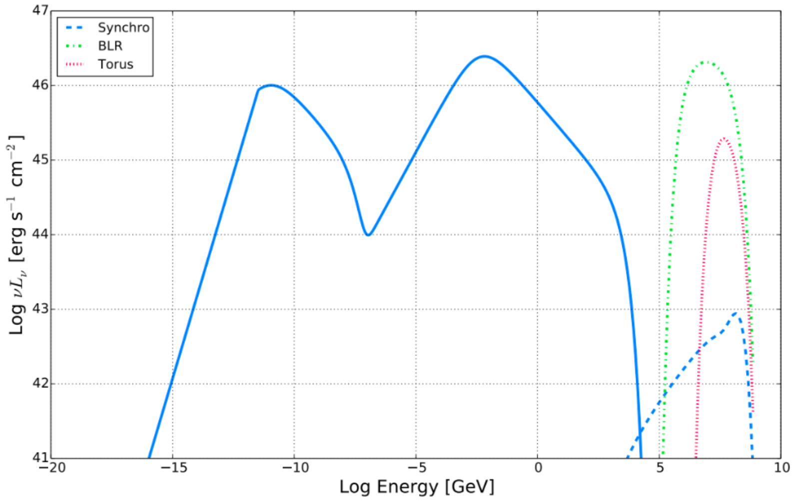

Figure 1.4: SED for a jetted-AGNs with a 20 MeV - 300 GeV luminosity of 10^{45} erg s^{-1} < L < 10^{46} erg s^{-1}. Blue solid line shows the SED derived by phenomenological models, while the red dotted line, green dash-dotted line and blue dashed line are respectively the neutrino spectrum obtained using the radiation of the torus, of the BLR and the internal synchrotron radiation as targets for the pγ reaction. Figure taken from Righi & Tavecchio (2020).

from the hadronic process. Finally there are some works where a lepto-hadronic model is used to the describe the high peak in the SEDs (e.g. Cerruti et al. 2011; Rodrigues et al. 2019).

As we can see from equation 1.28, through this type of processes it is not only possible to produce γ-ray photons but also neutrinos (e.g. Schroller et al. 2022). Both processes can occur only if the proton has enough energy to produce the pions in the final state (Berezinskii et al. 1990; Gaisser 1990). Considering, for example, the interaction between a proton and a photon produced by the disc with energy ϵ = 1 eV, placing in the center-of-mass reference frame, we see that the energy of the proton must be:

$$E_p = \frac{(m_p + m_\pi)^2 - m_\pi^2}{2\epsilon(1 - cos\theta)} \simeq \frac{m_p m_\pi}{\epsilon(1 - cos\theta)} \tag{1.30}$$

which with $\theta = \pi$ results E$_p \simeq 1 \times 10^{17}$ eV.

Furthermore, typically in these processes E$_\pi \sim \frac{1}{5}$ E$_p$ and E$_\nu \sim \frac{1}{4}$ E$_\pi$, where E$_\pi$ and E$_\nu$ are the energy of the pion and the energy of the neutrino, respectively. Therefore, we find that the energy of the emitted neutrinos is E$_\nu \sim 0.05$ E$_p$ (Guépin & Kotera 2017; Guépin 2020; Fang & Murase 2018; Dermer & Menon 2009). In Fig. 1.4 is shown a SED from radio to neutrino emission of a jetted-AGN.

Gamma-ray Absorption

The γ-ray photons emitted by astrophysical sources traverse vast distances before reaching Earth-bound observers. During their journey, they may encounter several absorption and interaction mechanisms, leading to a reduction in the overall observed flux. The primary causes of this energy loss are interactions with matter and interactions with background photons (e.g.

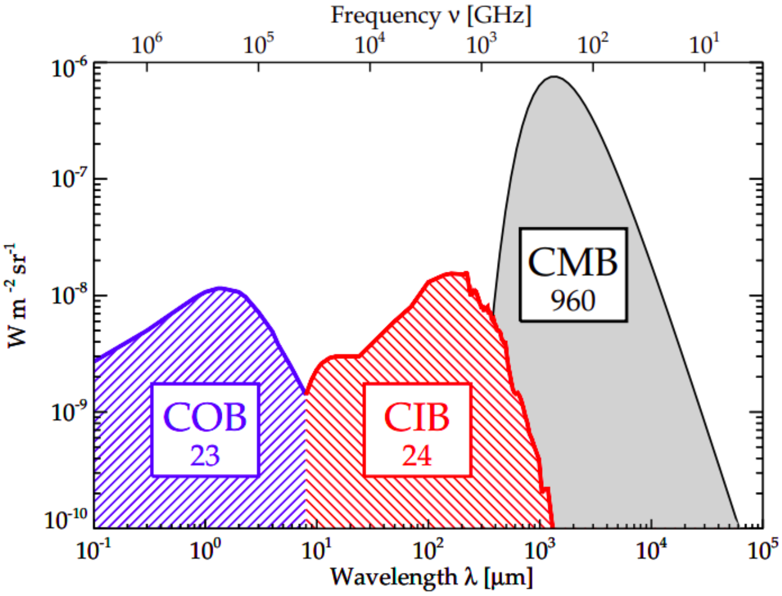

Figure 1.5: Schematic representations of the Spectral Energy Distributions (SEDs) for the most significant (in terms of intensity) backgrounds in the universe are depicted, along with their approximate brightness indicated in nW m^{-2}sr^{-1} within the corresponding boxes. Moving from right to left, these backgrounds include the Cosmic Microwave Background (CMB), the Cosmic Infrared Background (CIB), and the Cosmic Optical Background (COB). Figure taken from (Dole et al. 2006).

Cooray 2016). While γ-ray photons do interact with cosmic particles before reaching our space observatories, this interaction is negligible due to the low particle density in space (1 atom cm^{-3} in the interstellar medium and 10^{-5} atom cm^{-3} in the intergalactic medium).

The second mechanism, however, proves to be significant. It involves the interaction of background photons and the subsequent production of pairs: $\gamma + \gamma \longrightarrow \mathrm{e}^{+} + \mathrm{e}^{-}$. This process occurs when the center-of-mass energy of the photon-photon system exceeds twice the rest energy of the produced pair:

$$E_{\gamma 1} E_{\gamma 2}(1 - cos\theta) \sim 2(m_e c^2)^2 \tag{1.31}$$

At energies above 100 GeV, the Very High Energy (VHE) photons are mainly absorbed by the interaction with the *Extragalactic Background Light* (EBL). It refers to the diffuse radiation filling the universe, originating from the collective emission of stars, galaxies, and other astrophysical sources throughout cosmic history. This background light spans a wide range of wavelengths, from ultraviolet to microwaves, and provides crucial information about the universe's luminous history. The EBL is primarily composed of starlight emitted by stars within galaxies, as well as the integrated emission from AGNs. Additionally, processes such as the reprocessing of starlight by interstellar dust and the re-emission of absorbed light contribute to the EBL's complex structure. The SED of EBL is reported in Fig. 1.5.

2

The Unified Model for AGNs

Different sub-classes of AGNs are delineated based on various observable properties, often correlated with the orientation of their central engines and surrounding structures, as described by the AGN Unified Model (Urry & Padovani 1995; Frank et al. 2002; Beckmann & Shrader 2012). Figure 2.1 presents a simplified representation of AGNs, illustrating how the Unified Model allows for the classification of these sub-classes based on factors such as viewing angle and radiation intensity (see the schematic representation of the Unified Model in Tab. 2.2).

The first great dividing line is the one which separates radio-loud from radio-quiet objects. Among these, Seyfert galaxies are relatively bright and relatively close AGNs, identified by their characteristic emission line spectra, attributed to non-relativistic processes in the vicinity of a supermassive black hole. Conversely, the quasi-stellar objects (QSOs) are highly luminous and distant AGNs, often exhibiting broad emission lines and intense radiation across multiple wavelengths.

When the observer's line of sight intersects at a small angle with the jet of a radio-loud AGN, it results in the emergence in the so called class of blazars. These objects are characterized by their intense and variable emissions across various wavelengths, with notable prominence in the radio and gamma-ray bands. Finally, when the viewing angle is greater, the radio-loud AGNs can exhibit extended radio structures, associated with jets and lobes emanating from the central structure. These types of AGNs are called radio galaxies.

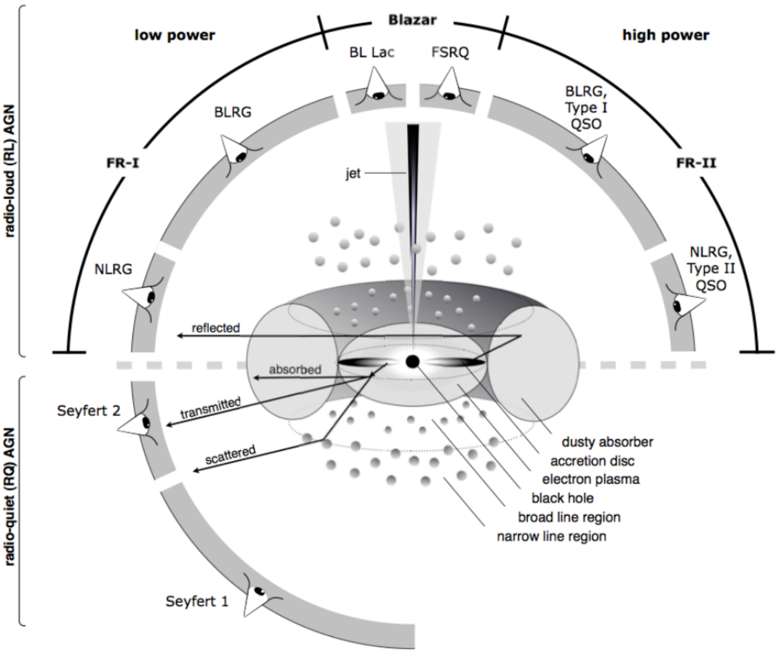

Figure 2.1: Schematic representation of the unified model for AGNs. The unified model suggests that the different types of AGNs (such as quasars, blazars, radio galaxies, and Seyfert galaxies) are primarily due to the viewing angle relative to the equatorial plane of the dusty and gaseous torus surrounding the supermassive black hole, and the possible presence of a jet of matter perpendicular to the accretion plane. This illustration shows the central black hole, the accretion disk, the relativistic jet, the dusty torus, the BLR and the NLR, highlighting how our point of view can influence the apparent nature of the observed AGN. Credit: Beckmann & Shrader (2012)

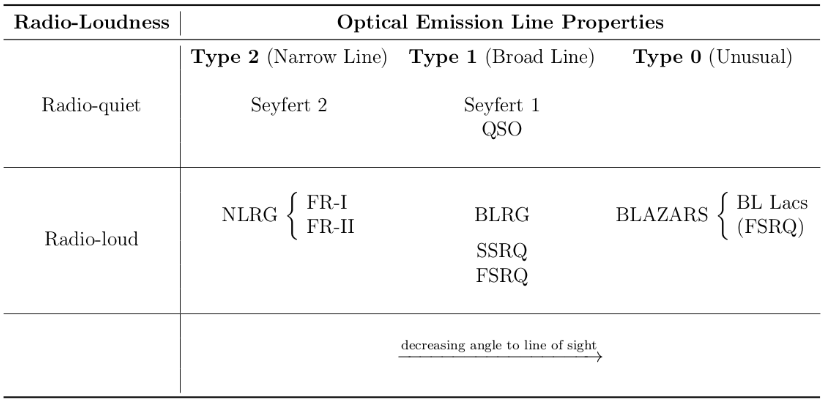

Radio-Loudness	**Optical Emission Line Properties**		
	Type 2 (Narrow Line)	**Type 1** (Broad Line)	**Type 0** (Unusual)
Radio-quiet	Seyfert 2	Seyfert 1 QSO	
Radio-loud	NLRG { FR-I FR-II	BLRG SSRQ FSRQ	BLAZARS { BL Lacs (FSRQ)
		$\xrightarrow{\text{decreasing angle to line of sight}}$	

Figure 2.2: Summary table for the classification of AGNs in the unified model. Classification based on both the radio-loudness and the optical properties of the sources. Notice that NLRG and BLRG stand for Narrow Line Radio Galaxy and Broad Line Radio Galaxy. Credit: Padovani (1999)

2.1.0 Radio-quiet AGNs

According to the Unified Model, radio-quiet AGNs represent one of the two primary classes of AGNs, distinguished by their radio brightness. Unlike their radio-loud counterparts, they exhibit weak or absent radio emission (Urry & Padovani 1995; Panessa et al. 2019). However, they display notable brightness across other wavelengths of the electromagnetic spectrum, particularly in the optical and X-ray bands (Urry & Padovani 1995; Wilson & Colbert 1995; Netzer 2013).

Several hypotheses exist regarding the weakness of radio-quiet AGNs in the radio spectrum. One possibility stems from the absence of relativistic jets, which typically emit significant radio brightness through synchrotron emission. In such instances, the differentiation between AGN categories transforms into jetted and non-jetted AGNs (Padovani et al. 2017). Another potential explanation lies in the surrounding medium of an AGN, which could absorb radio emission, resulting in weaker radio signals from radio-quiet AGNs compared to their radio-loud counterparts (Maini et al. 2016). Additionally, AGNs with high accretion rates may produce more high-energy radiation, such as UV, X-rays up to γ-rays, which could overshadow radio emissions, contributing to their reduced radio brightness.

Subsequently, radio-quiet AGNs can be further categorized based on their spectral properties, luminosity, and other observational characteristics, that will be elaborated upon in detail in the subsequent subsections.

2.1.1 Seyfert galaxies

Seyfert galaxies are a subclass of AGNs characterized by a non-stellar continuum and high ionization emission lines (Frank et al. 2002; Netzer 2013). These galaxies are named after the American astronomer Carl Seyfert, who first identified them in the 1940s (Seyfert 1943). Seyfert galaxies are typically found in spiral galaxies, although they can also occur in elliptical galaxies.

Seyfert galaxies are further classified into two main types based on their emission properties: Seyfert Type 1 and Seyfert Type 2, although intermediate types have also been defined. Seyfert Type 1 galaxies exhibit both broad and narrow emission lines in their spectra, while Seyfert Type 2 galaxies only display narrow emission lines, typically with higher [O III]/Hβ intensity ratios. This higher ratio arises because the emission line of [O III] is forbidden, so it is emitted as a narrow line, while Hβ, being permitted, can be emitted either as a broad line or a narrow line. Assuming that the broad lines come from the BLR and the narrow lines from the NLR, it is believed that the distinction between the two sub-classes arises from differences in the orientation of the obscuring material surrounding the central black hole. In Seyfert 1 galaxies, the observational angle allows for the interception of both the BLR and NLR, whereas in Seyfert 2 galaxies, the dusty torus prevents the observation of the BLR, leaving only the NLR visible, which extends beyond the size of the torus. This scenario is supported by studies in polarized light, which have managed to reveal broad emission lines originating from the BLR (Frank et al. 2002). In addition, Seyfert 2 appear to have higher radio fluxes, but weaker X-rays emissions. In Seyfert 1 galaxies, on the other hand, X-ray emission can be dominant, with a characteristic spectrum $F_\nu \propto \nu^{-0.7}$ in the 2-10 keV band.

There exists also a subclass of Seyfert 1 galaxies named as Narrow Line Seyfert 1 (NLSY1) galaxies, characterized by optical spectra in which the permitted lines show widths comparable to forbidden lines (Rakshit et al. 2018). In particular, the definition of NLSY1 galaxies predicts that the full-width at half maximum (FWHM) of the broad Hβ is < 2000 km s^{-1}. In addition, the flux ratio [O III]/Hβ < 3 is required to ensure that we have a direct view of the broad-line region (Osterbrock & Pogge 1985). Strong Fe II multiplets are often observed in NLSY1s, but this features are not part of the official classification criteria. The narrow FWHM of Hβ in NLSY1 galaxies is often attributed to a combination of factors (e.g. Järvelä et al. 2021, and reference therein). One explanation suggests that it results from low rotational velocity around a low- or intermediate-mass SMBH, typically less than 10^8 solar masses. This implies that NLS1s are accreting close to or even above the Eddington limit. Another possibility is that the narrow FWHM(Hβ) arises from a flattened Broad Line Region (BLR) observed face-on, causing the permitted lines to appear narrow due to the lack of Doppler broadening. This would imply that a smaller mass is not necessary. However, inclination-independent observational properties of NLS1s, such as their host galaxy morphologies and their different large-scale environments, indicate that the black hole masses could be genuinely small. Assuming that the black hole masses in NLS1s are small, they may be at an early stage of the AGN life cycle and will eventually grow into fully developed broad-line AGNs (Järvelä et al. 2021).

2.1.2 Quasars

The term "quasar" originates from "quasi-stellar radio source," a nod to their initial discovery when they resembled stars in early radio surveys (Netzer 2013). Quasars, a sub-class of AGNs, are renowned for their extraordinary luminosity across the electromagnetic spectrum, notably in the radio and optical bands. Despite their immense brightness, distinguishing between low-luminosity quasars and bright Type 1 Seyferts can be challenging, suggesting a continuum of similar objects partitioned into two classes due to observational constraints (Frank et al. 2002). Quasars typically outshine Seyfert galaxies, with an absolute magnitude in the B-band of the Johnson system (Johnson & Morgan 1953) M_{abs} < -23 for quasars (Osterbrock 1980). Among quasars, only about 10% exhibit strong radio emission, while the remaining 90% are referred to as QSOs, which exhibit weak or undetectable radio emissions (Frank et al. 2002). Radio-loud quasars are predominantly found in elliptical galaxies, though not exclusively, while radio-quiet ones are more common in spiral galaxies. Some radio-loud quasars exhibit apparent superluminal velocities in their radio-emitting plasma due to the relativistic motion of the jet, which is oriented toward the observer. Observed variability in these quasars tends to occur over timescales of years.

2.2.0 Radio-loud AGNs

Radio-loud AGNs represent approximately 10% of the total AGNs population (Padovani et al. 2017). These celestial sources emit copious amounts of radio power, distinguishing them from their radio-quiet counterpart. However, the optical properties of radio-quiet and radio-loud AGNs are strikingly similar, suggesting underlying commonalities in their emission mechanisms. The radio-loud AGN category encompasses a variety of intriguing objects, including radio galaxies, quasars, and blazars, each offering unique insights into the physics governing their energetic processes. Their distinguishing feature lies in the presence of powerful jets produced by SMBHs at their cores. These jets emit synchrotron radiation, with a power-law spectrum, $f(\nu) \propto \nu^{-\alpha}$, manifesting as the characteristic radio emission observed in radio-loud AGN.

The inclination of the central radio jet to the line of sight plays a crucial role in shaping the observed properties of radio-loud AGN. Core-dominated sources exhibit a "flat" spectrum (with a radio power-law index $\alpha_R < 0.5$), while lobe-dominated, weak-core sources often display a steeper spectrum ($\alpha_R > 0.5$) (Netzer 2013).

Similar to radio-quiets, the relative position of the torus to the observer is also significant in radio-loud AGNs. We distinguish Type 1 sources when the observer has a direct view of the central regions, such as the BLR and the jet, in contrast with Type 2 ones, where the torus obscures the central region from direct view.

Finally radio-loud AGNs tend to be more X-ray bright compared to radio-quiet AGNs of similar optical luminosity, indicating differences in their high-energy emission properties (Netzer 2013).

2.2.1 Radio galaxies

Extended radio sources, often referred to as radio galaxies, typically consist of a pair of lobes that can extend up to 50 kpc in diameter. These lobes are commonly found at distances ranging from a few hundred kpc to a few Mpc away from a central elliptical galaxy. The typical 10 MHz - 100 GHz of radio galaxy is a magnitude of 10^{46} erg s^{-1} (Kembhavi & Narlikar 1999). These galaxies are categorized into Fanaroff–Riley (FR) classes (Fanaroff & Riley 1974). FR I sources exhibit typically lower luminosity with respect to FR II. However, the luminosity boundary is not very sharp, and there is some overlap in the luminosities of FR I or FR II sources, classified according to their geometrical structures. FR I are generally characterized by a power at 14 GHz, $P14 < 10^{25}$ W Hz^{-1}, with a brightness that gradually diminishes with increasing distance from the central object (core-dominated), a phenomenon known as ‘limb darkening’ (Kembhavi & Narlikar 1999). In contrast, FR II sources typically possess $P14 > 10^{25}$ W Hz^{-1} and often display limb-brightened structures, often featuring bright spots or ‘hot spots’ a few kpc in size (lobe-dominated) (Kembhavi & Narlikar 1999). Radio galaxies classified as FR II are sometimes referred to as ‘classical doubles’. It is worth to note that, although FRIs are less luminous than FRIIs, they are more numerous. If optical emission lines are present, we classify them as narrow-line radio galaxies (NLRGs) if the lines are narrow, or as broad-line radio galaxies (BLRGs) if instead the lines are broad (Netzer 2013).

In addition, it is noteworthy that the central galaxy itself is frequently a radio source, which holds significance for several reasons (Frank et al. 2002). Firstly, they resemble quasi-stellar sources where the parent galaxy is substituted by a quasar. Secondly, the total energies involved in giant radio galaxies closely resemble those estimated for quasars. Thirdly, a radio galaxy's distance can be inferred from the galaxy redshift. Moreover, there exist physical connections between the radio lobes and the central galaxy or quasar, which serve as the primary power source for the lobes. Additionally, the continuum emission from the radio lobes, exhibiting characteristics such as an approximate power law spectrum and polarization, shares similarities with the emission from active nuclei, offering insights into the mechanism of energy production in active nuclei.

2.2.2 Blazars

Blazars are jetted AGNs with a jet pointing at a small angle, $\theta \lesssim 10^{\circ}$, toward the observer. They typically appear as point-like sources, although they sometimes display some extension in the radio band. The SED of blazars is dominated by the beamed emission from plasma moving relativistically in the jet (e.g. Padovani et al. 2017; Falomo et al. 2014), and it extends for more than 15 orders of magnitude in frequency, from radio to TeV energies (Urry & Padovani 1995; Costamante 2020). Due to this geometrical configuration, the emission is affected by the relativistic Doppler effect and usually appears superluminal. The apparent velocity can reach values of 40-50c, providing a lower limit for the Lorentz factor of $\Gamma \simeq 10 - 50$.

About luminosity, calculating the jet power directly from observations is challenging due to the beamed nature of the radiation. However, if the bulk Lorentz factor Γ is known (e.g., from superluminal motion), we can establish a solid lower limit for the jet power, which cannot be less than $L_{\rm obs}/\Gamma^2$ (Ghisellini et al. 2014). Assuming an efficiency of about 10% (e.g., Nemmen et al. 2012), the total jet power is roughly of the same order as, but generally greater than, the accretion disk luminosity (Ghisellini et al. 2014). Consequently, blazar jets are among the most efficient persistent engines in nature.

Blazars are powerful radio emitters (classified as radio-loud sources) and are also the brightest γ-ray sources in the extragalactic sky, often exhibiting extreme variability on timescales as short as minutes. A correlation between these two emission bands is observed (e.g. see Paiano et al. 2023, and Ulgiati et al. in preparation), and in the one-zone emission model (e.g. Ghisellini et al. 1985; Böttcher et al. 2013), it is assumed that both the radio and γ-ray emissions originate from a single region within the jet. In contrast, the multi-zone model (e.g. Potter & Cotter 2013) proposes that particles are accelerated and radiate throughout the jet in a more continuous manner, with the emissions arising from several distinct regions along the jet.

As previously discussed, the SED of jetted AGNs presents a double-peaked structure, given by the super-position of power-laws, $f(\nu) \propto \nu^{-\alpha}$, in the $f(\nu)$ vs ν diagram, with varying α across the spectrum. The radio emission is flat ($\alpha < 0.5$), optical/near-infrared spectral indices range from $\alpha_\nu \sim 0.5$ to 1.5, while X-ray emission is steeper, with $\alpha_\nu \sim 1.3$. γ-ray emission typically exhibits a spectral index $\alpha_\nu \sim 1$ (Falomo et al. 2014; Costamante et al. 2018, and references therein).

Historically, blazars are divided into two main classes based on differences in their optical spectra: i) FSRQs, characterized by prominent emission lines (Equivalent Width, $EW > 5\mathring{A}$), and ii) BL Lacertae objects (BLLs), which lack or have weak spectral lines(Equivalent Width, $EW < 5\mathring{A}$), presenting optical spectra described by a simple featureless power-law (Costamante et al. 2018). However, due to variability in both line and continuum emissions, there's significant overlap between the two classes, leading to misclassification, particularly when jet emission overwhelms the thermal emission of lines and the disc, termed "masquerading BLLs" (Giommi et al. 2013). Despite this, there's a substantial difference between FSRQs and BLLs: true BLLs have faint or no line emission (with much lower luminosities than FSRQs), weak or absent torus emission, and an under-luminous accretion disc. On the other hand, powerful FSRQs exhibit highly luminous discs, tori, and emission lines from BLR and NLR.

Recent estimates of black hole masses allow for estimations of luminosities in Eddington units, with a separation between the two classes occurring at $\mathrm{L}_{disc}/\mathrm{L}_{Edd} \sim 10^{-2}$, likely marking the transition between radiatively efficient, geometrically thin, optically thick accretion flows and radiatively inefficient, geometrically thick, optically thin accretion flows (Sbarrato et al. 2015). Consequently, new, more physically based definitions for "real" FSRQs and BLLs have been introduced, related to line luminosity in Eddington units (above or below 10^{-3}) (Ghisellini et al. 2011), or based on line composition. In detail, objects presenting high excitation emission lines (such as [OIII], [NeIII] or HeII) as in high-excitation galaxies (HEG, defined as galaxies with $[\mathrm{O\,III}]/\mathrm{H}_{\beta} > 3$, EW of $[\mathrm{O\,III}] > 3\ \mathring{A}$, associated with a strong AGN, with an high accretion rate) or low excitation lines, as in low excitation galaxies (e.g. Buttiglione et al. 2010; Padovani 2017).

Furthermore, another characteristic that distinguishes FSRQs from BLLs is the so-called Compton dominance (Costamante 2020). The Compton dominance is a dimensionless quantity defined as the ratio between the luminosity of the high-energy component (the second peak in the SED, ranging from X-ray to γ-ray emission) primarily due to inverse Compton scattering, and the luminosity of the lower-energy component (the first peak in the SED, ranging from radio to optical/UV) primarily due to synchrotron radiation. FSRQs typically exhibit a higher Compton dominance ($\mathrm{L}_{IC}/\mathrm{L}_{synch} \gtrsim 100$), indicating that their emission is dominated by high-energy photons generated through inverse Compton scattering, implying a stronger magnetic field and/or a higher electron energy density in the blazar jet. However, this could also be attributed to the fact that in FSRQs, the torus, disc, and BLR emit more intense radiation compared to BLLs, leading to a greater contribution from external (with respect the jet) seed photons for the inverse Compton process (Costamante 2020).

Blazars can also be categorized based on the position of the synchrotron peak (ν_p^s): low-synchrotron peaked (LSP) when $\nu_p^s < 10^{14}$ Hz, intermediate-synchrotron peaked (ISP) when 10^{14} Hz $< \nu_p^s < 10^{15}$ Hz, and high-synchrotron peaked (HSP) when $\nu_p^s > 10^{15}$ Hz (Padovani & Giommi 1995; Abdo et al. 2010a; Costamante 2020, and see Fig. 2.3). Another characteristic that distinguish the three classes is the slope of the 0.1 - 10 keV X-ray spectrum.

For LSP objects, the X-ray spectrum is predominantly influenced by the second hump of emission. In these objects, the optical band falls near the minimum point between the two SED peaks. Because the accretion disk and the torus have their peak emissions in the UV/X-ray and IR bands, respectively, they could influence the LSP SEDs and alter the double-peaked shape. This phenomenon is common in powerful FSRQs, facilitating the direct measurement of the accretion disk parameters and the black hole mass. Therefore, LSPs have a flat ($\alpha \lesssim 1$) X-ray spectrum and a steep ($\alpha \gtrsim 1$) γ-ray spectrum (see Fig. 2.3).

Intermediate sources are characterized by a concave X-ray spectrum, which reveals the transition between the two SED humps. In leptonic scenario, this region marks the shift from the tail end of the synchrotron emission to the onset of the IC emission, produced by the highest and lowest-energy electrons, respectively. As in LSP the accretion disk and the torus can be prominent and easily observable. In these objects, the γ-ray spectrum can appear either steep ($\alpha \gtrsim 1$) as in LSPs or flat ($\alpha \lesssim 1$), similar to HSPs (see Fig. 2.3).

In HSP sources, the X-ray spectrum is predominantly influenced by the synchrotron emission from high-energy electrons, typically exhibiting a steep slope. However, similar to LSP objects, the slope can become hard again due to the synchrotron peak moving through and beyond the observed X-ray band. When this occurs, the object is referred to as an "extreme BLL" (see Fig. 2.3). In HSPs, the γ-ray spectrum is flat ($\alpha \lesssim 1$), while the X-ray spectrum is steep ($\alpha \gtrsim 1$).

Since the early all-sky surveys in the γ-ray band, it has been evident that there is a continuity in the main physical properties of blazars, with variations in their observed characteristics being driven by differences in the electron energy distribution and the environment around the central black hole. FSRQs primarily appear as LSP blazars, exhibiting higher luminosity and greater Compton dominance. BLLs, on the other hand, span a broader range of SED types, from LSP to HSP to extreme BLLs, but generally have more similar luminosities at their two emission peaks.

The blazar sequence is a theoretical framework that classifies blazars based on the correlation between their synchrotron peak frequency and their bolometric luminosity. This framework posits that as the luminosity of a blazar increases, the peak frequency of its synchrotron emission shifts to lower energies. Additionally, it is observed that Compton dominance increases with total power.

This sequence is believed to result from different balances between electron acceleration and cooling processes (e.g. see Ghisellini & Tavecchio 2008; Ghisellini et al. 2017; Costamante 2020). More luminous objects, with bright accretion disks and broad emission lines, typically experience more substantial cooling through synchrotron radiation and inverse Compton scattering on relativistically boosted external photon fields. Consequently, their SEDs peak at lower energies (LSP-type) and exhibit higher Compton dominance. In contrast, blazars with less radiative cooling—due to lower jet luminosity, weaker magnetic fields, and the absence of significant external radiation fields—show their SED peaks at higher frequencies (HSP-type).

When SEDs are fitted with leptonic models, the Lorentz factor γ_{peak} of electrons emitting at the peak shows an inverse correlation with the total magnetic and radiative comoving energy density. This pattern aligns with the observed behavior of FSRQs and BLLs: FSRQs typically experience cooling dominated by external fields from BLR and/or molecular tori. As these structures scale with the disk luminosity ($\mathrm{R} \sim \mathrm{L}_{disc}^{1/2}$), the energy density within them (which scales as $\mathrm{L}_{disk}/\mathrm{R}^2$) remains relatively constant, keeping the cooling rate steady. Conversely, in BLLs, the radiative energy density varies with luminosity.

However, the validity of the blazar sequence as an intrinsic property of blazars is debated (e.g. Costamante 2020; Prandini & Ghisellini 2022). Some argue that the observed sequence

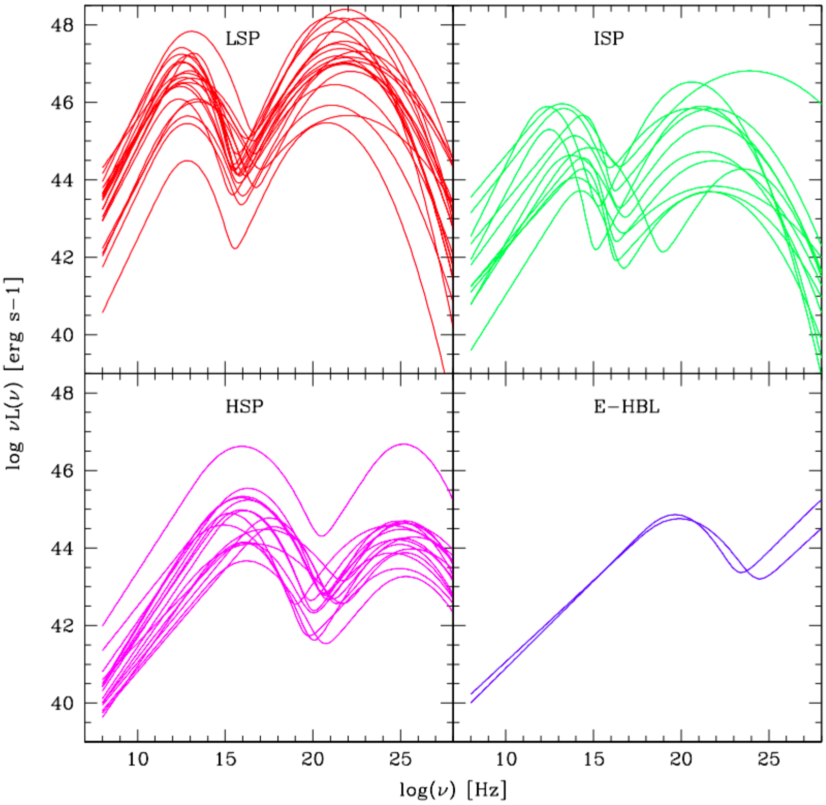

Figure 2.3: Analytic fits of the SEDs for a sample of 50 blazars are presented. The blazars are categorized into four different classes: LSP with $\nu_p^s < 10^{14}$ Hz (top left), ISP with 10^{14} Hz $< \nu_p^s < 10^{15}$ Hz (top right), HSP with $\nu_p^s > 10^{15}$ Hz (bottom left), and E-HSP with $\nu_p^s > 10^{17}$ Hz (bottom right). Credit: Paiano et al. (2017b).

could be the result of selection biases, as a significant portion of the BLL population lacks redshift measurements. It has been demonstrated that an asymmetric distribution of γ_{peak}, peaking around $\sim 10^3$ but with no luminosity correlation, along with minimal assumptions and a luminosity function $\propto L^{-3}$, could reproduce the observed data without invoking a blazar sequence (Giommi et al. 2012a). This alternative perspective suggests a substantial number of low-power LSP BLLs with SSC peaks in the 1-10 keV range. Future observations from eROSITA may shed light on this issue (Merloni et al. 2012).

Finally, blazars are considered possible neutrino emitters, highlighted by the association between the blazar TXS 0506+056 and the IceCube[1] neutrino event IceCube-170922A, marking the first extragalactic source-neutrino event association (IceCube Collaboration et al. 2018). In addition, FSRQs seem to be preferred in neutrino emission processes, as they produce more target photons for the hadronic processes that generate neutrinos (Böttcher 2019; Padovani et al. 2022; Kun et al. 2021). For example, Padovani et al. (2019) noted that TXS 0506+056, first associated as a BLL, is in reality a masquerading BLL.

Given that blazars constitute the most prominent extragalactic population in the γ-ray sky,

---

[1] IceCube is a neutrino observatory located at the South Pole. It consists of thousands of optical sensors embedded in a cubic kilometer of ice deep beneath the surface. These sensors are designed to detect the faint flashes of light produced when neutrinos interact with the ice. IceCube is primarily focused on detecting high-energy neutrinos, which can provide valuable information about some of the most energetic processes in the universe, such as those occurring in supernovae, black holes, and other astrophysical phenomena.

the search for new blazars is most effectively conducted within this energy band. The *Fermi* observatory (Atwood et al. 2009), having conducted a comprehensive all-sky survey at such high energies, is ideally suitable to detect blazars in large numbers.

3

The *Fermi* satellite

3.1.0 Introduction

The *Fermi Gamma-ray Space Telescope* (*Fermi*), formerly known as the *Gamma-ray Large Area Space Telescope* (*GLAST*) (de Angelis 2001), stands as a pivotal space observatory dedicated to γ-ray astronomy, succeeding the pioneering all-sky survey above 50 MeV conducted by *EGRET*. It represents a cornerstone of high-energy astrophysics, owing the significant scientific advancements it has led to this field since its launch.

The *Fermi* observatory was placed in space to meet specific observational requirements. Since the Earth's atmosphere blocks most γ-ray radiation (see Fig. 3.1), instruments designed to study these wavelengths need to be located outside the atmosphere. However, this imposes constraints on the size of the instruments (and thus the satellite) because the cost of launching increases with weight, and the size of rockets is limited. Given that some observatory performance parameters (such as photon collecting area and angular resolution) depended on the size of the instruments, it was necessary to consider these limitations during the satellite's construction.

Crafted through an international collaboration involving contributions from space agencies (NASA and the United States Department of Energy), high-energy particle physics institutes, and universities spanning the United States, Italy, France, Japan, and Sweden, *Fermi* embarked on its mission in June 2008. *Fermi* conducts a comprehensive all-sky survey every three hours, spanning an energy spectrum from 8 keV to 300 GeV.

The primary scientific objectives of this satellite encompass a multifaceted exploration of the cosmos (Atwood et al. 2009; Ackermann et al. 2012a; Meegan et al. 2009; de Angelis 2001):

- Unveiling the nature of unidentified γ-ray sources and elucidating the origins of diffuse emissions as revealed by *EGRET*;

- Deciphering the mechanisms of particle acceleration operative within celestial sources, with particular focus on AGNs, pulsars, pulsar wind nebulae, binary systems, supernova remnants, and solar phenomena;

- Understanding the high-energy dynamics of gamma-ray bursts (GRBs) and transient events;

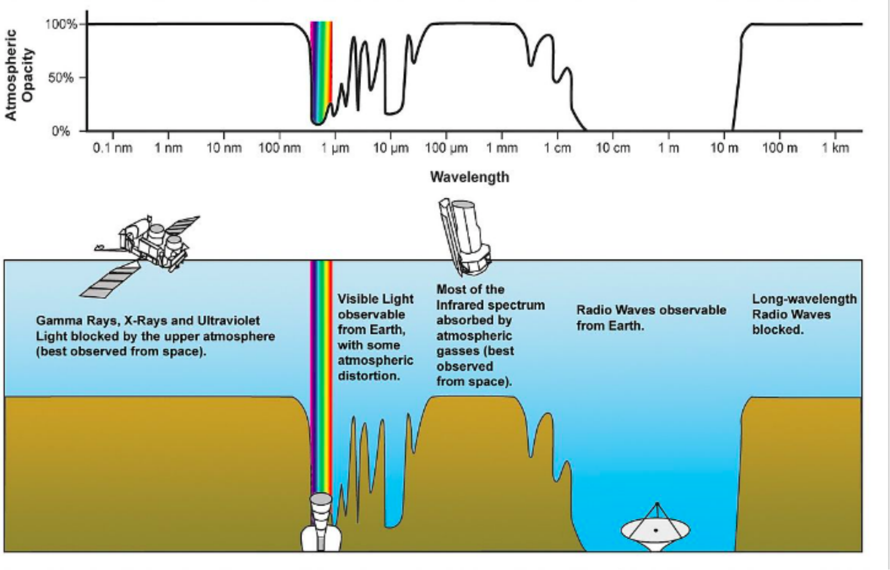

Figure 3.1: Atmospheric absorption at different wavelengths. Credits Summerer & Purcell (2009).

- Probing and discerning the nature of dark matter through γ-ray observations;
- Studying the BH accretion physics;
- Exploring the most extreme objects in the universe and constructing an all-sky catalogue of high-energy sources, providing crucial details about their spatial distribution and spectra spanning from 20 MeV to more than 50 GeV;
- Investigating the early universe and the cosmic evolution of high-energy sources up to redshifts $z > 6$.

3.1.1 Instruments on board of *Fermi*

To accomplish its ambitious goals, the *Fermi* telescope is equipped with two instruments: the *Gamma-ray Burst Monitor* (GBM) and the *Large Area Telescope* (LAT).

The *Gamma-ray Burst Monitor* (GBM) is a crucial component of the *Fermi* satellite, designed to detect and study transient sources and GRBs across a wide energy spectrum (Meegan et al. 2009). Comprising twelve thallium-activated sodium iodide scintillation counters and two bismuth germanate scintillation counters, the GBM covers the energy ranges from 8 keV to 1 MeV and from 200 keV to 40 MeV, respectively. The NaI detectors, sensitive in the lower energy range, from a few keV to about 1 MeV, provide burst triggers and locations, while the bismuth germanate ($Bi_4Ge_3O_{12}$) detectors extend the coverage to approximately 150 keV to 30 MeV, offering a complementary perspective. GBM operates with a programmable trigger algorithm, detecting GRBs through significant changes in count rate across at least two NaI scintillators. Time-tagged event data, recorded continuously with 5 μs resolution, supplies approximately 50 seconds of pre-trigger information for GRBs. Post-trigger, the GBM processor swiftly calculates preliminary position and spectral data for telemetry to the ground, facilitating potential

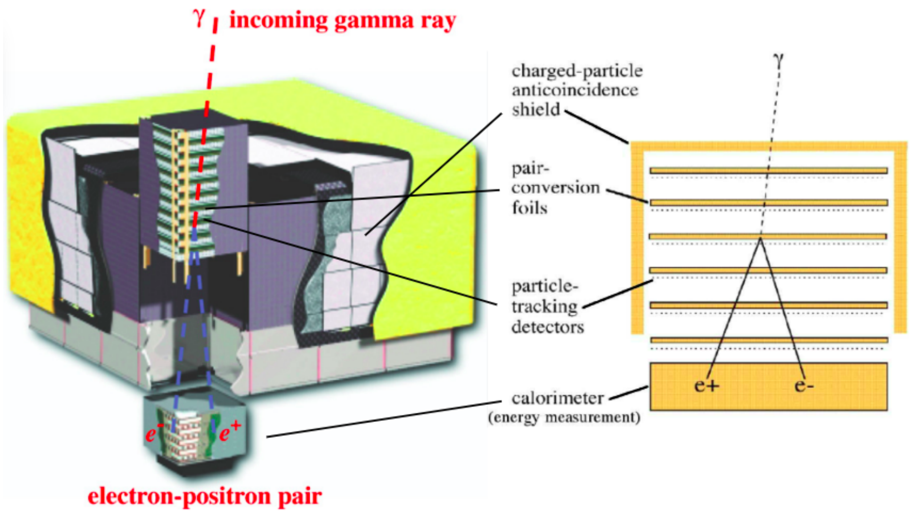

Figure 3.2: Schematic structure of the *Large Area Telescope*, from Atwood et al. (2009).

autonomous repositioning of *Fermi*. Expected to detect around 200 GRBs annually, GBM significantly enhances the scientific output of the *Fermi* Observatory, broadening the energy range for GRB observations and enabling prompt follow-up observations across various wavelengths by alerting the astronomical community instantaneously. Furthermore, GBM's secondary objective involves onboard computation of burst locations to enable spacecraft reorientation for observing delayed emission from bright bursts, thereby maximizing the utility of *Fermi*'s instruments in studying these cosmic events (see Meegan et al. 2009, for more details).

The LAT detector, the primary instrument on the *Fermi* mission, is an imaging, wide field-of-view (FoV), high-energy γ-ray telescope, covering the energy range from 20 MeV to more than 300 GeV (Atwood et al. 2009; Ackermann et al. 2012a; Grove & Johnson 2010). It is a pair-conversion telescope composed by a three detector system (see Fig. 3.2): a precision converter-tracker, to estimate the directions and the times of arrival of γ-ray photons, a calorimeter, to estimate the energies of photons, and a segmented anti-coincidence detector, to reject the background contamination triggered by cosmic-ray particles, maximizing the number of events associated to γ-rays. The term 'event types' refers to the different ways in which events are classified by the LAT based on the section of the detector where the γ-ray conversion occurs.

In addition to these three subsystems, a triggering and data acquisition system selects and records the most likely γ-ray candidate events for transmission to the ground.

Both the calorimeter and tracker are instruments consisting of 16 modules, often referred to as towers, arranged in a 4 × 4 grid. Each tower occupies a footprint of $\sim$ 37 cm × 37 cm and stands $\sim$ 85 cm tall, extending from the top of the tracker to the bottom of the calorimeter. The tracker serves as the crucial section where incoming γ-rays ideally convert to e^+e^- pairs and their trajectories are measured (Atwood et al. 2009; Ackermann et al. 2012a; Grove & Johnson 2010). Each tracker module has 18 (x,y) tracking planes, consisting of two layers (x and y) of single-sided silicon strip detectors. The 16 planes at the top of the tracker are interleaved with position-sensitive detectors made of high-Z material, primarily tungsten, organized into two distinct sections with notable differences in performance: the thin or front section and the thick or back section. The thin section consists of the first 12 paired layers, positioned closest to the converter foils composed of approximately 3% of a radiation length of tungsten. This arrangement minimizes the separation between the converter foils and the subsequent SSD planes, crucial for minimizing the effects of multiple scattering. The subsequent 4 layers, forming the thick or back section, feature tungsten converters $\sim$ 6 times thicker. The final two layers lack converters, as the tracker's trigger system requires signals in at least three adjacent x–y paired layers, making these layers insensitive to γ-rays. This strategic division of the tracker into two sections was driven by the need to balance conflicting requirements of achieving good angular resolution and maximizing the conversion probability of γ-rays. The tungsten foils were designed to ensure a roughly equal distribution of converted γ-rays across the thin and thick sections, facilitating accurate reconstruction of the incoming direction of the primary γ-ray at a later stage of analysis (Atwood et al. 2009; Ackermann et al. 2012a; Grove & Johnson 2010).

The LAT calorimeter comprises a 4×4 array of identical modules, each housing a hodoscopic array of 96 CsI(Tl) scintillation crystals with PIN photodiode readouts (Atwood et al. 2009; Ackermann et al. 2012a; Grove & Johnson 2010). These crystals are organized into eight layers of 12 crystals each, with alternating orientations by 90 degrees to form an x-y array. This arrangement enables each crystal to not only measure the energy deposited within its volume but also accurately pinpoint the location of that energy deposition in three dimensions. Consequently, this setup serves as an essential tool for initial background discrimination. Additionally, energy leakage corrections are implemented, particularly for showers with energies exceeding a few GeV, where leakage effects may be more pronounced. This correction process significantly enhances the energy resolution of the calorimeter (Atwood et al. 2009; Ackermann et al. 2012a; Grove & Johnson 2010).

The third subsystem of the LAT is the anticoincidence detector, responsible for rejecting background from charged particles (Atwood et al. 2009; Ackermann et al. 2012a; Grove & Johnson 2010). It consists of 25 scintillating plastic tiles covering the instrument's top and 16 tiles on each of its four sides, totaling 89 tiles. The anticoincidence detector dimensions range from 561 to 2650 cm^2 in surface area and 10 to 12 mm in thickness. Unlike the segmentation of the LAT tower modules, the anticoincidence detector segmentation is deliberately designed to prevent alignment of gaps between tiles with those in the tracker and calorimeter. The anticoincidence detector design specifications require rejecting incoming charged particles (which are identified by their emission of light flashes, resulting in their subsequent rejection) with an efficiency exceeding 99.97%, while allowing gamma rays to freely pass through its thin plastic scintillator tiles.

Finally the data acquisition system carries the data collected by the tracker, calorimeter, and anticoincidence detector subsystems (Atwood et al. 2009; Ackermann et al. 2012a; Grove & Johnson 2010). Using a multi-event triggering process and running various filter algorithms in parallel, the data acquisition system selects and records the most likely γ-ray candidate events, reducing the number of events transmitted to the ground. Besides hadronic-induced showers recognized as background events, the LAT also has to handle "ghost events"—remnants of electronic signals from particles that passed through the LAT a few microseconds before

Parameter	Value or Range
Energy range	20 MeV - 300 GeV
Effective area at normal incidence	9.500 cm^2
Energy resolution (equivalent Gaussian 1σ):	
100 MeV - 1 GeV (on-axis)	9% – 15 %
1 GeV - 10 GeV (on-axis)	8% – 9 %
10 GeV - 300 GeV (on-axis)	8.5% – 18 %
>10GeV(>60° incidence)	≤6%
Single photon angular resolution (space angle)	
on-axis, 68% containment radius:	
>10GeV	≤0°.15
1GeV	0°.6
100MeV	3°.5
on-axis, 95% containment radius	$< 3 \times \theta_{68\%}$
off-axis containment radius at 55°	< 1.7 × on-axis value
Field of View (FoV)	2.4 sr
Timing accuracy	<10μs
Event readout time (dead time)	26.5 μs

Table 3.1: Summary of LAT performance parameters, from Atwood et al. (2009).

the triggering particle. These ghost events complicate the analysis and event reconstruction, particularly at lower energies, affecting instrument performance. Additionally, the LAT performs rapid onboard scientific analysis to search for transient sources, enhancing its capability to detect and study γ-ray phenomena (see Atwood et al. 2009; Ackermann et al. 2012a; Grove & Johnson 2010, for more details).

3.1.2 LAT performance

In Tab. 3.1 are summarised the performances of the LAT instrument (Atwood et al. 2009; Ajello et al. 2021). They are primarily governed by four aspects: the LAT hardware design, the event reconstruction algorithms, the background selections and event quality selections. The performances are stored into the Instrument Response Functions (IRFs), that are generated by full detector Monte Carlo simulations of γ-rays and calibrated in beam tests and updated via on-orbit measurements (Ackermann et al. 2012a; Atwood et al. 2013; Bruel et al. 2018).

The key performance parameters are described as function of photon energy, incidence angle and conversion point within the instrument. The three main performance parameters are: the effective area, the Point Spread Function (PSF) and the energy resolution (Ackermann et al. 2012a).

The effective area, $A_{eff}(E,\hat{v}, s)$ is a crucial parameter for understanding the performance of LAT in detecting γ-rays. It represents the product of the cross-sectional geometrical collection area, the γ-ray conversion probability, and the efficiency of a given event selection (denoted by s) for a γ-ray with energy E and direction $\hat{v}$ in the LAT frame. This parameter effectively encapsulates the overall efficiency of the LAT in detecting γ-rays. The determination of the

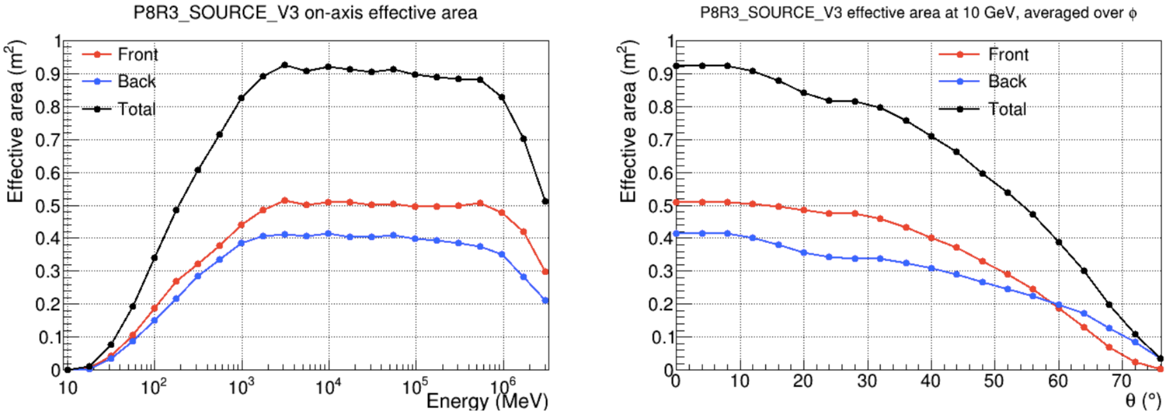

Figure 3.3: Left: Effective area versus energy for normal incidence photons (θ = 0). Right: Effective area versus incidence angle (θ) for 10 GeV photons. Taken from Rando (2022).

effective area is based on detailed Monte Carlo simulations that model γ-rays fully propagating through the instrument. These simulations take into account the complete sequence of interactions from the initial physics interactions within the detector material to the electronic signal processing, including the trigger and filter algorithms, and ultimately the event reconstruction and classification processes. Thus, the effective area provides a comprehensive measure of the LAT's detection capability, integrating both the physical properties of the instrument and the efficiency of its data analysis algorithms. In Fig. 3.3, the effective area is shown as a function of the energy for normal incidence photons (θ=0) and as a function of incidence angle theta for 10 GeV photons.

The PSF of LAT is a critical metric that defines the instrument's ability to resolve and accurately localize γ-ray point sources. The PSF is a function of several variables, including the energy of the incident photon, the inclination angle at which the photon strikes the detector, and the specific event class (a flag to indicate the quality of the events). The value of the PSF is primarily determined by the containment radius of the incoming γ-ray distribution and its profile. At lower energies ($\leq$100 MeV), the PSF is notably affected by multiple scatterings within the detector, which complicate the track reconstruction and broaden the PSF. This broadening at lower energies hampers the instrument's ability to precisely localize γ-ray sources. Consequently, the PSF is a crucial parameter for determining the localization accuracy and the positional error ellipse of the sources detected by LAT. The 68% and 95% containment angles of the acceptance weighted PSF for both the front/back and PSF event types is shown in Fig. 3.4.

Finally the acceptance weighted energy resolution (i.e. 68% containment half width of the reconstructed incoming photon energy) as a function of energy and the energy resolution as a function of incidence angle for 10 GeV photons, are shown in Fig. 3.5.

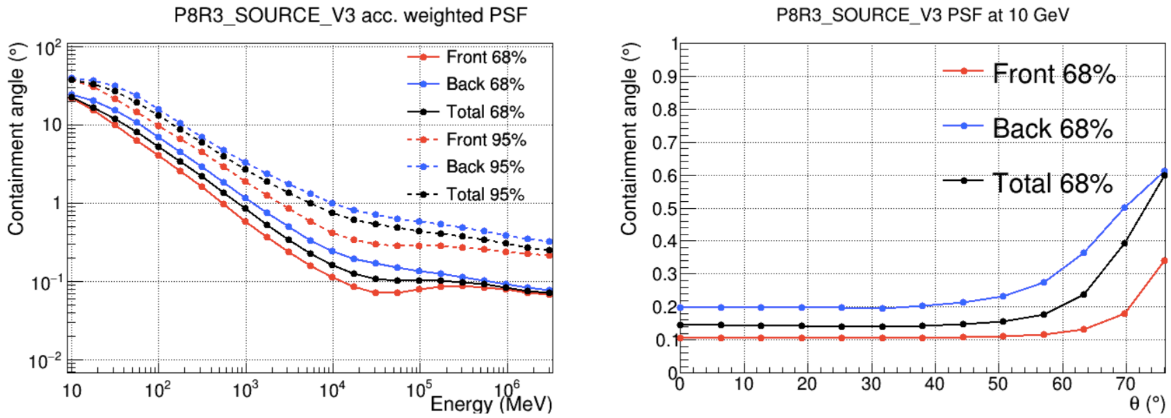

Figure 3.4: Left: Acceptance-weighted (acc. weighted) PSF containment angles at 68% and 95% for both front/back and PSF event types. Right: 68% containment angles as a function of incidence angle (theta) at 10 GeV. Taken from Rando (2022).

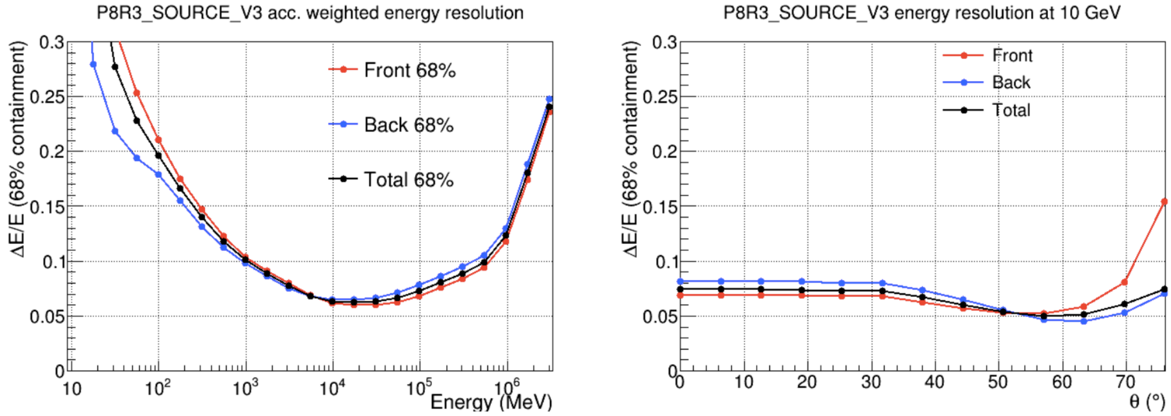

Figure 3.5: Left: Acceptance-weighted (acc. weighted) energy resolution (68% containment half-width of the reconstructed incoming photon energy) versus energy. Right: Energy resolution versus incidence angle for 10 GeV photons. Taken from Rando (2022).

3.2.0 The Fourth *Fermi* Gamma-ray LAT Catalog

Since its launch in June 2008, the *Fermi* satellite, utilizing the LAT detector, has been conducting a γ-ray sky survey to create a comprehensive map. Integrating the data over many years, the LAT collaboration has produced several releases of high-energy γ-ray source catalogs. The currently latest version of the catalog is the fourth version, the Fourth Fermi Gamma-ray LAT Catalog (4FGL, Abdollahi et al. 2020), in particular the Data Release 4 (Fermi Large Area Telescope Fourth Source Catalog Data Release 4 (4FGL-DR4), Ballet et al. 2023), which contains sources detected over 14 years of observations. The *Fermi* collaboration publishes a new data release of the same catalog when existing data are updated with new observations or corrections, but without significant changes in the methodology or criteria for source inclusion. This update improves the data quality and includes new sources detected in the period following the original catalog's publication.

The improvements of the fourth catalog over the previous one (the 3FGL catalog, which contains sources observed during the first four years of the satellite's operation Acero et al. 2015) have included an improvement on the angular resolution above 3 GeV, a 20% increment in acceptance (defined as the integral of the effective area over the field of view), the adoption of a new model to describe Galactic emission, and a doubling of the number of detected sources. Additionally, the emission of each source has been modeled using three spectral models (power-law, log normal, and power law with sub-exponential cutoff), compared to the single model (power-law) used in 3FGL. Finally, light curves have been constructed, and variability has been tested using two temporal bins (one year and two months) (see Abdollahi et al. 2020).

Data release 4: The data for the 4FGL-DR4 catalog span 14 years, from August 4, 2008 (15:43 UTC) to August 2, 2022 (21:53 UTC). Throughout most of this period, Fermi was in sky-scanning survey mode, alternating its viewing direction north and south of the zenith within each orbit, allowing nearly complete sky coverage approximately every three hours. Data intervals around solar flares and bright GRBs were excluded. The catalog covers an energy range from 50 MeV to 1 TeV (see Ballet et al. 2023).

A fundamental ingredient for the catalog building is having a robust model to account for the diffuse γ-ray background (Abdollahi et al. 2020; Ballet et al. 2023). This model includes various sources of diffuse emission, such as interactions of cosmic rays with interstellar gas and radiation fields, as well as contributions from unresolved extragalactic sources. Accurate modeling of the diffuse background is essential for distinguishing and characterizing individual γ-ray sources. By incorporating data from the Galactic plane, isotropic background, and known γ-ray sources, the model effectively separates diffuse and point source contributions, ensuring precise source detection and cataloging in the 4FGL.

Detection, localization and significance: The Test Statistic (TS) used to quantify how significantly a source stands out from the background is defined as follows: $\mathrm{TS} = 2\log\left(\frac{\mathcal{L}}{\mathcal{L}_{\prime}}\right)$. This statistic compares the maximum value of the likelihood function $\mathcal{L}$, which includes the source in the model, with $\mathcal{L}_{\prime}$, the likelihood value without the source (see Abdollahi et al. 2020).

The source detection process for the 4FGL catalog involves a detailed and iterative method to accurately identify and characterize gamma-ray sources. The sky was divided into 1728 tiles, each covering about 24 square degrees. Regions of Interest (RoIs) were defined with a 5-degree radius centered on these tiles. Data were binned into 16 energy bands from 100 MeV to 1 TeV and by event type (Front or Back). Only Front events were used for the two bands below 316 MeV to avoid poor PSF and contributions from the Earth's limb (see Abdollahi et al. 2020, for more details).

All point sources within each RoI and nearby sources contributing at least 1% were included. The spectral model parameters for sources within the central tile were adjusted to optimize the likelihood. An iterative process optimized each RoI independently and then repeated for those with significant changes, until convergence.

The isotropic diffuse source was globally refitted up to 10 GeV, and the Galactic diffuse emission was adjusted using an 8-layer map to ensure smooth transitions between RoIs (see Abdollahi et al. 2020, for more details). After convergence, source positions were updated, and new sources were added using the residual TS procedure. Sensitivity to the Galactic diffuse component was managed by limiting the precision to 2%, which increased the spectral fit uncertainty for the lowest energy bins.

The position of each source was determined by maximizing the likelihood relative to its position while keeping other parameters fixed. Ideally, with large statistics, the log-likelihood forms a quadratic shape in angular variables, assuming small offsets. The Localization Test Statistic (LTS) is defined as twice the log-likelihood ratio of a given position, compared to the maximum likelihood value obtained for that source; an LTS map is created by evaluating LTS across a grid of positions. The LTS distribution is fitted to a quadratic form to determine the uncertainty ellipse, including the position, major and minor axes, and orientation. The fitting process starts with an LTS distribution prediction based on current elliptical parameters, evaluates LTS at eight positions around a circle, and measures localization quality (LQ) by the sum of squared differences. The fitting adjusts the elliptical parameters to minimize LQ.

Only sources with TS > 25, corresponding to a significance slightly over 5σ, evaluated from the χ^2 distribution with 4 degrees of freedom (position and spectral parameters of a power-law source, Mattox et al. 1996), are included in the catalog.

Spectral fitting shapes and flux determination: The sources were fitted with three spectral models: power law, power law with sub-exponential cutoff, and log-normal (Abdollahi et al. 2020; Ballet et al. 2023). For all three spectral models, the normalization K, is defined at a reference energy E_0, where the error on K is minimal. This ensures the highest precision and reliability in the spectral fitting process, leading to more accurate and consistent results across different models.

The log-normal function (called in the catalog *LogParabola*) is defined such as:

$$\frac{dN}{dE} = K \left(\frac{E}{E_0}\right)^{-\alpha-\beta \, log(E/E_0)} \tag{3.1}$$

where α is the spectral slope at E_0, and β is the curvature.

The sub-exponentially cutoff power law function (called in the catalog *PLSuperExpCutoff*) is defined as such:

$$\frac{dN}{dE} = K \left(\frac{E}{E_0}\right)^{-\Gamma} exp\left(a(E_0^b - E^b)\right) \tag{3.2}$$

where Γ is the low-energy spectral slope, a is the exponential factor (with the correct units of measurement to ensure that the exponential function is dimensionless), and b is the exponential index.

Finally the power-law (called in the catalog *PowerLaw*) is defined as the Eq. 3.2, without the exponential term.

The power-law model is rarely applicable to astrophysical sources across the 50 MeV to 1 TeV range (Abdollahi et al. 2020; Ballet et al. 2023). Bright sources in the 4FGL catalog show significant downward curvature, and the power-law model tends to overestimate data at the spectrum's low energies where constraints are weak. Using a *LogParabola* shape for all sources would be ideal, but correlations at low energy make this unstable. So, the curved model is used when $\mathrm{TS}_{curv} > 9$ (3σ significance), where $\mathrm{TS}_{curv} = 2\log[\mathcal{L}(curved\, spectrum)/\mathcal{L}(power - law)]$. Sources with curved spectra are considered significant whenever TS > 25+9 = 34 because this threshold ensures both a robust detection (TS > 25) and a significant preference for a curved model over a power-law model (TScurv > 9). This dual criterion helps ensure that the detected sources are accurately characterized and not misrepresented by an inadequate model.

The source photon fluxes are reported across seven energy bands: 1) 50 to 100 MeV, 2) 100 to 300 MeV, 3) 300 MeV to 1 GeV, 4) 1 to 3 GeV, 5) 3 to 10 GeV, 6) 10 to 30 GeV, and 7) 30 to 300 GeV. These fluxes were determined by fixing the power-law index to the value obtained from fitting over the entire energy range. The scale factor, which serves as a multiplier for the model's predicted fluxes in each energy band, was then adjusted to best match the observed data. This adjustment allows for improved alignment between the model predictions and the actual measurements across the different energy bands. For sources with curved spectra, the photon index in each band was set to the geometric mean of the given energy bin.

3.3.0 Sources of the *Fermi* catalog

The 4FGL-DR4 catalog contains 7195 sources. 4765 of them are associated or identified with targets at other wavelengths and classified (Ballet et al. 2023).

The dominant class in the catalog is that of AGNs, with 3934 blazars, 53 radio galaxies, and 27 other types of AGNs. Blazars are divided into three sub-classes: 1490 BLLs, 820 FSRQs and 1624 Blazar Candidate of Uncertain type (BCUs). An object is classified as a BCU in the *Fermi* catalog when it displays characteristics typical of blazars but lacks sufficient data for definitive identification as either a BLL or a FSRQ (see Tolamatti et al. 2023, and references therein). The primary reasons for this classification include: inadequate or limited observational data, particularly in terms of optical spectra; the object exhibits intermediate or ambiguous properties between the two main blazar classes; spectral data of low quality hinder the identification of key

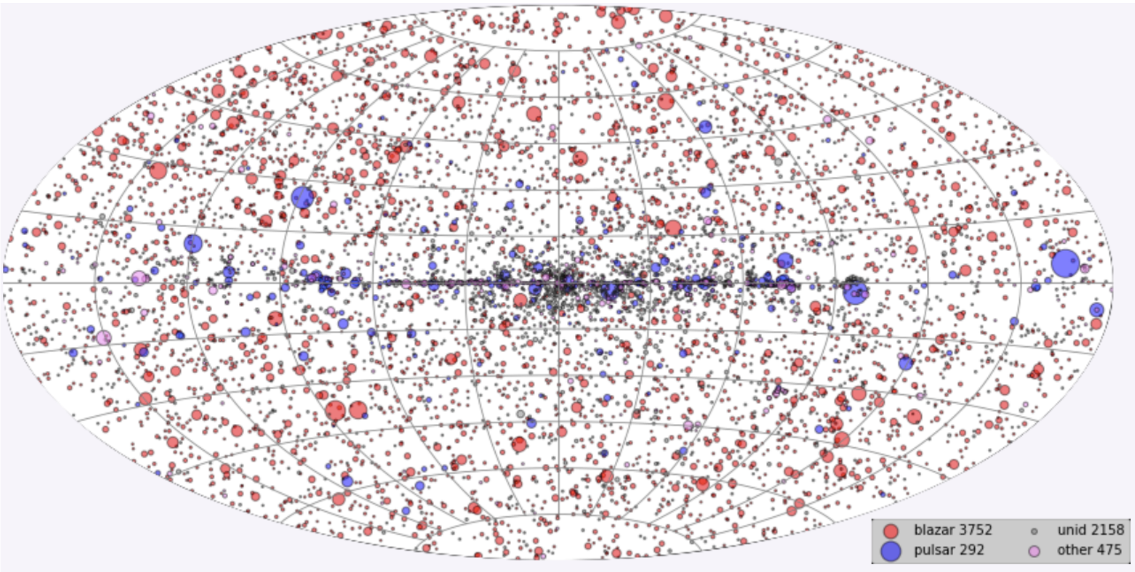

Figure 3.6: Full γ-ray sky map containing all sources of the 4FGL-DR3 catalog (Abdollahi et al. 2022). Taken from the Space Science Data Center (SSDC, https://www.ssdc.asi.it/).

spectral features and the estimation of redshift; insufficient multi-wavelength coverage to fully characterize the object's emission properties. It is worth to note that, over the years, the *Fermi* collaboration has collected the AGNs detected by the LAT detector into a sub-catalog of the main catalog. The Fourth LAT AGN Catalog, Data Release 3 (4LAC-DR3 Ajello et al. 2020, 2022) contains the AGNs detected in the first 12 yr of observations.

γ-ray emission can also come from non-active galaxies (Ballet et al. 2023). In addiction to three normal galaxies, Small Magellanic Cloud, Large Magellanic Cloud and M31, the 4FGL-DR4 catalog contains 6 Star Forming Regions (SFR) and 8 StarBurst Galaxies (SBG), in which cosmic rays accelerated by supernova remnants can produce γ-ray radiation through inelastic collisions with ambient gas particles and subsequent π^0-decay (e.g. Peng et al. 2019, and references therein). In this case, the γ-ray emission appears to be almost steady over time, unlike in blazars and jetted AGN in general, where the emission tends to be very variable. (Ballet et al. 2023).

Approximately 6% of the sources in the catalog are galactic objects: 320 pulsars, 22 pulsar wind nebulae, 45 supernova remnants, 34 globular clusters, 20 binary systems, and 8 novae (Ballet et al. 2023).

The full sky map of the Fourth *Fermi* Gamma-ray LAT Catalog, Data Release 3, (4FGL-DR3 Abdollahi et al. 2022) is shown in Fig. 3.6.

The association and classification of *Fermi* sources benefited from data obtained through several follow-up programs. Numerous research groups have applied various statistical methods (Ackermann et al. 2012b; Mirabal et al. 2012; Mao & Yu 2013) and neural network algorithms (Doert & Errando 2014; Salvetti et al. 2017a; Kaur et al. 2019a,b; Kerby et al. 2021; Kaur et al. 2023) to investigate and determine the nature of *Fermi* sources based on their γ-ray properties. Additionally, significant efforts have been directed towards identifying counterparts at other wavelengths. In particular, in radio band, follow-up campaigns were carried out above GHz frequencies by e.g. Kovalev (2009); Petrov et al. (2011, 2013); Hovatta et al. (2012, 2014); Schinzel et al. (2015, 2017) and below by Massaro et al. (2013); Nori et al. (2014); Giroletti et al. (2016). Simultaneously, other groups, such as Giommi et al. (2012b) and López-Caniego et al. (2013), have focused on submillimeter observations, while D'Abrusco et al. (2013) and Massaro et al. (2015b, and references therein) proposed AGN candidates, between *Fermi* sources, based on the infrared colors of lower energy counterparts. Follow-up campaigns in X-ray band was conducted by several group, such as Falcone et al. (2011); Landi et al. (2015); Salvetti et al. (2017b); Kaur et al. (2019a,b); Kerby et al. (2021); Kaur et al. (2023) and Marchesini et al. (2020), using the *Neil Gehrels Swift Observatory* (herafter, *Swift*), while, other groups, e.g. Maeda et al. (2011); Cheung et al. (2012); Kataoka et al. (2012); Takahashi et al. (2012) and Takeuchi et al. (2013), have used different satellites, such as the *Chandra X-ray Observatory* and *Suzaku* (formerly ASTRO-EII).

In any case, to accurately classify newly extra-galactic associated sources, it is crucial to perform spectroscopic optical observations, that, in addition, can provide estimates of their cosmological distances (see, e.g., Shaw et al. 2013a,b; Massaro et al. 2015b,a; Ricci et al. 2015; Álvarez Crespo et al. 2016a,b; Paiano et al. 2017d,c,a; Peña-Herazo et al. 2017; Landoni et al. 2018; Marchesi et al. 2018; Marchesini et al. 2019; Paliya et al. 2021). In contrast, for galactic objects, while optical observations can offer useful information, they are not as critical for classification.

Unassociated sources: However, the 4FGL-DR4 also contains a significant fraction of sources, about 30%, that remain unclassified and unassociated with lower energy sources, known as Unassociated Gamma-ray Sources (UGSs) (Ballet et al. 2023). The primary reason they remain unassociated and unclassified is the significant positional uncertainty of these γ-ray emitters, which is due to limited photon statistics [the average 100 MeV - 100 GeV γ-ray flux of the UGSs ($<F_{UGS}> \sim 5.3 \times 10^{-12}$ erg cm^{-2} s^{-1}) is lower compared to that of the associated sources ($<F_{ass}> \sim 1.6 \times 10^{-11}$ erg cm^{-2} s^{-1}), as noted by Ulgiati et al. (2024)] and the angular resolution of the LAT detector (3.5° at E = 100 MeV, 0.6° at 1 GeV, and greater than 0.15° at E > 10 GeV, see Tab. 3.1). This results in a large number of low-energy candidate counterparts (e.g., in the optical and radio bands) within the typical *Fermi* error boxes, making it challenging to attribute the γ-ray emission to a specific source.

Although UGSs are unassociated and unclassified, they still represent a significant component of the γ-ray sky. Given the predominance of blazars in the *Fermi* catalog, UGSs could potentially conceal new blazars or other AGN subclasses capable of emitting at GeV energies (as Narrow Line Seyfert-1 and Seyfert-like objects, for which only a few are known as γ-ray emitters). Consequently, UGSs are crucial for population and cosmic evolution studies (e.g. Ajello et al. 2014; Ghisellini et al. 2017). In addition to blazars, the UGS studies can lead to discovery new pulsars or binary systems; e.g., see Saz Parkinson et al. (2010) and Ransom et al. (2011).

Furthermore, the identification and classification of UGSs can improve our understanding of the γ-ray sky by potentially uncovering unknown astrophysical phenomena or source types (e.g., weakly interacting massive particle dark matter annihilating in Galactic subhalos Ackermann et al. 2012c; Coronado-Blázquez et al. 2019).

Approximately half of the UGSs are located within 10° of the Galactic plane. The Galactic plane is a region of intense diffuse γ-ray emission caused by processes such as the scattering of cosmic rays on interstellar gas and background radiation. This diffuse emission creates a strong background that makes it difficult to distinguish γ-ray point-like sources. Additionally, the Galactic plane is a very dense region of sources, notably pulsars, supernova remnants, and X-ray binary systems. This high density causes source overlap and a higher likelihood of confusing one source with another. Finally, the emission of dust and gas in the Galactic plane can obscure sources at other wavelengths, such as optical and radio. This makes it difficult to obtain counterparts in other bands of the electromagnetic spectrum, which are necessary to confirm the association of a γ-ray source.

Outside the Galactic plane ($b > 10°$), the percentage of Galactic sources decreases significantly. Pulsars, the second most common class in the catalog after AGNs, are rarely observed outside the Galactic plane. Young isolated pulsars ($t < 10^6$ years) are naturally clustered close to the plane, while older pulsars, which have had time to move away from the plane, do not have enough energy to emit in γ-rays (they cross the "γ-ray death line"). However, a handful of millisecond pulsars can be found outside the plane; being older objects, they have had time to leave the plane, and being powered by accretion, they have enough energy to emit in γ-rays. The dominant sources outside the plane are extragalactic objects, particularly AGNs, of which 98% are blazars.

Multi-wavelength follow-up observations are essential for identifying counterparts and confirming associations for UGSs. Observations in radio and optical bands are particularly crucial as they can provide precise localization and additional spectral information that complement the γ-ray data. However, the number of radio and optical sources is usually very high within the typical *Fermi* error box of UGSs (approximately 6 arcminutes). This high density of sources is particularly evident in regions like the Galactic plane, where significant background noise further complicates follow-up efforts. Crowded fields, or fields with many sources in general, make it challenging to identify the correct counterpart.

To break this degeneracy, at least outside the Galactic plane, the search for counterparts that emit in the X-ray band is particularly helpful. At these energies, the number of sources is smaller compared to the radio and optical bands. Moreover, searching for X-ray counterparts allows for reducing the size of the search regions, as X-ray telescopes like *Swift* generally have an angular resolution between a few and tens of arcseconds, which is significantly better than that of *Fermi*. In such regions, there is rarely a degeneracy of optical and/or radio counterparts.

Finally, analyzing the optical spectrum of the counterpart allows us to classify the source and determine if the object can be the counterpart of the γ-ray emission. Definitive confirmation is achieved by correlating the optical spectroscopy with the study of temporal variability across different bands and the SED of the object.

3.4.0 Goal of my PhD project

My PhD project aims at performing a multi-wavelength study of the unidentified γ-ray objects in the fourth *Fermi* catalog in order to provide an astrophysical association for each of them and also to find and to classify new AGNs. To enhance the chance of selecting extragalactic targets, I focus on the UGSs outside the Galactic plane ($|b| > 10°$).

For a given UGS, I search for possible X-ray, radio, and optical counterparts. Blazars (and AGNs in general) are known to be strong X-ray emitters, with both their γ-ray and X-ray emissions originating from the same component, the jet. The X-ray spectrum of the counterpart should exhibit behavior consistent with the γ-ray spectrum, suggesting a common emission mechanism (see Sec. 2.2.2). Additionally, blazars are strong radio emitters, with their jet-dominated emission peaking in radio flux density. Moreover, the radio emission should be correlated with the γ-ray emission, as both are emitted from the jet (e.g. see Paiano et al. 2023). Subsequently, I analyze the optical spectrum of the counterpart to provide a classification of the object. Finally, analysing the SED of the object, I verify the validity of the association.

Given that extragalactic UGS are distributed across the entire sky and are very numerous, and considering that UGS are generally faint, identifying their lower-energy counterparts requires sky surveys across all relevant bands, that are also sufficiently deep and sensitive. In the following paragraph, I will review which observatories have been utilized for this type of research and which surveys have been consulted.

4

X-ray, optical and radio facilities

In this chapter, I will describe the X-ray, optical, and radio facilities that were specifically utilized for this thesis work. The choice to use these observatories was driven by several factors: together, they offer comprehensive sky coverage, they have made their data publicly accessible, and they provide essential multi-wavelength observations that are crucial for studying UGSs.

For the X-ray band, the *Swift* satellite was employed. The *Neil Gehrels Swift Observatory*, commonly referred to as *Swift*, has been conducting a dedicated monitoring campaign on UGSs for over a decade, making it an ideal resource for this work. Its key advantage lies in its flexibility and long-term commitment to monitoring these sources, ensuring continuous coverage and rapid follow-up.

In the optical band, data were gathered from various large-scale sky surveys, including the *Panoramic Survey Telescope and Rapid Response System* (Pan-STARRS), the *Sloan Digital Sky Survey* (SDSS), the *Dark Energy Survey* (DES), the *SuperCOSMOS Sky Survey*, and *Gaia* (*Global Astrometric Interferometer for Astrophysics*). These surveys were selected because they provide deep imaging and extensive coverage, essential for pinpointing the optical counterparts of faint or distant UGSs.

For the radio band, the facilities used were the *Karl G. Jansky Very Large Array* (VLA), the *Rapid ASKAP Continuum Survey* (RACS) conducted by the *Australian Square Kilometre Array Pathfinder* (ASKAP), and the *Australia Telescope Compact Array* (ATCA). These instruments were chosen for their ability to deliver high-quality, wide-field radio images, offering coverage in regions of the sky that complement the optical and X-ray data. Though other radio observatories could provide higher angular resolution, the selected instruments are more suited for large-scale surveys, enabling efficient detection and follow-up of potential radio counterparts to the UGSs.

4.1.0 The *Swift* satellite

The *Neil Gehrels Swift Observatory*, previously known as the *Swift Gamma-Ray Burst Explorer* (hereafter the *Swift* satellite, or simply *Swift*), is a NASA space observatory launched in 2004 (Gehrels et al. 2004). Like γ-ray observatories, X-ray instruments must be placed in space due to significant atmospheric absorption (see Fig. 3.1). The *Swift* satellite orbits Earth at an altitude of approximately 600 km, completing one full orbit every 96.6 minutes. The initial mission duration was planned to be two years, but due to its scientific success and the good condition of the satellite and its onboard instruments, it has been extended several times and remains active.

Swift was initially conceived to study GRBs and monitor their afterglows in X-ray and UV/Visible light at the location of a burst. However, over the years, it has proven to be one of the most versatile missions ever launched.

Unlike many space missions, it prioritizes open science, ensuring that all collected data are promptly made available to the global scientific community (Gehrels et al. 2004). This policy of rapid data release has enabled a swift response to GRB events and facilitated timely follow-up observations across multiple wavelengths. By providing open access to its data, *Swift* democratizes research opportunities, allowing scientists from various institutions and countries to contribute to and benefit from its findings. This approach maximizes the scientific return on investment, as the global research community can immediately utilize and build upon *Swift*'s observations.

Among the various programs supported by the satellite, *Swift* has been used to monitor the center of our galaxy, a project that required several years of observation. In shorter-term projects, *Swift* mapped nearby galaxies in the ultraviolet, including a notable effort with the Large Magellanic Cloud. *Swift*'s Ultraviolet/Optical Telescope (UVOT) captured 2200 overlapping "snapshots" to cover the galaxy, producing the most detailed ultraviolet view to date. The satellite has also monitored supernova explosions and blazar flares, contributing to our understanding of the mechanisms behind these powerful and variable events. Additionally, *Swift* has followed up on X-ray transients discovered by MAXI satellite (Matsuoka et al. 2009) and studied the transition of X-ray binary systems into millisecond pulsars and black hole transients, providing valuable insights into these dynamic processes. It has also been used to study massive clusters and tidal disruption flares.

In particular, *Swift* is employed to search for X-ray and UV/optical counterparts of UGSs. For the past decade, it has been actively involved in a dedicated campaign focusing on these objects with its X-ray Telescope (XRT) (Stroh & Falcone 2013; Falcone et al. 2014). This Swift program includes pointed observations, typically lasting around 4 kiloseconds, of *Fermi* catalog sources with no currently known source associations at other wavelengths. For each *Fermi*-LAT localization ellipse, *Swift*-XRT obtains accurate source positions (within 5 arcseconds) for any detected X-ray sources, facilitating new blazar identification observations and pulsation searches across radio and γ-ray wavelengths.

4.1.1 Instruments

The *Swift* satellite is equipped with three co-aligned telescopes: the Burst Alert Telescope (BAT), the X-ray Telescope (XRT), and the Ultraviolet/Optical Telescope (UVOT). Notably, *Swift* lacks an onboard propulsion system. Instead, it utilizes momentum wheels for the pointing. The momentum buildup in these wheels is countered by magnetic torquers, ensuring stability. For celestial orientation, *Swift* relies on a combination of star trackers, Sun sensors, and magnetometers.

The Burst Alert Telescope: The Burst Alert Telescope (BAT) detector is a highly sensitive instrument ($\sim 10^{-8}$ erg cm^{-2} s^{-1}), capable to detect photons in the energy range 15-150 keV, with a precision of 1-4 arcmin. Its energy resolution is of $\sim$ 7 keV, and its large field of view (FOV) is 1.4 sr. In astronomy, this energy range is typically referred to the hard X-ray band or, alternatively, soft γ-rays.

BAT was initially designed to provide GRB triggers (see Barthelmy 2000; Gehrels et al. 2004; Barthelmy et al. 2005, for details), however over time, it has been utilized for a variety of other scientific purposes, such as the detection of X-ray transients, the study of AGNs, monitoring supernova explosions, and mapping the sky in X-ray and γ-ray bands.

BAT employs a coded mask to generate images of the sky based on the principle of pinhole imaging. This technology was chosen because it is extremely challenging to focus γ-rays using conventional mirror- or lens-based techniques. The structure consists of 52,000 5-mm lead shielding platelets arranged in a complex pattern one meter away from the 32,768 4-mm CZT (cadmium zinc telluride) platelets for hard X-ray detection (Gehrels et al. 2004).

BAT's primary objective is to identify any transient celestial high-energy phenomenon. This necessitates a wide field of view and good sensitivity. BAT can provide an object's location within 15 seconds of detection, within which time it determines whether the burst warrants a spacecraft slew and, if so, sends the position to the spacecraft.

The X-ray Telescope: The *Swift*/XRT detector is an instrument designed to study the X-ray radiation between the 0.2 - 10 keV energy range. XRT utilizes a set of nested, grazing incidence mirrors, known as a Wolter Type I telescope, to achieve high-resolution imaging (Gehrels et al. 2004; Burrows et al. 2005). These mirrors focus X-rays onto a CCD (Charge-Coupled Device) detector, which captures detailed images and data. To minimize noise, the CCD was originally cooled to -100°C using a thermo-electric cooler (TEC). However, after the TEC failure, the temperature is now maintained around -50°C using passive cooling. A thermal door protects the CCD from contamination and the harsh space environment until the instrument is fully operational.

Based on BeppoSAX and RXTE observations, it is expected that a typical X-ray afterglow will have a flux of 0.5–5 crab in the 0.2–10 keV band immediately after the burst (Gehrels et al. 2004). The XRT is therefore required to measure afterglow positions with accuracy better than 5 arcseconds within 100 s of a burst alert from the BAT instrument. The instrument technical characteristics are shown in Tab. 4.1.

The XRT operates in several modes, including imaging, photon-counting, and windowed timing. The photodiode mode (PD), intended for observing very bright sources (up to 60 Crab) without spatial resolution and providing a timing precision of 0.14 ms, was deactivated after a micrometeorite impact on May 27, 2005. This event caused a significant increase in background noise due to hot pixels, which cannot be mitigated during the read-out process in this mode.

The Ultraviolet/Optical Telescope: The ultraviolet and optical telescope (UVOT) is an instrument designed to detect photons in the UV/optical band, between 160 nm and 600 nm.

Telescope:	Wolter I (3.5 m focal length)
Detector:	e2v CCD-22
Detector Format:	600 × 600 pixels
Pixel Size:	40 μm × 40 μm
Readout Modes:	Image (IM) mode Photodiode (PD) mode Windowed Timing (WT) mode Photon-Counting (PC) mode
Pixel Scale:	2.36 arcseconds/pixel
Field of View:	23.6 × 23.6 arcminutes
PSF:	18 arcseconds HPD @ 1.5 keV 22 arcseconds HPD @ 8.1 keV
Position Accuracy:	3 arcseconds
Time Resolution:	0.14 ms, 1.8 ms, or 2.5 s
Energy Range:	0.2 - 10 keV
Energy Resolution:	140 eV @ 5.9 keV (at launch)
Effective Area:	~ 125 cm^2 @ 1.5 keV ~ 20 cm^2 @ 8.1 keV
Sensitivity:	2×10^{-14} erg cm^{-2} s^{-1} in 10^4 seconds
Operation:	Autonomous

Table 4.1: XRT Instrument Characteristics (Burrows et al. 2005).

This telescope adopts a modified Ritchey-Chrétien design with a primary mirror 30 centimeters wide (Gehrels et al. 2004).

UVOT is equipped with a versatile filter wheel that allows for various observation modes. It can capture broad colors of light (photometry) or even split light into its component colors to create a basic spectrum (grism spectra) for particularly bright GRBs. The heart of UVOT lies in its two highly sensitive photon-counting detectors, each paired with its own filter wheel. These filters allow for observations across the ultraviolet and visible spectrum, including dedicated filters for specific ultraviolet wavelengths.

For even wider field-of-view observations, a special magnifier can be used, although it does not work at ultraviolet wavelengths. Light detection is achieved by reading out the light-sensitive chip (CCD) within the detector at a very high rate. A clever technique called centroiding allows UVOT to achieve high resolution despite the physical size of its pixels. This essentially subdivides each pixel into smaller virtual ones, creating a much larger effective detection area. With a fast readout speed and minimal internal noise, UVOT offers exceptional sensitivity, rivaling that of much larger telescopes on the ground, while achieving sub-arcsecond resolution for precise measurements.

4.2.0 Optical telescopes

Optical telescopes are instruments designed to observe light in the visible spectrum (e.g. King 1955; Watson 2004). There are various types of optical telescopes, but the primarily are:

the refracting telescopes, which use lenses to gather and focus light, and reflecting telescopes, which use mirrors for the same purpose. Modern optical telescopes are often equipped with advanced technologies such as adaptive optics, which compensate for atmospheric distortions, and digital sensors that capture high-resolution images.

Ground-based optical observations face challenges from the Earth's atmosphere (see Fig. 3.1), which absorbs and distorts visible light due to water vapor, dust, and atmospheric turbulence, causing stars to twinkle and images to lose sharpness. To mitigate these issues, observatories are typically situated in high, dry, remote locations such as mountain tops and deserts. Despite these measures, space telescopes offer superior optical observations by operating above the atmosphere, eliminating atmospheric absorption and distortion. The Hubble Space Telescope, for instance, is renowned for its sharp, detailed images of the universe.

However, space telescopes are constrained by weight and size due to the requirements of launching them into space, limiting the size of their mirrors and optical systems and complicating maintenance and upgrades. The compromise between ground-based and space telescopes depends on the specific objectives of the observations.

4.2.1 The Pan-STARRS Telescope

The Panoramic Survey Telescope and Rapid Response System (Pan-STARRS) is an innovative astronomical observatory project situated at the Haleakalā Observatory in Hawaii, USA. The primary telescope, known as Pan-STARRS1 or PS1 (Chambers et al. 2016), is a 1.8-meter Ritchey–Chrétien telescope with a remarkable 3° field of view exceptionally large for its size. Originally conceived as a multi-telescope array, Pan-STARRS adopted a single-telescope approach due to the project's complexity and costs. PS1 houses what was the largest digital camera in the world at the time of its construction, capturing images with an astounding 1.4 billion pixels. This is achieved through a focal plane design that features an 8×8 array of 60 closely packed CCDs, known as Orthogonal Transfer Arrays (OTAs), each with a resolution of 4800×4800 pixels. These CCDs are further divided into 64 cells of 600×600 pixels. While the corner positions lack CCDs due to optical system limitations, the telescope's capabilities allow it to record objects down to an apparent magnitude of 22 with exposure times ranging from 30 to 60 seconds.

Panoramic Survey Telescope and Rapid Response System: The Pan-STARRS project is designed to conduct an extensive survey of the sky, focusing on the detection of moving or variable objects (Kaiser et al. 2002, 2010). Equipped with advanced cameras, telescopes, and computing facilities, Pan-STARRS produces highly accurate astrometry and photometry of objects in the northern sky (with a declination $\delta >$ -30°), covering optical and near-infrared bands. The survey operates in five photometric bands g, r, i, z, y spanning wavelengths from approximately 400 nm to 1100 nm (Kaiser et al. 2002, 2010). With its large field of view and short exposure times, Pan-STARRS can image around 6000 square degrees of the sky each night. The system can cover the entire visible sky from Hawaii, approximately 30,000 square degrees, in just 40 hours. This allows the entire sky to be surveyed four times per month. By the end of its initial three-year mission in April 2014, PS1 had imaged the sky 12 times in each of the five filters. The vast amounts of data generated are processed to detect changes in brightness or position, enabling the identification of objects of interest such as asteroids, comets, and transient astronomical events.

4.2.2 The Sloan telescope

The Sloan Telescope, a wide-angle optical instrument located at the Apache Point Observatory in New Mexico, is a cornerstone of the Sloan Digital Sky Survey (SDSS). It features a modified two-corrector Ritchey-Chrétien design with a 2.5-meter f/2.25 primary mirror, a 1.08-meter secondary mirror, a Gascoigne astigmatism corrector, and interchangeable aspheric correctors near the focal plane—one optimized for imaging and the other for spectroscopy (see Gunn et al. 2006, for more details). The telescope's final focal ratio of f/5 is well-suited for both spectroscopy and imaging, matching the requirements of its sophisticated instrumentation. The Sloan Telescope is equipped with a wide-area, multiband CCD camera and a pair of fiber-fed double spectrographs. The camera consists of 30 CCD chips, each with a resolution of 2048 × 2048 pixels, totaling approximately 120 megapixels. It operates across five optical filters (u, g, r, i, z) and is cooled to 190 kelvins to reduce noise, ensuring highly detailed photometric data collection (see Fukugita et al. 1996). This data is crucial for identifying celestial objects such as stars, galaxies, and quasars for further spectroscopic analysis. The multi-object/multi-fiber spectrograph processes thousands of spectral images, capturing flux versus wavelength (3800-9200 $\AA$) data for each object through individual optical fibers positioned on custom aluminum plates for each field of view (Wilson et al. 2019). Notable features of the Sloan Telescope include a wide-angle, low-distortion focal plane, highly precise motion control for time-delay-and-integrate (TDI) imaging, and a unique wind baffle/enclosure design to maximize image quality. First light was achieved in May 1998, and the telescope began regular survey operations in 2000, making it a versatile tool for rapidly switching between imaging and spectroscopic modes to adapt to changing observational conditions.

Sloan Digital Sky Survey: The Sloan Digital Sky Survey (SDSS) is one of the largest multi-spectral imaging and spectroscopic surveys of the sky (York et al. 2000). The project began in 2000, primarily funded by the Alfred P. Sloan Foundation, from which it derives its name, with the aim of mapping the universe by observing a large portion of the sky and collecting data on millions of celestial objects. Its goals include expanding our understanding of the large-scale evolution and structure of the universe, the formation of stars and galaxies, the history of the Milky Way, the nature of supermassive black holes, and the science behind dark energy.

To achieve its objectives, in addition to the scientific innovations of the telescope—such as the camera, spectrograph, wide-angle view, extraordinarily low-distortion focal plane, and extremely accurate drives—SDSS is equipped with a data acquisition system capable of reliably storing incoming data and providing real-time analysis for quality control, focus, and more. Furthermore, SDSS features a data processing system that can automatically and rapidly calibrate observations, identify objects, and measure their properties. This allows for the selection of spectroscopic targets shortly after the imaging data is acquired.

In the fifth phase of the survey, SDSS-V (Kollmeier et al. 2017), SDSS will collect data from ~ 6 million objects during its five-year lifetime (2020-2025). The data release DR18 (Almeida et al. 2023) is the first one for SDSS-V, and it is currently the latest release of the SDSS catalog.

4.2.3 Dark Energy Survey telescopes

The Dark Energy Survey (DES) is an ambitious astronomical project that employed the 4-meter Victor M. Blanco Telescope at the Cerro Tololo Inter-American Observatory in Chile (e.g. The Dark Energy Survey Collaboration 2005; Poppett 2024). Managed by the U.S. National Optical Astronomy Observatory (NOAO), this telescope was central to DES's mission to investigate the dynamics of the universe's expansion and the growth of its large-scale structure. The telescope's powerful observational capabilities were enhanced by the state-of-the-art Dark Energy Camera (DECam), which was specifically designed for DES (e.g. The Dark Energy Survey Collaboration 2005; Wester & Dark Energy Survey Collaboration 2005). DECam offers one of the widest fields of view for ground-based imaging, with a 2.2-degree diameter, and excels in capturing more sensitive images in the red part of the visible spectrum and the near-infrared compared to earlier instruments like those used in the SDSS.

A critical advancement provided by DECam is its enhanced quantum efficiency in the red and near-infrared portions of the spectrum, crucial for observing distant cosmic objects such as Type Ia supernovae and distant galaxies. As the universe expands, the light from these sources is redshifted to longer wavelengths. However, traditional CCDs (charge-coupled devices) face challenges in detecting this light due to silicon's transparency to infrared radiation. DECam's design overcomes this limitation, using CCDs made from high-resistivity silicon that are optimized for astronomical observations. These CCDs feature 15×15-micron pixels, allowing DECam to gather more light per pixel, thus compensating for lower sensitivity and ensuring high-quality data capture.

DECam's focal plane is composed of an array of 62 CCDs, each with 2048×4096 back-illuminated pixels, totaling 520 megapixels, plus an additional array of 12 CCDs for guiding, alignment, and focusing, contributing to a total of 570 megapixels. The focal plane is maintained at a cryogenic temperature of 173 K using liquid nitrogen, reducing thermal noise and ensuring high-quality images. The entire setup is kept under a vacuum of 1.3×10^{-9} atm to prevent condensation on the sensors.

Dark Energy Survey: The Dark Energy Survey (DES), officially launched in August 2013, was an international collaboration aimed at probing the mysteries of dark energy and the expansion of the universe. Over the course of its primary mission, which concluded in 2019, DES observed approximately 300 million galaxies across 758 nights. The survey focused on a vast region of the southern sky, covering 5000 square degrees. DES employed both visible and near-infrared bands, using filters in u, g, r, i, z, and Y bands similar to those used in the Sloan Digital Sky Survey (SDSS). This setup allowed DES to detect photometric redshifts up to $z \approx 1$, making it possible to study galaxies at varying distances and contributing significantly to our understanding of the cosmos (e.g. The Dark Energy Survey Collaboration 2005). The typical exposure cycle for each image took about two minutes: 90 seconds for exposure and 30 seconds for camera data readout and telescope repositioning. DES achieved a remarkable depth of 24th magnitude in the i band across its entire survey area, enabling the detection of extremely faint objects. Public access to all DES images is available through the NOIRLab Astro Data archives[1].

4.2.4 SuperCOSMOS Sky Survey telescopes

The SuperCOSMOS Sky Survey (SSS) is a comprehensive astronomical project aimed at digitizing and cataloging the vast photographic records of the night sky collected over several decades (Hambly et al. 2001). Conducted using the SuperCOSMOS microdensitometer at the Royal Observatory in Edinburgh, this survey meticulously scanned photographic plates from several major sky surveys, including the UK Schmidt Telescope (UKST) in Australia, the Palomar Observatory Sky Survey (POSS), and the ESO Schmidt Telescope in Chile. The SuperCOSMOS microdensitometer operates with a precision of 10 microns, producing images with a resolution of 0.67 arcseconds per pixel. This level of detail allows for the study of fine structures and faint objects that might have been overlooked in the original photographic plates. The data collection from these plates is instrumental in digitizing millions of individual stars, galaxies, and other celestial objects, thus preserving and extending the usefulness of decades-old astronomical data.

SuperCOSMOS Sky Survey: The primary goal of the SSS is to create a digital archive of these records, making high-resolution images of the sky accessible to astronomers. The survey spans a broad spectral range, including data from blue, red, and infrared bands, which enhances the ability to classify and analyze celestial objects based on their colors and brightness (Hambly et al. 2001). This archive covers approximately 20,000 square degrees of the sky, including both the northern and southern hemispheres. By digitizing millions of celestial objects, the SSS has provided invaluable data for a wide range of astronomical studies, from investigating stellar populations and the structure of our galaxy to examining the distribution of galaxies across the universe.

The survey also generates a variety of derived data products, such as object catalogs and astrometric measurements, which are essential for tasks like tracking the proper motion of stars over time. These resources allow for cross-referencing with other astronomical datasets and have been instrumental in the discovery of new celestial objects and in refining our understanding of the Milky Way and extragalactic astronomy. All data from the SuperCOSMOS Sky Survey is publicly accessible[2] and serves as a key resource for both professional astronomers and amateur stargazers alike. The survey's contributions have had a lasting impact on the field of astronomy, providing a bridge between the rich historical data of photographic plates and the modern digital era of astronomical research.

---

[1] https://datalab.noirlab.edu/sia.php

[2] http://www-wfau.roe.ac.uk/sss/halpha/hapixel.html

4.2.5 Gaia satellite

Gaia is a key mission within the European Space Agency's (ESA) scientific program, designed to create a detailed three-dimensional map of our galaxy, revealing its composition, formation, and evolution. Launched on December 19, 2013, Gaia is a continuation of the Hipparcos mission and is part of the Horizon 2000 scientific program. The mission aims to compile a catalog of approximately one billion stars, down to a magnitude of 20, with its primary objective being the measurement of astrometric data with unprecedented precision (e.g. see Perryman 2005).

Throughout its operational lifetime, Gaia will repeatedly measure the exact positions of these stars at different times, enabling the calculation of their proper motions with remarkable accuracy. For stars of magnitude 15, Gaia achieves a precision of around 20 microarcseconds, while for those of magnitude 20, the precision is within 200 microarcseconds (e.g. see Perryman 2005). By exploiting the parallax effect, Gaia will also determine the distances to these stars, with the highest accuracy achieved for the closest and brightest stars.

In addition to its astrometric capabilities, Gaia will perform photometric measurements across multiple wavelengths at different time intervals, which will allow it to determine the radial velocities of the stars. This comprehensive data set will enable Gaia to construct an exceptionally precise 3D map of the nearby portion of our Galaxy and a less detailed but still valuable map of more distant regions, using the brightest and most visible stars.

The mission will also measure a vast number of quasars, exoplanets, and solar system objects. The spacecraft's detector, a 1-gigapixel camera, is the largest ever launched into space, consisting of 106 CCDs arranged in a mosaic. Each CCD has 4500 × 1966 pixels, allowing Gaia to capture the fine details necessary for its high-precision measurements (e.g. see Perryman 2005).

4.3.0 Radio telescopes

A radio telescope is a type of directional radio antenna (either a single large parabolic antenna or an array of connected antennas) used in radio astronomy to detect and collect data from radio sources in space (e.g. Marr et al. 2015). The radio band is the portion of the electromagnetic spectrum that spans from a few Hz to thousands of GHz ($\sim$ 0.1 mm to over 100,000 km). Given the wavelengths to be detected and the weak nature of radio signals (necessitating a large collecting area and high resolving power), the diameter of the antenna(s) used is typically very large. The size of these observatories is feasible due to the low atmospheric opacity in this band (see Fig. 3.1), which permits the placement of antennas on the ground (even though production costs must always be taken into account).

To further increase the size of these observatories, radio telescopes are usually composed of an array of antennas. These act as a single large "virtual" antenna through the method of radio interferometry, which was invented by Martin Ryle and Antony Hewish (who won the Nobel Prize in 1974 for their work in radio interferometry) (e.g. Ryle et al. 1959; Ryle & Hewish 1960).

Interferometry is a key technique in radio astronomy (e.g. Hariharan 2007), leveraging the interference of electromagnetic waves to achieve high resolution by coherently combining data from widely spaced astronomical observatories. The distance between these observatories can range from meters to thousands of kilometers, directly impacting the resulting resolution. This approach circumvents the technical challenges of building large-aperture radio telescopes. Interferometry is employed across both optical and radio telescopes, offering resolution equivalent to a single mirror or telescope with an aperture corresponding to the distance between combined instruments. The contrast of interference fringes provides information on the observed object's size or angular separation between objects, such as star-planet systems. The angular resolution achievable by a telescope is determined by its diffraction limit, proportional to its diameter. Each fundamental unit in astronomical interferometry consists of a telescope pair, forming a baseline in the u,v space, where correlated signals are analyzed to reconstruct detailed radio source images.

4.3.1 Very Large Array

The Karl G. Jansky Very Large Array (VLA) is a centimeter-wavelength radio astronomy observatory located in New Mexico, USA (Thompson et al. 1980). It operates across a frequency range from $\sim$ 100 MHz to 50 GHz. The VLA consists of twenty-eight 25-meter radio telescopes arranged in a Y-shaped array, with twenty-seven telescopes operational at any given time while one undergoes maintenance. Each of the telescopes is mounted on double parallel railroad tracks, allowing the configuration of the array's radius and density to be adjusted, thereby optimizing between angular resolution (between 0.2 and 0.04 arcseconds) and surface brightness sensitivity.

The VLA is strategically located on a vast, flat plain in a region 2124 meters above sea level, far from major cities. This elevated and dry location is critical to the VLA's success, as it reduces the background noise caused by water molecules in the air. Humidity is, in fact, the primary source of noise for radio telescopes, as they operate in the same frequency range as radio waves emitted by water. Additionally, the region is surrounded by mountains, which act as a natural barrier against radio interference that could be generated by cities hundreds of miles away.

Very Large Array Sky Survey: On September 7, 2017, VLA started a survey of the northern sky (δ > -40°) in the S band (2 GHz < ν < 4 GHz) (Lacy et al. 2020). This is the third survey project of the facility, after the the NRAO VLA Sky Survey (NVSS) and Faint Images of the Radio Sky at Twenty-Centimeters (FIRST) in 1992, and it has the highest angular resolution (2.5") of any all-sky radio continuum survey to date. VLASS is divided in three phases, to be completed by the end of 2024. Its combined (3 epoch) sensitivity is 69 μJy RMS. In the first version of the catalog (Gordon et al. 2021) $\sim 2 \times 10^6$ sources were collected.

4.3.2 Australian Square Kilometre Array Pathfinder

The Australian Square Kilometre Array Pathfinder (ASKAP) is a cutting-edge radio telescope array located in the Mid West region of Western Australia, specifically in the radio-quiet Murchison district (Johnston et al. 2007, 2008; DeBoer et al. 2009; Hotan et al. 2021). This location, characterized by its low population density and minimal radio interference, is protected by both the Australian Commonwealth and Western Australia State Government through stringent regulatory measures. ASKAP consists of a two-dimensional array of 36 dish antennas, each 12 meters in diameter, working together as a single astronomical interferometer(Johnston et al. 2007). The baselines of this array range from 22 meters to 6 kilometers, providing a total collecting area of approximately 4000 m^2. Operating between 700 MHz and 1800 MHz, ASKAP excels in producing high-resolution snapshot images of 10 arcseconds.

ASKAP was designed as a synoptic telescope with a wide field-of-view, large spectral bandwidth, fast survey speed, and a significant number of simultaneous baselines. One of its most notable technical achievements is the advanced Phased Array Feed (PAF) receivers installed on its antennas. Each PAF includes 188 individual receivers, significantly extending the field of view of a 12-meter dish to 30 square degrees. The development and construction of these PAFs were particularly challenging, as they represented a novel application in radio astronomy and involved managing the largest data rate encountered by a radio telescope to date. This innovative technology positions ASKAP at the forefront of astronomical research, enabling it to explore cosmic phenomena with unprecedented detail and speed.

Rapid ASKAP Continuum Survey: The Rapid ASKAP Continuum Survey (RACS) is the first extensive sky survey utilizing the ASKAP telescope(McConnell et al. 2020). RACS revolutionizes survey science by enabling astronomers to map the entire sky in weeks instead of years, while offering improved resolution and sensitivity over earlier surveys at comparable wavelengths. As a precursor to the comprehensive, multi-year surveys planned for ASKAP, RACS covers the sky from declinations of -90° to +47°, spanning the full ASKAP band of 700 to 1800 MHz. The survey is divided into three frequency bands: RACS-low at 887.5 MHz, RACS-mid at 1367.5 MHz, and RACS-high at 1655.5 MHz, each with a bandwidth of 288 MHz. The angular resolution is approximately 15 arcseconds, and the sensitivity is around 300 μJy/beam. The complete catalogue (RACS-low, RACS-mid, and RACS-high) is expected to include about three million source components, complete with spectral index and polarization information.

RACS Data Release 1 (RACS DR1) is already available to the public, encompassing initial observations for RACS-low (central frequency of 887.5 MHz) within the declination range of -90° to +41° (Hale et al. 2021). This initial catalog contains approximately 2 million source components, marking a significant milestone in the ASKAP's survey capabilities.

4.3.3 Australian Telescope Compact Array

The Australia Telescope Compact Array (ATCA) is a prominent radio telescope located at the Paul Wild Observatory near Narrabri on Gomeroi Country, at an elevation of 237 meters above sea level (Frater et al. 1992). It comprises six 22-meter diameter antennas designed to observe the radio sky across a wide frequency range from 1.1 GHz to 105 GHz. Five of these antennas are mobile, able to be positioned along railway tracks spanning 44 fixed stations, while the sixth antenna remains fixed 3 kilometers west of the main east-west track, allowing for various observational configurations. The longest possible baseline for these configurations is 6 kilometers.

ATCA operates with 17 predefined configurations, with a subset offered each semester, optimized for minimal redundancy and maximum coverage during a 12-hour observation period. As an earth-rotation aperture synthesis radio interferometer, ATCA operates by using pairs of antennas that combine their time-delayed signals to derive visibility. This method, based on the van Cittert–Zernike theorem, allows the Fourier transformation of the spatial coherence function to produce an image with the same angular resolution as a single antenna with a diameter equal to the largest spacing, albeit with reduced sensitivity due to the smaller collecting area.

The telescope's imaging capabilities and component resolution within the field of view are assessed by plotting the baseline vectors' tracks as the Earth rotates, a plot known as the (u,v)-coverage. Full (u,v)-coverage requires observations in multiple configurations over twelve hours each, but most programs can be completed successfully with less. Sophisticated off-line processing techniques optimize single configuration imaging, ensuring reasonable image quality with minimal missing (u,v) coverage. Typically, using one to four configurations effectively balances dynamic range, (u,v) coverage, and time.

ATCA is most effective for observing southern objects at high angular resolutions. Full (u,v)-coverage is unattainable north of Declination -24°, highly elongated near Declination zero, and inaccessible for sources north of Declination +48° due to the telescope's +12° elevation limit. For lower angular resolutions, north-south and hybrid arrays improve (u,v)-coverage for equatorial sources, although the maximum north-south baseline is 214 meters.

5

Data analysis

5.1.0 The *Swift*/XRT data products generator

The *Swift*-XRT data products generator is an online tool provided by the *Swift* consortium that allows users to create custom data products from observations made by the *Swift*-XRT detector.

To use the generator, users access the tool for building XRT products[1] on the *Swift* Science Data Center website, select specific observations from the *Swift*-XRT archive by entering coordinates, target names, or observation IDs, and specify the desired parameters such as time intervals, energy bands, and regions of interest. Once the request is submitted, the tool processes the data through an automated pipeline and produces various products, including high-resolution images of the entire field of view or specific areas, source detection, source position, light curves tracking the brightness of a source over time, detailed spectra of the energy distribution of X-ray emissions, exposure maps showing the effective exposure time across the FOV, and event lists providing detailed information about detected X-ray events.

5.1.1 Source detection

The source detection process employs a variety of sophisticated techniques to ensure accurate identification and characterization of X-ray sources (Evans et al. 2020). The procedure begins with background estimation, a critical step where the background noise is assessed to differentiate between actual X-ray sources and random noise. This is achieved through adaptive smoothing combined with source masking, where the background is smoothed to reduce fluctuations, and known sources are masked out to prevent them from influencing the background estimate. The minimum smoothing scale is set to 15 pixels to balance between smooth background and maintaining spatial resolution.

Exposure maps are generated for each observation to account for variations in exposure time across the FOV. These maps help correct for areas with differing amounts of exposure, ensuring that the detected source intensities are accurately measured regardless of their position in the FOV.

---

[1] https://www.swift.ac.uk/user_objects/

For initial source detection, a sliding cell detection algorithm is employed. This algorithm scans the entire field of view using a detection cell, typically 20 pixels in size, to count the X-ray photons. It calculates the signal-to-noise ratio (SNR) by comparing the counts within the detection cell to the background estimate from the surrounding regions. A minimum SNR of 3 is required to identify a source, meaning the source signal must be at least three times stronger than the background noise (Evans et al. 2020).

Once potential sources are identified, region sizes for signal extraction are defined. Circular extraction regions are used for aperture photometry, usually set to a radius that encompasses 90% of the PSF at the observed energy. The PSF modeling accounts for variations with energy and off-axis angle, calibrated using in-flight data, which is crucial for accurate source localization and characterization.

Effective area corrections are derived from calibration data to account for the instrument's variations with energy, off-axis angle, and detector position. These corrections ensure that the measured source intensities are accurate and comparable across different observations and positions within the FOV.

In addition to analyzing individual observations, the process can involve stacking multiple observations. Image stacking involves aligning individual snapshot images on a common sky coordinate frame and co-adding them, along with their corresponding exposure maps. This method enhances the signal for faint sources by effectively increasing the total exposure time, allowing for the detection of weaker sources that might not be visible in single observations.

Pile-up, a phenomenon where multiple X-ray photons hit the detector within the same time frame, leading to distorted or merged signals, is addressed by identifying and flagging sources affected by pile-up. For flux calculations, the core of the PSF is excluded, and an annular region is used instead. The pile-up correction algorithm models the redistribution of photon energies to mitigate spectral distortions caused by pile-up (Evans et al. 2020).

The detailed steps of the detection process include preprocessing cleaned photon-counting mode data to remove artifacts and noise, initial candidate identification using the sliding cell algorithm, source verification through maximum likelihood fitting that incorporates the PSF model, and refinement with aperture photometry and adaptive background smoothing. Finally, the catalog is compiled with verified source positions, fluxes, and other parameters.

5.1.2 Source position

The source positions can be categorized into three distinct types based on their derivation methods and associated uncertainties (Goad et al. 2007; Evans et al. 2009). The standard position utilizes astrometry from *Swift*'s star-trackers, with source detection and localization methods akin to those in the 1SXPS catalog. This method provides a systematic astrometric uncertainty of 3.5" at 90% confidence, and additional options are available for refining the position. The enhanced position involves astrometry derived from field stars in UVOT images, leveraging the UVOT as a star tracker rather than for direct source detection. This approach offers a more precise systematic astrometric uncertainty of 1.4" at 90% confidence, but requires that the X-ray source be sufficiently bright for detection during individual UVOT exposures. Lastly, the astrometric position starts with the detection and localization of sources in XRT images, then aligns these with the 2MASS catalog. This method initially defaults to a standard position but can be enhanced by using all available data for improved accuracy, as it does not have a systematic error but depends on the number of X-ray sources used for alignment. Each type of position offers different trade-offs between systematic and statistical uncertainties, allowing for tailored precision based on observational constraints and requirements.

5.1.3 Spectral analysis

Spectral analysis of *Swift*/XRT data involves a series of detailed steps to ensure accurate interpretation of X-ray observations (see Evans et al. 2020).

Before diving into these steps, it is important to understand that *Swift*/XRT operates in two primary modes: Photon Counting (PC) and Windowed Timing (WT), each tailored to different observing conditions and scientific objectives.

PC mode is designed for high-resolution spectroscopy and is optimal for sources with relatively low count rates. In this mode, each X-ray photon is individually recorded, allowing for precise positional and energy information, which yields high spectral and spatial resolution. However, this mode is susceptible to pile-up effects when the source count rate exceeds approximately 0.6 counts per second. Pile-up occurs when multiple photons hit the same detector pixel within a short time frame, leading to overlapping events that distort the measured spectrum and compromise the accuracy of the analysis.

In contrast, WT mode is optimized for sources with higher count rates. It sacrifices spatial resolution to prioritize timing information by compressing two-dimensional position data into a one-dimensional format. In this mode, pile-up sensitivity is reduced due to the shorter readout interval (1.79 ms, compared to 2.5 s in PC mode), enabling WT mode to handle count rates of up to approximately 150 counts per second without significant distortion. While this reduces spatial detail relative to PC mode, WT mode is particularly effective for bright sources or rapidly variable targets where precise timing is crucial.

Now that we have reviewed the two modes in which *Swift*/XRT operates, we can explore how the spectrum is extracted for analysis. The process begins with the extraction of source and background counts from the event file. The extraction region for the source can have any shape but must be centered on the source to ensure accurate data collection. Typically, circular regions with a radius of 20 pixels are used for less bright targets, or 30 pixels for brighter ones. It is worth to note that circular regions can be used for both WT and PC modes. In cases where the source is affected by pile-up, the central region of the source must be excluded. In this case, an annular region is used, with the inner radius of the ring varying depending on the source intensity to limit the effects of pile-up (see Evans et al. 2020, for details).

Regarding the background spectrum, for PC mode, it is typically derived from a circular annulus surrounding the source, with an inner radius of 60 pixels (142 arcseconds) and an outer radius of 110 pixels (260 arcseconds). If this region extends beyond the detector's edge, it is adjusted accordingly while maintaining the central region fixed on the source. It is crucial that the background selection region does not contain any background sources. If evidence of sources is detected, they must be excluded by selecting an appropriate region that is distant from the source of interest. In WT mode, the background is extracted from the entire window, excluding a 120-pixel (283 arcseconds) wide box centered on the source (see Evans et al. 2020, for details). Similar care must be taken to ensure that the background region does not include any background sources.

To accurately interpret the data and account for instrumental effects, several additional steps are required. An Ancillary Response File (ARF) is generated to model the telescope's response to X-rays, correcting for factors such as detector sensitivity and effective area. Exposure maps are also created to correct for the loss of flux caused by some CCD pixels being non-functional or damaged, such as those affected by the micrometeoroid impact in May 2005. These maps adjust the observed flux for regions of the detector that are not used for data collection, ensuring that the recorded data accurately represents the source's emission. Another critical component is the Redistribution Matrix File (RMF), which describes how the telescope redistributes X-ray photons across different energy channels of the detector. The RMF accounts for the instrumental effects on the measured energy of the photons, allowing for precise calibration of the spectral data (Evans et al. 2020). Calibration data from the CALDB database are then applied to correct for various other instrumental effects, further ensuring that the spectral analysis accurately reflects the true characteristics of the observed source.

Once the spectral and calibration files are prepared, they are analyzed using the HeaSoft FTOOLS XSPEC, a software package for spectral fitting. To make the spectrum suitable for use in XSPEC, it is necessary to pass it through the FTOOL GRPPHA. The GRPPHA tool is used to group or bin the spectral data, consolidating counts into larger energy bins to improve the signal-to-noise ratio and make the data compatible with spectral fitting procedures. It takes as input the spectral and calibration files and gives as output a binned spectrum that includes counts, associated errors, calibration information, and details of the energy range, all formatted for advanced spectral analysis.

Various spectral models, such as power laws, blackbody radiation, thermal bremsstrahlung, and cyclotron models [bremsstrahlung and cyclotron are part of the Astrophysical Plasma Emission Code (APEC) model], are employed to fit the data. The fitting is performed within the 0.3-10 keV energy range using maximum likelihood statistics and the C-statistic. Galactic and intrinsic absorption are modeled using the PHABS component with abundances fixed according to Anders & Grevesse (1989). Finally, the observed and unabsorbed 0.3-10 keV fluxes are calculated to convert count rates into physical flux units. Throughout the analysis, visual inspection and statistical checks are employed to ensure the accuracy and reliability of the results.

5.2.0 Optical spectroscopy

Optical spectroscopy is a powerful analytical technique used to study the interaction of light with matter. It involves measuring and analyzing the light spectrum emitted, absorbed, or scattered by a sample, providing essential information about the sample's composition, structure, and physical properties. By dispersing light into its constituent wavelengths (or colors) using a prism or diffraction grating, optical spectroscopy enables the identification of specific wavelengths corresponding to electronic transitions within atoms or molecules. These transitions create distinct spectral lines or bands, which act as unique fingerprints for different elements or compounds.

As previously mentioned, optical spectroscopy is a fundamental tool for studying AGN and classifying UGSs. Optical spectra reveal crucial information about the structures surrounding the central SMBH, such as the BLR and NLR. The BLR and NLR are known to emit broad lines (with an equivalent width, $EW > 5\AA$) and narrow lines ($EW < 5\AA$), respectively, with wavelengths that fall within the optical band. Additionally, optical spectroscopy allows us to study the host galaxy, which can be identified in optical spectra by characteristic absorption lines typical of its stellar population. Depending on the ratio between AGN emission and that of the host galaxy, these absorption lines may be more or less prominent.

However, the role of optical spectroscopy in AGN studies extends beyond these aspects. Given the significant distances of AGN, they typically exhibit substantial redshifts. This redshift is observed in the spectra as the emission and absorption lines shift toward longer wavelengths. By identifying these lines in the optical spectra and measuring the shift in wavelength from their known laboratory values, we can accurately determine the distance to these objects. In the next paragraph, we will explore the techniques used for analyzing optical spectra of AGN in more detail.

5.2.1 Spectral analysis for AGNs

Spectral analysis begins with the identification of lines or line structures in emission or absorption. We know that the host galaxy typically exhibits absorption lines such as the calcium doublet, Ca II (3934 $\AA$, 3968 $\AA$), the G-band[2] (4305 $\AA$), Mg I (5175 $\AA$), and Na I (5893 $\AA$). As for AGN, we know that through the BLR and NLR, they produce emission lines such as: Hα (6563 $\AA$), Hβ (4861 $\AA$), [O II] (3727 $\AA$), the [O III] doublet (4959 $\AA$, 5007 $\AA$), and the [N II] doublet (6548 $\AA$, 6583 $\AA$). The effect of redshift is to shift the lines toward longer wavelengths, such that:

$$\lambda_{obs} = \lambda_{em}(1 + z) \tag{5.1}$$

where λ_{obs} is the observed line wavelength, λ_{em} is the emitted line wavelength, and z is the redshift.

---

[2] The G-band is an absorption feature in the optical spectrum of stars and galaxies, particularly noticeable in the spectra of older, cooler and low-mass stars (e.g., G-type and cooler), such as those found in the host galaxies of AGN. It is primarily due to the absorption by molecular CH (methylidyne) in the atmospheres of these stars.

However, within the optical spectrum of an AGN, there can also be other emission and absorption lines originating from sources distinct from the AGN and the host galaxy. One such example is telluric lines. Telluric lines are absorption features produced by Earth's atmosphere, specifically by molecules and atoms that absorb certain wavelengths of light. Common examples include the oxygen lines (e.g., O I at 5577 Å and 6300 Å), water vapor lines (e.g., H_2O in the near-infrared), and carbon dioxide bands (e.g., CO_2 in the infrared). Another example is lines originating from our Galaxy, which arise from components of the interstellar medium, such as the sodium D-lines (e.g., Na I D at 5890 Å and 5896 Å), the calcium H and K lines (e.g., Ca II H at 3968 Å and K at 3934 Å), and the magnesium triplet (e.g., Mg I at 5175 Å).

These lines can interfere with the analysis of astronomical spectra if not correctly subtracted during data reduction, potentially adding unwanted features or altering the observed intensities of the AGN and host galaxy lines. Fortunately, these lines are not affected by redshift and thus are easily recognizable in the spectrum, as they appear at fixed wavelengths.

Once a feature (or presumed feature) in the spectrum is identified, it is matched to a known laboratory line. By measuring the shift between the observed wavelength and the laboratory wavelength, the redshift is estimated and checked for compatibility with all the "non-spurious" features in the spectrum. If the redshift is consistent with all the lines, the distance to the observed object has been determined. If it is not consistent, the association between the feature and the laboratory line is incorrect and needs to be reassessed. In the case of line structures, the task is simpler as these are more easily recognized in the spectrum. From the broadening of the structure and the shift to longer wavelengths, the redshift can be determined, but it must still be verified against all other features present in the spectrum.

However, in some cases, it is not possible to identify spectral lines and therefore determine the redshift, as in the case of BLL objects where features are weak or absent, or when the spectrum is too noisy. In the latter case, there is little that can be done. For the former, it is sometimes possible to establish lower limits on the redshift. Occasionally, cold gas clouds lie between us and the BLL, leading to the appearance of absorption lines [such as Mg II (2800 $\AA$)] in the spectrum, which will have a redshift less than or equal to that of the BLL or the observed object. This allows us to set a lower limit on z. Another method for establishing a lower limit on z is based on the minimum equivalent width (EW_{min}, e.g. Sbarufatti et al. 2006).

The minimum equivalent width (EW_{min}) is a critical parameter used to estimate the lowest detectable strength of spectral lines within a given spectrum. It represents the smallest equivalent width that can be reliably measured given the noise level in the data. To determine EW_{min}, the spectrum is analyzed by calculating twice the root mean square (rms) of the equivalent width distribution across the normalized spectrum, where the spectrum has been normalized by dividing it by the best-fit power-law model of the continuum. The spectrum is typically divided into bins, with each bin being carefully chosen to be small enough to test individual portions of the spectrum for weak features, yet large enough to ensure that each segment contains a statistically significant amount of data. A typical bin width might be around 30 $\AA$, balancing the need for detailed analysis with the requirement for reliable measurements. The rms of the equivalent width distribution is then calculated within each bin. This rms value, multiplied by two, gives the

EW_{min}, reflecting the faintest possible spectral feature that could be distinguished above the noise. If no spectral lines exceed this threshold, the spectrum is classified as featureless or lineless. The lower limit on the redshift is then derived by assuming the characteristics of the host galaxy, often using a model of a typical elliptical galaxy (e.g. Urry et al. 2000; Sbarufatti et al. 2005). By placing the object on a nucleus-to-host flux ratio versus redshift diagram, the minimum redshift is determined based on the point where the spectral features of the host galaxy would fall below the EW_{min} threshold, thus remaining undetectable. This approach allows for a conservative estimate of the redshift, even in cases where the spectrum is devoid of prominent lines.

6

Search for the multi-wavelength counterparts of extragalactic UGSs

Results in short

This chapter addresses the search for lower-energy counterparts (X-ray, optical, and radio) of the extragalactic UGSs in the 4FGL-DR4 *Fermi* catalog (Ballet et al. 2023), which have also been observed by the *Neil Gehrels Swift Observatory* (Gehrels et al. 2004). The choice to exclude sources in the region of the Galactic plane is motivated by the primary interest in finding new AGNs (in particular new blazars), as sources at high Galactic latitudes are more likely to be extragalactic. Moreover, as described in chapter 4, for more than 10 years, the *Swift* satellite has been involved in a campaign dedicated to observing UGSs (Stroh & Falcone 2013; Falcone et al. 2014) and all data are available on the public archive[1].

The search for counterparts begins in the X-ray band, with the analysis of Swift/XRT data covering the positions of the UGSs. This allows us to reduce the degeneracy in the optical counterpart determination, as the number of X-ray sources in the typical *Fermi* error boxes (the average 99.7% containment radius is ~ 6 arcminutes, estimated over the entire range of LAT, see chapter 3 for details) is significantly smaller than in the optical band or even at lower energies. Furthermore, it also narrows the search region for identifying potential radio and optical counterparts, given that the angular resolution of the *Swift*/XRT detector is a few arcsec (see chapter 4 for details). Subsequently, starting from the X-ray positions and error boxes, we look for radio and optical counterparts, using several optical and radio catalogs.

Out of the 1284 extragalactic UGSs (with $|b| > 10°$) in the 4FGL-DR4 catalog, 714 were observed at least once by *Swift*/XRT. We detected, with a significance of $\geq 3\sigma$, at least one X-ray source within the *Fermi* error box for 274 of these γ-ray emitters. Among these, 193 UGSs have a single potential X-ray counterpart (referred to as UGS1), while 81 have multiple potential X-ray counterparts within the Fermi error box (referred to as UGS2). Of the UGS2, 54 have two X-ray counterparts, 11 have three, and the remaining 16 have more than three. Each UGS1 has an optical counterpart, and 113 also have a radio counterpart. To validate the potential counterparts, we compared their flux properties with those of the primary classes of γ-ray emitters identified by *Fermi*.

The work presented in this chapter is an integral part of the paper titled **Search for the multi-wavelength counterparts to extragalactic unassociated *Fermi* γ-ray sources**, submitted to the journal Astronomy & Astrophysics and recommended by the referee for the publication after moderate revisions.

6.1.0 Introduction

In 2023, the *Fermi* collaboration released the fourth catalog (4FGL-DR4), documenting 7195 sources detected over 14 years by the *Large Area Telescope* (LAT). Of these, 4765 sources have been identified, highlighting the dominance of extragalactic sources, particularly AGNs, with blazars being the most prevalent at 3934 objects.

About 30% of the sources in the 4FGL-DR4 catalog are classified as unassociated gamma-ray sources (UGSs), lacking known counterparts at lower energies. These UGSs represent a significant component of the high-energy sky, potentially hiding new blazars or AGN of various

---

[1] https://www.swift.ac.uk/swift_portal/

classes. Being generally faint objects (on average UGSs have lower γ-ray fluxes, $\sim 5.3 \times 10^{-12}$ erg cm^{-2} s^{-1}, with respect to associated AGN sources, $\sim 1.6 \times 10^{-11}$ erg cm^{-2} s^{-1}, in the 100 MeV to 100 GeV range), with lower γ-ray fluxes compared to associated AGN sources, UGSs might indicate higher redshift AGN populations or lower luminosity sources. Their investigation is crucial for population studies, the development of physical models, and the interpretation of cosmic evolution regarding γ-ray sources (Ajello et al. 2014; Ghisellini et al. 2017).

Identifying UGS counterparts presents challenges due to the large positional errors from *Fermi*, which arise from limited photon statistics and the angular resolution of the LAT detector. This results in the presence of tens to hundreds of potential low-energy candidate counterparts (e.g., in the optical and radio bands) within typical *Fermi* error boxes. Consequently, attributing γ-ray emission to a specific source among these candidates can be quite challenging.

This chapter focuses on UGSs from the 4FGL-DR4 catalog located outside the Galactic plane ($|b| > 10°$) that have also been observed by the *Neil Gehrels Swift Observatory* (Gehrels et al. 2004). The exclusion of sources in the Galactic plane is motivated by a primary interest in AGNs, as sources at high Galactic latitudes are more likely to be extragalactic. For over ten years, the *Swift* satellite has been involved in a campaign dedicated to observing UGSs, with all data available in a public archive[2].

The aim of the chapter is to find X-ray counterparts for a sample of UGSs. This approach reduces uncertainty in identifying optical counterparts, as the number of X-ray sources in typical *Fermi* error boxes is significantly smaller than in the optical band or at lower energies. Additionally, it narrows the search for potential radio and optical counterparts, given the better angular resolution of the *Swift*/XRT detector.

The chapter is structured as follows: Sec. 6.2 outlines the X-ray data reduction and analysis, automated through the use of a pipeline developed by our group; in Sec. 6.3 the search for the multi-wavelength counterparts is described; results are discussed in Sec. 6.4; Sec. 6.5 contains the discussion; while Sec. 6.6 contains the conclusions.

6.2.0 X-ray detection pipeline, data reduction and analysis

The number of UGSs in the 4FGL-DR4 catalog is 2430, of which 1284 are located outside of the Galactic plane region (with $|b| > 10°$). Out of those 1284 sources, 714 are covered by at least one *Swift*/XRT observation.

Given the large number of UGSs with available X-ray data, we developed a pipeline to reduce and automatize the data reduction and analysis process. The pipeline is Python based, performing source detection and spectral analysis on all of the available XRT observations overlapping the UGS positions. The HeaSoft FTOOLS version 6.30.1 (Nasa High Energy Astrophysics Science Archive Research Center (Heasarc) 2014) package was used for analysis. Using the data

---

[2] https://www.swift.ac.uk/swift_portal/

reduction tool provided by the UK *Swift* Science Data Centre[3] (Evans et al. 2020), for each UGS the pipeline takes the UGS position and performs the following:

- look for all the available Swift-XRT observations that cover the UGS positions within a cone search radius of 20 arcminutes;
- create a 0.3–10 keV *Swift*/XRT stacked image;
- run a source-detection algorithm (with an initial 1.5 σ significance cutoff);
- determine the position (with associated uncertainty) of any detected X-ray source within the *Swift*/XRT field of view (23.6' × 23.6'), around the position of the γ-ray emitter. If data acquired with the UV and Optical Telescope (UVOT) on board of Swift are available, it provides the enhanced source position corrected for astrometry (Goad et al. 2007);
- generate a list of X-ray detections (to which an ID is assigned), listing the position and the Signal-to-Noise Ratio (SNR) for each X-ray detected source.
- select detected sources that are within the 3σ *Fermi* error region of UGS sources with a SNR ≥ 3[4],
- for each of the selected X-ray detections, an average spectrum is produced. Circular (annular) extraction regions are used to extract the source (background) events, as described in Evans et al. (2009);
- each spectrum is grouped with the HeaSoft FTOOLS tool GRPPHA in order to accumulate at least 8 counts per energy bin. This choice is a compromise to maximize the degrees of freedom of the fit and the significance of the points, given the small number of collected counts for each X-ray source (the median value is $\sim$ 40 photons). Additionally, this grouping allows the use of χ^2 statistics for the analysis for most of the analysed spectra,
- finally, the 0.3 – 10 keV X-ray spectral analysis is performed using XSPEC version 12.12.1 (Arnaud 1996, 2022).

Since blazars are the dominant population in the 4FGL-DR4 catalog and are characterised by a non-thermal X-ray emission, we model the spectra of each detected X-ray source with an absorbed power law. In particular, we fit the data with the model TBABS*POWER-LAW in XSPEC, where TBABS describes the column density (nH) of the interstellar and intergalactic absorption, adopting the abundance set from Wilms et al. (2000). Given the small number of detected counts per source, the *nH* parameter was fixed to the Galactic line-of-sight value. Furthermore, in order to have a rough estimate of the source flux, we note that the power-law photon index was fixed to 2 for spectra that had no more than 2 or 3 spectral points. The photon index of 2 was determined as a reasonable average of the typical blazar slope (e.g. Padovani et al. 2017).

---

[3] https://www.swift.ac.uk/user_objects/

[4] The two axes of the 4FGL-DR4 error ellipses at a 95% confidence level have been increased by 50% in order to yield ~99% confidence level

6.3.0 Search for multi-wavelength counterparts

Taking the position of X-ray sources found within the UGS error ellipses, we search for their possible radio and optical counterparts. To do so, we take the ~99% confidence level error boxes on the X-ray positions (which is on average ~ 4 arcsec).

In the optical, we search for counterparts using the Sloan Digital Sky Survey (SDSS, Ahumada et al. 2020), the Panoramic Survey Telescope and Rapid Response System (PanSTARRS, Chambers et al. 2016) database, the Dark Energy Survey (DES, Abbott et al. 2021) and the SuperCOSMOS Sky Survey (SSS, Hambly et al. 2004). Once possible optical counterparts have been identified, we then searched the *GAIA* Early Data Release 3 (EDR3, Seabroke et al. 2021) archive to determine which sources have measured proper motions. The significance of the proper motion is calculated as the ratio between the proper motion and its uncertainty. A source is considered to have proper motion if the significance is $\geq 3\sigma$.

Two catalogues were used to search for possible radio counterparts: the Very Large Array Sky Survey (VLASS; Lacy et al. 2020), and the Rapid ASKAP Continuum Survey (RACS; Hale et al. 2021). If a radio counterpart is not significantly detected/reported in the radio catalogs but was within the survey region, we set an upper limit flux using the sensitivity threshold of the RACS survey (1.5 mJy at 5σ) for the sources located at $-90° < \delta < -40°$ and of VLASS survey (0.345 mJy at 5σ) for the objects at $-40° < \delta < +90°$.

In addition, we also conducted dedicated follow-up radio observations using the Australian Telescope Compact Array (ATCA) for a sample of 18 UGSs (see Table A.1). These 18 sources were selected either because the survey images showed a potential, but not highly significant radio counterpart [a $2\sigma \leq \mathrm{SNR} \leq 4\sigma$ detection from the analysis of the RACS and LOFAR (Shimwell et al. (LOw-Frequency ARray Two-metre Sky Survey 2022)) images], due to a lack of radio coverage of their sky position, or because the survey images showed intriguing extended radio structures. The data reduction and the main results of this campaign are reported in the Sec. A.1.

6.4.0 Results

Among the 714 UGSs with Swift/XRT observation, we find that 274 objects have at least one X-ray detection with a SNR ≥3 inside the *Fermi* error box. For 193 of them, only one possible counterpart in the Fermi error box was found (hereafter UGS1; see an example of a UGS1 source in the top panel of Fig. 6.1; the entire UGS1 sub-sample is shown in Sec. A.2), while 81 have more than one potential X-ray counterparts (hereafter UGS2; see an example of a UGS2 source in the bottom panel of Fig. 6.1). Details about the *Swift*/XRT observations and all X-ray detections related to UGS1 and UGS2 are in Tab. 6.1 and 6.2, respectively. For each X-ray detection, we performed X-ray spectral data analysis (see Sec. 6.5) and in Tab. 6.3 and 6.4, we report the results of the XRT spectral fitting for UGS1 and UGS2.

We find that, over a total of 431 possible X-ray counterparts, 384 sources can be well fit with

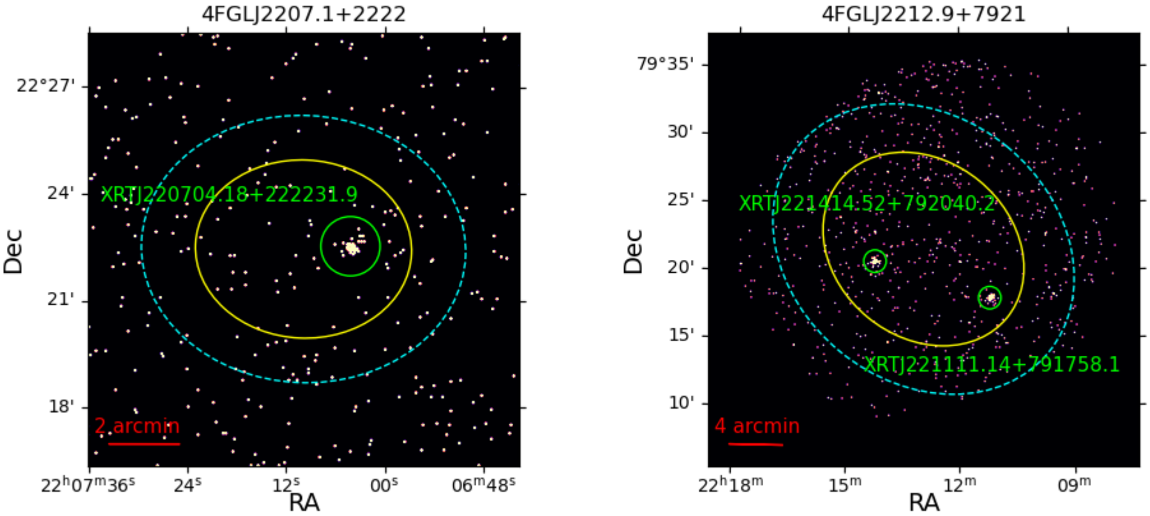

Figure 6.1: *Upper panel*: The X-ray skymap of 4FGL J22017.1+2222. The yellow and cyan ellipses are the 2σ and 3σ *Fermi* γ-ray error regions, respectively. The X-ray detection is shown with a green circular region.
Bottom panel: An X-ray skymap of 4FGL J2212.9+7921 with colours as described above.

a simple absorbed power-law ($0.8 \leq \chi^2_\nu \leq 1.2$). For other 36 sources, the fitting statistics are very poor (less than 3 spectral points) and hence we only estimated the flux by fixing the nH and the power-law index.

Comparing the distribution of absorbed 0.3–10 keV fluxes for UGS1 and UGS2 (see Fig. 6.2 , excluding sources that exhibit proper motion according to *GAIA*), we find that the UGS1 flux distribution follows a log-normal behaviour but the UGS2 distribution is less predictable, probably due to the dominance of spurious sources. The χ^2_ν from fitting the X-ray fluxes of UGS2 with a log-normal function indicated that the model does not fit the data well. To avoid underestimating the uncertainties, we introduced a systematic error into the data for the UGS2 and repeated the fit. The best-fitting results are reported in Tab. 6.7.

Using the position of each X-ray detection, we the list the potential optical and radio counterparts for UGS1 and UGS2 in Tab. 6.5 and 6.6, providing the optical coordinates, the magnitude in the g and r bands, the optical and the radio flux. Finally we report the radio-loudness parameter R defined as the ratio between the radio density flux, in the 2-4 GHz range, and the optical g-band density flux. Historically, sources with the R>10 are defined as radio-loud sources, otherwise are radio-quiet (Kellermann et al. 1989).

Over a total of 431 X-ray counterparts (193 for UGS1 and 238 for UGS2), we find that the *GAIA* survey reports a significant (> 3σ) proper motion for 41 and 63 optical counterparts of UGS1 and UGS2, respectively, strongly supporting for a possible Galactic origin.

6.4.1 UGS1 counterparts

All of 193 UGS1 X-ray counterparts are coincident with optical sources (see an example in Fig. 6.3 and the entire sample in Fig. A.2), that have g magnitudes spanning from 6.3 to

Table 6.1: Summary of a subsample (shown as example) of *Swift*/XRT detections within the 3σ *Fermi* error box of a list of UGS1 (UGS with a single potential X-ray counterpart), where a portion of the table is shown to demonstrate its form and content. The entire table is available in the Tab. A.2.

4FGL Name (1)	γ-ray detection (2) (σ)	Swift exposure (3) (ks)	*Swift*/XRT source (4)	RA (5) (J2000)	DEC (6) (J2000)	Positional error (7) (arcsec)	X-ray detection (8) (σ)
4FGL J0003.6+3059	13.1	4.9	XRT J000402.65+310219.8	1.0111	31.0388	4.6	3.7
4FGL J0004.4−4001	11.0	9.4	XRT J000434.22−400034.73	1.1426	-40.0096	2.9	7.7
4FGL J0006.6+4618	6.0	4.5	XRT J000652.09+461813.9	1.7170	46.3039	6.4	3.5
4FGL J0009.1−5012	9.7	4.8	XRT J000908.61−501000.9	2.2859	-50.1669	6.2	3.9
4FGL J0022.0−5921	12.4	4.6	XRT J002127.45−591946.3	5.3644	-59.3295	6.0	4.1
4FGL J0023.2+8412	3.4	1.8	XRT J002403.36+841352.6	6.0140	84.2313	8.0	3.4
4FGL J0023.6−4209	4.4	3.4	XRT J002303.59−420509.6	5.7650	-42.0860	2.9	5.0
4FGL J0025.4−4838	7.4	4.4	XRT J002536.94−483810.9	6.4039	-48.6364	3.0	5.6
4FGL J0026.1−0732	9.7	6.6	XRT J002611.55−073116.0	6.5481	-7.5211	2.4	22.6
4FGL J0027.0−1134	4.4	1.9	XRT J002710.11−113638.7	6.7921	-11.6108	3.2	5.1

Note. 1) 4FGL Name; 2) γ-ray detection significance as reported in the 4FGL catalog; 3) *Swift*/XRT exposure time; 4) Name of the *Swift*/XRT source; 5-6) Coordinates of the X-ray source; 7) X-ray positional error radius; 8) Detection significance of the X-ray source.

Table 6.2: Summary of a subsample (shown as example) of *Swift*/XRT detections within the 3σ *Fermi* error box of a list of UGS2 (UGS with more than one potential X-ray counterparts), where a portion of the table is shown to demonstrate its form and content. The entire table is available in the Tab. A.3.

4FGL Name (1)	γ-ray detection (2) (σ)	Swift exposure (3) (ks)	*Swift*/XRT source (4)	RA (5) (J2000)	DEC (6) (J2000)	Positional error (7) (arcsec)	X-ray detection (8) (σ)
4FGL J0017.1−4605	7.2	9.8	XRT J001708.63−460607.7	4.2859	-46.1021	2.9	6.5
			XRT J001750.81−460437.5	4.4617	-46.0771	4.2	4.7
			XRT J001705.00−460109.2	4.2709	-46.0192	7.7	3.0
4FGL J0031.0−2327	10.3	10.7	XRT J003120.53−233400.7	7.8355	-23.5669	2.5	19.5
			XRT J003039.79−232821.2	7.6658	-23.4725	6.6	3.6
4FGL J0040.2−2725	6.6	33.3	XRT J004016.42−271912.3	10.0684	-27.3201	2.0	25.2
			XRT J004023.77−272254.2	10.0991	-27.3817	7.0	5.6
			XRT J004026.07−272116.1	10.1086	-27.3545	7.0	5.6
			XRT J004035.80−272240.7	10.1492	-27.3780	7.6	4.4
			XRT J003954.35−272516.1	9.9764	-27.4211	6.0	3.9
4FGL J0045.8−1324	5.9	5.7	XRT J004602.94−132422.2	11.5123	-13.4062	7.0	7.7
			XRT J004608.32−132213.6	11.5347	-13.3704	3.5	5.2
			XRT J004611.48−132519.3	11.5479	-13.4220	3.5	4.4
			XRT J004539.41−132507.7	11.4142	-13.4188	4.3	4.0
			XRT J004602.97−131959.0	11.5124	-13.3331	6.0	3.2
			XRT J004555.20−132312.5	11.4800	-13.3868	3.5	3.2
4FGL J0102.3+1000	12.4	12.2	XRT J010226.89+095939.9	15.6121	9.9944	4.4	4.6
			XRT J010235.93+095832.4	15.6497	9.9757	6.0	3.7
			XRT J010220.73+095848.9	15.5864	9.9803	6.0	3.4
			XRT J010214.03+100258.4	15.5585	10.0496	3.6	3.3
4FGL J0118.3−6008	13.6	8.9	XRT J011823.22−600747.8	19.5967	-60.1300	4.3	4.9
			XRT J011848.17−600256.2	19.7007	-60.0489	5.5	3.3
4FGL J0122.4+1034	5.8	21.7	XRT J012223.64+103212.6	20.5985	10.5368	2.4	24.0
			XRT J012222.25+103116.2	20.5927	10.5212	4.7	6.2
4FGL J0126.3−6746	6.0	6.1	XRT J012610.88−674744.5	21.5453	-67.7957	3.0	6.6
			XRT J012622.53−674626.7	21.5939	-67.7741	4.3	3.9
4FGL J0132.9−4259	7.5	119.8	XRT J013346.96−430407.0	-43.0686	2.6	19.4	
			XRT J013401.65−425630.0	23.5069	-42.9417	3.5	12.6
			XRT J013339.96−425503.4	23.4165	-42.9176	3.5	8.5
			XRT J013347.80−430229.3	23.4491	-43.0415	3.5	7.9
			XRT J013316.63−425908.7	23.3193	-42.9858	3.5	7.6
			XRT J013308.39−425744.6	23.2849	-42.9624	3.5	6.9
			XRT J013359.11−430219.2	23.4963	-43.0387	3.5	5.6
			XRT J013347.00−430610.6	23.4459	-43.1029	3.5	5.6
			XRT J013339.30−425824.0	23.4138	-42.9733	6.0	3.0
4FGL J0140.4+5114	4.9	8.4	XRT J014107.78+510659.4	25.2824	51.1165	2.6	8.7
			XRT J014022.50+511313.3	25.0937	51.2204	4.6	6.9

Note. Labels are the same as in table 6.1.

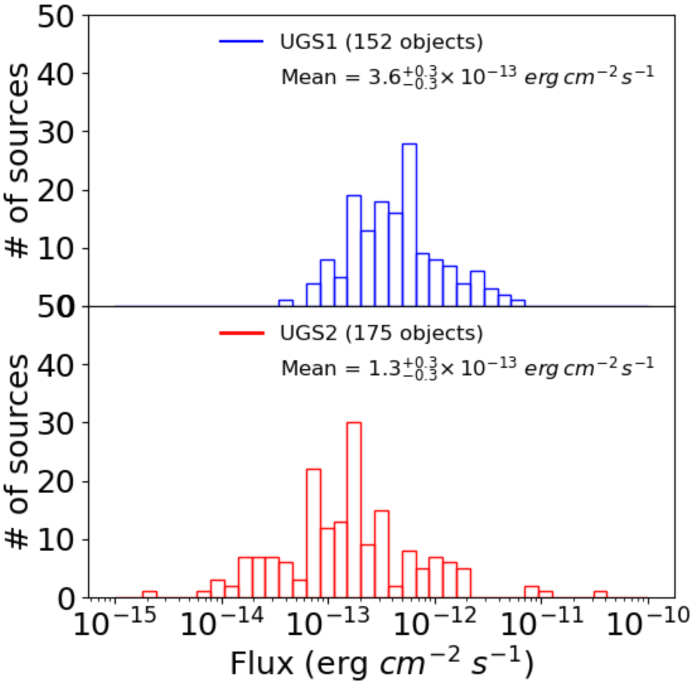

Figure 6.2: Absorbed 0.3–10 keV flux distributions for UGS1 and UGS2. It is worth noting that sources with proper motion are excluded from the histograms.

24.9 (from 14.9 to 24.9 excluding sources with proper motion), while their r magnitudes span from 6.7 to 24.9 (from 13.4 to 24.7 excluding sources with proper motion). The distribution of magnitudes in g-band and r-band are shown in Fig. 6.4.

Furthermore, 113 X-ray counterparts of the 193 UGS1 are also coincident with a radio source (105 excluding sources with proper motion). 33 UGS1 optical counterparts already have optical spectra available from the literature, which were presented in the Chapter 7 and in Ulgiati et al. (2024).

All X-ray sources coincident with a radio source from the VLASS and RACS catalogs, and for which we have an estimate of the optical magnitude in the g-band, are radio-loud, except for 4FGL J0641.4+3349/PAN J064111.22+334459.7 with R=2. This source is classified as a low redshift QSO on the basis of the absolute magnitude and the emission lines detected in the optical spectrum (see Monroe et al. 2016; Ulgiati et al. 2024, but also Chapter 7).

All the sources observed in the radio band using ATCA are radio-quiet except for 5 objects: 4FGL J0126.3−6746/SSS J012622.15−674623.0 (R = 1601) and 4FGL J1709.4−2127/PAN J170936.70−212838.9 (R = 90)[5], 4FGL J0536.1−1205/PAN J053626.80−120652.1 (already listed in the VLASS catalog, R = 216), 4FGL J0755.9-0515/PAN J075614.43−051718.9 (R =16) and 4FGL J1415.9-1504/PAN J141546.17−150229.0 (R = 13).

The other UGS1 X-ray sources that do not coincide with a radio source can be considered radio-quiet although for 30 of them the radio and R upper limit are poorly constrained (R > 10). For a comparison between the distribution of the R value in the UGS1 sub-sample and in *Fermi*

---

[5] Both are extended radio sources also listed in the RACS and VLASS catalogs, respectively.

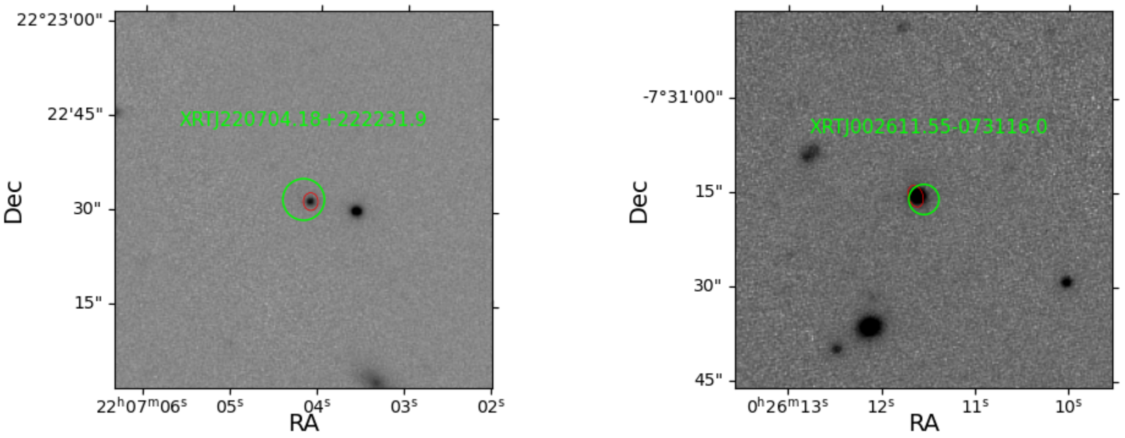

Figure 6.3: *Upper panel*: Optical r-band PanSTARRs image of 4FGL J2207.1+2222 counterpart. The green circle represent the error box of the X-ray counterpart and the red ellipses the error box of radio counterparts found within the VLASS catalog. *Bottom panel*: Optical r-band PanSTARRs image of 4FGL J0026.1-0732 counterpart. Color codes are as above.

blazars, see Fig. 6.5.

6.4.2 UGS2 counterparts

Of the UGS2 sample, 54 of them could be associated with two potential X-ray counterparts, of which 7 have both counterparts exhibiting proper motion, and 18 have only one counterpart with proper motion. For the latter 18 UGSs, only 8 of them have at least one non-moving object coincident with a radio source. Additionally, 11 UGS2 objects have three potential X-ray counterparts, and 16 have more than three X-ray counterparts. Similar to our approach with UGS1 sources, all potential X-ray counterparts of UGS2 that coincide with a radio source cataloged in VLASS or RACS, and for which we have an estimate of the optical magnitude in the g-band, are found to be radio-loud, except 3: 4FGL J0159.0+3313/XRT J015905.35+331257.8, 4FGL J1008.2−1000/XRT J100848.62−095450.2, and 4FGL J1407.7−3017/XRT J140806.82−302353.7, which are radio quiet. Investigating the optical images and the literature on these objects, we found that XRT J015905.35+331257.8 is located very close to a star ($\sim$ 25 arcsec), which probably compromises the measurement of the optical magnitude; XRT J100848.62−095450.2 is a Seyfert 1 (Véron-Cetty & Véron 2006) with a redshift of z=0.057253 (Jones et al. 2009); XRT J140806.82−302353.7 is a Seyfert 1 (Malizia et al. 2012) with redshift $z = 0.023456$ (Jones et al. 2009). The other UGS2 objects, which do not coincide with a radio object, are either radio-quiet or have an upper limit for R that exceeds the threshold of 10.

6.5.0 Discussion

We compare the main flux properties of the UGS X-ray counterparts with the main class of extragalactic γ-ray emitters detected by *Fermi* to characterize the nature of UGS counterparts and to test the goodness of our proposal. In particular, we confront the X-ray 0.3-10 keV flux

Table 6.3: Results of the X-ray spectral fitting for a list of UGS1 shown as example. The entire table is available in the Tab. A.4.

4FGL Name (1)	*Swift*/XRT source (2)	Count rate (3) [$\times10^{-3}$]	nH (4) [$\times10^{20}$]	Γ (5)	Norm. (6) 10^{-5}	absorbed flux (7) [$\times10^{-13}$]	χ^2_ν(dof) (8)
4FGL J0003.6+3059	XRT J000402.65+310219.8	$4.64^{+1.01}_{-1.01}$	6.8	2	$4.3^{+1.1}_{-1.1}$	$2.0^{+0.5}_{-0.5}$	0.01(1)
4FGL J0004.4−4001	XRT J000434.22−400034.7	$9.68^{+1.04}_{-1.04}$	1.2	$2.5^{+0.2}_{-0.2}$	$7.2^{+0.9}_{-0.9}$	$3.2^{+0.4}_{-0.4}$	0.9(8)
4FGL J0006.6+4618	XRT J000652.09+461813.9	$4.19^{+1.00}_{-1.00}$	11.0	2	$5.8^{+1.6}_{-1.6}$	$2.5^{+0.7}_{-0.7}$	-
4FGL J0009.1−5012	XRT J000908.61−501000.9	$4.53^{+1.01}_{-1.01}$	1.4	2	$4.7^{+1.5}_{-1.5}$	$2.5^{+0.8}_{-0.8}$	-
4FGL J0022.0−5921	XRT J002127.45−591946.3	$6.14^{+1.19}_{-1.19}$	1.4	2	$6.1^{+1.3}_{-1.3}$	$3.2^{+0.7}_{-0.7}$	0.7(2)
4FGL J0023.2+8412	XRT J002403.36+841352.6	$13.42^{+2.84}_{-2.84}$	11.0	2	$11.0^{+2.9}_{-2.9}$	$5.0^{+1.4}_{-1.4}$	1.2(1)
4FGL J0023.6−4209	XRT J002303.59-420509.6	$12.60^{+1.96}_{-1.96}$	1.4	$1.2^{+0.3}_{-0.3}$	$11.0^{+2.0}_{-2.0}$	$12.6^{+4.4}_{-3.5}$	0.8(3)
4FGL J0025.4−4838	XRT J002536.94−483810.9	$12.97^{+1.77}_{-1.77}$	1.8	$2.5^{+0.2}_{-0.2}$	$8.6^{+1.4}_{-1.4}$	$4.0^{+0.7}_{-0.7}$	1.8(4)
4FGL J0026.1−0732	XRT J002611.55−073116.0	$94.75^{+3.81}_{-3.81}$	4.0	$2.2^{+0.1}_{-0.1}$	$77.0^{+3.3}_{-3.3}$	$31.6^{+1.5}_{-1.4}$	0.7(66)
4FGL J0027.0−1134	XRT J002710.11−113638.7	$22.40^{+3.50}_{-3.50}$	2.9	$2.0^{+0.3}_{-0.3}$	$21.0^{+3.6}_{-3.6}$	$10.0^{+2.0}_{-2.1}$	1.0(3)

Note. 1) 4FGL Name; 2) Name of the *Swift*/XRT source; 3) *Swift*/XRT count rate; 4) Equivalent hydrogen column density (cm^{-2}), provided by the HI4PI Collaboration et al. (2016) database; 5) Power-law index; 6) Normalization factor (photons keV^{-1} cm^{-2} s^{-1}) at 1 keV; 7) Absorbed flux in the range 0.3–10 keV (erg cm^{-2} s^{-1}); 8) χ^2_ν (and the relative degrees of freedom).
The sources for which the χ^2_ν does not appear in the table have a spectral data quality too poor to allow for spectral fitting. For these sources, we just convert the observed source count rate into a flux (see text).

Table 6.4: Results of the X-ray spectral fitting for a list of UGS2 shown as example. The entire table is available in the Tab. A.5.

4FGL Name (1)	*Swift*/XRT source (2)	Count rate (3) [$\times10^{-3}$]	nH (4) [$\times10^{20}$]	Γ (5)	Norm. (6) 10^{-5}	absorbed flux (7) [$\times10^{-13}$]	χ^2_ν(dof) (8)
4FGL J0017.1−4605	XRT J001708.63−460607.7	$6.44^{+0.84}_{-0.84}$	1.6	$1.8^{+0.3}_{-0.3}$	$5.0^{+0.7}_{-0.7}$	$3.2^{+0.7}_{-0.7}$	0.6(6)
	XRT J001750.81−460437.5	$3.95^{+0.66}_{-0.66}$	1.6	$-0.1^{+0.5}_{-0.6}$	$1.3^{+0.5}_{-0.5}$	$12.6^{+13.1}_{-6.1}$	1.3(2)
	XRT J001705.00−460109.2	$1.47^{+0.42}_{-0.42}$	1.6	2	$1.1^{+0.4}_{-0.4}$	$0.6^{+0.2}_{-0.2}$	-
4FGL J0031.0−2327	XRT J003120.53−233400.7	$44.80^{+2.08}_{-2.08}$	1.7	$1.8^{+0.1}_{-0.1}$	$34.0^{+1.8}_{-1.8}$	$20.0^{+1.4}_{-1.3}$	0.9(50)
	XRT J003039.79-232821.2	$1.93^{+0.48}_{-0.48}$	1.7	2	$1.6^{+0.5}_{-0.5}$	$0.8^{+0.2}_{-0.2}$	-
4FGL J0040.2−2725	XRT J004016.42−271912.3	$22.59^{+0.83}_{-0.83}$	1.4	$2.7^{+0.1}_{-0.1}$	$16.0^{+0.6}_{-0.6}$	$6.3^{+0.3}_{-0.3}$	1.1(72)
	XRT J004023.77−272254.2	$1.32^{+0.22}_{-0.22}$	1.4	$7.2^{+0.3}_{-0.3}$	$0.4^{+0.1}_{-0.1}$	$3.2^{+1.0}_{-0.9}$	1.0(4)
	XRT J004026.07−272116.1	$1.51^{+0.23}_{-0.23}$	1.4	$2.5^{+0.2}_{-0.2}$	$1.3^{+0.2}_{-0.2}$	$0.5^{+0.1}_{-0.1}$	0.8(5)
	XRT J004035.80−272240.7	$0.91^{+0.19}_{-0.19}$	1.4	$1.1^{+0.6}_{-0.6}$	$0.5^{+0.1}_{-0.2}$	$0.6^{+0.5}_{-0.3}$	2.4(2)
	XRT J003954.35−272516.1	$0.63^{+0.16}_{-0.16}$	1.5	2	$0.4^{+0.1}_{-0.1}$	$0.3^{+0.1}_{-0.1}$	3.0(2)
4FGL J0045.8−1324	XRT J004602.94−132422.2	$4.00^{+0.44}_{-0.44}$	1.7	$2.2^{+0.2}_{-0.2}$	$3.3^{+0.4}_{-0.4}$	$1.6^{+0.2}_{-0.2}$	0.8(10)
	XRT J004608.32−132213.6	$1.90^{+0.32}_{-0.32}$	1.7	$1.1^{+0.3}_{-0.3}$	$1.1^{+0.3}_{-0.3}$	$1.6^{+0.5}_{-0.4}$	1.1(4)
	XRT J004611.48−132519.3	$1.68^{+0.30}_{-0.30}$	1.7	$1.7^{+0.4}_{-0.4}$	$1.8^{+0.3}_{-0.3}$	$1.3^{+0.8}_{-0.4}$	1.2(3)
	XRT J004539.41−132507.7	$0.87^{+0.23}_{-0.23}$	1.7	2	$0.8^{+0.2}_{-0.2}$	$0.4^{+0.1}_{-0.1}$	0.9(2)
	XRT J004602.97−131959.0	$0.39^{+0.20}_{-0.20}$	1.8	2	$0.5^{+0.2}_{-0.2}$	$0.3^{+0.1}_{-0.1}$	-
	XRT J004555.20−132312.5	$0.73^{+0.22}_{-0.22}$	1.7	2	$0.6^{+0.2}_{-0.2}$	$0.3^{+0.1}_{-0.1}$	2.4(1)
4FGL J0102.3+1000	XRT J010226.89+095939.9	$0.47^{+0.14}_{-0.14}$	4.3	$2.4^{+0.7}_{-0.8}$	$0.6^{+0.1}_{-0.1}$	$0.3^{+0.2}_{-0.1}$	1.1(2)
	XRT J010235.93+095832.4	$0.26^{+0.11}_{-0.11}$	4.3	2	$0.3^{+0.1}_{-0.1}$	$0.1^{+0.1}_{-0.1}$	-
	XRT J010220.73+095848.9	$0.36^{+0.12}_{-0.12}$	4.3	2	$0.4^{+0.1}_{-0.1}$	$0.2^{+0.1}_{-0.1}$	0.5(2)
	XRT J010214.03+100258.4	$0.39^{+0.12}_{-0.12}$	4.3	2	$0.3^{+0.1}_{-0.1}$	$0.2^{+0.1}_{-0.1}$	3.3(1)
4FGL J0118.3−6008	XRT J011823.22−600747.8	$3.98^{+0.70}_{-0.70}$	2.6	$2.1^{+0.4}_{-0.4}$	$3.8^{+0.7}_{-0.7}$	$2.0^{+0.8}_{-0.5}$	0.6(2)
	XRT J011848.17−600256.2	$2.24^{+0.52}_{-0.52}$	2.7	2	$2.3^{+0.6}_{-0.6}$	$1.3^{+0.3}_{-0.3}$	-
4FGL J0122.4+1034	XRT J012223.64+103212.6	$31.52^{+1.22}_{-1.22}$	5.5	$2.2^{+0.1}_{-0.1}$	$27.0^{+1.1}_{-1.1}$	$10.0^{+0.5}_{-0.5}$	1.2(70)
	XRT J012222.25+103116.2	$3.27^{+0.42}_{-0.42}$	5.5	$1.4^{+0.3}_{-0.3}$	$2.9^{+0.5}_{-0.5}$	$2.5^{+0.8}_{-0.6}$	0.7(7)
4FGL J0126.3−6746	XRT J012610.88−674744.5	$10.94^{+1.39}_{-1.39}$	3.2	$2.6^{+0.3}_{-0.2}$	$8.7^{+1.2}_{-1.2}$	$3.2^{+0.5}_{-0.5}$	0.8(6)
	XRT J012622.53−674626.7	$4.07^{+0.87}_{-0.87}$	3.2	2	$3.0^{+0.7}_{-0.7}$	$1.6^{+0.4}_{-0.4}$	1.2(2)
4FGL J0132.9-4259	XRT J013346.96−430407.0	$3.13^{+0.14}_{-0.14}$	1.7	$1.8^{+0.1}_{-0.1}$	$2.6^{+0.1}_{-0.1}$	$1.6^{+0.1}_{-0.1}$	0.9(66)
	XRT J013401.65−425630.0	$1.13^{+0.09}_{-0.09}$	1.8	$2.2^{+0.1}_{-0.1}$	$0.9^{+0.1}_{-0.1}$	$0.5^{+0.0}_{-0.1}$	1.0(29)
	XRT J013339.96−425503.4	$0.63^{+0.07}_{-0.07}$	1.8	$2.0^{+0.2}_{-0.2}$	$0.5^{+0.1}_{-0.1}$	$0.3^{+0.0}_{-0.0}$	1.0(17)
	XRT J013347.80−430229.3	$0.51^{+0.06}_{-0.06}$	1.7	$1.2^{+0.2}_{-0.2}$	$0.4^{+0.1}_{-0.1}$	$0.4^{+0.1}_{-0.1}$	1.4(14)
	XRT J013316.63−425908.7	$0.53^{+0.08}_{-0.08}$	1.7	$1.6^{+0.3}_{-0.3}$	$0.6^{+0.1}_{-0.1}$	$0.4^{+0.1}_{-0.1}$	0.3(9)
	XRT J013308.39-425744.6	$1.05^{+0.12}_{-0.12}$	1.7	$0.8^{+0.2}_{-0.2}$	$0.6^{+0.1}_{-0.1}$	$1.3^{+0.3}_{-0.2}$	0.9(10)
	XRT J013359.11−430219.2	$0.16^{+0.05}_{-0.05}$	1.7	$1.2^{+0.3}_{-0.3}$	$0.1^{+0.0}_{-0.0}$	$0.2^{+0.1}_{-0.0}$	1.3(7)
	XRT J013347.00−430610.6	$0.38^{+0.06}_{-0.06}$	1.7	$1.4^{+0.2}_{-0.2}$	$0.3^{+0.1}_{-0.1}$	$0.3^{+0.1}_{-0.1}$	1.0(8)
	XRT J013339.30−425824.0	$0.02^{+0.04}_{-0.04}$	1.8	$1.6^{+-1.6}_{-1.6}$	$0.0^{+0.0}_{-0.0}$	$0.0^{+1.0}_{-0.0}$	0.7(2)
4FGL J0140.4+5114	XRT J014107.78+510659.4	$13.89^{+1.41}_{-1.41}$	28.0	$1.8^{+0.3}_{-0.2}$	$19.0^{+3.4}_{-3.3}$	$7.9^{+1.6}_{-1.5}$	1.5(11)
-	XRT J014022.50+511313.3	$10.43^{+1.14}_{-1.14}$	29.0	$1.8^{+0.2}_{-0.2}$	$14.0^{+2.2}_{-2.2}$	$6.3^{+1.3}_{-1.1}$	0.6(9)

Note. Labels are the same as in table 6.3.

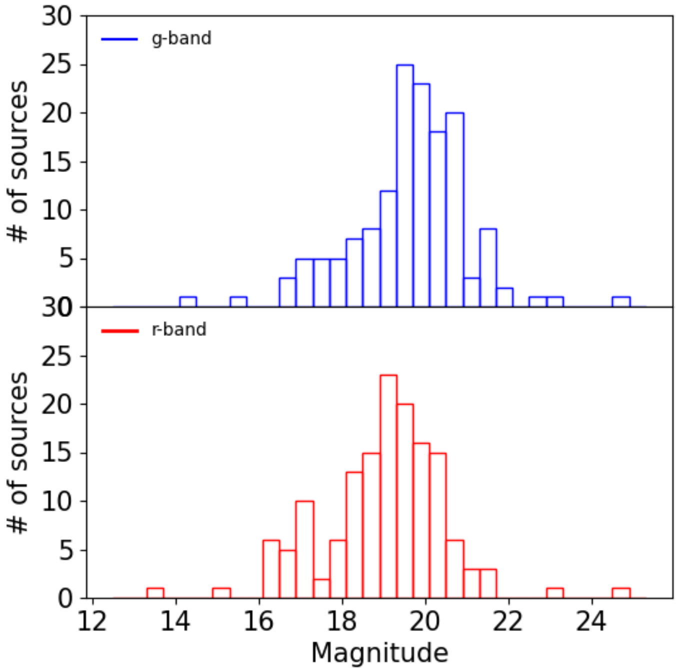

Figure 6.4: Distribution of magnitudes in the g-band (top) and r-band (bottom) for UGS1. Note that sources with proper motion have been excluded from the histogram.

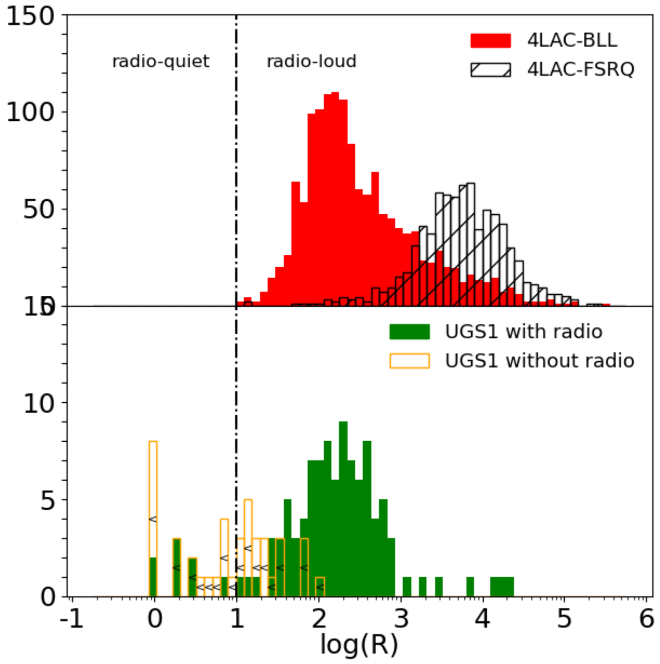

Figure 6.5: *Upper panel*: Distribution of the *radio-loudness* parameter (log(R)) value for 1409 objects classified as BLL and 771 objects as FSRQ of the 4LAC catalog. *Bottom panel*: Distribution of the *radio-loudness* value for the counterparts of UGS1. It is worth to note that the empty orange bars represent the upper limits on R for UGS1 withot a radio counterpart. The black dashed vertical line represent the *radio-loudness* parameter value (R = 10) that separates the radio-quiet from the radio-loud sources. It is worth noting that sources with proper motion are excluded from the histograms.

Table 6.5: MWL counterparts of a list of UGS1 shown as example.
A portion of the table is shown here to demonstrate its form and content. The entire table is available in the Tab. A.6.

4FGL Name (1)	*Swift*/XRT source (2)	Radio source (3)	Optical source (4)	RA (5) J2000	DEC (6) J2000	gmag(rmag) (7)	$f_\nu^{\rm opt}$ (8) [$\times 10^{-28}$]	$f_\nu^{\rm radio}$ (9)
4FGL J0003.6+3059	XRT J000402.65+310219.8	-	PANJ000402.51+310222.0	1.0105	31.0394	21.2(20.1)	1.2	<0.3
4FGL J0004.4−4001	XRT J000434.22−400034.7	VLASS1QLCIRJ000434.19-400033.6	DESJ000434.22−400035.1	1.1426	-40.0098	16.9(16.2)	63.1	32.5
4FGL J0006.6+4618	XRT J000652.09+461813.9	VLASS1QLCIRJ000652.31+461816.8	PANJ000652.33+461817.0	1.7180	46.3047	19.9(19.6)	4.0	2.6
4FGL J0009.1−5012	XRT J000908.61−501000.9*	-	DESJ000908.64−501000.6	2.2860	-50.1669	11.1(11.5)	13182.6	<0.6
4FGL J0022.0−5921	XRT J002127.45−591946.3	RACSJ002127.4−591949	DESJ002127.51−591948.0	5.3646	-59.3300	19.6(19.2)	5.2	93.4
4FGL J0023.2+8412	XRT J002403.36+841352.6	-	PANJ002405.61+841352.2	6.0234	84.2312	16.7(16.2)	75.9	<0.3
4FGL J0023.6−4209	XRT J002303.59-420509.6	-	DESJ002303.75−420508.6	5.7657	-42.0857	15.6(15.0)	208.9	<0.3
4FGL J0025.4−4838	XRT J002536.94−483810.9	RACSJ002536.8−483810	DESJ002536.92−483809.5	6.4039	-48.6360	19.8(19.4)	4.4	5.0
4FGL J0026.1−0732	XRT J002611.55−073116.0	VLASS1QLCIRJ002611.63−073115.5	PANJ002611.64−073115.8	6.5485	-7.5211	19.1(19.1)	8.3	6.4
4FGL J0027.0−1134	XRT J002710.11−113638.7	VLASS1QLCIRJ002710.12−113637.5	PANJ002710.12−113637.9	6.7922	-11.6105	17.1(16.3)	52.5	19.9

Note. 1) 4FGL Name; 2) X-ray source; 3) Radio source; 4) Optical source; 5) - 6) Coordinates of the optical counterpart. 7) g(r) magnitude of the optical source. 8) Optical density flux in unit of erg cm^{-2} s^{-1} Hz^{-1}. 9) Radio density flux (mJy); 10) *Radio-loudness* parameter.
* Sources with proper motion.

Table 6.6: MWL counterparts of a list of UGS2 shown as example.
A portion of the table is shown here to demonstrate its form and content. The entire table is available in the Tab. A.7.

4FGL Name (1)	*Swift*/XRT source (2)	Radio source (3)	Optical source (4)	RA (5) J2000	DEC (6) J2000	gmag(rmag) (7)	$f_\nu^{\rm opt}$ (8) [$\times 10^{-28}$]	$f_\nu^{\rm radio}$ (9)	*R* (10)
4FGL J0017.1−4605	XRT J001708.63−460607.7	ATCAJ001708.65−460607.0	DESJ001708.67−460606.9	4.2862	-46.1019	18.3(18.1)	17.4	0.1	1
	XRT J001750.81−460437.5	ATCAJ001750.67−460438.6	DESJ001750.66−460438.5	4.4611	-46.0774	17.8(17.9)	27.5	0.5	3
	XRT J001705.00−460109.2	-	DESJ001704.83−460110.1	4.2702	-46.0195	20.8(20.7)	1.7	<0.6	<37
4FGL J0031.0−2327	XRT J003120.53−233400.7	VLASS1QLCIRJ003120.56−233401.6	PANJ003120.55−233401.2	7.8356	-23.5670	20.1(19.0)	3.3	3.9	118
	XRT J003039.79-232821.2	-	PANJ003039.76−232822.3	7.6656	-23.4729	19.9(19.5)	4.0	<0.3	<9
4FGL J0040.2−2725	XRT J004016.42−271912.3	VLASS1QLCIRJ004016.40−271911.5	PANJ004016.41−271911.7	10.0684	-27.3199	18.8(18.6)	11.0	86.0	784
	XRT J004023.77−272254.2	-	PANJ004023.90−272255.4	10.0996	-27.3821	22.6(20.8)	-	<0.3	-
	XRT J004026.07−272116.1*	-	DESJ004026.16−272117.6	10.1090	-27.3549	14.8(14.2)	436.5	<0.3	<1
	XRT J004035.80−272240.7	-	PANJ004035.87−272242.0	10.1494	-27.3783	21.9(21.6)	0.6	<0.3	<55
	XRT J003954.35−272516.1	-	PANJ003954.09-272513.5	9.9754	-27.4204	21.2(21.1)	1.2	<0.3	<29
4FGL J0045.8−1324	XRT J004602.94−132422.2	VLASS1QLCIRJ004602.82−132422.1	PANJ004602.82−132422.4	11.5118	-13.4062	18.7(18.7)	12.0	8.1	68
	XRT J004608.32−132213.6	-	PANJ004608.44−132215.2	11.5352	-13.3709	18.5(18.6)	14.5	<0.3	<2
	XRT J004611.48−132519.3*	-	PANJ004611.47−132522.6	11.5478	-13.4229	17.6(16.4)	33.1	<0.3	<1
	XRT J004539.41−132507.7	VLASS1QLCIRJ004539.47−132508.0	-	-	-	-(-)	-	1.7	-
	XRT J004602.97−131959.0	-	PANJ004602.68−131958.9	11.5112	-13.3330	21.1(21.3)	1.3	<0.3	<26
	XRT J004555.20−132312.5	-	PANJ004555.27−132314.3	11.4803	-13.3873	−(21.2)	-	<0.3	-
4FGL J0102.3+1000	XRT J010226.89+095939.9	VLASS1QLCIRJ010226.69+095939.6	-	-	-	-(-)	-	6.5	-
	XRT J010235.93+095832.4	-	-	-	-	-(-)	-	<0.3	-
	XRT J010220.73+095848.9	-	PANJ010220.59+095847.5	15.5858	9.9799	20.1(20.0)	3.3	<0.3	<10
	XRT J010214.03+100258.4	-	-	-	-	-(-)	-	<0.3	-
4FGL J0118.3−6008	XRT J011823.22−600747.8	RACSJ011823.5−600749	DESJ011823.48−600751.3	19.5978	-60.1309	17.9(17.4)	25.1	96.8	385
	XRT J011848.17−600256.2	-	DESJ011848.16−600256.3	19.7007	-60.0490	19.0(18.9)	9.1	<0.6	<7
4FGL J0122.4+1034	XRT J012223.64+103212.6	VLASS1QLCIRJ012223.63+103213.3	PANJ012223.62+103213.2	20.5984	10.5370	20.1(19.8)	3.3	8.5	257
	XRT J012222.25+103116.2	-	PANJ012222.18+103118.2	20.5924	10.5217	21.3(19.5)	1.1	<0.3	<31
4FGL J0126.3−6746	XRT J012610.88−674744.5	RACSJ012610.7−674743	SSSJ012610.68−674742.6	21.5446	-67.7952	18.6(16.5)	13.2	8.4	64
	XRT J012622.53−674626.7	RACSJ012622.4−674610	SSSJ012622.15−674623.0	21.5924	-67.7731	20.1(19.4)	3.3	53.0	1601
4FGL J0132.9-4259	XRT J013346.96−430407.0	-	DESJ013346.86−430410.0	23.4453	-43.0695	20.8(19.7)	1.7	<0.6	<37
	XRT J013401.65−425630.0	-	DESJ013401.71−425630.9	23.5072	-42.9419	19.5(19.2)	5.8	<0.6	<11
	XRT J013339.96−425503.4	-	DESJ013339.96−425505.0	23.4165	-42.9181	19.6(19.1)	5.2	<0.6	<12
	XRT J013347.80−430229.3	-	DESJ013347.77−430230.0	23.4490	-43.0417	21.7(21.1)	0.8	<0.6	<84
	XRT J013316.63−425908.7	-	DESJ013316.78−425910.0	23.3199	-42.9861	19.8(19.5)	4.4	<0.6	<15
	XRT J013308.39-425744.6	-	DESJ013308.45−425747.2	23.2852	-42.9631	20.7(20.2)	1.9	<0.6	<34
	XRT J013359.11−430219.2	-	DESJ013359.30−430221.1	23.4971	-43.0392	21.2(23.0)	-	<0.6	-
	XRT J013347.00−430610.6	-	DESJ013347.16−430611.0	23.4465	-43.1031	20.7(20.7)	1.9	<0.6	<34
	XRT J013339.30−425824.0	-	DESJ013339.31−425825.8	23.4138	-42.9738	23.9(23.9)	0.1	<0.6	<639
4FGL J0140.4+5114	XRT J014107.78+510659.4	-	PANJ014107.96+510658.8	25.2832	51.1163	19.3(18.7)	6.9	<0.3	<5
	XRT J014022.50+511313.3	-	PANJ014022.76+511311.6	25.0948	51.2199	21.1(19.4)	1.3	<0.3	<26

Note. Labels are the same as in table 6.5

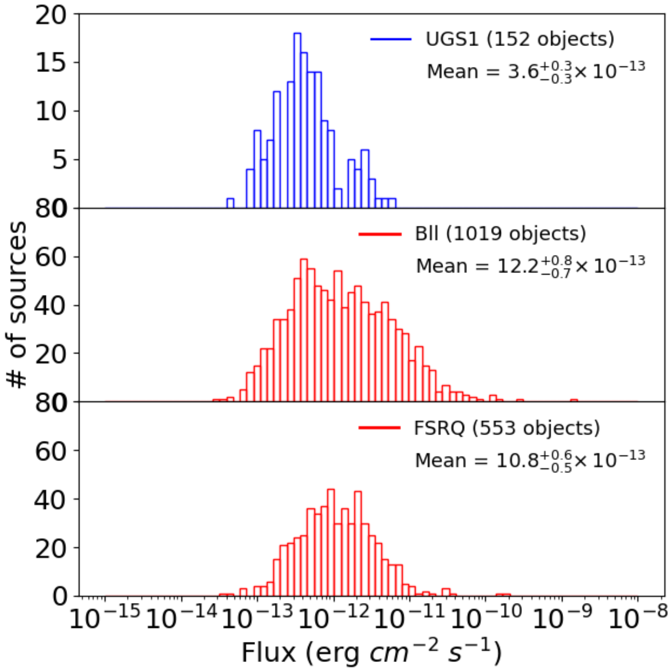

Figure 6.6: Absorbed 0.3–10 keV flux distributions for UGS1 (top), 4FGL-DR4 BLL (center) and 4FGL-DR4 FSRQ (bottom). It is worth noting that sources with proper motion are excluded from the histograms.

Table 6.7: Results of fits on X-ray flux distributions

Sample (1)	Mean (μ) (2) $\times 10^{-13}$ erg cm^{-2} s^{-1}	Standard (3) deviation(σ) $\times 10^{-13}$
UGS1	$3.6^{+0.3}_{-0.3}$	3.2
UGS2	$1.3^{+0.3}_{-0.3}$	1.8
4FGL-DR4 BLL	$12.2^{+0.8}_{-0.7}$	18.6
4FGL-DR4 FSRQ	$10.8^{+0.6}_{-0.5}$	11.9

Note. Results of lognormal fits on the distributions of X-ray fluxes in the different samples, where μ is the mean. 1): Sample under investigation; 2): Mean energy flux in the range 0.3–10 keV (erg cm^{-2} s^{-1}); 3): Standard deviation σ.

distribution of UGS1 with those of the 4FGL-DR4 blazars (see Fig. 6.6), where we carefully excluded Blazar Candidates of Uncertain type (BCU), since they could hide objects that are misclassified as blazars. As seen before, we adopted a log-normal function to describe the flux properties. However, we found that the flux distribution of 4FGL-DR4 BLL cannot be described log-normal distribution ($\chi^2_\nu \gg 1$ and p-value $\ll 0.05$)[6]. The results of the fit are reported in Tab. 6.7.

We note that the X-ray fluxes of UGS1 are generally lower than those of the 4FGL-DR4 blazars (expected values of the distributions in Tab. 6.7). A simple explanation for this behaviour is linked to the fact that UGSs are intrinsically weak γ-ray emitters, revealed by the ever-increasing exposure time (and hence the statistics) of the Fermi survey, which allows the detection of the sources with weakest fluxes.

These probably belong to the blazar population at large distances and/or may be AGN with a low nucleus-to-host flux ratio.

We further build the *color-color diagrams* considering the ratios of the absorbed fluxes at different energy bands, in particular $\log(F_{\mathrm{radio}}/F_X)$ and $\log(F_{\mathrm{optical}}/F_X)$ as a function of $\log(F_\gamma/F_X)$ for UGS1 (see Fig. 6.7) and UGS2 (see Fig. 6.8). In the same plots, we also included the 4FGL-DR4 blazars and 4FGL-DR4 Galactic sources (pulsars, pulsar wind nebulae, High Mass X-ray Binaries, Low Mass X-ray Binaries, and Supernova Remnants). For the 4FGL-DR4 sources which are not covered by *Swift*/XRT observations, we extract their X-ray fluxes from the 4XMM-DR13 catalog (Webb et al. 2020), in order to increase the number of sources with an estimated X-ray flux.

All Fermi AGNs ($\sim$ 98% are blazars and hence radio-loud) occupy a compact region in the two *color-color diagrams*, and it is possible to recognize two sub-regions: one populated by BLLs and one populated by FSRQs.

The upper panel of Fig. 6.7 shows that a fraction of UGS1 (filled red points) occupies the same region of the 4FGL-DR4 blazars (grey points). These are the sources for which there is also a radio detection and are radio-loud. This supports the classification with the class of radio-loud AGN and, for 19 objects this is confirmed spectroscopically (Ulgiati et al. 2024, but also Chapter 7).

The remaining UGS1 without radio signal, and for which a radio flux upper limit is provided, are marked as filled red triangles. These sources, along with the UGS1 for which a potential radio counterpart was found using ATCA, considered as radio-quiet objects, are located in the lower edge of the locus occupied by the Fermi blazars. On the other hand, taking into account the second diagram displayed in the bottom panel of Fig. 6.7, where the radio flux is not taken into account, these sources share the same region occupied by AGNs, suggesting a radio-quiet AGN nature. Of these sources, 10 of them were studied in Ulgiati et al. (2024) and in the Chapter 7 and, indeed, they belong to the class of the Seyfert/QSO on the basis of their optical spectrum.

The same analysis is performed for the UGS2 sample (see Fig. 6.8), where the degree of degeneracy of the number of the proposed counterparts leads to more speculative conclusions.

---

[6] To address this, we introduce a systematic error into the data before performing the log-normal fit, to avoid underestimating the uncertainty of the model parameters.

Also in this case, we have the same trend found for the UGS1 for which the radio-loud sources occupy the same region of 4FGL-DR4 blazars while the radio-quiet ones are located in a distinct region.

This work represent the basis for future studies on the investigation of UGSs. Future researches will intensify efforts to associate and classify these sources. Dedicated spectroscopic campaigns are being conducted with 10-meter-class optical telescopes, such as the Gran Telescopio Canarias (GTC) and the Large Binocular Telescope (LBT), to obtain high-quality spectra and characterize their optical properties. Further multi-wavelength investigations will focus on constructing detailed spectral energy distributions (SEDs) to provide an in-depth view of their emissions across the spectrum. The SED analysis aims to reveal insights into the physical mechanisms powering these objects, helping to distinguish between different classes of gamma-ray emitters (Paiano et al. 2017a, 2019; Ulgiati et al. 2024, as well as ongoing analyses by Ulgiati et al., Paiano et al., and in Chapter 8).

6.6.0 Conclusions

The primary aim of this work is to create a catalog of possible counterparts and list their multi-wavelength emission fluxes. Detailed studies on individual sources are ongoing: optical spectroscopic campaigns are being conducted using optical telescopes of 10 meter class, as the Gran Telescopio Canarias (GTC), and multi-wavelength study are focused on constructing the SEDs of these objects, with the aim of providing an overall view of their emission and gaining insights into the underlying physical processes (Paiano et al. 2017a, 2019; Ulgiati et al. 2024, and Ulgiati et al in preparation and Paiano et al in preparation).

This paper is one piece of the global puzzle in the study of extragalactic UGSs, a puzzle that will help shed light on these γ-ray emitters. New blazars and AGNs are discovered, further enriching our understanding of their population characteristics and how they fit into the larger framework of AGNs and their varied emission processes.

As a final remark, this chapter presents a comprehensive list of potential lower-energy counterparts (X-ray, optical, and radio) to extragalactic UGSs ($|b| > 10°$) from the *Fermi* 4FGL-DR4 catalog. The search for counterparts began in the X-ray band, analyzing *Swift*/XRT observations that covered the UGS regions. Of the 714 UGSs observed, 274 have at least one X-ray source within the 3σ *Fermi* error box, with a signal-to-noise ratio (SNR) ≥ 3. Among these, 193 have only one possible X-ray counterpart (denoted as UGS1), and 81 have multiple possible X-ray counterparts (denoted as UGS2).

All 193 X-ray counterparts of UGS1 are coincident with optical sources, of which 113 are also coincident with radio sources. All X-ray sources coincident with a radio source from the VLASS and RACS catalogs, and for which optical magnitudes in the g-band were available, are radio-loud, except for 4FGL J0641.4+3349/PAN J064111.22+334459.7, which has an R value of 2. The UGS1 sources not coincident with radio objects are likely radio-quiet sources. A subset of these sources was observed using the ATCA facility, and although several were detected, they are still confirmed to be radio-quiet.

Regarding the UGS2 sample, similarly to UGS1, all potential X-ray counterparts of UGS2s that coincide with a radio source cataloged in VLASS or RACS, and for which g-band optical magnitudes are available, are found to be radio-loud, except for 4FGL J0159.0+3313/XRT J015905.35+331257.8, 4FGL J1008.2−1000/XRT J100848.62−095450.2, and 4FGL J1407.7−3017/XRT J140806.82−302353.7. More studies on the broadband properties of these 2 sources are therefore needed to constrain their nature.

Finally, it was noted that UGSs exhibit lower flux across all bands compared to sources already associated and identified in the 4FGL-DR4 catalog. Using color-color diagrams, $\log(F_{\mathrm{radio}}/F_X)$ and $\log(F_{\mathrm{optical}}/F_X)$ as functions of $\log(F_\gamma/F_X)$, we observed that both UGS1 and UGS2 sources coincident with radio sources occupy the same regions of the diagram as blazars (or generally, radio-loud AGNs). The remaining UGS1 sources not coincident with radio objects occupy a distinct region populated by mainly radio-quiet AGNs (see Ulgiati et al. 2024). For UGS2 sources not coincident with radio objects, due to a high level of degeneracy and the likelihood of spurious sources, they occupy a less constrained region.

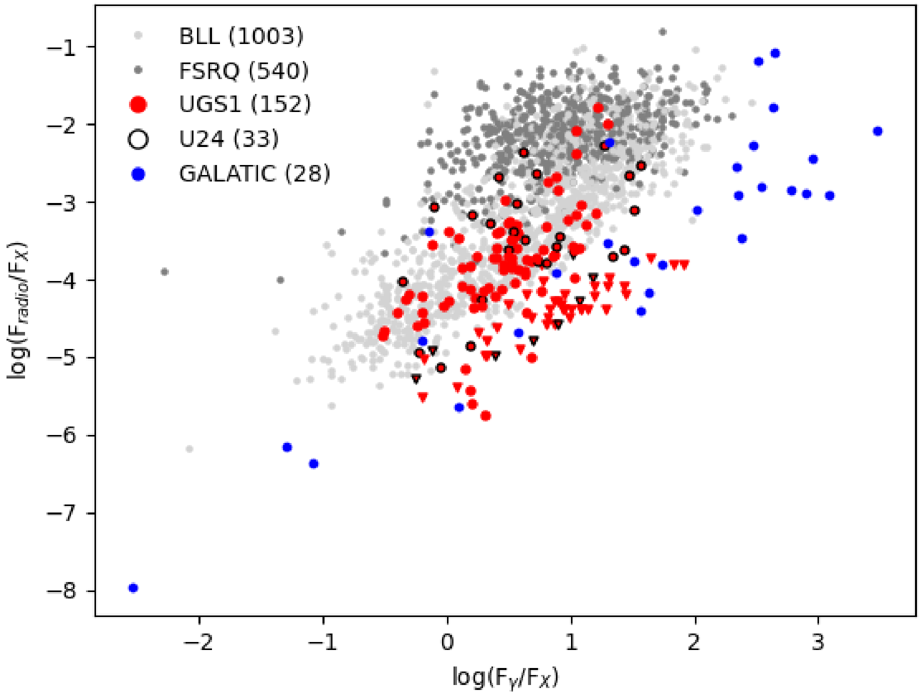

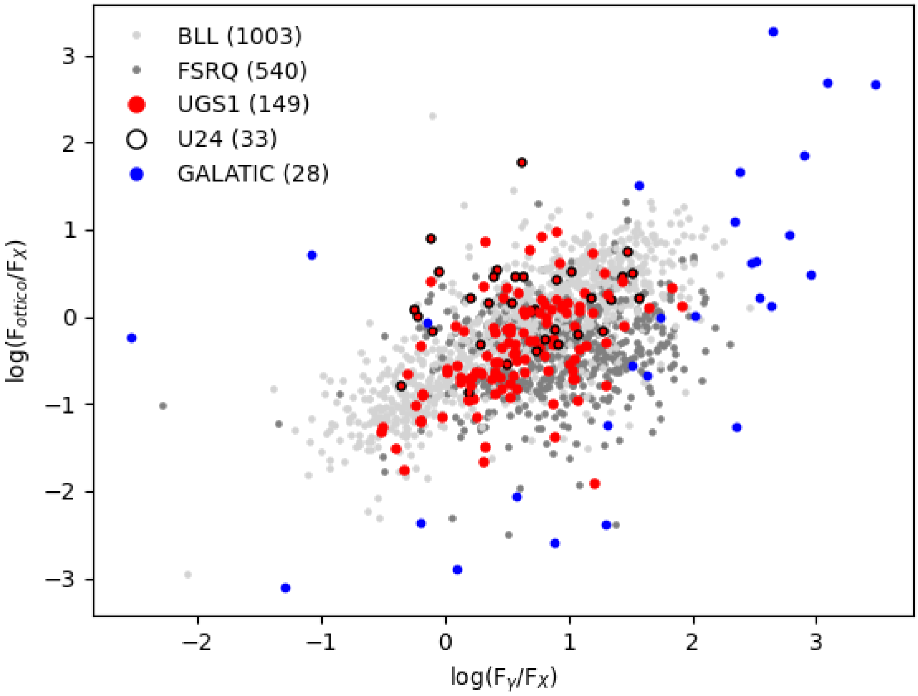

Figure 6.7: log(F_{radio}/F_X) vs log(F_γ/F_X) (top) and log($F_{optical}/F_X$) vs log(F_γ/F_X) (bottom) diagrams and for 4FGL-DR4 BLL (light grey), 4FGL-DR4 FSRQ (grey), UGS1 (red) and 4FGL-DR4 Galactic sources (blue). Sources already analyzed in (Ulgiati et al. 2024) are underlined with a black edge around the points. It is worth noting that sources with proper motion or lacking g-band magnitude estimates are not included in the plot.

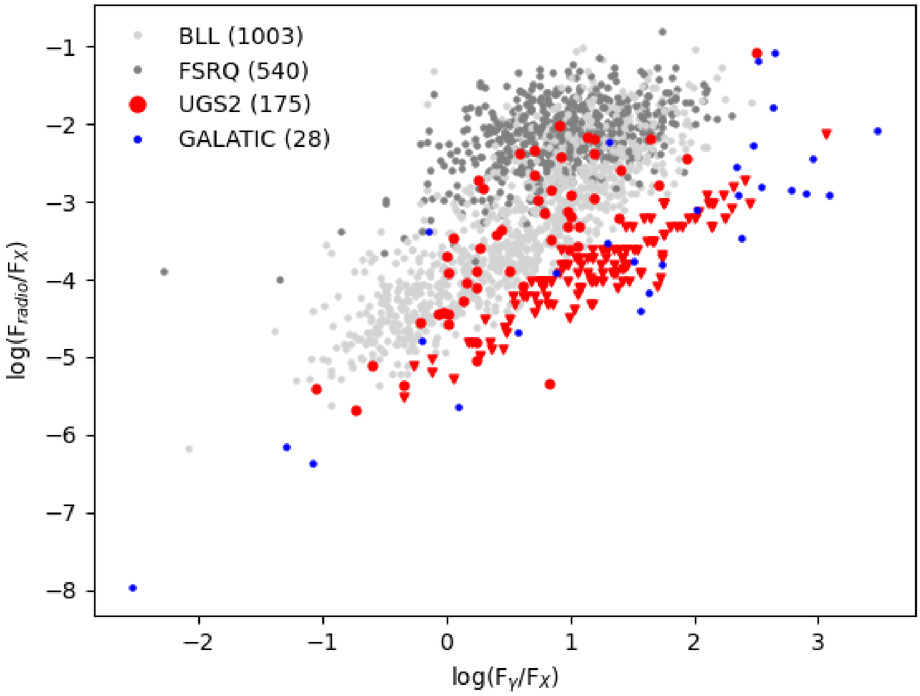

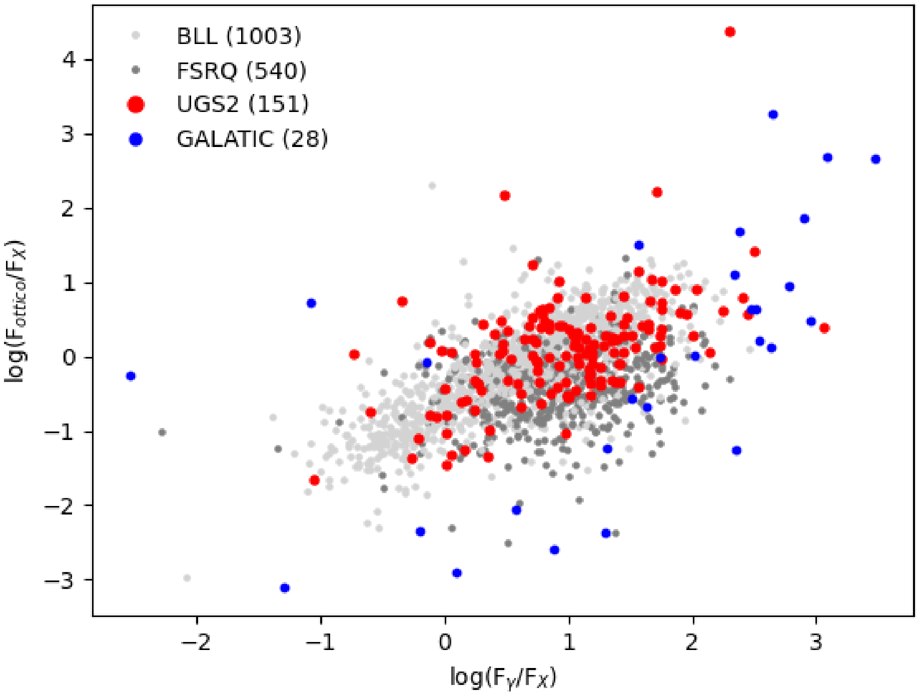

Figure 6.8: $\log(F_{\mathrm{radio}}/F_X)$ vs $\log(F_\gamma/F_X)$ (top) and $\log(F_{\mathrm{optical}}/F_X)$ vs $\log(F_\gamma/F_X)$ (bottom) diagrams and for 4FGL-DR4 BLL (light grey), 4FGL-DR4 FSRQ (grey), UGS2 (red) and 4FGL-DR4 Galactic sources (blue). It is worth noting that sources with proper motion, those lacking an optical counterpart, or those without g-band magnitude estimates are not included in the plot.

7

Spectroscopy of a Sample of UGSs

Results in short

This chapter discusses the optical spectroscopy of a sample of 33 UGSs, for which only one X-ray source, detected by the *Swift* satellite (see Chapter 6 for more details), was found within the *Fermi* error boxes, and for which an optical spectrum had already been reported in the literature. As discussed in Chapters 1 and 3, the analysis of optical spectra is a crucial step in the association and classification of extra-galactic UGSs.

We found that among the 33 UGS analysed, 21 of them can be classified as BLL objects. Among these we were able to provide the redshift for 8 of them while for 2 others we established a lower limit to the redshift by detecting intervening absorption. The other 12 objects display optical spectra with prominent emission lines ($0.036<z<1.65$). These spectra are characterized by both broad and narrow emission lines with the exception of 3 sources. Of these, 1 displays only broad emission lines, while the other 2 exclusively exhibit narrow lines. On the basis of the radio/optical flux ratio, all BLL objects in this study are radio loud. Among the 12 sources with prominent emission lines, 4 can be classified as radio loud, while at least 5 of the 12 sources with prominent lines are radio quiet. This is somewhat unexpected comparing with the radio-loudness distribution of the 4FGL-associated blazars (see Fig. 6.5 and Chapter 6 for more details).

The work presented in this chapter was published under the title "**Spectroscopy of a Sample of Unidentified Gamma-ray *Fermi* Sources**" in Monthly Notices of the Royal Astronomical Society, Volume 530, Issue 4, June 2024, Pages 4626–4647, (`https://doi.org/10.1093/mnras/stae587`).

7.1.0 Introduction

Several efforts have been made over the years in order to associate and classify UGSs. Various statistical algorithms (Ackermann et al. 2012a; Mirabal et al. 2012; Mao & Yu 2013) and neural network classifiers (Doert & Errando 2014; Salvetti et al. 2017a; Kaur et al. 2019a,b; Kerby et al. 2021; Kaur et al. 2023), based on γ-ray spectral features and variability information, have been developed with the aim to distinguish blazars from other γ-ray source populations. Other works were focused on the search for counterparts at other wavelengths. In the radio band Petrov et al. (2013), Nori et al. (2014), Schinzel et al. (2015), Schinzel et al. (2017), Bruzewski et al. (2021), Bruzewski et al. (2022) provided radio counterparts of UGSs using ATCA and LOFAR data. D'Abrusco et al. (2013) and Massaro et al. (2015b, and references therein) proposed AGN candidates on the basis of the colours of the infrared (IR) counterparts in the Wide-field Infrared Survey Explorer (WISE) survey (Wright et al. 2010). Searches using X-ray data has been performed by Falcone et al. (2011), Takahashi et al. (2012), Landi et al. (2015), Salvetti et al. (2017b), Kaur et al. (2019a), Kaur et al. (2019b), Kerby et al. (2021), Kaur et al. (2023) and Marchesini et al. (2020), while a multi-wavelength approach has been adopted by Acero et al. (2013), Paiano et al. (2017b), Fronte et al. (2023). Moreover, numerous pulsars have been discovered among the UGSs through timing studies from the γ-ray band to the radio band (Abdo et al. 2013; Wu 2018; Li et al. 2018, and references therein).

The firm classification of the *Fermi* sources requires spectroscopy of the optical counterpart. Optical spectra act as the fingerprints of these objects, enabling their extragalactic nature and classification to be determined. Shaw et al. (2012, 2013c) studied the optical spectra of about 500 sources of the second *Fermi* catalog (2FGL, Nolan et al. 2012), confirming the blazar nature of these objects and estimating a redshift (or a lower limit) for each of them. D'Abrusco et al. (2013), Massaro et al. (2015b, 2016) and references therein, focused on the association and classification of the UGSs of the second and third *Fermi* (3FGL, Acero et al. 2015) catalogs: among a sample of ~600 candidates, they classified ~200 blazars using selection criteria based on the infrared (IR) colors of counterparts in the WISE survey. Paiano et al. (2017d,c, 2020, 2021, 2023) analyzed the optical spectra of ~150 BLL objects (or candidates) identified as TeV (or TeV candidate) emitters and/or potential neutrino sources. In addition, Paiano et al. (2017a, 2019) focused on the association and classification of UGSs from the second and third *Fermi* catalogs. All sources exhibited an AGN optical spectrum (44 as BLLs, 1 QSO, 1 NLSy1 and 2 objects with a Seyfert 2 type spectrum). A recent summary of spectroscopic observations on blazar *Fermi* sources can be found in Paliya et al. (2021).

In this chapter, we report the results of the association study for a sample of 33 UGSs of the 4FGL-DR3 catalogue (Abdollahi et al. 2022) that have only one X-ray counterpart in the *Fermi* error ellipse and for which an optical spectrum is already available in literature or in public surveys, providing details about the main spectral properties and the classification.

This chapter is structured as follows: in Sec. 7.2, we introduce the sample under consideration, in Sec. 7.3 we present the main results from the analysis of the optical spectra and multi-wavelength data, in the Sec. 7.4 we give notes on individual objects, and finally in Sec. 7.5 we summarize and discuss the main properties of the sample in a multi-wavelength point of view.

7.2.0 Definition of sample

We found that among the UGS1 sub-sample (UGSs with only one potential X-ray counterpart; see Chapter 6 for details and for the procedure of searching for counterparts), 33 objects have a X-ray counterpart which has already an optical spectrum in literature, in ASCII or FITS format.

The main information of the *Swift*/XRT observations and results of the X-ray analysis for this sub-sample of the entire list of UGS studied are summarized in Tab. 7.1. In Tab. 7.2 we list the multi-wavelength counterparts of each UGS. For this work we decided to perform an additional search[1] for any uncatalogued radio sources using public radio images provided through LOFAR in the northern hemisphere and RACS in the southern hemisphere. Additionally, for the search for optical counterparts, the United States Naval Observatory (USNO, Monet et al. 2003)

---

[1] The radio detection was performed by applying two circular regions: one around the source (found through the search for the centroid, or in the absence of an obvious source on the position of the X-ray source) of size 10 arcsec, and the other in a region without of radio sources, of size 50 arcsec, to estimate the background. The ratio between the maximum flux in the source region and the rms of the background region gives the SNR of the detection.

Table 7.1: X-ray info of the 33 UGSs sample

4FGL Name	γ-ray significance (σ)	*Swift* exp. time (ks)	XRT counterpart	RA (J2000)	DEC (J2000)	X-ray positional error radius (")	X-ray significance (σ)
4FGLJ0023.6-4209	5.1	3.4	XRTJ002303.5-420509.6	5.76496	-42.08601	2.9	5.0
4FGLJ0112.0+3442	4.8	4.7	XRTJ011124.8+344154.1	17.85359	34.69837	4.7	4.0
4FGLJ0117.9+1430	6.1	6.6	XRTJ011804.7+143159.5	19.51996	14.53322	3.0	4.7
4FGLJ0202.7+3133	4.3	10.5	XRTJ020242.1+313211.3	30.67554	31.53649	2.5	10.3
4FGLJ0251.1-1830	11.0	7.7	XRTJ025111.7-183111.1	42.79877	-18.51976	2.7	8.9
4FGLJ0259.0+0552	23.2	4.9	XRTJ025857.5+055244.4	44.73982	5.87900	3.4	5.2
4FGLJ0641.4+3349	4.4	3.6	XRTJ064111.2+334502.0	100.29683	33.75056	3.7	13.8
4FGLJ0838.5+4013	4.1	3.9	XRTJ083902.9+401546.9	129.76240	40.26303	3.0	4.4
4FGLJ0938.8+5155	6.1	10.6	XRTJ093834.5+515454.7	144.64375	51.91522	6.1	3.8
4FGLJ1016.1-4247	12.8	6.1	XRTJ101620.7-424723.2	154.08659	-42.78978	2.7	8.6
4FGLJ1039.2+3258	9.8	5.1	XRTJ103852.1+325651.9	159.71738	32.94776	3.0	4.6
4FGLJ1049.8+2741	6.5	5.5	XRTJ104938.7+274212.0	162.41124	27.70335	2.9	5.8
4FGLJ1125.1+4811	4.5	50.5	XRTJ112526.0+480922.8	171.35839	48.15634	5.4	4.3
4FGLJ1131.6+4657	6.3	4.6	XRTJ113142.3+470009.2	172.92651	47.00256	2.6	6.0
4FGLJ1146.0-0638	13.5	3.3	XRTJ114600.8-063853.9	176.50361	-6.64831	3.1	6.7
4FGLJ1256.8+5329	5.6	5.6	XRTJ125630.5+533202.2	194.12725	53.53397	6.4	4.2
4FGLJ1308.7+0347	9.7	3.6	XRTJ130832.2+034405.3	197.13445	3.73483	4.0	5.5
4FGLJ1346.5+5330	10.3	3.9	XRTJ134545.1+533252.4	206.43811	53.54791	2.2	13.5
4FGLJ1410.7+7405	22.9	11.7	XRTJ141045.6+740509.8	212.69026	74.08608	7.2	4.5
4FGLJ1430.6+1543	4.8	1.6	XRTJ143057.9+154556.0	217.74133	15.76529	3.1	5.4
4FGLJ1535.9+3743	18.1	10.7	XRTJ153550.5+374056.8	233.96065	37.68245	4.6	4.1
4FGLJ1539.1+1008	5.6	6.2	XRTJ153848.5+101841.7	234.70214	10.31159	3.2	5.0
4FGLJ1544.9+3218	6.5	13.9	XRTJ154433.1+322148.5	236.13813	32.36349	2.6	10.1
4FGLJ1554.2+2008	10.6	8.2	XRTJ155424.1+201125.3	238.60069	20.19041	2.0	34.5
4FGLJ1555.3+2903	5.1	3.5	XRTJ155513.0+290328.0	238.80422	29.05779	3.5	10.9
4FGLJ1631.8+4144	8.0	3.7	XRTJ163146.8+414631.8	247.94510	41.77550	2.6	8.9
4FGLJ1648.7+4834	5.7	4.2	XRTJ164900.5+483409.1	252.25233	48.56921	2.8	5.7
4FGLJ2030.0-0310	4.5	4.5	XRTJ203014.3-030722.8	307.55974	-3.12276	2.8	11.0
4FGLJ2207.1+2222	7.5	4.8	XRTJ220704.1+222231.8	331.76740	22.37552	3.3	5.0
4FGLJ2240.3-5241	11.8	5.8	XRTJ224017.55-524112.3	340.07314	-52.68676	3.6	3.4
4FGLJ2317.7+2839	10.7	14.1	XRTJ231740.1+283955.4	349.41730	28.66540	5.8	4.3
4FGLJ2323.1+2040	6.2	3.3	XRTJ232320.30+203523.6	350.83459	20.58990	4.2	3.5
4FGLJ2353.2+3135	9.0	28.0	XRTJ235319.39+313616.9	358.3308	31.6047	3.5	8.2

Note. Column 1: 4FGL Name of the target; Column 2: γ-ray detection significance as reported in the 4FGL catalog; Column 3: *Swift*/XRT exposure time; Column 4: X-ray counterpart detected from our *Swift*/XRT analysis (Names report the acronym of the XRT detector plus the J2000 sexagesimal coordinates); Column 5-6: Coordinates of the proposed X-ray counterpart in degrees; Column 7: X-ray positional error radius in arcsecs; Column 8: Detection significance of the X-ray counterpart.

survey was also used. In Fig. A.1 we show the *Fermi* error boxes superimposed to the X-ray images (first 33 sub-figures). Fig. A.2 contains the optical images (Fig. A.2) taken from the PANSTARRs, DES and NOIRLab Astro Data database with the overlay of the proposed X-ray and radio counterparts (first 33 sub-figures). Details of the multi-wavelength study, including the X-ray and the optical skymaps for the entire UGS sample with at least one X-ray detection are presented in Ulgiati et al., (submitted) and in Chapter 6.

7.3.0 Results

The available and downloaded optical spectra found in literature of our 33 UGS sample (see Tab. 7.3 for the references) are shown in Fig. 7.1. The spectra are dereddened for the Galaxy contribution, applying the extinction law by Cardelli et al. (1989) and assuming the E(B-V) values provided by the NASA/IPAC infrared science archive [2]. Note that for 2 objects (4FGLJ0023.6-4209 and 4FGLJ2030.0-0310) the spectra, taken from the 6dF survey, are not

---

[2] https://irsa.ipac.caltech.edu/applications/DUST/

Table 7.2: Multi-wavelength counterparts proposed for the sample of 33 UGSs

4FGL Name	XRT counterpart	Radio counterpart	Optical counterpart	RA J2000	DEC J2000
4FGLJ0023.6-4209	XRTJ002303.5-420509.6	RACSJ002303.61-420509.57	DESJ002303.74-420508.4	5.765596	-42.08569
4FGLJ0112.0+3442	XRTJ011124.8+344154.1	VLASS1QLCIRJ011124.83+344154.5	SDSSJ011124.86+344154.6	17.853583	34.698500
4FGLJ0117.9+1430	XRTJ011804.7+143159.5	-	SDSSJ011804.83+143158.6	19.520125	14.532944
4FGLJ0202.7+3133	XRTJ020242.1+313211.3	VLASS1QLCIRJ020242.03+313211.0	SDSSJ020242.06+313210.9	19.520125	14.532944
4FGLJ0251.1-1830	XRTJ025111.7-183111.1	VLASS1QLCIRJ025111.53-183112.3	PANJ025111.53-183112.7	42.798000	-18.520167
4FGLJ0259.0+0552	XRTJ025857.5+055244.4	VLASS1QLCIRJ025857.55+055244.0	SDSSJ025857.55+055243.9	44.739792	5.878861
4FGLJ0641.4+3349	XRTJ064111.24+334502.0	VLASS1QLCIRJ064111.20+334459.6	PANJ064111.22+334459.7	100.296750	33.749917
4FGLJ0838.5+4013	XRTJ083902.9+401546.9	VLASS1QLCIRJ083903.07+401545.6	SDSSJ083903.08+401545.6	129.762833	40.262667
4FGLJ0938.8+5155	XRTJ093834.5+515454.7	LoTSS093834.68+515451.8	SDSSJ093834.72+515452.3	144.644667	51.914528
4FGLJ1016.1-4247	XRTJ101620.7-424723.2	ATCAJ101620.76-424723.1	USNOJ101620.67-424722.6	154.086125	-42.789611
4FGLJ1039.2+3258	XRTJ103852.1+325651.9	VLASS1QLCIRJ103852.17+325651.9	SDSSJ103852.17+325651.6	159.717375	32.947667
4FGLJ1049.8+2741	XRTJ104938.7+274212.0	VLASS1QLCIRJ104938.81+274213.1	SDSSJ104938.79+274213.0	162.411625	27.703611
4FGLJ1125.1+4811	XRTJ112526.0+480922.8	-	SDSSJ112526.27+480922.0	171.359458	48.156111
4FGLJ1131.6+4657	XRTJ113142.3+470009.2	VLASS1QLCIRJ113142.36+470009.4	SDSSJ113142.27+470008.6	172.926125	47.002389
4FGLJ1146.0-0638	XRTJ114600.8-063853.9	VLASS1QLCIR114600.87-063854.5	USNOB1-0833-0250645	176.504000	-6.648556
4FGLJ1256.8+5329	XRTJ125630.5+533202.2	-	SDSSJ125630.43+533204.3	194.126792	53.534528
4FGLJ1308.7+0347	XRTJ130832.2+034405.3	-	SDSSJ130832.10+034403.9	197.133750	3.734417
4FGLJ1346.5+5330	XRTJ134545.1+533252.4	VLASS1QLCIRJ134545.34+533252.1	SDSSJ134545.36+533252.3	206.439000	53.547861
4FGLJ1410.7+7405	XRTJ141045.6+740509.8	JVLAJ141046.00+740511.2*	PANJ141045.95+740510.8	212.691458	74.086333
4FGLJ1430.6+1543	XRTJ143057.9+154555.0	-	SDSSJ143058.03+154555.6	217.741792	15.765444
4FGLJ1535.9+3743	XRTJ153550.56+374056.8	VLASS1QLCIR J153550.56+374055.5	SDSSJ153550.54+374055.6	233.960583	37.682111
4FGLJ1539.1+1008	XRTJ153848.5+101841.7	-	SDSSJ153848.47+101843.2	234.701958	10.312000
4FGLJ1544.9+3218	XRTJ154433.1+322148.5	VLASS1QLCIRJ154433.20+322149.1	SDSSJ154433.19+322149.1	236.138292	32.363639
4FGLJ1554.2+2008	XRTJ155424.1+201125.3	VLASS1QLCIRJ155424.15+201125.5	SDSSJ155424.12+201125.4	238.600500	20.190389
4FGLJ1555.3+2903	XRTJ155513.0+290328.0	VLASS1QLCIRJ155512.89+290330.0	SDSSJ155512.91+290329.9	238.803792	29.058306
4FGLJ1631.8+4144	XRTJ163146.8+414631.8	VLASS1QLCIRJ163146.74+414632.7	SDSSJ163146.72+414632.8	247.944667	41.775778
4FGLJ1648.7+4834	XRTJ164900.5+483409.1	VLASS1QLCIRJ164900.35+483411.7	SDSSJ164900.34+483411.8	252.251417	48.569944
4FGLJ2030.0-0310	XRTJ203014.3-030722.8	ATCAJ203014.27-030721.8	PANJ203014.27-030722.5	307.559458	-3.122933
4FGLJ2207.1+2222	XRTJ220704.1+222231.8	VLASS1QLCIRJ220704.09+222231.5	SDSSJ220704.10+222231.4	331.767083	22.375389
4FGLJ2240.3-5241	XRTJ224017.55-524112.3	RACS224017.79-524111.1	DESJ224017.71-524113.7	340.073792	-52.687139
4FGLJ2317.7+2839	XRTJ231740.1+283955.4	VLASS1QLCIRJ231740.21+283955.8	SDSSJ231740.00+283955.7	349.416667	28.665472
4FGLJ2323.1+2040	XRTJ232320.30+203523.6	VLASS1QLCIRJ232319.95+203523.7	SDSSJ232320.34+203523.4	350.834772	20.589860
4FGLJ2353.2+3135	XRTJ235319.39+313616.9	VLASS1QLCIRJ235319.50+313616.8	SDSSJ235319.54+313616.7	358.331417	31.604639

Note. Column 1: 4FGL Name of the target; Column 2: X-ray counterpart; Column 3: Radio counterpart (Names report the acronym of the radio facility plus the J2000 sexagesimal coordinates); Column 4: Optical counterpart; Column 5-6: Coordinates of the optical counterpart in degrees.
(*) Radio source proposed by (Marchesini et al. 2023a)

Table 7.3: Optical properties of the 33 UGSs

4FGL Name	Optical counterpart	g	r	Spectrum Reference	Line type	Redshift	Spectrum Class
4FGLJ0023.6-4209	DESJ002303.74-420508.4	15.6	15.0	6dF	e	0.053	Type-2
4FGLJ0112.0+3442	SDSSJ011124.86+344154.6	19.4	19.0	SDSS	e,g	0.3997	BLL
4FGLJ0117.9+1430	SDSSJ011804.83+143158.6	18.7	18.3	SDSS	e	0.129	Type-1
4FGLJ0202.7+3133	SDSSJ020242.06+313210.9	18.7	18.4	SDSS	-	? *	BLL
4FGLJ0251.1-1830	PANJ025111.53-183112.7	20.2	19.6	Paiano et al. (2019)	i	>0.615	BLL
4FGLJ0259.0+0552	SDSSJ025857.55+055243.9	18.6	18.3	Paiano et al. (2019)	-	?	BLL
4FGLJ0641.4+3349	PANJ064111.22+334459.7	17.1	16.4	Monroe et al. (2016)	e	0.1657	Type-1
4FGLJ0838.5+4013	SDSSJ083903.08+401545.6	18.2	17.0	SDSS	g	0.1945	BLG
4FGLJ0938.8+5155	SDSSJ093834.72+515452.3	20.3	20.1	SDSS	e	0.4168	Type-1
4FGLJ1016.1-4247	USNOJ101620.67-424722.6	19.3	18.2	Rajagopal et al. (2023)	-	?	BLL
4FGLJ1039.2+3258	SDSSJ103852.17+325651.6	19.7	18.9	SDSS	-	? *	BLL
4FGLJ1049.8+2741	SDSSJ104938.79+274213.0	18.2	17.3	SDSS, de Menezes et al. (2019)	g	0.144	BLG
4FGLJ1125.1+4811	SDSSJ112526.27+480922.0	20.3	20.2	SDSS	e	1.649	Type-1
4FGLJ1131.6+4657	SDSSJ113142.27+470008.6	17.5	16.5	SDSS	g	0.1255	BLG
4FGLJ1146.0-0638	USNOB1-0833-0250645	19.5	19.7	Paiano et al. (2019)	g	0.6407	BLL
4FGLJ1256.8+5329	SDSSJ125630.43+533204.3	20.6	20.3	SDSS	e	0.996	Type-1
4FGLJ1308.7+0347	SDSSJ130832.10+034403.9	17.2	17.3	SDSS	e	0.6193	Type-1
4FGLJ1346.5+5330	SDSSJ134545.36+533252.3	17.0	16.6	SDSS	e	0.1359	Type-1
4FGLJ1410.7+7405	PANJ141045.95+740510.8	19.2	19.3	Marchesini et al. (2023b)	-	?	BLL
4FGLJ1430.6+1543	SDSSJ143058.03+154555.6	17.4	16.9	SDSS	e	0.1633	Type-1
4FGLJ1535.9+3743	SDSSJ153550.54+374055.6	19.7	19.4	SDSS	e	0.6255	Type-1
4FGLJ1539.1+1008	SDSSJ153848.47+101843.2	18.3	18.0	SDSS	e	0.2345	Type-1
4FGLJ1544.9+3218	SDSSJ154433.19+322149.1	18.7	18.4	SDSS	-	? *	BLL
4FGLJ1554.2+2008	SDSSJ155424.12+201125.4	18.1	17.2	SDSS	g	0.2225	BLG
4FGLJ1555.3+2903	SDSSJ155512.91+290329.9	18.2	17.2	SDSS	g	0.1767	BLG
4FGLJ1631.8+4144	SDSSJ163146.72+414632.8	20.5	20.4	SDSS	-	? *	BLL
4FGLJ1648.7+4834	SDSSJ164900.34+483411.8	19.4	19.1	SDSS	-	? *	BLL
4FGLJ2030.0-0310	PANJ203014.27-030722.5	16.8	16.2	6dF	e	0.036	Type-2
4FGLJ2207.1+2222	SDSSJ220704.10+222231.4	20.4	19.9	SDSS	-	? *	BLL
4FGLJ2240.3-5241	DESJ224017.71-524113.7	18.1	17.4	Desai et al. (2019)	-	?	BLL
4FGLJ2317.7+2839	SDSSJ231740.00+283955.7	19.6	19.1	SDSS	-	? *	BLL
4FGLJ2323.1+2040	SDSSJ232320.34+203523.4	14.4	13.4	Marcha et al. (1996)	g	0.036	BLG
4FGLJ2353.2+3135	SDSSJ235319.54+313616.7	20.5	20.5	SDSS	i	>0.8809*	BLL

Note. Column 1: 4FGL Name of the target; Column 2: Optical counterpart; Column 3-4: magnitude in g and r band from PANSTARRs; Column 5: Reference of the optical spectrum; Column 6: Type of the detected lines: e = emission lines, g = absoption lines from the host galaxy, i = intervening absorption lines; Column 7: Redshift; Column 7: Classification based on the optical spectrum.
(*) New redshift estimates reported for the first time by this work. It is worth noting that, for a given number of sources, the literature redshift was disproved and then they are not known (except in one case, where we determined a lower limit). Details are reported in Sec. 7.4

flux calibrated and dereddened. Although they are useful for the redshift determination, no information of the magnitude of the source and line luminosities can be derived.

From the redshifts deduced from the analysis of the optical spectra and/or the presence of a power-law component (typical of the BLL), it was possible to asses the extragalacic nature of the sources.

For 20 out of 33 objects, clear spectral features are found that allow us to derive their redshift (see Tab. 7.3). We determine the position of the emission and absorption lines performing accurate search of the centroids, by computing the barycenter of each line after subtraction of the underlined continuum. The redshift is determined by comparing the found wavelenght centroids of each line with the expected rest-frame wavelenghts. After checking that all lines provide consistent results, we derived the final redshift from the average. 11 sources do not reveal intrinsic spectral features. For 7 sources, the optical spectrum exhibits absorption lines of the host galaxy stellar population (Ca II 3934,3968, G-band 4305, Mg I5175, and Na I 5893), 12 objects present only emission lines, and for one case (4FGLJ0112.0+3442) both emission and absorption lines are present.

We can classify 21 sources as BLL: 15 with spectra characterized by a power-law emission and another 6 with a strong signature of the stellar population due to the host galaxy (labelled as galaxy-dominated BLL (BLG) in Tab. 7.3). The redshift of 7 BLLs has been determined through the detection of the host galaxy absorption lines. The redshifts are in the interval $0.04 < z < 0.64$ and the average value is <z> = 0.2 ± 0.1, in agreement with the typical BLL redshift distribution (Padovani et al. 2017; Garofalo et al. 2019). For 2 BLLs, 4FGLJ0251.0-1830 (Paiano et al. 2019, for details) and 4FGLJ2353.0+3135 (see Fig. 7.1), we can detect only intervening absorption systems due to MgII 2899 that allow us to provide a spectroscopic redshift lower limit.

The spectra of the remaining 12 objects all have prominent emission lines (mainly CIII], MgII, [OII], H_β, [OIII], H_α, [N II] and [SII]), most of them showing a type-1 spectrum with broad and narrow emission lines. One high redshift source ($z \geq 1$) displays only broad emission lines. 4FGLJ0117.9+1430 can be classified as a Narrow Line Seyfert 1 (see details in Sec. 7.4), while the other 11 have a Seyfert/QSO-like spectrum.

To better analyze the intrinsic properties of the AGN as the source of the γ-ray emission, we separated the nuclear and host galaxy components, using r-band images from the PANSTARRs, SDSS, and DES databases for 15 sources with redshift < 0.5 and/or a significant host galaxy contribution. The AIDA software (Uslenghi & Falomo 2011) was used for image decomposition, enabling us to isolate the nuclear component and determine key photometric and morphological characteristics of the host galaxy, such as absolute magnitude, effective radius, and Sersic index n [3].

From this r-band image decomposition, we found that all 15 galaxies with redshift $z < 0.5$ are resolved, except for 4FGLJ0112.0+3442. The decomposition results are presented in Tab. 7.4.

The optical properties and the multi-wavelength emission data of the 33 UGS are summarized

---

[3] The surface brightness profile of a galaxy is described by the Sersic law: $\frac{I(r)}{I(e)} = exp(- b_n ((\frac{r}{R_e})^{\frac{1}{n}} - 1))$, where I_e is the light intensity at the effective radius R_e, the major-axis effective radius encompassing half of the total flux, and n is the Sersic index, with b_n a constant depending on n.

Table 7.4: Results of the analysis and decomposition of the PANSTARRs images

4FGL Name	z	r	r_n	r_h	$M(r)_h$	R_e	n	N/H
4FGLJ0023.6-4209*	0.053	14.9	>18.5	14.9	-21.9	6.8	1.4	<0.05
4FGLJ0112.0+3442	0.3997	18.7	19.0	20.4	>-21.3	7*	4	4
4FGLJ0117.9+1430	0.129	18.2	19.4	18.5	-20.4	2.0	4	0.4
4FGLJ0641.4+3349	0.1657	16.3	17.1	16.7	-22.8	7*	5	0.7
4FGLJ0838.5+4013	0.1945	16.9	19.1	16.7	-23.1	10.5	4	0.1
4FGLJ0938.8+5155	0.4168	19.8	20.4	20.6	-21.2	10.7	4	1
4FGLJ1049.8+2741	0.144	17.2	19.0	17.2	-21.9	5.1	4	0.25
4FGLJ1131.6+4657	0.1255	16.4	18.9	16.3	-22.5	7.6	4	0.1
4FGLJ1346.5+5330	0.1359	16.4	17.8	16.7	-22.3	4	4	0.4
4FGLJ1430.6+1543	0.1633	16.8	18.0	17.1	-22.3	5.9	2.1	0.4
4FGLJ1539.1+1008	0.2345	17.9	18.3	19.2	-21.1	3.6	3.0	2.5
4FGLJ1554.2+2008	0.2225	16.9	18.3	17.2	-23.0	7.9	4	0.4
4FGLJ1555.3+2903	0.1767	17.0	19.3	17.0	-22.6	7.3	4	0.1
4FGLJ2030.0-0310	0.036	16.1	18.8	16.1	-19.8	1.1	1.9	0.1
4FGLJ2323.1+2040*	0.038	13.6	>17.0	13.6	-22.5	6.5	4	<0.05

Note. Column 1: *Fermi* name, Column 2: Redshift, Column 3: r from aperture photometry of the PANSTARRs image, Column 4-5: apparent magnitude of the nucleus (r_n) and of the host galaxy (r_h) derived by the imaging analysis, Column 6: Absolute magnitude of the host galaxy, Column 7: Effective radius (kpc), Column 8: Sersic index n, Column 9: Galaxy flux to nucleus flux ratio.
(*) For 4FGLJ0023.6-4209 the DES image is used and for 4FGLJ2323.1+2040 we used the SDSS image.

in Tab. 7.5[4]. While γ-ray, optical and radio fluxes come from catalogs, the X-ray fluxes are extracted through spectral fits (see Sec. 6.2 for details).

For each source, we evaluate the *radio-loudness* parameter R (see Chapter 1 and Sec. 6.4 for the definition of *radio-loudness*), and we present the results in Tab. 7.5. We classify sources as radio loud or radio quiet using the historical threshold of R>10 (Kellermann et al. 1989). All BLL sources in our sample are found to be radio loud. About the other 12 sources, 4 sources (4FGLJ0023.6-4209, 4FGLJ0938.8+5155, 4FGLJ1346.5+5330 and 4FGLJ1535.9+3743) can be classified as radio-loud, 2 have $R < 10$, and 6 are not detected in the radio images, allowing us to put an upper limit on R.

Based on the absolute magnitude (M_{abs} <-23 for QSO, e.g. Osterbrock 1980) and the optical imaging analysis (see details in Chapter 6), 4 sources have the typical luminosity of the QSO: 4FGLJ1535.9+3743 is a radio-loud quasar and 4FGLJ1125.1+4811, 4FGLJ1256.8+5329 and 4FGLJ1308.7+0347 radio quiet quasars. The other 8 objects can be classified as Seyfert galaxies.

---

[4] We adopted concordance cosmology (e.g. Seehars et al. 2016) assuming Hubble constant $H_0 = 70$ km s^{-1} Mpc^{-1}, matter density $\Omega_{m,0} = 0.3$, and dark energy density $\Omega_{\Lambda,0} = 0.7$.

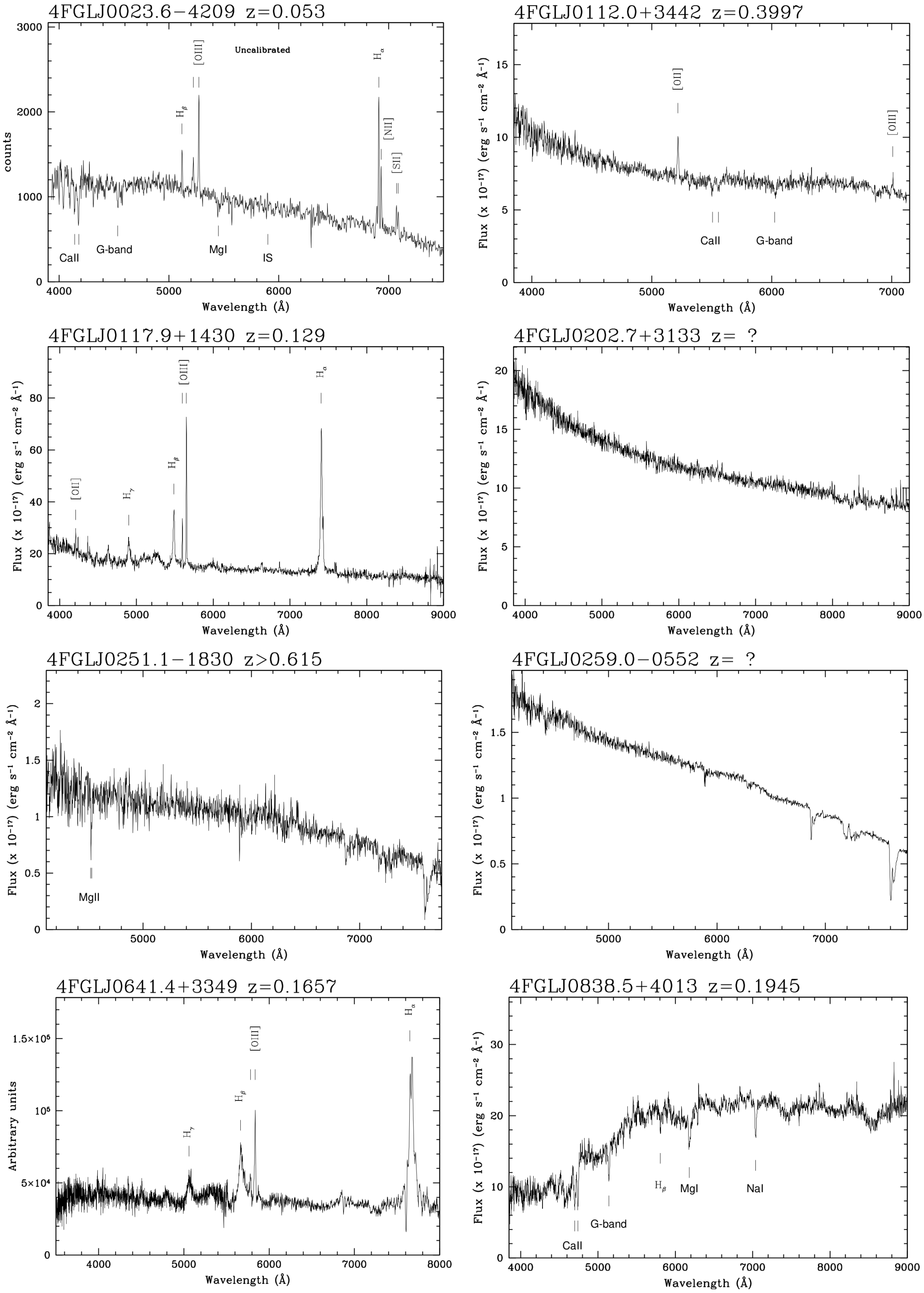

Figure 7.1: Optical spectra of the counterparts of UGS with only one X-ray detection within the 3σ *Fermi* error ellipses (see text and Tab. 2 and 3 for details).

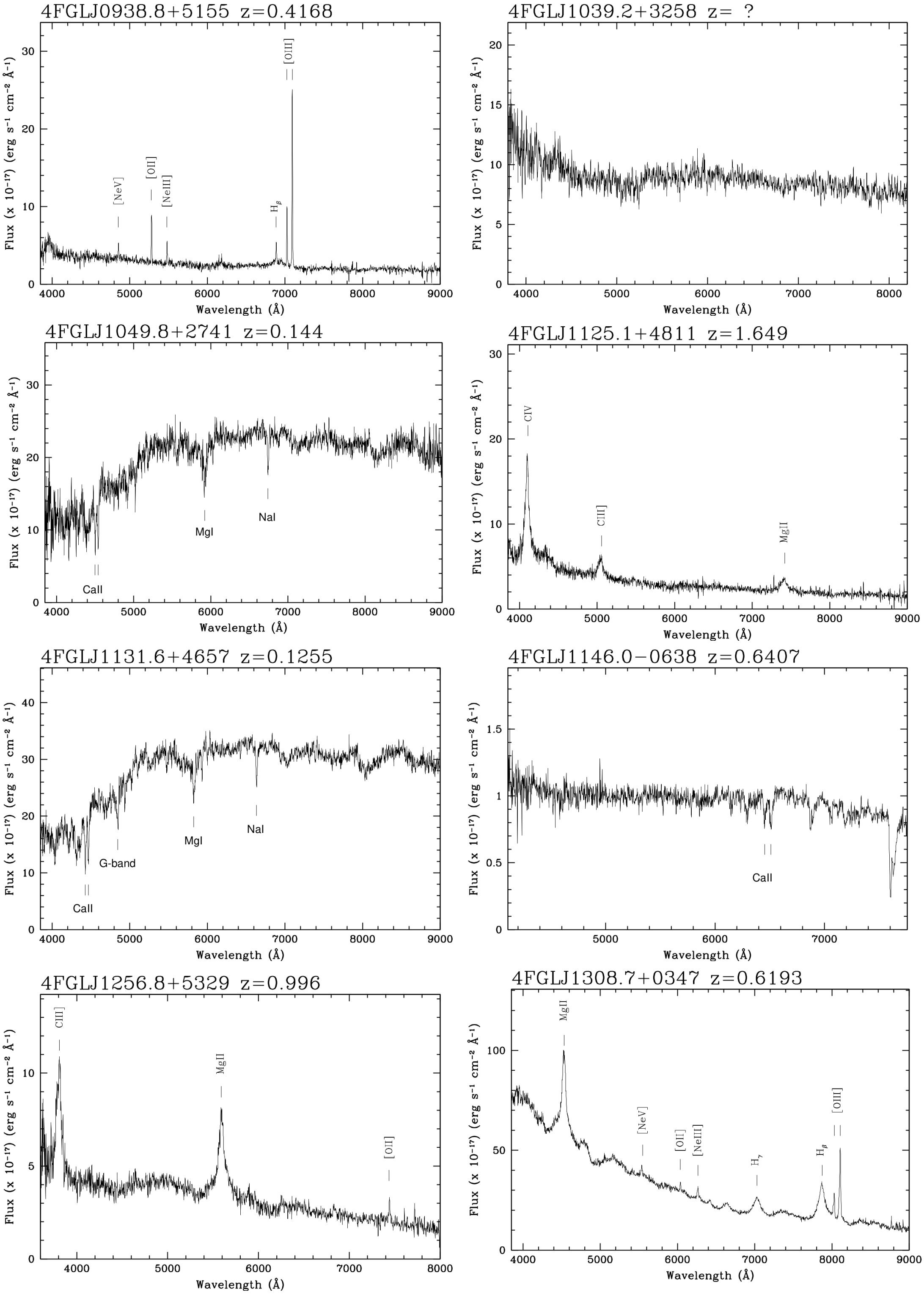

Figure 7.1: Continued.

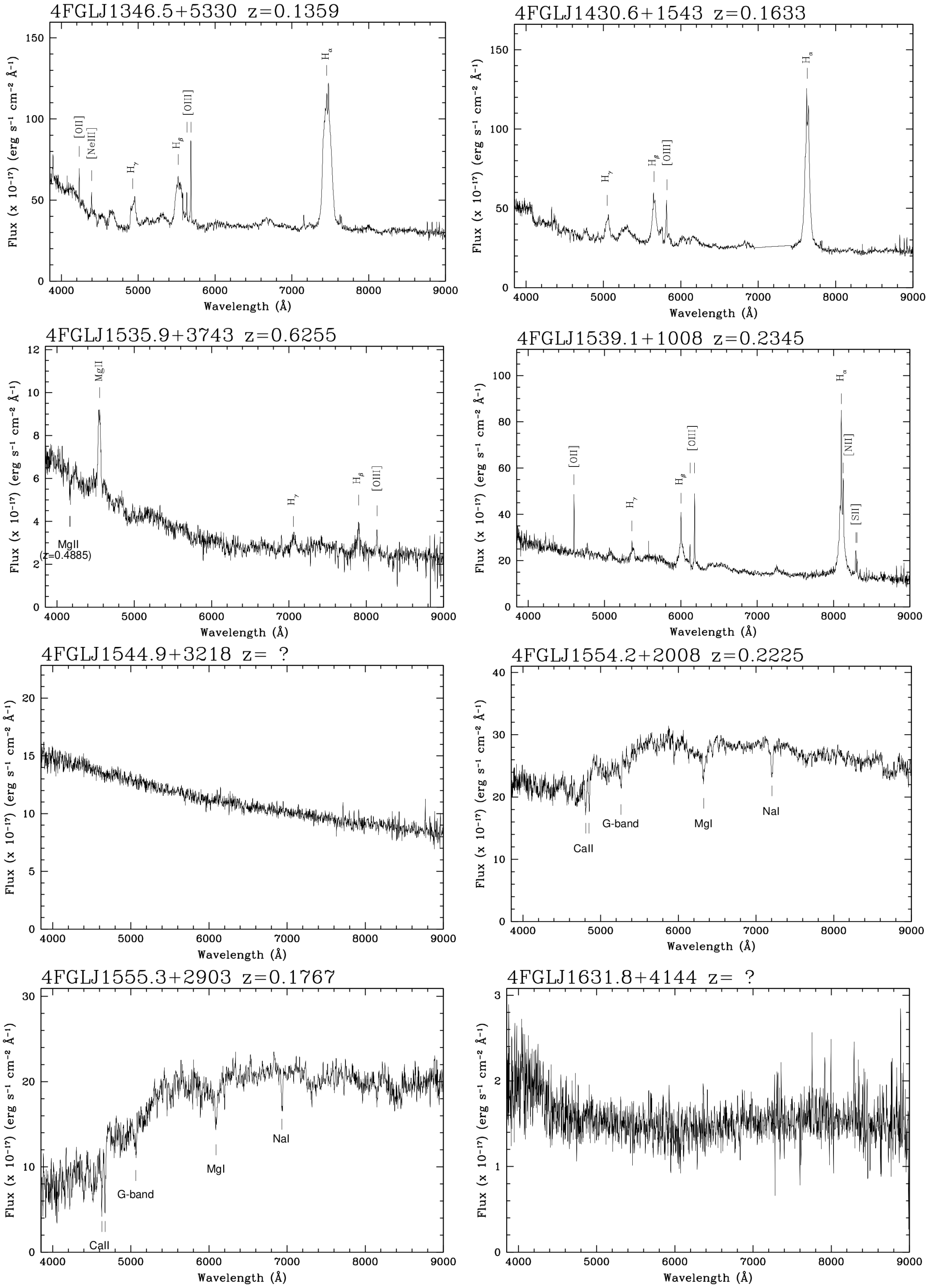

Figure 7.1: Continued.

7.4.0 Notes on Individual Sources

4FGLJ0023.6-4209 - DESJ002303.74-420508.4: In the *Swift*/XRT image we find the source XRTJ002303.5-420509.6 as the likely X-ray counterpart for this UGS. It coincides with the optical source DESJ002303.74-420508.4 (g=15.6), and the radio source J002303.61-420509.57, detected from the analysis of radio RACS data covering the UGS sky region (see first 33 sub-figures of Fig. A.2). The radio source appears point-like and it has a density flux F = 3.3 mJy that corresponds to a radio-loudness R>15 (see Tab. 7.4 and 7.5). In the uncalibrated 6dF Galaxy Redshift survey optical spectrum, we are able to detect prominent and narrow emission lines attributed to H_β 4861, [O III] 4959,5007 , H_α 6563, [N II] 6583 and [S II] 6717,6731 at z = 0.053. No broad lines are found. The emission line properties of this object are typical of Seyfert 2 galaxies and from a inspection of the optical image (see first 33 sub-figures of Fig. A.2) the host galaxy appears as spiral galaxy. Given the remarkably proximity ($z < 0.053$), the γ-ray luminosity of 4FGLJ0023.6-4209 is $\sim 10^{43}$ erg/s, one of the weakest of our sample.

4FGLJ0112.0+3442 - SDSSJ011124.86+344154.6: From the *Swift/XRT* analysis, we reveal the X-ray source XRTJ011124.8+344154.1 within the *Fermi* error box. The sources is positionally coincident with the radio source VLASS1QLCIRJ011124.83+344154.5 and the optical source SDSSJ011124.86+344154.6. The optical spectrum, available in the SDSS archive, shows [O II] and [O III] emission lines and the Ca II doublet absorption lines consistent with redshift z=0.3397. Given the power-law shape of the spectrum, the source can be classified as a BLL. It is worth to note that this UGS is 1 of 3 sources listed in the 4FGL that lies within the event radius of the neutrino event IceCube-230511A[5].

4FGLJ0117.9+1430 - SDSSJ011804.83+143158.6: Within the *Fermi* error box of this UGS, we detect the X-ray source XRTJ011804.7+143159.5 coincident with the optical source SDSSJ011804.83+143158.6 (g = 18.7). No radio counterpart is found in the NVSS and VLASS catalogue. From the RACS data we can estimate the radio flux upper limit of 4.2 mJy/beam (within 5σ). The SDSS spectrum clearly shows prominent emission lines (H_δ 4102, H_γ 4340, H_β 4861 and [O III] 4959,5007) at z = 0.129. We note that the Balmer lines show broad components and in particular, based on the H_β 4861 width (FWHM~500 km/s) and on the line ratio ([OIII] 5007/H_β)~1 (see e.g. Komossa 2008), we can classify the source as a NLSy1, according to that reported by Rakshit et al. (2017).

4FGLJ0202.7+3133 - SDSSJ020242.06+313210.9: We propose the source XRTJ020242.13+313211.4, found in the *Swift*/XRT skymap, as the X-ray counterpart for this UGS, spatially coincident with the optical object SDSSJ020242.06+313210.9 (g =

---

[5] https://gcn.nasa.gov/circulars/33773?page=5

18.7) and the radio source VLASS1QLCIRJ020242.03+313211.0. The SDSS spectrum appears featureless and exhibits the characteristic power-law continuum of the BLL.

4FGLJ0641.4+3349 - PANJ064111.22+334459.7: From the *Swift*/XRT imaging analysis, in the 4FGL error box of this γ-ray emitter, we find the X-ray source XRTJ064111.24+334502.0, coincident with the radio source VLASS1QLCIRJ064111.20+334459.6 (1.2 mJy) and the optical source PANJ064111.22+334459.7 (g=17.1). The spectrum of the optical source, available in Monroe et al. (2016), shows prominent narrow emission lines due [OIII] 4959, 5007 and broad H_γ 4340, H_β 4861 and H_α 6564 emission lines at redshift z=0.1657. On the basis of the absolute magnitude, the radio-loudness R ~2.5 and the emission lines properties, this object can be classified as a low redshift radio quiet QSO.

4FGLJ0838.5+4013 - SDSSJ083903.08+401545.6: Inside the *Fermi* error box of this UGS we find the X-ray source XRTJ083902.9+401546.9 coincident with the radio source VLASS1QLCIRJ083903.07+401545.6 (Joffre et al. 2022) and the optical source SDSSJ083903.08+401545.6. Kaur et al. (2023) and Joffre et al. (2022) through a machine learning analysis proposed the X-ray object as a BLL candidate. The SDSS spectrum is dominated by a galactic component and we can identify several absorption lines (Ca II, G-band, Mg I, and Na II) at $z = 0.1945$ due to old stellar population of the host galaxy. The source can be classify as a galaxy-dominated BLL in agreement with what reported in the BZCAT catalog.

4FGLJ0938.8+5155 - SDSSJ093834.72+515452.3: Through the inspection of *Swift*/XRT data, we find the X-ray source XRTJ093834.5+515454.7 inside the 3σ *Fermi* error ellipse. Analysing radio data of the LoTSS survey we found a radio detection J093834.68+515451.8 (0.6mJy) coincident with the X-ray source. A SDSS spectrum available for the optical counterpart SDSSJ093834.72+515452.3 (g=20.3) shows prominent and narrow emission lines attributed to [O II], H_γ, H_β, [O III], H_α and [N II] consistent with z=0.4168. A broad component is present for the H_β and H_α. Based on this information, the target can be classified as a radio loud QSO.

4FGLJ1039.2+3258 - SDSSJ103852.17+325651.6: We propose the X-ray source XRTJ103852.1+325651.9 found inside the *Fermi* error box of this γ-ray emitter as the likely lower energy counterpart. It is coincident with the radio source VLASS1QLCIRJ103852.17+325651.9 and the optical source SDSSJ103852.17+325651.6. The modest quality SDSS spectrum, reported also in de Menezes et al. (2019) and associated to the IR source WISEJ103852.20+325651.7, appears featureless typical of BLL, although a possible weak signature of CaII break at ~5200 can be recognized yelding a tentative redshift of 0.32.

4FGLJ1049.8+2741 - SDSSJ104938.79+274213.0: Inside the 4FGL sky region of this UGS we find the X-ray source XRTJ104938.7+274212.0, that spatially coincides with the the radio source VLASS1QLCIRJ104938.81+274213.1 and the optical source SDSSJ104938.79+274213.0 (g=18.2). The optical spectrum provided by the SDSS survey is dominated by the component of the elliptical host galaxy (N/H=0.25 see Tab. 7.4) and a number of relevant absorption features are present: the CaII doublet, G-band, MgI and NaI at z=0.144.

4FGLJ1125.1+4811 - SDSSJ112526.27+480922.0: We find the X-ray source XRTJ112526.0+480922.8 inside the γ-ray 3σ error ellipse of this UGS. It is spatially coincident with the optical source SDSSJ112526.27+480922.0 (g=20.3). From the analysis of LOTSS radio data, no radio counterpart is found, in agreement with Gürkan et al. (2019). In the optical spectrum, obtained by the SDSS survey, we can detect broad emission lines attributed to CIV, C III and Mg II consistent with z=1.649. On the basis of this spectrum and of the MWL information, we can classify this source as a radio-quiet QSO. Within 4σ *Fermi* error box of this γ-ray emitter, another X-ray source is present, XRTJ112432.5+480741.0, coincident with the radio source VLASS1QLCIRJ112432.64+480739.9 and the optical source SDSSJ112432.65+480740.7 (g=22.7). An optical spectrum is available in the SDSS archive for this source. The power-law trend of the spectrum, absent of emission or absorption lines, indicates that the object is a BLL.

4FGLJ1131.6+4657 - SDSSJ113142.27+470008.6: The *Swift*/XRT analysis reveals the source XRTJ113142.3+470009.2 as X-ray counterpart of this UGS. The radio source VLASS1QLCIRJ113142.36+470009.4 and the optical source SDSSJ113142.27+470008.6 are coincident with the X-ray emission. The SDSS survey provides the optical spectrum with absorption lines (Ca II, G-band, MgI, Ca+Fe and NaI) due to the old stellar population of the elliptical host galaxy. The spectral lines are consistent with a redshift $z = 0.1255$ and the source can be classify as a galaxy-dominated BLL.

4FGLJ1256.8+5329 - SDSSJ125630.43+533204.3: The analysis of *Swift*/XRT data reveals only the X-ray source XRTJ125630.5+533202.2 within the *Fermi* error box of this γ-ray emitter. It is coincident with the optical source SDSSJ125630.43+533204.3. The optical spectrum exhibits broad emission lines due to CIII] and MgII at z=0.996. Also the narrow (EW=11.1) emission line due to [O II] at 7439 is present. We can classify the source as a QSO. From radio catalogs and the analysis of LoTSS data, no radio emission is coincident with the X-ray/optical counterpart.

4FGLJ1308.7+0347 - SDSSJ130832.10+034403.9: For this UGS, we find the X-ray source XRTJ130832.2+034405.3 slightly out of the *Fermi* error ellipse reported in the 4FGL-DR3, but inside the 3σ error box (see Sec. 7.2). From the analysis of the SDSS optical spectrum we can detect prominent broad emission lines attributed to Mg II, H_γ, H_β and the doublet of narrow lines due to [O III]. The redshift of the source is z=0.6193. From our analysis of RACS radio data and from that reported by Rusinek-Abarca & Sikora (2021) using LoTSS data, no radio object is detected coincident with the optical counterpart that can be classified as a radio quiet QSO.

4FGLJ1346.5+5330 - SDSSJ134545.36+533252.3: The X-ray counterpart for this UGS, found by our *Swift*/XRT analysis, is XRTJ134545.1+533252.4. It coincides with the radio source VLASS1QLCIRJ134545.34+533252.1 and in the optical with SDSSJ134545.36+533252.3. The SDSS optical spectrum is a Seyfert 1-like (as also proposed by Wang et al. 2009) and exhibits several emission lines: narrow emission lines due to [OII], [OIII] and [OI] and the emission lines attributed to H_δ, H_γ, H_β and H_α that show a very prominent broad emission component. These lines set the source at z=0.1359. From the radio analysis of LOFAR Two Metre Sky Survey data, Pajdosz-Śmierciak et al. (2022) show that the source exhibits a structure composed of a compact radio core, two-sided S-shaped jets and the radio luminosity characteristic of FR I radio galaxies.

4FGLJ1430.6+1543 - SDSSJ143058.03+154555.6: In the *Swift*/XRT skymap and within the *Fermi* error box of this γ-ray emitter we find the X-ray source XRTJ143057.9+154555.0 coincident with the optical source SDSSJ143058.03+154555.6. The optical spectrum, available in the SDSS archive, shows prominent and broad emission lines such as H_γ, H_β, H_α together with the narrow lines due to the [O III] doublet at z=0.1633 and consistent with a Seyfert-1 spectrum. In the radio band, no counterpart is detected (Coziol et al. 2017).

4FGLJ1535.9+3743 - SDSSJ153550.54+374055.6: Analysing the *Swift*/XRT data we find the X-ray source XRTJ153550.56+374056.8 inside the UGS *Fermi* error box. It is coincident with the radio source VLASS1QLCIRJ153550.56+374055.5 (26 mJy) and the optical source SDSSJ153550.54+374055.6 for which the spectrum is available. The spectrum shows a prominent emission line at 4551 due to MgII, a weak and broad emission line attributed to H_β and the faint and narrow line of [OIII]. The redshift is z=0.6255. We note that also an intervening MgII absorption line is detected at ~4167 (z=0.4885). On the basis of the radio-loudness parameter (R~550) and the absolute optical magnitude (M_g = -23.2) the source appears to be a radio loud quasar.

4FGLJ1539.1+1008 - SDSSJ153848.47+101843.2: From the *Swift*/XRT image, we find that the source XRTJ153848.5+101841.7 is a possible UGS X-ray counterpart. It is coincident with the optical source SDSSJ153848.47+101843.2. No radio emission is present (Coziol et al. 2017). The SDSS spectrum displays narrow lines due to [OII], [OIII] and [SII], H_β and H_α emission lines with broad and narrow components. This can be classified as a Seyfert-1-like spectrum and sets the source at z=0.2345.

4FGLJ1544.9+3218 - SDSSJ154433.19+322149.1: From the analysis of *Swift*/XRT data, we propose the X-ray source XRTJ154433.1+322148.5, coincident with the radio source VLASS1QLCIRJ154433.20+322149.1 and the optical source SDSSJ154433.19+322149.1, as lower energy counterpart of the γ-ray emitter. In the SDSS archive the optical spectrum is available showing the power-law shape and appearing featureless. We therefore classify the source as a BLL with unknown redshift.

4FGLJ1554.2+2008 - SDSSJ155424.12+201125.4: The optical source SDSSJ155424.12+201125.4 and the radio source VLASS1QLCIRJ155424.15+201125.5 are spatially coincident with the X-ray object XRTJ155424.1+201125.3 found inside the positional error box of this UGS and proposed as the likely counterpart. The optical spectrum of this source is provided by the SDSS survey and it is dominated by a galactic component with the presence of moderate non-thermal emission. Clear absorption features of the stellar population are detected, in particular Ca II 3934, 3968, G-band 4305, Mg I 5157, and NaI 5893 at z=0.2225. We classified the source as a BLG. It is also notably that the source is one of the possible counterparts of the neutrino event IceCube-110521A (Giommi et al. 2020; Padovani et al. 2022).

4FGLJ1555.3+2903 - SDSSJ155512.91+290329.9: By the *Swift*/XRT data analysis, we found the X-ray source XRTJ155513.01+290328.0 inside the 4FGL-DR3 error box of this UGS, that coincides with the radio emitter VLASS1QLCIRJ155512.89+290330.0 and the optical source SDSSJ155512.91+290329.9. The SDSS spectrum is available and absorption lines due to Ca II doublet, G-band, Mg I and NaII are clearly detected at z=0.1747, allowing us to classify the source as a galaxy-dominated BLL.

4FGLJ1631.8+4144 - SDSSJ163146.72+414632.8: XRTJ163146.8+414631.8 is the only X-ray source detected inside the 4FGL-DR3 position error box and it is coincident with the radio source VLASS1QLCIRJ163146.74+414632.7 and the optical object SDSSJ163146.72+414632.8. In the SDSS spectrum the continuum is very flat and no emission lines are detected, allowing us to classify the source as a BLL. A possible CaII absorption doublet is present at ∼6800 yielding a tentative redshift of z=0.721.

4FGLJ1648.7+4834 - SDSSJ164900.34+483411.8: Through the *Swift*/XRT image analysis, we find the X-ray source XRTJ163146.8+414631.8 inside the positional error box of this UGS. We propose the spatially coincident objects VLASS1QLCIRJ163146.74+414632.7 and SDSSJ164900.34+483411.8 (g = 19.4) as radio and optical counterparts. Our optical spectrum exhibits a featureless power-law continuum typical of BLL.

4FGLJ2030.0-0310 - PANJ203014.27-030722.56: The *Swift*/XRT image reveals the X-ray object XRTJ203014.3-030722.8 inside the 4FGL error box that is spatially coincident with the optical source PANJ203014.27-030722.56. RACS radio image reveals an hint of radio emission at the position of the X-ray source. As such, we observed 4FGLJ2030.0-0310 sky region with the Australia Telescope Compact Array (ATCA)[6]. We detected the source with a SNR $> 13\ \sigma$ and we measured a radio flux density of 0.40 ± 0.03 mJy at 2.1 GHz, corresponding to a radio-loudness R=3.5 (see Tab. 7.4 and 7.5). The uncalibrated 6dF Galaxy Redshift survey optical spectrum shows prominent and narrow emission lines attributed to H_β 4861, [O III] 4959,5007 , H_α 6563, [N II] 6583 and [S II] 6717,6731 at z=0.036. No broad lines are found, therefore the spectrum can be classified as Type 2. Considering the very low redshift, the absolute optical magnitude (M_g = -19.2) and the host galaxy properies from the analysis of the optical image (see Tab.7.4), the source should be classified as a Seyfert-2 galaxy hosted by a dwarf galaxy. It is important to mention that, given its remarkably close proximity (z=0.036), this object has a γ-ray luminosity of approximately $2{\times}10^{42}$ erg/s, which is one of the lowest in our sample.

4FGLJ2207.1+2222 - SDSSJ220704.10+222231.4: The analysis of *Swift*-XRT imaging data reveals one X-ray object XRTJ220704.1+222231.8 in the 4FGL-DR3 error box that is spatially coincident with the optical source SDSSJ220704.10+222231.4 (g=20.4) and the radio source VLASS1QLCIRJ220704.09+222231.5. The SDSS optical spectrum is characterized by a power-law emission and appears featureless typical of BLL. It is worth noting that this UGS is one of two sources listed in the 4FGL that lie within the event radius of the neutrino event IceCube-221210A[7].

4FGLJ2317.7+2839 - SDSSJ231740.00+283955.7: Inside the *Fermi* error box of this UGS, we detected the X-ray source XRTJ231740.1+283955.4, coincident with the radio source VLASS1QLCIRJ231740.21+283955.8 and the optical source SDSSJ231740.00+283955.7.

---

[6] The observations were carried out over two epochs, (2023-07-04 17:25:20 – 20:53:10 UT and 2023-07-05 13:07:30 – 20:49:30 UT). For both observations we used PKS 1934−638 for primary flux and bandpass calibration, and PKS 2044−027 for secondary gain calibration. Data were recorded at a central frequency of 2.1 GHz with 2 GHz of bandwidth composed of 2048 1-MHz channels. Raw data were then edited for radio frequency interference (RFI), calibrated, and imaged following standard procedures (details in `https://casaguides.nrao.edu/index.php/ATCA_Tutorials`) in the Common Astronomy Software Applications for radio astronomy (CASA, version 5.1.2; CASA Team et al. 2022)

[7] https://gcn.nasa.gov/circulars/33040?page=12

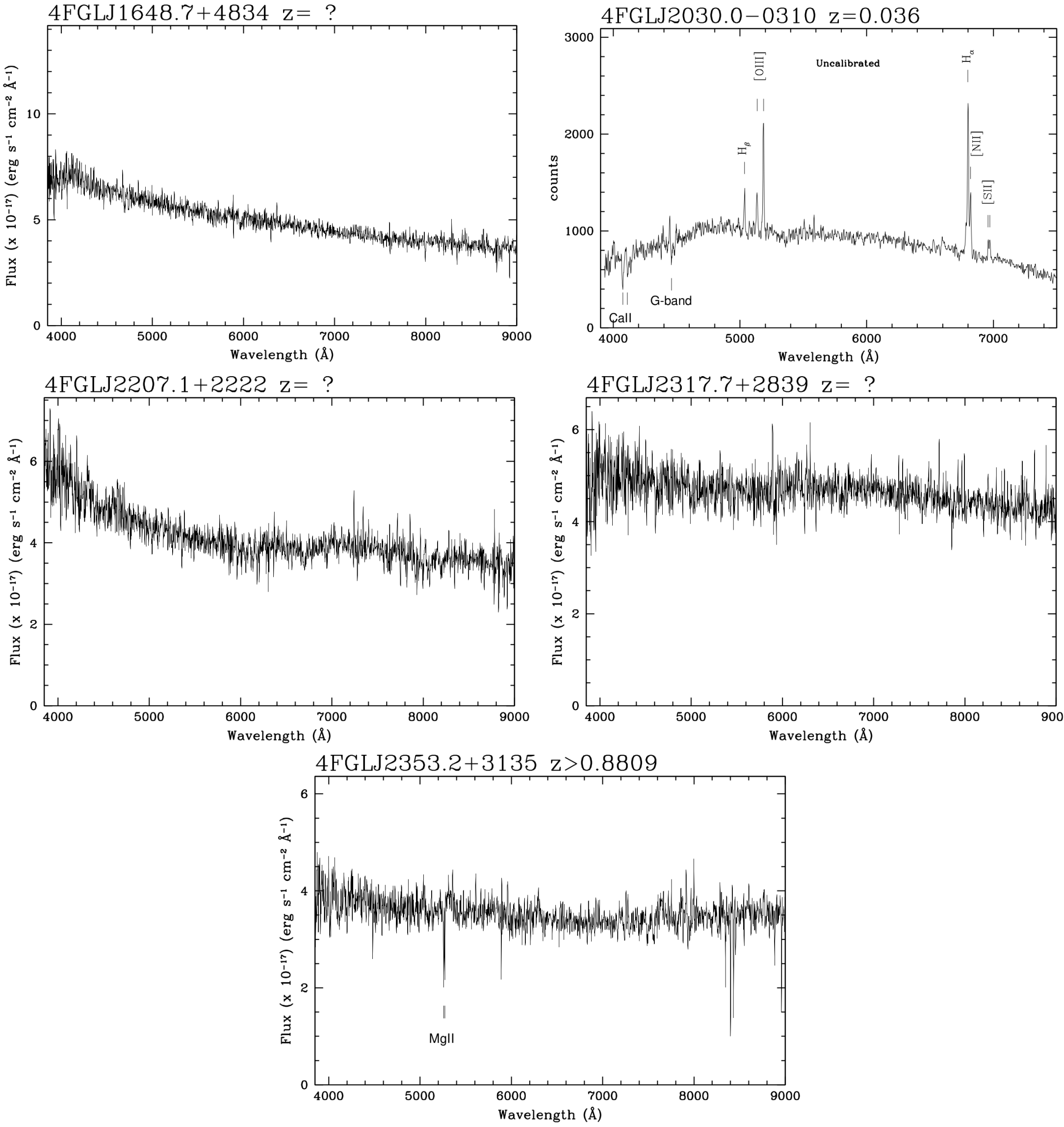

Figure 7.1: Continued.

The optical spectrum, available in the SDSS archive, appears featureless with a power-law continuum. This source is therefore a BLL with redshift unknown.

4FGLJ2353.2+3135 - SDSSJ235319.54+313616.7: Through the *Swift*/XRT data analysis, we find that the X-ray source XRTJ235319.1+313613.4 is inside the 4FGL-DR3 position error box. The radio object VLASS1QLCIR J235319.50+313616.8 and the optical source SDSSJ235319.54+313616.7 are coincident with the X-ray emitter. The optical spectrum, available in the SDSS archive, is flat and characterized by a power-law continuum typical of BLL. It is clearly possible to detect an intervening absorption system due to MgII allowing us to set a redshift lower limit of $z > 0.8809$.

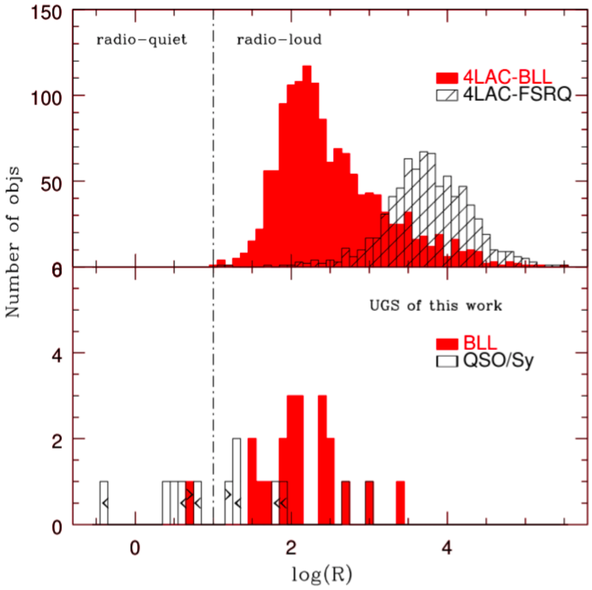

Figure 7.2: *Upper panel*: Distribution of the *radio-loudness* parameter (log(R)) value for 1409 objects classified as BLL and 771 objects as FSRQ of the 4LAC catalog. *Bottom panel*: Distribution of the *radio-loudness* value for the counterparts of the 33 UGS of this work. The black dashed vertical line represent the *radio-loudiness* parameter value (R = 10) that separates the radio-quiet from the radio-loud sources.

7.5.0 Summary and conclusions

We have examined a set of 33 UGS counterparts for which an optical spectrum was recovered in the literature. From the spectroscopic analysis we found that all counterparts are extragalactic objects: 21 sources have been classified as BLL, while the others 12 are AGN with prominent emission lines.

In particular we found that among the 21 BLL, 7 are notable for having their redshift determined solely through the detection of absorption lines due to the host galaxy, while 1 object (4FGLJ0112.0+3442) exhibits both absorption and emission lines. For 2 BLLs, spectroscopic redshift lower limit can be set on the based of the detection of intervening absorption lines. The others have a featureless spectrum, described by a power-law shape, and the redshift is unknown.

The average γ-ray luminosity of the BLL in the sample ($<L_\gamma> = 10^{44}$ erg s^{-1}), is found significantly lower than that ($<L_\gamma> \sim 10^{45}$ erg s^{-1}) of ~900 BLL of the 4FGL-DR3 catalog (see also Tab. 7.6). While, regarding radio band, all BLL are radio-loud sources. It is worth noting that 4FGLJ1410.7+7405 identified as a candidate Radio Weak BLL (RWBL) by Marchesini et al. (2023a) and Massaro et al. (2017), turns out to instead be a radio loud BLL using the radio flux value estimated in the same work by Marchesini et al. (2023a). From the imaging decomposition (see Tab. 7.4), the absolute magnitude of their host galaxies in the optical r-band is in the range -23.1<M(r)<-21.2, with <M(r)>=-22.4. These values are consistent with that typical of BLL host galaxies <Mr>=-22.9 (Urry et al. 2000; Sbarufatti et al. 2005). The indication is therefore that these UGSs identified as BLL belong to the same population of already identified *Fermi* BLL, covering the faint tail of this luminosity *Fermi* BLL distribution (see Tab. 7.6).

The other 12 UGS of this study are characterized by optical spectra with strong emission lines and constitute ∼40% of the total of our studied sources. This fraction is in fact in agreement with the larger statistics of the Fourth Catalog of AGNs detected by *Fermi* - Data Release 3 (4LAC-DR3, Ajello et al. 2020, 2022) (∼ 1400 BLL and ∼ 800 FSRQ) and it is much greater than ∼10% found in our earlier studies of UGS (Paiano et al. 2017a, 2019) for which only 3 objects showed a spectrum not compatible with a BLL classification. Note that they were based on the 2FGL and 3FGL catalogues (Nolan et al. 2012; Acero et al. 2015) which explored fluxes sensibly higher than those examined here (see Tab. 7.6).

More specifically, we found 1 radio-loud quasar (4FGLJ1535.9+3743), 3 radio-quiet quasars (4FGLJ1125.1+4811, 4FGLJ1256.8+5329 and 4FGLJ1308.7+0347) and 8 Seyfert-like objects. 4FGLJ0023.6-4209 and 4FGLJ2030.0-0310, 2 Type-2 AGN, are the closest sources of the sample with $z \leq 0.05$ and have the smallest γ-ray luminosity (see Tab. 7.5). 4FGLJ0117.9+1430 is classified as a NLSy1 (see the note of the source in Section 7.4). This increases the total number of objects classified as Seyfert of the 4FGL-DR3 catalog (8 NLSy and 3 Seyfert).

It is of interest to compare the values of the *radio-loudness (R)* found in our sample of 33 objects with the results of 4LAC, which are summarized in the distribution reported in Fig. 7.2. It is apparent that our 21 BLL have R indexes which are in the low part of the distribution. The median value is R=120 to be compared with that R=230 for the 4LAC BLL. We also compared the distribution of R values of the 12 objects with prominent emission lines with the 4LAC FSRQ one. We found a significant difference and, as expected for the case of Seyfert galaxies, their *radio-loudness* value is well below the 4LAC FSRQ one (median R=5600; see Fig. 7.2).

The presence of a sizeable fraction of radio faint objects, in particular ≥ 5 sources have R smaller than 10, among the UGS counterparts is somewhat unexpected but not implausible (Massaro et al. 2017; Järvelä et al. 2021). The obvious comment is that our current search for UGS counterparts is completely independent of the radio brightness, which is gathered *a posteriori*, it rather depends on the choose of the significance of the X-ray detection. In spite of the rather small sample the issue of radio quiet counterparts of γ-ray sources is of potentially great interest since they may represent a poorly explored type of γ-ray objects.

Future analyses will expand this work to an additional set of ∼ 60 UGS counterparts, for which we have obtained optical spectroscopic data from large telescopes such as the Large Binocular Telescope (LBT) and Gran Telescopio Canarias (GTC) (Paiano et al., in prep.).

Table 7.5: Multi-wavelength fluxes and luminosities of the lower energy counterparts of the 33 UGSs

4FGL Name	F_γ	$f_\nu^{\rm radio}$	F_X	$f_\nu^{\rm opt}$	L_γ	$L_{\rm radio}$	L_X	M_g (M_r)	R
BLL and BLG	[$\times 10^{-12}$]		[$\times 10^{-13}$]	[$\times 10^{-28}$]	[$\times 10^{45}$]	[$\times 10^{40}$]	[$\times 10^{44}$]		
4FGLJ0112.0+3442	1.4	41	2.5	6.3	0.9	74	1.5	-22.3 (-22.7)	450
4FGLJ0202.7+3133	1.0	15	3.8	12	-	-	-	-	125
4FGLJ0251.1-1830	1.8	8.8	5.5	3.3	-	-	-	-	265
4FGLJ0259.0+0552	6.8	5.8	4.1	13	-	-	-	-	45
4FGLJ0838.5+4013	0.9	24	4.6	19	0.1	8.3	0.5	-21.7 (-22.9)	290
4FGLJ1016.1-4247	3.1	7.2	5.8	6.9	-	-	-	-	100
4FGLJ1039.2+3258	2.7	6.1	2.9	4.8	-	-	-	-	130
4FGLJ1049.8+2741	1.4	7.2	2.9	19	0.1	1.3	0.2	-21.0 (-21.9)	80
4FGLJ1131.6+4657	1.1	92	4.5	36	0.1	1.2	0.2	-21.3 (-22.3)	920
4FGLJ1146.0-0638	3.1	5.8	5.4	5.8	5.7	32	10	-23.4 (-23.2)	100
4FGLJ1410.7+7405	3.6	2.4	1.1	7.6	-	-	-	-	30
4FGLJ1544.9+3218	1.4	12	3.6	12	-	-	-	-	100
4FGLJ1554.2+2008	2.7	42	6.1	21	0.4	20	10	-22.1 (-23.0)	240
4FGLJ1555.3+2903	1.1	22	3.2	19	0.1	6.1	0.3	-21.5 (-22.5)	320
4FGLJ1631.8+4144	1.3	0.8	8.1	2.3	-	-	-	-	35
4FGLJ1648.7+4834	1.2	2.5	6.0	6.3	-	-	-	-	40
4FGLJ2207.1+2222	1.7	6.5	2.6	2.5	-	-	-	-	260
4FGLJ2240.3-5241	6.2	29	1.9	21	-	-	-	-	135
4FGLJ2317.7+2839	2.8	4.5	0.8	5.2	-	-	-	-	90
4FGLJ2323.1+2040	2.4	2.4	4.9	631.0	0.01	0.03	0.02	-21.9 (-23.0)	>5
4FGLJ2353.2+3135	3.6	61	1.5	2.3	-	-	-	-	2650
Objects with prominent lines									
4FGLJ0023.6-4209	1.1	3.3	12	209	0.01	0.02	0.08	-21.3 (-21.9)	>15
4FGLJ0117.9+1430	2.9	<4.2	4.9	12	0.1	<0.03	0.2	-20.2 (-20.6)	<65
4FGLJ0641.4+3349	1.3	1.2	28	53	0.1	0.3	2.3	-22.4 (-23.1)	2.5
4FGLJ0938.8+5155	1.2	0.6	0.7	2.8	0.8	0.06	0.5	-21.5 (-21.7)	25
4FGLJ1125.1+4811	0.8	<0.6	0.4	2.8	14.5	<1.5	7.0	-25.1 (-25.2)	<20
4FGLJ1256.8+5329	2.7	<1.6	1.7	2.1	14.7	<1.3	9.1	-23.5 (-23.8)	<75
4FGLJ1308.7+0347	2.0	<0.2	7.5	48	3.3	<1.0	13	-25.6 (-25.5)	<0.5
4FGLJ1346.5+5330	3.0	250	44	58	0.2	39	2.3	-22.0 (-22.4)	900
4FGLJ1430.6+1543	0.9	<1.0	14	40	0.1	<0.2	1.1	-22.1 (-22.6)	<4.5
4FGLJ1535.9+3743	4.9	26	1.1	4.8	8.5	6.6	2.0	-23.2 (-23.5)	540
4FGLJ1539.1+1008	2.2	<1.0	3.1	17	0.4	<0.5	0.5	-22.0 (-22.3)	<6.0
4FGLJ2030.0-0310	0.7	0.4	11	69	0.002	0.003	0.03	-19.2 (-19.8)	3.5

Note. Column 1: 4FGL Name of the target; Column 2: γ-ray flux (erg cm^{-2} s^{-1}) in the 100 MeV to 100 GeV range; Column 3: Radio density flux (mJy); Column 4: X-ray flux (erg cm^{-2} s^{-1}) in the 0.3-10 keV range; Column 5: Optical density flux (erg cm^{-2} s^{-1} Hz^{-1}) ; Column 6-7-8: γ-ray, radio and X-ray luminosity (erg s^{-1}); Column 9: g-band and r-band absolute magnitude of the target (derived from PANSTARRs images); Column 10: *radio-loudness* define as the ratio between radio flux density and optical flux density of the nuclear component.

Table 7.6: Statistics on Redshift, Flux and Luminosity; Comparison of the 33 UGS sample with Paiano et al. (2017a, 2019) sample and 4FGL-DR3 catalog

Sample	$< z >$	F_γ (erg cm^{-2} s^{-1}) $\times 10^{-12}$	L_γ (erg s^{-1}) $\times 10^{45}$
8 BLL/BLG of this work	0.2	1.4 ± 0.4	0.1 ± 0.1
12 QSO/Seyfert-like of this work	0.2	1.3 ± 0.7	0.3 ± 0.3
875 BLL of 4LAC	0.3	3.1 ± 1.7	1.2 ± 1.1
792 FSRQ of 4LAC	1.1	5.5 ± 3.4	45 ± 40
24 BLL-UGS of Paiano et al 2017,2019	0.4	2.9 ± 1.0	2.0 ± 1.3
3 QSO/Sy-like UGS of Paiano et al 2017,2019	0.3	4.7 ± 1.4	0.6 ± 0.1

Note. Column 1: Sample under investigation; Column 2: Median redshift; Column 3: Median energy flux from 4FGL catalog in the 100 MeV to 100 GeV range; Column 4: median luminosity.
The reported uncertainty indicates the rms of the distribution.

8

Characterization of a sample of γ-ray active galactic nuclei

Results in short

In this chapter, we provide a detailed characterization of a sample of 77 UGSs, previously associated in this thesis (see Chapter 7 and Ulgiati et al. 2024), as well as in other studies conducted by Paiano et al. (2017a, 2019). Specifically, we investigate the emission of these objects across the entire electromagnetic spectrum through a comprehensive analysis of their SEDs. This allows us to study the association between the low-energy counterparts and the γ-ray detections, infer the locations of the emissions at different wavelengths, and classify blazars into their sub-classes: low synchrotron peak (LSP), intermediate synchrotron peak (ISP), and high synchrotron peak (HSP). Additionally, we search for potential masquerading BLLs within this sample by comparing their absolute and relative emission intensities to threshold values designed to identify this subclass of sources.

We initially classified the objects in our sample (all of which are AGNs) based on their radio-loudness, finding 64 sources as radio-loud class and 13 as radio-quiet. Subsequently, we compared the emission properties of these objects with those of blazars in the 4FGL-DR4 *Fermi* catalog. While blazars are the prototypical extragalactic γ-ray sources, we note that the γ-ray sky also contains a small, but potentially astrophysically significant, population of Seyfert galaxies, radio galaxies, and non-active galaxies, where, in this latter case, γ-ray emission is linked to star-forming processes.

Blazars typically show a correlation between their γ-ray luminosity and their 1.4 GHz radio power. We placed our sample sources on the L_γ vs. $P_{1.4\mathrm{GHz}}$ diagram, and observed that while the radio-loud objects follow the same trend as 4FGL-DR4 blazars, the radio-quiet sources deviate from it. Taking these preliminary findings into account, we conducted a more in-depth study of these objects, analyzing their emission across the entire electromagnetic spectrum.

We plotted the SEDs of all sources in the sample, including both radio-loud and radio-quiet sources, and compared them to LSP, ISP, and HSP blazar templates. The multi-wavelength analysis reveals that the radio-loud sources in our sample exhibit coherent multi-wavelength emission across the spectrum, characterized by a double-peak structure typically ascribed to jet activity (although in some cases, host galaxy contributions were also evident). We therefore classify these source according to the location of the synchrotron emission peak in their SEDs, as LSP, ISP, or HSP sources. The majority are classified as HSP (46 objects), with 11 as ISP and 7 as LSP.

In the search for masquerading BLL, we found 9 candidate sources, representing approximately 15% of the radio-loud sample, with a possible upper limit of 30%. This proportion is lower than in previous studies, where Paiano et al. (2023) found a percentage of masquerading BLL of 34%.

For the sources associated with radio-quiet AGNs, it was found that the SEDs do not exhibit a double-peak structure typical of jetted AGNs. Similarly, there is no evidence of jet activity at low energies, which typically manifests as flat-spectrum radio emission with $\alpha \lesssim 0.5$. In the absence of a jet, if the γ-ray emission comes from the proposed counterpart, it must have another physical origin.

We explored the possibility that the γ-ray emission originated from star-forming processes. A known relationship exists between the 1.4 GHz radio power and γ-ray luminosity in star-forming regions (see Peng et al. 2019). Assuming that the observed radio emission in these radio-quiet AGNs was entirely due to star formation, we estimated the expected γ-ray luminosity according to the L_γ vs. $P_{1.4\mathrm{GHz}}$ relationship. However, we found that the expected γ-ray emission was, on average, three orders of magnitude lower than the observed values, ruling out star formation as the source of the high-energy emission. The absence of a jet and/or star formation processes makes it more difficult to reconcile the γ-ray emission with the lower energy emission. We searched therefore for possible alternative counterparts for these 13 γ-ray sources.We compared the SEDs of potential alternative counterparts with those of LSP, ISP, and HSP blazars. The research revealed new potential low-energy counterparts for 7 out of the 13 γ-ray sources, whose emissions across the spectrum were consistent with jet activity. Investigating the relationship for the newly identified counterparts in the L_γ vs. $P_{1.4\mathrm{GHz}}$ diagram, we found that they follow the trend of *Fermi* blazars. This supports the hypothesis that they are likely blazar-type objects and could be associated with the detected γ-ray emission. These source will be subject of a spectroscopic campaign, which will provide a definitive classification for these objects and strengthen the proposed associations.

For the remaining 6 sources, no plausible alternative counterparts were found within the 3σ γ-ray error boxes. For these sources, further analysis are therefore needed, to investigate the origin of the γ-ray emission.

8.1.0 Introduction

Fifteen years have elapsed since the launch of the *Fermi* satellite, significantly enhancing our understanding of the γ-ray sky. In 2023, the *Fermi* collaboration released the incremental version of the fourth catalogue (4FGL-DR4, Abdollahi et al. 2020; Ballet et al. 2023), which reports the sources detected over the 14 years of observations by the *Large Area Telescope* (LAT) detector. Of the total 7195 objects in the catalog, 4765 have been associated or identified at other wavelengths thanks to either a positional overlap in the sky, measurements of correlated variability, and/or multi-wavelength spectral properties (Abdollahi et al. 2020; Ballet et al. 2023). The catalogue includes both Galactic sources and extragalactic sources, with the latter which dominate the γ-ray sky. AGNs (AGN), and in particular blazars (with 3934 objects reported in the catalog), represent the most abundant class of these extragalactic sources. The γ-ray sky is also populated by a small but possibly astrophysically relevant fraction of Seyfert galaxies and radio galaxies (Cheung & Fermi LAT Collaboration 2010; Abdo et al. 2010b; Ackermann et al. 2011; Grandi 2012; Paliya et al. 2015; Angioni et al. 2017; Rieger 2017; Järvelä et al. 2021; Ye et al. 2023; Ballet et al. 2023). γ-ray emission can also come from non-active galaxies. For example, in star-forming and starburst galaxies, cosmic rays accelerated by supernova remnants can produce γ-ray radiation through inelastic collisions with ambient gas particles and subsequent π^0-decay (Peng et al. 2019, and references therein). In this case γ-ray emission appears to be almost steady over time, at variance with blazars and jetted AGN in general, where instead it appears to be very variable (Ballet et al. 2023).

In the 4FGL-DR4 catalog, a significant fraction of sources, approximately 30%, remain unassociated and unclassified, known as unassociated gamma-ray sources (UGSs). As extensively specified in the previous chapters, UGSs represent a significant component of the γ-ray sky (see Chapter 3, 6, and 7 for more details).

The association and classification of the UGSs is a fundamental goal of our research group (Paiano et al. 2017a, 2019; Ulgiati et al. 2024, Ulgiati et al. (submitted), Paiano et al. 2025 (in prep)). Since we are interested in searching for AGNs, we focused on those UGSs that have a high galactic latitude ($|b| > 10°$), which have a greater probability to be extragalactic. Moreover, in 2015, an observational campaign has been launched, aimed at the study and classification of blazars (with a particular focus on BLLs) and other classes of AGN, utilizing optical spectroscopy with large diameter telescopes (in the 8-10 m range) such as the Gran Telescopio Canarias (GTC) and the Large Binocular Telescope (LBT). These telescopes were selected due to their high spectral resolution, which provides the opportunity to detect the faint features expected in BLLs.

In this chapter we build the multi-frequency SEDs for the sample of 77 sources analysed in Paiano et al. (2017a, 2019), and Ulgiati et al. (2024), where we studied the optical spectroscopy, in order to have a multi-wavelength picture of these objects. This will allow us to characterize the emission over the entire spectrum, to infer the locations of the emissions at different wavelengths, and divide blazars according to their sub-classes: low-synchrotron peaked (LSP), intermediate-synchrotron peaked (ISP) and high-synchrotron peaked (HSP). Furthermore, we also want to search for any masquerading BLL in the sample. In the context of astrophysics, "masquerading BLL" refers to certain objects that are intrinsically flat-spectrum radio quasars (FSRQs) but appear similar to BLL objects, due to the overwhelming effect of their bright, Doppler-boosted jet continuum. This strong jet emission can obscure their emission lines, making them look like BLLs despite being FSRQs. The term highlights the misclassification that can occur when observing these objects, as their true nature is masked by the jet's brightness. Identifying masquerading BLLs is important for deepening our understanding of the diverse AGN population. By refining classifications and improving the accuracy of our astrophysical surveys, we ensure that the data we collect accurately reflects the true nature of these sources. Additionally, recognizing these objects sheds light on jet dynamics and the underlying processes driving AGN activity, ultimately enhancing our comprehension of cosmic evolution and the mechanisms behind high-energy emissions.

The chapter is structured as follows: in Sec. 8.2, the criterion used for associating the UGS with their lower-energy counterparts is described; in Sec. 8.3, the SEDs are constructed; in Sec. 8.4, the dependence of γ-ray luminosity and 1.4 GHz radio power is tested to investigate the possibility that a jet is the origin of the γ-ray emission; the results are discussed in Sec. 8.5, where the origin of the γ-ray emission is debated; finally, the conclusions are reported in Sec. 8.6.

8.2.0 Source multi-wavelength associations

The process of searching for lower energy counterparts (compared to the γ-ray band) started from the identification of a X-ray source within the *Fermi* error boxes of the UGSs (see Paiano et al. 2017a, 2019; Ulgiati et al. 2024, Ulgiati et al. submitted and Chapter 6 for more details). For this research we analysed *Swift*/XRT data covering the γ-ray positions. Starting from the X-ray coordinates and uncertainties, we looked for radio and optical counterparts that are positionally coincident (see Sec. 6.3).

8.2.1 Radio-loud and radio-quiet sources in our UGS sample

A characteristic that distinguishes blazars and radio galaxies is their brightness in the radio band. The radio-loudness parameter R is defined as the ratio between the radio flux (in the range 2 - 4 GHz) and the optical flux of an object. Sources with R > 10 are considered radio-loud (Kellermann et al. 1989). Blazars and radio galaxies are radio-loud sources (see Chapter 6 and 7, but also Padovani et al. 2017; Ballet et al. 2023; Ulgiati et al. 2024, and Ulgiati et al., submitted), while Seyfert galaxies and QSOs are typically radio-quiet (Padovani et al. 2017, and reference therein).

We estimate R values for our objects and the results are reported in Table 8.1. For sources without a cataloged radio counterpart and lacking a flux estimate in the literature, we established an upper limit on the flux, according to the radio survey covering the UGS sky region. For sources with a declination greater than -40°, we used the detection threshold given by the VLASS catalogue (0.345 mJy at 5σ), while for sources below this declination, we used the detection threshold from the RACS catalogue (1.5 mJy at 5σ). A total of 13 sources are found to be radio-quiet (see Tab. 7.5 and 8.1). This is an unexpected and potentially interesting result, since they could represent a type of γ-ray objects that is still relatively unexplored, and having a multi-wavelength view of these objects is bound to shed light on the matter. Finally, we constructed the SEDs for all objects in the sample.

8.3.0 Construction and properties of the broadband SED of UGSs

We utilized the online tool VOU-Blazars V2.00, (Chang et al. 2020) to gather multifrequency data for each UGS and to build the multi-wavelength SED, exploiting its capability to scan a variety of catalogues (detailed in Sec. A.5) for flux measurements that span a broad spectrum of the electromagnetic range. To complete the multi-wavelength SED we also include the radio flux upper limits, for those sources without a catalogued radio counterpart, and X-ray spectral points deriving from our XRT spectra analysis (see Sec. 6.2 and Ulgiati et al. submitted for more details). Given the temporal variability of AGNs, it is possible to have multiple spectral points at the same frequency. However, we want to analyze the average behavior of the objects. For this reason, we decided to average the spectral points for each frequency. Following the approach used in Paiano et al. (2017b), we overlayed the SED with a curve that emulates the typical double-peaked shape of blazars. This shape, as detailed in Equation 1 of Paiano et al. (2017b), includes both a synchrotron emission peak at lower frequencies and an inverse Compton (IC) peak at higher frequencies. These two peaks are modeled through an analytic form that combines two power laws with exponential cutoffs to match the distinct rise and decline of each component. Specifically, the model's parameters allow for adjustment of the amplitude, width, and peak frequency of each component, to follow the SED of a generic blazar (Paiano et al. 2017b, for more details). Additionally, we incorporate the template of a giant elliptical host galaxy at the object's redshift (Coleman et al. 1980).

The SEDs of radio-loud sources are reported in Fig. A.3. The SEDs of the radio-quiet objects will be presented in subsection 8.5.3 (see Fig. 8.5), where the associations will be discussed in detail.

8.4.0 The jet as the source of γ-ray radiation

For blazars, the γ-ray emission is generated by non-thermal processes, with the jet acting as the dominant structure for radiation production in this band. There is a correlation between γ-ray luminosity and 1.4 GHz radio power in jetted-AGNs (e.g. see Paiano et al. 2023). We compare the γ-ray luminosities and radio powers of our UGSs. For the objects for which the redshift

Table 8.1: Multi-wavelength parameters for the objects under analysis.

4FGL Name	$f_\nu^{\rm radio}$	$f_\nu^{\rm opt}$	Fractional variability γ-ray	R	L_γ erg s^{-1}	$P_{1.4\rm GHz}$ W Hz^{-1}	Redshift Reference	Redshift
		[$\times 10^{-28}$]						
4FGL J0004.0+0840	16.5	3.0	0.5 ± 0.5	332	>46.2	>26.0	Paiano et al. (2019)	>1.5035
4FGL J0006.4+0135	5.8	2.8	-	364	45.6	25.0	Paiano et al. (2019)	0.787
4FGL J0023.6−4209	1.4	208.9	0.7 ± 0.3	1	42.8	22.2	Ulgiati et al. (2024)	0.053
3FGL J0031.6+0938	<0.4	7.6	-	<5	44.9	<22.9	Paiano et al. (2019)	0.2207
4FGL J0049.1+4223	4.5	4.8	-	210	44.7	24.0	Paiano et al. (2017a)	0.302
4FGL J0102.4+0942	10.0	6.9	0.5 ± 0.3	145	45.2	24.7	Paiano et al. (2017a)	0.42
4FGL J0112.0+3442	41.3	6.3	-	655	44.9	25.2	Ulgiati et al. (2024)	0.3997
4FGL J0117.9+1430	<1.8	12.0	0.5 ± 0.2	<15	44.1	<23.1	Ulgiati et al. (2024)	0.129
4FGL J0158.8+0101	45.8	1.0	-	1003	45.5	25.4	Paiano et al. (2019)	0.4537
4FGL J0202.7+3133	15.1	12	-	126	>44.6	>24.7	this chapter	**>0.35***
4FGL J0234.3−0628	4.8	4.8	-	210	>45.6	>24.7	Paiano et al. (2019)	>0.63
4FGL J0238.7+2555	10.6	3.3	-	303	45.3	25.0	Paiano et al. (2017a)	0.584
4FGL J0251.1−1830	8.8	3.3	0.2 ± 0.4	291	>45.4	>25.0	Paiano et al. (2019)	>0.615
4FGL J0259.0+0552	5.8	13.2	0.5 ± 0.1	44	>46.3	>24.9	Paiano et al. (2019)	>0.7*
4FGL J0305.1−1608	35.6	10.0	0.3 ± 0.2	100	45.0	25.0	Paiano et al. (2017a)	0.312
4FGL J0338.5+1302	13.4	16.0	0.4 ± 0.1	63	>45.9	>24.7	Paiano et al. (2017a)	>0.382
4FGL J0409.8−0359	55.6	4.8	0.5 ± 0.1	210	>46.0	>25.9	Paiano et al. (2017a)	>0.7*
4FGL J0414.6−0842	28.4	7.6	0.6 ± 0.4	132	>44.8	>25.0	Paiano et al. (2019)	>0.35*
4FGL J0506.9+0323	18.4	11.0	-	91	>43.9	>23.7	Paiano et al. (2019)	>0.1*
4FGL J0641.4+3349	1.2	52.5	-	2	44.1	23.2	Ulgiati et al. (2024)	0.1657
4FGL J0644.6+6039	20.4	8.3	0.5 ± 0.1	121	>45.8	>25.3	Paiano et al. (2017a)	>0.581
4FGL J0838.5+4013	24.0	17.4	-	138	43.9	24.4	Ulgiati et al. (2024)	0.1945
4FGL J0848.7+7017	26.1	4.0	-	252	>46.3	>26.0	Paiano et al. (2019)	>1.2435
4FGL J0930.5+5132	7.3	3.3	-	303	43.9	23.8	Paiano et al. (2019)	0.1893
4FGL J0937.9−1434	15.3	13.0	0.6 ± 0.2	76	44.8	24.5	Paiano et al. (2017a)	0.287
4FGL J0938.8+5155	0.1	2.8	0.3 ± 0.4	3	44.9	22.9	Ulgiati et al. (2024)	0.4168
4FGL J0952.8+0712	25.9	6.9	0.5 ± 0.3	145	45.2	25.4	Paiano et al. (2017a)	0.574
4FGL J1016.1−4247	7.8	5.2	0.0 ± 1.5	149	>45.8	>25.0	this chapter	**>0.65***
4FGL J1039.2+3258	6.1	4.8	-	128	45.0	24.2	this chapter	**0.32***
4FGL J1049.5+1548	30.0	63.0	0.2 ± 0.1	16	45.4	24.9	Paiano et al. (2017a)	0.326
4FGL J1049.8+2741	7.2	19.1	0.1 ± 1.1	38	43.9	23.6	Ulgiati et al. (2024)	0.144
4FGL J1125.1+4811	<0.3	2.8	0.5 ± 0.9	<13	45.9	<24.2	Ulgiati et al. (2024)	1.649
4FGL J1128.8+3757	28.3	1.7	0.8 ± 0.2	577	>46.6	>26.1	Paiano et al. (2017a)	>1.211
4FGL J1131.6+4657	73.9	36.3	0.6 ± 0.3	204	43.8	24.5	Ulgiati et al. (2024)	0.1255
4FGL J1146.0−0638	5.8	5.8	-	100	45.7	24.8	Paiano et al. (2019)	0.6407
4FGL J1223.5+0818	9.5	10.0	0.6 ± 0.2	100	>45.8	>25.1	Paiano et al. (2019)	>0.7187
4FGL J1223.9+7954	37.2	6.9	-	145	44.8	25.1	Paiano et al. (2017a)	0.375
4FGL J1234.7−0434	<0.4	13.1	0.4 ± 0.5	<3	44.7	<23.2	Paiano et al. (2019)	0.2765
4FGL J1256.8+5329	<0.3	2.1	0.4 ± 0.3	<17	46.2	<24.2	Ulgiati et al. (2024)	0.996
3FGLJ1258.4+2123	15.1	2.3	-	661	46.0	25.2	Paiano et al. (2019)	0.6265
4FGL J1308.7+0347	<0.3	47.9	0.2 ± 0.4	<1	45.6	<23.3	Ulgiati et al. (2024)	0.6193
4FGL J1340.8−0409	14.6	48.0	0.3 ± 0.2	21	44.8	24.3	Paiano et al. (2017a)	0.223
4FGL J1346.5+5330	248.1	57.5	0.3 ± 0.1	431	44.3	25.1	Ulgiati et al. (2024)	0.1359
4FGL J1410.7+7405	2.2	7.6	0.3 ± 0.1	29	>45.6	>24.3	this chapter	**>0.55***
4FGL J1411.5−0723	56.0	25.0	-	40	>45.7	>25.9	Paiano et al. (2017a)	>0.72*
4FGL J1430.6+1543	<0.3	39.8	0.7 ± 0.3	<1	43.9	<22.9	Ulgiati et al. (2024)	0.1633
4FGL J1511.8−0513	15.1	36.0	0.2 ± 0.1	28	>45.7	>24.9	Paiano et al. (2017a)	>0.45
4FGL J1526.1−0831	24.0	17.0	0.5 ± 0.2	58	>45.2	>25.0	Paiano et al. (2019)	>0.40*
4FGL J1535.9+3743	26.3	4.4	1.0 ± 0.2	603	46.0	25.5	Ulgiati et al. (2024)	0.6255
4FGL J1539.1+1008	<0.3	17.4	-	<2	44.7	<23.2	Ulgiati et al. (2024)	0.2345
4FGL J1541.7+1413	27.8	16.0	0.1 ± 0.5	63	44.5	24.6	Paiano et al. (2019)	0.223
4FGL J1544.9+3218	12.0	12.0	-	100	44.6	24.5	this chapter	**0.3***
4FGL J1554.2+2008	42.0	20.9	-	201	44.6	24.7	Ulgiati et al. (2024)	0.2225
4FGL J1555.3+2903	21.7	19.1	0.5 ± 0.4	114	44.0	24.2	Ulgiati et al. (2024)	0.1767
4FGL J1631.8+4144	0.8	2.3	0.4 ± 0.3	34	>45.3	>24.0	this chapter	**>0.65***
4FGL J1648.7+4834	2.5	6.3	-	40.0	>45.3	>24.4	this chapter	**>0.6***
4FGL J1704.2+1234	18.9	10.0	0.7 ± 0.2	100	45.5	25.0	Paiano et al. (2017a)	0.452
4FGL J1704.5−0527	9.7	13.0	0.2 ± 0.1	76	46.4	25.1	Paiano et al. (2017a)	>0.7*
4FGL J2030.0−0310	0.3	69.2	-	1	42.5	21.2	Ulgiati et al. (2024)	0.036
4FGL J2115.2+1218	10.2	48.0	0.6 ± 0.2	21	>45.5	>24.8	Paiano et al. (2017a)	>0.497
4FGL J2150.7−1750	13.1	33.0	0.1 ± 0.2	30	44.6	24.1	Paiano et al. (2019)	0.1855
4FGL J2207.1+2222	6.5	2.5	0.7 ± 0.3	258	45.2	24.6	this chapter	**0.45***
4FGL J2209.7−0451	15.1	11.0	-	91	45.4	24.8	Paiano et al. (2019)	0.3967
4FGL J2212.4+0708	<0.3	2.1	-	<13	46.5	<24.4	Paiano et al. (2019)	1.0
4FGL J2228.6−1636	15.8	11.0	0.9 ± 0.2	91	45.5	25.1	Paiano et al. (2019)	0.525
4FGL J2229.1+2254	3.3	10.0	-	100	45.0	24.2	Paiano et al. (2019)	0.440
4FGL J2240.3-5241	31.0	22.9	0.4 ± 0.2	135	>46.1	>25.6	this chapter	**>0.65***
4FGL J2244.6+2502	9.2	10.0	0.1 ± 1.0	100	45.7	25.0	Paiano et al. (2019)	0.650
4FGL J2245.9+1544	6.2	8.3	0.4 ± 0.1	121	45.9	24.8	Paiano et al. (2019)	0.5965
4FGL J2250.4+1748	36.7	3.0	0.5 ± 0.2	332	45.3	25.1	Paiano et al. (2019)	0.3437
4FGL J2317.7+2839	4.5	5.2	0.6 ± 0.2	86	>45.4	>24.5	this chapter	**>0.5***
4FGL J2321.5−1619	7.3	63.0	0.8 ± 0.2	16	45.8	25.0	Paiano et al. (2019)	0.6938
4FGL J2323.1+2040	160.4	631	-	25	42.9	23.7	Ulgiati et al. (2024)	0.038
4FGL J2346.7+0705	184.4	44.0	0.4 ± 0.1	23	44.9	25.1	Paiano et al. (2017a)	0.171
4FGL J2353.2+3135	60.6	2.3	0.5 ± 0.2	2646	>46.2	>26.1	Ulgiati et al. (2024)	>0.8809
4FGL J2358.3+3830	24.9	16.0	0.5 ± 0.1	63	44.8	24.4	Paiano et al. (2019)	0.2001
4FGL J2358.5−1808	15.8	30.0	0.2 ± 0.1	33	>45.1	>24.4	Paiano et al. (2019)	>0.25*

Note. Column 1: 4FGL Name of the target; Column 2: 2 - 4 GHz radio density flux (mJy); Column 3: g-band optical density flux (erg cm^{-2} s^{-1} Hz^{-1}); Column 4: Fractional variability in γ-ray band; Column 5: *radio-loudness* R defined as the ratio between radio flux density and optical flux density of the nuclear component; Column 6: Logarithm of the 0.1-100 GeV γ-ray luminosity (erg s^{-1}); Column 7: Logarithm of the 1.4 GHz radio power (W Hz^{-1}); Column 8: Reference of the redshift; Column 9: Redshift.

(*) Photometric redshift.

Boldface: New photometric redshift estimate.

measurement is lacking (BLL with featureless optical spectra), we estimated a photometric redshift by overlaying a host galaxy template (a giant elliptical galaxy) at different redshifts onto the SEDs, using the *Firmamento* software (Tripathi et al. 2024). When the SED exhibits a signature of host galaxy emission, we derive the redshift to align the host galaxy template with the IR/optical emission.

When the SED lacks evidence of host galaxy emission, additional considerations are required: blazar emission is highly variable, while that of the host galaxy remains constant. By analyzing the IR/optical light curves, we can constrain the host galaxy's flux to be no greater than the minimum observed flux, providing a lower limit on the photometric redshift. For objects lacking IR/optical light curves, we establish an upper limit on the redshift using the method proposed by Landt et al. (2002). Landt et al. (2002) studied how the shape of the optical spectrum changes depending on the ratio between the non-thermal flux and the host galaxy flux. They observed that the host galaxy's contribution becomes negligible in the optical spectrum when the non-thermal flux exceeds that of the galaxy by a factor $\gtrsim 10$. Therefore, when a source's optical spectrum is described by a featureless power-law, we can place an upper limit on the host galaxy's flux, and thus derive a lower limit for the redshift (see Chang et al. 2019, for details).

We report in Table 8.1 the L_γ, the $P_{1.4GHz}$ and the redshift of the sources in our sample, and in Fig. 8.1 the L_γ vs. $P_{1.4GHz}$ diagram , where we compare our sources (black and red points) with 4FGL-DR4 jetted-AGNs (grey points). Since not all sources have flux measurements at 1.4 GHz, we estimate the flux at this frequency by interpolating, using a power-law model, the available data points at $\nu_{VLASS} = 3$ GHz, $\nu_{RACS} = 887.5$ MHz, and $\nu_{LOFAR} = 144$ MHz. We assume a spectral index of $\alpha = 0$ for blazars, due to their flat radio spectrum, and $\alpha = 0.7$ for other AGN classes.

UGSs with radio flux upper limits or classified as radio-quiet deviate from the region occupied by jetted sources, as their radio power is too low relative to their γ-ray power. This sub-sample is unlikely to contain jetted-AGNs.

8.5.0 Discussion

8.5.1 The case of radio-loud sources

Analysing the multi-wavelength SEDs of the radio-loud objects of our UGS sample (64 sources on a total of 77, see Fig. A.3), we can note that the spectral behavior of the proposed counterpart is compatible with γ-ray emission. The radio emission appears to be flat ($\alpha < 0.5$, according to the SEDs template of jetted AGN reported in Fig. 2.3) and there is clear evidence of the presence of a jet (expressed by the double peak structure of SEDs), which is realistically the origin of the high-energy (HE, E>100 MeV) spectrum. The emission in the X-ray band is consistent with that in the γ-ray regime, suggesting a common emission mechanism between these two components: the LSP blazars have a flat ($\alpha \lesssim 1$) X-ray spectrum, and a steep ($\alpha \gtrsim 1$) γ-ray spectrum; for the HSP blazars, the γ-ray spectrum is instead flat ($\alpha \lesssim 1$) and the X-ray spectrum is steep ($\alpha \gtrsim 1$). This is evident in the SEDs of the radio-loud AGNs in our sample,

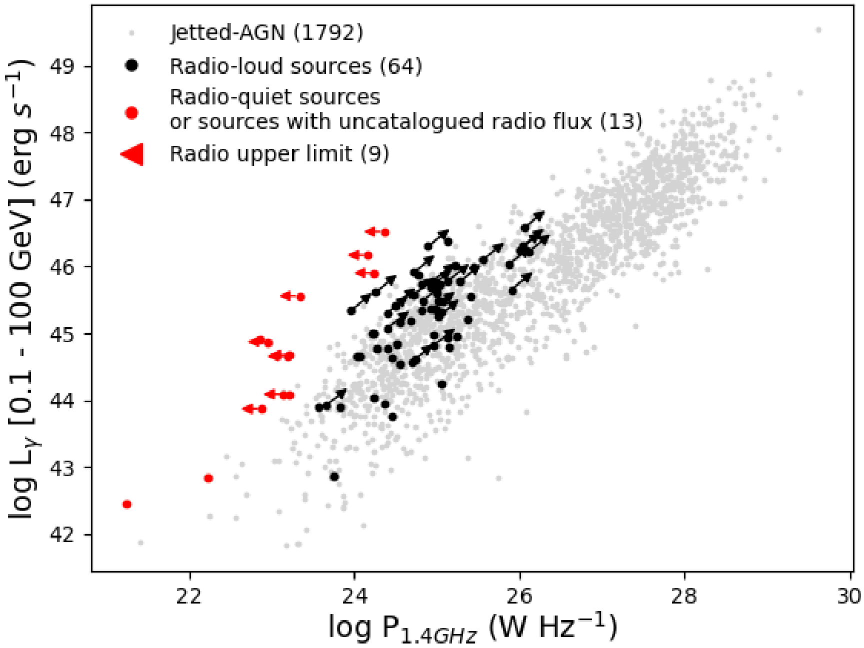

Figure 8.1: $L_{\gamma-ray}$ vs. $P_{1.4GHz}$ for our sample (black and red points) and the comparison sample, represented by 4FGL-DR4 jetted-AGNs (light-grey points). The red points are either radio-quiet sources or sources with uncatalogued radio flux. Diagonal arrows denote lower limits on redshift and therefore powers, horizontal arrows represent radio luminosity upper limits.

reinforcing our proposed association.

It is worth to note the case of XRT J235825.17+382856.4/PAN J235825.17+382856.4, that shows a Seyfert 2 -like optical spectrum[1], and the typical HSP blazar behaviour in its multi-wavelength SED. Its strong radio emission indicates that the jet is likely aligned with the observer, consistent with its blazar-like SED. Probably this object is a low-luminosity FSRQ, given that its absolute magnitude derived by the analysis of the PanSTARRS imaging is $M_g \sim -21.6$.

While objects dominated by the nuclear component exhibit a double-peaked SED shape, characteristic of blazar-like sources, 6 objects reveal a prominent host galaxy that stands out from the non-thermal component.

Beyond the classification based on the characteristics of optical spectra, we can also categorize these objects as LSP, ISP or HSP, according to their ν_p^s, which was estimated using BlaST. This is a machine-learning algorithm that provides an automatic measure of this parameter from the binned SED without any need for manual data preparation, taking also into account the possible presence of emission from dust in the host galaxy (IR bump) and the accretion disk (blue bump) (Glauch et al. 2022). The results of the classification are reported in Table 8.2. As expected, HSPs are the dominant class, which is typical for *Fermi* catalogues, especially for BLLs.

---

[1] All spectra produced by our research group are collected in ZBLLAC, https://web.oapd.inaf.it/zbllac/

Table 8.2: Classification of radio-loud sources according to the position of the synchrotron peak.

Name	ν_p^s (Hz)	Classification
4FGL J0004.0+0840	14.4 ± 1.1	ISP
4FGL J0006.4+0135	15.1 ± 0.8	HSP
4FGL J0049.1+4223	15.7 ± 0.6	HSP
4FGL J0102.4+0942	14.7 ± 0.6	ISP
4FGL J0112.0+3442	14.2 ± 1.7	ISP
4FGL J0158.8+0101	13.0 ± 0.9	LSP
4FGL J0202.7+3133	15.3 ± 0.7	HSP
4FGL J0234.3−0628	15.1 ± 0.8	HSP
4FGL J0238.7+2555	16.5 ± 0.8	HSP
4FGL J0251.1−1830	16.1 ± 1.0	HSP
4FGL J0259.0+0552	15.6 ± 0.9	HSP
4FGL J0305.1−1608	15.7 ± 2.0	HSP
4FGL J0338.5+1302	15.7 ± 0.6	HSP
4FGL J0409.8−0359	14.1 ± 0.7	ISP
4FGL J0414.6−0842	14.1 ± 1.2	ISP
4FGL J0506.9+0323	15.4 ± 0.6	HSP
4FGL J0644.6+6039	16.2 ± 1.0	HSP
4FGL J0838.5+4013	15.8 ± 0.8	HSP
4FGL J0848.7+7017	13.7 ± 1.1	LSP
4FGL J0930.5+5132	15.1 ± 0.8	HSP
4FGL J0937.9−1434	15.3 ± 0.6	HSP
4FGL J0952.8+0712	15.4 ± 2.1	HSP
4FGL J1016.1−4247	15.8 ± 0.7	HSP
4FGL J1039.2+3258	15.1 ± 1.4	HSP
4FGL J1049.8+2741	15.8 ± 0.8	HSP
4FGL J1049.5+1548	14.8 ± 0.8	ISP
4FGL J1128.8+3757	13.9 ± 0.9	LSP
4FGL J1131.6+4657	15.6 ± 1.1	HSP
4FGL J1146.0−0638	16.1 ± 0.7	HSP
4FGL J1223.5+0818	16.1 ± 1.2	HSP
4FGL J1223.9+7954	14.9 ± 1.4	ISP
3FGL J1258.4+2123	16.6 ± 0.8	HSP
4FGL J1340.8−0409	15.2 ± 0.8	HSP
4FGL J1346.5+5330	13.6 ± 1.7	LSP
4FGL J1410.7+7405	15.2 ± 0.7	HSP
4FGL J1411.5−0723	15.6 ± 0.9	HSP
4FGL J1511.8−0513	17.1 ± 1.0	HSP
4FGL J1526.1−0831	15.5 ± 0.7	HSP
4FGL J1535.9+3743	13.5 ± 1.2	LSP
4FGL J1541.7+1413	15.5 ± 0.8	HSP
4FGL J1544.9+3218	15.5 ± 0.8	HSP
4FGL J1554.2+2008	17.4 ± 1.4	HSP
4FGL J1555.3+2903	15.8 ± 1.1	HSP
4FGL J1631.8+4144	16.1 ± 0.7	HSP
4FGL J1648.7+4834	16.0 ± 1.6	HSP
4FGL J1704.2+1234	16.1 ± 1.1	HSP
4FGL J1704.5−0527	16.0 ± 1.0	HSP
4FGL J2115.2+1218	15.4 ± 0.6	HSP
4FGL J2150.7−1750	14.6 ± 1.0	ISP
4FGL J2207.1+2222	16.0 ± 0.8	HSP
4FGL J2209.7−0451	15.4 ± 0.7	HSP
4FGL J2228.6−1636	14.6 ± 0.6	ISP
4FGL J2229.1+2254	17.1 ± 0.9	HSP
4FGL J2240.3−5241	14.5 ± 0.9	ISP
4FGL J2244.6+2502	15.5 ± 0.6	HSP
4FGL J2245.9+1544	15.8 ± 1.4	HSP
4FGL J2250.4+1748	13.6 ± 1.3	LSP
4FGL J2317.7+2839	15.0 ± 0.6	HSP
4FGL J2321.5−1619	16.0 ± 0.8	HSP
4FGL J2323.1+2040	14.6 ± 1.0	ISP
4FGL J2346.7+0705	15.3 ± 0.5	HSP
4FGL J2353.2+3135	12.9 ± 1.0	LSP
4FGL J2358.3+3830	16.3 ± 0.9	HSP
4FGL J2358.5−1808	15.6 ± 0.6	HSP

Note. Column 1: Name; Column 2: Logarithm of the synchrotron peak frequency, ν_p^s (Hz); Column 3: Classification.

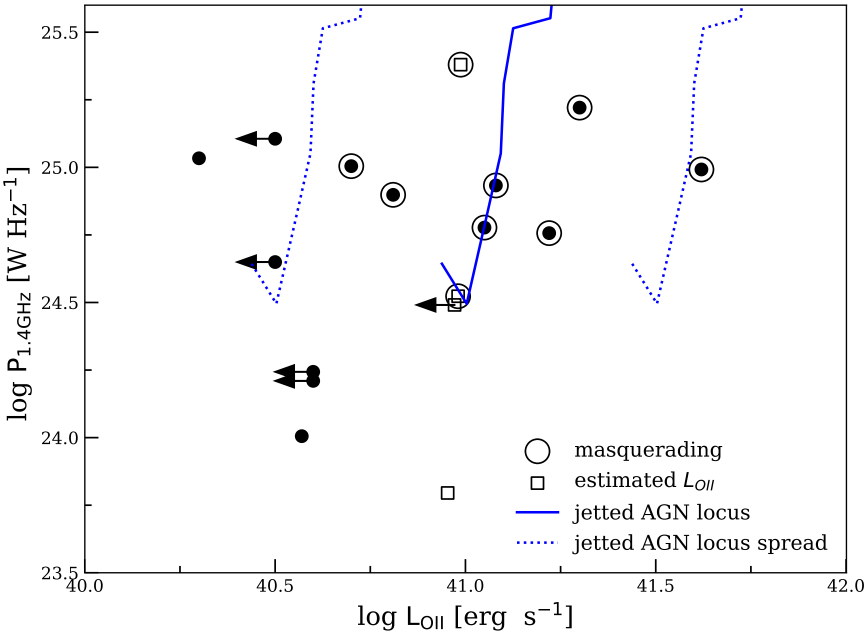

Figure 8.2: $P_{1.4\text{GHz}}$ vs. $L_{[\text{OII}]}$ for the objects in our sample having [O II] information (black filled circles), with masquerading sources highlighted (larger empty circles). Sources for which $L_{[\text{OII}]}$ has been estimated from $L_{[\text{OIII}]}$ are denoted by black empty squares. The solid blue line is the locus of jetted quasars, with the two dotted lines indicating a spread of 0.5 dex, which includes most of the points in Figure 4 of Kalfountzou et al. (2012) (converted from radio powers in W Hz^{-1} sr^{-1} and line powers in W). The arrows denote upper limits on $L_{[\text{OII}]}$.

8.5.2 Unveiling masquerading BLLs among radio-loud UGS

Padovani et al. (2019), Padovani et al. (2022) and Paiano et al. (2023) used four parameters for the classification of masquerading BLLs. These are: (1) location on the radio power – [OII] emission line power, $P_{1.4\text{GHz}} - L_{[\text{OII}]}$, diagram, which defines the locus of jetted (radio-loud) quasars; (2) a radio power $P_{1.4\text{GHz}} > 10^{26}$ W Hz^{-1}, since high-excitation galaxies (HEGs), the class to which FSRQs belong, become the dominant population in the radio sky above this value; (3) an Eddington ratio, i.e. the ratio between the (accretion-related) observed luminosity, L_{acc}, and the Eddington luminosity[2], $L_{\text{acc}}/L_{\text{Edd}} \gtrsim 0.01$, which is again typical of HEGs (Padovani et al. 2017); (4) a γ-ray Eddington ratio $L_\gamma/L_{\text{Edd}} \gtrsim 0.1$, where L_γ is the rest-frame, k-corrected, γ-ray power between 0.1 and 100 GeV.

Since L_{acc} cannot be directly determined for these sources, an indirect approach is applied, using the relationships between L_{acc} and the emission line luminosities $L_{[\text{OII}]}$ and $L_{[\text{OIII}]}$ (Punsly & Zhang (2011); see also Padovani et al. 2019 for more details.). As stressed by Paiano et al. (2023) parameters (3) and (4) are the least certain given their dependence on L_{acc} and M_{BH}. This is even more important in our case since, not having individual measurements, we had to assume the typical value for blazars of $M_{\text{BH}} = 6.3 \times 10^8 M_\odot$ (e.g., Padovani et al. 2022 and references therein).

---

[2] The Eddington luminosity is $L_{\text{Edd}} = 1.26 \times 10^{46}$ $(M/10^8 \text{M}_\odot)$ erg s^{-1}, where $\text{M}_\odot$ is one solar mass.

Table 8.3: Masquerading BLL properties.

Name	4FGL Name	z	$P_{1.4\mathrm{GHz}} - L_{[\mathrm{OII}]}$	$P_{1.4\mathrm{GHz}}$	$L_{\mathrm{acc}}/L_{\mathrm{Edd}}$	$L_{\gamma}/L_{\mathrm{Edd}}$
SDSS J000359.23+08413	4FGL J0004.0+0840	>1.5035	–	I	–	✓
SDSS J011124.86+34415	4FGL J0112.0+3442	0.3997	✓	I	✗	✗
SDSS J015852.77+01013	4FGL J0158.8+0101	0.4537	✓	I	✗	✗
SDSS J025857.55+05524	4FGL J0259.0+0552	>0.6000	–	I	–	✓
SDSS J030515.00−16081	4FGL J0305.1−1608	0.3120	✓	I	✓	✗
USNOB1−1602-0082223	4FGL J0848.7+7017	>1.2435	–	✓	–	✓
SDSS J104939.30+15483	4FGL J1049.5+1548	0.3260	✓	I	✓	✗
SDSS J112903.20+37565	4FGL J1128.8+3757	>1.2110	–	✓	–	✓
SDSS J125821+212351	3FGL J1258.4+2123	0.6265	–	I	–	✓
SDSS J154150.16+14143	4FGL J1541.7+1413	0.2230	✓	I	✗	✗
SDSS J170409.60+12342	4FGL J1704.2+1234	0.4520	✓	I	✓	✗
USNOB0845−0308445	4FGL J1704.5−0527	>0.3000	–	I	–	✓
SDSS J220941.70-04511	4FGL J2209.7-0451	0.3967	✓	I	✓	✗
DES J224017.71−524113	4FGL J2240.3−5241	>0.6500	–	I	–	✓
SDSS J224436.70+25034	4FGL J2244.6+2502	0.6500	✓	I	✓	✗
NVSS J224604.90+15443	4FGL J2245.9+1544	0.5965	✓	I	✓	✗
SDSS J235319.54+31361	4FGL J2353.2+3135	>0.8809	–	✓	–	✓
USNOB1−0718−1032041	4FGL J2358.5−1808	>0.7000	–	I	–	✓

Notes. '✓' implies that the condition is met, 'I' that the condition is not met but this does not mean this is not a masquerading BLL, '✗' that the condition is not met, and '–' that no information is available.

Fig. 8.2 shows the location of our sources with [OII] on the $P_{1.4\mathrm{GHz}} - L_{[\mathrm{OII}]}$ diagram [3]. Nine objects are close to the locus of jetted quasars and are therefore *bona fide* masquerading BLLs, six of which also have $L_{\mathrm{acc}}/L_{\mathrm{Edd}} \geq 0.01$[4]. One source (USNOB0754−0223141 counterpart of 4FGLJ0937.9−1434) has an $L_{[\mathrm{OII}]}$ upper limit right on the locus. However, given that this object has no other HEG-like property and no [O III] detection we are not including it within the masquerading source sample.

Table 8.3 lists the 18 sources which are qualified as masquerading according to at least one parameter. Three BLLs without emission line information have $P_{1.4\mathrm{GHz}} > 10^{26}$ W Hz^{-1} (and $L_{\gamma}/L_{\mathrm{Edd}} > 0.1$), while for the remaining 6 the classification is based only on $L_{\gamma}/L_{\mathrm{Edd}}$, as $L_{\mathrm{acc}}/L_{\mathrm{Edd}}$ requires emission lines. Based on the discussion above, we regard the latter objects as only candidate masquerading BLLs. Therefore, of the 61 sources with redshift information, $\sim 15\%$ (possibly $\sim 30\%$), are of the masquerading type, which is somewhat smaller than the value of $\gtrsim 34\%$ derived by Paiano et al. (2023) for a sample of possible neutrino sources.

8.5.3 The case of radio-quiet sources

Regarding the radio-quiet sources in the sample, we note that most of these objects do not exhibit radio emission (thus, we had to set upper limits), making it difficult to confirm the presence of a jet structure that, as mentioned in the introduction, reaches its maximum flux density in the radio. This is strengthened by the analysis conducted in Sec. 8.4, where we observed that

---

[3] As done in Paiano et al. (2023) for four objects for which only [OIII] was available we converted $L_{[\mathrm{OIII}]}$ to $L_{[\mathrm{OII}]}$ using Figure 7 of Kalfountzou et al. (2012).

[4] One more source, SDSS J011124.86+344154.6 (4FGL J0112.0+3442), has $L_{\mathrm{acc}}/L_{\mathrm{Edd}} = 0.009$ but falls very close to the locus of jetted AGN.

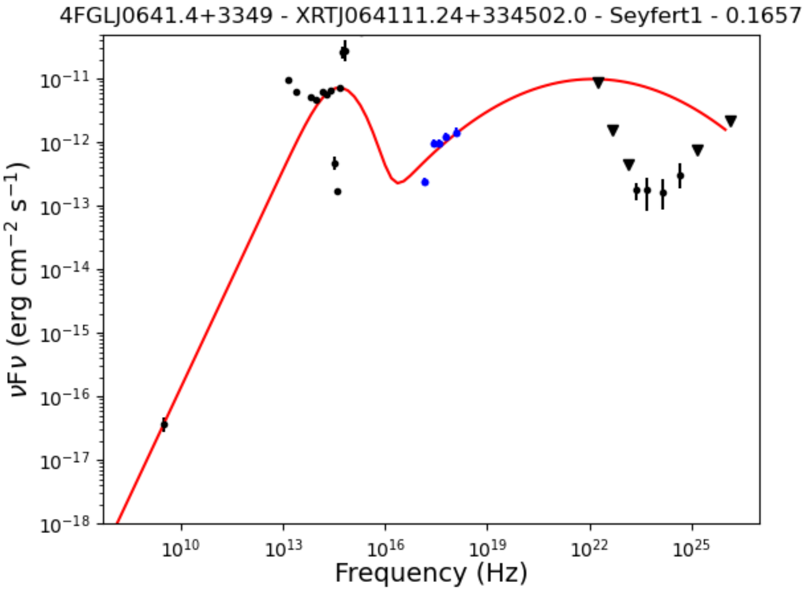

Figure 8.3: SED of XRT J064111.24+334502.0, proposed counterpart in Ulgiati et al. (2024) for the UGS 4FGL J0641.4+3349. Black spectral point are from VOU-Blazar, blue points from our analysis. The points with a triangle shape are upper limits.

these objects deviate from the behavior of jetted AGN-like sources. The SEDs confirm for these objects an emission that differs from a double-peak trend. When a double-peak curve is overlaid on the SEDs, it is observed that the spectral slope in the X-ray band is not compatible with that in the γ-ray band (see an example in Fig. 8.3, to compare with the Fig. 2.3; all cases are discussed in subsection 8.5.3). Due to the absence of a jet, the γ-ray emission cannot obviously be associated to it. As for the IR-X-ray emission, however, it appears to have a thermal origin.

Having ruled out the presence of a jet in these sources, we explore possible alternatives for the origin of their γ-ray emission.

Gamma-ray emission from star-formation-related processes? As mentioned in Sec. 8.1, γ-ray photons can be produced through star-formation-related (SFR) processes. Since the γ-ray emission from starburst galaxies is constant over time, we decided to investigate the fractional variability (FV) of the radio-quiet objects.

We notice that the mean value of the FV parameter for our entire sample is consistent with that of the 4FGL AGNs ($\langle FV^{AGN}_{4FGL-DR4}\rangle = 0.6 \pm 0.4$, compared to $\langle FV_{sample}\rangle = 0.5 \pm 0.2$). Regarding radio-quiet objects, while three of them (4FGL J0023.6−4209, 4FGL J0117.9+1430 and 4FGL J1430.6+1543) show variability, in other three cases (4FGL J0938.8+5155, 4FGL J1125.1+4811 and 4FGL J1234.7−0434) the FV parameter is compatible with 0 (in the remaining objects the parameter is not available). Therefore, in these 3 objects γ-ray emission could stem from SFR processes. However, even ~15% of the 4FGL-DR4 AGNs have an FV parameter compatible with 0, which demonstrates that this condition is necessary but not sufficient to identify starburst galaxies. We therefore decided to perform a different test.

Considering the L_γ vs. $P_{1.4\text{GHz}}$ relationship reported in Peng et al. (2019) for star-forming galaxies is it possible to infer the level of γ-ray emission due to SFR process (within the hypothesis

Table 8.4: Comparison between the predicted γ-ray luminosity due to SFR processes and the estimated luminosity from the fluxes reported in the 4FGL-DR4 for the radio-quiet sample.

ID	4FGL Name	Optical counterpart	$P_{1.4\mathrm{GHz}}$ (W Hz^{-1})	$L^{SFP}_{1-500GeV}$ (erg s^{-1})	$L^{Fermi}_{1-500GeV}$ (erg s^{-1})
1	4FGL J0023.6−4209	DES J002303.74-420508.4	22.2	$40.3^{+0.6}_{-0.6}$	42.7
2	3FGL J0031.6+0938	SDSS J003159.86+093618.4	<22.9	$41.2^{+0.6}_{-0.6}$	44.2
3	4FGL J0117.9+1430	SDSS J011804.83+143158.6	<23.1	$<41.4^{+0.6}_{-0.6}$	43.6
4	4FGL J0641.4+3349	PAN J064111.22+334459.7	23.2	$41.6^{+0.6}_{-0.6}$	44.0
5	4FGL J0938.8+5155	SDSS J093834.72+515452.3	22.9	$41.2^{+0.6}_{-0.6}$	44.8
6	4FGL J1125.1+4811	SDSS J112526.27+480922.0	<24.2	$<42.9^{+0.6}_{-0.6}$	46.0
7	4FGL J1234.7−0434	PAN J123448.05-043245.2	23.2	$41.6^{+0.6}_{-0.6}$	44.6
8	4FGL J1256.8+5329	SDSS J125630.43+533204.3	<24.2	$<42.9^{+0.6}_{-0.6}$	45.6
9	4FGL J1308.7+0347	SDSS J130832.10+034403.9	<23.3	$<41.7^{+0.6}_{-0.6}$	45.5
10	4FGL J1430.6+1543	SDSS J143058.03+154555.6*	<22.9	$<41.1^{+0.6}_{-0.6}$	43.6
11	4FGL J1539.1+1008	SDSS J153848.47+101843.2*	<23.2	$<41.6^{+0.6}_{-0.6}$	44.2
12	4FGL J2030.0−0310	PAN J203014.27-030722.5	21.2	$38.9^{+0.6}_{-0.6}$	42.4
13	4FGL J2212.4+0708	SDSS J221230.98+070652.5	<24.4	$<43.0^{+0.6}_{-0.6}$	46.4

Note. Column 1: Identification number; Column 2: 4FGL Name; Column 3: Optical counterpart; Column 4: Logarithm of the 1.4 GHz radio power (W Hz^{-1}); Column 5: Logarithm of the γ-ray luminosity predicted by the L_γ vs. $P_{1.4\mathrm{GHz}}$ relationship for SFR processes (erg s^{-1}). The reported uncertainty is at a 1 σ confidence level and was estimated from Figure 3 of Peng et al. (2019); Column 6: Logarithm of the γ-ray luminosity estimated from the 4FGL-DR4 catalogued flux (erg s^{-1}).
(*) L_{radio} is measured at 1.4 GHz.

that all radio emission is due to the latter). We report in Table 8.4 the results of this analysis, comparing the cataloged γ-ray emission with the predicted one. The formula reported in Peng et al. (2019) involves the use of monochromatic radio continuum power at 1.4 GHz. As shown in Table 8.4, the predicted γ-ray emission is significantly lower than the cataloged values, typically by about three orders of magnitude. This suggests that star-forming-related processes are unlikely to be the source of the *Fermi* emission.

Notes of individual sources and possible alternative counterparts

Given the challenges in attributing the γ-ray emission in our sample of radio-quiet sources to either jet activity or star formation processes, we have delved deeper into the analysis to explore alternative counterparts. The original proposed counterparts are selected to be the unique X-ray sources with SNR $\geq 3\sigma$ contained within the 3σ *Fermi* error regions of these UGSs. We decide to decrease the detection threshold (SNR $< 3\sigma$) for the X-ray counterparts, and to investigate potential radio counterparts regardless of the presence of an X-ray source. The radio catalogues primarily used for this research are VLASS and RACS.

Below we present detailed notes on each examined individual sources:

- 4FGL J0023.6−4209: The proposed counterpart is the Seyfert 2 XRT J002303.59-420509.6/DES J002303.74-420508.4 (see Sec. 7.4, Fig. 8.4 and Ulgiati et al. (2024)). Based on the SED presented in Fig. 8.5, we can conclude that the multi-wavelength

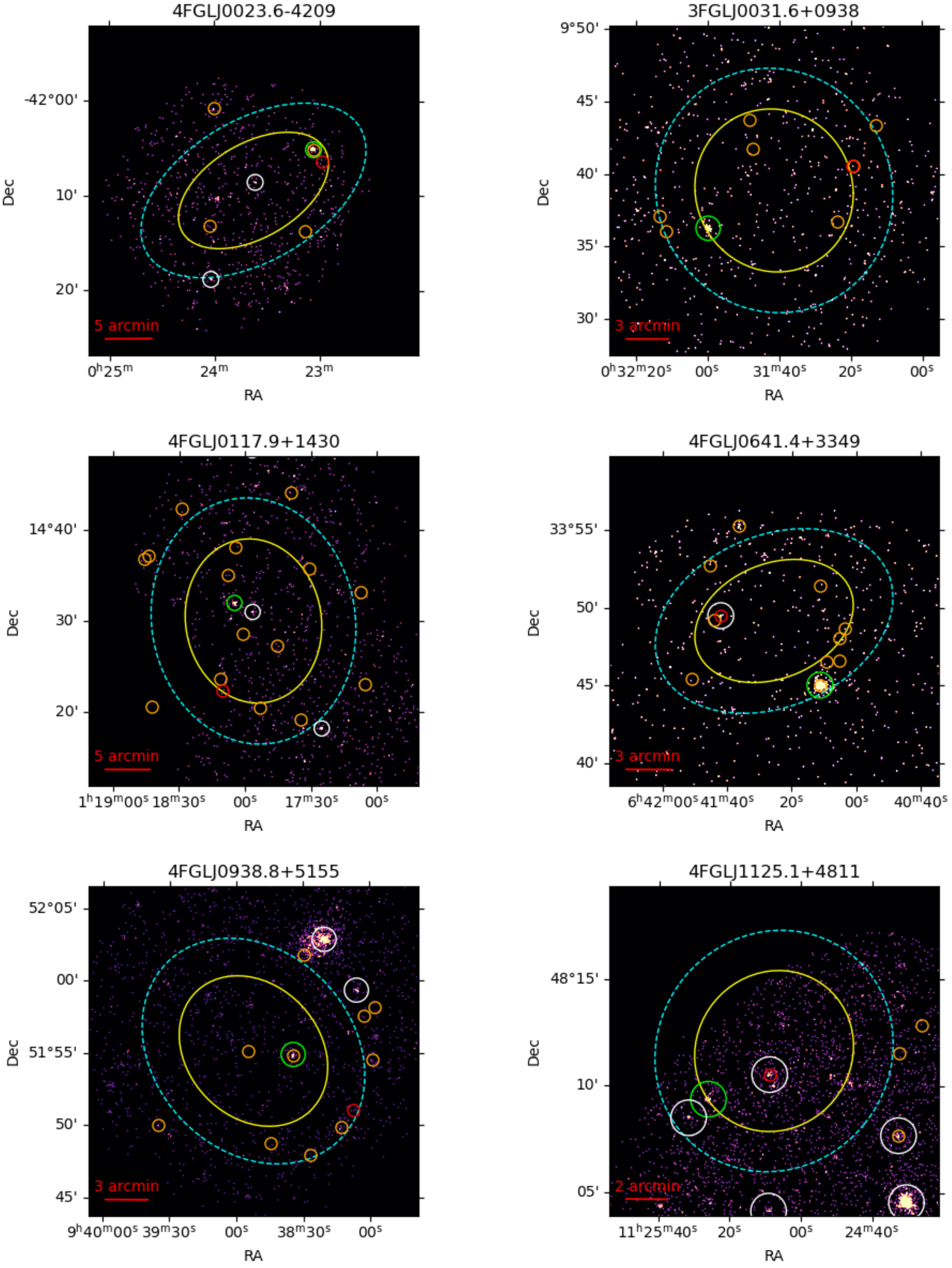

Figure 8.4: X-ray skymaps for 13 UGSs with disputed associations. The yellow and cyan ellipses are respectively the 2σ and 3σ *Fermi* γ-ray error regions. X-ray detections, found through *Swift*/XRT analysis, are reported in green (counterpart proposed in Ulgiati et al. (2024)) and white (other X-ray sources). Radio detections are reported in red (alternative counterpart proposed in this chapter) and orange (other radio sources).

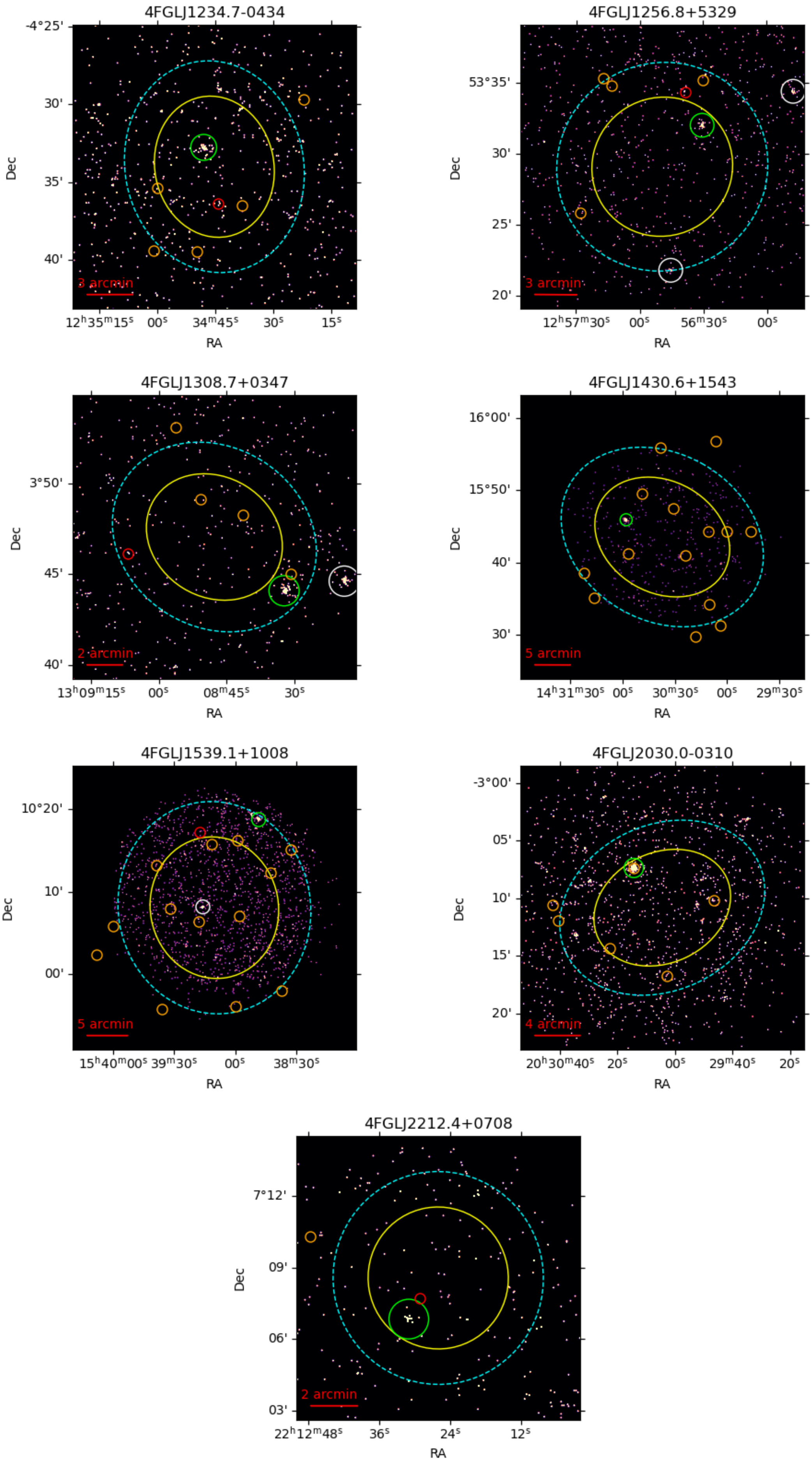

Figure 8.4. Continued.

emission of this object is not consistent with that of a blazar (see Fig. 2.3 for comparison). It does not exhibit a flat radio spectrum ($\alpha < 0.5$), and furthermore, both the X-ray and γ-ray spectra are flat, which contradicts the characteristics of jet-like emission. For this source, according to the spectroscopic classification, the likely origin of the X-ray component of XRT J002303.59-420509.6 is the disk, while that of the infrared one is the dusty torus.

Within the error region of this UGS there are two other X-ray sources: XRT J002402.05-421851.6 and XRT J002336.81-420837.1, both with a SNR = 1.6. XRT J002402.05-421851.6 has the same inconsistency as DES J002303.74-420508.4, without a jet visible in the SED and a flat X-ray spectrum. XRT J002336.81-420837.1 is a star, so it can not emit γ-rays.

In the radio band, we find that four sources are coincident with the γ-ray position (see Fig. 8.4), but only two of them are also coincident with an optical source. Building the SEDs for these objects, we find that the radio source RACS J002258.9−420624, coincident with the optical source DES J002259.06-420624.5 (g = 22.8), has the radio/optical spectrum consistent with the γ-ray one (see Fig. 8.5 and Fig. 2.3 as comparison), even though this source is not detected in the X-ray band. The SED exhibits a hint of a double-peak shape and also shows a flat radio spectrum. This could be a clue for the presence of a jet and, according to its synchrotron frequency peak (ν_p^s = 14.2 ± 2.9), it can be classified as an ISP blazar. This can be a possible counterpart of 4FGL J0023.6−4209; however, the absence of X-ray detection introduces some uncertainty regarding the association. Optical spectroscopy may provide further confirmation.

Regarding the other radio source, RACS J002402.90-421309.0, it has poor spectral coverage, which does not allow for SED analysis.

- 3FGLJ0031.6+0938: The proposed counterpart of this γ-ray emitter is the X-ray source XRT J003159.86+093618.4, which coincides with the optical source SDSS J003159.86+093618.4, exhibiting a narrow-line Seyfert 1 (NLSy1) optical spectrum (Paiano et al. 2019). Although the SED shows a blazar-like double-peak trend (see Fig. 2.3), the source is not detected in the radio band. This complicates the association and leads us to search for potential alternative counterparts in the field.

  There are no other possible X-ray counterparts in the 3σ *Fermi* error region (see Fig. 8.4). Investigating possible alternative counterparts among the radio sources coincident with the γ-ray emission, we find that the radio source VLASS1QLCIR J003119.56+094033.3, coincident with the optical source SDSS J003119.60+094033.0 (g=20.6), which has a spectrum published in the SDSS DR16 archive, is identified as a FSRQ ($M_g \sim -25.8$) at z=2.40604 (Ahumada et al. 2020). Given the low-energy emission trend, it is unlikely that this HSP blazar (ν_p^s = 15.1 ± 2.3) is the counterpart of the γ-ray emission, as such a system would require a very strong Compton dominance [5]. Five additional radio sources are located within the error box of this UGS (see Fig. 8.4), but only two show an optical emission, VLASS1QLCIR J003213.25+093703.8 and RACS J003147.4+094145. Both present a radio to optical spectrum consistent with a non-active galaxy, so incompatible with a γ-ray emission. Therefore, there are no plausible alternative counterparts for 3FGL J0031.6+0938.

- 4FGL J0117.9+1430: Two X-ray sources are detected within the *Fermi* error region of this UGS: the NLSY1 SDSS J011804.83+143158.6 with a SNR = 4.7 and XRT J011756.53+143059.8 with a SNR = 1.8. We proposed in the Sec. 7.4 and in Ulgiati et al. (2024) the NLSY1 as the possible low energy counterpart of this UGS. In this case as well, the SED shows a double-peak trend (see Fig. 8.5), although the source is not detected in the radio band. We are also searching for potential alternative counterparts for this source.

  Nine radio source are present within the γ-ray error ellipse (see Fig. 8.4), but only three of them are also coincident with an optical source. One of them (VLASS1QLCIR J011734.73+141910.2) is a star. VLASS1QLCIR J011808.08+143504.7 is coincident with the optical source SDSS J011808.07+143504.7, which appears to be an elliptical galaxy at redshift 0.427 (Ahumada et al. 2020) with a steep radio spectrum ($\alpha > 0.5$). The spectrum of the counterpart is typical of a non-active galaxy, and when compared with the γ-ray emission, it is too low to justify a continuity in emission. The other radio source is VLASS1QLCIR J011810.42+142217.9, which is coincident with the optical source SDSS J011810.39+142218.2. The IR and optical emissions are consistent with a giant elliptical galaxy at z ~ 0.5. The SED is consistent with an LSP source ($\nu_p^s = 12.8 \pm 1.2$) with a high Compton dominance (see Fig. 8.5). This could be the counterpart of the UGS.

- 4FGL J0641.4+3349: This UGS contain two X-ray sources within its error region: XRT J064111.2+334502.0 with SNR = 13.8 and XRT J064142.06+334930.5 with SNR = 1.7. XRT J064111.2+334502.0 is a Seyfert 1 galaxy (see Sec. 7.4, Fig. 8.4 and Ulgiati et al. (2024)) at z=0.1657. The SED of this object reveals that the γ-ray emission is too low to be compatible with the rest of the spectrum for a jetted source (see Fig. 8.5, and Fig. 2.3). The trend of the SED up to the X-ray band is consistent with that of a classical Seyfert, indicating that the X-ray emission is of thermal origin. The other X-ray source, XRT J064142.06+334930.5, is coincident with the radio source VLASS1QLCIR J064142.03+334927.5 and the optical source PAN J064142.10+334927.7. There is no optical spectrum available in the literature. The low energy emission is consistent with the γ-ray one (Fig. 8.5). From the modeling of the low energy peak it is possible to estimate a photometric redshift z ~ 0.4 (see Chang et al. 2019 for details). According

---

[5] The Compton dominance quantifies the relative strength of the γ-ray emission compared to the X-ray emission and indicates the importance of Compton scattering processes in the production of high-energy photons within the blazar jets

to the position of the synchrotron frequency peak (ν_p^s = 14.4 ± 1.0), this source can be classified as an ISP blazar. Spectroscopic observations will be performed in order to confirm the classification of this object. Within the *Fermi* error box of this UGS, there are eight other radio sources (see Fig. 8.4). Only one of these coincides with an optical source, VLASS1QLCIR J064144.15+334913.1. However, this is a star, which we can therefore exclude as a potential counterpart.

- 4FGL J0938.8+5155: The counterpart proposed in the Sec. 7.4 and in Ulgiati et al. (2024) for this UGS is the QSO SDSS J093834.72+515452.3. Observing the multi-wavelength SED (Fig. 8.5) we note that both X-ray and γ-ray spectra appear flat, trend not compatible for a jetted-AGN.

  There are no additional X-ray counterparts within the γ-ray error region, and, however, five radio sources are found (Fig. 8.4), none of which exhibit X-ray emission or low-energy characteristics consistent with the γ-ray flux based on SED analysis. Only VLASS1QLCIR J093807.91+515103.7 shows both radio and optical emissions compatible with the high-energy data (Fig. 8.5). This source's SED suggests a potential double-peak structure and a flat radio spectrum, despite its lack of X-ray detection. It coincides with SDSS J093807.91+515103.8, an object reported in the literature with a featureless optical spectrum characteristic of a BLL (Ahumada et al. 2020). The source is likely an ISP blazar, with ν_p^s = 14.6 ± 1.2, and based on modeling of the low-energy peak, its photometric redshift can be at approximately z ~ 0.3.

- 4FGL J1125.1+4811: Our proposed counterpart for this γ-ray emitter is the X-ray source XRT J112526.01+480922.8, coincident with the optical source SDSS J112526.27+480922.0 (see Sec. 7.4 and Ulgiati et al. (2024)). From the SED (see Fig. 8.5), the X-ray and γ-ray spectra are flat, so inconsistent with each other assuming the *blazar-like* double-peak SED. Subsequently, new *Swift* observations were made in the region of this UGS, significantly increasing the statistics and revealing two new sources: XRT J112508.81+481032.4, with a SNR = 4.2 σ, and XRT J112531.47+480832.1, with a SNR = 2.6 σ (see Fig. 8.4). While the first X-ray source can not be associated with any optical source, XRT J112508.81+481032.4 coincides with a radio source VLASS1QLCIR J112508.90+481033.7 and the optical object SDSS J112508.91+481033.4, for which a SDSS spectrum is available (Ahumada et al. 2020). The spectrum has a power-law shape and appears to be featureless, indicating a BLL nature. The multi-wavelength SED shows a double-peaked ISP blazar shape(ν_p^s = 14.4 ± 1.0). These elements suggests XRT J112508.81+481032.4 as the most likely counterpart of this γ-ray emitter.

- 4FGL J1234.7−0434: The X-ray source XRT J123448.00-043246.2, aligned with the optical source PAN J123448.05-043245.2, was suggested as a potential counterpart in

Paiano et al. (2019), showing a Seyfert-2 like optical spectrum. The multi-wavelength SED of this object deviates from the typical double-peak trend of jetted AGNs, and it is also not detected in the radio band, making difficult to reconcile the γ-ray emission with that at lower energies (Fig. 8.5, and Fig. 2.3). There are no other possible X-ray counterparts in the 3σ *Fermi* error region (see Fig. 8.4). We find that there are four radio sources contained in the γ-ray error box of this γ-ray emitter (see Fig. 8.4). VLASS1QLCIR J123449.72-043929.1 is not coincident with an optical source, RACS J123459.9-043522 and VLASS1QLCIR J123438.16-043631.7 are a star and a galaxy respectively, so they can not be considered as good counterparts of this UGS. The radio emitter VLASS1QLCIR J123444.23-043622.2, coincident with the optical source PAN J123444.21-043622.4, has a radio-optical SED compatible with the γ-ray emission of this UGS (Fig. 8.5). Furthermore, it is worth to note that 4FGL J1234.7−0434 is also contained in the 3HSP catalogue (Chang et al. 2019) (it has $\nu_p^s = 14.5 \pm 1.4$), associated with the source 3HSP J123444.2-043622. This association was subsequently included in the 4FGL-DR3 catalog (Abdollahi et al. 2022), following the work by Paiano et al. (2019).

- 4FGL J1256.8+5329: This UGS contains two X-ray sources within its error region: XRT J125630.5+533202.2 with a SNR=4.2 and XRT J125645.37+532150.4 with SNR=2.4. XRT J125630.5+533202.2 is coincident with the optical source SDSS J125630.43+533204.3 (see Sec. 7.4, Fig. 8.4 and Ulgiati et al. (2024)). Its SED exhibit a double-peak shape, although the source is not detected in the radio band (Fig. 8.5).

  XRT J125645.37+532150.4 is coincident with the optical source SDSS J125645.08+532148.3 and the multi-wavelength SED is consistent with a non-active galaxy (it does not exhibit a flat radio spectrum, and it has a thermal IR/optical spectrum, typical of a non-active galaxy). Therefore it can not be the counterpart of the UGS.

  Within the *Fermi* error region of this UGS, there are four radio sources, including CRATES J125637+533417 (VLASS1QLCIR J125638.62+533423.5). This source exhibits an SED (see Fig. 8.5) with a double-peak shape characteristic of an LSP, with $\nu_p^s = 12.9 \pm 0.8$ (see Fig. 2.3 for a typical LSP SED). In the IR/optical range, there is a suggestion of elliptical host galaxy emission, allowing an estimated photometric redshift of approximately $z \sim 0.45$ (see details in Sec. 8.4). Spectroscopic observations would help clarify the nature of this source, which is a good candidate as an alternative counterpart. As for the remaining radio sources, none show optical counterparts, except for VLASS1QLCIR J125739.13+533422.7, which appears to be a non-active galaxy and thus an unlikely counterpart to the γ-ray emitter (the SED does not show a flat radio spectrum, and in the IR/optical band, only a thermal component from the galaxy appears).

- 4FGL J1308.7+0347: The proposed counterpart for this γ-ray emitter is the X-ray source XRT J130832.27+034405.4, coincident with the optical source SDSS J130832.10+034403.9

(details in the Sec. 7.4 and in Ulgiati et al. (2024)). Its SED does not show a double-peak shape, nor a flat radio spectrum. According to the spectroscopic classification (see Fig. 7.1 and Sec. 7.4), the likely origin of the X-ray component of XRT J130832.27+034405.4 is the disk, while that of the infrared one is the dusty torus, which would not justify its γ-ray emission (Fig. 8.5). There are no other possible X-ray counterparts in the 3σ *Fermi* error region (see Fig. 8.4).

From the search for potential radio counterparts within the error region, two radio sources have been identified (see Fig. 8.4). The first, VLASS1QLCIR J130906.79+034608.0, coincides with the optical source SDSS J130906.78+034607.5. Its optical spectrum (Ahumada et al. 2020) appears featureless, indicating a likely BLL-like nature. Based on multi-wavelength SED analysis, the synchrotron frequency peak is set at ν_p^s = 12.9 ± 1.0 (see Fig. 2.3), classifying it as a low-synchrotron-peaked (LSP) blazar. However, the low-energy emission trend suggests that this source is unlikely to be the counterpart of the γ-ray emission, as such a system would require a significant Compton dominance. The second radio source, RACS J130856.2+035304, coincides with an optical source, which exhibit a *Gaia* proper motion (see Chapter 6 for details), with a stellar-like SED. In conclusion, we find that no plausible alternative counterparts for this UGS can be proposed.

- 4FGL J1430.6+1543: We identify the source XRT J143057.9+154556.0, coinciding with the Seyfert 1 galaxy SDSS J143058.03+154555.6, as a potential counterpart (see Sec. 7.4). However, when assuming a double-peak blazar-like SED, the observed radio and X-ray emissions do not align with the expected γ-ray flux, which appears too low (see Fig. 8.5). Within the γ-ray error region, we find 10 radio sources (see Fig. 8.4), but none coincide with an optical counterpart. Consequently, we conclude that no alternative counterparts can be proposed for this UGS.

- 4FGL J1539.1+1008: The low energy counterpart proposed for this UGS in the Sec. 7.4 and in Ulgiati et al. (2024) is the X-ray source XRT J153848.5+101841.7, classified as a Seyfert 1 galaxy. The SED (see Fig. 8.5) exhibit a double-peak shape, although the source has not radio detection in the literature. In the absence of a flat radio spectrum, it is difficult to connect the γ-ray emission with this source. In the *Fermi* error region of this UGS, there is another X-ray source that does not coincide with any optical counterpart.

  Within the γ-ray error ellipse (see Fig. 8.4), we identified two interesting radio objects, both of which have optical spectra available in the SDSS archive.

  The first, VLASS1QLCIR J153917.29+101713.6, is an AGN at a redshift of z=0.09692 (Ahumada et al. 2020). However, due to the lack of X-ray detection and a flat radio spectrum, this association is unlikely, and we cannot consider it a potential counterpart for the γ-ray detection. The second source, VLASS1QLCIR J153938.94+101311.6, coincides with the spiral galaxy SDSS J153938.96+101311.7, located at z = 0.034 (Ahumada et al.

2020). Further analysis is required to investigate these alternative associations. Regarding the other radio sources found within the UGS error box, the majority do not coincide with optical counterparts, and there are insufficient spectral data points available to construct and analyze the multi-wavelength SED. Therefore, no plausible alternative counterparts can be proposed for this UGS.

- 4FGL J2030.0−0310: Our proposed counterpart XRT J203014.34-030721.9, coincident with the Seyfert 2 galaxy PAN J203014.27-030722.56, displays a multi-wavelength SED (Fig. 8.5) where the γ-ray emission is comparatively weak relative to the radio and X-ray components, assuming a typical blazar-like double-peak structure. Within the *Fermi* error box, three additional radio sources are present (see Fig. 8.4), although none of them can be associated to any optical or X-ray sources. Consequently, no alternative counterpart candidates emerge from the analysis of this UGS.

- 4FGL J2212.4+0708: The X-ray source XRT J221230.98+070652.5, coinciding with the optical source SDSS J221230.98+070652.5, has been suggested as the counterpart of this UGS (Paiano et al. 2019). From multi-wavelength analysis (Fig. 8.5), the SED displays a double-peak shape with a pronounced γ-ray cut-off, though no radio data are currently available.

  Only one radio source, RACS J221229.1+070744, is found within the γ-ray error box (see Fig. 8.4) and coincides with the optical source SDSS J221229.11+070743.9. This source lacks the flat radio spectrum typical of jet-dominated objects, and the γ-ray emission is too intense to be plausibly associated with the observed low-energy emission. This characteristic weakens the likelihood of an association between the radio source and the γ-ray emission.

We have updated the L_γ vs. $P_{1.4GHz}$ diagram (Fig. 8.6), including the 7 new "alternative" proposed counterparts identified starting from the radio sources within the UGS region, regardless of X-ray emission presence or significance. These sources fall within the region typically occupied by jetted AGNs, supporting the hypothesis that they are likely blazar-type objects and could be associated with the detected γ-ray emission. Regarding the UGSs 4FGL J0023.6-4209 and 4FGL J1234.7-0434, they do not appear in the plot because their new counterparts lack redshift information. This is due to the absence of an IR/optical light curve and insufficient optical coverage in the SEDs. In any case, as stated in the introduction, more conclusive classification of these sources could be achieved through optical spectral analysis, making them a priority for an upcoming spectroscopic campaign.

For 6 objects, no alternative counterparts were identified, leaving the initial candidates proposed in Chapter 7 and in Paiano et al. (2017a, 2019) as the most probable associations for these UGSs. However, further analyses are required to clarify the emission mechanisms at play and to fully interpret the observed SEDs.

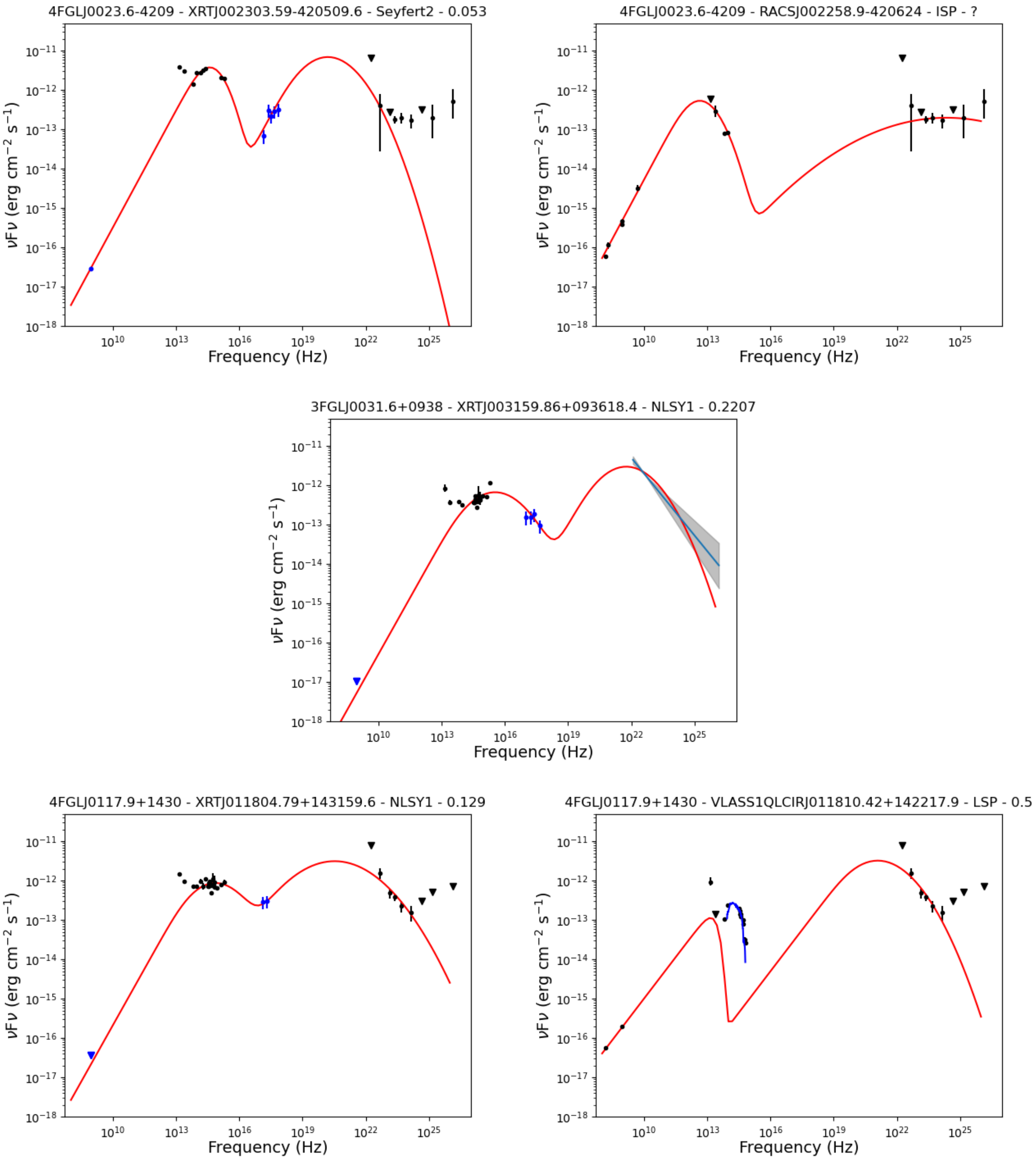

Figure 8.5: Left: SED of the counterpart proposed in Ulgiati et al. (2024) or Paiano et al. (2017a) or Paiano et al. (2019). Right: SED of the alternative counterpart proposed in this chapter. In the case where only one SED is available for the UGS (the SED of the counterpart proposed in the previous works), it means that besides the counterpart proposed in previous works, there are no other better counterparts within the Fermi error box. At the top of the figure, the name of the UGS, the proposed counterpart, the counterpart's classification, and its redshift are displayed (if marked with a '*', the redshift is photometric; otherwise, it is spectroscopic). Black point are from VOU-Blazar, blue points from our analysis. The points with a triangle shape are upper limits. The red curve emulates the typical double-peaked shape of blazars, while the blue one is the template of a giant host galaxy at the object's redshift. It is worth noting that we did not overlay a host galaxy template for the Seyferts, as they are typically hosted in spiral galaxies, and a corresponding template is not available in the SSDC's SED Builder tool.

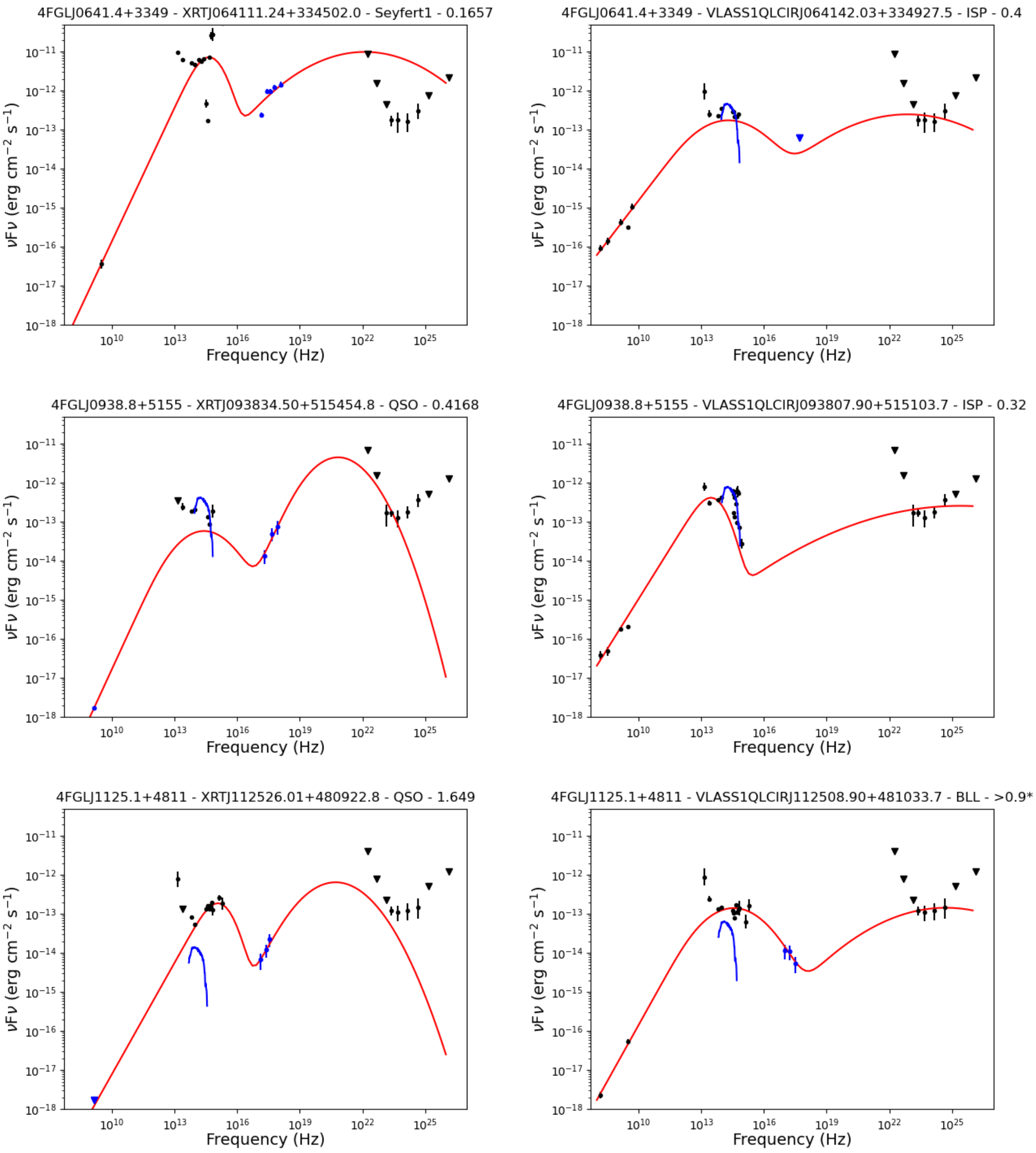

Fig: 8.5: Continued.

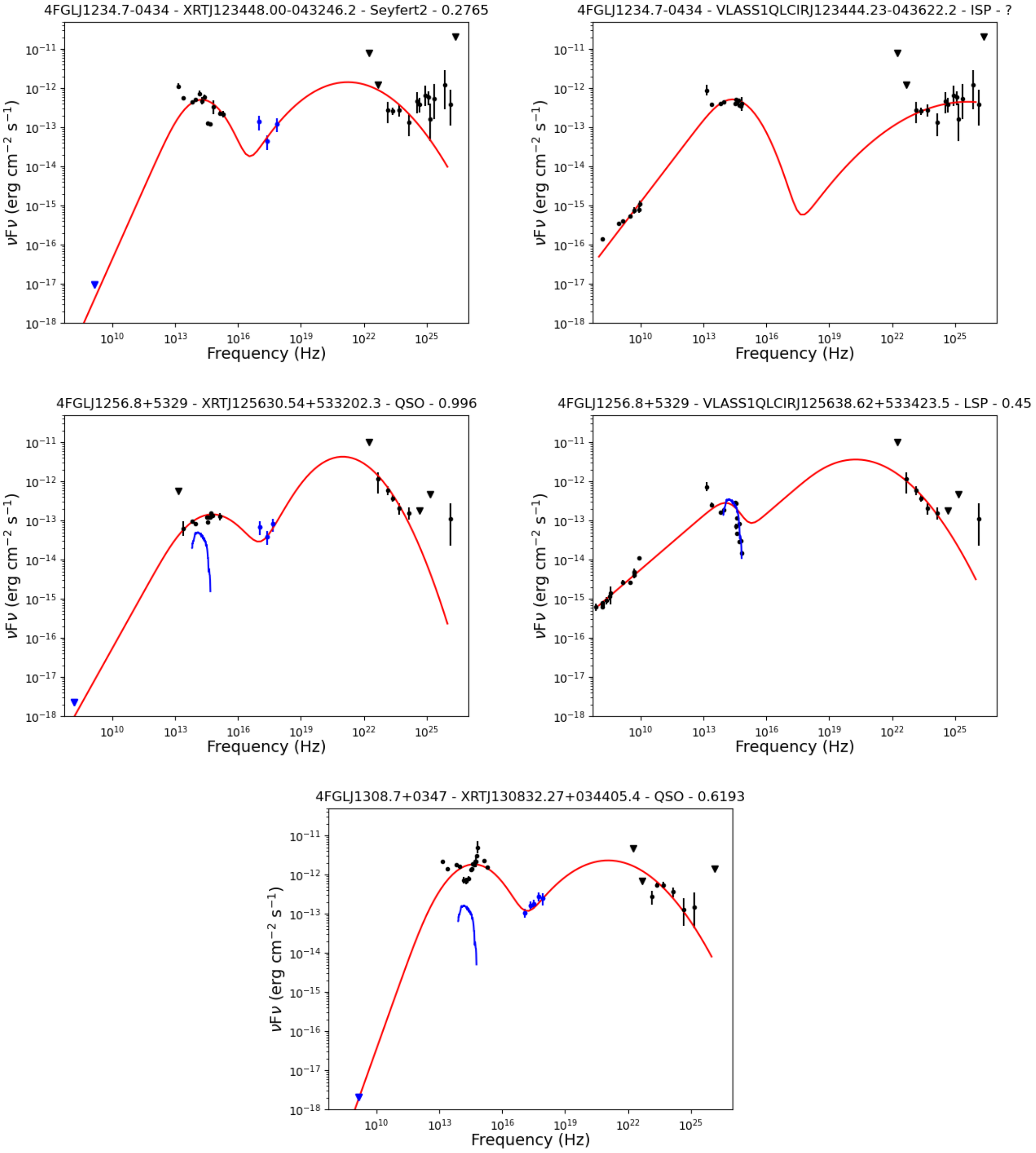

Fig: 8.5: Continued.

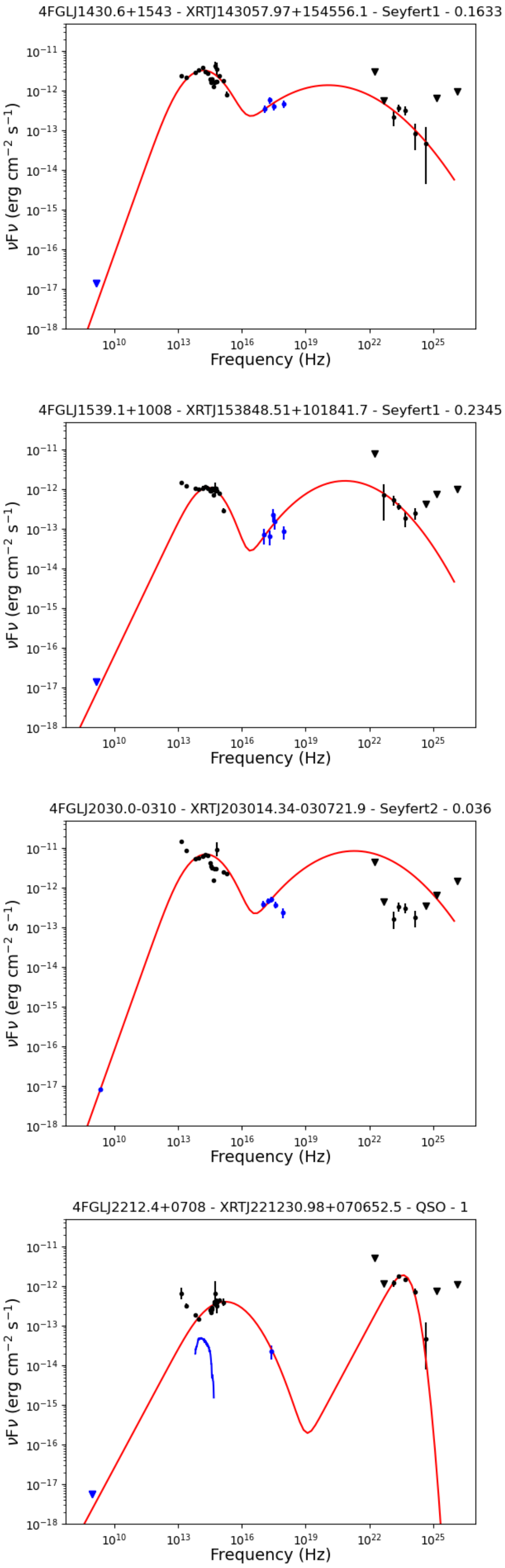

Fig: 8.5: Continued.

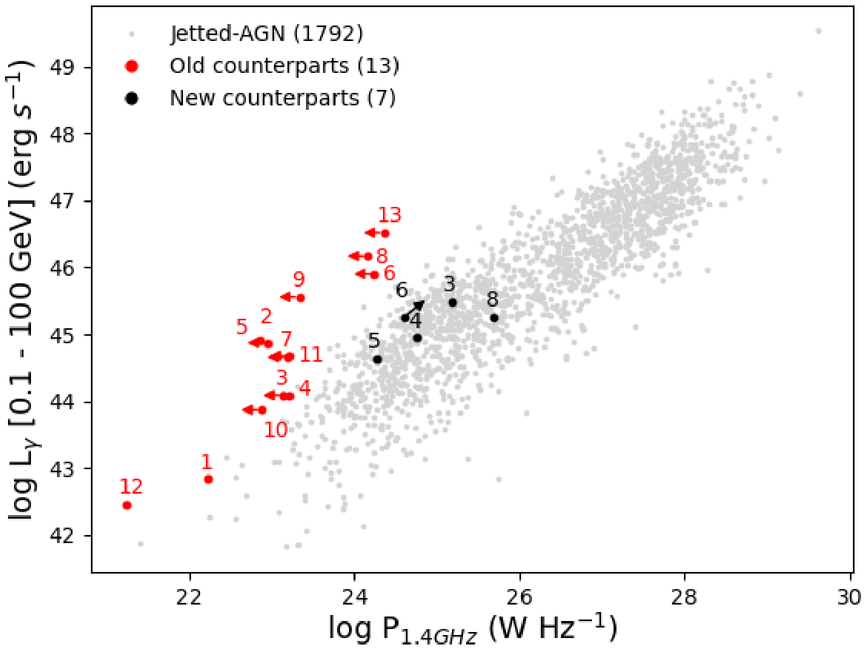

Figure 8.6: $L_{\gamma-ray}$ vs. $P_{1.4GHz}$ for the alternative counterpart (black), the previously proposed counterparts (red), shown to track the UGS evolution in the plot, and for the comparison sample, the 4FGL-DR4 jetted-AGNs (light-grey points). Diagonal arrows denote lower limits on redshift and therefore powers, horizontal arrows represent radio luminosity upper limits. To each UGS, an identifying number has been assigned, as shown in Table 8.4. It is worth noting that among the sources marked in red, some overlap. This is the case for the sources marked as 3 and 4, 7 and 11, 2 and 5.

Table 8.5 summarize the results obtained in the search for alternative counterparts for the 13 radio-quiet sources in the sample.

8.6.0 Conclusions

We analyzed the multi-wavelength emission of a sample of 77 UGSs and their lower-energy counterparts, as proposed in Paiano et al. (2017a, 2019) and Ulgiati et al. (2024). Our objective was to characterize their SEDs, identify potential new masquerading BLLs, and investigate the proposed association between the γ-ray flux and lower-energy emissions.

The multi-wavelength analysis reveals that the radio-loud sources in our sample exhibit SEDs consistent with the characteristic double-peak structure typical of blazars. This classification allows us to categorize them further as LSP, ISP, or HSP sources, based on the location of the synchrotron emission peak in their SEDs. The majority are classified as HSP (46 objects), with 11 as ISP and 7 as LSP.

In the search for masquerading BLL, 9 candidates are identified based on their absolute and relative emission intensities, representing approximately 15% of the radio-loud sample, with a possible upper limit of 30%. This proportion is slightly lower than in previous studies, where Paiano et al. (2023) found a percentage of masquerading BLL of 34% among a sample of neutrino

Table 8.5: Lower energy counterpart for γ-ray sources analysed in this chapter

ID	4FGL Name	Counterpart proposed in the Chapter 7	Alternative counterpart	Class	z	Reference
1	4FGL J0023.6−4209	XRT J002303.59−420509.6	RACS J002258.9−420624	ISP	?	this chapter
2	3FGL J0031.6+0938	XRT J003159.86+093618.4	-	NLSY1	0.2207	Paiano et al. (2019)
3	4FGL J0117.9+1430	XRT J011804.79+143159.6	VLASS1QLCIR J011810.42+142217.9	LSP	0.5^*	this chapter
4	4FGL J0641.4+3349	XRT J064111.24+334502.0	VLASS1QLCIR J064142.03+334927.5	ISP	0.4^*	Chang et al. (2019)
5	4FGL J0938.8+5155	XRT J093834.50+515454.8	VLASS1QLCIR J093807.91+515103.7	BLL	0.3^*	this chapter
6	4FGL J1125.1+4811	XRT J112526.01+480922.8	VLASS1QLCIR J112508.90+481033.7	BLL	$>0.9^*$	this chapter
7	4FGL J1234.7−0434	XRT J123448.00−043246.2	VLASS1QLCIR J123444.23−043622.2	ISP	?	this chapter
8	4FGL J1256.8+5329	XRT J125630.54+533202.3	VLASS1QLCIR J125638.62+533423.5	LSP	0.45^*	this chapter
9	4FGL J1308.7+0347	XRT J130832.27+034405.4	-	QSO	0.6193	Ahumada et al. (2020)
10	4FGL J1430.6+1543	XRT J143057.97+154556.1	-	Seyfert 1	0.1633	Ahumada et al. (2020)
11	4FGL J1539.1+1008	XRT J153848.51+101841.7	-	Seyfert 1	0.2345	Ahumada et al. (2020)
12	4FGL J2030.0−0310	XRT J203014.34−030721.9	-	Seyfert 2	0.036	Jones et al. (2009)
13	4FGL J2212.4+0708	XRT J221230.98+070652.5	-	QSO	1	Paiano et al. (2019)

Note. Column 1: Identification number; Column 2: 4FGL Name; Column 3: Name of the counterpart proposed in the Chapter 7; Column 4: Name of the alternative counterpart proposed in this chapter; Column 5: Classification; Column 6: redshift (z); Column 7: Reference of the redshift.
(*) photometric redshift.

emitter blazars.

For the 13 radio-quiet objects (mainly classified Seyfert/QSO galaxies), the multi-wavelength SED cannot be attributed to jet emissions or star formation processes. This makes it challenging to reconcile the observed γ-ray emission with that of their lower-energy counterparts. Consequently, we explored potential alternative counterparts by examining the radio sources within the UGS error ellipses, independently of their X-ray detection or significance. Among these, we identified possible alternative counterparts for 7 out of the 13 sources, while no plausible alternatives were found for the remaining 6. The investigation of these new counterparts will form the basis for an upcoming spectroscopic campaign, aimed at refining their classifications and further validating the proposed associations.

9

Summary and Conclusions

This thesis project focused on the association and classification of extragalactic unassociated gamma-ray sources (UGSs) identified in the fourth *Fermi* catalog. UGSs represent a significant fraction of the high-energy sky, potentially hiding new blazars or AGN of various classes. The main goal was to identify multi-wavelength counterparts to these UGSs and to discover new sources within these categories. Typically, UGSs are faint in the γ-ray regime, exhibiting lower fluxes compared to associated AGN emitting in γ-ray. This characteristic may suggest the presence of AGNs at higher redshifts or lower luminosity sources. Investigating these sources is essential for population studies, advancing physical models, and enhancing our understanding of cosmic evolution in relation to γ-ray emissions. The association procedure is based on the search for X-ray counterparts of the UGSs by analyzing images provided by the *Swift*/XRT satellite covering the UGS sky regions.

In addition to the X-ray analysis, I investigated the optical and radio sources within the uncertainty regions of the candidate X-ray counterparts of UGS, by consulting various catalogs and conducting targeted observations. Such an effort led to the compilation of a list of potential X-ray, optical, and radio counterparts for UGS1 and UGS2.

The association for the UGS1 is simpler and straightforward: all UGS1 sources were found to be coincident with optical emitters, and 113 were also associated with radio objects. For UGS2 the degree of degeneracy is high, and counting how many of them have at least one optical and/or radio counterpart provides little useful information.

To study the potential of these counterparts for association with UGSs, I compared their absolute and relative fluxes to those of known blazars in the fourth *Fermi* catalog, which serve as prototypes for extragalactic γ-ray emitters. The analysis reveals that UGS counterparts generally exhibit lower fluxes than those of 4FGL-DR4 blazars. Furthermore, the radio-loud sources in the sample occupy regions similar to those of Fermi blazars on *color-color* diagrams ($\log(F_{radio}/F_X)$ and $\log(F_{optical}/F_X)$ as functions of $\log(F_\gamma/F_X)$), suggesting a possible blazar nature. In contrast, radio-quiet sources are found in distinct, more isolated regions in the diagrams, indicating a different type of AGN with characteristics unlike those of the Fermi blazars, and warranting further analysis to confirm their association.

Among the UGS1 sources, 33 of them are coincident with optical counterparts whose spectra were already available in the literature but had not been analyzed in detail. The study of their optical spectra is crucial for determining the extragalactic origin of UGSs, to measure the redshift, and to classify them into various AGN subclasses. All of these 33 objects were classified as AGNs, comprising 21 BL Lacs, 1 flat spectrum radio quasar (FSRQ), 1 radio galaxy, and 10 Seyferts and quasi-stellar objects (QSOs). The unexpected presence of radio-quiet objects (Seyferts and QSOs) as potential counterparts is particularly intriguing, given that all AGNs listed in the fourth *Fermi* catalog are radio-loud.

A multi-wavelength study was conducted to characterize these 33 objects, along with an addition of 44 unidentified γ-ray sources from the second and third *Fermi* catalogs that were previously associated and classified by Paiano et al. (2017a, 2019). This study involved an analysis of their spectral energy distributions (SEDs) to examine their properties and provide a classification. Additionally, new masquerading BL Lac objects were identified based on emission intensities.

Based on the radio-loudness parameter, 64 sources were classified as radio-loud and 13 as radio-quiet AGN. The analysis of the radio-loud sources reveals that their SEDs are consistent with the typical SEDs observed in *Fermi* blazars (Ballet et al. 2023), suggesting that jet emission likely drives as the primary contributor across the radio to γ-ray spectrum. Accordingly, these objects can be categorized into four blazar subclasses based on the synchrotron peak position in their SEDs: 46 HSP, 11 ISP, and 7 LSP. Notably, 9 sources, about 15% of the sample (with a potential upper limit of 30%) are candidates for masquerading BL Lac objects. This fraction is somewhat lower than the $\gtrsim$ 34% reported in previous studies focusing on masquerading BL Lacs within samples of neutrino-emitting blazars (Padovani et al. 2022; Paiano et al. 2023).

For the 13 radio-quiet AGN, the multi-wavelength SED profile diverges significantly from that observed in jetted AGNs. Their SEDs lack the characteristic double-peak structure, suggesting the absence of a jet and complicating any direct correlation between their γ-ray emission and lower-energy emissions. Since γ-ray production typically requires non-thermal processes, and with the jet ruled out as the emission source, I investigated the possibility that the γ-ray emission might arise from star formation processes within the host galaxy. This analysis, however, revealed inconsistencies between the γ-ray and lower-energy emissions. Consequently, I examined alternative counterparts by analyzing radio sources that fall within the γ-ray error box, irrespective of the presence or significance of X-ray emission. This search identified good alternative counterparts for 7 of the 13 UGSs, each showing a broad-band SED with a double-peaked structure characteristic of jetted AGNs. Such sources will be the targets of an upcoming observational campaign for classification confirmation and association verification. For the remaining 6 sources, no alternative counterparts were identified and a more deep analyses is needed to probe the origin of their γ-ray emissions.

The objectives of my thesis have been successfully achieved, with potential multi-wavelength counterparts identified for 40% of the extragalactic unassociated gamma-ray sources (UGSs) from the fourth *Fermi* catalog, totaling 274 sources. Among these, 193 have only one potential counterpart (UGS1), while 81 have more than one (UGS2). Within the UGS1 group, 33 sources have been classified as blazars or other classes of AGNs in this thesis, and $\sim$ 60 have been observed with optical spectroscopy. From the analysis of this sample, these sources have also been identified as blazars and AGNs, and will be included in forthcoming publications currently in preparation. This work has enriched the understanding of these high-energy sources and underscores the importance of such findings in advancing the field of high-energy astrophysics.

This work illustrates the complexity of the counterpart identification process for UGSs, which involves a series of complementary steps. Identifying potential counterparts across X-ray and other wavelengths emphasizes the necessity of a multi-wavelength approach, employing various observational and analytical techniques. It includes optical spectroscopy, which is crucial for providing a robust classification of the optical counterparts, and multi-band SED analysis, which allows us to study the properties and origin of the emissions. The adopted approach not only allows for the classification of UGS into various types of AGN, particularly the different classes of blazars, but also assists in identifying peculiar and rare sources, such as masquerading BLL.

A

Appendix

A.1.0 ATCA data

As part of the dedicated ATCA program, we observed 20 X-ray sources between 13-16 June 2023, for a total of 240 hours of ATCA time. For primary flux and bandpass calibration we used the source PKS B1934−638, while for gain calibrations we used a bright, nearby ($< 7^\circ$ away from our target) compact source[1]. Data were recorded at central frequencies of either 2.1 GHz, or simultaneously at 5.5 GHz and 9GHz, with 2 GHz of bandwidth at each central frequency. Raw data were then edited for radio frequency interference (RFI), calibrated, and imaged following standard procedures[2] in the Common Astronomy Software Applications for radio astronomy (CASA, version 5.1.2; CASA Team et al. 2022). Imaging typically used a Briggs robust parameter of 0 to balance sensitivity and angular resolution, as well as suppress sidelobes that create image noise from bright sources in the field.

Our ATCA campaign detected 14 potential radio counterparts for many UGS (table A.1). It is worth noting, that three X-ray objects in this sample, XRT J053626.88−120653.4 (the possible X-ray counterpart of the UGS 4FGL J0536.1−1205), XRT J012622.53−674626.7 (the possible X-ray counterpart of the UGS 4FGL J0126.3−6746) and XRT J170936.55−212840.3 (the possible X-ray counterpart of the UGS 4FGL J1709.4−2127), already had a radio detection and flux estimation from the radio catalogs analyzed prior to our ATCA observations. However, while XRT J053626.88−120653.4 was observed to confirm the detection (since it did not have a source detection in RACS) XRT J012622.53−674626.7 and XRT J170936.55−212840.3 exhibit an extended morphology. Therefore, they are are interesting targets.

XRT J012622.53−674626.7 pops-up in the RACS images as a point-like object at the position of the X-ray source, with an extended radio lobe, seemingly moving away from the object (see Fig. A.1). This behavior is sometimes observed in blazars at low radio frequencies (see for example MKN 421, Baghel et al. 2024). ATCA data (at 5GHz and 9GHz) confirm the presence of a jet coming from the point-like source, coinciding with the X-ray source XRT J012622.53−674626.7. In fact we can see in both 5GHz and 9GHz data a radio spot coincident with the X-ray source

---

[1] https://www.narrabri.atnf.csiro.au/calibrators/

[2] `https://casaguides.nrao.edu/index.php/ATCA_Tutorials`

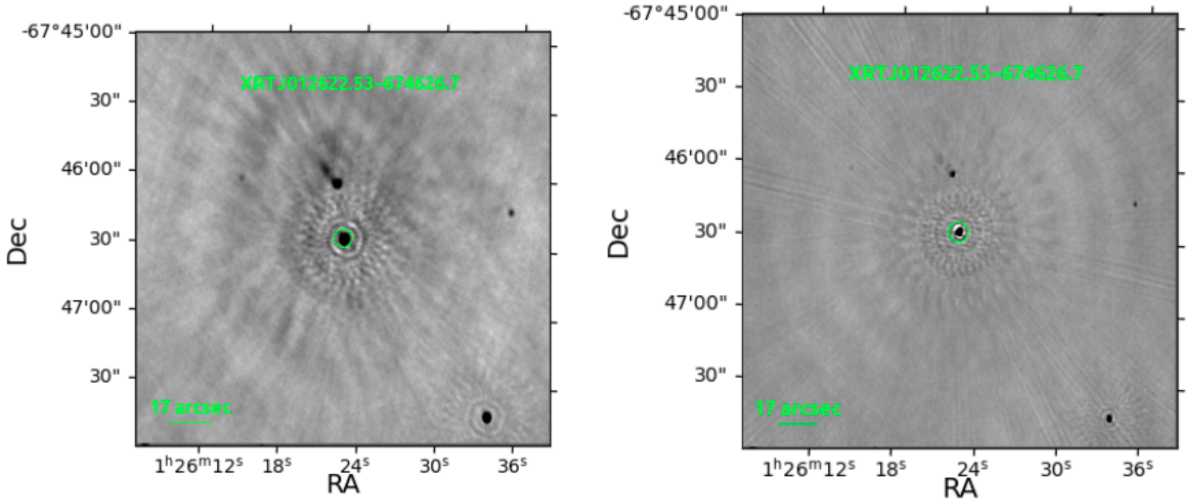

Figure A.1: Radio skymaps at 5GHz (top panel) and 9 GHz (bottom panel) for the counterpart SSS J012610.68−674742.6 of the UGS 4FGL J0126.3−6746. The green circle represent the error box of the X-ray counterpart XRT J012622.53−674626.7.

and one propagating from it. However while in the 9 GHz data the two spot are closer (~ 25.16 arcsec) one from each other and closer to the X-ray source, in the 5 GHz they are farther (~ 25.28 arcsec) according to a propagating jet (higher frequency is expected to be closer to the central SMBH, see e.g. Blandford & Königl (1979); Marscher & Gear (1985)).

For XRT J170936.55−212840.3, it is worth noting that the SNR of the detection of the possible X-ray counterpart does not exceed the threshold of 3σ set in this paper (for this source, we have SNR ~ 2.8). However, analyzing the radio images acquired from the RACS survey shows that this object exhibits a morphology typical of type 2 radio galaxy [named FR II after the two astronomers who discovered and classified them, Fanaroff and Riley (Fanaroff & Riley 1974)]. These class of sources present an extended radio structure with two distinct radio lobes symmetrically positioned relative to the AGN (which position is identified by a X-ray emission, how observed by us in the case of XRT J170936.55−212840.3), lobes that dominate the radio emission (see Fig. A.2). Since only a few FR II have been associated with Fermi gamma-ray objects (see Grandi et al. 2012; Bruni et al. 2022; Ballet et al. 2023), discovering and associating new FR II holds significant importance. Both 5GHz and 9 GHz ATCA data we acquired from this source show a two lobes morphology typical of FR II radio galaxies.

We believe that XRT J012622.53−674626.7 and XRT J170936.55−212840.3 are intriguing sources that worth further analysis to uncover their nature and assess whether they could be the correct counterparts of their respective UGSs. For this reason, our group is currently conducting optical spectroscopic campaigns, and the results will soon be published in a forthcoming paper, which is currently in preparation (Paiano et al, in prep).

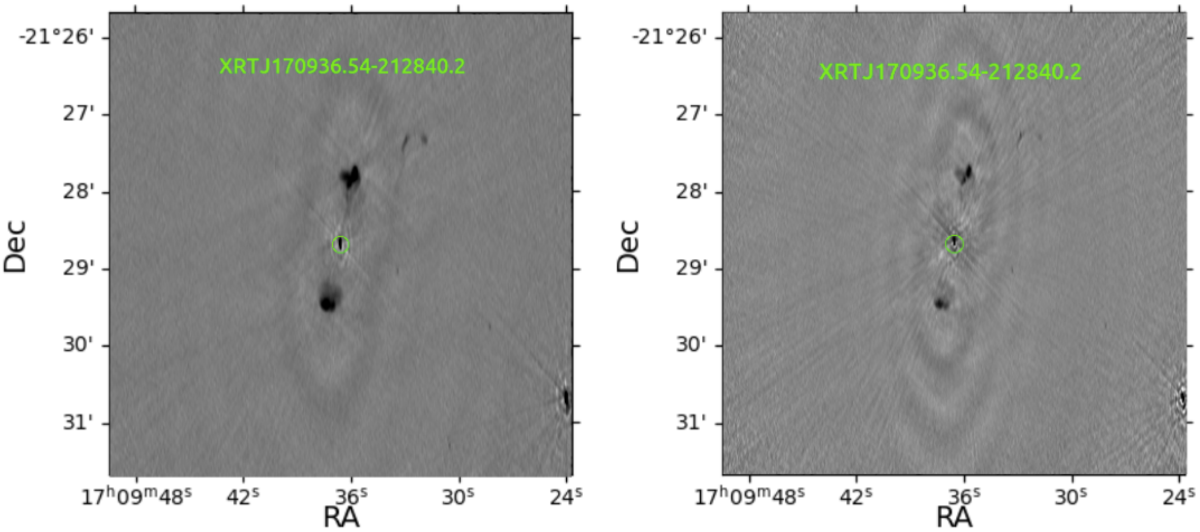

Figure A.2: Radio skymaps at 5GHz (top panel) and 9 GHz (bottom panel) for the counterpart PAN J170936.70−212838.9 of the UGS 4FGL J1709.4−2127. The green circle represent the error box of the X-ray counterpart XRT J170936.55−212840.3.

Table A.1: ATCA radio observations of 18 UGS sources.

4FGL Name (1)	*Swift*/XRT (2)	Observation (3) frequency (GHz)	Radio detection (4) significance (σ)	Flux (mJy) (5)	RA (6)	Dec (7)
4FGL J0017.1−4605	XRT J001708.63−460607.7	2.1	6.0	0.078 ± 0.013	00:17:08.65	−46:06:07.0
	XRT J001750.81−460437.5	2.1	44.1	0.618 ± 0.014	00:17:50.67	−46:04:38.6
4FGL J0054.4−1503	XRT J005431.46−145804.7	2.1	8.2	0.148 ± 0.018	00:54:31.58	−14:58:02.5
4FGL J0126.3−6746	XRT J012622.53−674626.7*	5.5	39.8	15.9 ± 0.4	01:26:22.16	−67:46:23.3
		9.0	21.0	21.0 ± 1.0		
4FGL J0536.1−1205	XRT J053626.88−120653.4	2.1	50.0	10.0 ± 0.2	05:36:26.79	−12:06:52.8
4FGL J0624.7−4903	XRT J062419.86−490640.2	2.1	4.3	0.17 ± 0.04	06:24:19.66	−49:06:36.4
4FGL J0755.9−0515	XRT J075614.46−051719.2	2.1	3.2	0.19 ± 0.06	07:56:14.44	−05:17:20.4
4FGL J0800.1−5531	XRT J075949.42−553253.8	2.1		< 0.06	-	-
4FGL J0957.7−3510	XRT J095637.78−351644.9	2.1	12.0	0.24 ± 0.02	09:56:37.83	−35:16:44.5
4FGL J1415.9−1504	XRT J141546.05−150231.4	2.1	25.7	1.54 ± 0.06	14:15:46.18	−15:02:29.7
4FGL J1517.7−4446	XRT J151727.58−444254.5	2.1	4.1	0.172 ± 0.042	15:17:27.61	−44:42:50.4
4FGL J1709.4−2127	XRT J170936.55−212840.3*	5.5	56.3	5.07 ± 0.09	17:09:36.59	−21:28:38.0
		9.0	92.7	5.56 ± 0.06		
4FGL J1813.7−6846	XRT J181307.54−684706.7	2.1		< 0.05	-	-
4FGL J1848.7−6307	XRT J184838.07−630537.8	2.1		< 0.09	-	-
4FGL J2029.5−4237	XRT J202914.15−423532.1	2.1	16.0	0.32 ± 0.02	20:29:14.18	−42:35:30.0
4FGL J2030.0−0310	XRT J203014.34−030721.9	2.1	13.3	0.40 ± 0.03	20:30:14.27	−03:07:21.8
4FGL J2241.4−8327	XRT J224201.49−832743.9	2.1	7.0	0.21 ± 0.03	22:42:01.56	−83:27:43.1
4FGL J2255.4−3253	XRT J225507.15−324816.8	2.1		< 0.06	-	-
4FGL J2326.9−4139	XRT J232653.20−412713.8	2.1		-	-	-
4FGL J2336.9−8427	XRT J233625.43−842650.6	2.1		-	-	-

Note. 1) 4FGL Name; 2) Name of the *Swift*/XRT source; 3) Observation frequency (GHz); 4) Detection significance of the radio source; 5) Radio density flux (mJy); 6-7) Coordinates of the radio source.
(*) Extended radio source.

A.2.0 X-RAY SKYMAPS

In the online material the X-ray skymaps for UGS analysed in this paper are shown. The yellow and cyan ellipses are respectively the 2σ and 3σ *Fermi* γ-ray error regions. X-ray detection, found through *Swift*/XRT analysis, are reported in green with circles, for sources within the *Fermi* error boxes, and with asterisks, for sources outside the *Fermi* error boxes.

A.3.0 TABLES

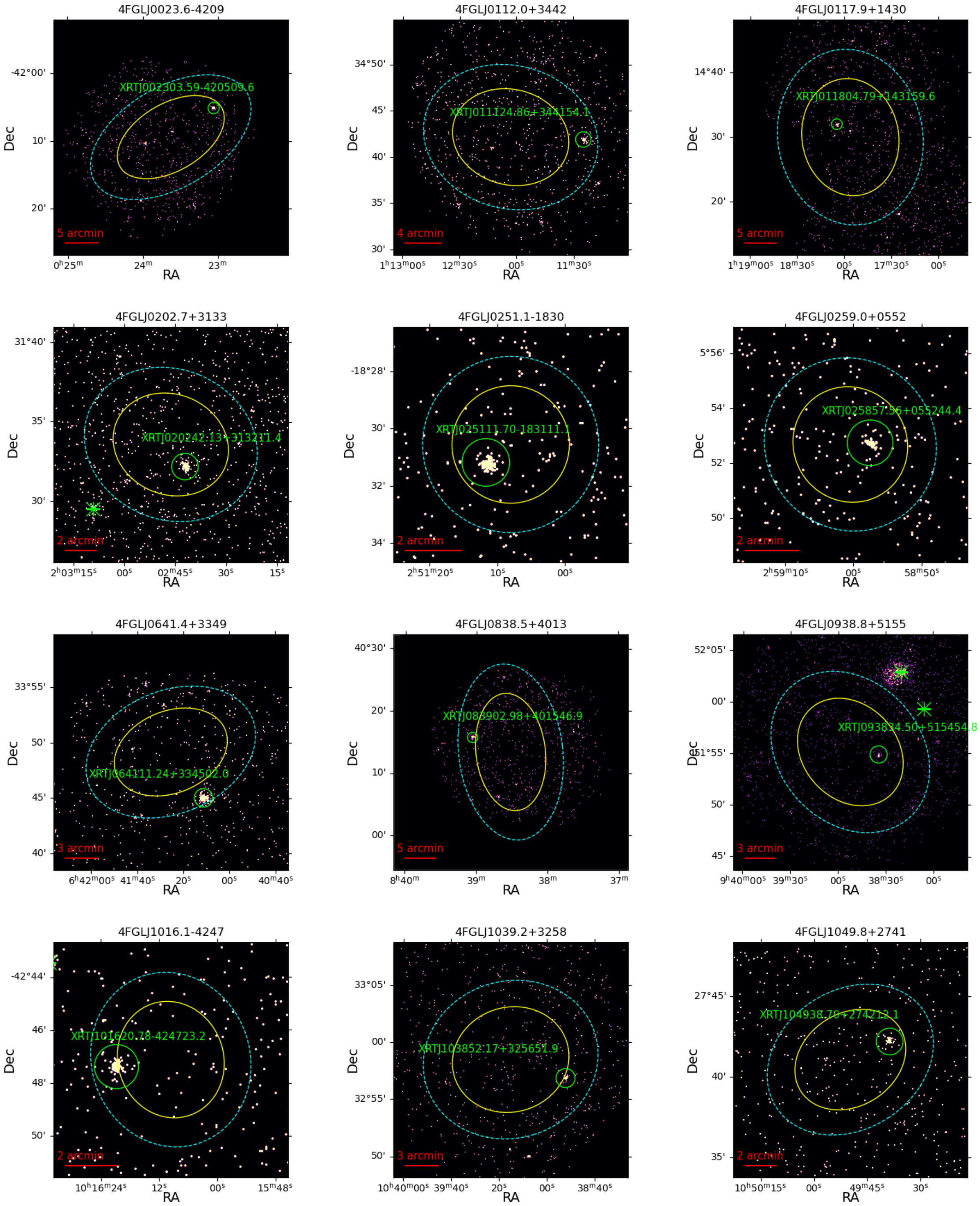

Figure A.1: X-ray skymaps for UGS1. The yellow and cyan ellipses are respectively the 2σ and 3σ *Fermi* γ-ray error regions. X-ray detection are reported in green.

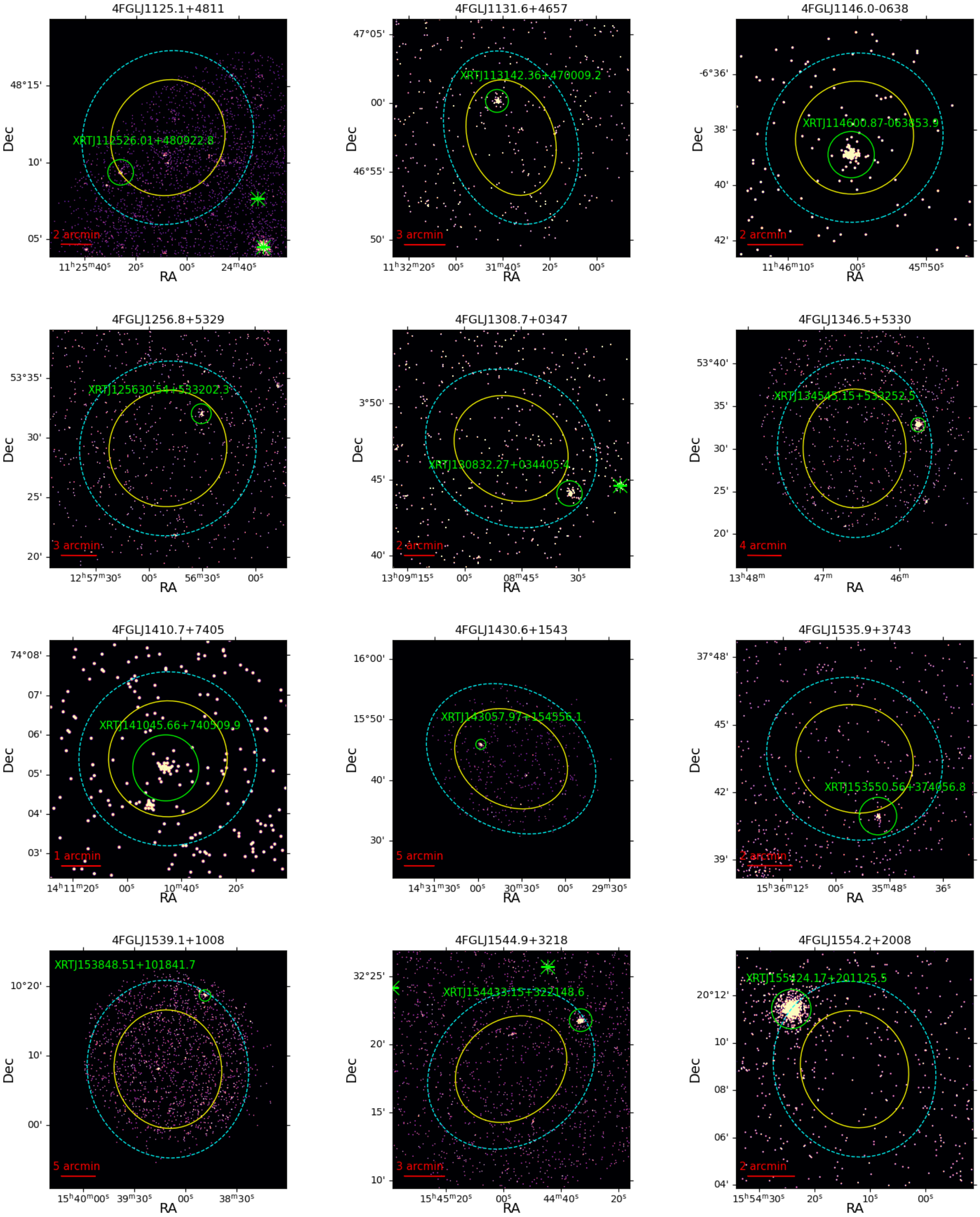

Figure A.1: Continued

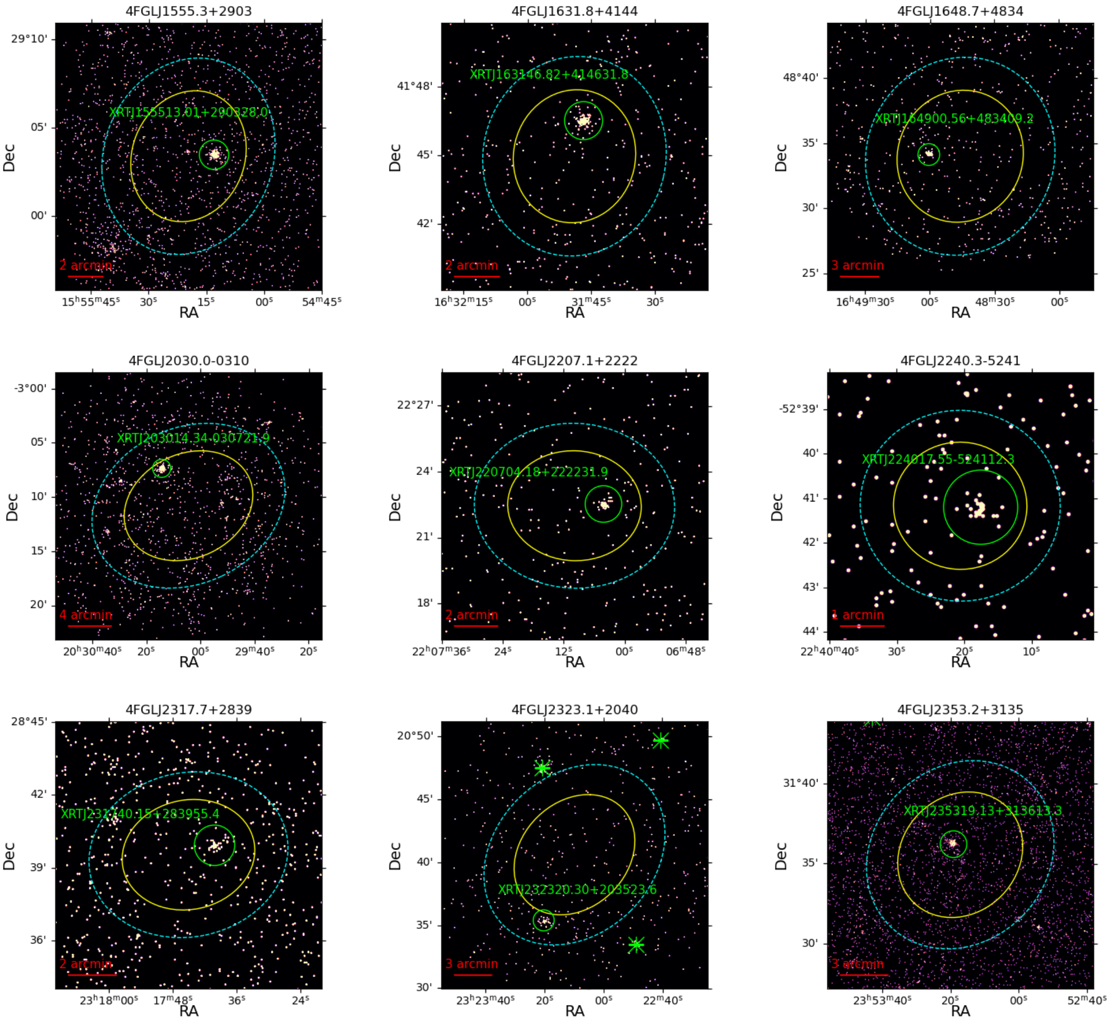

Figure A.1: Continued

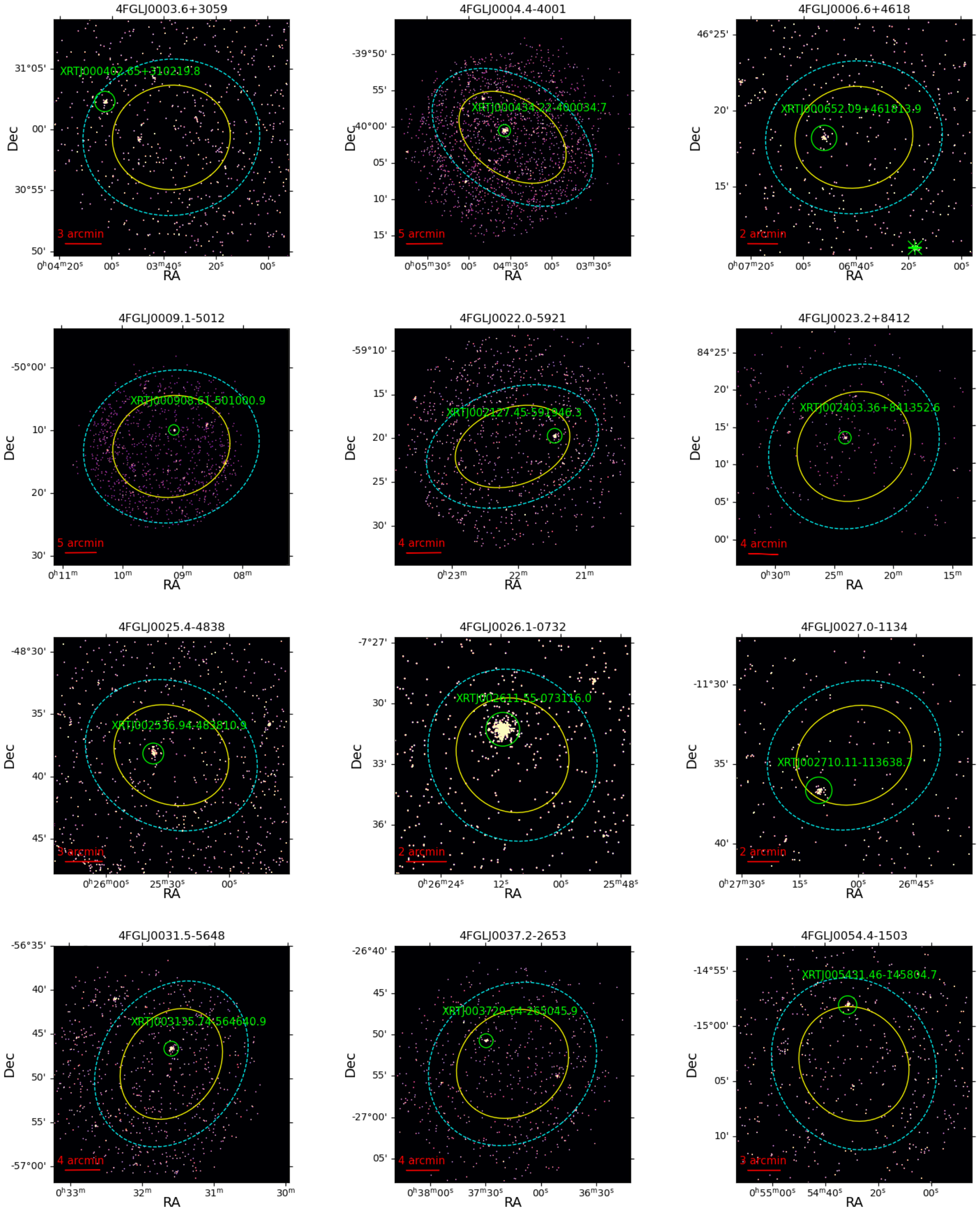

Figure A.1: Continued.

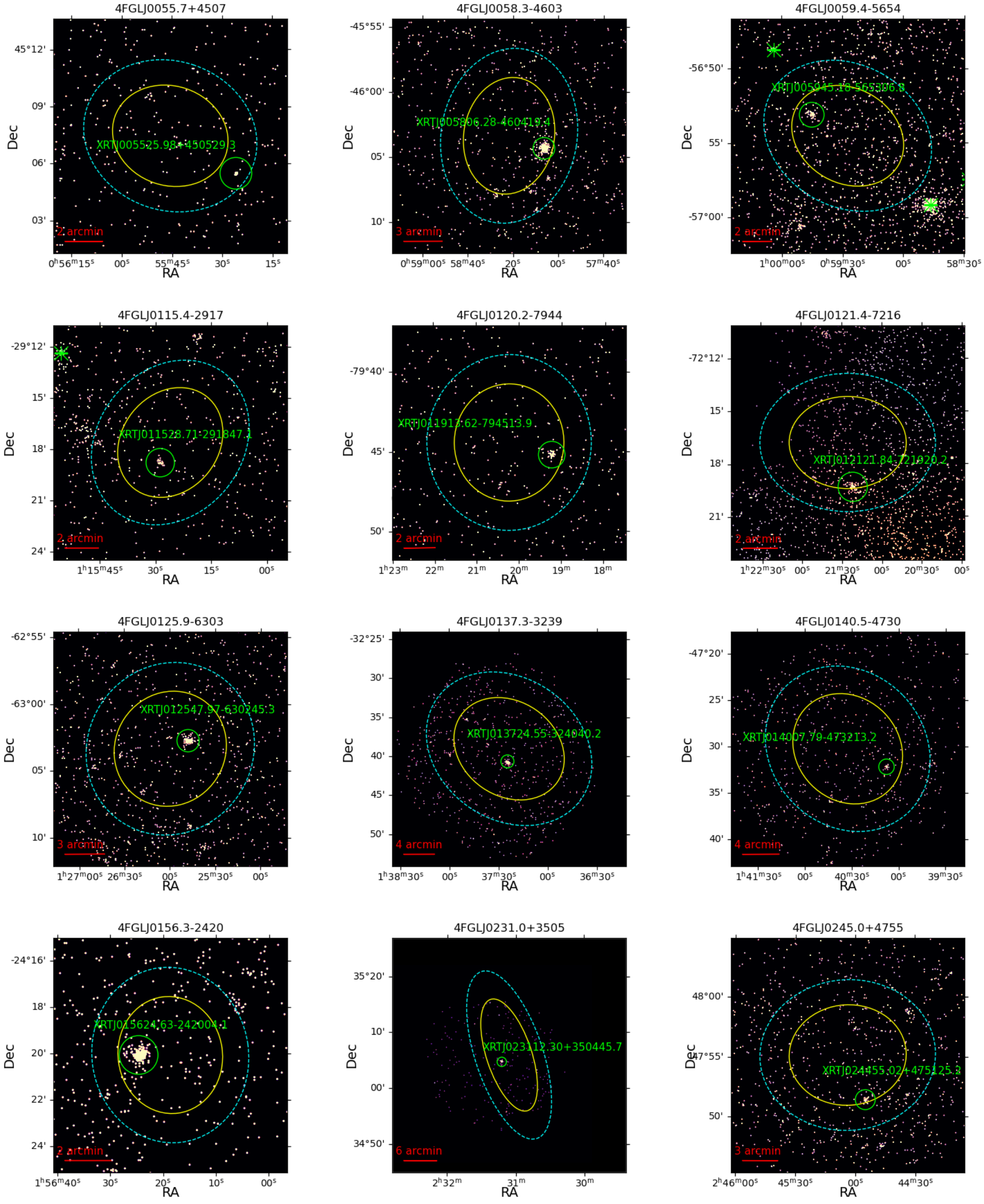

Figure A.1: Continued.

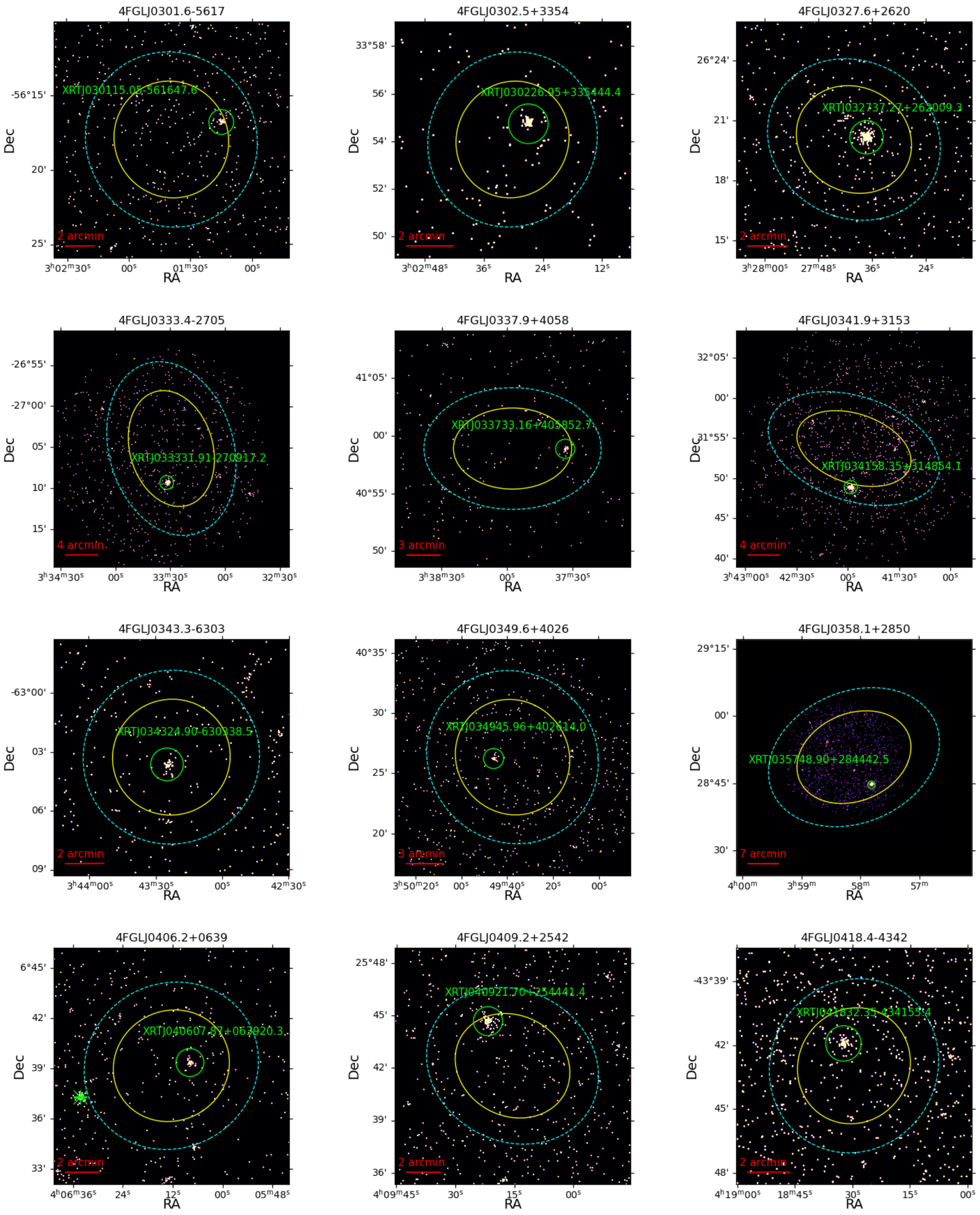

Figure A.1: Continued.

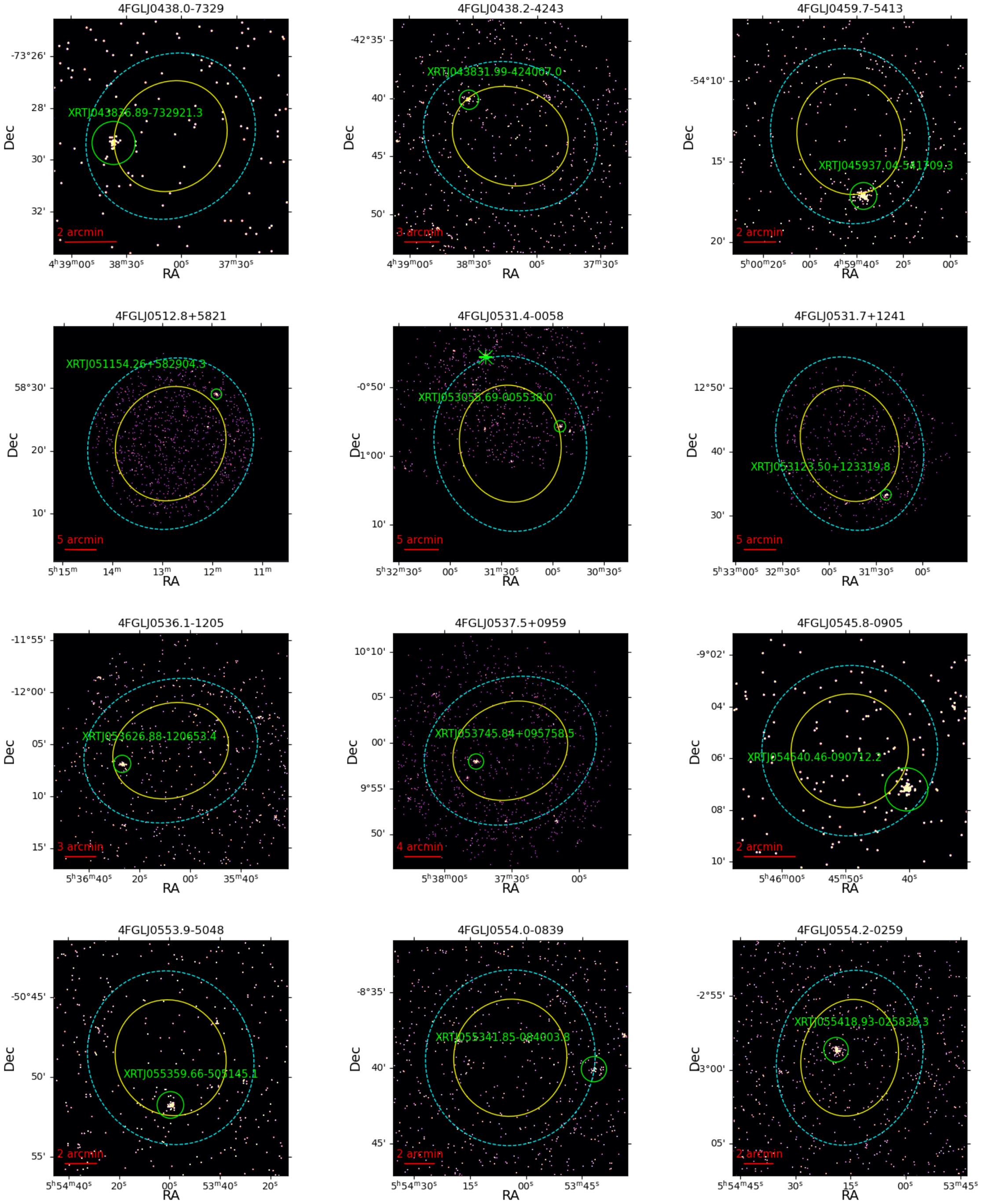

Figure A.1: Continued.

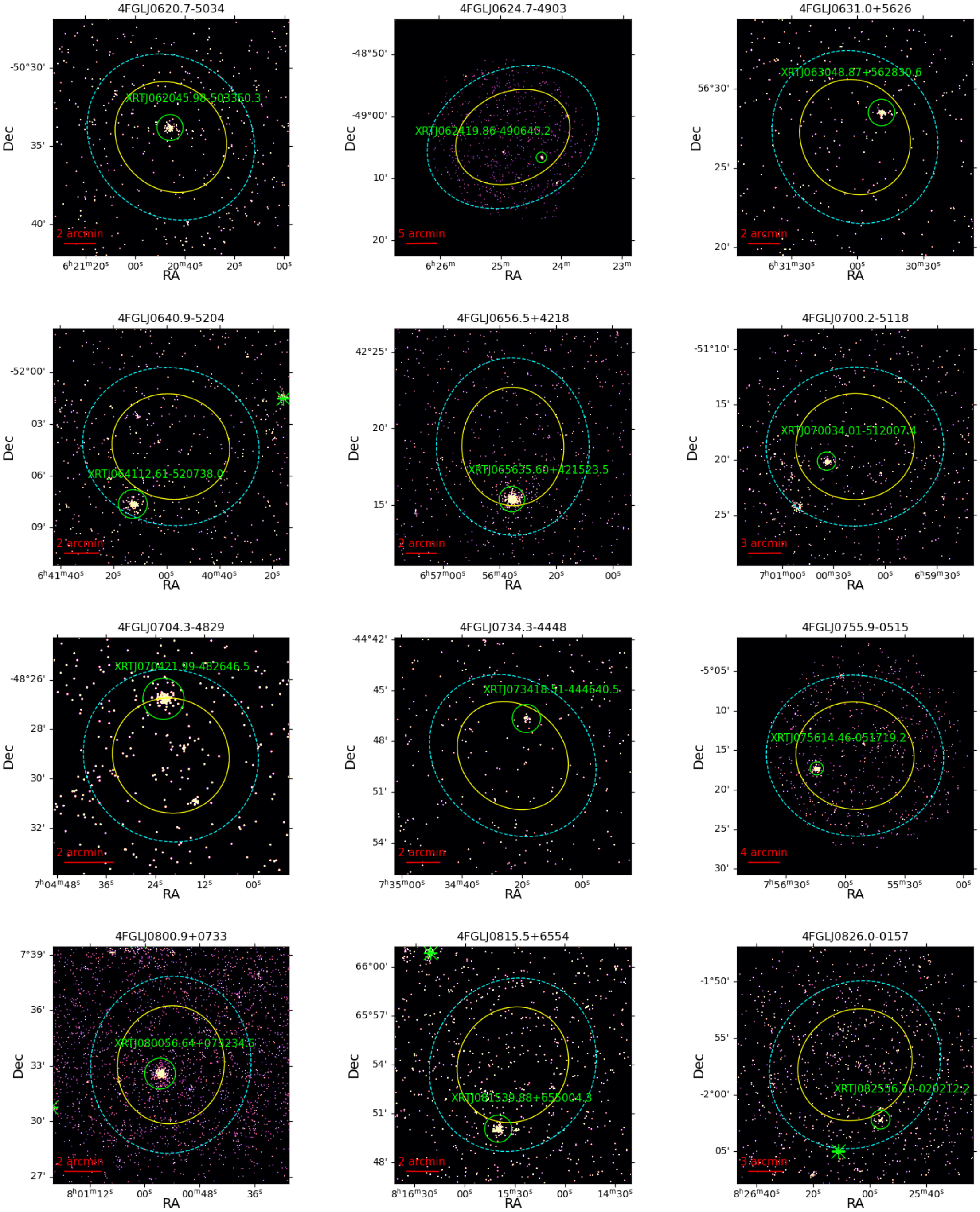

Figure A.1: Continued.

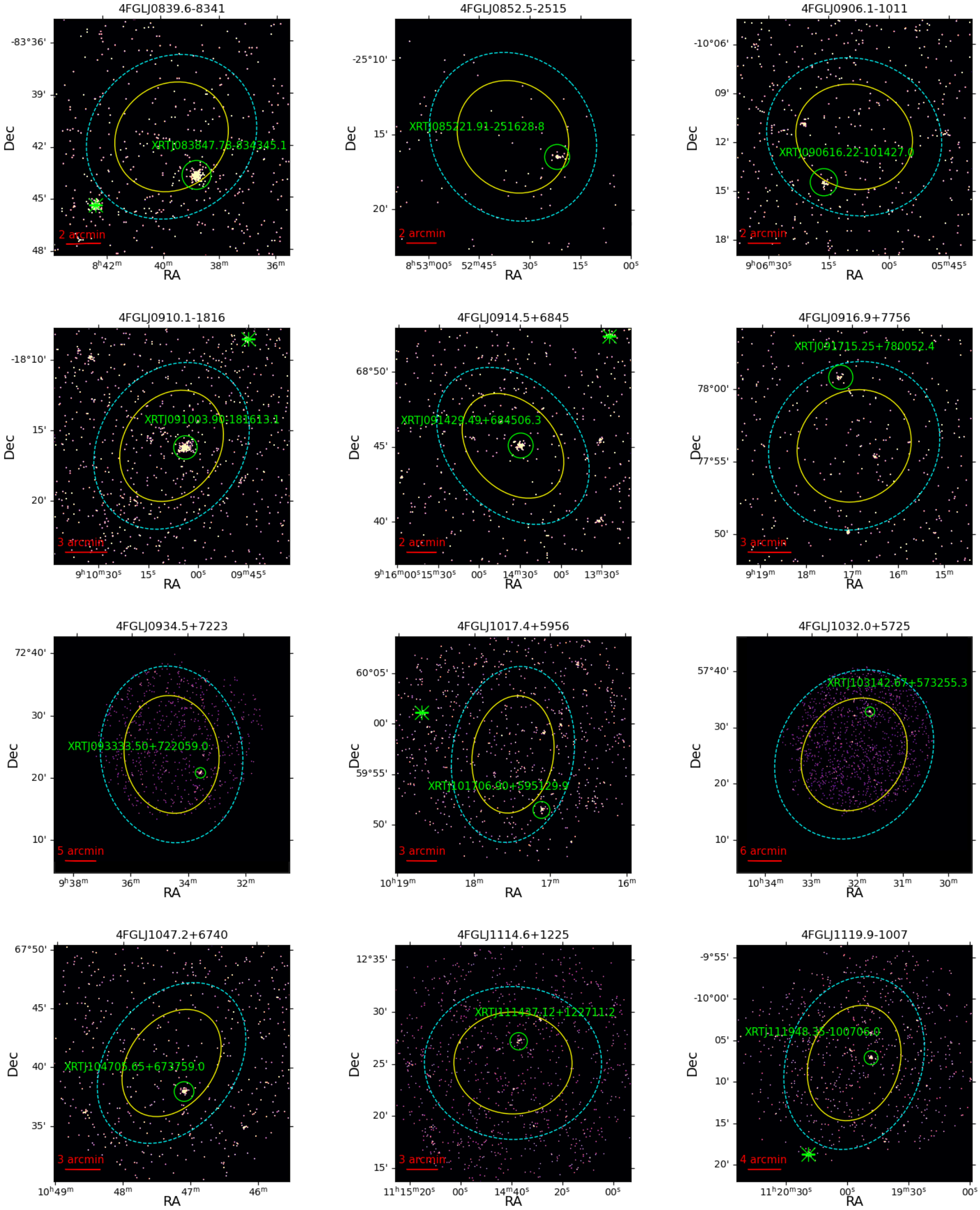

Figure A.1: Continued.

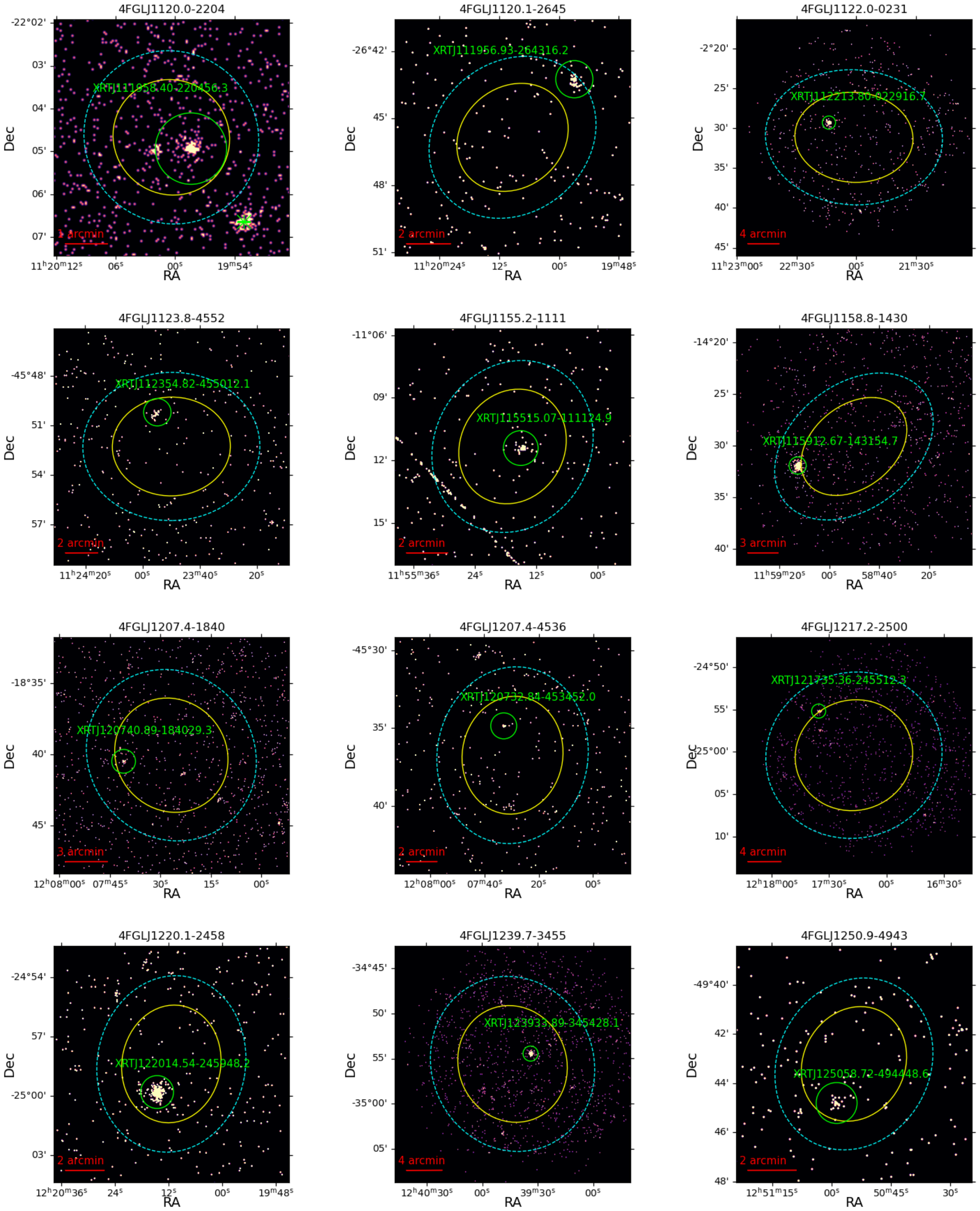

Figure A.1: Continued.

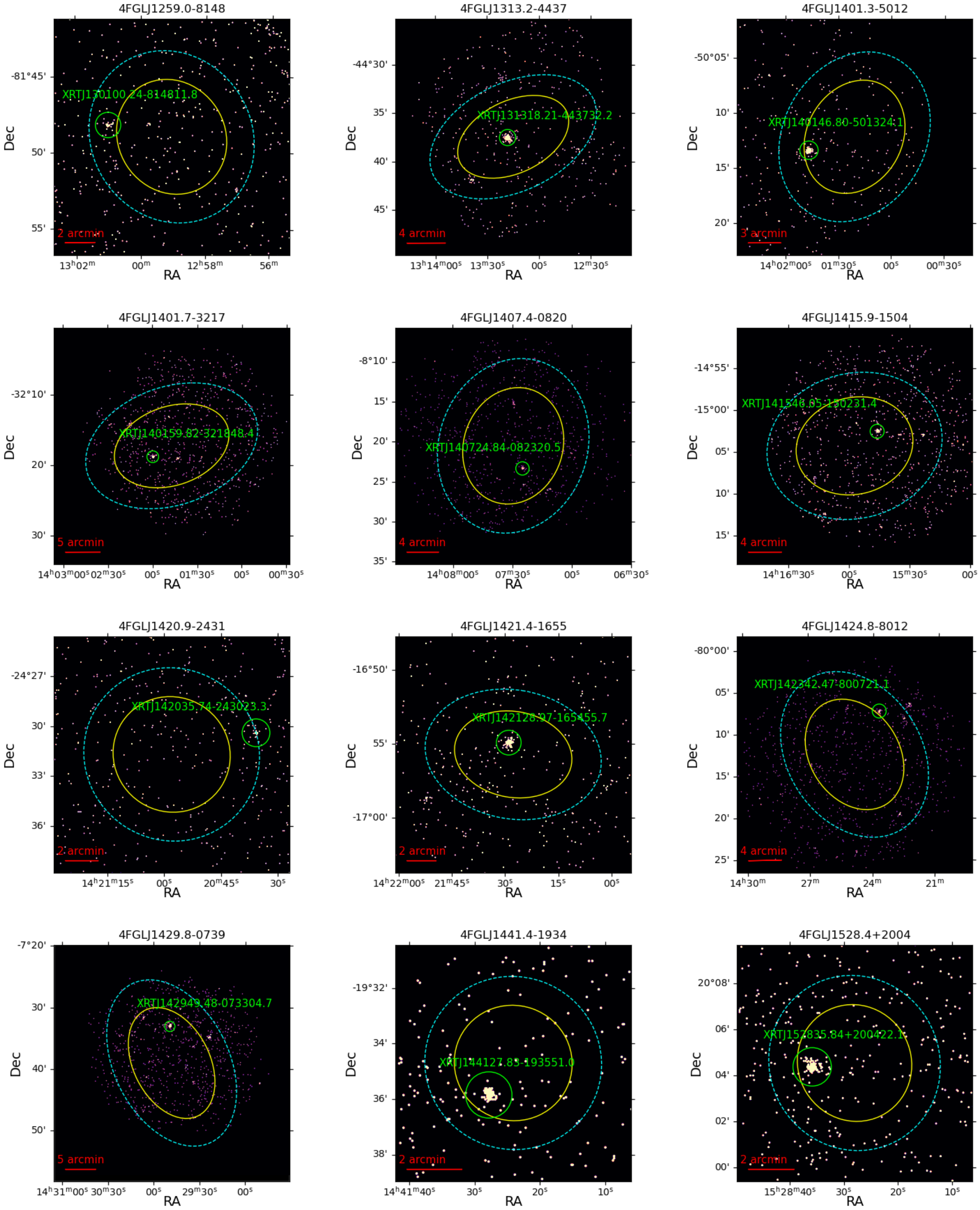

Figure A.1: Continued.

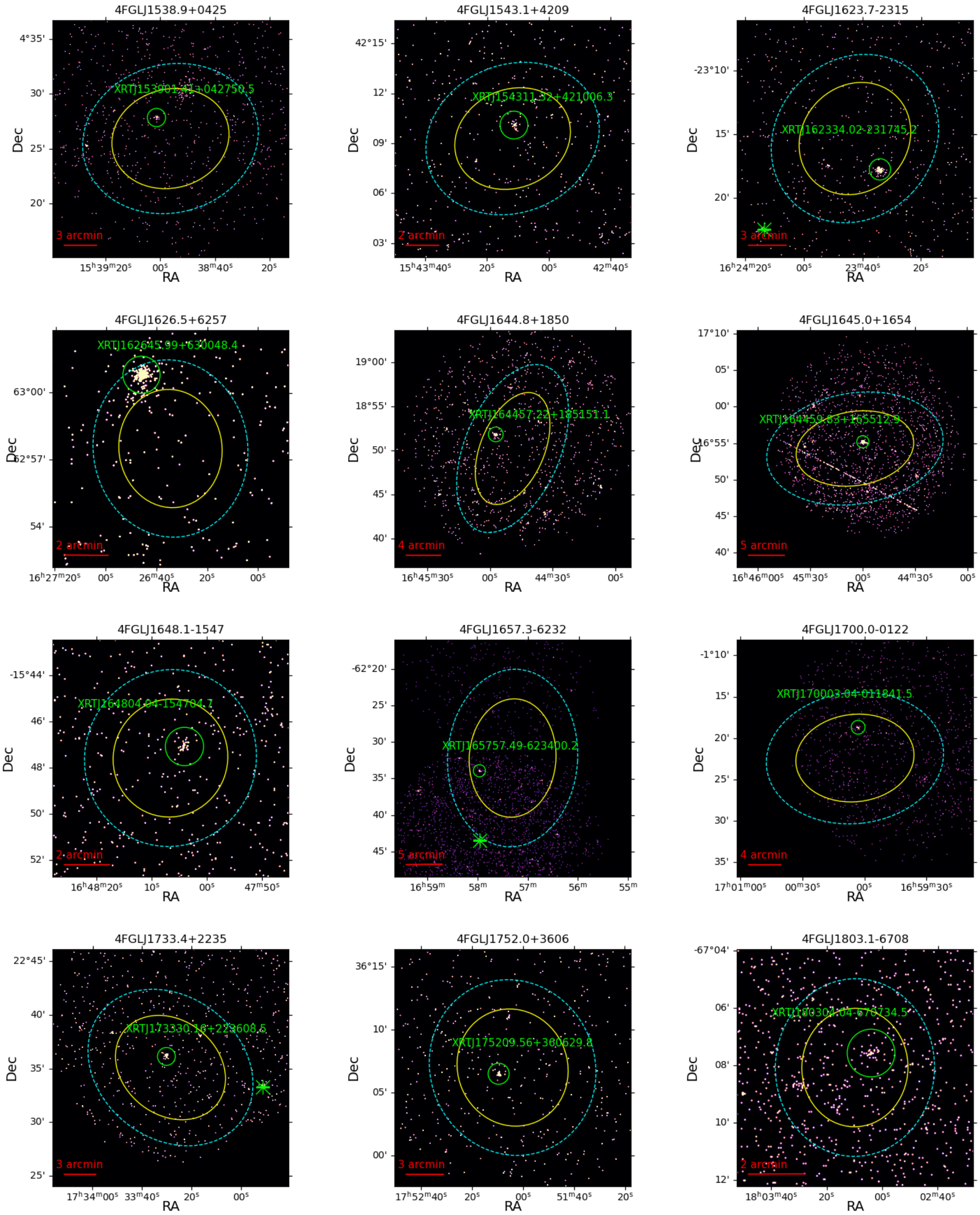

Figure A.1: Continued.

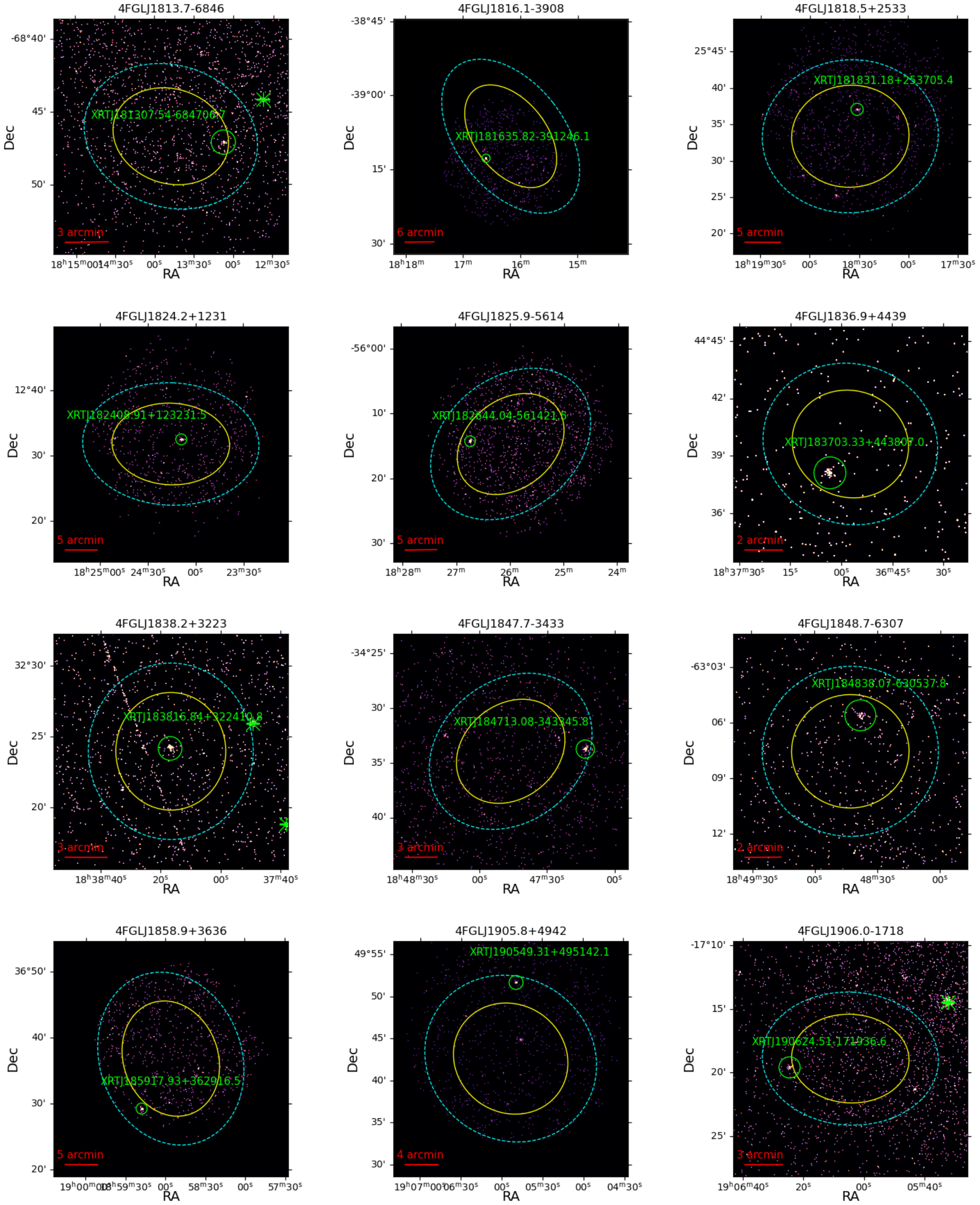

Figure A.1: Continued.

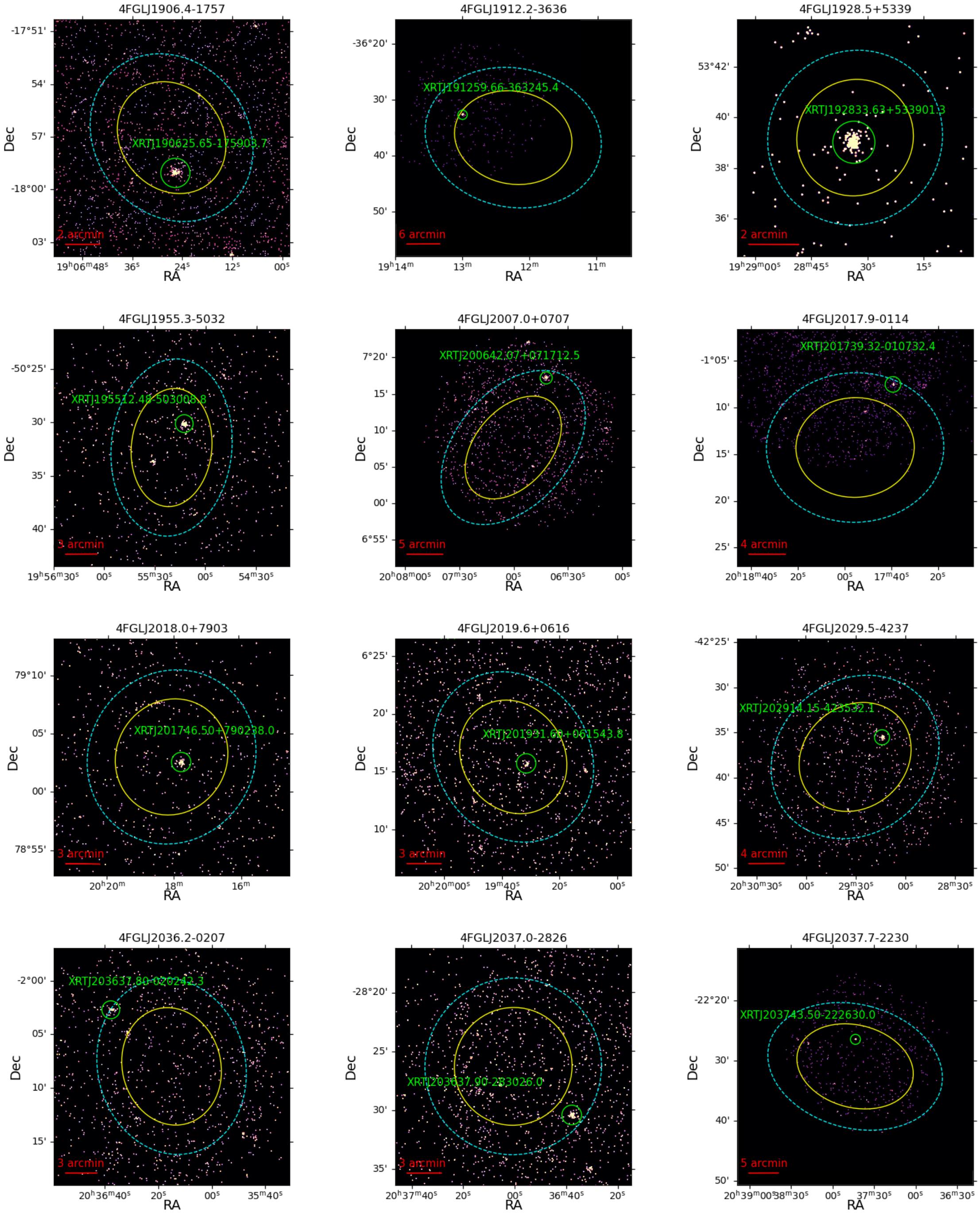

Figure A.1: Continued.

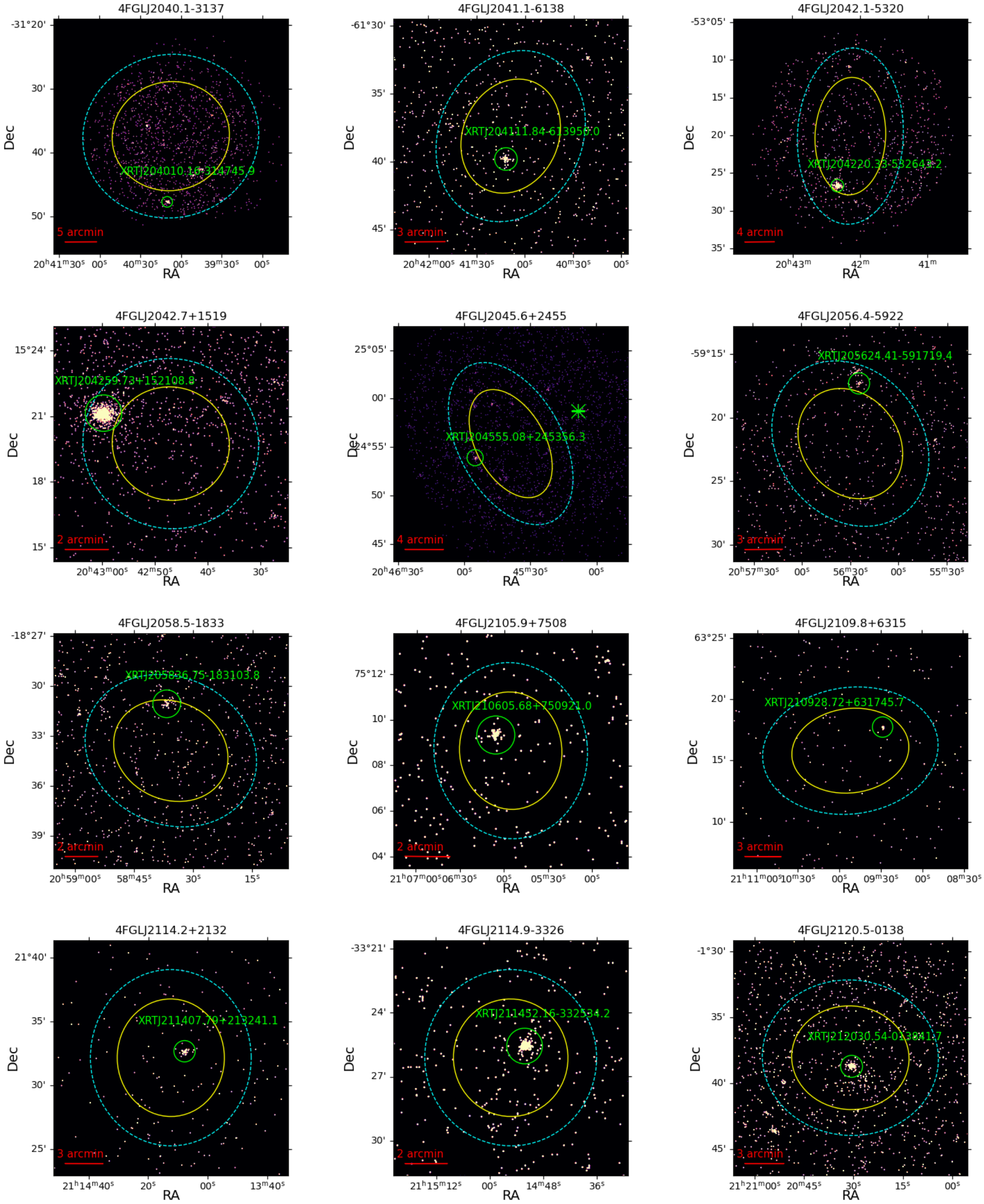

Figure A.1: Continued.

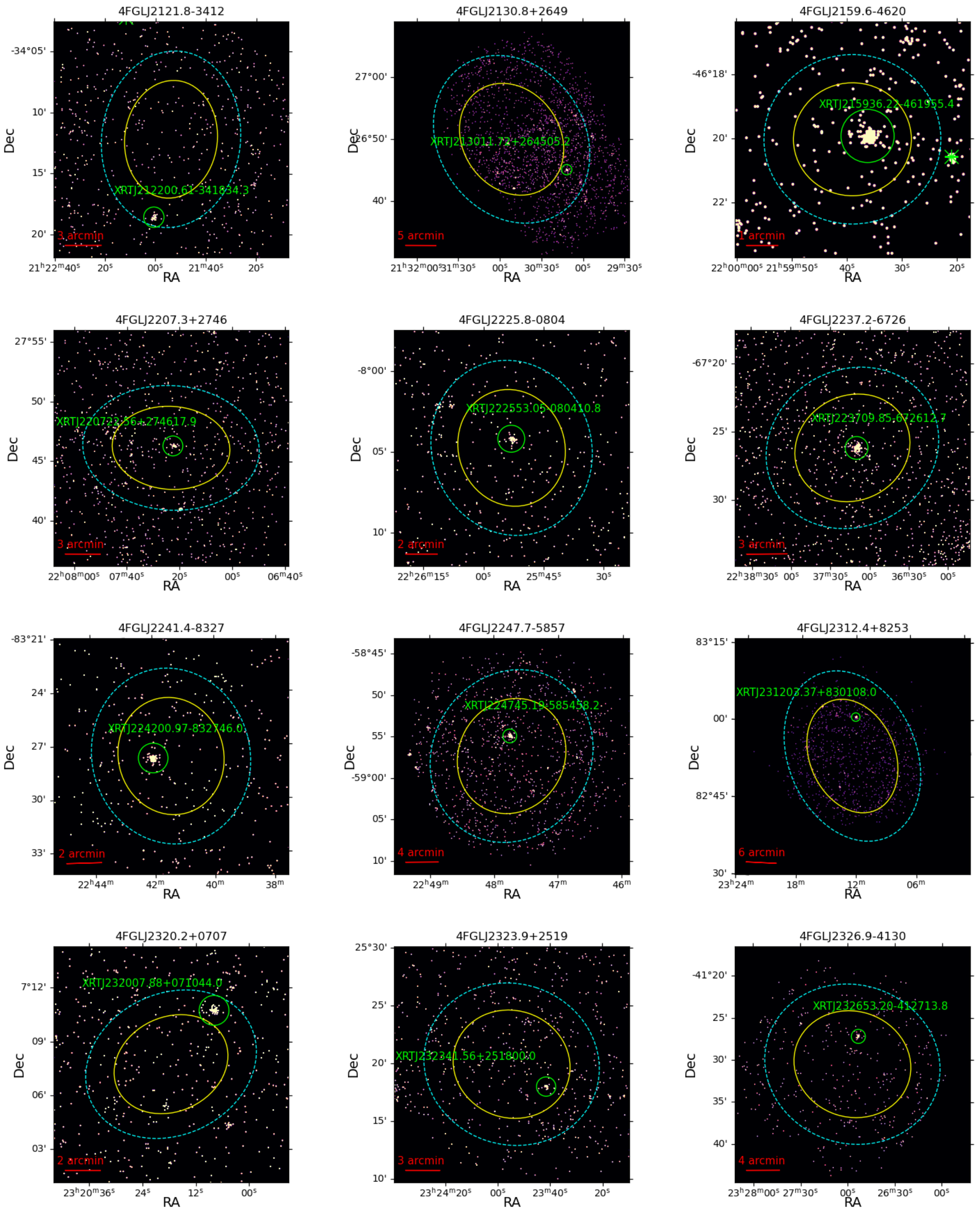

4FGLJ2121.8-3412

4FGLJ2130.8+2649

4FGLJ2159.6-4620

4FGLJ2207.3+2746

4FGLJ2225.8-0804

4FGLJ2237.2-6726

4FGLJ2241.4-8327

4FGLJ2247.7-5857

4FGLJ2312.4+8253

4FGLJ2320.2+0707

4FGLJ2323.9+2519

4FGLJ2326.9-4130

Figure A.1: Continued.

Table A.2: Summary of *Swift*/XRT detections within the 3σ *Fermi* error box of UGS1 (UGS with a single potential X-ray counterpart).

4FGL Name (1)	γ-ray detection (2) (σ)	Swift exposure (3) (ks)	*Swift*/XRT source (4)	RA (5) (J2000)	DEC (6) (J2000)	Positional error (7) (arcsec)	X-ray detection (8) (σ)
4FGLJ0003.6+3059	13.1	4.9	XRT000402.65+310219.8	1.0111	31.0388	4.6	3.7
4FGLJ0004.4-4001	11.0	9.4	XRTJ000434.22-400034.7	1.1426	-40.0096	2.9	7.7
4FGLJ0006.6+4618	6.0	4.5	XRTJ000652.09+461813.9	1.7170	46.3039	6.4	3.5
4FGLJ0009.1-5012	9.7	4.8	XRTJ000908.61-501000.9	2.2859	-50.1669	6.2	3.9
4FGLJ0022.0-5921	12.4	4.6	XRTJ002127.45-591946.3	5.3644	-59.3295	6.0	4.1
4FGLJ0023.2+8412	3.4	1.8	XRTJ002403.36+841352.6	6.0140	84.2313	8.0	3.4
4FGLJ0023.6-4209	4.4	3.4	XRTJ002303.59-420509.6	5.7650	-42.0860	2.9	5.0
4FGLJ0025.4-4838	7.4	4.4	XRTJ002536.94-483810.9	6.4039	-48.6364	3.0	5.6
4FGLJ0026.1-0732	9.7	6.6	XRTJ002611.55-073116.0	6.5481	-7.5211	2.4	22.6
4FGLJ0027.0-1134	4.4	1.9	XRTJ002710.11-113638.7	6.7921	-11.6108	3.2	5.1
4FGLJ0031.5-5648	7.6	4.3	XRTJ003135.74-564640.9	7.8989	-56.7780	3.3	5.3
4FGLJ0037.2-2653	4.1	3.3	XRTJ003729.64-265045.9	9.3735	-26.8461	3.8	4.0
4FGLJ0054.4-1503	3.9	3.0	XRTJ005431.46-145804.7	13.6311	-14.9680	3.8	3.8
4FGLJ0055.7+4507	4.5	5.3	XRTJ005525.98+450529.3	13.8582	45.0915	5.6	3.2
4FGLJ0058.3-4603	5.7	5.5	XRTJ005806.28-460419.4	14.5262	-46.0721	2.5	16.2
4FGLJ0059.4-5654	25.9	11.6	XRTJ005945.18-565306.8	14.9383	-56.8852	7.6	4.2
4FGLJ0112.0+3442	4.9	4.7	XRTJ011124.86+344154.1	17.8536	34.6984	4.7	4.0
4FGLJ0115.4-2917	7.3	7.0	XRTJ011528.71-291847.1	18.8696	-29.3131	7.3	3.1
4FGLJ0117.9+1430	7.0	6.6	XRTJ011804.79+143159.6	19.5200	14.5332	3.0	4.7
4FGLJ0120.2-7944	4.9	4.2	XRTJ011913.62-794513.9	19.8068	-79.7538	3.0	5.4
4FGLJ0121.4-7216	5.2	23.7	XRTJ012121.84-721920.2	20.3410	-72.3223	3.5	3.7
4FGLJ0125.9-6303	5.3	6.0	XRTJ012547.97-630245.3	21.4499	-63.0459	3.0	8.4
4FGLJ0137.3-3239	5.3	3.5	XRTJ013724.55-324040.2	24.3523	-32.6778	2.9	6.2
4FGLJ0140.5-4730	5.0	3.6	XRTJ014007.79-473213.2	25.0325	-47.5370	6.9	3.0
4FGLJ0156.3-2420	13.9	8.7	XRTJ015624.63-242004.1	29.1026	-24.3345	2.3	14.3
4FGLJ0202.7+3133	4.1	10.5	XRTJ020242.13+313211.4	30.6755	31.5365	2.5	10.3
4FGLJ0231.0+3505	4.2	1.0	XRTJ023112.30+350445.7	37.8013	35.0794	3.0	4.9
4FGLJ0245.0+4755	4.8	6.0	XRTJ024455.02+475125.2	41.2293	47.8570	7.2	3.3
4FGLJ0251.1-1830	10.5	7.7	XRTJ025111.70-183111.1	42.7988	-18.5198	2.7	8.9
4FGLJ0259.0+0552	28.7	4.9	XRTJ025857.56+055244.4	44.7398	5.8790	3.4	5.2
4FGLJ0301.6-5617	11.1	5.4	XRTJ030115.05-561647.6	45.3127	-56.2799	4.6	4.3
4FGLJ0302.5+3354	7.3	3.7	XRTJ030226.95+335444.4	45.6123	33.9123	3.7	5.7
4FGLJ0327.6+2620	6.3	3.2	XRTJ032737.27+262009.3	51.9053	26.3359	2.5	11.2
4FGLJ0333.4-2705	7.5	4.0	XRTJ033331.91-270917.2	53.3829	-27.1548	2.7	8.1
4FGLJ0337.9+4058	5.9	1.6	XRTJ033733.16+405852.7	54.3882	40.9813	5.2	3.3
4FGLJ0341.9+3153	7.1	6.3	XRTJ034158.35+314854.1	55.4931	31.8150	5.2	10.5
4FGLJ0343.3-6303	14.9	4.0	XRTJ034324.90-630338.5	55.8538	-63.0607	3.6	4.0
4FGLJ0349.6+4026	7.4	4.9	XRTJ034945.96+402614.0	57.4415	40.4372	5.6	3.1
4FGLJ0358.1+2850	4.9	6.9	XRTJ035748.90+284442.5	59.4537	28.7451	2.5	13.1
4FGLJ0406.2+0639	5.9	5.8	XRTJ040607.87+063920.3	61.5328	6.6556	4.5	4.5
4FGLJ0409.2+2542	7.7	6.8	XRTJ040921.70+254441.4	62.3404	25.7448	2.7	7.5
4FGLJ0418.4-4342	4.4	8.4	XRTJ041832.35-434155.4	64.6348	-43.6987	3.6	5.2
4FGLJ0438.0-7329	14.1	3.9	XRTJ043836.89-732921.3	69.6537	-73.4892	3.1	4.5
4FGLJ0438.2-4243	7.0	4.3	XRTJ043831.99-424007.0	69.6333	-42.6686	3.3	4.3
4FGLJ0459.7-5413	8.8	4.1	XRTJ045937.04-541709.3	74.9043	-54.2859	2.6	9.0
4FGLJ0512.8+5821	6.2	5.1	XRTJ051154.26+582904.3	77.9761	58.4845	3.6	4.3
4FGLJ0531.4-0058	4.4	4.3	XRTJ053055.69-005538.0	82.7321	-0.9272	4.8	3.4
4FGLJ0531.7+1241	6.5	3.6	XRTJ053123.50+123319.8	82.8479	12.5555	4.6	3.5
4FGLJ0536.1-1205	5.3	4.1	XRTJ053626.88-120653.4	84.1120	-12.1148	2.9	5.5
4FGLJ0537.5+0959	5.1	5.1	XRTJ053745.84+095758.5	84.4410	9.9662	3.0	5.2
4FGLJ0545.8-0905	10.0	4.4	XRTJ054540.46-090712.2	86.4186	-9.1201	3.1	5.6
4FGLJ0553.9-5048	11.6	3.9	XRTJ055359.66-505145.1	88.4986	-50.8625	2.9	5.8
4FGLJ0554.0-0839	4.9	7.4	XRTJ055341.85-084003.8	88.4244	-8.6677	4.8	3.3
4FGLJ0554.2-0259	5.8	7.5	XRTJ055418.93-025838.3	88.5789	-2.9773	3.3	6.0
4FGLJ0620.7-5034	6.6	5.1	XRTJ062045.98-503350.3	95.1916	-50.5640	2.8	7.1
4FGLJ0624.7-4903	6.8	3.6	XRTJ062419.86-490640.2	96.0828	-49.1112	4.2	3.5
4FGLJ0631.0+5626	6.2	4.1	XRTJ063048.87+562830.6	97.7036	56.4752	2.8	6.1
4FGLJ0640.9-5204	4.5	6.5	XRTJ064112.61-520738.0	100.3026	-52.1272	2.6	10.8
4FGLJ0641.4+3349	5.4	3.6	XRTJ064111.24+334502.0	100.2968	33.7506	3.7	13.8
4FGLJ0656.5+4218	6.2	8.4	XRTJ065635.60+421523.5	104.1483	42.2565	2.4	23.3
4FGLJ0700.2-5118	7.7	3.6	XRTJ070034.01-512007.4	105.1417	-51.3354	2.7	8.6
4FGLJ0704.3-4829	9.7	7.0	XRTJ070421.99-482646.5	106.0916	-48.4463	2.6	11.0
4FGLJ0734.3-4448	5.9	4.0	XRTJ073418.51-444640.5	113.5771	-44.7779	4.4	3.3
4FGLJ0755.9-0515	7.7	3.5	XRTJ075614.46-051719.2	119.0603	-5.2887	2.6	11.2

Note. 1) 4FGL Name; 2) γ-ray detection significance as reported in the 4FGL catalog; 3) *Swift*/XRT exposure time; 4) Name of the *Swift*/XRT source; 5-6) Coordinates of the X-ray source; 7) X-ray positional error radius; 8) Detection significance of the X-ray source.

Table A.2: Summary of *Swift*/XRT detections within the 3σ *Fermi* error box of UGS1 (UGS with a single potential X-ray counterpart). Continued.

4FGL Name (1)	γ-ray detection (2) (σ)	Swift exposure (3) (ks)	*Swift*/XRT source (4)	RA (5) (J2000)	DEC (6) (J2000)	Positional error (7) (arcsec)	X-ray detection (8) (σ)
4FGLJ0800.9+0733	9.1	35.8	XRTJ080056.64+073234.5	120.2360	7.5429	2.1	18.6
4FGLJ0815.5+6554	4.7	9.1	XRTJ081539.88+655004.3	123.9162	65.8345	4.3	10.5
4FGLJ0826.0-0157	7.2	6.7	XRTJ082556.10-020212.2	126.4838	-2.0367	4.2	4.2
4FGLJ0838.5+4013	4.0	3.9	XRTJ083902.98+401546.9	129.7624	40.2630	3.0	4.4
4FGLJ0839.6-8341	5.2	4.6	XRTJ083847.78-834345.1	129.6991	-83.7292	3.4	12.0
4FGLJ0852.5-2515	5.7	1.1	XRTJ085221.91-251628.8	133.0913	-25.2747	3.2	3.9
4FGLJ0906.1-1011	6.2	3.9	XRTJ090616.22-101427.0	136.5676	-10.2408	3.8	3.3
4FGLJ0910.1-1816	7.0	7.5	XRTJ091003.90-181613.1	137.5162	-18.2703	2.6	11.5
4FGLJ0914.5+6845	9.1	4.3	XRTJ091429.49+684506.3	138.6229	68.7518	3.2	5.3
4FGLJ0916.9+7756	6.7	3.2	XRTJ091715.25+780052.4	139.3135	78.0145	4.8	3.0
4FGLJ0934.5+7223	5.4	4.1	XRTJ093333.50+722059.0	143.3896	72.3497	5.5	3.7
4FGLJ0938.8+5155	6.4	10.6	XRTJ093834.50+515454.8	144.6438	51.9152	6.1	3.8
4FGLJ1016.1-4247	15.1	6.1	XRTJ101620.78-424723.2	154.0866	-42.7898	2.7	8.6
4FGLJ1017.4+5956	6.1	5.7	XRTJ101706.90+595129.9	154.2787	59.8583	5.6	3.3
4FGLJ1032.0+5725	4.6	5.4	XRTJ103142.67+573255.3	157.9278	57.5487	5.1	3.8
4FGLJ1039.2+3258	9.5	5.1	XRTJ103852.17+325651.9	159.7174	32.9478	3.0	4.6
4FGLJ1047.2+6740	8.9	3.8	XRTJ104705.65+673759.0	161.7735	67.6330	3.1	5.1
4FGLJ1049.8+2741	6.8	5.5	XRTJ104938.70+274212.1	162.4112	27.7034	2.9	5.8
4FGLJ1114.6+1225	4.0	5.2	XRTJ111437.12+122711.2	168.6547	12.4531	4.0	3.7
4FGLJ1119.9-1007	7.9	4.3	XRTJ111948.35-100706.0	169.9514	-10.1183	3.5	4.4
4FGLJ1120.0-2204	64.3	65.0	XRTJ111958.40-220456.3	169.9933	-22.0823	3.5	8.6
4FGLJ1120.1-2645	13.3	3.9	XRTJ111956.93-264316.2	169.9872	-26.7212	4.4	4.4
4FGLJ1122.0-0231	9.4	3.2	XRTJ112213.80-022916.7	170.5575	-2.4880	2.7	7.1
4FGLJ1123.8-4552	10.7	3.7	XRTJ112354.82-455012.2	170.9784	-45.8367	3.4	4.0
4FGLJ1125.1+4811	4.0	50.5	XRTJ112526.01+480922.8	171.3584	48.1563	5.4	4.3
4FGLJ1131.6+4657	8.5	4.6	XRTJ113142.36+470009.2	172.9265	47.0026	2.6	6.0
4FGLJ1146.0-0638	15.0	3.3	XRTJ114600.87-063853.9	176.5036	-6.6483	3.1	6.7
4FGLJ1155.2-1111	6.5	4.3	XRTJ115515.07-111124.9	178.8128	-11.1903	3.3	4.8
4FGLJ1158.8-1430	8.0	5.2	XRTJ115912.67-143154.7	179.8028	-14.5319	2.4	18.1
4FGLJ1207.4-1840	5.0	9.5	XRTJ120740.89-184029.3	181.9204	-18.6748	4.6	3.2
4FGLJ1207.4-4536	15.1	3.7	XRTJ120732.84-453452.0	181.8868	-45.5811	4.2	3.4
4FGLJ1217.2-2500	7.4	5.1	XRTJ121735.36-245512.3	184.3973	-24.9201	5.4	3.4
4FGLJ1220.1-2458	8.6	4.3	XRTJ122014.54-245948.2	185.0606	-24.9967	2.5	14.3
4FGLJ1239.7-3455	5.1	5.7	XRTJ123933.89-345428.1	189.8912	-34.9078	2.8	7.7
4FGLJ1250.9-4943	17.2	4.5	XRTJ125058.72-494448.6	192.7447	-49.7468	5.4	3.7
4FGLJ1256.8+5329	5.3	5.6	XRTJ125630.54+533202.3	194.1273	53.5340	6.4	4.2
4FGLJ1259.0-8148	15.0	3.6	XRTJ130100.24-814811.8	195.2510	-81.8033	6.0	3.2
4FGLJ1308.7+0347	10.9	3.6	XRTJ130832.27+034405.4	197.1344	3.7348	4.0	5.5
4FGLJ1313.2-4437	4.9	2.1	XRTJ131318.21-443732.2	198.3259	-44.6256	2.1	11.5
4FGLJ1346.5+5330	11.9	3.9	XRTJ134545.15+533252.5	206.4381	53.5479	2.2	13.5
4FGLJ1401.3-5012	5.7	1.7	XRTJ140146.80-501324.1	210.4450	-50.2234	2.8	9.4
4FGLJ1401.7-3217	8.2	3.4	XRTJ140159.82-321848.4	210.4992	-32.3135	4.7	3.1
4FGLJ1407.4-0820	4.4	3.6	XRTJ140724.84-082320.5	211.8535	-8.3890	4.0	3.1
4FGLJ1410.7+7405	23.3	11.7	XRTJ141045.66+740509.9	212.6903	74.0861	7.2	4.5
4FGLJ1415.9-1504	6.8	3.5	XRTJ141546.05-150231.4	213.9419	-15.0420	3.0	4.6
4FGLJ1420.9-2431	12.5	3.6	XRTJ142035.74-243023.3	215.1489	-24.5065	4.2	3.8
4FGLJ1421.4-1655	5.9	2.1	XRTJ142128.97-165455.7	215.3707	-16.9155	2.3	8.3
4FGLJ1424.8-8012	7.1	3.4	XRTJ142342.47-800721.1	215.9270	-80.1225	3.9	3.7
4FGLJ1429.8-0739	8.8	3.9	XRTJ142949.48-073304.7	217.4562	-7.5513	2.8	7.1
4FGLJ1430.6+1543	4.1	1.6	XRTJ143057.97+154556.1	217.7415	15.7656	3.5	4.3
4FGLJ1441.4-1934	11.5	4.7	XRTJ144127.83-193551.0	220.3659	-19.5975	2.7	7.4
4FGLJ1528.4+2004	5.8	6.2	XRTJ152835.84+200422.1	232.1493	20.0728	3.9	8.8
4FGLJ1535.9+3743	18.5	10.7	XRTJ153550.56+374056.8	233.9606	37.6825	4.6	4.1
4FGLJ1538.9+0425	6.2	3.6	XRTJ153901.41+042750.5	234.7559	4.4640	4.3	3.1
4FGLJ1539.1+1008	6.7	6.2	XRTJ153848.51+101841.7	234.7021	10.3116	3.2	5.0
4FGLJ1543.1+4209	6.8	5.0	XRTJ154311.32+421006.3	235.7971	42.1684	4.8	3.4
4FGLJ1544.9+3218	7.2	13.9	XRTJ154433.15+322148.6	236.1381	32.3635	2.6	10.1
4FGLJ1554.2+2008	11.9	8.2	XRTJ155424.17+201125.5	238.6007	20.1904	2.0	34.5
4FGLJ1555.3+2903	6.1	15.6	XRTJ155513.01+290328.0	238.8042	29.0578	3.5	10.9
4FGLJ1623.7-2315	5.6	3.8	XRTJ162334.02-231745.2	245.8917	-23.2959	5.4	7.6
4FGLJ1626.5+6257	7.2	4.6	XRTJ162645.99+630048.4	246.6916	63.0134	2.5	12.9
4FGLJ1631.8+4144	8.2	3.7	XRTJ163146.82+414631.8	247.9451	41.7755	2.6	8.9
4FGLJ1644.8+1850	8.9	4.8	XRTJ164457.22+185151.1	251.2384	18.8642	4.4	4.5
4FGLJ1645.0+1654	6.0	5.7	XRTJ164459.83+165512.9	251.2493	16.9202	2.7	7.6

Note. Labels are the same as in Table A.2.

Table A.2: Summary of *Swift*/XRT detections within the 3σ *Fermi* error box of UGS1 (UGS with a single potential X-ray counterpart). Continued.

4FGL Name (1)	γ-ray detection (2) (σ)	Swift exposure (3) (ks)	*Swift*/XRT source (4)	RA (5) (J2000)	DEC (6) (J2000)	Positional error (7) (arcsec)	X-ray detection (8) (σ)
4FGLJ1648.1-1547	9.8	10.0	XRTJ164804.04-154704.7	252.0169	-15.7846	5.2	4.1
4FGLJ1648.7+4834	7.0	4.2	XRTJ164900.56+483409.2	252.2523	48.5692	2.8	5.7
4FGLJ1657.3-6232	5.4	8.8	XRTJ165757.49-623400.2	254.4896	-62.5667	5.9	4.2
4FGLJ1700.0-0122	5.2	3.2	XRTJ170003.04-011841.5	255.0127	-1.3115	4.8	3.1
4FGLJ1733.4+2235	7.7	4.4	XRTJ173330.16+223608.5	263.3757	22.6024	3.4	3.8
4FGLJ1752.0+3606	11.4	3.4	XRTJ175209.56+360629.8	268.0399	36.1083	3.3	4.0
4FGLJ1803.1-6708	22.9	13.6	XRTJ180304.04-670734.5	270.7668	-67.1262	6.0	3.3
4FGLJ1813.7-6846	12.3	13.6	XRTJ181307.54-684706.7	273.2814	-68.7852	6.0	3.8
4FGLJ1816.1-3908	5.5	1.8	XRTJ181635.82-391246.1	274.1492	-39.2128	3.3	4.3
4FGLJ1818.5+2533	6.3	7.2	XRTJ181831.18+253705.4	274.6299	25.6182	5.8	3.6
4FGLJ1824.2+1231	5.5	3.6	XRTJ182408.91+123231.5	276.0371	12.5421	3.6	4.0
4FGLJ1825.9-5614	6.6	4.1	XRTJ182644.04-561421.5	276.6835	-56.2393	3.7	4.6
4FGLJ1836.9+4439	4.9	4.3	XRTJ183703.33+443807.0	279.2639	44.6353	3.5	4.1
4FGLJ1838.2+3223	9.5	7.5	XRTJ183816.84+322410.8	279.5702	32.4030	3.2	4.9
4FGLJ1847.7-3433	6.8	3.7	XRTJ184713.08-343345.8	281.8045	-34.5627	3.0	5.7
4FGLJ1848.7-6307	4.9	4.1	XRTJ184838.07-630537.8	282.1586	-63.0938	4.3	3.8
4FGLJ1858.9+3636	9.6	3.2	XRTJ185917.93+362916.5	284.8247	36.4879	3.5	3.7
4FGLJ1905.8+4942	12.0	5.4	XRTJ190549.31+495142.1	286.4554	49.8617	6.7	3.8
4FGLJ1906.0-1718	8.2	13.8	XRTJ190624.51-171936.6	286.6021	-17.3268	4.0	3.7
4FGLJ1906.4-1757	10.6	12.6	XRTJ190625.65-175903.7	286.6069	-17.9844	5.4	8.0
4FGLJ1912.2-3636	4.4	0.9	XRTJ191259.66-363245.4	288.2486	-36.5459	4.5	4.0
4FGLJ1928.5+5339	5.0	2.0	XRTJ192833.63+533901.3	292.1401	53.6504	2.3	10.6
4FGLJ1955.3-5032	8.0	3.6	XRTJ195512.48-503008.8	298.8020	-50.5024	2.7	7.6
4FGLJ2007.0+0707	5.4	4.9	XRTJ200642.07+071712.5	301.6753	7.2868	4.1	3.5
4FGLJ2017.9-0114	6.3	12.2	XRTJ201739.32-010732.4	304.4138	-1.1257	4.4	3.5
4FGLJ2018.0+7903	7.0	4.2	XRTJ201746.50+790238.0	304.4438	79.0439	3.8	5.1
4FGLJ2019.6+0616	5.0	7.5	XRTJ201931.60+061543.8	304.8816	6.2622	4.7	3.3
4FGLJ2029.5-4237	12.3	3.6	XRTJ202914.15-423532.1	307.3089	-42.5922	3.2	4.5
4FGLJ2030.0-0310	4.6	4.5	XRTJ203014.34-030721.9	307.5597	-3.1228	2.8	7.7
4FGLJ2036.2-0207	7.3	5.2	XRTJ203637.80-020242.3	309.1575	-2.0451	4.9	3.5
4FGLJ2037.0-2826	15.9	9.5	XRTJ203637.90-283026.0	309.1579	-28.5072	2.8	6.7
4FGLJ2037.7-2230	4.6	1.7	XRTJ203743.50-222630.0	309.4312	-22.4417	4.3	3.2
4FGLJ2040.1-3137	4.0	6.4	XRTJ204010.16-314745.9	310.0423	-31.7961	3.3	5.0
4FGLJ2041.1-6138	11.6	4.9	XRTJ204111.84-613950.0	310.2993	-61.6639	3.0	5.4
4FGLJ2042.1-5320	5.5	3.8	XRTJ204220.33-532643.2	310.5847	-53.4453	2.5	12.3
4FGLJ2042.7+1519	10.7	30.4	XRTJ204259.73+152108.8	310.7489	15.3524	1.9	27.2
4FGLJ2045.6+2455	3.9	7.9	XRTJ204555.08+245356.3	311.4795	24.8990	3.6	4.5
4FGLJ2056.4-5922	12.2	5.3	XRTJ205624.41-591719.4	314.1017	-59.2887	8.0	3.0
4FGLJ2058.5-1833	4.7	8.7	XRTJ205836.75-183103.8	314.6531	-18.5177	6.2	4.3
4FGLJ2105.9+7508	11.1	7.9	XRTJ210605.68+750921.0	316.5237	75.1558	3.6	5.4
4FGLJ2109.8+6315	4.6	1.9	XRTJ210928.72+631745.7	317.3696	63.2960	4.6	4.4
4FGLJ2114.2+2132	4.9	1.1	XRTJ211407.79+213241.1	318.5325	21.5448	3.1	4.9
4FGLJ2114.9-3326	10.1	4.5	XRTJ211452.16-332534.2	318.7173	-33.4262	2.5	12.1
4FGLJ2120.5-0138	7.1	7.5	XRTJ212030.54-013841.7	320.1273	-1.6449	2.7	9.0
4FGLJ2121.8-3412	4.4	4.3	XRTJ212200.61-341834.3	320.5026	-34.3095	4.6	4.3
4FGLJ2130.8+2649	4.4	13.4	XRTJ213011.72+264505.2	322.5488	26.7514	5.7	4.3
4FGLJ2159.6-4620	13.6	8.6	XRTJ215936.22-461955.4	329.9009	-46.3321	2.7	8.4
4FGLJ2207.1+2222	9.8	4.8	XRTJ220704.18+222231.9	331.7674	22.3755	3.3	5.0
4FGLJ2207.3+2746	5.4	4.8	XRTJ220722.56+274617.9	331.8440	27.7716	3.9	3.4
4FGLJ2225.8-0804	8.9	4.6	XRTJ222553.05-080410.8	336.4711	-8.0697	3.9	4.4
4FGLJ2237.2-6726	8.5	5.4	XRTJ223709.85-672612.7	339.2910	-67.4369	2.8	7.6
4FGLJ2240.3-5241	11.5	5.8	XRTJ224017.55-524112.3	340.0731	-52.6868	3.6	3.4
4FGLJ2241.4-8327	12.8	3.9	XRTJ224200.97-832746.0	340.5040	-83.4628	6.0	6.8
4FGLJ2247.7-5857	7.7	5.2	XRTJ224745.19-585458.2	341.9383	-58.9162	2.9	6.9
4FGLJ2312.4+8253	4.3	4.5	XRTJ231203.37+830108.0	348.0140	83.0189	6.0	4.8
4FGLJ2317.7+2839	10.5	14.1	XRTJ231740.15+283955.4	349.4173	28.6654	5.8	4.3
4FGLJ2320.2+0707	7.3	6.8	XRTJ232007.88+071044.0	350.0328	7.1789	3.6	6.1
4FGLJ2323.1+2040	6.7	3.3	XRTJ232320.30+203523.6	350.8346	20.5899	4.2	3.5
4FGLJ2323.9+2519	7.4	3.9	XRTJ232341.56+251800.0	350.9232	25.3000	6.0	3.1
4FGLJ2326.9-4130	7.0	2.4	XRTJ232653.20-412713.8	351.7217	-41.4538	3.9	3.4
4FGLJ2331.6+4430	7.0	6.0	XRTJ233129.51+443104.3	352.8730	44.5179	5.4	4.7
4FGLJ2336.9-8427	6.6	4.1	XRTJ233625.43-842650.6	354.1060	-84.4474	4.7	6.0
4FGLJ2337.7-2903	7.4	5.9	XRTJ233730.35-290237.9	354.3764	-29.0438	2.6	9.7
4FGLJ2347.9-5106	23.0	8.5	XRTJ234804.68-510745.2	357.0195	-51.1292	6.7	3.4
4FGLJ2353.2+3135	8.6	28.0	XRTJ235319.12+313613.4	358.3297	31.6037	4.0	8.2

Note. Labels are the same as in Table A.2.

Table A.3: Summary of *Swift*/XRT detections within the 3σ *Fermi* error box of UGS2 (UGS with more than one potential X-ray counterparts).

4FGL Name (1)	γ-ray detection (2) (σ)	Swift exposure (3) (ks)	*Swift*/XRT source (4)	RA (5) (J2000)	DEC (6) (J2000)	Positional error (7) (arcsec)	X-ray detection (8) (σ)
4FGLJ0017.1-4605	7.2	9.8	XRTJ001708.63-460607.7	4.2859	-46.1021	2.9	6.5
			XRTJ001750.81-460437.5	4.4617	-46.0771	4.2	4.7
			XRTJ001705.00-460109.2	4.2709	-46.0192	7.7	3.0
4FGLJ0031.0-2327	10.3	10.7	XRTJ003120.53-233400.7	7.8355	-23.5669	2.5	19.5
			XRTJ003039.79-232821.2	7.6658	-23.4725	6.6	3.6
4FGLJ0040.2-2725	6.6	33.3	XRTJ004016.42-271912.3	10.0684	-27.3201	2.0	25.2
			XRTJ004023.77-272254.2	10.0991	-27.3817	7.0	5.6
			XRTJ004026.07-272116.1	10.1086	-27.3545	7.0	5.6
			XRTJ004035.80-272240.7	10.1492	-27.3780	7.6	4.4
			XRTJ003954.35-272516.1	9.9764	-27.4211	6.0	3.9
4FGLJ0045.8-1324	5.9	5.7	XRTJ004602.94-132422.2	11.5123	-13.4062	7.0	7.7
			XRTJ004608.32-132213.6	11.5347	-13.3704	3.5	5.2
			XRTJ004611.48-132519.3	11.5479	-13.4220	3.5	4.4
			XRTJ004539.41-132507.7	11.4142	-13.4188	4.3	4.0
			XRTJ004602.97-131959.0	11.5124	-13.3331	6.0	3.2
			XRTJ004555.20-132312.5	11.4800	-13.3868	3.5	3.2
4FGLJ0102.3+1000	12.4	12.2	XRTJ010226.89+095939.9	15.6121	9.9944	4.4	4.6
			XRTJ010235.93+095832.4	15.6497	9.9757	6.0	3.7
			XRTJ010220.73+095848.9	15.5864	9.9803	6.0	3.4
			XRTJ010214.03+100258.4	15.5585	10.0496	3.6	3.3
4FGLJ0118.3-6008	13.6	8.9	XRTJ011823.22-600747.8	19.5967	-60.1300	4.3	4.9
			XRTJ011848.17-600256.2	19.7007	-60.0489	5.5	3.3
4FGLJ0122.4+1034	5.8	21.7	XRTJ012223.64+103212.6	20.5985	10.5368	2.4	24.0
			XRTJ012222.25+103116.2	20.5927	10.5212	4.7	6.2
4FGLJ0126.3-6746	6.0	6.1	XRTJ012610.88-674744.5	21.5453	-67.7957	3.0	6.6
			XRTJ012622.53-674626.7	21.5939	-67.7741	4.3	3.9
4FGLJ0132.9-4259	7.5	119.8	XRTJ013346.96-430407.0	23.4457	-43.0686	2.6	19.4
			XRTJ013401.65-425630.0	23.5069	-42.9417	3.5	12.6
			XRTJ013339.96-425503.4	23.4165	-42.9176	3.5	8.5
			XRTJ013347.80-430229.3	23.4491	-43.0415	3.5	7.9
			XRTJ013316.63-425908.7	23.3193	-42.9858	3.5	7.6
			XRTJ013308.39-425744.6	23.2849	-42.9624	3.5	6.9
			XRTJ013359.11-430219.2	23.4963	-43.0387	3.5	5.6
			XRTJ013347.00-430610.6	23.4459	-43.1029	3.5	5.6
			XRTJ013339.30-425824.0	23.4138	-42.9733	6.0	3.0
4FGLJ0140.4+5114	4.9	8.4	XRTJ014107.78+510659.4	25.2824	51.1165	2.6	8.7
			XRTJ014022.50+511313.3	25.0937	51.2204	4.6	6.9
4FGLJ0159.0+3313	9.0	3.4	XRTJ015906.95+331227.3	29.7790	33.2076	2.5	14.1
			XRTJ015905.35+331257.8	29.7723	33.2161	3.0	5.1
			XRTJ015927.92+331107.7	29.8663	33.1855	5.2	3.3
4FGLJ0159.8-2234	5.8	11.8	XRTJ015947.54-223254.4	29.9481	-22.5484	5.1	6.0
			XRTJ020016.59-222940.5	30.0691	-22.4946	4.4	4.4
			XRTJ015957.01-223136.3	29.9876	-22.5267	4.7	3.7
4FGLJ0209.8+2626	6.5	7.6	XRTJ020946.75+262530.4	32.4448	26.4251	2.4	18.5
			XRTJ020950.60+263253.3	32.4609	26.5481	3.5	5.4
4FGLJ0240.2-0248	6.1	12.6	XRTJ024002.02-024321.6	40.0084	-2.7227	2.6	11.7
			XRTJ024004.57-024504.3	40.0191	-2.7512	3.0	11.0
			XRTJ024024.23-025336.4	40.1010	-2.8934	5.8	4.5
4FGLJ0251.4+4646	3.9	15.8	XRTJ025027.22+464729.1	42.6134	46.7914	2.0	26.1
			XRTJ025117.49+464501.7	42.8229	46.7505	5.8	4.4
4FGLJ0252.0-3657	4.7	3.4	XRTJ025139.26-365715.2	42.9136	-36.9542	3.0	9.6
			XRTJ025149.15-370144.5	42.9548	-37.0290	6.2	6.4
			XRTJ025145.81-365713.8	42.9409	-36.9538	3.5	6.2
			XRTJ025207.48-365438.4	43.0312	-36.9107	3.5	4.9
4FGLJ0447.2+2446	9.3	6.3	XRTJ044739.31+244227.7	71.9138	24.7077	6.7	3.8
			XRTJ044709.75+243701.5	71.7906	24.6171	6.0	3.2
4FGLJ0535.3+0934	5.6	4.2	XRTJ053512.72+093645.2	83.8030	9.6126	5.2	5.8
			XRTJ053447.47+094026.3	83.6978	9.6740	5.6	5.0
			XRTJ053508.19+094254.2	83.7841	9.7151	5.7	4.4
4FGLJ0539.2-6333	6.9	6.8	XRTJ053842.39-632820.0	84.6766	-63.4722	2.5	10.8
			XRTJ054002.73-633214.6	85.0114	-63.5374	7.9	3.4
4FGLJ0544.8+5209	4.2	6.5	XRTJ054424.68+521515.7	86.1029	52.2544	5.1	4.2
			XRTJ054457.19+520852.8	86.2383	52.1480	6.0	3.4

Note. Labels are the same as in table A.2.

Table A.3: Summary of *Swift*/XRT detections within the 3σ *Fermi* error box of UGS2 (UGS with more than one potential X-ray counterparts). Continued

4FGL Name (1)	γ-ray detection (2) (σ)	Swift exposure (3) (ks)	*Swift*/XRT source (4)	RA (5) (J2000)	DEC (6) (J2000)	Positional error (7) (arcsec)	X-ray detection (8) (σ)
4FGLJ0546.5-1100	6.4	73.0	XRTJ054730.24-112151.5	86.8760	-11.3643	3.5	6.5
			XRTJ054631.01-112023.3	86.6292	-11.3398	3.6	5.4
			XRTJ054719.62-110938.9	86.8318	-11.1608	6.0	4.9
			XRTJ054706.34-112139.1	86.7764	-11.3608	6.0	4.5
			XRTJ054649.72-111754.3	86.7071	-11.2984	3.5	4.0
			XRTJ054628.95-112059.0	86.6206	-11.3497	3.6	3.6
			XRTJ054632.75-110505.3	86.6365	-11.0848	4.9	3.2
			XRTJ054736.04-111141.3	86.9002	-11.1948	3.5	3.0
4FGLJ0610.8-4911	5.5	7.6	XRTJ061100.18-491036.2	92.7507	-49.1767	2.5	17.2
			XRTJ061031.81-491222.5	92.6325	-49.2062	4.7	4.5
4FGLJ0611.5-2918	5.8	4.2	XRTJ061141.70-291618.0	92.9237	-29.2717	3.5	3.9
			XRTJ061216.02-291702.3	93.0667	-29.2840	4.0	3.1
4FGLJ0617.6-4028	6.3	7.2	XRTJ061646.98-402143.4	94.1958	-40.3621	2.4	4.0
			XRTJ061724.11-402212.8	94.3505	-40.3702	3.5	3.6
			XRTJ061818.54-403400.9	94.5773	-40.5669	3.9	3.1
4FGLJ0633.9+5840	5.2	9.1	XRTJ063359.74+584034.2	98.4989	58.6762	6.1	3.3
			XRTJ063342.26+584642.7	98.4261	58.7785	7.0	3.1
4FGLJ0639.1-8009	5.1	53.6	XRTJ064059.59-801126.2	100.2483	-80.1906	2.6	17.5
			XRTJ063617.46-801350.5	99.0727	-80.2307	3.5	10.1
			XRTJ064125.96-801048.5	100.3582	-80.1801	3.5	5.4
			XRTJ063719.22-801230.2	99.3301	-80.2084	6.0	4.4
			XRTJ064012.99-801725.0	100.0541	-80.2903	6.0	4.1
			XRTJ063555.23-800813.0	98.9801	-80.1369	4.2	3.9
			XRTJ064047.38-802414.7	100.1974	-80.4041	3.9	3.7
			XRTJ063641.31-801124.9	99.1721	-80.1903	4.1	3.3
			XRTJ064049.32-801255.8	100.2055	-80.2155	6.0	3.0
4FGLJ0723.9+5702	3.5	6.2	XRTJ072351.47+565734.6	110.9644	56.9596	3.2	6.8
			XRTJ072328.63+565908.8	110.8693	56.9858	6.7	3.5
4FGLJ0737.4+6535	6.9	70.4	XRTJ073655.73+653540.7	114.2322	65.5946	2.4	20.7
			XRTJ073711.73+653344.9	114.2989	65.5625	7.0	7.3
4FGLJ0738.6+1311	7.2	5.6	XRTJ073843.59+131328.3	114.6816	13.2245	3.2	4.8
			XRTJ073848.93+130755.1	114.7039	13.1320	5.8	3.3
4FGLJ0751.2-0029	4.2	84.8	XRTJ075119.14-002748.8	117.8298	-0.4636	3.5	8.2
			XRTJ075104.16-003305.6	117.7673	-0.5515	3.5	4.9
4FGLJ0800.1-5531	3.0	8.0	XRTJ075949.42-553253.8	119.9559	-55.5483	5.6	4.2
			XRTJ080013.52-553407.9	120.0563	-55.5689	4.0	4.0
4FGLJ0849.5+2710	4.4	8.4	XRTJ084957.80+271614.1	132.4908	27.2706	3.9	3.6
			XRTJ084936.07+270127.6	132.4003	27.0243	6.9	3.4
4FGLJ0903.5+4057	5.8	20.0	XRTJ090314.64+405600.2	135.8110	40.9334	2.1	19.2
			XRTJ090342.94+405501.1	135.9289	40.9170	3.9	6.0
4FGLJ0949.8+7551	9.9	7.4	XRTJ095017.79+754457.7	147.5741	75.7494	4.5	5.6
			XRTJ095133.13+754839.3	147.8881	75.8109	5.3	3.4
4FGLJ0952.9+1351	4.4	9.2	XRTJ095245.54+134723.5	148.1898	13.7899	3.8	8.9
			XRTJ095250.40+135218.5	148.2100	13.8718	3.5	6.6
4FGLJ0958.6-0522	7.0	3.4	XRTJ095833.81-052139.9	149.6409	-5.3611	2.7	8.7
			XRTJ095813.64-052441.3	149.5568	-5.4115	3.8	3.8
4FGLJ1008.2-1000	5.0	8.6	XRTJ100848.62-095450.2	152.2026	-9.9139	1.9	50.3
			XRTJ100802.55-095919.3	152.0106	-9.9887	3.2	6.2
			XRTJ100749.49-094911.9	151.9562	-9.8200	3.9	4.1
4FGLJ1018.1-2705	6.3	8.7	XRTJ101750.36-270552.8	154.4598	-27.0980	2.5	15.2
			XRTJ101801.35-271234.0	154.5056	-27.2095	6.0	3.0
4FGLJ1018.1-4051	4.8	7.6	XRTJ101807.55-404407.6	154.5314	-40.7355	3.7	4.5
			XRTJ101801.63-405519.5	154.5068	-40.9221	3.2	4.3
			XRTJ101725.04-404436.3	154.3543	-40.7434	4.2	3.8
			XRTJ101717.29-404759.7	154.3220	-40.7999	4.3	3.7
			XRTJ101820.43-404813.8	154.5851	-40.8038	6.0	3.1
4FGLJ1036.5-1809	6.7	10.9	XRTJ103610.62-181315.4	159.0443	-18.2209	4.4	3.9
			XRTJ103625.96-180011.3	159.1082	-18.0031	4.5	3.8
4FGLJ1106.7+3623	17.1	6.0	XRTJ110622.38+363319.7	166.5933	36.5555	3.2	4.8
			XRTJ110710.07+361655.1	166.7920	36.2820	3.7	3.9
			XRTJ110635.95+362648.9	166.6498	36.4469	5.7	3.8
			XRTJ110612.40+363126.6	166.5516	36.5241	3.8	3.2

Note. Labels are the same as in table A.2.

Table A.3: Summary of *Swift*/XRT detections within the 3σ *Fermi* error box of UGS2 (UGS with more than one potential X-ray counterparts). Continued

4FGL Name (1)	γ-ray detection (2) (σ)	Swift exposure (3) (ks)	*Swift*/XRT source (4)	RA (5) (J2000)	DEC (6) (J2000)	Positional error (7) (arcsec)	X-ray detection (8) (σ)
4FGLJ1111.4+0137	5.0	4.4	XRTJ111114.26+013427.6	167.8094	1.5743	2.5	12.6
			XRTJ111206.06+013526.7	168.0252	1.5907	3.2	4.7
			XRTJ111159.79+013642.6	167.9991	1.6118	3.9	4.1
			XRTJ111106.07+014559.8	167.7753	1.7666	3.3	3.9
4FGLJ1126.0-5007	9.4	30.0	XRTJ112624.22-500806.5	171.6009	-50.1351	2.0	22.9
			XRTJ112628.32-500842.8	171.6180	-50.1452	5.3	5.7
			XRTJ112533.68-500549.2	171.3903	-50.0970	5.0	4.7
			XRTJ112605.11-501020.5	171.5213	-50.1724	3.5	4.1
4FGLJ1151.2-2929	4.5	3.3	XRTJ115118.17-292744.4	177.8257	-29.4623	4.5	6.8
			XRTJ115110.12-292917.2	177.7922	-29.4881	4.8	3.1
4FGLJ1224.6+7011	6.7	20.7	XRTJ122502.59+702038.4	186.2608	70.3440	3.5	8.6
			XRTJ122457.12+700723.3	186.2380	70.1231	3.3	5.2
			XRTJ122531.06+701250.5	186.3794	70.2140	7.9	3.3
4FGLJ1243.7+1727	4.8	8.8	XRTJ124326.39+172935.9	190.8600	17.4933	2.6	7.9
			XRTJ124351.64+172643.2	190.9651	17.4453	5.0	4.0
4FGLJ1326.0+3507	14.0	11.3	XRTJ132544.62+350442.7	201.4359	35.0785	3.2	6.0
			XRTJ132608.87+350836.9	201.5369	35.1436	3.8	5.9
			XRTJ132622.45+350622.4	201.5935	35.1062	3.7	5.0
4FGLJ1336.5-4655	3.3	21.6	XRTJ133618.81-465738.9	204.0784	-46.9608	3.2	16.0
			XRTJ133548.08-465905.6	203.9503	-46.9849	4.3	4.4
4FGLJ1407.7-3017	11.5	18.0	XRTJ140806.82-302353.7	212.0284	-30.3982	1.9	51.3
			XRTJ140759.93-303047.2	211.9997	-30.5131	2.7	6.6
4FGLJ1408.6-2917	12.0	6.7	XRTJ140809.87-292241.0	212.0411	-29.3781	4.8	4.2
			XRTJ140807.26-291615.1	212.0303	-29.2709	7.8	3.2
			XRTJ140826.77-292222.7	212.1115	-29.3730	3.9	3.2
4FGLJ1438.0+0219	5.8	8.2	XRTJ143809.82+021804.1	219.5409	2.3011	5.2	3.6
			XRTJ143743.99+021934.5	219.4333	2.3262	5.5	3.2
4FGLJ1444.8+3645	5.0	6.2	XRTJ144529.77+364615.6	221.3740	36.7710	3.8	3.6
			XRTJ144401.00+364415.3	221.0042	36.7376	5.8	3.5
4FGLJ1452.0-4148	6.0	10.4	XRTJ145149.46-414503.3	222.9561	-41.7509	2.1	19.0
			XRTJ145224.64-414953.4	223.1027	-41.8315	6.2	4.2
4FGLJ1454.3-3946	4.1	3.3	XRTJ145411.28-395523.4	223.5470	-39.9232	2.9	5.6
			XRTJ145347.13-394451.0	223.4464	-39.7475	3.1	4.9
4FGLJ1504.6+4343	5.8	4.2	XRTJ150425.17+434105.0	226.1049	43.6847	2.5	11.3
			XRTJ150507.23+435002.6	226.2801	43.8341	2.7	10.0
4FGLJ1513.0-3118	7.4	3.3	XRTJ151244.55-311650.1	228.1856	-31.2806	2.7	7.9
			XRTJ151258.83-311746.4	228.2451	-31.2962	4.2	3.0
4FGLJ1514.8+4448	24.4	15.4	XRTJ151436.48+445002.0	228.6520	44.8339	4.6	4.6
			XRTJ151451.10+444953.1	228.7129	44.8314	4.7	4.3
4FGLJ1517.7-4446	12.0	5.0	XRTJ151727.58-444254.5	229.3649	-44.7152	3.2	4.5
			XRTJ151810.81-444734.7	229.5451	-44.7930	7.5	3.7
4FGLJ1557.2+3822	4.6	9.2	XRTJ155712.37+382030.2	239.3015	38.3417	3.1	6.7
			XRTJ155656.77+382825.8	239.2365	38.4738	5.3	3.7
4FGLJ1637.5+3005	3.8	9.5	XRTJ163739.22+301009.3	249.4134	30.1692	2.6	8.5
			XRTJ163738.33+300503.1	249.4097	30.0842	3.5	5.2
			XRTJ163727.99+300954.6	249.3666	30.1652	4.4	3.9
			XRTJ163647.31+300555.1	249.1971	30.0986	4.7	3.1
			XRTJ163735.81+301310.8	249.3992	30.2197	6.2	3.0
4FGLJ1651.7-7241	3.9	5.1	XRTJ165151.61-724308.5	252.9650	-72.7190	2.9	6.7
			XRTJ165139.31-724639.6	252.9138	-72.7777	7.7	3.1
4FGLJ1821.6+6636	9.1	8.4	XRTJ182108.75+663542.0	275.2865	66.5950	6.6	3.3
			XRTJ182204.70+663715.0	275.5196	66.6208	5.5	3.1
4FGLJ1845.3+5605	5.3	5.3	XRTJ184556.92+561002.4	281.4872	56.1673	2.6	5.3
			XRTJ184641.97+561617.3	281.6749	56.2715	4.3	5.1
4FGLJ2012.1-5234	6.9	3.7	XRTJ201213.56-523248.9	303.0565	-52.5469	2.7	7.4
			XRTJ201144.43-523444.5	302.9351	-52.5790	6.0	3.3
4FGLJ2046.9-5409	5.3	12.0	XRTJ204700.86-541245.8	311.7536	-54.2127	2.7	8.5
			XRTJ204722.68-540906.1	311.8445	-54.1517	3.8	5.1
			XRTJ204643.60-540604.1	311.6816	-54.1011	7.0	3.4
4FGLJ2054.2+6904	15.4	21.3	XRTJ205359.10+690518.6	313.4962	69.0885	5.9	4.7
			XRTJ205353.18+690141.5	313.4716	69.0282	4.3	4.6
4FGLJ2122.3+7653	6.8	177.3	XRTJ212204.08+765830.1	320.5170	76.9750	3.6	4.5
			XRTJ212156.89+765308.0	320.4871	76.8855	6.0	3.8
4FGLJ2122.5+0345	5.8	11.2	XRTJ212228.37+034511.1	320.6182	3.7531	2.7	7.7
			XRTJ212212.36+035254.2	320.5515	3.8817	4.5	3.9
4FGLJ2134.3-0319	3.9	5.4	XRTJ213415.13-032439.2	323.5630	-3.4109	2.7	5.2
			XRTJ213418.47-032327.5	323.5770	-3.3910	5.6	3.0

Note. Labels are the same as in table A.2.

Table A.3: Summary of *Swift*/XRT detections within the 3σ *Fermi* error box of UGS2 (UGS with more than one potential X-ray counterparts). Continued

4FGL Name (1)	γ-ray detection (2) (σ)	Swift exposure (3) (ks)	*Swift*/XRT source (4)	RA (5) (J2000)	DEC (6) (J2000)	Positional error (7) (arcsec)	X-ray detection (8) (σ)
4FGLJ2141.4+0733	7.9	20.8	XRTJ214147.51+074216.2	325.4480	7.7045	7.7	5.4
			XRTJ214125.72+073257.3	325.3572	7.5492	4.3	4.2
4FGLJ2144.7-5640	4.8	13.6	XRTJ214429.66-563848.6	326.1236	-56.6468	2.1	12.4
			XRTJ214503.13-564500.8	326.2630	-56.7502	4.3	5.6
4FGLJ2153.0-6442	5.3	5.2	XRTJ215306.90-644444.4	328.2788	-64.7457	2.1	11.1
			XRTJ215326.50-644310.5	328.3604	-64.7196	2.6	5.6
4FGLJ2212.9+7921	5.5	2.2	XRTJ221111.14+791758.1	332.7964	79.2995	3.2	5.8
-	5.5	2.2	XRTJ221414.52+792040.2	333.5605	79.3445	4.8	5.0
4FGLJ2222.9+1507	5.2	5.6	XRTJ222253.97+151053.6	335.7249	15.1816	5.9	4.4
			XRTJ222239.38+151053.7	335.6641	15.1816	4.1	3.4
4FGLJ2223.0+2704	5.2	51.4	XRTJ222217.67+270747.9	335.5736	27.1300	3.9	13.2
			XRTJ222305.55+265733.0	335.7731	26.9592	3.2	10.2
			XRTJ222334.34+270113.8	335.8931	27.0205	3.7	8.2
			XRTJ222244.77+270423.6	335.6865	27.0732	3.5	7.9
			XRTJ222247.02+270103.3	335.6959	27.0176	3.5	6.5
			XRTJ222228.30+265743.6	335.6179	26.9621	3.5	6.5
			XRTJ222301.89+265603.4	335.7579	26.9343	3.5	4.6
			XRTJ222314.49+271025.5	335.8104	27.1737	4.7	4.2
			XRTJ222310.54+271308.1	335.7939	27.2189	4.9	4.2
			XRTJ222239.51+270453.8	335.6646	27.0816	3.5	4.0
			XRTJ222250.46+270432.3	335.7103	27.0756	5.2	3.9
			XRTJ222313.70+270849.2	335.8071	27.1470	5.9	3.1
4FGLJ2311.6-4427	7.1	6.1	XRTJ231145.87-443221.0	347.9411	-44.5392	3.5	3.9
			XRTJ231134.44-443617.8	347.8935	-44.6050	6.4	3.8
4FGLJ2324.6+3115	4.3	34.8	XRTJ232458.69+312709.9	351.2445	31.4527	3.1	7.8
			XRTJ232402.93+312019.8	351.0122	31.3388	3.7	7.5
			XRTJ232457.35+311340.3	351.2389	31.2279	6.0	4.3
			XRTJ232441.72+311002.0	351.1738	31.1672	3.6	4.0
4FGLJ2338.1+0411	6.4	26.8	XRTJ233830.54+041900.0	354.6273	4.3167	2.4	24.6
			XRTJ233742.04+041003.2	354.4252	4.1676	2.6	12.3
			XRTJ233833.66+041321.8	354.6402	4.2227	3.5	5.1
			XRTJ233731.09+040634.4	354.3796	4.1095	3.5	4.9
			XRTJ233737.43+040814.6	354.4060	4.1374	3.5	4.7
			XRTJ233735.13+041029.1	354.3964	4.1747	4.1	4.6
			XRTJ233741.42+040736.8	354.4226	4.1269	3.5	3.8
			XRTJ233824.88+040520.3	354.6037	4.0890	3.7	3.4
4FGLJ2344.7-4234	4.2	15.6	XRTJ234413.10-423935.9	356.0546	-42.6599	7.0	7.2
			XRTJ234431.22-423308.8	356.1301	-42.5525	8.7	3.4
4FGLJ2351.4-2818	6.0	4.8	XRTJ235137.78-281824.6	357.9074	-28.3068	4.5	5.2
			XRTJ235136.96-282157.3	357.9040	-28.3659	4.4	4.6
4FGLJ2359.3+1444	7.8	14.7	XRTJ235937.37+144848.9	359.9057	14.8136	3.5	4.9
			XRTJ235919.60+144156.1	359.8317	14.6989	4.8	4.7
			XRTJ235838.47+144512.3	359.6603	14.7534	4.5	4.1
			XRTJ235918.00+144851.8	359.8250	14.8144	4.4	3.8
			XRTJ235953.96+145523.9	359.9748	14.9233	4.5	3.8
			XRTJ235923.02+144833.7	359.8459	14.8094	5.2	3.2
			XRTJ235923.02+144833.7	359.8459	14.8094	5.2	3.2

Note. Labels are the same as in table A.2.

Table A.4: Results of the X-ray spectral fitting for UGS1.

4FGL Name (1)	*Swift*/XRT source (2)	Count rate (3) [$\times 10^{-3}$]	nH (4) [$\times 10^{20}$]	Γ (5)	Norm. (6) 10^{-5}	absorbed flux (7) [$\times 10^{-13}$]	χ^2_ν(dof) (8)
4FGLJ0003.6+3059	XRTJ000402.65+310219.8	$4.64^{+1.01}_{-1.01}$	6.8	2	$4.3^{+1.1}_{-1.1}$	$2.0^{+0.5}_{-0.5}$	0.01(1)
4FGLJ0004.4-4001	XRTJ000434.22-400034.7	$9.68^{+1.04}_{-1.04}$	1.2	$2.5^{+0.2}_{-0.2}$	$7.2^{+0.9}_{-0.9}$	$3.2^{+0.4}_{-0.4}$	0.9(8)
4FGLJ0006.6+4618	XRTJ000652.09+461813.9	$4.19^{+1.00}_{-1.00}$	11.0	2	$5.8^{+1.6}_{-1.6}$	$2.5^{+0.7}_{-0.7}$	-
4FGLJ0009.1-5012	XRTJ000908.61-501000.9	$4.53^{+1.01}_{-1.01}$	1.4	2	$4.7^{+1.5}_{-1.5}$	$2.5^{+0.8}_{-0.8}$	-
4FGLJ0022.0-5921	XRTJ002127.45-591946.3	$6.14^{+1.19}_{-1.19}$	1.4	2	$6.1^{+1.3}_{-1.3}$	$3.2^{+0.7}_{-0.7}$	0.7(2)
4FGLJ0023.2+8412	XRTJ002403.36+841352.6	$13.42^{+2.84}_{-2.84}$	11.0	2	$11.0^{+2.9}_{-2.9}$	$5.0^{+1.4}_{-1.4}$	1.2(1)
4FGLJ0023.6-4209	XRTJ002303.59-420509.6	$12.60^{+1.96}_{-1.96}$	1.4	$1.2^{+0.3}_{-0.3}$	$11.0^{+2.0}_{-2.0}$	$12.6^{+4.4}_{-3.5}$	0.8(3)
4FGLJ0025.4-4838	XRTJ002536.94-483810.9	$12.97^{+1.77}_{-1.77}$	1.8	$2.5^{+0.2}_{-0.2}$	$8.6^{+1.4}_{-1.4}$	$4.0^{+0.7}_{-0.7}$	1.8(4)
4FGLJ0026.1-0732	XRTJ002611.55-073116.0	$94.75^{+3.81}_{-3.81}$	4.0	$2.2^{+0.1}_{-0.1}$	$77.0^{+3.3}_{-3.3}$	$31.6^{+1.5}_{-1.4}$	0.7(66)
4FGLJ0027.0-1134	XRTJ002710.11-113638.7	$22.40^{+3.50}_{-3.50}$	2.9	$2.0^{+0.3}_{-0.3}$	$21.0^{+3.6}_{-3.6}$	$10.0^{+2.0}_{-2.1}$	1.0(3)
4FGLJ0031.5-5648	XRTJ003135.74-564640.9	$10.50^{+1.59}_{-1.59}$	1.3	$2.3^{+0.4}_{-0.3}$	$9.2^{+1.6}_{-1.6}$	$4.0^{+1.0}_{-0.8}$	0.3(3)
4FGLJ0037.2-2653	XRTJ003729.64-265045.9	$7.55^{+1.56}_{-1.56}$	1.4	2	$6.0^{+1.3}_{-1.3}$	$3.2^{+0.7}_{-0.7}$	0.8(2)
4FGLJ0054.4-1503	XRTJ005431.46-145804.7	$11.60^{+1.42}_{-1.42}$	1.9	$2.7^{+0.3}_{-0.3}$	$8.6^{+1.2}_{-1.2}$	$4.0^{+0.6}_{-0.5}$	0.7(6)
4FGLJ0055.7+4507	XRTJ005525.98+450529.3	$3.72^{+0.95}_{-0.95}$	13.0	2	$15.0^{+4.0}_{-4.0}$	$6.3^{+1.6}_{-1.6}$	-
4FGLJ0058.3-4603	XRTJ005806.28-460419.4	$59.25^{+3.30}_{-3.30}$	1.5	$1.6^{+0.1}_{-0.1}$	$37.0^{+2.4}_{-2.4}$	$25.1^{+1.8}_{-1.7}$	1.0(36)
4FGLJ0059.4-5654	XRTJ005945.18-565306.8	$2.71^{+0.55}_{-0.55}$	2.3	$2.2^{+0.5}_{-0.6}$	$2.0^{+0.5}_{-0.5}$	$1.0^{+0.4}_{-0.3}$	0.1(1)
4FGLJ0112.0+3442	XRTJ011124.86+344154.1	$5.22^{+1.10}_{-1.10}$	6.0	2	$5.2^{+1.1}_{-1.1}$	$2.5^{+0.6}_{-0.6}$	0.3(2)
4FGLJ0115.4-2917	XRTJ011528.71-291847.1	$2.09^{+0.57}_{-0.57}$	2.1	2	$2.0^{+0.6}_{-0.5}$	$1.0^{+0.3}_{-0.3}$	0.5(13)
4FGLJ0117.9+1430	XRTJ011804.79+143159.6	$14.49^{+2.49}_{-2.49}$	4.0	$2.8^{+0.3}_{-0.3}$	$13.0^{+2.5}_{-2.5}$	$5.0^{+1.0}_{-0.9}$	1.1(2)
4FGLJ0120.2-7944	XRTJ011913.62-794513.9	$9.72^{+1.56}_{-1.56}$	7.3	$2.3^{+0.6}_{-0.7}$	$8.6^{+1.6}_{-1.6}$	$3.2^{+2.1}_{-0.9}$	2.8(3)
4FGLJ0121.4-7216	XRTJ012121.84-721920.2	$1.66^{+0.54}_{-0.54}$	31.0	$3.1^{+0.7}_{-0.7}$	$7.6^{+1.9}_{-2.0}$	$1.0^{+0.4}_{-0.3}$	0.3(3)
4FGLJ0125.9-6303	XRTJ012547.97-630245.3	$17.68^{+1.75}_{-1.75}$	2.3	$1.6^{+0.2}_{-0.2}$	$16.0^{+1.6}_{-1.7}$	$10.0^{+2.3}_{-1.9}$	0.5(10)
4FGLJ0137.3-3239	XRTJ013724.55-324040.2	$16.77^{+2.22}_{-2.22}$	2.6	$2.4^{+0.2}_{-0.2}$	$14.0^{+1.9}_{-2.0}$	$6.3^{+1.1}_{-0.9}$	0.4(5)
4FGLJ0140.5-4730	XRTJ014007.79-473213.2	$4.08^{+1.11}_{-1.11}$	2.0	2	$3.0^{+0.9}_{-0.9}$	$1.6^{+0.5}_{-0.5}$	-
4FGLJ0156.3-2420	XRTJ015624.63-242004.1	$29.55^{+1.86}_{-1.86}$	1.4	$2.5^{+0.1}_{-0.1}$	$21.0^{+1.5}_{-1.5}$	$10.0^{+0.7}_{-0.7}$	1.0(26)
4FGLJ0202.7+3133	XRTJ020242.13+313211.4	$12.67^{+1.12}_{-1.12}$	6.5	$3.1^{+0.2}_{-0.2}$	$12.0^{+1.2}_{-1.2}$	$4.0^{+0.4}_{-0.4}$	0.5(14)
4FGLJ0231.0+3505	XRTJ023112.30+350445.7	$37.71^{+6.23}_{-6.23}$	6.7	$1.4^{+0.7}_{-0.8}$	$36.0^{+7.2}_{-8.1}$	$31.6^{+61.7}_{-16.8}$	1.7(2)
4FGLJ0245.0+4755	XRTJ024455.02+475125.2	$3.10^{+0.78}_{-0.78}$	24.0	2	$5.1^{+1.4}_{-1.4}$	$2.0^{+0.6}_{-0.5}$	-
4FGLJ0251.1-1830	XRTJ025111.70-183111.1	$14.41^{+1.39}_{-1.39}$	3.3	$2.1^{+0.2}_{-0.2}$	$12.0^{+1.2}_{-1.2}$	$5.0^{+0.6}_{-0.6}$	0.6(11)
4FGLJ0259.0+0552	XRTJ025857.56+055244.4	$9.38^{+1.44}_{-1.44}$	13.0	$2.2^{+0.3}_{-0.4}$	$12.0^{+2.0}_{-2.1}$	$4.0^{+1.3}_{-1.0}$	0.4(3)
4FGLJ0301.6-5617	XRTJ030115.05-561647.6	$6.98^{+1.18}_{-1.18}$	1.1	$2.8^{+0.4}_{-0.3}$	$4.6^{+0.9}_{-0.9}$	$2.0^{+0.3}_{-0.4}$	0.2(2)
4FGLJ0302.5+3354	XRTJ030226.95+335444.4	$12.34^{+1.86}_{-1.86}$	16.0	$2.6^{+0.4}_{-0.5}$	$17.0^{+2.9}_{-2.9}$	$5.0^{+1.7}_{-1.2}$	0.6(3)
4FGLJ0327.6+2620	XRTJ032737.27+262009.3	$19.50^{+0.74}_{-0.74}$	17.0	$2.4^{+0.1}_{-0.1}$	$25.0^{+1.1}_{-1.1}$	$6.3^{+0.3}_{-0.3}$	1.0(77)
4FGLJ0333.4-2705	XRTJ033331.91-270917.2	$23.53^{+2.44}_{-2.44}$	0.7	$2.0^{+0.2}_{-0.2}$	$19.0^{+2.1}_{-2.1}$	$10.0^{+1.7}_{-1.5}$	0.8(9)
4FGLJ0337.9+4058	XRTJ033733.16+405852.7	$12.07^{+2.88}_{-2.88}$	28.0	2	$16.0^{+4.5}_{-4.5}$	$6.3^{+1.6}_{-1.7}$	-
4FGLJ0341.9+3153	XRTJ034158.35+314854.1	$21.74^{+1.91}_{-1.91}$	26.0	$1.1^{+0.1}_{-0.1}$	$13.0^{+1.9}_{-1.9}$	$15.8^{+1.9}_{-2.0}$	2.3(15)
4FGLJ0343.3-6303	XRTJ034324.90-630338.5	$7.52^{+1.42}_{-1.42}$	4.2	$3.1^{+0.5}_{-0.5}$	$7.4^{+2.1}_{-2.2}$	$2.5^{+0.7}_{-0.6}$	0.4(1)
4FGLJ0349.6+4026	XRTJ034945.96+402614.0	$3.60^{+0.89}_{-0.89}$	37.0	2	$5.5^{+1.5}_{-1.5}$	$2.0^{+0.6}_{-0.5}$	-
4FGLJ0358.1+2850	XRTJ035748.90+284442.5	$30.48^{+2.12}_{-2.12}$	12.0	$1.5^{+0.1}_{-0.1}$	$30.0^{+2.8}_{-2.8}$	$20.0^{+2.4}_{-2.2}$	0.4(23)
4FGLJ0406.2+0639	XRTJ040607.87+063920.3	$5.81^{+1.03}_{-1.03}$	18.0	$2.5^{+0.4}_{-0.4}$	$8.9^{+1.7}_{-1.8}$	$2.5^{+0.8}_{-0.6}$	0.1(2)
4FGLJ0409.2+2542	XRTJ040921.70+254441.4	$10.95^{+1.20}_{-1.20}$	16.0	$2.7^{+0.3}_{-0.3}$	$17.0^{+1.9}_{-2.0}$	$4.0^{+0.7}_{-0.6}$	0.8(8)
4FGLJ0418.4-4342	XRTJ041832.35-434155.4	$2.76^{+0.36}_{-0.36}$	1.7	$2.3^{+0.3}_{-0.3}$	$2.4^{+0.3}_{-0.3}$	$1.0^{+0.2}_{-0.1}$	1.0(8)
4FGLJ0438.0-7329	XRTJ043836.89-732921.3	$7.51^{+1.43}_{-1.43}$	12.0	2	$8.7^{+1.9}_{-1.9}$	$4.0^{+0.9}_{-0.9}$	1.1(2)
4FGLJ0438.2-4243	XRTJ043831.99-424007.0	$7.64^{+1.36}_{-1.36}$	1.6	$2.2^{+0.3}_{-0.3}$	$6.2^{+1.1}_{-1.1}$	$3.2^{+0.7}_{-0.7}$	0.8(2)
4FGLJ0459.7-5413	XRTJ045937.04-541709.3	$28.79^{+2.68}_{-2.68}$	1.5	$2.3^{+0.2}_{-0.1}$	$20.0^{+2.1}_{-2.1}$	$10.0^{+1.2}_{-1.1}$	1.4(12)
4FGLJ0512.8+5821	XRTJ051154.26+582904.3	$6.53^{+1.17}_{-1.17}$	34.0	$1.6^{+0.5}_{-0.5}$	$10.0^{+3.5}_{-3.3}$	$6.3^{+3.5}_{-2.3}$	0.2(2)
4FGLJ0531.4-0058	XRTJ053055.69-005538.0	$5.91^{+1.38}_{-1.38}$	26.0	2	$13.0^{+3.4}_{-3.4}$	$5.0^{+1.3}_{-1.3}$	-
4FGLJ0531.7+1241	XRTJ053123.50+123319.8	$6.66^{+1.40}_{-1.40}$	37.0	2	$57.0^{+15.0}_{-15.0}$	$20.0^{+5.2}_{-5.5}$	2.7(1)
4FGLJ0536.1-1205	XRTJ053626.88-120653.4	$11.87^{+1.74}_{-1.74}$	16.0	$2.9^{+0.5}_{-0.5}$	$19.0^{+3.3}_{-3.4}$	$4.0^{+1.5}_{-1.0}$	0.2(3)
4FGLJ0537.5+0959	XRTJ053745.84+095758.5	$7.21^{+0.99}_{-0.99}$	32.0	$2.1^{+0.5}_{-0.5}$	$12.0^{+2.8}_{-2.8}$	$4.0^{+1.6}_{-1.1}$	1.0(5)
4FGLJ0545.8-0905	XRTJ054540.46-090712.2	$11.09^{+1.61}_{-1.61}$	31.0	$1.8^{+0.3}_{-0.3}$	$13.0^{+2.9}_{-2.9}$	$6.3^{+1.6}_{-1.4}$	1.8(4)
4FGLJ0553.9-5048	XRTJ055359.66-505145.1	$14.04^{+1.93}_{-1.93}$	4.9	$2.1^{+0.3}_{-0.3}$	$11.0^{+1.7}_{-1.7}$	$5.0^{+1.2}_{-1.0}$	1.0(4)
4FGLJ0554.0-0839	XRTJ055341.85-084003.8	$2.45^{+0.61}_{-0.61}$	30.0	2	$4.0^{+1.1}_{-1.1}$	$1.6^{+0.4}_{-0.4}$	-
4FGLJ0554.2-0259	XRTJ055418.93-025838.3	$8.12^{+1.07}_{-1.07}$	34.0	$1.9^{+0.3}_{-0.3}$	$12.0^{+2.4}_{-2.4}$	$4.0^{+0.9}_{-0.8}$	0.9(5)
4FGLJ0620.7-5034	XRTJ062045.98-503350.3	$15.12^{+1.75}_{-1.75}$	4.9	$2.3^{+0.3}_{-0.3}$	$13.0^{+1.7}_{-1.7}$	$5.0^{+1.0}_{-0.8}$	0.7(7)
4FGLJ0624.7-4903	XRTJ062419.86-490640.2	$6.01^{+1.33}_{-1.33}$	3.8	2	$6.2^{+1.6}_{-1.6}$	$3.2^{+0.8}_{-0.8}$	-

Note. 1) 4FGL Name; 2) Name of the *Swift*/XRT source; 3) *Swift*/XRT count rate; 4) Equivalent hydrogen column density (cm^{-2}), provided by the HI4PI Collaboration et al. (2016) database; 5) Power-law index; 6) Normalization factor (photons keV^{-1} cm^{-2} s^{-1}) at 1 keV; 7) Absorbed flux in the range 0.3–10 keV (erg cm^{-2} s^{-1}); 8) χ^2_ν (and the relative degrees of freedom).
The sources for which the χ^2_ν does not appear in the table have a spectral data quality too poor to allow for spectral fitting. For these sources, we just convert the observed source count rate into a flux (see text).

Table A.4: Results of the X-ray spectral fitting for UGS1. Continued

4FGL Name (1)	*Swift*/XRT source (2)	Count rate (3) [$\times10^{-3}$]	nH (4) [$\times10^{20}$]	Γ (5)	Norm. (6) 10^{-5}	absorbed flux (7) [$\times10^{-13}$]	χ^2_ν(dof) (8)
4FGLJ0631.0+5626	XRTJ063048.87+562830.6	$14.09^{+1.88}_{-1.88}$	11.0	$2.6^{+0.3}_{-0.3}$	$17.0^{+2.4}_{-2.4}$	$5.0^{+1.2}_{-0.9}$	0.9(5)
4FGLJ0640.9-5204	XRTJ064112.61-520738.0	$22.95^{+1.91}_{-1.91}$	5.2	$2.3^{+0.2}_{-0.2}$	$16.0^{+1.6}_{-1.6}$	$6.3^{+0.8}_{-0.8}$	3.2(15)
4FGLJ0641.4+3349	XRTJ064111.24+334502.0	$68.21^{+4.40}_{-4.40}$	23.0	$2.1^{+0.1}_{-0.1}$	$82.0^{+7.5}_{-7.6}$	$25.1^{+2.4}_{-2.7}$	1.1(27)
4FGLJ0656.5+4218	XRTJ065635.60+421523.5	$79.41^{+3.10}_{-3.10}$	13.0	$2.3^{+0.1}_{-0.1}$	$87.0^{+3.8}_{-3.8}$	$25.1^{+1.2}_{-1.1}$	0.7(68)
4FGLJ0700.2-5118	XRTJ070034.01-512007.4	$28.00^{+2.82}_{-2.82}$	5.7	$1.9^{+0.2}_{-0.2}$	$24.0^{+2.8}_{-2.9}$	$12.6^{+1.9}_{-1.9}$	0.8(10)
4FGLJ0704.3-4829	XRTJ070421.99-482646.5	$21.39^{+1.77}_{-1.77}$	5.3	$2.7^{+0.1}_{-0.1}$	$19.0^{+1.7}_{-1.7}$	$6.3^{+0.6}_{-0.6}$	1.1(16)
4FGLJ0734.3-4448	XRTJ073418.51-444640.5	$4.17^{+1.07}_{-1.07}$	26.0	2	$5.7^{+1.5}_{-1.5}$	$2.0^{+0.5}_{-0.5}$	-
4FGLJ0755.9-0515	XRTJ075614.46-051719.2	$46.32^{+3.64}_{-3.64}$	10.0	$1.8^{+0.2}_{-0.2}$	$39.0^{+4.3}_{-4.5}$	$20.0^{+3.0}_{-3.0}$	1.2(17)
4FGLJ0800.9+0733	XRTJ080056.64+073234.5	$13.13^{+0.63}_{-0.63}$	3.0	$2.7^{+0.1}_{-0.1}$	$11.0^{+0.6}_{-0.6}$	$4.0^{+0.2}_{-0.2}$	0.7(46)
4FGLJ0815.5+6554	XRTJ081539.88+655004.3	$14.81^{+1.30}_{-1.30}$	4.6	$2.1^{+0.2}_{-0.2}$	$14.0^{+1.4}_{-1.4}$	$6.3^{+0.9}_{-0.8}$	1.2(13)
4FGLJ0826.0-0157	XRTJ082556.10-020212.2	$4.44^{+0.84}_{-0.84}$	4.6	$1.5^{+0.4}_{-0.4}$	$3.7^{+0.8}_{-0.9}$	$3.2^{+1.3}_{-1.0}$	1.0(2)
4FGLJ0838.5+4013	XRTJ083902.98+401546.9	$9.89^{+1.61}_{-1.61}$	3.8	$2.0^{+0.4}_{-0.5}$	$9.5^{+1.8}_{-1.8}$	$5.0^{+2.6}_{-1.5}$	0.6(2)
4FGLJ0839.6-8341	XRTJ083847.78-834345.1	$39.99^{+3.00}_{-3.00}$	17.0	$2.3^{+0.1}_{-0.1}$	$52.0^{+4.4}_{-4.5}$	$15.8^{+1.5}_{-1.4}$	0.9(20)
4FGLJ0852.5-2515	XRTJ085221.91-251628.8	$28.32^{+5.16}_{-5.16}$	14.0	2	$41.0^{+8.5}_{-8.5}$	$15.8^{+3.2}_{-3.3}$	0.1(2)
4FGLJ0906.1-1011	XRTJ090616.22-101427.0	$4.94^{+1.24}_{-1.24}$	5.1	2	$4.2^{+1.2}_{-1.2}$	$2.0^{+0.6}_{-0.6}$	-
4FGLJ0910.1-1816	XRTJ091003.90-181613.1	$22.14^{+1.73}_{-1.73}$	8.7	$2.4^{+0.2}_{-0.2}$	$23.0^{+1.9}_{-1.9}$	$7.9^{+1.0}_{-0.9}$	0.5(18)
4FGLJ0914.5+6845	XRTJ091429.49+684506.3	$13.51^{+1.81}_{-1.81}$	5.3	$2.0^{+0.3}_{-0.3}$	$11.0^{+1.7}_{-1.7}$	$5.0^{+1.4}_{-1.1}$	1.8(5)
4FGLJ0916.9+7756	XRTJ091715.25+780052.4	$4.93^{+1.28}_{-1.28}$	1.9	2	$3.3^{+1.0}_{-1.0}$	$1.6^{+0.5}_{-0.5}$	-
4FGLJ0934.5+7223	XRTJ093333.50+722059.0	$5.97^{+1.25}_{-1.25}$	2.9	2	$5.7^{+1.2}_{-1.2}$	$3.2^{+0.7}_{-0.7}$	0.4(2)
4FGLJ0938.8+5155	XRTJ093834.50+515454.8	$2.30^{+0.49}_{-0.49}$	1.3	2	$1.3^{+0.4}_{-0.4}$	$0.8^{+0.2}_{-0.2}$	3.5(2)
4FGLJ1016.1-4247	XRTJ101620.78-424723.2	$19.81^{+2.32}_{-2.32}$	14.0	$2.8^{+0.3}_{-0.3}$	$23.0^{+2.9}_{-2.9}$	$6.3^{+1.1}_{-0.9}$	1.7(8)
4FGLJ1017.4+5956	XRTJ101706.90+595129.9	$3.03^{+0.76}_{-0.76}$	1.1	2	$3.3^{+0.9}_{-0.9}$	$1.6^{+0.4}_{-0.4}$	-
4FGLJ1032.0+5725	XRTJ103142.67+573255.3	$4.46^{+0.71}_{-0.71}$	0.7	$1.1^{+0.3}_{-0.3}$	$2.9^{+0.6}_{-0.6}$	$4.0^{+1.4}_{-1.1}$	0.4(3)
4FGLJ1039.2+3258	XRTJ103852.17+325651.9	$6.82^{+1.18}_{-1.18}$	1.7	$2.2^{+0.5}_{-0.5}$	$6.0^{+1.2}_{-1.2}$	$3.2^{+1.5}_{-0.9}$	0.8(2)
4FGLJ1047.2+6740	XRTJ104705.65+673759.0	$9.85^{+1.66}_{-1.66}$	1.6	$2.3^{+0.4}_{-0.4}$	$7.2^{+1.4}_{-1.4}$	$3.2^{+0.9}_{-0.7}$	0.5(2)
4FGLJ1049.8+2741	XRTJ104938.70+274212.1	$9.01^{+1.30}_{-1.30}$	2.0	$2.7^{+0.3}_{-0.3}$	$6.9^{+1.1}_{-1.1}$	$3.2^{+0.5}_{-0.5}$	0.2(4)
4FGLJ1114.6+1225	XRTJ111437.12+122711.2	$4.09^{+0.92}_{-0.92}$	1.9	2	$5.6^{+1.5}_{-1.5}$	$3.2^{+0.8}_{-0.8}$	-
4FGLJ1119.9-1007	XRTJ111948.35-100706.0	$7.05^{+1.32}_{-1.32}$	5.1	$2.3^{+0.6}_{-0.6}$	$6.8^{+1.5}_{-1.6}$	$2.5^{+1.6}_{-0.8}$	0.0(1)
4FGLJ1120.0-2204	XRTJ111958.40-220456.3	$1.49^{+0.16}_{-0.16}$	4.4	$1.8^{+0.2}_{-0.2}$	$1.1^{+0.1}_{-0.1}$	$0.6^{+0.1}_{-0.1}$	1.9(11)
4FGLJ1120.1-2645	XRTJ111956.93-264316.2	$8.84^{+1.55}_{-1.55}$	6.1	$2.2^{+0.4}_{-0.4}$	$7.8^{+1.5}_{-1.5}$	$3.2^{+1.1}_{-0.8}$	1.2(2)
4FGLJ1122.0-0231	XRTJ112213.80-022916.7	$24.86^{+2.82}_{-2.82}$	5.6	$2.6^{+0.2}_{-0.2}$	$21.0^{+2.5}_{-2.5}$	$7.9^{+1.2}_{-1.0}$	1.6(8)
4FGLJ1123.8-4552	XRTJ112354.82-455012.2	$5.93^{+1.32}_{-1.32}$	13.0	2	$5.4^{+1.5}_{-1.5}$	$2.5^{+0.7}_{-0.7}$	1.3(1)
4FGLJ1125.1+4811	XRTJ112526.01+480922.8	$0.60^{+0.14}_{-0.14}$	1.6	2	$0.7^{+0.2}_{-0.2}$	$0.4^{+0.1}_{-0.1}$	1.3(2)
4FGLJ1131.6+4657	XRTJ113142.36+470009.2	$12.56^{+1.68}_{-1.68}$	1.8	$2.2^{+0.3}_{-0.3}$	$9.4^{+1.5}_{-1.5}$	$5.0^{+1.3}_{-1.0}$	1.0(4)
4FGLJ1146.0-0638	XRTJ114600.87-063853.9	$14.34^{+1.32}_{-1.32}$	3.3	$2.2^{+0.2}_{-0.2}$	$12.0^{+1.2}_{-1.2}$	$5.0^{+0.7}_{-0.6}$	1.0(12)
4FGLJ1155.2-1111	XRTJ115515.07-111124.9	$8.62^{+1.50}_{-1.50}$	3.6	$1.9^{+0.4}_{-0.4}$	$8.2^{+1.5}_{-1.6}$	$4.0^{+1.4}_{-1.0}$	0.9(3)
4FGLJ1158.8-1430	XRTJ115912.67-143154.7	$80.62^{+3.94}_{-3.94}$	4.8	$2.2^{+0.1}_{-0.1}$	$69.0^{+3.7}_{-3.7}$	$31.6^{+2.3}_{-2.1}$	1.0(45)
4FGLJ1207.4-1840	XRTJ120740.89-184029.3	$1.90^{+0.47}_{-0.47}$	4.9	2	$1.7^{+0.5}_{-0.5}$	$0.8^{+0.2}_{-0.2}$	-
4FGLJ1207.4-4536	XRTJ120732.84-453452.0	$4.99^{+1.00}_{-1.00}$	9.9	2	$18.0^{+4.2}_{-4.2}$	$7.9^{+1.8}_{-1.8}$	2.8(2)
4FGLJ1217.2-2500	XRTJ121735.36-245512.3	$3.73^{+0.89}_{-0.89}$	11.0	2	$5.4^{+1.4}_{-1.4}$	$2.5^{+0.7}_{-0.6}$	-
4FGLJ1220.1-2458	XRTJ122014.54-245948.2	$60.42^{+3.80}_{-3.80}$	10.0	$1.9^{+0.1}_{-0.1}$	$55.0^{+4.1}_{-4.1}$	$25.1^{+2.4}_{-2.2}$	0.9(29)
4FGLJ1239.7-3455	XRTJ123933.89-345428.1	$15.29^{+1.67}_{-1.67}$	6.5	$1.9^{+0.2}_{-0.2}$	$13.0^{+1.6}_{-1.6}$	$6.3^{+1.1}_{-1.1}$	1.1(9)
4FGLJ1250.9-4943	XRTJ125058.72-494448.6	$5.08^{+1.10}_{-1.10}$	18.0	2	$6.0^{+1.4}_{-1.4}$	$2.5^{+0.6}_{-0.6}$	1.5(2)
4FGLJ1256.8+5329	XRTJ125630.54+533202.3	$5.36^{+1.02}_{-1.02}$	1.6	$2.1^{+0.9}_{-1.0}$	$3.4^{+0.8}_{-0.9}$	$1.6^{+2.4}_{-0.6}$	2.7(1)
4FGLJ1259.0-8148	XRTJ130100.24-814811.8	$5.16^{+1.26}_{-1.26}$	17.0	2	$6.4^{+1.8}_{-1.8}$	$2.5^{+0.7}_{-0.7}$	-
4FGLJ1308.7+0347	XRTJ130832.27+034405.4	$11.67^{+1.41}_{-1.41}$	2.2	$1.7^{+0.2}_{-0.2}$	$11.0^{+1.5}_{-1.5}$	$7.9^{+1.6}_{-1.5}$	0.4(7)
4FGLJ1313.2-4437	XRTJ131318.21-443732.2	$81.25^{+6.25}_{-6.25}$	10.0	$2.4^{+0.1}_{-0.1}$	$70.0^{+6.2}_{-6.2}$	$25.1^{+2.4}_{-2.7}$	1.6(19)
4FGLJ1346.5+5330	XRTJ134545.15+533252.5	$78.72^{+3.18}_{-3.18}$	1.1	$1.5^{+0.1}_{-0.1}$	$55.0^{+2.6}_{-2.6}$	$39.8^{+2.8}_{-2.7}$	0.8(67)
4FGLJ1401.3-5012	XRTJ140146.80-501324.1	$71.06^{+6.56}_{-6.56}$	27.0	$1.3^{+0.2}_{-0.2}$	$57.0^{+9.7}_{-9.4}$	$50.1^{+8.8}_{-8.4}$	0.8(12)
4FGLJ1401.7-3217	XRTJ140159.82-321848.4	$5.75^{+1.38}_{-1.38}$	6.2	2	$5.6^{+1.6}_{-1.6}$	$2.5^{+0.7}_{-0.7}$	-
4FGLJ1407.4-0820	XRTJ140724.84-082320.5	$6.02^{+1.36}_{-1.36}$	2.9	2	$4.3^{+1.2}_{-1.2}$	$2.0^{+0.6}_{-0.6}$	1.8(1)
4FGLJ1410.7+7405	XRTJ141045.66+740509.9	$2.62^{+0.53}_{-0.53}$	2.4	$2.6^{+0.4}_{-0.4}$	$2.7^{+0.5}_{-0.5}$	$1.3^{+0.3}_{-0.3}$	0.1(2)
4FGLJ1415.9-1504	XRTJ141546.05-150231.4	$10.57^{+1.79}_{-1.79}$	7.8	$3.1^{+0.4}_{-0.4}$	$12.0^{+2.3}_{-2.4}$	$4.0^{+0.8}_{-0.7}$	0.0(2)
4FGLJ1420.9-2431	XRTJ142035.74-243023.3	$6.84^{+1.47}_{-1.47}$	7.9	2	$9.8^{+2.6}_{-2.6}$	$5.0^{+1.3}_{-1.3}$	3.8(2)
4FGLJ1421.4-1655	XRTJ142128.97-165455.7	$20.79^{+1.69}_{-1.69}$	8.9	$2.0^{+0.2}_{-0.2}$	$19.0^{+1.8}_{-1.8}$	$7.9^{+1.2}_{-1.0}$	0.6(17)
4FGLJ1424.8-8012	XRTJ142342.47-800721.1	$7.81^{+1.57}_{-1.57}$	14.0	2	$18.0^{+3.9}_{-3.9}$	$7.9^{+1.8}_{-1.8}$	0.5(2)
4FGLJ1429.8-0739	XRTJ142949.48-073304.7	$19.71^{+2.29}_{-2.29}$	5.5	$2.2^{+0.2}_{-0.2}$	$18.0^{+2.2}_{-2.2}$	$7.9^{+1.4}_{-1.3}$	0.5(7)
4FGLJ1430.6+1543	XRTJ143057.97+154556.1	$35.23^{+3.56}_{-3.56}$	1.8	$2.0^{+0.2}_{-0.2}$	$27.0^{+3.0}_{-3.0}$	$15.8^{+2.3}_{-2.0}$	1.0(10)
4FGLJ1441.4-1934	XRTJ144127.83-193551.0	$16.65^{+1.91}_{-1.91}$	10.0	$2.4^{+0.3}_{-0.3}$	$18.0^{+2.3}_{-2.3}$	$6.3^{+1.5}_{-1.1}$	0.8(7)

Note. Labels are the same as in table A.4.

Table A.4: Results of the X-ray spectral fitting for UGS1. Continued

4FGL Name (1)	*Swift*/XRT source (2)	Count rate (3) $[\times 10^{-3}]$	nH (4) $[\times 10^{20}]$	Γ (5)	Norm. (6) 10^{-5}	absorbed flux (7) $[\times 10^{-13}]$	χ^2_ν(dof) (8)
4FGLJ1528.4+2004	XRTJ152835.84+200422.1	$18.36^{+1.74}_{-1.74}$	6.2	$2.0^{+0.2}_{-0.2}$	$16.0^{+1.7}_{-1.8}$	$7.9^{+1.4}_{-1.2}$	1.4(12)
4FGLJ1535.9+3743	XRTJ153550.56+374056.8	$2.57^{+0.52}_{-0.52}$	1.3	2	$2.1^{+0.5}_{-0.5}$	$1.3^{+0.3}_{-0.3}$	1.3(2)
4FGLJ1538.9+0425	XRTJ153901.41+042750.5	$4.18^{+1.18}_{-1.18}$	5.0	2	$4.1^{+1.2}_{-1.2}$	$2.0^{+0.6}_{-0.6}$	-
4FGLJ1539.1+1008	XRTJ153848.51+101841.7	$6.73^{+1.15}_{-1.15}$	3.8	$2.0^{+0.3}_{-0.3}$	$6.5^{+1.2}_{-1.2}$	$3.2^{+0.7}_{-0.7}$	1.6(3)
4FGLJ1543.1+4209	XRTJ154311.32+421006.3	$4.55^{+1.01}_{-1.01}$	2.5	2	$4.3^{+1.2}_{-1.2}$	$2.0^{+0.6}_{-0.5}$	1.5(1)
4FGLJ1544.9+3218	XRTJ154433.15+322148.6	$10.16^{+0.87}_{-0.87}$	2.7	$2.5^{+0.2}_{-0.1}$	$8.8^{+0.8}_{-0.8}$	$4.0^{+0.4}_{-0.4}$	0.6(15)
4FGLJ1554.2+2008	XRTJ155424.17+201125.5	$152.60^{+4.33}_{-4.33}$	4.0	$2.0^{+0.0}_{-0.0}$	$120.0^{+3.8}_{-3.9}$	$63.1^{+3.0}_{-2.8}$	1.1(117)
4FGLJ1555.3+2903	XRTJ155513.01+290328.0	$9.68^{+0.82}_{-0.82}$	3.8	$2.4^{+0.2}_{-0.1}$	$7.8^{+0.7}_{-0.7}$	$3.2^{+0.3}_{-0.3}$	1.0(16)
4FGLJ1623.7-2315	XRTJ162334.02-231745.2	$23.22^{+2.52}_{-2.52}$	29.0	$1.2^{+0.2}_{-0.2}$	$21.0^{+3.9}_{-3.8}$	$20.0^{+3.5}_{-3.0}$	0.3(9)
4FGLJ1626.5+6257	XRTJ162645.99+630048.4	$47.95^{+3.26}_{-3.26}$	2.0	$2.0^{+0.1}_{-0.1}$	$36.0^{+2.7}_{-2.7}$	$20.0^{+1.9}_{-1.8}$	1.0(23)
4FGLJ1631.8+4144	XRTJ163146.82+414631.8	$26.80^{+1.84}_{-1.84}$	0.9	$2.5^{+0.1}_{-0.1}$	$18.0^{+1.4}_{-1.4}$	$7.9^{+0.6}_{-0.7}$	1.2(23)
4FGLJ1644.8+1850	XRTJ164457.22+185151.1	$7.17^{+1.26}_{-1.26}$	8.1	$2.7^{+0.4}_{-0.4}$	$7.5^{+1.5}_{-1.5}$	$2.5^{+0.7}_{-0.6}$	1.3(2)
4FGLJ1645.0+1654	XRTJ164459.83+165512.9	$14.01^{+1.66}_{-1.66}$	6.4	$2.4^{+0.2}_{-0.2}$	$13.0^{+1.6}_{-1.6}$	$5.0^{+0.7}_{-0.7}$	1.3(8)
4FGLJ1648.1-1547	XRTJ164804.04-154704.7	$2.27^{+0.51}_{-0.51}$	30.0	2	$3.8^{+0.8}_{-0.8}$	$1.3^{+0.3}_{-0.3}$	1.1(2)
4FGLJ1648.7+4834	XRTJ164900.56+483409.2	$12.09^{+1.73}_{-1.73}$	1.7	$1.9^{+0.3}_{-0.3}$	$10.0^{+1.6}_{-1.6}$	$6.3^{+2.2}_{-1.5}$	0.5(4)
4FGLJ1657.3-6232	XRTJ165757.49-623400.2	$3.28^{+0.66}_{-0.66}$	18.0	$3.9^{+0.6}_{-0.5}$	$4.0^{+1.1}_{-1.1}$	$0.8^{+0.2}_{-0.2}$	5.2(2)
4FGLJ1700.0-0122	XRTJ170003.04-011841.5	$4.08^{+1.21}_{-1.21}$	16.0	2	$9.2^{+1.9}_{-1.6}$	$2.5^{+0.8}_{-0.7}$	0.3(14)
4FGLJ1733.4+2235	XRTJ173330.16+223608.5	$5.53^{+1.17}_{-1.17}$	6.8	2	$5.1^{+1.1}_{-1.1}$	$2.5^{+0.6}_{-0.6}$	0.2(2)
4FGLJ1752.0+3606	XRTJ175209.56+360629.8	$8.27^{+1.60}_{-1.60}$	3.2	2	$8.3^{+1.8}_{-1.8}$	$4.0^{+0.8}_{-0.8}$	0.4(2)
4FGLJ1803.1-6708	XRTJ180304.04-670734.5	$1.48^{+0.45}_{-0.45}$	7.7	$1.5^{+0.5}_{-0.5}$	$0.9^{+0.4}_{-0.3}$	$0.8^{+0.4}_{-0.3}$	0.9(20)
4FGLJ1813.7-6846	XRTJ181307.54-684706.7	$1.49^{+0.39}_{-0.39}$	11.0	2	$1.6^{+0.4}_{-0.4}$	$0.8^{+0.2}_{-0.2}$	0.5(2)
4FGLJ1816.1-3908	XRTJ181635.82-391246.1	$17.00^{+3.19}_{-3.19}$	12.0	$3.4^{+0.3}_{-0.4}$	$4.2^{+1.8}_{-1.6}$	$31.6^{+10.1}_{-9.2}$	1.4(2)
4FGLJ1818.5+2533	XRTJ181831.18+253705.4	$2.94^{+0.67}_{-0.67}$	17.0	2	$3.4^{+0.9}_{-0.9}$	$1.3^{+0.3}_{-0.3}$	-
4FGLJ1824.2+1231	XRTJ182408.91+123231.5	$7.95^{+1.54}_{-1.54}$	23.0	2	$11.0^{+2.5}_{-2.5}$	$4.0^{+0.9}_{-0.9}$	1.2(2)
4FGLJ1825.9-5614	XRTJ182644.04-561421.5	$7.96^{+1.50}_{-1.50}$	9.9	$2.2^{+0.8}_{-0.7}$	$9.1^{+1.9}_{-1.9}$	$3.2^{+2.7}_{-1.1}$	2.1(2)
4FGLJ1836.9+4439	XRTJ183703.33+443807.0	$5.86^{+1.20}_{-1.20}$	7.5	2	$2.8^{+0.9}_{-0.9}$	$1.3^{+0.4}_{-0.4}$	5.6(2)
4FGLJ1838.2+3223	XRTJ183816.84+322410.8	$4.92^{+0.87}_{-0.87}$	11.0	$0.6^{+0.3}_{-0.3}$	$2.1^{+0.7}_{-0.6}$	$6.3^{+1.8}_{-1.6}$	0.9(3)
4FGLJ1847.7-3433	XRTJ184713.08-343345.8	$13.17^{+1.96}_{-1.96}$	10.0	$1.8^{+0.3}_{-0.3}$	$15.0^{+2.7}_{-2.7}$	$7.9^{+2.3}_{-1.9}$	0.3(4)
4FGLJ1848.7-6307	XRTJ184838.07-630537.8	$5.84^{+1.30}_{-1.30}$	7.9	2	$5.5^{+1.3}_{-1.3}$	$2.5^{+0.6}_{-0.6}$	1.2(2)
4FGLJ1858.9+3636	XRTJ185917.93+362916.5	$7.43^{+1.58}_{-1.58}$	10.0	2	$12.0^{+2.5}_{-2.5}$	$5.0^{+1.0}_{-1.0}$	0.0(2)
4FGLJ1905.8+4942	XRTJ190549.31+495142.1	$4.23^{+0.92}_{-0.92}$	6.7	2	$2.0^{+0.7}_{-0.7}$	$1.0^{+0.3}_{-0.3}$	6.2(2)
4FGLJ1906.0-1718	XRTJ190624.51-171936.6	$3.60^{+0.93}_{-0.93}$	15.0	2	$4.4^{+1.4}_{-1.4}$	$2.0^{+0.6}_{-0.6}$	-
4FGLJ1906.4-1757	XRTJ190625.65-175903.7	$7.46^{+0.85}_{-0.85}$	17.0	$0.4^{+0.2}_{-0.2}$	$2.5^{+0.6}_{-0.6}$	$10.0^{+1.7}_{-1.7}$	1.0(10)
4FGLJ1912.2-3636	XRTJ191259.66-363245.4	$16.96^{+2.92}_{-2.92}$	11.0	$1.6^{+0.4}_{-0.4}$	$15.0^{+3.4}_{-3.5}$	$10.0^{+3.8}_{-2.9}$	0.6(2)
4FGLJ1928.5+5339	XRTJ192833.63+533901.3	$74.07^{+6.12}_{-6.12}$	17.0	$2.1^{+0.2}_{-0.2}$	$78.0^{+8.4}_{-8.6}$	$25.1^{+4.4}_{-3.7}$	1.9(16)
4FGLJ1955.3-5032	XRTJ195512.48-503008.8	$23.09^{+2.58}_{-2.58}$	5.0	$1.9^{+0.2}_{-0.2}$	$19.0^{+2.4}_{-2.4}$	$10.0^{+2.0}_{-1.7}$	0.8(8)
4FGLJ2007.0+0707	XRTJ200642.07+071712.5	$4.07^{+0.85}_{-0.85}$	18.0	$2.5^{+0.7}_{-0.8}$	$7.4^{+1.8}_{-1.9}$	$2.0^{+2.5}_{-0.8}$	3.1(1)
4FGLJ2017.9-0114	XRTJ201739.32-010732.4	$1.77^{+0.40}_{-0.40}$	11.0	2	$2.1^{+0.5}_{-0.5}$	$1.0^{+0.3}_{-0.3}$	2.5(2)
4FGLJ2018.0+7903	XRTJ201746.50+790238.0	$9.89^{+1.57}_{-1.57}$	11.0	$1.9^{+0.4}_{-0.4}$	$9.9^{+1.9}_{-2.0}$	$5.0^{+1.6}_{-1.3}$	0.6(3)
4FGLJ2019.6+0616	XRTJ201931.60+061543.8	$2.87^{+0.63}_{-0.63}$	15.0	2	$3.3^{+0.8}_{-0.8}$	$1.3^{+0.3}_{-0.3}$	0.5(2)
4FGLJ2029.5-4237	XRTJ202914.15-423532.1	$8.37^{+1.58}_{-1.58}$	4.2	$0.2^{+0.3}_{-0.3}$	$2.7^{+1.0}_{-0.9}$	$15.8^{+5.5}_{-4.6}$	0.8(2)
4FGLJ2030.0-0310	XRTJ203014.34-030721.9	$33.18^{+2.76}_{-2.76}$	6.7	$2.7^{+0.2}_{-0.1}$	$32.0^{+2.8}_{-2.8}$	$10.0^{+1.0}_{-0.9}$	0.6(16)
4FGLJ2036.2-0207	XRTJ203637.80-020242.3	$3.87^{+0.89}_{-0.89}$	9.8	2	$4.6^{+1.2}_{-1.2}$	$2.0^{+0.5}_{-0.5}$	-
4FGLJ2037.0-2826	XRTJ203637.90-283026.0	$6.93^{+0.88}_{-0.88}$	5.4	$1.7^{+0.2}_{-0.2}$	$5.7^{+0.8}_{-0.8}$	$3.2^{+0.6}_{-0.5}$	0.8(6)
4FGLJ2037.7-2230	XRTJ203743.50-222630.0	$3.46^{+0.57}_{-0.57}$	4.1	$1.2^{+0.6}_{-0.7}$	$11.0^{+3.5}_{-3.2}$	$12.6^{+37.5}_{-8.1}$	0.3(3)
4FGLJ2040.1-3137	XRTJ204010.16-314745.9	$6.89^{+1.18}_{-1.18}$	6.2	$1.2^{+0.5}_{-0.5}$	$4.9^{+1.7}_{-1.6}$	$5.0^{+2.4}_{-1.8}$	2.3(3)
4FGLJ2041.1-6138	XRTJ204111.84-613950.0	$9.98^{+1.46}_{-1.46}$	6.6	$2.2^{+0.3}_{-0.3}$	$10.0^{+1.6}_{-1.6}$	$4.0^{+0.8}_{-0.7}$	0.2(4)
4FGLJ2042.1-5320	XRTJ204220.33-532643.2	$58.07^{+3.97}_{-3.97}$	3.2	$2.1^{+0.1}_{-0.1}$	$46.0^{+3.4}_{-3.4}$	$20.0^{+1.9}_{-1.8}$	0.7(23)
4FGLJ2042.7+1519	XRTJ204259.73+152108.8	$34.54^{+1.17}_{-1.17}$	8.9	$2.4^{+0.1}_{-0.1}$	$41.0^{+1.5}_{-1.5}$	$15.8^{+0.7}_{-0.7}$	0.8(87)
4FGLJ2045.6+2455	XRTJ204555.08+245356.3	$1.06^{+0.19}_{-0.19}$	17.0	$1.0^{+0.3}_{-0.3}$	$0.8^{+0.2}_{-0.2}$	$1.0^{+0.3}_{-0.3}$	0.2(4)
4FGLJ2056.4-5922	XRTJ205624.41-591719.4	$2.84^{+0.80}_{-0.80}$	6.3	2	$3.2^{+1.0}_{-0.8}$	$1.6^{+0.5}_{-0.4}$	0.4(13)
4FGLJ2058.5-1833	XRTJ205836.75-183103.8	$3.06^{+0.63}_{-0.63}$	6.1	2	$2.6^{+0.6}_{-0.6}$	$1.3^{+0.3}_{-0.3}$	0.1(2)
4FGLJ2105.9+7508	XRTJ210605.68+750921.0	$5.54^{+0.86}_{-0.86}$	26.0	$2.0^{+0.3}_{-0.3}$	$7.3^{+1.5}_{-1.5}$	$2.5^{+0.7}_{-0.6}$	0.8(3)
4FGLJ2109.8+6315	XRTJ210928.72+631745.7	$8.45^{+1.35}_{-1.35}$	42.0	$4.6^{+0.4}_{-0.5}$	$35.0^{+6.5}_{-6.6}$	$2.5^{+0.5}_{-0.5}$	2.4(3)

Note. Labels are the same as in table A.4.

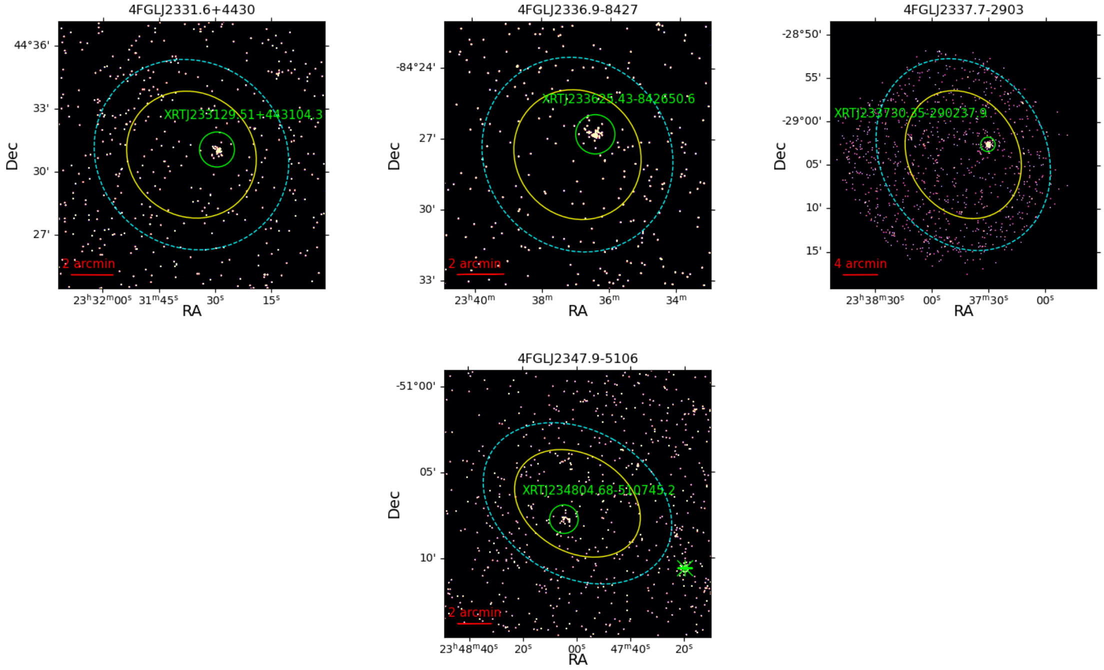

Figure A.1: Continued.

Table A.4: Results of the X-ray spectral fitting for UGS1. Continued

4FGL Name (1)	*Swift*/XRT source (2)	Count rate (3) [×10^{-3}]	nH (4) [×10^{20}]	Γ (5)	Norm. (6) 10^{-5}	absorbed flux (7) [×10^{-13}]	χ^2_ν(dof) (8)
4FGLJ2114.2+2132	XRTJ211407.79+213241.1	$21.54^{+2.21}_{-2.21}$	12.0	$2.6^{+0.2}_{-0.2}$	$24.0^{+2.6}_{-2.6}$	$6.3^{+0.8}_{-0.8}$	1.1(10)
4FGLJ2114.9-3326	XRTJ211452.16-332534.2	$40.65^{+3.04}_{-3.04}$	9.7	$2.4^{+0.1}_{-0.1}$	$45.0^{+3.6}_{-3.6}$	$15.8^{+1.5}_{-1.7}$	0.5(19)
4FGLJ2120.5-0138	XRTJ212030.54-013841.7	$14.93^{+1.44}_{-1.44}$	4.8	$2.1^{+0.2}_{-0.2}$	$14.0^{+1.5}_{-1.5}$	$6.3^{+1.1}_{-0.9}$	0.7(11)
4FGLJ2121.8-3412	XRTJ212200.61-341834.3	$6.32^{+1.24}_{-1.24}$	7.5	2	$7.4^{+1.6}_{-1.6}$	$3.2^{+0.6}_{-0.7}$	0.2(2)
4FGLJ2130.8+2649	XRTJ213011.72+264505.2	$2.73^{+0.51}_{-0.51}$	12.0	$1.8^{+0.4}_{-0.4}$	$3.1^{+0.7}_{-0.7}$	$1.6^{+0.7}_{-0.5}$	0.0(2)
4FGLJ2159.6-4620	XRTJ215936.22-461955.4	$12.74^{+1.25}_{-1.25}$	1.2	$2.6^{+0.2}_{-0.2}$	$10.0^{+1.1}_{-1.1}$	$4.0^{+0.5}_{-0.4}$	0.2(10)
4FGLJ2207.1+2222	XRTJ220704.18+222231.9	$7.95^{+1.33}_{-1.33}$	9.8	$2.9^{+0.3}_{-0.3}$	$9.3^{+1.6}_{-1.6}$	$2.5^{+0.4}_{-0.4}$	0.5(3)
4FGLJ2207.3+2746	XRTJ220722.56+274617.9	$3.90^{+0.95}_{-0.95}$	8.4	2	$6.2^{+1.6}_{-1.6}$	$2.5^{+0.7}_{-0.6}$	-
4FGLJ2225.8-0804	XRTJ222553.05-080410.8	$6.95^{+1.27}_{-1.27}$	5.2	$1.2^{+0.4}_{-0.4}$	$5.3^{+1.2}_{-1.3}$	$6.3^{+3.0}_{-2.1}$	1.8(2)
4FGLJ2237.2-6726	XRTJ223709.85-672612.7	$17.61^{+1.86}_{-1.86}$	2.9	$1.9^{+0.2}_{-0.2}$	$16.0^{+1.9}_{-1.9}$	$10.0^{+1.7}_{-1.7}$	0.8(9)
4FGLJ2240.3-5241	XRTJ224017.55-524112.3	$3.88^{+0.87}_{-0.87}$	1.3	2	$3.4^{+0.8}_{-0.8}$	$2.0^{+0.5}_{-0.4}$	0.3(2)
4FGLJ2241.4-8327	XRTJ224200.97-832746.0	$18.65^{+2.22}_{-2.22}$	13.0	$1.2^{+0.2}_{-0.2}$	$14.0^{+2.7}_{-2.7}$	$15.8^{+3.6}_{-3.3}$	0.8(7)
4FGLJ2247.7-5857	XRTJ224745.19-585458.2	$13.83^{+1.67}_{-1.67}$	1.9	$2.4^{+0.3}_{-0.3}$	$9.7^{+1.3}_{-1.3}$	$4.0^{+0.6}_{-0.6}$	1.4(7)
4FGLJ2312.4+8253	XRTJ231203.37+830108.0	$6.00^{+0.77}_{-0.77}$	16.0	$2.9^{+0.3}_{-0.3}$	$11.0^{+1.3}_{-1.3}$	$2.5^{+0.4}_{-0.4}$	0.8(7)
4FGLJ2317.7+2839	XRTJ231740.15+283955.4	$1.58^{+0.37}_{-0.37}$	8.7	2	$1.7^{+0.4}_{-0.4}$	$0.8^{+0.2}_{-0.2}$	1.1(2)
4FGLJ2320.2+0707	XRTJ232007.88+071044.0	$7.40^{+1.07}_{-1.07}$	7.6	$1.9^{+0.3}_{-0.4}$	$7.4^{+1.2}_{-1.2}$	$4.0^{+1.5}_{-1.0}$	1.9(4)
4FGLJ2323.1+2040	XRTJ232320.30+203523.6	$8.81^{+1.68}_{-1.68}$	4.9	2	$10.0^{+2.2}_{-2.2}$	$5.0^{+1.2}_{-1.1}$	1.6(2)
4FGLJ2323.9+2519	XRTJ232341.56+251800.0	$3.87^{+1.07}_{-1.07}$	5.3	2	$6.3^{+1.7}_{-1.7}$	$3.2^{+0.8}_{-0.8}$	-
4FGLJ2326.9-4130	XRTJ232653.20-412713.8	$9.41^{+2.05}_{-2.05}$	1.6	2	$5.5^{+1.6}_{-1.6}$	$3.2^{+0.9}_{-0.9}$	-
4FGLJ2331.6+4430	XRTJ233129.51+443104.3	$5.35^{+0.99}_{-0.99}$	15.0	$2.4^{+0.7}_{-0.6}$	$7.6^{+1.6}_{-1.8}$	$2.0^{+1.0}_{-0.6}$	1.4(2)
4FGLJ2336.9-8427	XRTJ233625.43-842650.6	$13.15^{+1.82}_{-1.82}$	11.0	$1.9^{+0.3}_{-0.3}$	$14.0^{+2.2}_{-2.2}$	$6.3^{+1.5}_{-1.3}$	1.0(5)
4FGLJ2337.7-2903	XRTJ233730.35-290237.9	$23.34^{+2.01}_{-2.01}$	1.8	$2.3^{+0.2}_{-0.2}$	$19.0^{+1.8}_{-1.8}$	$7.9^{+1.0}_{-0.9}$	0.9(14)
4FGLJ2347.9-5106	XRTJ234804.68-510745.2	$2.36^{+0.55}_{-0.55}$	1.4	2	$1.7^{+0.5}_{-0.5}$	$1.0^{+0.3}_{-0.3}$	-
4FGLJ2353.2+3135	XRTJ235319.12+313613.4	$3.27^{+0.37}_{-0.37}$	5.8	$1.9^{+0.2}_{-0.2}$	$3.0^{+0.4}_{-0.4}$	$1.6^{+0.3}_{-0.3}$	0.4(10)

Note. Labels are the same as in table A.4.

Table A.5: Results of the X-ray spectral fitting for UGS2.

4FGL Name (1)	*Swift*/XRT source (2)	Count rate (3) [$\times10^{-3}$]	nH (4) [$\times10^{20}$]	Γ (5)	Norm. (6) 10^{-5}	absorbed flux (7) [$\times10^{-13}$]	χ^2_ν(dof) (8)
4FGLJ0017.1-4605	XRTJ001708.63-460607.7	$6.44^{+0.84}_{-0.84}$	1.6	$1.8^{+0.3}_{-0.3}$	$5.0^{+0.7}_{-0.7}$	$3.2^{+0.7}_{-0.7}$	0.6(6)
	XRTJ001750.81-460437.5	$3.95^{+0.66}_{-0.66}$	1.6	$-0.1^{+0.5}_{-0.6}$	$1.3^{+0.5}_{-0.5}$	$12.6^{+13.1}_{-6.1}$	1.3(2)
	XRTJ001705.00-460109.2	$1.47^{+0.42}_{-0.42}$	1.6	2	$1.1^{+0.4}_{-0.4}$	$0.6^{+0.2}_{-0.2}$	-
4FGLJ0031.0-2327	XRTJ003120.53-233400.7	$44.80^{+2.08}_{-2.08}$	1.7	$1.8^{+0.1}_{-0.1}$	$34.0^{+1.8}_{-1.8}$	$20.0^{+1.4}_{-1.3}$	0.9(50)
	XRTJ003039.79-232821.2	$1.93^{+0.48}_{-0.48}$	1.7	2	$1.6^{+0.5}_{-0.5}$	$0.8^{+0.2}_{-0.2}$	-
4FGLJ0040.2-2725	XRTJ004016.42-271912.3	$22.59^{+0.83}_{-0.83}$	1.4	$2.7^{+0.1}_{-0.1}$	$16.0^{+0.6}_{-0.6}$	$6.3^{+0.3}_{-0.3}$	1.1(72)
	XRTJ004023.77-272254.2	$1.32^{+0.22}_{-0.22}$	1.4	$7.2^{+0.3}_{-0.3}$	$0.4^{+0.1}_{-0.1}$	$3.2^{+1.0}_{-0.9}$	1.0(4)
	XRTJ004026.07-272116.1	$1.51^{+0.23}_{-0.23}$	1.4	$2.5^{+0.2}_{-0.2}$	$1.3^{+0.2}_{-0.2}$	$0.5^{+0.1}_{-0.1}$	0.8(5)
	XRTJ004035.80-272240.7	$0.91^{+0.19}_{-0.19}$	1.4	$1.1^{+0.6}_{-0.6}$	$0.5^{+0.1}_{-0.2}$	$0.6^{+0.5}_{-0.3}$	2.4(2)
	XRTJ003954.35-272516.1	$0.63^{+0.16}_{-0.16}$	1.5	2	$0.4^{+0.1}_{-0.1}$	$0.3^{+0.1}_{-0.1}$	3.0(2)
4FGLJ0045.8-1324	XRTJ004602.94-132422.2	$4.00^{+0.44}_{-0.44}$	1.7	$2.2^{+0.2}_{-0.2}$	$3.3^{+0.4}_{-0.4}$	$1.6^{+0.2}_{-0.2}$	0.8(10)
	XRTJ004608.32-132213.6	$1.90^{+0.32}_{-0.32}$	1.7	$1.1^{+0.3}_{-0.3}$	$1.1^{+0.3}_{-0.3}$	$1.6^{+0.5}_{-0.4}$	1.1(4)
	XRTJ004611.48-132519.3	$1.68^{+0.30}_{-0.30}$	1.7	$1.7^{+0.4}_{-0.4}$	$1.8^{+0.3}_{-0.3}$	$1.3^{+0.8}_{-0.4}$	1.2(3)
	XRTJ004539.41-132507.7	$0.87^{+0.23}_{-0.23}$	1.7	2	$0.8^{+0.2}_{-0.2}$	$0.4^{+0.1}_{-0.1}$	0.9(2)
	XRTJ004602.97-131959.0	$0.39^{+0.20}_{-0.20}$	1.8	2	$0.5^{+0.2}_{-0.2}$	$0.3^{+0.1}_{-0.1}$	-
	XRTJ004555.20-132312.5	$0.73^{+0.22}_{-0.22}$	1.7	2	$0.6^{+0.2}_{-0.2}$	$0.3^{+0.1}_{-0.1}$	2.4(1)
4FGLJ0102.3+1000	XRTJ010226.89+095939.9	$0.47^{+0.14}_{-0.14}$	4.3	$2.4^{+0.7}_{-0.8}$	$0.6^{+0.1}_{-0.1}$	$0.3^{+0.2}_{-0.1}$	1.1(2)
	XRTJ010235.93+095832.4	$0.26^{+0.11}_{-0.11}$	4.3	2	$0.3^{+0.1}_{-0.1}$	$0.1^{+0.1}_{-0.1}$	-
	XRTJ010220.73+095848.9	$0.36^{+0.12}_{-0.12}$	4.3	2	$0.4^{+0.1}_{-0.1}$	$0.2^{+0.1}_{-0.1}$	0.5(2)
	XRTJ010214.03+100258.4	$0.39^{+0.12}_{-0.12}$	4.3	2	$0.3^{+0.1}_{-0.1}$	$0.2^{+0.1}_{-0.1}$	3.3(1)
4FGLJ0118.3-6008	XRTJ011823.22-600747.8	$3.98^{+0.70}_{-0.70}$	2.6	$2.1^{+0.4}_{-0.4}$	$3.8^{+0.7}_{-0.7}$	$2.0^{+0.8}_{-0.5}$	0.6(2)
	XRTJ011848.17-600256.2	$2.24^{+0.52}_{-0.52}$	2.7	2	$2.3^{+0.6}_{-0.6}$	$1.3^{+0.3}_{-0.3}$	-
4FGLJ0122.4+1034	XRTJ012223.64+103212.6	$31.52^{+1.22}_{-1.22}$	5.5	$2.2^{+0.1}_{-0.1}$	$27.0^{+1.1}_{-1.1}$	$10.0^{+0.5}_{-0.5}$	1.2(70)
	XRTJ012222.25+103116.2	$3.27^{+0.42}_{-0.42}$	5.5	$1.4^{+0.3}_{-0.3}$	$2.9^{+0.5}_{-0.5}$	$2.5^{+0.8}_{-0.6}$	0.7(7)
4FGLJ0126.3-6746	XRTJ012610.88-674744.5	$10.94^{+1.39}_{-1.39}$	3.2	$2.6^{+0.3}_{-0.2}$	$8.7^{+1.2}_{-1.2}$	$3.2^{+0.5}_{-0.5}$	0.8(6)
	XRTJ012622.53-674626.7	$4.07^{+0.87}_{-0.87}$	3.2	2	$3.0^{+0.7}_{-0.7}$	$1.6^{+0.4}_{-0.4}$	1.2(2)
4FGLJ0132.9-4259	XRTJ013346.96-430407.0	$3.13^{+0.14}_{-0.14}$	1.7	$1.8^{+0.1}_{-0.1}$	$2.6^{+0.1}_{-0.1}$	$1.6^{+0.1}_{-0.1}$	0.9(66)
	XRTJ013401.65-425630.0	$1.13^{+0.09}_{-0.09}$	1.8	$2.2^{+0.1}_{-0.1}$	$0.9^{+0.1}_{-0.1}$	$0.5^{+0.0}_{-0.1}$	1.0(29)
	XRTJ013339.96-425503.4	$0.63^{+0.07}_{-0.07}$	1.8	$2.0^{+0.2}_{-0.2}$	$0.5^{+0.1}_{-0.1}$	$0.3^{+0.0}_{-0.0}$	1.0(17)
	XRTJ013347.80-430229.3	$0.51^{+0.06}_{-0.06}$	1.7	$1.2^{+0.2}_{-0.2}$	$0.4^{+0.1}_{-0.1}$	$0.4^{+0.1}_{-0.1}$	1.4(14)
	XRTJ013316.63-425908.7	$0.53^{+0.08}_{-0.08}$	1.7	$1.6^{+0.3}_{-0.3}$	$0.6^{+0.1}_{-0.1}$	$0.4^{+0.1}_{-0.1}$	0.3(9)
	XRTJ013308.39-425744.6	$1.05^{+0.12}_{-0.12}$	1.7	$0.8^{+0.2}_{-0.2}$	$0.6^{+0.1}_{-0.1}$	$1.3^{+0.3}_{-0.2}$	0.9(10)
	XRTJ013359.11-430219.2	$0.16^{+0.05}_{-0.05}$	1.7	$1.2^{+0.3}_{-0.3}$	$0.1^{+0.0}_{-0.0}$	$0.2^{+0.1}_{-0.0}$	1.3(7)
	XRTJ013347.00-430610.6	$0.38^{+0.06}_{-0.06}$	1.7	$1.4^{+0.2}_{-0.2}$	$0.3^{+0.1}_{-0.1}$	$0.3^{+0.1}_{-0.1}$	1.0(8)
	XRTJ013339.30-425824.0	$0.02^{+0.04}_{-0.04}$	1.8	$1.6^{+-1.6}_{-1.6}$	$0.0^{+0.0}_{-0.0}$	$0.0^{+1.0}_{-0.0}$	0.7(2)
4FGLJ0140.4+5114	XRTJ014107.78+510659.4	$13.89^{+1.41}_{-1.41}$	28.0	$1.8^{+0.3}_{-0.2}$	$19.0^{+3.4}_{-3.3}$	$7.9^{+1.6}_{-1.5}$	1.5(11)
	XRTJ014022.50+511313.3	$10.43^{+1.14}_{-1.14}$	29.0	$1.8^{+0.2}_{-0.2}$	$14.0^{+2.2}_{-2.2}$	$6.3^{+1.3}_{-1.1}$	0.6(9)
4FGLJ0159.0+3313	XRTJ015906.95+331227.3	$9.18^{+0.42}_{-0.42}$	6.8	$3.8^{+0.1}_{-0.1}$	$4.0^{+0.3}_{-0.3}$	$1.6^{+0.1}_{-0.1}$	5.1(46)
	XRTJ015905.35+331257.8	$0.86^{+0.16}_{-0.16}$	6.8	$2.2^{+0.3}_{-0.3}$	$0.9^{+0.2}_{-0.2}$	$0.4^{+0.1}_{-0.1}$	0.8(6)
	XRTJ015927.92+331107.7	$1.16^{+0.16}_{-0.16}$	6.9	$1.4^{+0.3}_{-0.3}$	$0.8^{+0.2}_{-0.2}$	$0.6^{+0.2}_{-0.2}$	1.1(6)
4FGLJ0159.8-2234	XRTJ015947.54-223254.4	$3.05^{+0.33}_{-0.33}$	1.6	$2.6^{+0.2}_{-0.2}$	$2.4^{+0.3}_{-0.3}$	$1.0^{+0.1}_{-0.1}$	0.6(10)
	XRTJ020016.59-222940.5	$2.38^{+0.29}_{-0.29}$	1.6	$1.7^{+0.3}_{-0.3}$	$2.0^{+0.3}_{-0.3}$	$1.3^{+0.3}_{-0.3}$	0.7(7)
	XRTJ015957.01-223136.3	$1.62^{+0.26}_{-0.26}$	1.6	$1.6^{+0.3}_{-0.4}$	$1.8^{+0.3}_{-0.3}$	$1.3^{+0.7}_{-0.4}$	2.0(5)
4FGLJ0209.8+2626	XRTJ020946.75+262530.4	$54.23^{+2.68}_{-2.68}$	6.3	$1.9^{+0.1}_{-0.1}$	$44.0^{+2.4}_{-2.4}$	$20.0^{+1.4}_{-1.3}$	0.9(45)
	XRTJ020950.60+263253.3	$6.19^{+0.94}_{-0.94}$	6.2	$1.4^{+0.3}_{-0.3}$	$5.0^{+1.0}_{-1.0}$	$4.0^{+1.1}_{-1.0}$	1.1(4)
4FGLJ0240.2-0248	XRTJ024002.02-024321.6	$14.33^{+1.07}_{-1.07}$	2.9	$1.9^{+0.1}_{-0.1}$	$12.0^{+1.0}_{-1.0}$	$6.3^{+0.8}_{-0.7}$	0.8(20)
	XRTJ024004.57-024504.3	$12.89^{+1.01}_{-1.01}$	2.9	$1.8^{+0.1}_{-0.1}$	$10.0^{+0.9}_{-0.9}$	$6.3^{+0.8}_{-0.7}$	0.9(18)
	XRTJ024024.23-025336.4	$3.91^{+0.81}_{-0.81}$	2.8	2	$2.9^{+0.8}_{-0.8}$	$1.6^{+0.5}_{-0.4}$	4.7(2)
4FGLJ0251.4+4646	XRTJ025027.22+464729.1	$52.30^{+1.84}_{-1.84}$	24.0	$-5.2^{+0.1}_{-0.1}$	$8.9^{+0.7}_{-0.7}$	$79.4^{+3.7}_{-3.6}$	2.0(92)
	XRTJ025117.49+464501.7	$1.92^{+0.37}_{-0.37}$	23.0	$1.7^{+0.5}_{-0.5}$	$2.6^{+0.8}_{-0.9}$	$1.3^{+0.6}_{-0.4}$	1.1(2)
4FGLJ0252.0-3657	XRTJ025139.26-365715.2	$2.83^{+0.28}_{-0.28}$	2.5	$1.7^{+0.1}_{-0.1}$	$2.2^{+0.2}_{-0.2}$	$1.6^{+0.2}_{-0.2}$	1.1(15)
	XRTJ025149.15-370144.5	$1.34^{+0.21}_{-0.21}$	2.5	$1.7^{+0.3}_{-0.3}$	$1.1^{+0.2}_{-0.2}$	$0.8^{+0.2}_{-0.2}$	0.6(6)
	XRTJ025145.81-365713.8	$1.23^{+0.20}_{-0.20}$	2.5	$0.8^{+0.2}_{-0.2}$	$0.5^{+0.1}_{-0.1}$	$1.0^{+0.2}_{-0.2}$	2.9(6)
	XRTJ025207.48-365438.4	$0.89^{+0.17}_{-0.17}$	2.5	$1.3^{+0.4}_{-0.5}$	$0.7^{+0.2}_{-0.2}$	$0.6^{+0.5}_{-0.2}$	0.5(3)
4FGLJ0447.2+2446	XRTJ044739.31+244227.7	$3.95^{+0.83}_{-0.83}$	35.0	2	$5.1^{+1.3}_{-1.3}$	$1.6^{+0.4}_{-0.4}$	2.5(2)
	XRTJ044709.75+243701.5	$3.05^{+0.71}_{-0.71}$	35.0	2	$4.5^{+1.4}_{-1.4}$	$1.6^{+0.5}_{-0.5}$	-
4FGLJ0535.3+0934	XRTJ053512.72+093645.2	$10.78^{+1.65}_{-1.65}$	33.0	$4.1^{+0.6}_{-0.6}$	$39.0^{+10.0}_{-9.8}$	$4.0^{+1.5}_{-1.0}$	1.3(3)
	XRTJ053447.47+094026.3	$9.70^{+1.56}_{-1.56}$	33.0	$2.8^{+0.5}_{-0.5}$	$22.0^{+4.5}_{-4.7}$	$4.0^{+1.5}_{-1.0}$	0.7(3)
	XRTJ053508.19+094254.2	$7.58^{+1.38}_{-1.38}$	33.0	$2.8^{+0.5}_{-0.5}$	$17.0^{+4.2}_{-4.4}$	$3.2^{+1.1}_{-0.8}$	1.4(2)
4FGLJ0539.2-6333	XRTJ053842.39-632820.0	$21.49^{+1.80}_{-1.80}$	4.5	$2.2^{+0.1}_{-0.1}$	$19.0^{+1.7}_{-1.7}$	$7.9^{+0.8}_{-0.9}$	0.7(16)
	XRTJ054002.73-633214.6	$2.48^{+0.64}_{-0.64}$	5.2	2	$2.7^{+0.7}_{-0.7}$	$1.3^{+0.3}_{-0.3}$	-
4FGLJ0544.8+5209	XRTJ054424.68+521515.7	$4.14^{+0.81}_{-0.81}$	30.0	2	$7.4^{+1.6}_{-1.6}$	$2.5^{+0.5}_{-0.6}$	0.6(2)
	XRTJ054457.19+520852.8	$3.34^{+0.74}_{-0.74}$	30.0	2	$6.8^{+1.8}_{-1.8}$	$2.5^{+0.7}_{-0.7}$	-

Note. Labels are the same as in table A.4.

Table A.5: Results of the X-ray spectral fitting for UGS2. Continued

4FGL Name (1)	*Swift*/XRT source (2)	Count rate (3) [$\times10^{-3}$]	nH (4) [$\times10^{20}$]	Γ (5)	Norm. (6) 10^{-5}	absorbed flux (7) [$\times10^{-13}$]	χ^2_ν(dof) (8)
4FGLJ0546.5-1100	XRTJ054730.24-112151.5	$0.91^{+0.13}_{-0.13}$	28.0	$3.8^{+0.3}_{-0.3}$	$2.2^{+0.3}_{-0.3}$	$0.3^{+0.0}_{-0.0}$	2.6(6)
	XRTJ054631.01-112023.3	$0.57^{+0.10}_{-0.10}$	27.0	$1.1^{+0.3}_{-0.3}$	$0.6^{+0.2}_{-0.2}$	$0.8^{+0.2}_{-0.2}$	0.7(4)
	XRTJ054719.62-110938.9	$0.34^{+0.09}_{-0.09}$	29.0	$2.8^{+0.5}_{-0.6}$	$0.9^{+0.2}_{-0.2}$	$0.2^{+0.1}_{-0.0}$	0.3(2)
	XRTJ054706.34-112139.1	$0.39^{+0.09}_{-0.09}$	28.0	$1.8^{+0.6}_{-0.6}$	$0.6^{+0.2}_{-0.2}$	$0.3^{+0.2}_{-0.1}$	0.0(2)
	XRTJ054649.72-111754.3	$0.24^{+0.08}_{-0.08}$	28.0	$0.9^{+0.7}_{-0.9}$	$0.2^{+0.1}_{-0.1}$	$0.3^{+0.3}_{-0.2}$	2.3(1)
	XRTJ054628.95-112059.0	$0.25^{+0.08}_{-0.08}$	27.0	2	$0.3^{+0.1}_{-0.1}$	$0.1^{+0.1}_{-0.1}$	3.0(2)
	XRTJ054632.75-110505.3	$0.39^{+0.11}_{-0.11}$	28.0	2	$0.6^{+0.2}_{-0.2}$	$0.3^{+0.1}_{-0.1}$	-
	XRTJ054736.04-111141.3	$0.10^{+0.06}_{-0.06}$	29.0	2	$0.1^{+0.1}_{-0.1}$	$0.0^{+0.0}_{-0.0}$	-
4FGLJ0610.8-4911	XRTJ061100.18-491036.2	$50.03^{+2.59}_{-2.59}$	4.5	$2.0^{+0.1}_{-0.1}$	$39.0^{+2.2}_{-2.2}$	$20.0^{+1.4}_{-1.3}$	0.9(40)
	XRTJ061031.81-491222.5	$4.50^{+0.81}_{-0.81}$	4.4	$1.3^{+0.5}_{-0.6}$	$5.6^{+1.1}_{-1.1}$	$6.3^{+8.8}_{-3.2}$	1.9(2)
4FGLJ0611.5-2918	XRTJ061141.70-291618.0	$6.25^{+1.27}_{-1.27}$	3.0	2	$6.0^{+1.3}_{-1.3}$	$3.2^{+0.6}_{-0.7}$	0.6(2)
	XRTJ061216.02-291702.3	$4.35^{+1.07}_{-1.07}$	2.9	2	$4.9^{+1.3}_{-1.3}$	$2.5^{+0.7}_{-0.6}$	-
4FGLJ0617.6-4028	XRTJ061646.98-402143.4	$327.80^{+9.33}_{-9.33}$	8.6	$1.3^{+0.0}_{-0.0}$	$370.0^{+14.0}_{-14.0}$	$316.2^{+14.9}_{-14.2}$	0.8(126)
	XRTJ061724.11-402212.8	$4.04^{+0.82}_{-0.82}$	8.6	$2.7^{+0.5}_{-0.5}$	$3.8^{+0.9}_{-1.0}$	$1.3^{+0.4}_{-0.3}$	4.8(2)
	XRTJ061818.54-403400.9	$2.89^{+0.77}_{-0.77}$	8.2	2	$2.6^{+0.8}_{-0.8}$	$1.3^{+0.4}_{-0.4}$	-
4FGLJ0633.9+5840	XRTJ063359.74+584034.2	$2.05^{+0.50}_{-0.50}$	7.8	2	$2.4^{+0.6}_{-0.6}$	$1.0^{+0.3}_{-0.3}$	-
	XRTJ063342.26+584642.7	$1.79^{+0.46}_{-0.46}$	7.7	2	$1.7^{+0.5}_{-0.5}$	$0.8^{+0.2}_{-0.2}$	-
4FGLJ0639.1-8009	XRTJ064059.59-801126.2	$6.81^{+0.37}_{-0.37}$	20.0	$1.8^{+0.1}_{-0.1}$	$8.0^{+0.6}_{-0.6}$	$4.0^{+0.4}_{-0.4}$	1.0(42)
	XRTJ063617.46-801350.5	$2.41^{+0.22}_{-0.22}$	19.0	$0.5^{+0.1}_{-0.2}$	$0.8^{+0.2}_{-0.2}$	$3.2^{+0.5}_{-0.5}$	2.4(15)
	XRTJ064125.96-801048.5	$0.86^{+0.14}_{-0.14}$	20.0	$1.5^{+0.4}_{-0.4}$	$1.2^{+0.3}_{-0.3}$	$0.8^{+0.3}_{-0.2}$	0.0(4)
	XRTJ063719.22-801230.2	$0.34^{+0.10}_{-0.10}$	19.0	2	$0.2^{+0.1}_{-0.1}$	$0.1^{+0.0}_{-0.0}$	4.3(2)
	XRTJ064012.99-801725.0	$0.39^{+0.11}_{-0.11}$	20.0	$1.4^{+0.6}_{-0.6}$	$0.4^{+0.2}_{-0.2}$	$0.3^{+0.2}_{-0.1}$	0.6(1)
	XRTJ063555.23-800813.0	$0.50^{+0.11}_{-0.11}$	19.0	$0.9^{+0.5}_{-0.6}$	$0.5^{+0.2}_{-0.2}$	$0.8^{+0.6}_{-0.3}$	0.9(2)
	XRTJ064047.38-802414.7	$0.68^{+0.15}_{-0.15}$	20.0	$1.6^{+0.5}_{-0.5}$	$0.8^{+0.3}_{-0.3}$	$0.5^{+0.2}_{-0.2}$	0.1(1)
	XRTJ063641.31-801124.9	$0.22^{+0.09}_{-0.09}$	19.0	2	$0.2^{+0.1}_{-0.1}$	$0.1^{+0.0}_{-0.0}$	-
	XRTJ064049.32-801255.8	$0.35^{+0.10}_{-0.10}$	20.0	2	$0.4^{+0.1}_{-0.1}$	$0.2^{+0.1}_{-0.1}$	3.1(2)
4FGLJ0723.9+5702	XRTJ072351.47+565734.6	$9.84^{+1.31}_{-1.31}$	6.1	$2.1^{+0.4}_{-0.4}$	$9.0^{+1.3}_{-1.4}$	$4.0^{+1.5}_{-1.0}$	1.5(5)
	XRTJ072328.63+565908.8	$3.04^{+0.76}_{-0.76}$	6.0	2	$4.6^{+1.3}_{-1.3}$	$2.0^{+0.6}_{-0.5}$	-
4FGLJ0737.4+6535	XRTJ073655.73+653540.7	$7.55^{+0.34}_{-0.34}$	5.0	$1.4^{+0.1}_{-0.1}$	$5.1^{+0.3}_{-0.3}$	$4.0^{+0.3}_{-0.3}$	1.3(63)
	XRTJ073711.73+653344.9	$1.11^{+0.14}_{-0.14}$	4.9	$0.3^{+0.2}_{-0.3}$	$0.5^{+0.1}_{-0.1}$	$2.0^{+0.6}_{-0.5}$	2.2(9)
4FGLJ0738.6+1311	XRTJ073843.59+131328.3	$6.20^{+1.09}_{-1.09}$	6.2	$2.0^{+0.5}_{-0.5}$	$6.5^{+1.4}_{-1.4}$	$3.2^{+2.2}_{-1.1}$	3.1(2)
	XRTJ073848.93+130755.1	$3.37^{+0.80}_{-0.80}$	6.0	2	$3.9^{+1.1}_{-1.1}$	$2.0^{+0.5}_{-0.5}$	-
4FGLJ0751.2-0029	XRTJ075119.15-002749.0	$1.10^{+0.14}_{-0.14}$	6.0	$2.0^{+0.2}_{-0.2}$	$1.40^{+0.18}_{-0.18}$	$0.6^{+0.1}_{-0.1}$	1.4(15)
	XRTJ075104.16-003305.6	$0.37^{+0.08}_{-0.08}$	6.5	$0.5^{+0.3}_{-0.4}$	$0.2^{+0.1}_{-0.1}$	$0.6^{+0.2}_{-0.2}$	0.7(3)
4FGLJ0800.1-5531	XRTJ075949.42-553253.8	$3.21^{+0.66}_{-0.66}$	24.0	2	$4.5^{+1.0}_{-1.0}$	$1.6^{+0.3}_{-0.4}$	0.3(2)
	XRTJ080013.52-553407.9	$2.92^{+0.63}_{-0.63}$	24.0	2	$3.8^{+0.9}_{-0.9}$	$1.6^{+0.4}_{-0.4}$	1.4(2)
4FGLJ0849.5+2710	XRTJ084957.80+271614.1	$2.70^{+0.62}_{-0.62}$	4.0	2	$1.3^{+0.5}_{-0.5}$	$0.6^{+0.2}_{-0.2}$	-
	XRTJ084936.07+270127.6	$2.38^{+0.59}_{-0.59}$	3.9	2	$2.7^{+0.7}_{-0.7}$	$1.3^{+0.3}_{-0.3}$	-
4FGLJ0903.5+4057	XRTJ090314.64+405600.2	$21.78^{+1.06}_{-1.06}$	1.6	$2.0^{+0.1}_{-0.1}$	$17.0^{+0.9}_{-0.9}$	$7.9^{+0.6}_{-0.5}$	0.9(47)
	XRTJ090342.94+405501.1	$2.71^{+0.39}_{-0.39}$	1.6	$2.0^{+0.3}_{-0.3}$	$2.4^{+0.4}_{-0.4}$	$1.3^{+0.4}_{-0.3}$	0.4(4)
4FGLJ0949.8+7551	XRTJ095017.79+754457.7	$6.12^{+0.95}_{-0.95}$	2.7	$1.6^{+0.5}_{-0.5}$	$4.9^{+0.9}_{-0.9}$	$4.0^{+2.3}_{-1.4}$	0.9(3)
	XRTJ095133.13+754839.3	$2.71^{+0.66}_{-0.66}$	2.8	2	$3.4^{+0.9}_{-0.9}$	$1.6^{+0.4}_{-0.4}$	0.3(1)
4FGLJ0952.9+1351	XRTJ095250.40+135218.5	$8.15^{+0.97}_{-0.97}$	3.0	$2.5^{+0.2}_{-0.2}$	$6.9^{+0.9}_{-0.9}$	$3.2^{+0.5}_{-0.4}$	0.2(6)
	XRTJ095245.55+134723.6	$12.20^{+1.20}_{-1.20}$	3.0	$2.0^{+0.2}_{-0.2}$	$9.0^{+1.0}_{-1.0}$	$5.0^{+0.9}_{-0.7}$	2.4(11)
4FGLJ0958.6-0522	XRTJ095833.81-052139.9	$33.71^{+3.23}_{-3.23}$	3.3	$1.9^{+0.2}_{-0.2}$	$32.0^{+3.2}_{-3.2}$	$15.8^{+2.8}_{-2.4}$	0.4(11)
	XRTJ095813.64-052441.3	$8.01^{+1.88}_{-1.88}$	3.4	$2.7^{+0.5}_{-0.5}$	$6.9^{+1.5}_{-1.6}$	$2.5^{+0.7}_{-0.6}$	0.1(1)
4FGLJ1008.2-1000	XRTJ100848.62-095450.2	$261.20^{+5.41}_{-5.41}$	6.6	$2.0^{+0.0}_{-0.0}$	$290.0^{+6.9}_{-6.9}$	$125.9^{+2.9}_{-2.9}$	1.2(200)
	XRTJ100802.55-095919.3	$6.67^{+0.91}_{-0.91}$	6.7	$1.6^{+0.2}_{-0.2}$	$5.5^{+0.9}_{-0.9}$	$4.0^{+0.8}_{-0.8}$	0.9(5)
	XRTJ100749.49-094911.9	$3.43^{+0.67}_{-0.67}$	6.8	2	$4.0^{+0.9}_{-0.9}$	$2.0^{+0.4}_{-0.4}$	0.9(2)
4FGLJ1018.1-2705	XRTJ101750.36-270552.8	$34.23^{+2.01}_{-2.01}$	7.6	$1.6^{+0.1}_{-0.1}$	$27.0^{+2.1}_{-2.1}$	$20.0^{+1.9}_{-1.8}$	0.8(32)
	XRTJ101801.35-271234.0	$1.63^{+0.49}_{-0.49}$	7.5	2	$2.1^{+0.6}_{-0.6}$	$1.0^{+0.3}_{-0.3}$	-
4FGLJ1018.1-4051	XRTJ101807.55-404407.6	$4.31^{+0.80}_{-0.80}$	17.0	$2.4^{+0.5}_{-0.5}$	$6.0^{+1.3}_{-1.4}$	$1.6^{+0.7}_{-0.4}$	0.7(2)
	XRTJ101801.63-405519.5	$4.20^{+0.78}_{-0.78}$	17.0	$2.5^{+0.7}_{-0.6}$	$5.6^{+1.3}_{-1.5}$	$1.6^{+0.7}_{-0.4}$	1.4(2)
	XRTJ101725.04-404436.3	$3.39^{+0.77}_{-0.77}$	18.0	2	$5.4^{+1.3}_{-1.3}$	$2.0^{+0.5}_{-0.4}$	0.8(2)
	XRTJ101717.29-404759.7	$3.63^{+0.78}_{-0.78}$	18.0	2	$5.2^{+1.2}_{-1.2}$	$2.0^{+0.5}_{-0.4}$	1.1(2)
	XRTJ101820.43-404813.8	$2.43^{+0.62}_{-0.62}$	17.0	2	$2.6^{+0.8}_{-0.8}$	$1.0^{+0.3}_{-0.3}$	-
4FGLJ1036.5-1809	XRTJ103610.62-181315.4	$2.37^{+0.50}_{-0.50}$	5.6	2	$2.9^{+0.7}_{-0.7}$	$1.3^{+0.3}_{-0.3}$	1.8(2)
	XRTJ103625.96-180011.3	$2.03^{+0.45}_{-0.45}$	5.7	2	$2.3^{+0.5}_{-0.5}$	$1.0^{+0.2}_{-0.2}$	0.9(2)

Note. Labels are the same as in table A.4.

Table A.5: Results of the X-ray spectral fitting for UGS2. Continued

4FGL Name (1)	*Swift*/XRT source (2)	Count rate (3) $[\times10^{-3}]$	nH (4) $[\times10^{20}]$	Γ (5)	Norm. (6) 10^{-5}	absorbed flux (7) $[\times10^{-13}]$	χ^2_ν(dof) (8)
4FGLJ1106.7+3623	XRTJ110622.38+363319.7	$3.31^{+0.41}_{-0.41}$	2.4	$2.4^{+0.3}_{-0.3}$	$3.1^{+0.4}_{-0.4}$	$1.3^{+0.2}_{-0.2}$	0.6(6)
	XRTJ110710.07+361655.1	$4.30^{+0.89}_{-0.89}$	2.4	2	$3.3^{+0.8}_{-0.8}$	$1.6^{+0.4}_{-0.4}$	2.4(2)
	XRTJ110635.95+362648.9	$3.35^{+0.41}_{-0.41}$	2.4	$1.0^{+0.3}_{-0.3}$	$1.8^{+0.4}_{-0.4}$	$3.2^{+1.1}_{-0.9}$	1.3(7)
	XRTJ110612.40+363126.6	$2.88^{+0.42}_{-0.42}$	2.6	$1.5^{+0.2}_{-0.2}$	$2.4^{+0.4}_{-0.4}$	$2.0^{+0.6}_{-0.5}$	1.6(4)
4FGLJ1111.4+0137	XRTJ111114.26+013427.6	$46.02^{+3.29}_{-3.29}$	4.3	$1.9^{+0.1}_{-0.1}$	$37.0^{+3.0}_{-3.0}$	$20.0^{+1.9}_{-2.2}$	0.7(22)
	XRTJ111206.06+013526.7	$8.80^{+1.46}_{-1.46}$	4.5	$1.1^{+0.4}_{-0.4}$	$7.9^{+1.7}_{-1.7}$	$10.0^{+5.8}_{-3.7}$	0.6(2)
	XRTJ111159.79+013642.6	$5.67^{+1.19}_{-1.19}$	4.5	2	$3.4^{+1.0}_{-1.0}$	$1.6^{+0.5}_{-0.4}$	4.7(2)
	XRTJ111106.07+014559.8	$5.63^{+1.17}_{-1.17}$	4.2	2	$6.6^{+1.4}_{-1.4}$	$3.2^{+0.7}_{-0.7}$	0.7(2)
4FGLJ1126.0-5007	XRTJ112624.22-500806.5	$21.32^{+0.86}_{-0.86}$	16.0	$1.9^{+0.1}_{-0.1}$	$22.0^{+1.1}_{-1.1}$	$10.0^{+0.5}_{-0.5}$	1.1(72)
	XRTJ112628.32-500842.8	$4.29^{+0.41}_{-0.41}$	16.0	$1.8^{+0.1}_{-0.1}$	$4.6^{+0.5}_{-0.5}$	$2.5^{+0.3}_{-0.3}$	1.0(16)
	XRTJ112533.68-500549.2	$1.37^{+0.24}_{-0.24}$	16.0	$2.3^{+0.4}_{-0.5}$	$2.1^{+0.4}_{-0.4}$	$0.6^{+0.2}_{-0.2}$	0.9(3)
	XRTJ112605.11-501020.5	$0.37^{+0.16}_{-0.16}$	16.0	2	$0.3^{+0.2}_{-0.2}$	$0.1^{+0.1}_{-0.1}$	-
4FGLJ1151.2-2929	XRTJ115118.17-292744.4	$21.53^{+2.59}_{-2.59}$	6.2	$2.3^{+0.3}_{-0.3}$	$21.0^{+2.7}_{-2.7}$	$7.9^{+1.8}_{-1.5}$	0.7(6)
	XRTJ115110.12-292917.2	$5.22^{+1.32}_{-1.32}$	6.2	2	$9.7^{+2.6}_{-2.6}$	$5.0^{+1.3}_{-1.3}$	-
4FGLJ1224.6+7011	XRTJ122502.59+702038.4	$4.68^{+0.50}_{-0.50}$	1.9	$2.0^{+0.2}_{-0.2}$	$3.6^{+0.4}_{-0.4}$	$2.0^{+0.3}_{-0.3}$	0.9(10)
	XRTJ122457.12+700723.3	$7.28^{+1.15}_{-1.15}$	2.0	$2.0^{+0.3}_{-0.3}$	$5.4^{+1.0}_{-1.0}$	$3.2^{+0.7}_{-0.7}$	1.8(3)
	XRTJ122531.06+701250.5	$0.79^{+0.22}_{-0.22}$	2.0	2	$0.8^{+0.2}_{-0.2}$	$0.4^{+0.1}_{-0.1}$	-
4FGLJ1243.7+1727	XRTJ124326.39+172935.9	$13.69^{+1.28}_{-1.28}$	1.8	$1.9^{+0.2}_{-0.2}$	$9.5^{+1.0}_{-1.1}$	$5.0^{+0.7}_{-0.7}$	1.1(12)
	XRTJ124351.64+172643.2	$2.88^{+0.57}_{-0.57}$	1.8	$3.0^{+0.6}_{-0.6}$	$2.2^{+0.6}_{-0.6}$	$1.0^{+0.2}_{-0.2}$	1.7(2)
4FGLJ1326.0+3507	XRTJ132544.62+350442.7	$4.68^{+0.67}_{-0.67}$	1.0	$1.4^{+0.3}_{-0.3}$	$3.2^{+0.6}_{-0.6}$	$3.2^{+1.0}_{-0.8}$	1.0(5)
	XRTJ132608.87+350836.9	$4.22^{+0.63}_{-0.63}$	1.0	$2.3^{+0.3}_{-0.3}$	$2.5^{+0.5}_{-0.5}$	$1.3^{+0.3}_{-0.3}$	3.6(3)
	XRTJ132622.45+350622.4	$3.51^{+0.59}_{-0.59}$	1.0	$2.7^{+0.4}_{-0.4}$	$2.4^{+0.5}_{-0.5}$	$1.0^{+0.2}_{-0.2}$	0.5(2)
4FGLJ1336.5-4655	XRTJ133618.81-465738.9	$15.75^{+0.87}_{-0.87}$	14.0	$2.9^{+0.1}_{-0.1}$	$22.0^{+1.3}_{-1.3}$	$5.0^{+0.4}_{-0.3}$	1.1(37)
	XRTJ133548.08-465905.6	$1.22^{+0.27}_{-0.27}$	14.0	$1.9^{+0.4}_{-0.4}$	$1.5^{+0.4}_{-0.4}$	$0.6^{+0.2}_{-0.2}$	1.2(2)
4FGLJ1407.7-3017	XRTJ140806.82-302353.7	$142.30^{+2.45}_{-2.45}$	4.4	$1.5^{+0.0}_{-0.0}$	$99.0^{+2.5}_{-2.6}$	$79.4^{+1.9}_{-1.8}$	2.2(272)
	XRTJ140759.93-303047.2	$3.84^{+0.43}_{-0.43}$	4.4	$2.3^{+0.2}_{-0.2}$	$4.2^{+0.5}_{-0.5}$	$1.6^{+0.2}_{-0.2}$	1.3(10)
4FGLJ1408.6-2917	XRTJ140809.87-292241.0	$4.24^{+0.76}_{-0.76}$	4.4	$1.9^{+0.5}_{-0.5}$	$5.4^{+1.0}_{-1.0}$	$3.2^{+2.1}_{-1.0}$	0.4(2)
	XRTJ140807.26-291615.1	$2.82^{+0.69}_{-0.69}$	4.4	2	$2.4^{+0.7}_{-0.7}$	$1.3^{+0.4}_{-0.4}$	-
	XRTJ140826.77-292222.7	$1.53^{+0.41}_{-0.41}$	4.4	2	$1.5^{+0.5}_{-0.5}$	$0.8^{+0.3}_{-0.3}$	-
4FGLJ1438.0+0219	XRTJ143809.82+021804.1	$2.61^{+0.35}_{-0.35}$	3.3	$1.6^{+0.3}_{-0.3}$	$2.2^{+0.4}_{-0.4}$	$1.6^{+0.5}_{-0.4}$	1.3(7)
	XRTJ143743.99+021934.5	$1.75^{+0.53}_{-0.53}$	3.2	2	$1.7^{+0.5}_{-0.5}$	$0.8^{+0.2}_{-0.2}$	-
4FGLJ1444.8+3645	XRTJ144529.77+364615.6	$3.40^{+0.77}_{-0.77}$	1.1	2	$2.6^{+0.7}_{-0.7}$	$1.6^{+0.5}_{-0.4}$	-
	XRTJ144401.00+364415.3	$3.63^{+0.80}_{-0.80}$	1.1	2	$3.3^{+0.8}_{-0.8}$	$1.6^{+0.4}_{-0.4}$	1.5(2)
4FGLJ1452.0-4148	XRTJ145149.46-414503.3	$40.68^{+2.04}_{-2.04}$	11.0	$2.4^{+0.1}_{-0.1}$	$44.0^{+2.4}_{-2.4}$	$15.8^{+1.1}_{-1.1}$	1.0(46)
	XRTJ145224.64-414953.4	$2.62^{+0.60}_{-0.60}$	11.0	$2.9^{+0.6}_{-0.6}$	$3.5^{+0.8}_{-0.8}$	$1.0^{+0.3}_{-0.2}$	0.8(2)
4FGLJ1454.3-3946	XRTJ145411.28-395523.4	$15.95^{+2.24}_{-2.24}$	9.9	$2.6^{+0.3}_{-0.3}$	$19.0^{+3.1}_{-3.2}$	$6.3^{+1.6}_{-1.3}$	1.7(4)
	XRTJ145347.13-394451.0	$10.68^{+1.87}_{-1.87}$	10.0	$2.0^{+0.6}_{-0.7}$	$16.0^{+3.8}_{-3.9}$	$7.9^{+10.3}_{-3.7}$	3.3(2)
4FGLJ1504.6+4343	XRTJ150425.17+434105.0	$27.16^{+2.18}_{-2.18}$	1.6	$1.8^{+0.1}_{-0.1}$	$18.0^{+1.6}_{-1.6}$	$10.0^{+1.2}_{-1.1}$	1.0(16)
	XRTJ150507.23+435002.6	$25.08^{+2.21}_{-2.21}$	1.6	$1.8^{+0.2}_{-0.2}$	$20.0^{+2.0}_{-2.0}$	$12.6^{+1.9}_{-1.6}$	1.2(14)
4FGLJ1513.0-3118	XRTJ151244.55-311650.1	$30.31^{+3.08}_{-3.08}$	16.0	$3.0^{+0.2}_{-0.2}$	$46.0^{+4.9}_{-4.9}$	$10.0^{+1.2}_{-1.3}$	0.7(10)
	XRTJ151258.83-311746.4	$4.74^{+1.28}_{-1.28}$	16.0	2	$13.0^{+3.5}_{-3.5}$	$5.0^{+1.4}_{-1.4}$	-
4FGLJ1514.8+4448	XRTJ151436.48+445002.0	$2.44^{+0.42}_{-0.42}$	2.3	$1.1^{+0.4}_{-0.4}$	$1.4^{+0.3}_{-0.3}$	$2.0^{+1.0}_{-0.7}$	1.5(2)
	XRTJ151451.10+444953.1	$2.23^{+0.40}_{-0.40}$	2.3	$2.0^{+0.5}_{-0.5}$	$1.8^{+0.4}_{-0.4}$	$1.0^{+0.4}_{-0.3}$	1.0(2)
4FGLJ1517.7-4446	XRTJ151727.58-444254.5	$7.23^{+1.27}_{-1.27}$	21.0	$2.3^{+0.6}_{-0.6}$	$10.0^{+2.2}_{-2.3}$	$3.2^{+1.8}_{-1.0}$	0.5(2)
	XRTJ151810.81-444734.7	$4.28^{+1.01}_{-1.01}$	21.0	2	$23.0^{+6.6}_{-6.6}$	$10.0^{+2.9}_{-2.8}$	1.6(1)
4FGLJ1557.2+3822	XRTJ155712.37+382030.2	$7.20^{+0.91}_{-0.91}$	1.5	$2.1^{+0.2}_{-0.2}$	$5.5^{+0.8}_{-0.8}$	$2.5^{+0.4}_{-0.4}$	1.1(6)
	XRTJ155656.77+382825.8	$2.32^{+0.53}_{-0.53}$	1.4	2	$1.8^{+0.4}_{-0.4}$	$1.0^{+0.3}_{-0.2}$	1.9(2)
4FGLJ1637.5+3005	XRTJ163739.22+301009.3	$11.24^{+1.11}_{-1.11}$	2.1	$0.1^{+0.2}_{-0.2}$	$2.5^{+0.5}_{-0.5}$	$15.8^{+2.8}_{-2.4}$	1.8(11)
	XRTJ163738.33+300503.1	$4.11^{+0.68}_{-0.68}$	2.1	$1.8^{+0.3}_{-0.3}$	$3.2^{+0.6}_{-0.6}$	$2.0^{+0.5}_{-0.4}$	0.7(3)
	XRTJ163727.99+300954.6	$2.32^{+0.52}_{-0.52}$	2.0	2	$2.0^{+0.5}_{-0.5}$	$1.0^{+0.2}_{-0.2}$	0.5(2)
	XRTJ163647.31+300555.1	$1.74^{+0.46}_{-0.46}$	2.0	2	$1.6^{+0.5}_{-0.5}$	$0.8^{+0.2}_{-0.2}$	-
	XRTJ163735.81+301310.8	$2.26^{+0.51}_{-0.51}$	2.0	2	$2.4^{+0.6}_{-0.6}$	$1.3^{+0.3}_{-0.3}$	0.0(1)
4FGLJ1651.7-7241	XRTJ165151.61-724308.5	$13.26^{+1.66}_{-1.66}$	8.6	$1.1^{+0.2}_{-0.2}$	$6.4^{+1.2}_{-1.2}$	$7.9^{+1.6}_{-1.5}$	2.6(7)
	XRTJ165139.31-724639.6	$3.36^{+0.90}_{-0.90}$	8.4	2	$4.2^{+1.2}_{-1.2}$	$2.0^{+0.6}_{-0.5}$	-
4FGLJ1821.6+6636	XRTJ182108.75+663542.0	$3.10^{+0.51}_{-0.51}$	5.5	$1.7^{+0.5}_{-0.6}$	$2.0^{+0.5}_{-0.6}$	$1.3^{+0.6}_{-0.4}$	1.8(3)
	XRTJ182204.70+663715.0	$1.46^{+0.36}_{-0.36}$	5.8	2	$1.8^{+0.4}_{-0.4}$	$0.8^{+0.2}_{-0.2}$	0.1(2)

Note. Labels are the same as in table A.4.

Table A.5: Results of the X-ray spectral fitting for UGS2. Continued

4FGL Name (1)	*Swift*/XRT source (2)	Count rate (3)	nH (4)	Γ (5)	Norm. (6)	absorbed flux (7)	χ^2_ν(dof) (8)
		[$\times10^{-3}$]	[$\times10^{20}$]		10^{-5}	[$\times10^{-13}$]	
4FGLJ1845.3+5605	XRTJ184556.92+561002.4	$9.18^{+1.40}_{-1.40}$	4.9	$1.2^{+0.5}_{-0.5}$	$6.0^{+1.5}_{-1.6}$	$6.3^{+3.7}_{-2.4}$	1.0(4)
	XRTJ184641.97+561617.3	$15.11^{+1.92}_{-1.92}$	4.9	$1.2^{+0.3}_{-0.3}$	$14.0^{+2.2}_{-2.3}$	$15.8^{+5.5}_{-4.4}$	0.2(5)
4FGLJ2012.1-5234	XRTJ201213.56-523248.9	$22.87^{+2.54}_{-2.54}$	5.6	$2.2^{+0.2}_{-0.2}$	$20.0^{+2.4}_{-2.4}$	$7.9^{+1.2}_{-1.2}$	1.1(8)
	XRTJ201144.43-523444.5	$5.96^{+1.34}_{-1.34}$	5.6	2	$5.8^{+1.3}_{-1.3}$	$2.5^{+0.6}_{-0.6}$	0.5(2)
4FGLJ2046.9-5409	XRTJ204700.86-541245.8	$8.28^{+0.86}_{-0.86}$	3.4	$2.0^{+0.2}_{-0.2}$	$6.7^{+0.7}_{-0.7}$	$3.2^{+0.5}_{-0.5}$	0.8(10)
	XRTJ204722.68-540906.1	$3.27^{+0.55}_{-0.55}$	3.3	$2.2^{+0.4}_{-0.4}$	$2.5^{+0.5}_{-0.5}$	$1.3^{+0.5}_{-0.3}$	4.1(3)
	XRTJ204643.60-540604.1	$1.46^{+0.37}_{-0.37}$	3.3	2	$1.3^{+0.4}_{-0.4}$	$0.6^{+0.2}_{-0.2}$	-
4FGLJ2054.2+6904	XRTJ205359.10+690518.6	$1.48^{+0.28}_{-0.28}$	32.0	$0.9^{+0.3}_{-0.4}$	$1.1^{+0.4}_{-0.4}$	$1.6^{+0.5}_{-0.5}$	0.3(2)
	XRTJ205353.18+690141.5	$1.66^{+0.30}_{-0.30}$	32.0	$2.1^{+0.3}_{-0.3}$	$2.7^{+0.7}_{-0.7}$	$0.8^{+0.2}_{-0.2}$	1.0(3)
4FGLJ2122.3+7653	XRTJ212204.08+765830.1	$0.10^{+0.04}_{-0.04}$	22.0	$1.4^{+0.4}_{-0.4}$	$0.1^{+0.1}_{-0.1}$	$0.1^{+0.0}_{-0.0}$	1.2(3)
	XRTJ212156.89+765308.0	$0.09^{+0.03}_{-0.03}$	22.0	$2.0^{+0.7}_{-0.8}$	$0.2^{+0.1}_{-0.1}$	$0.1^{+0.1}_{-0.0}$	1.6(1)
4FGLJ2122.5+0345	XRTJ212228.37+034511.1	$7.18^{+0.84}_{-0.84}$	7.0	$0.8^{+0.5}_{-0.6}$	$28.0^{+5.8}_{-5.5}$	$50.1^{+104.8}_{-29.7}$	1.1(6)
	XRTJ212212.36+035254.2	$2.79^{+0.58}_{-0.58}$	7.4	$0.4^{+0.9}_{-1.4}$	$2.9^{+0.9}_{-1.2}$	$10.0^{+71.3}_{-7.1}$	0.1(1)
4FGLJ2134.3-0319	XRTJ213415.13-032439.2	$6.22^{+1.17}_{-1.17}$	3.9	$-0.9^{+1.0}_{-1.0}$	$17.0^{+4.0}_{-6.9}$	$1000.0^{+3677.4}_{-868.2}$	1.6(2)
	XRTJ213418.47-032327.5	$3.17^{+0.82}_{-0.82}$	3.9	2	$2.9^{+0.8}_{-0.8}$	$1.6^{+0.5}_{-0.5}$	-
4FGLJ1106.7+3623	XRTJ110622.38+363319.7	$3.31^{+0.41}_{-0.41}$	2.4	$2.4^{+0.3}_{-0.3}$	$3.1^{+0.4}_{-0.4}$	$1.3^{+0.2}_{-0.2}$	0.6(6)
	XRTJ110710.07+361655.1	$4.30^{+0.89}_{-0.89}$	2.4	2	$3.3^{+0.8}_{-0.8}$	$1.6^{+0.4}_{-0.4}$	2.4(2)
	XRTJ110635.95+362648.9	$3.35^{+0.41}_{-0.41}$	2.4	$1.0^{+0.3}_{-0.3}$	$1.8^{+0.4}_{-0.4}$	$3.2^{+1.1}_{-0.9}$	1.3(7)
	XRTJ110612.40+363126.6	$2.88^{+0.42}_{-0.42}$	2.6	$1.5^{+0.2}_{-0.2}$	$2.4^{+0.4}_{-0.4}$	$2.0^{+0.6}_{-0.5}$	1.6(4)
4FGLJ1111.4+0137	XRTJ111114.26+013427.6	$46.02^{+3.29}_{-3.29}$	4.3	$1.9^{+0.1}_{-0.1}$	$37.0^{+3.0}_{-3.0}$	$20.0^{+1.9}_{-2.2}$	0.7(22)
	XRTJ111206.06+013526.7	$8.80^{+1.46}_{-1.46}$	4.5	$1.1^{+0.4}_{-0.4}$	$7.9^{+1.7}_{-1.7}$	$10.0^{+5.8}_{-3.7}$	0.6(2)
	XRTJ111159.79+013642.6	$5.67^{+1.19}_{-1.19}$	4.5	2	$3.4^{+1.0}_{-1.0}$	$1.6^{+0.5}_{-0.4}$	4.7(2)
	XRTJ111106.07+014559.8	$5.63^{+1.17}_{-1.17}$	4.2	2	$6.6^{+1.4}_{-1.4}$	$3.2^{+0.7}_{-0.7}$	0.7(2)
4FGLJ1126.0-5007	XRTJ112624.22-500806.5	$21.32^{+0.86}_{-0.86}$	16.0	$1.9^{+0.1}_{-0.1}$	$22.0^{+1.1}_{-1.1}$	$10.0^{+0.5}_{-0.5}$	1.1(72)
	XRTJ112628.32-500842.8	$4.29^{+0.41}_{-0.41}$	16.0	$1.8^{+0.1}_{-0.1}$	$4.6^{+0.5}_{-0.5}$	$2.5^{+0.3}_{-0.3}$	1.0(16)
	XRTJ112533.68-500549.2	$1.37^{+0.24}_{-0.24}$	16.0	$2.3^{+0.4}_{-0.5}$	$2.1^{+0.4}_{-0.4}$	$0.6^{+0.2}_{-0.2}$	0.9(3)
	XRTJ112605.11-501020.5	$0.37^{+0.16}_{-0.16}$	16.0	2	$0.3^{+0.2}_{-0.2}$	$0.1^{+0.1}_{-0.1}$	-
4FGLJ1151.2-2929	XRTJ115118.17-292744.4	$21.53^{+2.59}_{-2.59}$	6.2	$2.3^{+0.3}_{-0.3}$	$21.0^{+2.7}_{-2.7}$	$7.9^{+1.8}_{-1.5}$	0.7(6)
	XRTJ115110.12-292917.2	$5.22^{+1.32}_{-1.32}$	6.2	2	$9.7^{+2.6}_{-2.6}$	$5.0^{+1.3}_{-1.3}$	-
4FGLJ1224.6+7011	XRTJ122502.59+702038.4	$4.68^{+0.50}_{-0.50}$	1.9	$2.0^{+0.2}_{-0.2}$	$3.6^{+0.4}_{-0.4}$	$2.0^{+0.3}_{-0.3}$	0.9(10)
	XRTJ122457.12+700723.3	$7.28^{+1.15}_{-1.15}$	2.0	$2.0^{+0.3}_{-0.3}$	$5.4^{+1.0}_{-1.0}$	$3.2^{+0.7}_{-0.7}$	1.8(3)
	XRTJ122531.06+701250.5	$0.79^{+0.22}_{-0.22}$	2.0	2	$0.8^{+0.2}_{-0.2}$	$0.4^{+0.1}_{-0.1}$	-
4FGLJ1226.8-4907	XRTJ122734.62-491204.2	$13.23^{+2.05}_{-2.05}$	18.0	$1.4^{+0.3}_{-0.3}$	$15.0^{+3.4}_{-3.4}$	$12.6^{+4.8}_{-3.7}$	0.1(4)
4FGLJ1243.7+1727	XRTJ124326.39+172935.9	$13.69^{+1.28}_{-1.28}$	1.8	$1.9^{+0.2}_{-0.2}$	$9.5^{+1.0}_{-1.1}$	$5.0^{+0.7}_{-0.7}$	1.1(12)
	XRTJ124351.64+172643.2	$2.88^{+0.57}_{-0.57}$	1.8	$3.0^{+0.6}_{-0.6}$	$2.2^{+0.6}_{-0.6}$	$1.0^{+0.2}_{-0.2}$	1.7(2)
4FGLJ1326.0+3507	XRTJ132544.62+350442.7	$4.68^{+0.67}_{-0.67}$	1.0	$1.4^{+0.3}_{-0.3}$	$3.2^{+0.6}_{-0.6}$	$3.2^{+1.0}_{-0.8}$	1.0(5)
	XRTJ132608.87+350836.9	$4.22^{+0.63}_{-0.63}$	1.0	$2.3^{+0.3}_{-0.3}$	$2.5^{+0.5}_{-0.5}$	$1.3^{+0.3}_{-0.3}$	3.6(3)
	XRTJ132622.45+350622.4	$3.51^{+0.59}_{-0.59}$	1.0	$2.7^{+0.4}_{-0.4}$	$2.4^{+0.5}_{-0.5}$	$1.0^{+0.2}_{-0.2}$	0.5(2)
4FGLJ1336.5-4655	XRTJ133618.81-465738.9	$15.75^{+0.87}_{-0.87}$	14.0	$2.9^{+0.1}_{-0.1}$	$22.0^{+1.3}_{-1.3}$	$5.0^{+0.4}_{-0.3}$	1.1(37)
	XRTJ133548.08-465905.6	$1.22^{+0.27}_{-0.27}$	14.0	$1.9^{+0.4}_{-0.4}$	$1.5^{+0.4}_{-0.4}$	$0.6^{+0.2}_{-0.2}$	1.2(2)
4FGLJ1407.7-3017	XRTJ140806.82-302353.7	$142.30^{+2.45}_{-2.45}$	4.4	$1.5^{+0.0}_{-0.0}$	$99.0^{+2.5}_{-2.6}$	$79.4^{+1.9}_{-1.8}$	2.2(272)
	XRTJ140759.93-303047.2	$3.84^{+0.43}_{-0.43}$	4.4	$2.3^{+0.2}_{-0.2}$	$4.2^{+0.5}_{-0.5}$	$1.6^{+0.2}_{-0.2}$	1.3(10)
4FGLJ1408.6-2917	XRTJ140809.87-292241.0	$4.24^{+0.76}_{-0.76}$	4.4	$1.9^{+0.5}_{-0.5}$	$5.4^{+1.0}_{-1.0}$	$3.2^{+2.1}_{-1.0}$	0.4(2)
	XRTJ140807.26-291615.1	$2.82^{+0.69}_{-0.69}$	4.4	2	$2.4^{+0.7}_{-0.7}$	$1.3^{+0.4}_{-0.4}$	-
	XRTJ140826.77-292222.7	$1.53^{+0.41}_{-0.41}$	4.4	2	$1.5^{+0.5}_{-0.5}$	$0.8^{+0.3}_{-0.3}$	-
4FGLJ1438.0+0219	XRTJ143809.82+021804.1	$2.61^{+0.35}_{-0.35}$	3.3	$1.6^{+0.3}_{-0.3}$	$2.2^{+0.4}_{-0.4}$	$1.6^{+0.5}_{-0.4}$	1.3(7)
	XRTJ143743.99+021934.5	$1.75^{+0.53}_{-0.53}$	3.2	2	$1.7^{+0.5}_{-0.5}$	$0.8^{+0.2}_{-0.2}$	-
4FGLJ1444.8+3645	XRTJ144529.77+364615.6	$3.40^{+0.77}_{-0.77}$	1.1	2	$2.6^{+0.7}_{-0.7}$	$1.6^{+0.5}_{-0.4}$	-
	XRTJ144401.00+364415.3	$3.63^{+0.80}_{-0.80}$	1.1	2	$3.3^{+0.8}_{-0.8}$	$1.6^{+0.4}_{-0.4}$	1.5(2)
4FGLJ1452.0-4148	XRTJ145149.46-414503.3	$40.68^{+2.04}_{-2.04}$	11.0	$2.4^{+0.1}_{-0.1}$	$44.0^{+2.4}_{-2.4}$	$15.8^{+1.1}_{-1.1}$	1.0(46)
	XRTJ145224.64-414953.4	$2.62^{+0.60}_{-0.60}$	11.0	$2.9^{+0.6}_{-0.6}$	$3.5^{+0.8}_{-0.8}$	$1.0^{+0.3}_{-0.2}$	0.8(2)
4FGLJ1454.3-3946	XRTJ145411.28-395523.4	$15.95^{+2.24}_{-2.24}$	9.9	$2.6^{+0.3}_{-0.3}$	$19.0^{+3.1}_{-3.2}$	$6.3^{+1.6}_{-1.3}$	1.7(4)
	XRTJ145347.13-394451.0	$10.68^{+1.87}_{-1.87}$	10.0	$2.0^{+0.6}_{-0.7}$	$16.0^{+3.8}_{-3.9}$	$7.9^{+10.3}_{-3.7}$	3.3(2)
4FGLJ1504.6+4343	XRTJ150425.17+434105.0	$27.16^{+2.18}_{-2.18}$	1.6	$1.8^{+0.1}_{-0.1}$	$18.0^{+1.6}_{-1.6}$	$10.0^{+1.2}_{-1.1}$	1.0(16)
	XRTJ150507.23+435002.6	$25.08^{+2.21}_{-2.21}$	1.6	$1.8^{+0.2}_{-0.2}$	$20.0^{+2.0}_{-2.0}$	$12.6^{+1.9}_{-1.6}$	1.2(14)
4FGLJ1513.0-3118	XRTJ151244.55-311650.1	$30.31^{+3.08}_{-3.08}$	16.0	$3.0^{+0.2}_{-0.2}$	$46.0^{+4.9}_{-4.9}$	$10.0^{+1.2}_{-1.3}$	0.7(10)
	XRTJ151258.83-311746.4	$4.74^{+1.28}_{-1.28}$	16.0	2	$13.0^{+3.5}_{-3.5}$	$5.0^{+1.4}_{-1.4}$	-
4FGLJ1514.8+4448	XRTJ151436.48+445002.0	$2.44^{+0.42}_{-0.42}$	2.3	$1.1^{+0.4}_{-0.4}$	$1.4^{+0.3}_{-0.3}$	$2.0^{+1.0}_{-0.7}$	1.5(2)
	XRTJ151451.10+444953.1	$2.23^{+0.40}_{-0.40}$	2.3	$2.0^{+0.5}_{-0.5}$	$1.8^{+0.4}_{-0.4}$	$1.0^{+0.4}_{-0.3}$	1.0(2)
4FGLJ1517.7-4446	XRTJ151727.58-444254.5	$7.23^{+1.27}_{-1.27}$	21.0	$2.3^{+0.6}_{-0.6}$	$10.0^{+2.2}_{-2.3}$	$3.2^{+1.8}_{-1.0}$	0.5(2)
	XRTJ151810.81-444734.7	$4.28^{+1.01}_{-1.01}$	21.0	2	$23.0^{+6.6}_{-6.6}$	$10.0^{+2.9}_{-2.8}$	1.6(1)

Note. Labels are the same as in table A.4.

Table A.5: Results of the X-ray spectral fitting for UGS2. Continued

4FGL Name (1)	*Swift*/XRT source (2)	Count rate (3) [$\times10^{-3}$]	nH (4) [$\times10^{20}$]	Γ (5)	Norm. (6) 10^{-5}	absorbed flux (7) [$\times10^{-13}$]	χ^2_ν(dof) (8)
4FGLJ1557.2+3822	XRTJ155712.37+382030.2	$7.20^{+0.91}_{-0.91}$	1.5	$2.1^{+0.2}_{-0.2}$	$5.5^{+0.8}_{-0.8}$	$2.5^{+0.4}_{-0.4}$	1.1(6)
	XRTJ155656.77+382825.8	$2.32^{+0.53}_{-0.53}$	1.4	2	$1.8^{+0.4}_{-0.4}$	$1.0^{+0.3}_{-0.2}$	1.9(2)
4FGLJ1637.5+3005	XRTJ163739.22+301009.3	$11.24^{+1.11}_{-1.11}$	2.1	$0.1^{+0.2}_{-0.2}$	$2.5^{+0.5}_{-0.5}$	$15.8^{+2.8}_{-2.4}$	1.8(11)
	XRTJ163738.33+300503.1	$4.11^{+0.68}_{-0.68}$	2.1	$1.8^{+0.3}_{-0.3}$	$3.2^{+0.6}_{-0.6}$	$2.0^{+0.5}_{-0.4}$	0.7(3)
	XRTJ163727.99+300954.6	$2.32^{+0.52}_{-0.52}$	2.0	2	$2.0^{+0.5}_{-0.5}$	$1.0^{+0.2}_{-0.2}$	0.5(2)
	XRTJ163647.31+300555.1	$1.74^{+0.46}_{-0.46}$	2.0	2	$1.6^{+0.5}_{-0.5}$	$0.8^{+0.2}_{-0.2}$	-
	XRTJ163735.81+301310.8	$2.26^{+0.51}_{-0.51}$	2.0	2	$2.4^{+0.6}_{-0.6}$	$1.3^{+0.3}_{-0.3}$	0.0(1)
4FGLJ1651.7-7241	XRTJ165151.61-724308.5	$13.26^{+1.66}_{-1.66}$	8.6	$1.1^{+0.2}_{-0.2}$	$6.4^{+1.2}_{-1.2}$	$7.9^{+1.6}_{-1.5}$	2.6(7)
	XRTJ165139.31-724639.6	$3.36^{+0.90}_{-0.90}$	8.4	2	$4.2^{+1.2}_{-1.2}$	$2.0^{+0.6}_{-0.5}$	-
4FGLJ1821.6+6636	XRTJ182108.75+663542.0	$3.10^{+0.51}_{-0.51}$	5.5	$1.7^{+0.5}_{-0.6}$	$2.0^{+0.5}_{-0.6}$	$1.3^{+0.6}_{-0.4}$	1.8(3)
	XRTJ182204.70+663715.0	$1.46^{+0.36}_{-0.36}$	5.8	2	$1.8^{+0.4}_{-0.4}$	$0.8^{+0.2}_{-0.2}$	0.1(2)
4FGLJ1845.3+5605	XRTJ184556.92+561002.4	$9.18^{+1.40}_{-1.40}$	4.9	$1.2^{+0.5}_{-0.5}$	$6.0^{+1.5}_{-1.6}$	$6.3^{+3.7}_{-2.4}$	1.0(4)
	XRTJ184641.97+561617.3	$15.11^{+1.92}_{-1.92}$	4.9	$1.2^{+0.3}_{-0.3}$	$14.0^{+2.2}_{-2.3}$	$15.8^{+5.5}_{-4.4}$	0.2(5)
4FGLJ2012.1-5234	XRTJ201213.56-523248.9	$22.87^{+2.54}_{-2.54}$	5.6	$2.2^{+0.2}_{-0.2}$	$20.0^{+2.4}_{-2.4}$	$7.9^{+1.2}_{-1.2}$	1.1(8)
	XRTJ201144.43-523444.5	$5.96^{+1.34}_{-1.34}$	5.6	2	$5.8^{+1.3}_{-1.3}$	$2.5^{+0.6}_{-0.6}$	0.5(2)
4FGLJ2046.9-5409	XRTJ204700.86-541245.8	$8.28^{+0.86}_{-0.86}$	3.4	$2.0^{+0.2}_{-0.2}$	$6.7^{+0.7}_{-0.7}$	$3.2^{+0.5}_{-0.5}$	0.8(10)
	XRTJ204722.68-540906.1	$3.27^{+0.55}_{-0.55}$	3.3	$2.2^{+0.4}_{-0.4}$	$2.5^{+0.5}_{-0.5}$	$1.3^{+0.5}_{-0.3}$	4.1(3)
	XRTJ204643.60-540604.1	$1.46^{+0.37}_{-0.37}$	3.3	2	$1.3^{+0.4}_{-0.4}$	$0.6^{+0.2}_{-0.2}$	-
4FGLJ2054.2+6904	XRTJ205359.10+690518.6	$1.48^{+0.28}_{-0.28}$	32.0	$0.9^{+0.3}_{-0.4}$	$1.1^{+0.4}_{-0.4}$	$1.6^{+0.5}_{-0.5}$	0.3(2)
	XRTJ205353.18+690141.5	$1.66^{+0.30}_{-0.30}$	32.0	$2.1^{+0.3}_{-0.3}$	$2.7^{+0.7}_{-0.7}$	$0.8^{+0.2}_{-0.2}$	1.0(3)
4FGLJ2122.3+7653	XRTJ212204.08+765830.1	$0.10^{+0.04}_{-0.04}$	22.0	$1.4^{+0.4}_{-0.4}$	$0.1^{+0.1}_{-0.1}$	$0.1^{+0.0}_{-0.0}$	1.2(3)
	XRTJ212156.89+765308.0	$0.09^{+0.03}_{-0.03}$	22.0	$2.0^{+0.7}_{-0.8}$	$0.2^{+0.1}_{-0.1}$	$0.1^{+0.1}_{-0.0}$	1.6(1)
4FGLJ2122.5+0345	XRTJ212228.37+034511.1	$7.18^{+0.84}_{-0.84}$	7.0	$0.8^{+0.5}_{-0.6}$	$28.0^{+5.8}_{-5.5}$	$50.1^{+104.8}_{-29.7}$	1.1(6)
	XRTJ212212.36+035254.2	$2.79^{+0.58}_{-0.58}$	7.4	$0.4^{+0.9}_{-1.4}$	$2.9^{+0.9}_{-1.2}$	$10.0^{+71.3}_{-7.1}$	0.1(1)
4FGLJ2134.3-0319	XRTJ213415.13-032439.2	$6.22^{+1.17}_{-1.17}$	3.9	$-0.9^{+1.0}_{-1.0}$	$17.0^{+4.0}_{-6.9}$	$1000.0^{+3677.4}_{-868.2}$	1.6(2)
	XRTJ213418.47-032327.5	$3.17^{+0.82}_{-0.82}$	3.9	2	$2.9^{+0.8}_{-0.8}$	$1.6^{+0.5}_{-0.5}$	-
4FGLJ2141.4+0733	XRTJ214147.51+074216.2	$2.49^{+0.37}_{-0.37}$	5.8	$1.8^{+0.3}_{-0.3}$	$2.5^{+0.4}_{-0.5}$	$1.3^{+0.4}_{-0.3}$	0.6(4)
	XRTJ214125.72+073257.3	$1.33^{+0.28}_{-0.28}$	5.6	$1.1^{+0.4}_{-0.5}$	$1.1^{+0.3}_{-0.3}$	$1.6^{+0.9}_{-0.6}$	0.2(2)
4FGLJ2144.7-5640	XRTJ214429.66-563848.6	$14.95^{+1.13}_{-1.13}$	2.9	$2.2^{+0.1}_{-0.1}$	$13.0^{+1.0}_{-1.0}$	$6.3^{+0.6}_{-0.6}$	0.9(25)
	XRTJ214503.13-564500.8	$2.71^{+0.49}_{-0.49}$	2.9	$2.4^{+0.3}_{-0.3}$	$2.5^{+0.5}_{-0.5}$	$1.0^{+0.2}_{-0.2}$	0.3(3)
4FGLJ2153.0-6442	XRTJ215306.90-644444.4	$30.88^{+2.47}_{-2.47}$	3.5	$2.4^{+0.2}_{-0.2}$	$24.0^{+2.1}_{-2.1}$	$10.0^{+1.2}_{-1.1}$	1.0(16)
	XRTJ215326.50-644310.5	$9.25^{+1.40}_{-1.40}$	3.5	$2.0^{+0.3}_{-0.3}$	$8.6^{+1.4}_{-1.4}$	$4.0^{+1.3}_{-1.0}$	1.4(4)
4FGLJ2212.9+7921	XRTJ221111.14+791758.1	$12.17^{+1.69}_{-1.69}$	19.0	$3.0^{+0.4}_{-0.4}$	$17.0^{+2.7}_{-2.7}$	$3.2^{+0.7}_{-0.6}$	1.3(4)
	XRTJ221414.52+792040.2	$8.30^{+1.20}_{-1.20}$	18.0	$0.8^{+0.3}_{-0.3}$	$5.1^{+1.4}_{-1.3}$	$10.0^{+2.9}_{-2.4}$	0.2(4)
4FGLJ2222.9+1507	XRTJ222253.97+151053.6	$5.88^{+1.05}_{-1.05}$	4.7	$2.4^{+0.3}_{-0.3}$	$5.8^{+1.1}_{-1.1}$	$2.5^{+0.6}_{-0.5}$	0.1(2)
	XRTJ222239.38+151053.7	$4.17^{+0.91}_{-0.91}$	4.7	2	$1.7^{+0.6}_{-0.6}$	$0.8^{+0.3}_{-0.3}$	6.1(2)
4FGLJ2223.0+2704	XRTJ222217.67+270747.9	$4.54^{+0.32}_{-0.32}$	7.5	$1.6^{+0.1}_{-0.1}$	$4.4^{+0.4}_{-0.4}$	$3.2^{+0.3}_{-0.3}$	0.7(27)
	XRTJ222305.55+265733.0	$2.59^{+0.24}_{-0.24}$	7.0	$1.7^{+0.2}_{-0.2}$	$2.7^{+0.3}_{-0.3}$	$1.6^{+0.3}_{-0.3}$	0.7(15)
	XRTJ222334.34+270113.8	$1.89^{+0.20}_{-0.20}$	6.8	$1.5^{+0.2}_{-0.2}$	$1.9^{+0.3}_{-0.3}$	$1.6^{+0.4}_{-0.3}$	0.4(10)
	XRTJ222244.77+270423.6	$1.68^{+0.20}_{-0.20}$	7.3	$2.0^{+0.3}_{-0.2}$	$1.6^{+0.2}_{-0.2}$	$0.8^{+0.2}_{-0.1}$	1.2(10)
	XRTJ222247.02+270103.3	$1.13^{+0.17}_{-0.17}$	7.2	$1.4^{+0.2}_{-0.2}$	$1.0^{+0.2}_{-0.2}$	$0.8^{+0.2}_{-0.1}$	0.5(7)
	XRTJ222228.30+265743.6	$1.90^{+0.26}_{-0.26}$	7.3	$1.9^{+0.2}_{-0.2}$	$2.3^{+0.3}_{-0.4}$	$1.0^{+0.2}_{-0.2}$	1.0(6)
	XRTJ222301.89+265603.4	$0.89^{+0.17}_{-0.17}$	7.1	$2.3^{+0.9}_{-0.7}$	$0.8^{+0.2}_{-0.2}$	$0.3^{+0.2}_{-0.1}$	3.4(3)
	XRTJ222314.49+271025.5	$0.48^{+0.12}_{-0.12}$	7.1	$2.0^{+0.8}_{-3.0}$	$0.4^{+0.1}_{-0.4}$	$0.2^{+3.3}_{-0.1}$	3.0(2)
	XRTJ222310.54+271308.1	$0.36^{+0.11}_{-0.11}$	7.2	2	$0.3^{+0.1}_{-0.1}$	$0.2^{+0.1}_{-0.1}$	1.3(2)
	XRTJ222239.51+270453.8	$0.43^{+0.12}_{-0.12}$	7.3	$2.5^{+0.7}_{-0.7}$	$0.5^{+0.1}_{-0.1}$	$0.2^{+0.1}_{-0.1}$	0.2(2)
	XRTJ222250.46+270432.3	$0.37^{+0.12}_{-0.12}$	7.2	$2.7^{+0.5}_{-0.5}$	$0.5^{+0.1}_{-0.1}$	$0.2^{+0.1}_{-0.0}$	1.1(2)
	XRTJ222313.70+270849.2	$0.21^{+0.09}_{-0.09}$	7.1	2	$0.3^{+0.1}_{-0.1}$	$0.2^{+0.1}_{-0.1}$	-
4FGLJ2311.6-4427	XRTJ231145.87-443221.0	$5.16^{+0.95}_{-0.95}$	1.2	$2.9^{+0.5}_{-0.5}$	$3.7^{+0.9}_{-1.0}$	$1.6^{+0.4}_{-0.4}$	0.2(1)
	XRTJ231134.44-443617.8	$4.74^{+0.93}_{-0.93}$	1.2	$0.5^{+0.6}_{-0.7}$	$3.1^{+0.9}_{-1.0}$	$10.0^{+14.5}_{-5.5}$	0.1(1)
4FGLJ2324.6+3115	XRTJ232458.69+312709.9	$2.98^{+0.35}_{-0.35}$	10.0	$1.2^{+0.2}_{-0.2}$	$2.8^{+0.5}_{-0.5}$	$3.2^{+0.6}_{-0.6}$	0.7(9)
	XRTJ232402.93+312019.8	$2.47^{+0.30}_{-0.30}$	10.0	$1.6^{+0.2}_{-0.3}$	$2.3^{+0.4}_{-0.4}$	$1.6^{+0.4}_{-0.3}$	1.7(9)
	XRTJ232457.35+311340.3	$0.74^{+0.17}_{-0.17}$	10.0	$2.4^{+0.6}_{-0.7}$	$1.0^{+0.2}_{-0.3}$	$0.3^{+0.2}_{-0.1}$	1.5(2)
	XRTJ232441.72+311002.0	$0.57^{+0.16}_{-0.16}$	10.0	$2.6^{+0.6}_{-0.7}$	$0.8^{+0.2}_{-0.2}$	$0.3^{+0.1}_{-0.1}$	1.1(1)

Note. Labels are the same as in table A.4.

Table A.5: Results of the X-ray spectral fitting for UGS2. Continued

4FGL Name (1)	*Swift*/XRT source (2)	Count rate (3) [×10^{-3}]	nH (4) [×10^{20}]	Γ (5)	Norm. (6) 10^{-5}	absorbed flux (7) [×10^{-13}]	χ^2_ν(dof) (8)
4FGLJ2338.1+0411	XRTJ233830.54+041900.0	$27.37^{+1.04}_{-1.04}$	6.9	$2.4^{+0.1}_{-0.1}$	$25.0^{+1.1}_{-1.1}$	$7.9^{+0.4}_{-0.4}$	2.7(66)
	XRTJ233742.04+041003.2	$7.76^{+0.56}_{-0.56}$	6.9	$2.3^{+0.1}_{-0.1}$	$7.6^{+0.6}_{-0.6}$	$3.2^{+0.3}_{-0.3}$	0.8(22)
	XRTJ233833.66+041321.8	$1.29^{+0.25}_{-0.25}$	6.8	$2.1^{+0.3}_{-0.3}$	$1.4^{+0.3}_{-0.3}$	$0.6^{+0.2}_{-0.2}$	0.7(3)
	XRTJ233731.09+040634.4	$1.86^{+0.33}_{-0.33}$	6.9	$1.7^{+0.3}_{-0.3}$	$2.2^{+0.4}_{-0.5}$	$1.3^{+0.4}_{-0.3}$	0.2(3)
	XRTJ233737.43+040814.6	$1.14^{+0.23}_{-0.23}$	6.9	$1.6^{+0.4}_{-0.4}$	$1.3^{+0.3}_{-0.3}$	$1.0^{+0.5}_{-0.3}$	0.5(2)
	XRTJ233735.13+041029.1	$1.17^{+0.24}_{-0.24}$	6.9	$1.5^{+0.8}_{-0.9}$	$0.9^{+0.3}_{-0.4}$	$0.6^{+0.7}_{-0.3}$	1.8(2)
	XRTJ233741.42+040736.8	$0.82^{+0.21}_{-0.21}$	6.9	$-0.3^{+1.6}_{0.4}$	$0.5^{+0.4}_{-0.5}$	$7.9^{+178.3}_{-7.0}$	1.0(1)
	XRTJ233824.88+040520.3	$0.69^{+0.18}_{-0.18}$	6.7	2	$0.9^{+0.3}_{-0.3}$	$0.4^{+0.1}_{-0.1}$	0.6(1)
4FGLJ2344.7-4234	XRTJ234413.10-423935.6	$4.49^{+0.62}_{-0.62}$	1.6	$1.8^{+0.3}_{-0.3}$	$3.70^{+0.57}_{-0.57}$	$2.5^{+0.7}_{-0.6}$	0.5(8)
	XRTJ234431.22-423308.8	$2.27^{+0.64}_{-0.64}$	1.6	2	$2.3^{+0.7}_{-0.7}$	$1.3^{+0.4}_{-0.4}$	0.1(1)
4FGLJ2351.4-2818	XRTJ235137.78-281824.6	$10.40^{+1.51}_{-1.51}$	1.7	$1.9^{+0.3}_{-0.3}$	$8.3^{+1.3}_{-1.3}$	$5.0^{+1.6}_{-1.2}$	1.2(4)
	XRTJ235136.96-282157.3	$7.58^{+1.31}_{-1.31}$	1.7	$2.0^{+0.3}_{-0.3}$	$5.5^{+1.0}_{-1.0}$	$3.2^{+0.8}_{-0.7}$	1.9(3)
4FGLJ2359.3+1444	XRTJ235937.37+144848.9	$2.37^{+0.43}_{-0.43}$	3.8	$1.1^{+0.5}_{-0.6}$	$2.2^{+0.5}_{-0.5}$	$2.5^{+3.0}_{-1.2}$	0.3(2)
	XRTJ235919.60+144156.1	$1.67^{+0.39}_{-0.39}$	3.8	$2.0^{+1.6}_{-1.3}$	$1.3^{+0.3}_{-0.3}$	$0.6^{+1.8}_{-0.3}$	3.2(1)
	XRTJ235838.47+144512.3	$3.00^{+0.58}_{-0.58}$	3.7	$1.2^{+0.4}_{-0.5}$	$2.2^{+0.6}_{-0.6}$	$2.5^{+1.5}_{-1.0}$	0.3(1)
	XRTJ235918.00+144851.8	$1.47^{+0.36}_{-0.36}$	3.8	2	$1.1^{+0.3}_{-0.3}$	$0.5^{+0.1}_{-0.1}$	2.3(2)
	XRTJ235953.96+145523.9	$3.25^{+0.67}_{-0.67}$	3.7	2	$3.1^{+0.8}_{-0.8}$	$1.6^{+0.4}_{-0.4}$	2.5(2)
	XRTJ235923.02+144833.7	$1.16^{+0.32}_{-0.32}$	3.8	2	$1.1^{+0.3}_{-0.3}$	$0.5^{+0.1}_{-0.2}$	-
	XRTJ235923.02+144833.7	$1.16^{+0.32}_{-0.32}$	3.8	2	$1.1^{+0.3}_{-0.3}$	$0.5^{+0.1}_{-0.2}$	-

Note. Labels are the same as in table A.4.

A.4.0 OPTICAL SKY MAPS

In the online material the optical skymaps for the UGS1 (UGS with single possible X-ray counterpart) analysed in this paper are shown. The green circle represent the error box of the X-ray counterpart and the red ellipses the error box of radio counterparts.

Table A.6: MWL counterparts of UGS1.

4FGL Name (1)	*Swift*/XRT source (2)	Radio source (3)	Optical source (4)	RA (5) J2000	DEC (6) J2000	gmag(rmag) (7)	$f_\nu^{\rm opt}$ (8) [$\times 10^{-28}$]	$f_\nu^{\rm radio}$ (9)	*R* (10)
4FGL J0003.6+3059	XRT J000402.65+310219.8	-	PANJ000402.51+310222.0	1.0105	31.0394	21.2(20.1)	1.2	<0.3	<29
4FGL J0004.4-4001	XRT J000434.22-400034.7	VLASS1QLCIRJ000434.19-400033.6	DESJ000434.22-400035.1	1.1426	-40.0098	16.9(16.2)	63.1	32.5	51
4FGL J0006.6+4618	XRT J000652.09+461813.9	VLASS1QLCIRJ000652.31+461816.8	PANJ000652.33+461817.0	1.7180	46.3047	19.9(19.6)	4	2.6	64
4FGL J0009.1-5012	XRT J000908.61-501000.9*	-	DESJ000908.64-501000.6	2.2860	-50.1669	11.1(11.5)	13182.6	<0.6	<1
4FGL J0022.0-5921	XRT J002127.45-591946.3	RACSJ002127.4-591949	DESJ002127.51-591948.0	5.3646	-59.3300	19.6(19.2)	5.2	93.4	1780
4FGL J0023.2+8412	XRT J002403.36+841352.6	-	PANJ002405.61+841352.2	6.0234	84.2312	16.7(16.2)	75.9	<0.3	<1
4FGL J0023.6-4209	XRT J002303.59-420509.6	-	DESJ002303.75-420508.6	5.7657	-42.0857	15.6(15.0)	208.9	1.4	1
4FGL J0025.4-4838	XRT J002536.94-483810.9	RACSJ002536.8-483810	DESJ002536.92-483809.5	6.4039	-48.6360	19.8(19.4)	4.4	5	114
4FGL J0026.1-0732	XRT J002611.55-073116.0	VLASS1QLCIRJ002611.63-073115.5	PANJ002611.64-073115.8	6.5485	-7.5211	19.1(19.1)	8.3	6.4	77
4FGL J0027.0-1134	XRT J002710.11-113638.7	VLASS1QLCIRJ002710.12-113637.5	PANJ002710.12-113637.9	6.7922	-11.6105	17.1(16.3)	52.5	19.9	38
4FGL J0031.5-5648	XRT J003135.74-564640.9	RACSJ003135.4-564641	DESJ003135.47-564641.4	7.8978	-56.7782	19.9(19.5)	4	7.3	183
4FGL J0037.2-2653	XRT J003729.64-265045.9	RACSJ003729.6-265045	PANJ003729.52-265045.3	9.3730	-26.8459	19.2(18.8)	7.6	2.7	35
4FGL J0054.4-1503	XRT J005431.46-145804.7	ATCAJ005431.58-145802.5	PANJ005431.59-145803.2	13.6316	-14.9676	19.5(19.1)	5.8	0.1	2
4FGL J0055.7+4507	XRT J005525.98+450529.3*	-	PANJ005526.16+450530.1	13.8590	45.0917	8.7(7.5)	120226.4	<0.3	<1
4FGL J0058.3-4603	XRT J005806.28-460419.4	RACSJ005806.0-460417	DESJ005806.21-460418.9	14.5259	-46.0719	20.9(20.3)	1.6	6.7	422
4FGL J0059.4-5654	XRT J005945.18-565306.8	-	DESJ005944.68-565305.3	14.9362	-56.8848	20.3(19.2)	2.8	<0.6	<23
4FGL J0112.0+3442	XRT J011124.86+344154.1	VLASS1QLCIRJ011124.83+344154.5	PANJ011124.86+344154.6	17.8536	34.6985	19.4(19.0)	6.3	41.3	655
4FGL J0115.4-2917	XRT J011528.71-291847.1	VLASS1QLCIRJ011528.95-291843.8	PANJ011528.96-291844.3	18.8707	-29.3123	20.3(19.3)	2.8	6.4	232
4FGL J0117.9+1430	XRT J011804.79+143159.6	-	PANJ011804.84+143158.7	19.5201	14.5330	18.7(18.3)	12	<1.8	<15
4FGL J0120.2-7944	XRT J011913.62-794513.9	-	SSSJ011913.77-794512.3	19.8068	-79.7535	20.7(-)	1.9	<0.6	<34
4FGL J0121.4-7216	XRT J012121.82-721919.9	RACSJ012122.7-721920	SSSJ012122.09-721918.0	20.3420	-72.3217	20.1(19.5)	3.3	1.7	52
4FGL J0125.9-6303	XRT J012547.97-630245.3	RACSJ012548.1-630243	DESJ012548.19-630245.1	21.4508	-63.0459	19.7(19.1)	4.8	30.3	633
4FGL J0137.3-3239	XRT J013724.55-324040.2	VLASS1QLCIRJ013724.50-324038.7	DESJ013724.50-324039.3	24.3521	-32.6776	20.2(19.2)	3	9	297
4FGL J0140.5-4730	XRT J014007.79-473213.2	-	DESJ014007.90-473209.5	25.0329	-47.5360	17.8(17.0)	27.5	<0.6	<2
4FGL J0156.3-2420	XRT J015624.63-242004.1	VLASS1QLCIRJ015624.53-242003.1	PANJ015624.55-242003.7	29.1023	-24.3344	18.4(17.8)	15.8	4.4	28
4FGL J0202.7+3133	XRT J020242.13+313211.4	VLASS1QLCIRJ020242.03+313211.0	PANJ020242.06+313211.0	30.6753	31.5364	18.7(18.4)	12	15.1	126
4FGL J0231.0+3505	XRT J023112.30+350445.7	VLASS1QLCIRJ023112.15+350444.5	PANJ023112.18+350444.6	37.8008	35.0791	20.0(19.6)	3.6	4.9	135
4FGL J0245.0+4755	XRT J024455.02+475125.2	-	PANJ024454.82+475129.2	41.2284	47.8581	19.6(19.2)	5.2	<0.3	<7
4FGL J0251.1-1830	XRT J025111.70-183111.1	VLASS1QLCIRJ025111.53-183112.3	PANJ025111.53-183112.7	42.7981	-18.5202	20.2(19.6)	3	8.8	291
4FGL J0259.0+0552	XRT J025857.56+055244.4	VLASS1QLCIRJ025857.55+055244.0	PANJ025857.56+055243.9	44.7398	5.8789	18.6(18.3)	13.2	5.8	44
4FGL J0301.6-5617	XRT J030115.05-561647.6	RACSJ030115.0-561643	DESJ030114.88-561646.7	45.3120	-56.2797	23.3(23.3)	0.2	30.3	17429
4FGL J0302.5+3354	XRT J030226.95+335444.4	VLASS1QLCIRJ030226.99+335445.9	PANJ030227.04+335445.8	45.6127	33.9127	19.3(19.1)	6.9	11.9	171
4FGL J0327.6+2620	XRT J032737.27+262009.3	VLASS1QLCIRJ032737.28+262010.9	PANJ032737.29+262011.0	51.9054	26.3364	20.7(19.9)	1.9	7.1	373
4FGL J0333.4-2705	XRT J033331.91-270917.2	VLASS1QLCIRJ033331.93-270916.1	PANJ033331.93-270916.5	53.3831	-27.1546	20.0(19.5)	3.6	6	164
4FGL J0337.9+4058	XRT J033733.16+405852.7*	-	PANJ033732.99+405856.4	54.3875	40.9824	14.3(17.9)	691.8	<0.3	<1
4FGL J0341.9+3153	XRT J034158.35+314854.1*	-	PANJ034158.45+314856.3	55.4936	31.8157	18.4(16.2)	15.8	<0.3	<2
4FGL J0343.3-6303	XRT J034324.90-630338.5	RACSJ034324.7-630337	DESJ034324.84-630337.3	55.8535	-63.0604	18.9(18.7)	10	9	90
4FGL J0349.6+4026	XRT J034945.96+402614.0	-	PANJ034945.92+402615.4	57.4413	40.4376	20.7(19.6)	1.9	<0.3	<18
4FGL J0358.1+2850	XRT J035748.90+284442.5	-	PANJ035748.94+284443.3	59.4539	28.7454	17.6(16.8)	33.1	<0.3	<1
4FGL J0406.2+0639	XRT J040607.87+063920.3	VLASS1QLCIRJ040607.92+063922.2	PANJ040607.94+063922.0	61.5331	6.6561	20.8(19.6)	1.7	12.1	695
4FGL J0409.2+2542	XRT J040921.70+254441.4*	VLASS1QLCIRJ040921.71+254442.0	PANJ040921.74+254442.0	62.3406	25.7450	19.6(19.9)	5.2	8.1	153
4FGL J0418.4-4342	XRT J041832.35-434155.4	-	DESJ041832.26-434156.2	64.6344	-43.6990	21.5(20.8)	0.9	<0.6	<70
4FGL J0438.0-7329	XRT J043836.89-732921.3*	RACSJ043837.1-732920	SSSJ043836.94-732921.9	69.6541	-73.4895	17.6(15.5)	33.1	20.6	62
4FGL J0438.2-4243	XRT J043831.99-424007.0	RACSJ043831.9-424007	DESJ043832.00-424006.8	69.6334	-42.6686	19.4(18.3)	6.3	41.5	658
4FGL J0459.7-5413	XRT J045937.04-541709.3	RACSJ045938.1-541659	DESJ045936.98-541707.4	74.9041	-54.2854	19.6(19.5)	5.2	3.8	73
4FGL J0512.8+5821	XRT J051154.26+582904.3	-	PANJ051154.44+582902.7	77.9768	58.4841	17.9(17.2)	25.1	<0.3	<1
4FGL J0531.4-0058	XRT J053055.69-005538.0*	-	PANJ053055.62-005540.0	82.7318	-0.9278	17.1(15.8)	52.5	<0.3	<1
4FGL J0531.7+1241	XRT J053123.50+123319.8*	-	PANJ053123.49+123320.5	82.8479	12.5557	11.7(11.7)	7585.8	<0.3	<1
4FGL J0536.1-1205	XRT J053626.88-120653.4	VLASS1QLCIRJ053626.79-120651.8	PANJ053626.80-120652.1	84.1117	-12.1145	20.4(18.6)	2.5	5.4	216
4FGL J0537.5+0959	XRT J053745.84+095758.5	VLASS1QLCIRJ053745.89+095758.8	PANJ053745.92+095758.7	84.4413	9.9663	21.5(20.2)	0.9	7.4	809
4FGL J0545.8-0905	XRT J054540.46-090712.2	VLASS1QLCIRJ054540.49-090708.4	PANJ054540.48-090708.7	86.4187	-9.1191	-(21.2)	-	-	-
4FGL J0553.9-5048	XRT J055359.66-505145.1	RACSJ055359.6-505143	DESJ055359.66-505143.9	88.4986	-50.8622	19.2(18.8)	7.6	18.6	246
4FGL J0554.0-0839	XRT J055341.85-084003.8	VLASS1QLCIRJ055341.90-084001.5	PANJ055418.94-025836.0	88.5807	-2.9760	-(-)	-	-	-
4FGL J0554.2-0259	XRT J055418.93-025838.3	VLASS1QLCIRJ055418.93-025835.7	PANJ055418.94-025836.0	88.5789	-2.9767	21.6(20.9)	0.8	6	726
4FGL J0620.7-5034	XRT J062045.98-503350.3	RACSJ062046.1-503352	DESJ062046.12-503350.9	95.1922	-50.5641	18.3(17.1)	17.4	38.4	221
4FGL J0624.7-4903	XRT J062419.86-490640.2	ATCAJ062419.66-490636.4	DESJ062419.71-490636.1	96.0821	-49.1100	19.2(19.1)	7.6	0.1	2
4FGL J0631.0+5626	XRT J063048.87+562830.6	VLASS1QLCIRJ063048.97+562830.6	PANJ063048.95+562831.1	97.7040	56.4753	20.6(19.9)	2.1	2.7	127
4FGL J0640.9-5204	XRT J064112.61-520738.0*	-	SSSJ064112.50-520738.8	100.3021	-52.1274	11.1(9.6)	13182.6	<0.6	<1
4FGL J0641.4+3349	XRT J064111.24+334502.0	VLASS1QLCIRJ064111.20+334459.6	PANJ064111.23+334459.7	100.2968	33.7499	17.1(16.4)	52.5	1.2	2
4FGL J0656.5+4218	XRT J065635.60+421523.5	VLASS1QLCIRJ065635.57+421524.0	PANJ065635.59+421524.1	104.1483	42.2567	20.1(19.8)	3.3	6.9	208
4FGL J0700.2-5118	XRT J070034.01-512007.4	RACSJ070034.4-511956	SSSJ070033.82-512006.8	105.1406	-51.3350	19.6(18.7)	5.2	12.7	243
4FGL J0704.3-4829	XRT J070421.99-482646.5	RACSJ070421.8-482647	SSSJ070421.82-482647.3	106.0911	-48.4466	20.7(19.8)	1.9	6.1	320
4FGL J0734.3-4448	XRT J073418.51-444640.5*	RACSJ073418.4-444642	SSSJ073418.48-444640.9	113.5771	-44.7781	20.8(19.1)	1.7	20.8	1194
4FGL J0755.9-0515	XRT J075614.46-051719.2	ATCAJ075614.44-051720.4	PANJ075614.43-051718.9	119.0601	-5.2886	21.5(21.4)	0.9	0.1	16

Note. 1) 4FGL Name; 2) X-ray source; 3) Radio source; 4) Optical source; 5) - 6) Coordinates of the optical counterpart. 7) g(r) magnitude of the optical source. 8) Optical density flux in unit of erg cm^{-2} s^{-1} Hz^{-1}. 9) Radio density flux (mJy); 10) *Radio-loudness* parameter.
* Sources with proper motion.

Table A.6: MWL counterparts of UGS1. Continued

4FGL Name (1)	*Swift*/XRT source (2)	Radio source (3)	Optical source (4)	RA (5) J2000	DEC (6) J2000	gmag(rmag) (7)	$f_\nu^{\rm opt}$ (8) [$\times 10^{-28}$]	$f_\nu^{\rm radio}$ (9)	*R* (10)
4FGL J0800.9+0733	XRT J080056.64+073234.5	VLASS1QLCIRJ080056.54+073235.2	PANJ080056.57+073235.1	120.2357	7.5431	18.3(18.1)	17.4	5.5	32
4FGL J0815.5+6554	XRT J081539.88+655004.3	VLASS1QLCIRJ081539.78+655004.3	PANJ081539.81+655004.5	123.9159	65.8346	20.0(19.6)	3.6	15.4	423
4FGL J0826.0-0157	XRT J082556.10-020212.2	-	PANJ082556.04-020211.9	126.4835	-2.0366	20.0(19.8)	3.6	<0.3	<10
4FGL J0838.5+4013	XRT J083902.98+401546.9	VLASS1QLCIRJ083903.07+401545.6	PANJ083903.08+401545.6	129.7629	40.2627	18.3(17.0)	17.4	24	138
4FGL J0839.6-8341	XRT J083847.78-834345.1	-	SSSJ083847.95-834343.2	129.6990	-83.7290	19.8(19.0)	4.4	<0.6	<15
4FGL J0852.5-2515	XRT J085221.91-251628.8*	VLASS1QLCIRJ085221.95-251627.6	PANJ085221.94-251628.1	133.0914	-25.2745	19.9(19.5)	4	35.4	889
4FGL J0906.1-1011	XRT J090616.22-101427.0	-	PANJ090616.14-101426.2	136.5672	-10.2406	21.4(21.2)	1	<0.3	<35
4FGL J0910.1-1816	XRT J091003.90-181613.1	VLASS1QLCIRJ091003.90-181612.1	PANJ091003.88-181612.5	137.5162	-18.2701	20.7(19.7)	1.9	4.3	226
4FGL J0914.5+6845	XRT J091429.49+684506.3	VLASS1QLCIRJ091429.67+684508.4	PANJ091429.69+684508.5	138.6237	68.7523	19.6(19.3)	5.2	19.8	377
4FGL J0916.9+7756	XRT J091715.25+780052.4	-	PANJ091713.71+780055.4	139.3071	78.0154	20.9(19.9)	1.6	<0.3	<22
4FGL J0934.5+7223	XRT J093333.50+722059.0	-	PANJ093333.67+722101.2	143.3903	72.3503	19.0(18.3)	9.1	<0.3	<4
4FGL J0938.8+5155	XRT J093834.50+515454.8	-	PANJ093834.73+515452.4	144.6447	51.9145	20.3(20.1)	2.8	0.1	3
4FGL J1016.1-4247	XRT J101620.78-424723.2	RACSJ101620.4-424721	SSSJ101620.65-424722.4	154.0861	-42.7896	19.6(18.3)	5.2	7.8	149
4FGL J1017.4+5956	XRT J101706.90+595129.9	-	PANJ101706.88+595135.6	154.2787	59.8599	19.6(18.9)	5.2	<0.3	<7
4FGL J1032.0+5725	XRT J103142.67+573255.3	-	PANJ103143.27+573252.6	157.9303	57.5479	22.0(21.4)	0.6	<0.3	<60
4FGL J1039.2+3258	XRT J103852.17+325651.9	VLASS1QLCIRJ103852.17+325651.9	PANJ103852.18+325651.7	159.7174	32.9477	19.7(18.9)	4.8	6.1	128
4FGL J1047.2+6740	XRT J104705.65+673759.0	VLASS1QLCIRJ104705.95+673757.9	PANJ104705.92+673758.1	161.7747	67.6328	20.6(20.3)	2.1	8.7	418
4FGL J1049.8+2741	XRT J104938.70+274212.1	VLASS1QLCIRJ104938.81+274213.1	PANJ104938.79+274213.0	162.4116	27.7036	18.2(17.3)	19.1	7.2	38
4FGL J1114.6+1225	XRT J111437.12+122711.2	VLASS1QLCIRJ111437.00+122713.1	PANJ111437.02+122713.1	168.6542	12.4536	21.3(21.1)	1.1	3.8	343
4FGL J1119.9-1007	XRT J111948.35-100706.0	VLASS1QLCIRJ111948.42-100706.8	PANJ111948.42-100707.2	169.9517	-10.1187	19.5(19.2)	5.8	10.6	185
4FGL J1120.0-2204	XRT J111958.40-220456.3*	-	PANJ111958.31-220456.4	169.9930	-22.0823	15.6(15.7)	208.9	<0.3	<1
4FGL J1120.1-2645	XRT J111956.93-264316.2	VLASS1QLCIRJ111957.09-264314.1	PANJ111957.07-264314.8	169.9878	-26.7208	20.9(20.6)	1.6	2.3	147
4FGL J1122.0-0231	XRT J112213.80-022916.7	VLASS1QLCIRJ112213.71-022913.7	PANJ112213.71-022914.2	170.5571	-2.4873	19.4(18.7)	6.3	29.4	466
4FGL J1123.8-4552	XRT J112354.82-455012.2	-	GAIAJ112355.30-455018.9	170.9804	-45.8386	19.5(-)	5.8	<0.6	<11
4FGL J1125.1+4811	XRT J112526.01+480922.8	-	PANJ112526.28+480922.0	171.3595	48.1561	20.3(20.2)	2.8	<0.3	<13
4FGL J1131.6+4657	XRT J113142.36+470009.2	VLASS1QLCIRJ113142.36+470009.4	PANJ113142.27+470008.6	172.9261	47.0024	17.5(16.5)	36.3	73.9	204
4FGL J1146.0-0638	XRT J114600.87-063853.9	VLASS1QLCIRJ114600.87-063854.5	PANJ114600.86-063854.8	176.5036	-6.6486	19.5(19.7)	5.8	5.8	100
4FGL J1155.2-1111	XRT J115515.07-111124.9	RACSJ115514.8-111121	PANJ115514.85-111122.6	178.8119	-11.1896	20.7(20.2)	1.9	7.2	378
4FGL J1158.8-1430	XRT J115912.67-143154.7	VLASS1QLCIRJ115912.63-143154.5	PANJ115912.62-143154.9	179.8026	-14.5319	19.4(19.0)	6.3	5.8	92
4FGL J1207.4-1840	XRT J120740.89-184029.3	-	PANJ120740.60-184031.0	181.9192	-18.6753	20.2(19.9)	3	<0.3	<11
4FGL J1207.4-4536	XRT J120732.84-453452.0*	-	SSSJ120732.77-453452.0	181.8864	-45.5812	7.5(6.7)	363078.1	<0.6	<1
4FGL J1217.2-2500	XRT J121735.36-245512.3	-	PANJ121735.18-245512.8	184.3966	-24.9202	19.8(19.7)	4.4	<0.3	<8
4FGL J1220.1-2458	XRT J122014.54-245948.2	VLASS1QLCIRJ122014.53-245948.2	PANJ122014.55-245948.6	185.0606	-24.9968	20.0(19.4)	3.6	8.2	227
4FGL J1239.7-3455	XRT J123933.89-345428.1	RACSJ123933.4-345426	SSSJ123933.61-345427.3	189.8902	-34.9075	20.3(18.5)	2.8	15.8	574
4FGL J1250.9-4943	XRT J125058.72-494448.6*	RACSJ125059.0-494447	SSSJ125059.00-494448.1	192.7455	-49.7473	19.2(18.4)	7.6	63.3	834
4FGL J1256.8+5329	XRT J125630.54+533202.3	-	PANJ125630.44+533204.3	194.1268	53.5345	20.6(20.3)	2.1	<0.3	<17
4FGL J1259.0-8148	XRT J130100.24-814811.8*	-	SSSJ130100.03-814813.3	195.2506	-81.8037	19.1(18.8)	8.3	<0.6	<8
4FGL J1308.7+0347	XRT J130832.27+034405.4	-	PANJ130832.10+034404.0	197.1338	3.7344	17.2(17.3)	47.9	<0.3	<1
4FGL J1313.2-4437	XRT J131318.21-443732.2	RACSJ131318.5-443724	SSSJ131318.14-443731.4	198.3257	-44.6253	21.5(50.0)	0.9	9.9	1087
4FGL J1346.5+5330	XRT J134545.15+533252.5	VLASS1QLCIRJ134545.34+533252.1	PANJ134545.36+533252.3	206.4390	53.5479	17.0(16.6)	57.5	248.1	431
4FGL J1401.7-3217	XRT J140159.82-321848.4	RACSJ140159.4-321845	SSSJ140459.47-321844.9	210.4979	-32.3124	21.4(20.6)	1	149.7	14971
4FGL J1401.3-5012	XRT J140146.80-501324.1	-	SSSJ140146.68-501321.7	210.4447	-50.2227	17.2(16.8)	47.9	<0.6	<1
4FGL J1407.4-0820	XRT J140724.84-082320.5	-	PANJ140724.83-082317.8	211.8535	-8.3883	18.6(18.6)	13.2	<0.3	<3
4FGL J1410.7+7405	XRT J141045.66+740509.9	VLASS1QLCIRJ141046.08+740510.9	PANJ141045.95+740510.9	212.6915	74.0864	19.2(19.3)	7.6	2.2	29
4FGL J1415.9-1504	XRT J141546.05-150231.4	ATCAJ141546.18-150229.7	PANJ141546.17-150229.0	213.9424	-15.0414	19.0(18.5)	9.1	2.0	13
4FGL J1420.9-2431	XRT J142035.74-243023.3*	-	PANJ142035.89-243024.6	215.1495	-24.5068	8.1(7.5)	208929.6	<0.3	<1
4FGL J1421.4-1655	XRT J142128.97-165455.7	VLASS1QLCIRJ142128.99-165455.7	PANJ142128.99-165456.1	215.3708	-16.9156	20.1(19.8)	3.3	2.5	76
4FGL J1424.8-8012	XRT J142342.47-800721.1*	-	SSSJ142343.91-800719.0	215.9332	-80.1219	14.6(13.2)	524.8	<0.6	<1
4FGL J1429.8-0739	XRT J142949.48-073304.7	-	PANJ142949.48-073304.4	217.4562	-7.5512	17.5(16.6)	36.3	<0.3	<1
4FGL J1430.6+1543	XRT J143057.97+154556.1	-	PANJ143058.03+154555.6	217.7418	15.7655	17.4(16.9)	39.8	<0.3	<1
4FGL J1441.4-1934	XRT J144127.83-193551.0	VLASS1QLCIRJ144127.96-193552.1	PANJ144127.97-193552.5	220.3665	-19.5979	19.7(19.0)	4.8	4.1	87
4FGL J1528.4+2004	XRT J152835.84+200422.1	VLASS1QLCIRJ152835.77+200420.3	PANJ152835.77+200420.1	232.1490	20.0723	20.7(20.2)	1.9	3.3	174
4FGL J1535.9+3743	XRT J153550.56+374056.8	VLASS1QLCIRJ153550.56+374055.5	PANJ153550.54+374055.5	233.9606	37.6821	19.8(19.3)	4.4	26.3	603
4FGL J1538.9+0425	XRT J153901.41+042750.5	-	PANJ153901.46+042750.7	234.7561	4.4641	20.8(19.7)	1.7	<0.3	<20
4FGL J1539.1+1008	XRT J153848.51+101841.7	-	PANJ153848.48+101843.3	234.7020	10.3120	18.3(18.0)	17.4	<0.3	<2
4FGL J1543.1+4209	XRT J154311.32+421006.3	VLASS1QLCIRJ154310.97+421008.0	PANJ154310.95+421008.1	235.7956	42.1689	20.3(20.1)	2.8	1.8	67
4FGL J1544.9+3218	XRT J154433.15+322148.6	VLASS1QLCIRJ154433.20+322149.1	PANJ154433.20+322149.1	236.1383	32.3636	18.7(18.4)	12	12	100
4FGL J1554.2+2008	XRT J155424.17+201125.5	VLASS1QLCIRJ155424.15+201125.5	PANJ155424.13+201125.4	238.6005	20.1904	18.1(17.2)	20.9	42	201
4FGL J1555.3+2903	XRT J155513.01+290328.0	VLASS1QLCIRJ155512.89+290330.0	PANJ155512.91+290329.9	238.8038	29.0583	18.2(17.2)	19.1	21.7	114
4FGL J1623.7-2315	XRT J162334.02-231745.2*	-	PANJ162334.00-231744.5	245.8917	-23.2957	21.3(20.5)	1.1	<0.3	<31
4FGL J1626.5+6257	XRT J162645.99+630048.4	VLASS1QLCIRJ162646.06+630048.4	PANJ162646.06+630048.4	246.6919	63.0134	19.0(18.0)	9.1	9.2	101
4FGL J1631.8+4144	XRT J163146.82+414631.8	VLASS1QLCIRJ163146.74+414632.7	PANJ163146.72+414632.7	247.9447	41.7758	20.5(20.4)	2.3	0.8	34
4FGL J1644.8+1850	XRT J164457.22+185151.1	-	PANJ164457.16+185149.1	251.2382	18.8636	19.2(18.7)	7.6	<0.3	<5
4FGL J1645.0+1654	XRT J164459.83+165512.9	VLASS1QLCIRJ164459.81+165512.4	PANJ164459.80+165512.3	251.2492	16.9201	19.2(18.2)	7.6	11.4	150

Note. Labels are the same as in table A.6.

Table A.6: MWL counterparts of UGS1. Continued

4FGL Name (1)	*Swift*/XRT source (2)	Radio source (3)	Optical source (4)	RA (5) J2000	DEC (6) J2000	gmag(rmag) (7)	$f_\nu^{\rm opt}$ (8) [× 10^{-28}]	$f_\nu^{\rm radio}$ (9)	*R* (10)
4FGL J1648.1-1547	XRT J164804.04-154704.7*	VLASS1QLCIRJ164804.19-154701.0	PANJ164804.27-154702.6	252.0178	-15.7841	19.0(18.3)	9.1	6.1	67
4FGL J1648.7+4834	XRT J164900.56+483409.2	VLASS1QLCIRJ164900.35+483411.7	PANJ164900.83+483408.1	252.2535	48.5689	19.4(19.1)	6.3	2.5	40
4FGL J1657.3-6232	XRT J165757.49-623400.2*	-	SSSJ165757.16-623400.0	254.4880	-62.5666	10.0(7.2)	36307.8	<0.6	<1
4FGL J1700.0-0122	XRT J170003.04-011841.5*	-	PANJ170003.04-011842.7	255.0127	-1.3118	16.2(15.0)	120.2	<0.3	<1
4FGL J1733.4+2235	XRT J173330.16+223608.5	-	PANJ173330.32+223611.8	263.3763	22.6033	17.7(17.0)	30.2	<0.3	<1
4FGL J1752.0+3606	XRT J175209.56+360629.8	VLASS1QLCIRJ175209.76+360627.7	PANJ175209.74+360627.7	268.0406	36.1077	20.3(20.3)	2.8	1	38
4FGL J1803.1-6708	XRT J180304.04-670734.5*	-	SSSJ180304.23-670735.9	270.7674	-67.1266	20.4(19.1)	2.5	<0.6	<25
4FGL J1813.7-6846	XRT J181307.54-684706.7	-	SSSJ181307.48-684706.2	273.2815	-68.7850	20.6(20.6)	2.1	<0.6	<31
4FGL J1816.1-3908	XRT J181635.82-391246.1*	-	SSSJ181635.99-391246.6	274.1500	-39.2129	17.1(16.8)	52.5	<0.3	<1
4FGL J1818.5+2533	XRT J181831.18+253705.4*	-	PANJ181831.17+253707.3	274.6299	25.6187	15.4(14.7)	251.2	<0.3	<1
4FGL J1824.2+1231	XRT J182408.91+123231.5*	-	PANJ182408.89+123233.3	276.0370	12.5426	19.9(19.2)	4	<0.3	<9
4FGL J1825.9-5614	XRT J182644.04-561421.5*	-	SSSJ182643.76-561419.7	276.6822	-56.2389	14.6(13.2)	524.8	<0.6	<1
4FGL J1836.9+4439	XRT J183703.33+443807.0	-	PANJ183703.46+443809.0	279.2644	44.6358	-(20.7)	-	-	-
4FGL J1838.2+3223	XRT J183816.84+322410.8*	-	PANJ183816.82+322411.3	279.5701	32.4031	20.8(20.7)	1.7	<0.3	<20
4FGL J1847.7-3433	XRT J184713.08-343345.8	-	SSSJ184713.08-343345.5	281.8046	-34.5627	22.1(-)	0.5	<0.3	<66
4FGL J1848.7-6307	XRT J184838.07-630537.8*	-	SSSJ184838.23-630535.6	282.1595	-63.0932	19.9(19.0)	4	<0.6	<16
4FGL J1858.9+3636	XRT J185917.93+362916.5*	-	PANJ185917.94+362914.0	284.8248	36.4872	12.8(12.2)	2754.2	<0.3	<1
4FGL J1905.8+4942	XRT J190549.31+495142.1	-	PANJ190549.43+495143.2	286.4560	49.8620	19.6(18.4)	5.2	<0.3	<7
4FGL J1906.0-1718	XRT J190624.51-171936.6	-	PANJ190624.58-171936.5	286.6024	-17.3268	19.7(18.9)	4.8	<0.3	<7
4FGL J1906.4-1757	XRT J190625.65-175903.7*	-	PANJ190625.86-175900.5	286.6078	-17.9835	19.4(18.4)	6.3	<0.3	<5
4FGL J1912.2-3636	XRT J191259.66-363245.4*	-	SSSJ191259.70-363244.7	288.2488	-36.5458	20.6(19.1)	2.1	<0.3	<17
4FGL J1928.5+5339	XRT J192833.63+533901.3	VLASS1QLCIRJ192833.55+533902.4	PANJ192833.58+533902.5	292.1399	53.6507	20.4(19.5)	2.5	3.3	132
4FGL J1955.3-5032	XRT J195512.48-503008.8	RACSJ195512.5-503008	SSSJ195512.56-503008.3	298.8024	-50.5022	19.9(18.0)	4	13.5	340
4FGL J2007.0+0707	XRT J200642.07+071712.5*	-	PANJ200642.33+071717.2	301.6764	7.2881	15.5(14.3)	229.1	<0.3	<1
4FGL J2017.9-0114	XRT J201739.32-010732.4	-	PANJ201739.10-010729.9	304.4129	-1.1250	-(21.5)	-	-	-
4FGL J2018.0+7903	XRT J201746.50+790238.0	VLASS1QLCIRJ201746.03+790237.6	PANJ201746.06+790237.9	304.4419	79.0439	20.0(19.6)	3.6	2.8	77
4FGL J2019.6+0616	XRT J201931.60+061543.8	-	PANJ201931.62+061540.2	304.8817	6.2612	20.6(20.5)	2.1	<0.3	<17
4FGL J2029.5-4237	XRT J202914.15-423532.1	ATCAJ225730.73-410226.2	DESJ202914.16-423530.9	307.3090	-42.5919	20.0(19.0)	3.6	0.3	7
4FGL J2030.0-0310	XRT J203014.34-030721.9	-	PANJ203014.28-030722.6	307.5595	-3.1229	16.8(16.2)	69.2	0.3	1
4FGL J2036.2-0207	XRT J203637.80-020242.3	-	PANJ203637.34-020239.0	309.1556	-2.0442	19.5(19.3)	5.8	<0.3	<6
4FGL J2037.0-2826	XRT J203637.90-283026.0	VLASS1QLCIRJ203637.77-283026.0	PANJ203637.78-283026.5	309.1574	-28.5074	20.1(20.2)	3.3	225.9	6822
4FGL J2037.7-2230	XRT J203743.50-222630.0*	-	PANJ203743.54-222631.0	309.4314	-22.4419	11.3(11.9)	10964.8	<0.3	<1
4FGL J2040.1-3137	XRT J204010.16-314745.9*	-	SSSJ204009.96-315750.9	310.0422	-31.7968	20.6(-)	2.1	<0.3	<17
4FGL J2041.1-6138	XRT J204111.84-613950.0*	RACSJ204111.9-613949	DESJ204112.07-613949.3	310.3003	-61.6637	19.2(18.5)	7.6	50.4	664
4FGL J2042.1-5320	XRT J204220.33-532643.2	RACSJ204220.4-532643	DESJ204220.36-532643.0	310.5849	-53.4453	20.4(19.9)	2.5	8.6	341
4FGL J2042.7+1519	XRT J204259.73+152108.8*	VLASS1QLCIRJ204259.74+152108.3	PANJ204259.72+152108.1	310.7489	15.3523	16.9(17.0)	63.1	10.9	17
4FGL J2045.6+2455	XRT J204555.08+245356.3	-	PANJ204554.97+245359.0	311.4791	24.8997	18.8(17.8)	11	<0.3	<3
4FGL J2056.4-5922	XRT J205624.41-591719.4	RACSJ205624.4-591723	DESJ205623.45-591720.4	314.0977	-59.2890	24.9(24.7)	0	8.2	20527
4FGL J2058.5-1833	XRT J205836.75-183103.8	-	PANJ205836.86-183105.5	314.6536	-18.5182	20.3(19.6)	2.8	<0.3	<13
4FGL J2105.9+7508	XRT J210605.68+750921.0	VLASS1QLCIRJ210605.50+750920.5	PANJ210605.48+750920.8	316.5228	75.1558	21.4(20.4)	1	4.4	441
4FGL J2109.8+6315	XRT J210928.72+631745.7*	-	PANJ210928.82+631744.3	317.3701	63.2956	6.3(6.7)	1096478.2	<0.3	<1
4FGL J2114.2+2132	XRT J211407.79+213241.1	VLASS1QLCIRJ211407.74+213240.9	PANJ211407.76+213240.8	318.5323	21.5447	19.9(18.8)	4	18.7	470
4FGL J2114.9-3326	XRT J211452.16-332534.2	VLASS1QLCIRJ211452.08-332532.9	PANJ211452.10-332533.5	318.7171	-33.4260	19.2(18.3)	7.6	5.2	69
4FGL J2120.5-0138	XRT J212030.54-013841.7	VLASS1QLCIRJ212030.62-013840.2	PANJ212030.60-013840.41	320.1275	-1.6446	19.5(18.8)	5.8	6	104
4FGL J2121.8-3412	XRT J212200.61-341834.3	VLASS1QLCIRJ212200.78-341835.8	SSSJ212200.77-341836.6	320.5032	-34.3101	19.8(19.1)	4.4	9	206
4FGL J2130.8+2649	XRT J213011.72+264505.2*	-	PANJ213011.83+264505.4	322.5493	26.7515	19.9(19.9)	4	<0.3	<9
4FGL J2159.6-4620	XRT J215936.22-461955.4	RACSJ215935.9-461953	DESJ215936.12-461953.7	329.9005	-46.3316	18.9(18.6)	10	5.5	55
4FGL J2207.1+2222	XRT J220704.18+222231.9	VLASS1QLCIRJ220704.09+222231.5	PANJ220704.10+222231.4	331.7671	22.3754	20.4(19.9)	2.5	6.5	258
4FGL J2207.3+2746	XRT J220722.56+274617.9	VLASS1QLCIRJ220722.39+274617.9	PANJ220722.41+274617.9	331.8434	27.7717	20.3(20.1)	2.8	3.4	124
4FGL J2225.8-0804	XRT J222553.05-080410.8	VLASS1QLCIRJ222553.12-080409.4	PANJ222553.15-080415.1	336.4715	-8.0709	20.9(19.9)	1.6	8.4	528
4FGL J2237.2-6726	XRT J223709.85-672612.7	RACSJ223709.6-672613	SSSJ223709.73-672613.3	339.2905	-67.4370	19.9(18.4)	4	10.8	270
4FGL J2240.3-5241	XRT J224017.55-524112.3	RACSJ224017.8-524114	DESJ224017.72-524113.8	340.0739	-52.6872	18.0(17.3)	22.9	31	135
4FGL J2241.4-8327	XRT J224200.97-832746.0	ATCAJ224201.46-832743.1	SSSJ224201.62-832744.0	340.5062	-83.4622	19.6(17.6)	5.2	0.2	3
4FGL J2247.7-5857	XRT J224745.19-585458.2	RACSJ224745.2-585457	DESJ224745.18-585457.6	341.9383	-58.9160	20.7(20.4)	1.9	5.2	271
4FGL J2312.4+8253	XRT J231203.37+830108.0*	-	PANJ231201.73+830111.3	348.0072	83.0198	15.0(13.4)	363.1	<0.3	<1
4FGL J2317.7+2839	XRT J231740.15+283955.4	VLASS1QLCIRJ231740.21+283955.8	PANJ231740.23+283955.8	349.4176	28.6655	19.6(19.1)	5.2	4.5	86
4FGL J2320.2+0707	XRT J232007.88+071044.0*	-	PANJ232007.94+071044.1	350.0331	7.1789	10.1(9.4)	33113.1	<0.3	<1
4FGL J2323.1+2040	XRT J232320.30+203523.6	VLASS1QLCIRJ232320.32+203522.2	PANJ232320.34+203523.5	350.8348	20.5899	14.4(13.4)	631	160.4	25
4FGL J2323.9+2519	XRT J232341.56+251800.0*	-	PANJ232341.34+251801.4	350.9222	25.3004	8.4(8.2)	158489.3	<0.3	<1
4FGL J2326.9-4130	XRT J232653.20-412713.8	-	DESJ232653.06-412710.9	351.7211	-41.4530	17.8(17.6)	27.5	<0.6	<2
4FGL J2331.6+4430	XRT J233129.51+443104.3	VLASS1QLCIRJ233129.03+443102.3	PANJ233129.06+443102.4	352.8711	44.5173	21.0(20.2)	1.4	6.9	480
4FGL J2336.9-8427	XRT J233625.43-842650.6	-	SSSJ233627.60-842651.55	354.1141	-84.4477	20.8(19.7)	1.7	0.2	12
4FGL J2337.7-2903	XRT J233730.35-290237.9	VLASS1QLCIRJ233730.46-290236.5	PANJ233730.46-290237.2	354.3769	-29.0437	20.0(18.9)	3.6	4.1	113
4FGL J2347.9-5106	XRT J234804.68-510745.2	-	DESJ234804.68-510742.3	357.0195	-51.1284	19.8(19.8)	4.4	<0.6	<15
4FGL J2353.2+3135	XRT J235319.54+313616.7	VLASS1QLCIRJ235319.50+313616.8	PANJ235319.55+313616.8	358.3314	31.6047	20.5(20.5)	2.3	60.6	2646

Note. Labels are the same as in table A.6.

Table A.7: MWL counterpartsof UGS2.

4FGL Name (1)	*Swift*/XRT source (2)	Radio source (3)	Optical source (4)	RA (5) J2000	DEC (6) J2000	gmag(rmag) (7)	f_ν^{opt} (8) [$\times 10^{-28}$]	f_ν^{radio} (9)	*R* (10)
4FGLJ0017.1-4605	XRTJ001708.63-460607.7	ATCAJ001708.65-460607.0	DESJ001708.67-460606.9	4.2862	-46.1019	18.3(18.1)	17.4	0.1	1
	XRTJ001750.81-460437.5	ATCAJ001750.67-460438.6	DESJ001750.66-460438.5	4.4611	-46.0774	17.8(17.9)	27.5	0.5	3
-	XRTJ001705.00-460109.2	-	DESJ001704.83-460110.1	4.2702	-46.0195	20.8(20.7)	1.7	<0.6	<37
4FGLJ0031.0-2327	XRTJ003120.53-233400.7	VLASS1QLCIRJ003120.56-233401.6	PANJ003120.55-233401.2	7.8356	-23.5670	20.1(19.0)	3.3	3.9	118
-	XRTJ003039.79-232821.2	-	PANJ003039.76-232822.3	7.6656	-23.4729	19.9(19.5)	4.0	<0.3	<9
4FGLJ0040.2-2725	XRTJ004016.42-271912.3	VLASS1QLCIRJ004016.40-271911.5	PANJ004016.41-271911.7	10.0684	-27.3199	18.8(18.6)	11.0	86.0	784
-	XRTJ004023.77-272254.2	-	PANJ004023.90-272255.4	10.0996	-27.3821	22.6(20.8)	-	<0.3	-
	XRTJ004026.07-272116.1*	-	DESJ004026.16-272117.6	10.1090	-27.3549	14.8(14.2)	436.5	<0.3	<1
-	XRTJ004035.80-272240.7	-	PANJ004035.87-272242.0	10.1494	-27.3783	21.9(21.6)	0.6	<0.3	<55
-	XRTJ003954.35-272516.1	-	PANJ003954.09-272513.5	9.9754	-27.4204	21.2(21.1)	1.2	<0.3	<29
4FGLJ0045.8-1324	XRTJ004602.94-132422.2	VLASS1QLCIRJ004602.82-132422.1	PANJ004602.82-132422.4	11.5118	-13.4062	18.7(18.7)	12.0	8.1	68
-	XRTJ004608.32-132213.6	-	PANJ004608.44-132215.2	11.5352	-13.3709	18.5(18.6)	14.5	<0.3	<2
-	XRTJ004611.48-132519.3*	-	PANJ004611.47-132522.6	11.5478	-13.4229	17.6(16.4)	33.1	<0.3	<1
-	XRTJ004539.41-132507.7	VLASS1QLCIRJ004539.47-132508.0	-	-	-	-(-)	-	1.7	-
-	XRTJ004602.97-131959.0	-	PANJ004602.68-131958.9	11.5112	-13.3330	21.1(21.3)	1.3	<0.3	<26
-	XRTJ004555.20-132312.5	-	PANJ004555.27-132314.3	11.4803	-13.3873	–(21.2)	-	<0.3	-
4FGLJ0102.3+1000	XRTJ010226.89+095939.9	VLASS1QLCIRJ010226.69+095939.6	-	-	-	-(-)	-	6.5	-
-	XRTJ010235.93+095832.4	-	-	-	-	-(-)	-	<0.3	-
-	XRTJ010220.73+095848.9	-	PANJ010220.59+095847.5	15.5858	9.9799	20.1(20.0)	3.3	<0.3	<10
-	XRTJ010214.03+100258.4	-	-	-	-	-(-)	-	<0.3	-
4FGLJ0118.3-6008	XRTJ011823.22-600747.8	RACSJ011823.5-600749	DESJ011823.48-600751.3	19.5978	-60.1309	17.9(17.4)	25.1	96.8	385
-	XRTJ011848.17-600256.2	-	DESJ011848.16-600256.3	19.7007	-60.0490	19.0(18.9)	9.1	<0.6	<7
4FGLJ0122.4+1034	XRTJ012223.64+103212.6	VLASS1QLCIRJ012223.63+103213.3	PANJ012223.62+103213.2	20.5984	10.5370	20.1(19.8)	3.3	8.5	257
-	XRTJ012222.25+103116.2	-	PANJ012222.18+103118.2	20.5924	10.5217	21.3(19.5)	1.1	<0.3	<31
4FGLJ0126.3-6746	XRTJ012610.88-674744.5	RACSJ012610.7-674743	SSSJ012610.68-674742.6	21.5446	-67.7952	18.6(16.5)	13.2	8.4	64
-	XRTJ012622.53-674626.7	RACSJ012622.4-674610	SSSJ012622.15-674623.0	21.5924	-67.7731	20.1(19.4)	3.3	53.0	1601
4FGLJ0132.9-4259	XRTJ013346.96-430407.0	-	DESJ013346.86-430410.0	23.4453	-43.0695	20.8(19.7)	1.7	<0.6	<37
-	XRTJ013401.65-425630.0	-	DESJ013401.71-425630.9	23.5072	-42.9419	19.5(19.2)	5.8	<0.6	<11
-	XRTJ013339.96-425503.4	-	DESJ013339.96-425505.0	23.4165	-42.9181	19.6(19.1)	5.2	<0.6	<12
-	XRTJ013347.80-430229.3	-	DESJ013347.77-430230.0	23.4490	-43.0417	21.7(21.1)	0.8	<0.6	<84
	XRTJ013316.63-425908.7	-	DESJ013316.78-425910.0	23.3199	-42.9861	19.8(19.5)	4.4	<0.6	<15
-	XRTJ013308.39-425744.6	-	DESJ013308.45-425747.2	23.2852	-42.9631	20.7(20.2)	1.9	<0.6	<34
-	XRTJ013359.11-430219.2	-	DESJ013359.30-430221.1	23.4971	-43.0392	21.2(23.0)	-	<0.6	-
-	XRTJ013347.00-430610.6	-	DESJ013347.16-430611.0	23.4465	-43.1031	20.7(20.7)	1.9	<0.6	<34
-	XRTJ013339.30-425824.0	-	DESJ013339.31-425825.8	23.4138	-42.9738	23.9(23.9)	0.1	<0.6	<639
4FGLJ0140.4+5114	XRTJ014107.78+510659.4	-	PANJ014107.96+510658.8	25.2832	51.1163	19.3(18.7)	6.9	<0.3	<5
-	XRTJ014022.50+511313.3	-	PANJ014022.76+511311.6	25.0948	51.2199	21.1(19.4)	1.3	<0.3	<26
4FGLJ0159.0+3313	XRTJ015906.95+331227.3*	-	PANJ015907.09+331226.8	29.7795	33.2075	10.9(6.5)	15848.9	<0.3	<1
	XRTJ015905.35+331257.8	VLASS1QLCIRJ015905.17+331257.7	PANJ015905.20+331257.6	29.7717	33.2160	16.1(17.2)	131.8	4.8	4
-	XRTJ015927.92+331107.7	-	PANJ015928.11+331107.4	29.8671	33.1854	20.4(20.2)	2.5	<0.3	<14
4FGLJ0159.8-2234	XRTJ015947.54-223254.4	RACSJ015946.9-223251	PANJ015947.53-223300.8	29.9481	-22.5502	22.0(21.4)	0.6	4.7	814
	XRTJ020016.59-222940.5	-	PANJ020016.76-222940.8	30.0698	-22.4947	18.4(18.4)	15.8	<0.3	<2
-	XRTJ015957.01-223136.3*	-	PANJ015957.00-223138.7	29.9875	-22.5274	12.3(12.0)	4365.2	<0.3	<1
4FGLJ0209.8+2626	XRTJ020946.75+262530.4	VLASS1QLCIRJ020946.71+262530.9	PANJ020946.73+262531.0	32.4447	26.4253	21.0(20.6)	1.4	3.9	268
-	XRTJ020950.60+263253.3	-	PANJ020950.74+263255.9	32.4614	26.5489	18.5(17.5)	14.5	<0.3	<2
4FGLJ0240.2-0248	XRTJ024002.02-024321.6	-	PANJ024001.91-024322.0	40.0079	-2.7228	18.2(18.3)	19.1	<0.3	<2
	XRTJ024004.57-024504.3	-	PANJ024004.51-024502.6	40.0188	-2.7507	18.4(17.9)	15.8	<0.3	<2
-	XRTJ024024.23-025336.4	VLASS1QLCIRJ024024.38-025334.0	PANJ024024.37-025334.3	40.1015	-2.8929	19.3(18.9)	6.9	5.5	79
4FGLJ0251.4+4646	XRTJ025027.22+464729.1	VLASS1QLCIRJ025027.17+464729.3	PANJ025027.19+464729.3	42.6133	46.7915	17.7(17.0)	30.2	4.5	15
-	XRTJ025117.49+464501.7	VLASS1QLCIRJ025117.66+464504.3	PANJ025117.68+464504.4	42.8237	46.7512	20.4(20.1)	2.5	38.1	1517
4FGLJ0252.0-3657	XRTJ025139.26-365715.2	-	DESJ025139.16-365714.3	42.9132	-36.9540	21.7(20.6)	0.8	<0.3	<45
-	XRTJ025149.15-370144.5	-	DESJ025149.10-370146.7	42.9546	-37.0296	20.1(20.0)	3.3	<0.3	<10
-	XRTJ025145.81-365713.8	-	DESJ025145.76-365713.4	42.9407	-36.9537	23.2(21.8)	0.2	<0.3	<181
-	XRTJ025207.48-365438.4	-	DESJ025207.53-365437.3	43.0314	-36.9104	21.7(21.5)	0.8	<0.3	<45
4FGLJ0447.2+2446	XRTJ044739.31+244227.7	VLASS1QLCIRJ044739.26+244225.6	-	-	-	-(-)	-	1.6	-
-	XRTJ044709.75+243701.5	-	PANJ044709.74+243658.3	71.7906	24.6162	21.0(19.4)	1.4	<0.3	<24
4FGLJ0535.3+0934	XRTJ053512.72+093645.2*	-	PANJ053512.69+093645.1	83.8029	9.6125	11.3(13.0)	10964.8	<0.3	<1
	XRTJ053447.47+094026.3*	-	PANJ053447.50+094029.0	83.6979	9.6747	19.0(17.7)	9.1	<0.3	<4
-	XRTJ053508.19+094254.2*	-	PANJ053508.34+094253.7	83.7847	9.7149	13.2(12.5)	1905.5	<0.3	<1
4FGLJ0539.2-6333	XRTJ053842.39-632820.0	RACSJ053842.1-632819	-	-	-	-(-)	-	4.5	-
-	XRTJ054002.73-633214.6*	-	SSSJ054002.82-633216.0	85.0119	-63.5378	18.7(17.0)	12.0	<0.6	<5
4FGLJ0544.8+5209	XRTJ054424.68+521515.7	-	PANJ054424.73+521516.2	86.1031	52.2545	20.9(20.5)	1.6	<0.3	<22
-	XRTJ054457.19+520852.8	VLASS1QLCIRJ054457.11+520851.1	PANJ054457.11+520851.2	86.2379	52.1476	21.0(19.7)	1.4	4.4	306

Note. Labels are the same as in table A.6

Table A.7: MWL counterpartsof UGS2. Continued

4FGL Name (1)	*Swift*/XRT source (2)	Radio source (3)	Optical source (4)	RA (5) J2000	DEC (6) J2000	gmag(rmag) (7)	$f_\nu^{\rm opt}$ (8) [$\times 10^{-28}$]	$f_\nu^{\rm radio}$ (9)	*R* (10)
4FGLJ0546.5-1100	XRTJ054730.24-112151.5*	-	PANJ054730.28-112151.9	86.8761	-11.3644	14.8(13.8)	436.5	<0.3	<1
-	XRTJ054631.01-112023.3	-	PANJ054631.13-112026.6	86.6297	-11.3407	20.5(21.4)	2.3	<0.3	<15
-	XRTJ054719.62-110938.9	-	PANJ054719.59-110940.1	86.8316	-11.1611	21.2(20.7)	1.2	<0.3	<29
-	XRTJ054706.34-112139.1	-	-	-	-	-(-)	-	<0.3	-
-	XRTJ054649.72-111754.3	-	PANJ054649.71-111755.9	86.7071	-11.2989	21.7(20.6)	0.8	<0.3	<45
-	XRTJ054628.95-112059.0*	-	PANJ054628.72-112100.5	86.6197	-11.3501	15.0(13.9)	363.1	<0.3	<1
-	XRTJ054632.75-110505.3	-	PANJ054632.64-110510.5	86.6360	-11.0862	20.6(20.1)	2.1	<0.3	<17
-	XRTJ054736.04-111141.3*	-	PANJ054736.01-111143.4	86.9000	-11.1954	11.4(10.5)	10000.0	<0.3	<1
4FGLJ0610.8-4911	XRTJ061100.18-491036.2	-	DESJ061100.16-491035.0	92.7507	-49.1764	20.8(20.5)	1.7	<0.6	<37
-	XRTJ061031.81-491222.5*	-	DESJ061031.94-491221.8	92.6331	-49.2061	15.3(15.4)	275.4	<0.6	<1
4FGLJ0611.5-2918	XRTJ061141.70-291618.0	VLASS1QLCIRJ061141.65-291618.5	PANJ061141.66-291618.8	92.9236	-29.2719	20.6(20.2)	2.1	1.9	90
-	XRTJ061216.02-291702.3	-	PANJ061215.95-291659.6	93.0665	-29.2832	18.3(18.2)	17.4	<0.3	<2
4FGLJ0617.6-4028	XRTJ061646.98-402143.4	RACSJ061646.7-402144	DESJ061647.02-402142.8	94.1959	-40.3619	18.5(18.1)	14.5	8.7	60
	XRTJ061724.11-402212.8*	-	DESJ061724.12-402213.5	94.3505	-40.3704	14.3(14.1)	691.8	<0.6	<1
-	XRTJ061818.54-403400.9	-	DESJ061818.37-403400.8	94.5766	-40.5669	19.7(18.5)	4.8	<0.6	<13
4FGLJ0633.9+5840	XRTJ063359.74+584034.2	VLASS1QLCIRJ063359.69+584035.8	PANJ063359.72+584035.8	98.4988	58.6766	20.1(19.2)	3.3	1.9	57
-	XRTJ063342.26+584642.7	-	PANJ063342.58+584643.6	98.4274	58.7788	20.6(20.2)	2.1	<0.3	<17
4FGLJ0639.1-8009	XRTJ064059.59-801126.2*	-	SSSJ064059.67-801125.8	100.2484	-80.1904	20.9(20.3)	1.6	<0.6	<40
-	XRTJ063617.46-801350.5	-	-	-	-	-(-)	-	<0.6	-
-	XRTJ064125.96-801048.5	-	SSSJ064126.18-801047.1	100.3589	-80.1800	21.1(20.2)	1.3	<0.6	<49
-	XRTJ063719.22-801230.2	-	-	-	-	-(-)	-	<0.6	-
	XRTJ064012.99-801725.0	-	-	-	-	-(-)	-	<0.6	-
-	XRTJ063555.23-800813.0	-	-	-	-	-(-)	-	<0.6	-
-	XRTJ064047.38-802414.7	-	-	-	-	-(-)	-	<0.6	-
-	XRTJ063641.31-801124.9	-	SSSJ063640.72-801126.5	99.1700	-80.1907	21.4(19.8)	1.0	<0.6	<64
-	XRTJ064049.32-801255.8	-	-	-	-	-(-)	-	<0.6	-
4FGLJ0723.9+5702	XRTJ072351.47+565734.6*	-	PANJ072351.61+565735.0	110.9650	56.9597	18.7(19.2)	12.0	<0.3	<3
-	XRTJ072328.63+565908.8*	-	PANJ072328.93+565908.9	110.8705	56.9858	9.6(12.5)	-	<0.3	-
4FGLJ0737.4+6535	XRTJ073655.73+653540.7	-	PANJ073655.87+653541.7	114.2328	65.5949	13.7(10.6)	1202.3	<0.3	<1
-	XRTJ073711.73+653344.9*	-	PANJ073711.66+653347.6	114.2986	65.5632	18.8(18.5)	11.0	<0.3	<3
4FGLJ0738.6+1311	XRTJ073843.59+131328.3*	-	PANJ073843.67+131327.4	114.6819	13.2243	16.8(14.6)	69.2	<0.3	<1
-	XRTJ073848.93+130755.1	VLASS1QLCIRJ073848.96+130758.3	PANJ073848.98+130758.2	114.7041	13.1328	20.1(19.1)	3.3	15.6	470
4FGLJ0751.2-0029	XRTJ075104.16-003305.6	-	PANJ075104.20-003305.9	117.7675	-0.5516	21.4(-)	1	<0.3	<35
-	XRTJ075119.14-002748.8	VLASS1QLCIRJ075119.20-002748.9	PANJ075119.20-002749.1	117.8300	-0.4636	18.6(17.8)	13.2	17.0	129
4FGLJ0800.1-5531	XRTJ075949.42-553253.8	-	SSSJ075949.46-553254.7	119.9565	-55.5485	19.0(18.3)	9.1	<0.6	<7
-	XRTJ080013.52-553407.9	-	SSSJ080013.53-553408.9	120.0561	-55.5692	19.2(17.4)	7.6	<0.6	<8
4FGLJ0849.5+2710	XRTJ084957.80+271614.1	-	PANJ084957.80+271616.0	132.4908	27.2711	21.9(20.7)	0.6	<0.3	<55
-	XRTJ084936.07+270127.6	-	PANJ084936.00+270125.8	132.4000	27.0238	19.7(19.7)	4.8	<0.3	<7
4FGLJ0903.5+4057	XRTJ090314.64+405600.2	VLASS1QLCIRJ090314.69+405559.7	PANJ090314.71+405559.9	135.8113	40.9333	18.2(17.3)	19.1	19.6	103
-	XRTJ090342.94+405501.1	VLASS1QLCIRJ090343.18+405503.1	PANJ090343.20+405503.1	135.9300	40.9175	20.4(20.1)	2.5	2.9	114
4FGLJ0949.8+7551	XRTJ095017.79+754457.7*	-	PANJ095017.78+754503.1	147.5741	75.7509	17.1(19.0)	52.5	<0.3	<1
-	XRTJ095133.13+754839.3*	-	PANJ095134.82+754840.5	147.8951	75.8113	13.5(12.9)	1445.4	<0.3	<1
4FGLJ0952.9+1351	XRTJ095250.40+135218.5	VLASS1QLCIRJ095250.47+135216.7	PANJ095250.48+135216.4	148.2104	13.8712	20.5(19.7)	2.3	34.2	1491
-	XRTJ095245.54+134723.5*	-	PANJ095245.55+134721.1	148.1897	13.7892	11.9(11.4)	6310.0	<0.3	<1
4FGLJ0958.6-0522	XRTJ095833.81-052139.9	VLASS1QLCIRJ095833.75-052140.2	PANJ095833.74-052140.5	149.6406	-5.3613	18.7(18.3)	12.0	22.5	187
-	XRTJ095813.64-052441.3	-	PANJ095813.66-052439.0	149.5569	-5.4108	18.4(17.7)	15.8	<0.3	<2
4FGLJ1008.2-1000	XRTJ100848.62-095450.2	VLASS1QLCIRJ100848.60-095450.9	PANJ100848.59-095450.9	152.2025	-9.9141	15.3(14.9)	275.4	1.9	1
	XRTJ100802.55-095919.3*	VLASS1QLCIRJ100802.80-095918.3	PANJ100802.34-095919.7	152.0098	-9.9888	19.4(19.3)	6.3	83.9	1330
-	XRTJ100749.49-094911.9	-	PANJ100749.35-094912.1	151.9556	-9.8200	19.9(19.5)	4.0	<0.3	<9
4FGLJ1018.1-2705	XRTJ101750.36-270552.8	VLASS1QLCIRJ101750.30-270550.3	PANJ101750.36-270552.2	154.4598	-27.0978	20.5(18.8)	2.3	13.1	571
-	XRTJ101801.35-271234.0	-	-	-	-	-(-)	-	<0.3	-
4FGLJ1018.1-4051	XRTJ101807.55-404407.6*	-	-	-	-	-(-)	-	<0.6	-
-	XRTJ101801.63-405519.5	RACSJ101801.2-405519	SSSJ101801.34-405518.2	154.5057	-40.9217	20.0(19.7)	3.6	74.5	2051
	XRTJ101725.04-404436.3	-	SSSJ101725.01-404434.3	154.3543	-40.7429	20.1(20.2)	3.3	<0.6	<19
-	XRTJ101717.29-404759.7*	RACSJ101717.0-404755	SSSJ101717.07-404757.0	154.3212	-40.7992	19.0(18.1)	9.1	366.6	4020
-	XRTJ101820.43-404813.8*	-	SSSJ101820.59-404814.6	154.5857	-40.8043	18.8(18.4)	11.0	<0.6	<6
4FGLJ1036.5-1809	XRTJ103610.62-181315.4*	-	PANJ103610.60-181315.7	159.0441	-18.2210	13.7(13.4)	1202.3	<0.3	<1
-	XRTJ103625.96-180011.3	-	PANJ103625.85-180010.8	159.1077	-18.0030	19.9(19.7)	4.0	<0.3	<9

Note. Labels are the same as in table A.6

Table A.7: MWL counterpartsof UGS2. Continued

4FGL Name (1)	*Swift*/XRT source (2)	Radio source (3)	Optical source (4)	RA (5) J2000	DEC (6) J2000	gmag(rmag) (7)	f_ν^{opt} (8) [$\times 10^{-28}$]	f_ν^{radio} (9)	*R* (10)
4FGLJ1106.7+3623	XRTJ110622.38+363319.7	-	PANJ110622.46+363321.2	166.5936	36.5559	17.5(17.4)	36.3	<0.3	<1
-	XRTJ110710.07+361655.1	-	PANJ110710.14+361652.6	166.7922	36.2813	18.8(18.4)	11.0	<0.3	<3
-	XRTJ110635.95+362648.9	-	PANJ110636.53+362649.9	166.6522	36.4472	20.3(20.4)	2.8	<0.3	<13
-	XRTJ110612.40+363126.6	-	PANJ110612.38+363128.1	166.5516	36.5245	20.7(21.2)	1.9	<0.3	<18
4FGLJ1111.4+0137	XRTJ111114.26+013427.6	VLASS1QLCIRJ111114.27+013428.4	PANJ111114.29+013428.3	167.8095	1.5745	19.4(18.4)	6.3	5.2	82
-	XRTJ111206.06+013526.7	VLASS1QLCIRJ111206.04+013524.5	PANJ111206.05+013524.4	168.0252	1.5901	18.9(17.7)	10.0	1.1	11
-	XRTJ111159.79+013642.6*	-	PANJ111159.80+013646.9	167.9992	1.6130	20.3(19.0)	2.8	<0.3	<13
-	XRTJ111106.07+014559.8	-	PANJ111105.95+014558.6	167.7748	1.7663	18.9(18.4)	10.0	<0.3	<3
4FGLJ1126.0-5007	XRTJ112624.22-500806.5	-	-	-	-	-(-)	-	<0.6	-
-	XRTJ112628.32-500842.8*	-	SSSJ112628.29-500843.2	171.6178	-50.1453	19.5(18.1)	5.8	<0.6	<11
-	XRTJ112533.68-500549.2*	-	SSSJ112533.70-500549.1	171.3906	-50.0970	17.4(16.3)	39.8	<0.6	<2
-	XRTJ112605.11-501020.5	-	-	-	-	-(-)	-	<0.6	-
4FGLJ1151.2-2929	XRTJ115118.17-292744.4	RACSJ115118.2-292740	PANJ115118.12-292744.9	177.8255	-29.4625	19.9(19.5)	4.0	3.0	74
-	XRTJ115110.12-292917.2*	-	PANJ115110.30-292920.4	177.7929	-29.4890	9.7(9.3)	47863.0	<0.3	<1
4FGLJ1224.6+7011	XRTJ122502.59+702038.4	-	PANJ122502.68+702040.0	186.2611	70.3444	19.1(19.2)	8.3	<0.3	<4
	XRTJ122457.12+700723.3*	-	PANJ122456.98+700723.6	186.2374	70.1232	13.8(13.3)	-	<0.3	-
-	XRTJ122531.06+701250.5	-	PANJ122531.52+701249.5	186.3813	70.2138	20.9(20.7)	1.6	<0.3	<22
4FGLJ1243.7+1727	XRTJ124326.39+172935.9	-	PANJ124326.49+172937.4	190.8604	17.4937	17.8(17.8)	27.5	<0.3	<1
-	XRTJ124351.64+172643.2	VLASS1QLCIRJ124351.77+172644.3	PANJ124351.76+172644.4	190.9657	17.4457	19.7(19.4)	4.8	8.7	183
4FGLJ1326.0+3507	XRTJ132544.62+350442.7	-	PANJ132544.50+350446.1	201.4354	35.0795	20.6(20.1)	2.1	<0.3	<17
	XRTJ132608.87+350836.9*	-	PANJ132608.81+350837.8	201.5367	35.1438	9.2(13.1)	-	<0.3	-
-	XRTJ132622.45+350622.4	-	PANJ132622.19+350624.5	201.5925	35.1068	20.1(19.7)	3.3	<0.3	<10
4FGLJ1336.5-4655	XRTJ133618.81-465738.9*	-	SSSJ133618.76-465737.2	204.0781	-46.9604	14.5(12.6)	575.4	<0.6	<1
-	XRTJ133548.08-465905.6	-	SSSJ133547.96-465902.3	203.9500	-46.9840	20.5(19.5)	2.3	<0.6	<28
4FGLJ1407.7-3017	XRTJ140806.82-302353.7	RACSJ140806.7-302352	SSSJ140806.77-302353.9	212.0283	-30.3982	14.0(15.4)	912.0	2.4	<1
-	XRTJ140759.93-303047.2*	-	PANJ140759.99-303048.9	212.0000	-30.5136	12.7(12.2)	3020.0	<0.3	<1
4FGLJ1408.6-2917	XRTJ140809.87-292241.0	-	PANJ140809.98-292238.1	212.0416	-29.3773	19.8(18.8)	4.4	<0.3	<8
	XRTJ140807.26-291615.1	-	PANJ140807.12-291613.8	212.0297	-29.2705	21.4(20.8)	1.0	<0.3	<35
-	XRTJ140826.77-292222.7*	-	PANJ140826.79-292221.2	212.1116	-29.3725	21.4(21.2)	1.0	<0.3	<35
4FGLJ1438.0+0219	XRTJ143809.82+021804.1	-	PANJ143809.84+021805.5	219.5410	2.3015	21.0(20.9)	1.4	<0.3	<24
-	XRTJ143743.99+021934.5	-	PANJ143744.13+021935.0	219.4339	2.3264	20.5(20.2)	2.3	<0.3	<15
4FGLJ1444.8+3645	XRTJ144529.77+364615.6	-	PANJ144529.62+364614.8	221.3734	36.7708	18.6(18.2)	13.2	<0.3	<3
-	XRTJ144401.00+364415.3	-	PANJ144400.94+364416.5	221.0039	36.7379	21.0(20.5)	1.4	<0.3	<24
4FGLJ1452.0-4148	XRTJ145149.46-414503.3	RACSJ145149.3-414503	SSSJ145149.30-414504.1	222.9558	-41.7509	20.2(18.7)	3.0	4.1	134
-	XRTJ145224.64-414953.4*	RACSJ145224.4-414953	SSSJ145224.54-414954.2	223.1025	-41.8315	20.1(19.5)	3.3	19.8	599
4FGLJ1454.3-3946	XRTJ145411.28-395523.4*	-	SSSJ145411.24-395523.0	223.5467	-39.9232	12.6(11.1)	3311.3	<0.3	<1
-	XRTJ145347.13-394451.0*	-	SSSJ145346.76-394450.5	223.4455	-39.7474	7.5(6.6)	363078.1	<0.3	<1
4FGLJ1504.6+4343	XRTJ150425.17+434105.0	VLASS1QLCIRJ150425.13+434106.7	PANJ150425.11+434106.6	226.1046	43.6852	17.9(17.4)	25.1	2.7	11
-	XRTJ150507.23+435002.6	-	PANJ150507.31+435004.8	226.2804	43.8347	17.4(16.6)	39.8	<0.3	<1
4FGLJ1513.0-3118	XRTJ151244.55-311650.1*	-	PANJ151244.45-311648.6	228.1852	-31.2802	12.1(11.3)	5248.1	<0.3	<1
-	XRTJ151258.83-311746.4*	-	SSSJ151258.65-311746.0	228.2446	-31.2960	14.3(11.6)	691.8	<0.3	<1
4FGLJ1514.8+4448	XRTJ151436.48+445002.0	VLASS1QLCIRJ151436.64+445003.9	PANJ151436.63+445004.1	228.6526	44.8345	20.1(19.2)	3.3	36.0	1087
-	XRTJ151451.10+444953.1	-	PANJ151451.16+444955.0	228.7132	44.8319	20.3(19.8)	2.8	<0.3	<13
4FGLJ1517.7-4446	XRTJ151727.58-444254.5*	ATCAJ151727.61-444250.4	SSSJ151727.59-444254.9	229.3650	-44.7152	17.9(17.8)	25.1	0.1	1
-	XRTJ151810.81-444734.7*	-	SSSJ151810.86-444736.3	229.5452	-44.7935	8.2(5.8)	190546.1	<0.6	<1
4FGLJ1557.2+3822	XRTJ155712.37+382030.2	VLASS1QLCIRJ155712.27+382033.1	PANJ155712.27+382032.9	239.3011	38.3425	20.4(19.3)	2.5	2.2	89
-	XRTJ155656.77+382825.8*	-	PANJ155657.00+382827.5	239.2375	38.4743	22.0(21.3)	0.6	<0.3	<60
4FGLJ1637.5+3005	XRTJ163739.22+301009.3	-	PANJ163739.21+301012.8	249.4134	30.1702	19.6(18.7)	5.2	<0.3	<7
-	XRTJ163738.33+300503.1	-	PANJ163738.15+300503.7	249.4090	30.0844	18.9(18.2)	10.0	<0.3	<3
	XRTJ163727.99+300954.6	-	PANJ163728.13+300953.0	249.3672	30.1647	20.3(19.9)	2.8	<0.3	<13
-	XRTJ163647.31+300555.1	-	-	-	-	-(-)	-	<0.3	-
-	XRTJ163735.81+301310.8*	-	PANJ163735.95+301310.9	249.3998	30.2197	16.6(15.4)	83.2	<0.3	<1
4FGLJ1651.7-7241	XRTJ165151.61-724308.5*	RACSJ165151.8-724307	SSSJ165151.99-724307.3	252.9667	-72.7186	19.1(17.0)	8.3	11.7	141
-	XRTJ165139.31-724639.6*	RACSJ165139.1-724643	SSSJ165139.39-724639.4	252.9147	-72.7776	20.1(19.2)	3.3	82.9	2505
4FGLJ1821.6+6636	XRTJ182108.75+663542.0	-	PANJ182109.26+663543.2	275.2886	66.5953	21.5(20.8)	0.9	<0.3	<38
-	XRTJ182204.70+663715.0*	-	PANJ182205.43+663716.4	275.5226	66.6212	20.3(19.7)	2.8	<0.3	<13
4FGLJ1845.3+5605	XRTJ184556.92+561002.4	-	PANJ184556.89+561002.1	281.4870	56.1673	17.4(16.7)	39.8	<0.3	<1
-	XRTJ184641.97+561617.3	-	PANJ184642.21+561614.2	281.6759	56.2706	20.9(19.7)	1.6	<0.3	<22
4FGLJ2012.1-5234	XRTJ201213.56-523248.9	RACSJ201213.7-523251	DESJ201213.72-523251.1	303.0572	-52.5475	19.3(18.8)	6.9	14.5	209
-	XRTJ201144.43-523444.5*	-	DESJ201144.51-523443.5	302.9355	-52.5788	20.2(18.8)	3.0	<0.6	<21
4FGLJ2046.9-5409	XRTJ204700.86-541245.8	RACSJ204700.9-541246	DESJ204700.73-541245.5	311.7531	-54.2126	20.3(19.4)	2.8	94.6	3436
	XRTJ204722.68-540906.1*	-	DESJ204722.64-540904.1	311.8444	-54.1512	16.0(15.9)	144.5	<0.6	<1
-	XRTJ204643.60-540604.1	-	DESJ204643.51-540605.6	311.6813	-54.1016	20.4(20.3)	2.5	<0.6	<25
4FGLJ2054.2+6904	XRTJ205359.10+690518.6*	-	PANJ205359.00+690519.7	313.4958	69.0888	20.9(20.2)	1.6	<0.3	<22
-	XRTJ205353.18+690141.5	-	-	-	-	-(-)	-	<0.3	-
4FGLJ2122.5+0345	XRTJ212228.37+034511.1*	-	PANJ212228.31+034510.5	320.6180	3.7529	12.2(11.1)	4786.3	<0.3	<1
-	XRTJ212212.36+035254.2	-	PANJ212212.42+035254.6	320.5518	3.8819	20.1(20.0)	3.3	37.8	1141
4FGLJ2122.3+7653	XRTJ212204.08+765830.1	-	-	-	-	-(-)	-	<0.3	-
-	XRTJ212156.89+765308.0	VLASS1QLCIRJ212156.35+765308.2	PANJ212156.28+765308.5	320.4845	76.8857	21.5(21.0)	0.9	<0.3	<38
4FGLJ2134.3-0319	XRTJ213415.13-032439.2*	-	PANJ213415.07-032438.5	323.5628	-3.4107	7.3(6.6)	436515.8	<0.3	<1
-	XRTJ213418.47-032327.5	-	PANJ213418.68-032328.4	323.5778	-3.3912	19.1(18.4)	8.3	<0.3	<4

Note. Labels are the same as in table A.6

Table A.7: MWL counterpartsof UGS2. Continued

4FGL Name (1)	*Swift*/XRT source (2)	Radio source (3)	Optical source (4)	RA (5) J2000	DEC (6) J2000	gmag(rmag) (7)	f_ν^{opt} (8) [$\times 10^{-28}$]	f_ν^{radio} (9)	*R* (10)
4FGLJ2141.4+0733	XRTJ214147.51+074216.2	-	PANJ214147.63+074216.1	325.4485	7.7045	20.2(19.3)	3.0	<0.3	<11
-	XRTJ214125.72+073257.3	-	PANJ214125.73+073257.3	325.3572	7.5493	21.1(20.8)	1.3	<0.3	<26
4FGLJ2144.7-5640	XRTJ214429.66-563848.6*	RACSJ214429.5-563849	DESJ214429.56-563849.0	326.1232	-56.6470	20.7(20.4)	1.9	11.1	585
-	XRTJ214503.13-564500.8	-	DESJ214502.80-564502.4	326.2617	-56.7507	19.6(19.3)	5.2	<0.6	<12
4FGLJ2153.0-6442	XRTJ215306.90-644444.4*	RACSJ215307.1-644444	DESJ215306.98-644444.4	328.2791	-64.7457	19.6(19.4)	5.2	3.0	58
-	XRTJ215326.50-644310.5*	-	DESJ215326.61-644310.2	328.3609	-64.7195	12.8(12.6)	2754.2	<0.6	<1
4FGLJ2212.9+7921	XRTJ221111.14+791758.1*	-	PANJ221111.34+791800.2	332.7973	79.3001	13.3(12.7)	1737.8	<0.3	<1
-	XRTJ221414.52+792040.2	VLASS1QLCIRJ221416.21+792043.3	PANJ221415.84+792041.8	333.5660	79.3449	19.9(19.4)	4.0	9.3	233
4FGLJ2222.9+1507	XRTJ222253.97+151053.6	-	PANJ222253.85+151054.7	335.7244	15.1819	19.0(18.5)	9.1	<0.3	<4
-	XRTJ222239.38+151053.7	-	PANJ222239.13+151056.2	335.6630	15.1823	20.8(20.1)	1.7	<0.3	<20
4FGLJ2223.0+2704	XRTJ222217.67+270747.9	RACSJ222217.6+270755	PANJ222217.63+270753.1	335.5735	27.1314	19.3(17.4)	6.9	10.1	146
-	XRTJ222305.55+265733.0	-	PANJ222305.56+265733.3	335.7732	26.9592	20.6(20.5)	2.1	<0.3	<17
-	XRTJ222334.34+270113.8	-	PANJ222334.45+270112.3	335.8936	27.0201	20.3(19.7)	2.8	<0.3	<13
-	XRTJ222244.77+270423.6	-	PANJ222244.80+270422.8	335.6867	27.0730	20.5(20.0)	2.3	<0.3	<15
-	XRTJ222247.02+270103.3*	-	PANJ222247.02+270102.6	335.6959	27.0174	21.4(20.9)	1.0	<0.3	<35
-	XRTJ222228.30+265743.6	-	PANJ222228.38+265742.9	335.6183	26.9619	19.6(19.3)	5.2	<0.3	<7
-	XRTJ222301.89+265603.4	-	PANJ222301.75+265606.5	335.7573	26.9351	20.8(21.4)	1.7	<0.3	<20
-	XRTJ222314.49+271025.5*	-	PANJ222314.46+271024.8	335.8103	27.1736	19.8(19.7)	4.4	<0.3	<8
-	XRTJ222310.54+271308.1	-	PANJ222310.51+271309.2	335.7938	27.2192	21.0(20.6)	1.4	<0.3	<24
-	XRTJ222239.51+270453.8	-	PANJ222239.39+270453.3	335.6641	27.0815	21.7(21.4)	0.8	<0.3	<45
-	XRTJ222250.46+270432.3*	-	PANJ222250.60+270434.8	335.7108	27.0763	14.2(14.0)	758.6	<0.3	<1
-	XRTJ222313.70+270849.2	-	PANJ222313.68+270849.3	335.8070	27.1470	20.1(20.0)	3.3	<0.3	<10
4FGLJ2311.6-4427	XRTJ231145.87-443221.0	RACSJ231145.7-443219	DESJ231146.02-443220.5	347.9418	-44.5390	20.1(19.5)	3.3	8.4	252
-	XRTJ231134.44-443617.8	-	DESJ231134.66-443620.0	347.8944	-44.6056	19.6(18.6)	5.2	<0.6	<12
4FGLJ2324.6+3115	XRTJ232458.69+312709.9	VLASS1QLCIRJ232458.70+312709.7	PANJ232458.72+312709.7	351.2447	31.4527	20.4(20.1)	2.5	215.1	8562
-	XRTJ232402.93+312019.8	-	PANJ232402.65+312021.2	351.0110	31.3392	19.7(19.6)	4.8	<0.3	<7
-	XRTJ232457.35+311340.3	-	PANJ232457.59+311334.7	351.2400	31.2263	20.4(19.9)	2.5	<0.3	<14
-	XRTJ232441.72+311002.0	-	PANJ232441.58+311002.3	351.1733	31.1673	21.4(21.3)	1.0	<0.3	<35
4FGLJ2338.1+0411	XRTJ233830.54+041900.0*	-	PANJ233830.52+041859.7	354.6272	4.3166	10.9(10.4)	15848.9	<0.3	<1
-	XRTJ233742.04+041003.2	VLASS1QLCIRJ233742.01+041003.3	PANJ233741.99+041003.0	354.4250	4.1675	19.5(18.8)	5.8	23.7	412
-	XRTJ233833.66+041321.8	-	PANJ233833.51+041320.6	354.6396	4.2224	21.0(20.3)	1.4	<0.3	<24
-	XRTJ233731.09+040634.4	-	PANJ233731.08+040633.9	354.3795	4.1094	19.8(19.6)	4.4	<0.3	<8
-	XRTJ233737.43+040814.6	-	-	-	-	-(-)	-	<0.3	-
-	XRTJ233735.13+041029.1	-	PANJ233735.06+041028.6	354.3961	4.1746	19.1(18.7)	8.3	<0.3	<4
-	XRTJ233741.42+040736.8*	-	PANJ233741.39+040738.5	354.4224	4.1274	21.9(20.6)	0.6	<0.3	<55
-	XRTJ233824.88+040520.3	VLASS1QLCIRJ233824.90+040517.7	PANJ233824.77+040518.7	354.6032	4.0885	20.5(20.1)	2.3	18.0	788
4FGLJ2344.7-4234	XRTJ234413.10-423935.9	-	GAIAJ234413.01-423944.2	356.0542	-42.6623	19.7(-)	4.8	<0.6	<13
-	XRTJ234431.22-423308.8	RACSJ234430.9-423314	SSSJ234431.21-423314.4	356.1300	-42.5540	18.7(18.6)	12	12.9	108
4FGLJ2351.4-2818	XRTJ235137.78-281824.6	-	PANJ235137.66-281827.7	357.9069	-28.3077	18.0(21.7)	22.9	<0.3	<2
-	XRTJ235136.96-282157.3	VLASS1QLCIRJ235136.72-282152.9	PANJ235136.74-282154.0	357.9031	-28.3650	13.8(13.2)	1096.5	49.6	5
4FGLJ2359.3+1444	XRTJ235937.37+144848.9	RACSJ235937.2+144834	-	-	-	-(-)	-	8.6	-
-	XRTJ235919.60+144156.1*	-	PANJ235919.72+144157.6	359.8322	14.6993	20.1(19.6)	3.3	<0.3	<10
-	XRTJ235838.47+144512.3*	-	PANJ235838.60+144513.0	359.6608	14.7536	20.4(20.1)	2.5	<0.3	<14
-	XRTJ235918.00+144851.8	-	PANJ235918.04+144853.6	359.8252	14.8149	18.8(18.4)	11.0	<0.3	<3
-	XRTJ235953.96+145523.9	-	PANJ235953.94+145519.5	359.9748	14.9221	21.4(21.2)	1.0	<0.3	<35
-	XRTJ235953.96+145523.9	-	PANJ235953.94+145519.5	359.9748	14.9221	21.4(21.2)	1.0	<0.3	<35

Note. Labels are the same as in table A.6

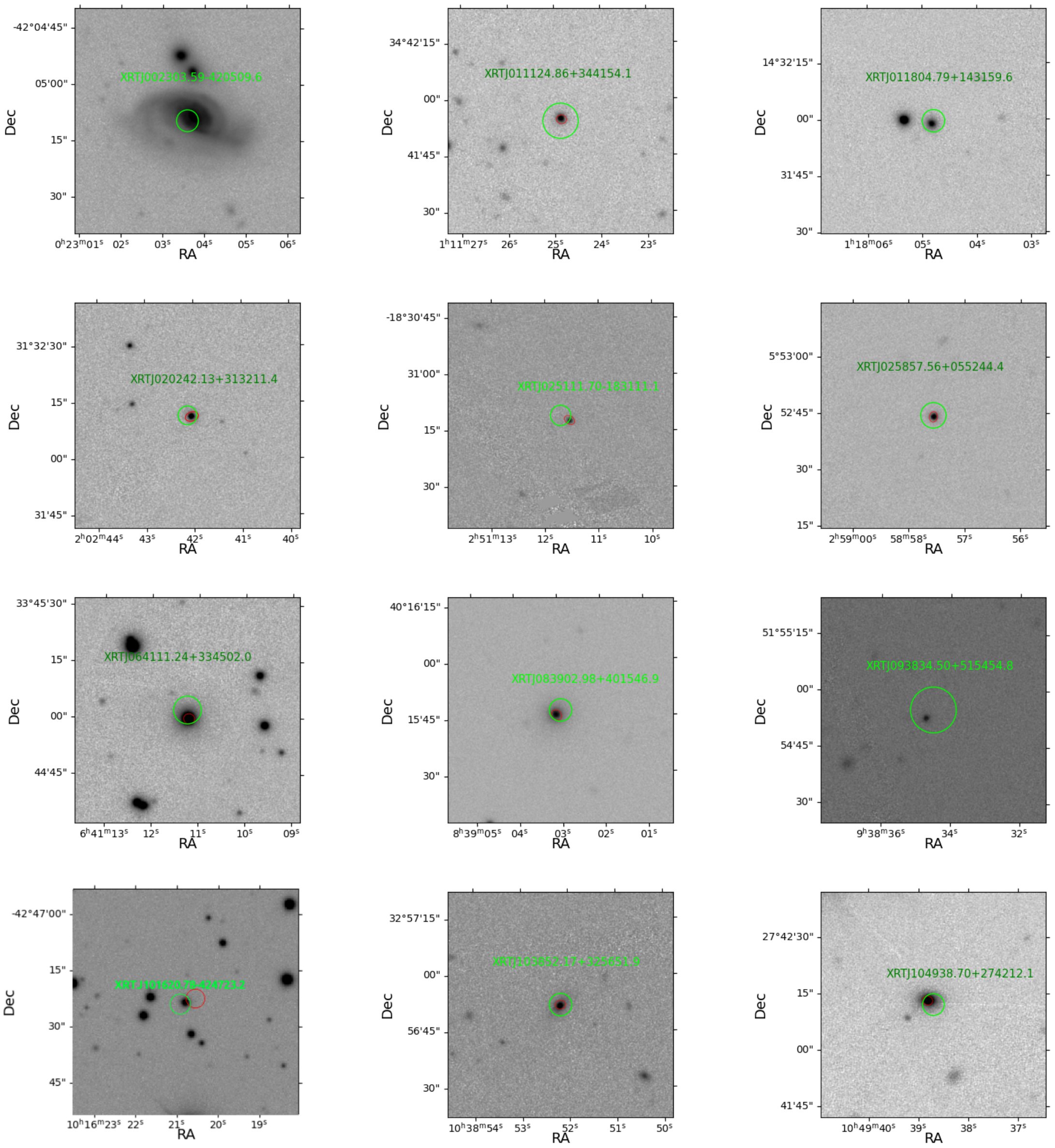

Figure A.2: Optical r-band skymaps for the UGS1 counterparts. The green circle represent the error box of the X-ray counterpart and the red ellipses the error box of radio counterparts.

A.5.0 VOU-BLAZARS catalogues

The catalogues queried in VOU-BLAZARS are: NVSS, FIRST, SUMSS, VLASSQL, 2SXPS, SDS82, 1OUSX, RASS, XMMSL2, 4XMM-DR11, BMW, WGACAT, IPC2E, IPCSL, ChandraCSC2, MAXI, eROSITA-EDR, ZWCLUSTERS, PSZ2, ABELL, MCXC, 5BZCat, SDSS-WHL, SWXCS, 3HSP, *Fermi*GRB, MilliQuas, BROS, MST9Y, PULSAR, F2PSR, F357cat, XRT-DEEP, WISH352, GLEAM, TGSS150, VLSSR, LoTSS, PMN, GB6, GB87, ATPMN, AT20G, NORTH20, CRATES, F357det, KUEHR, PCNT, PCCS44, PCCS70, PCCS100, PCCS143, PCCS217, PCCS353, PCCS2, ALMA, SPIRE, H-ATLAS-DR1, H-ATLAS-DR2, HATLAS-DR2NGP, H-ATLAS-DR2SGP, AKARIBSC, IRAS-PSC, WISE, WISEME, NEOWISE, 2MASS, USNO, SDSS, HSTGSC, PanSTARRS, GAIA, SMARTS, UVOT, GALEX, XMMOM, CMA, EXOSAT, XRTSPEC, OUSXB, OUSXG, OULC, BAT105m, BEPPOSAX, NuBlazar, 3FHL,

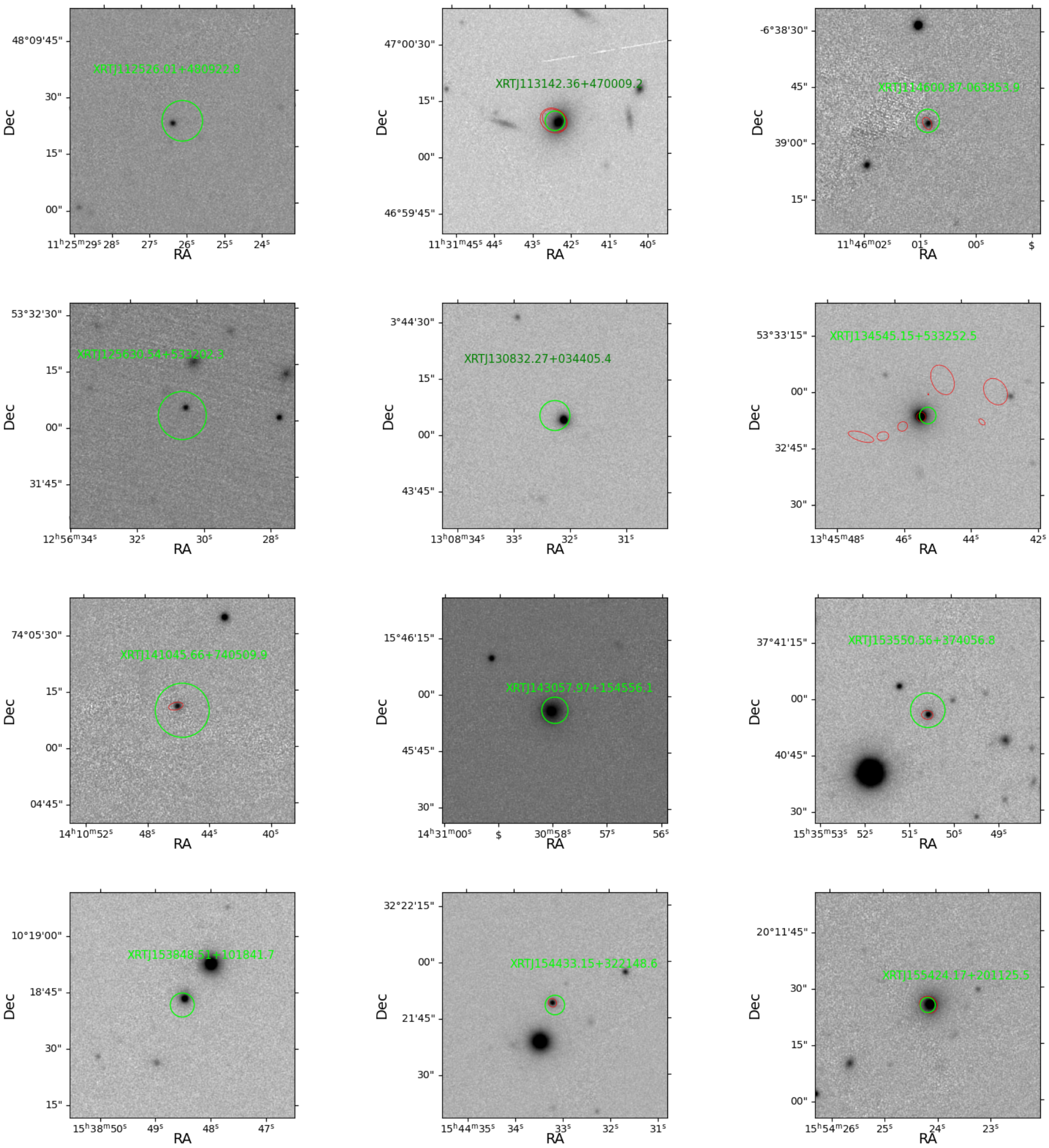

Figure A.2: Continued.

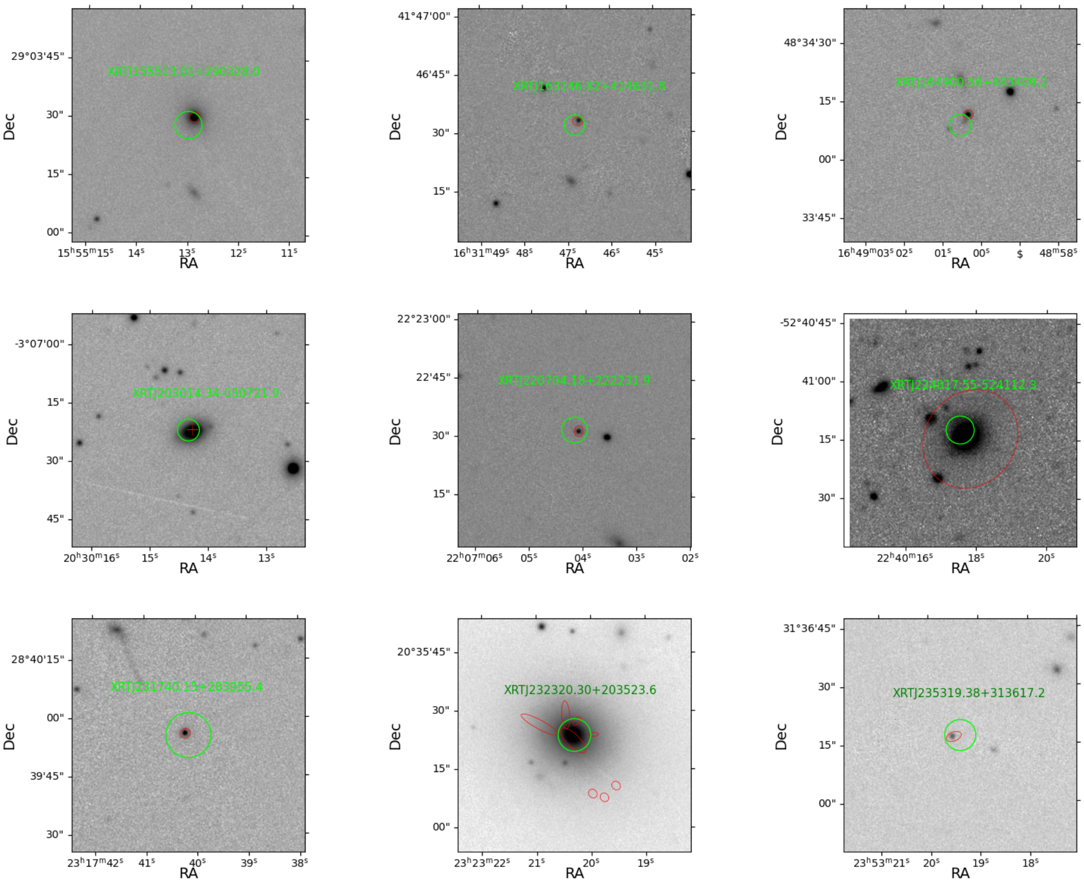

Figure A.2: Continued

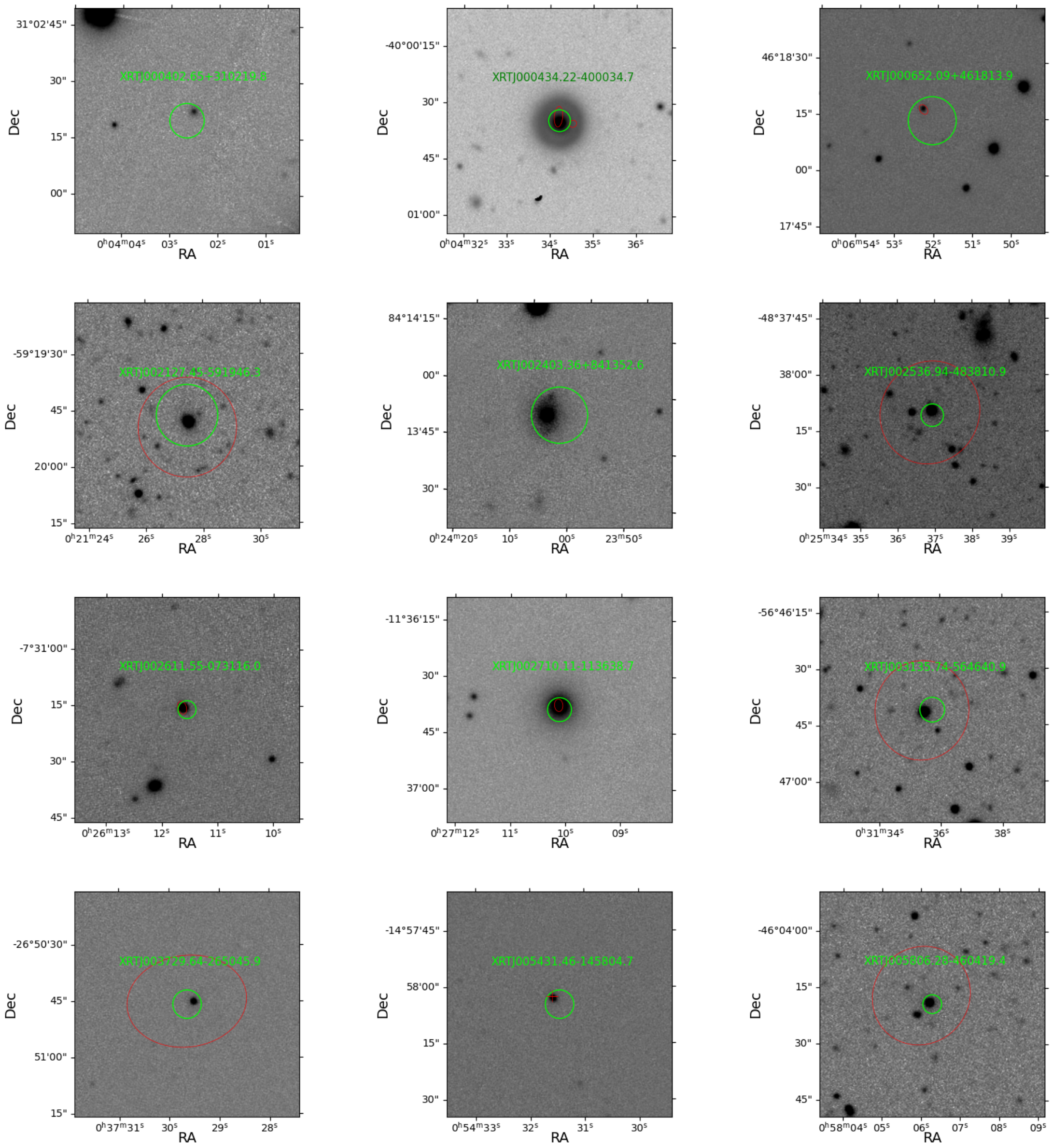

Figure A.2: Continued.

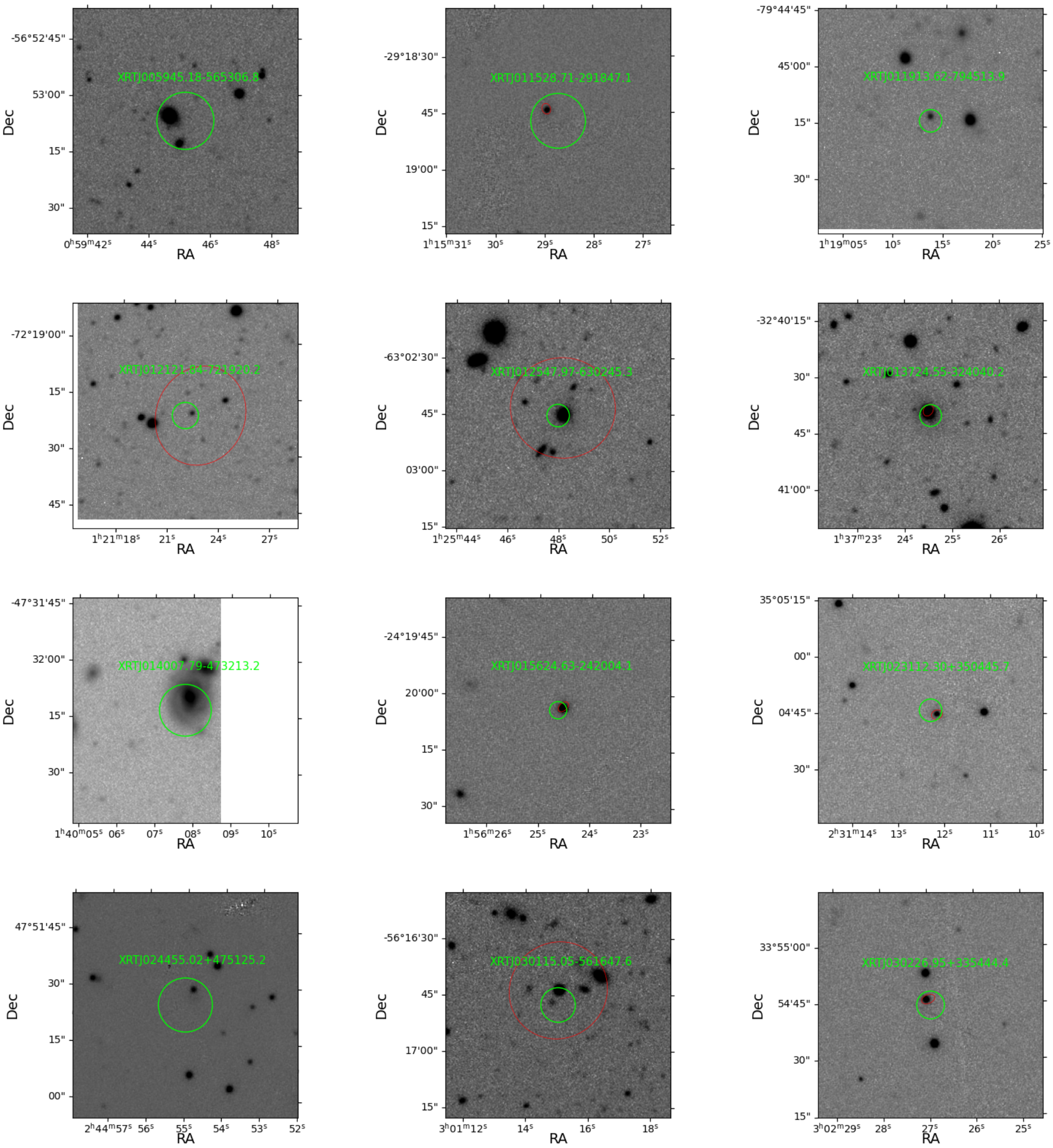

Figure A.2: Continued.

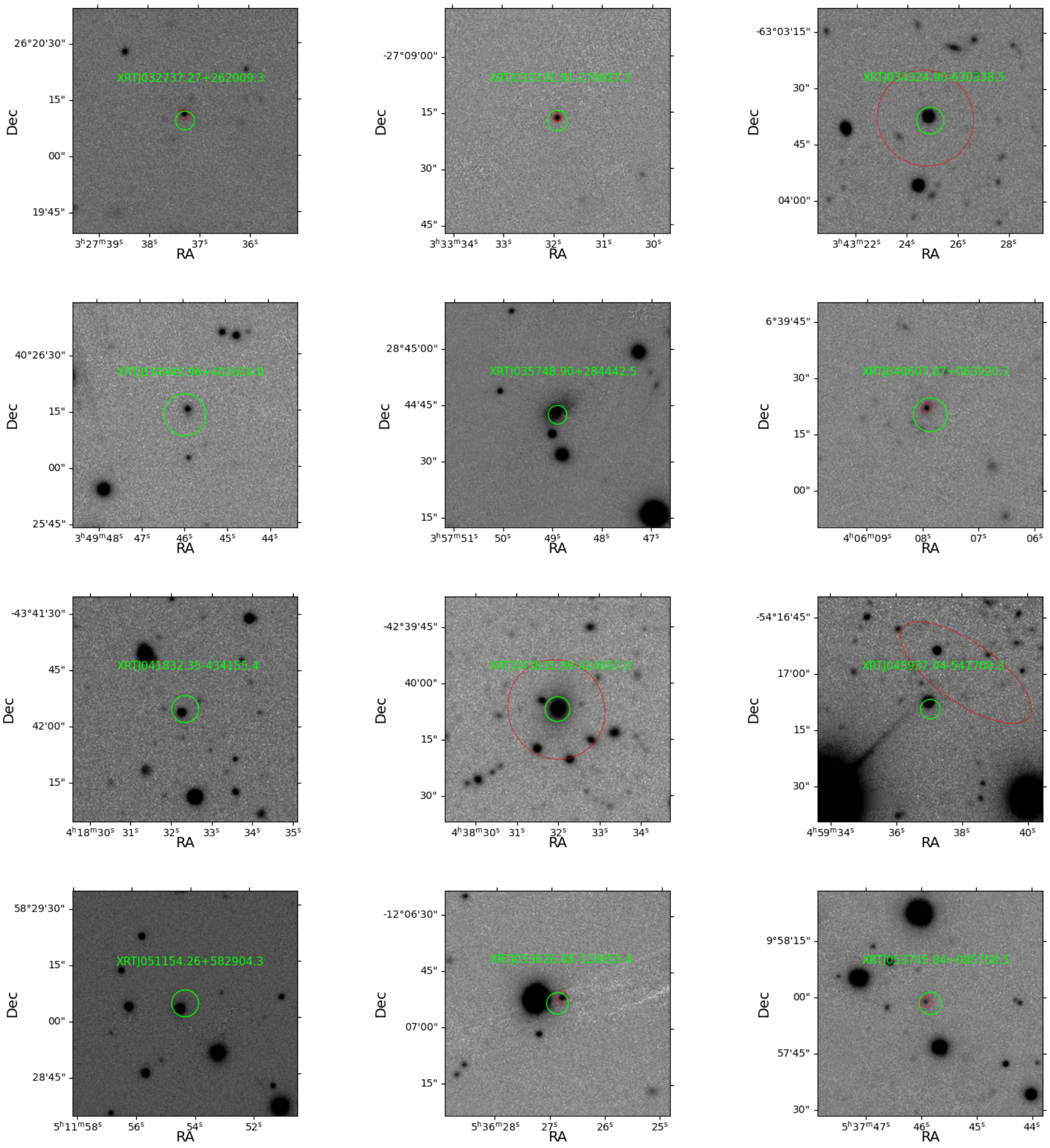

Figure A.2: Continued.

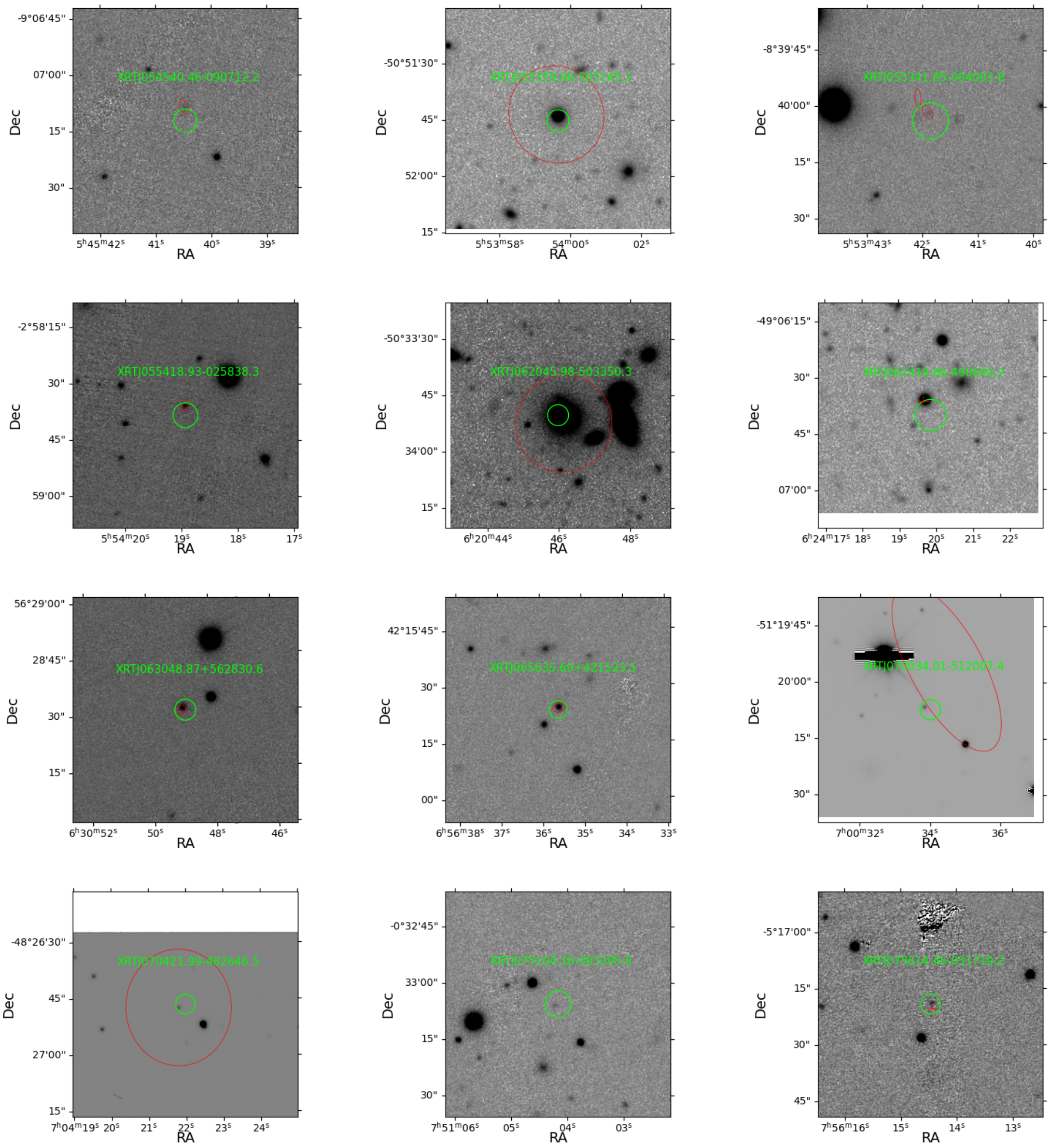

Figure A.2: Continued.

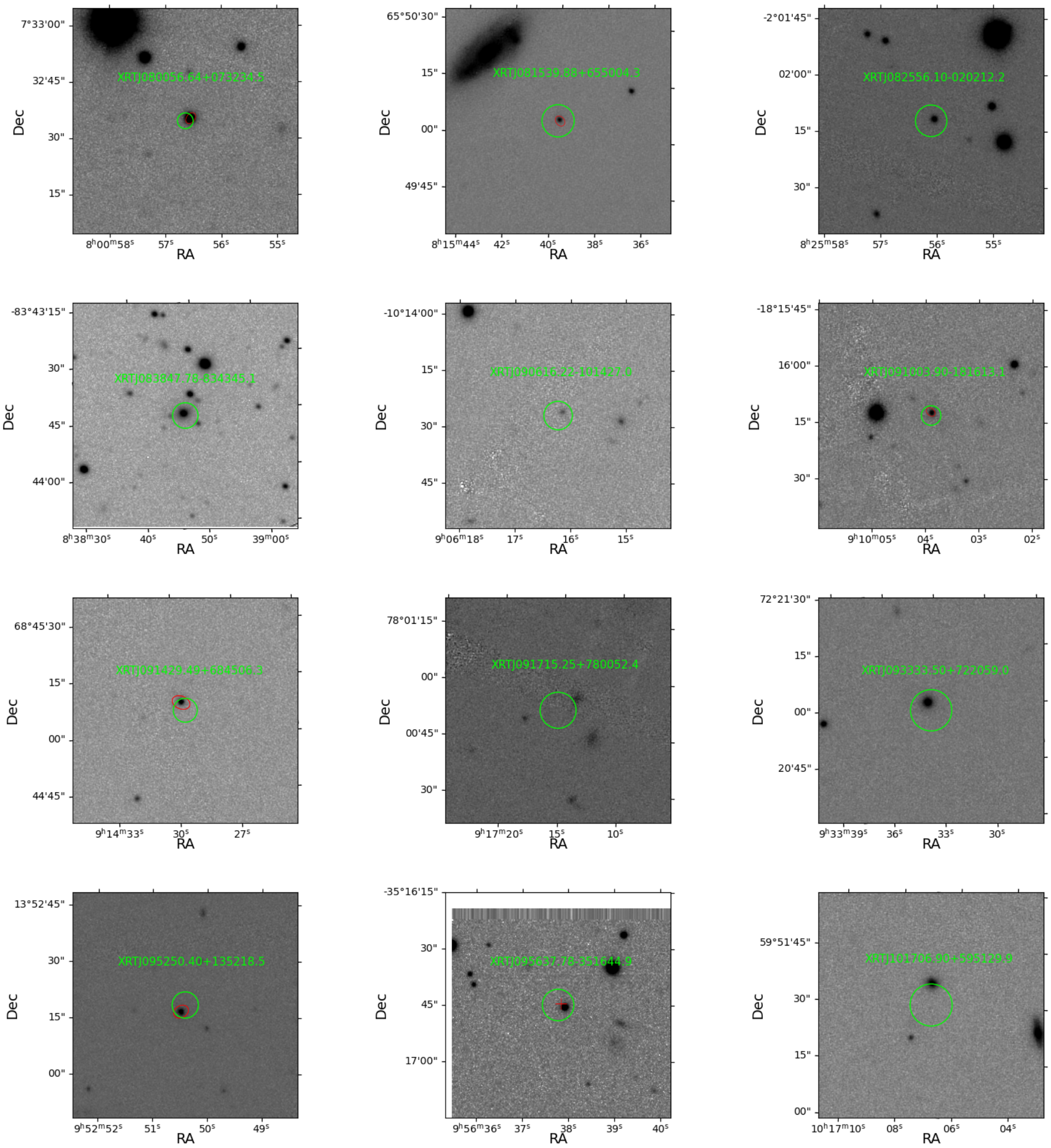

Figure A.2: Continued.

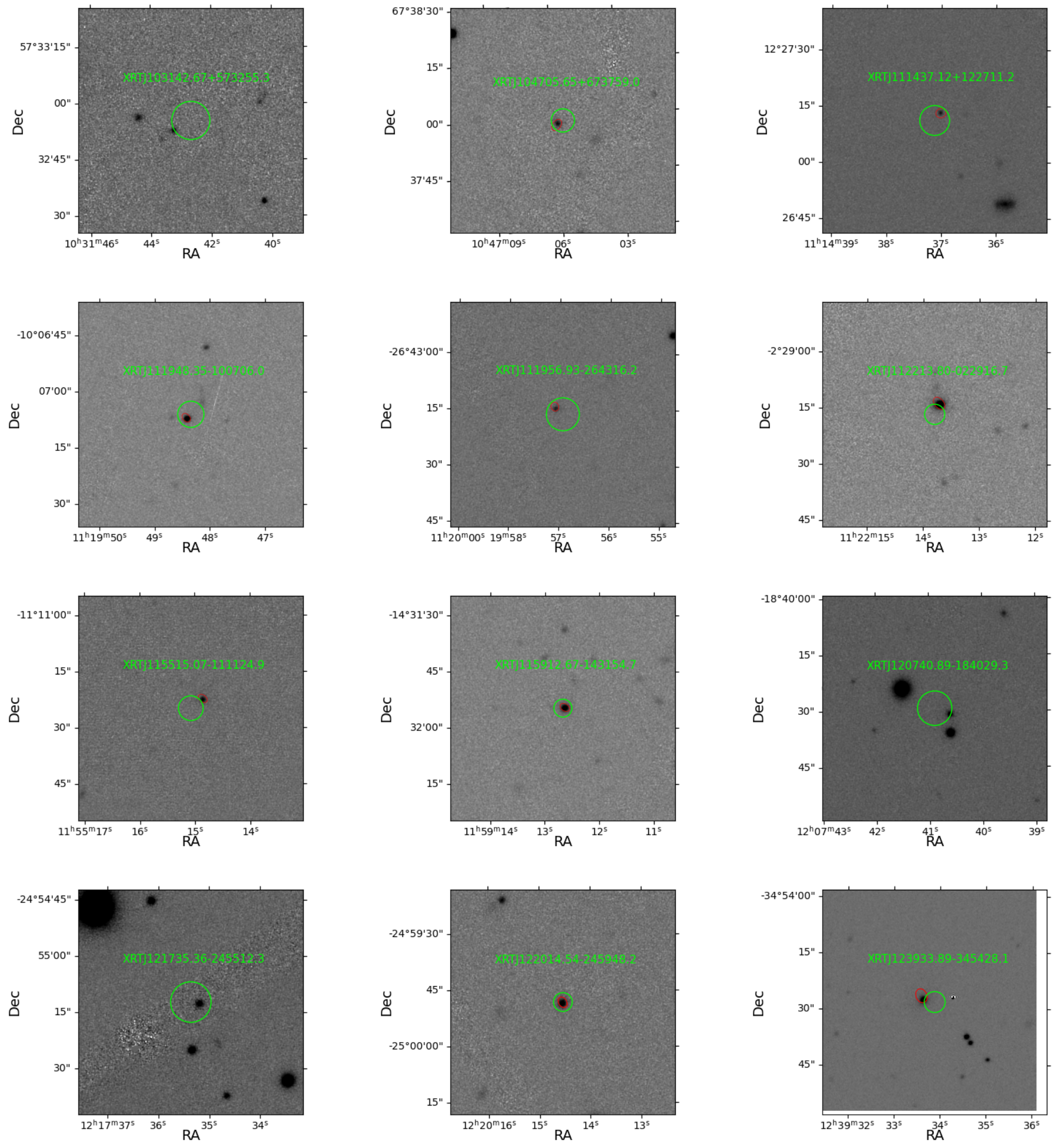

Figure A.2: Continued.

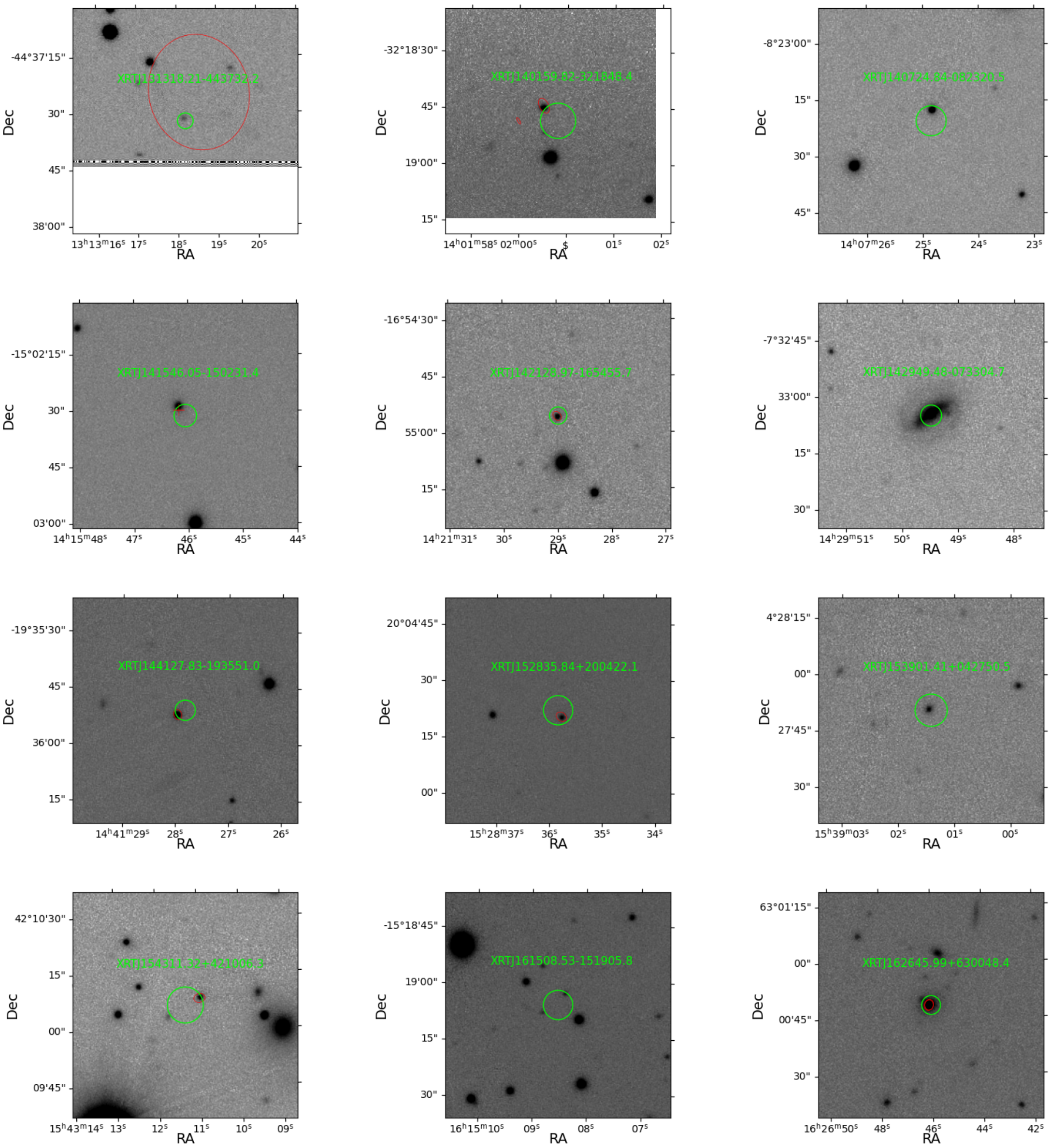

Figure A.2: Continued.

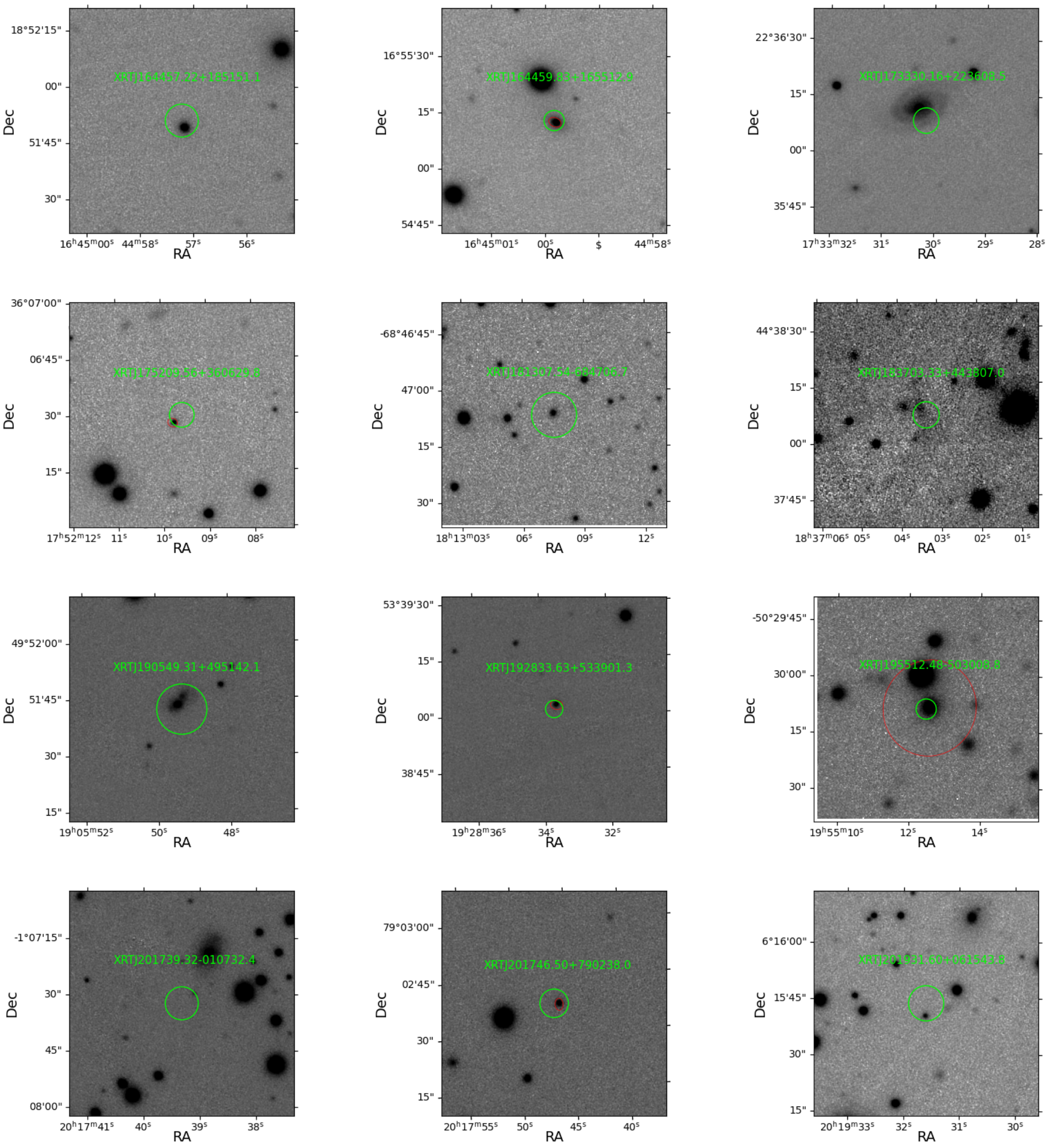

Figure A.2: Continued.

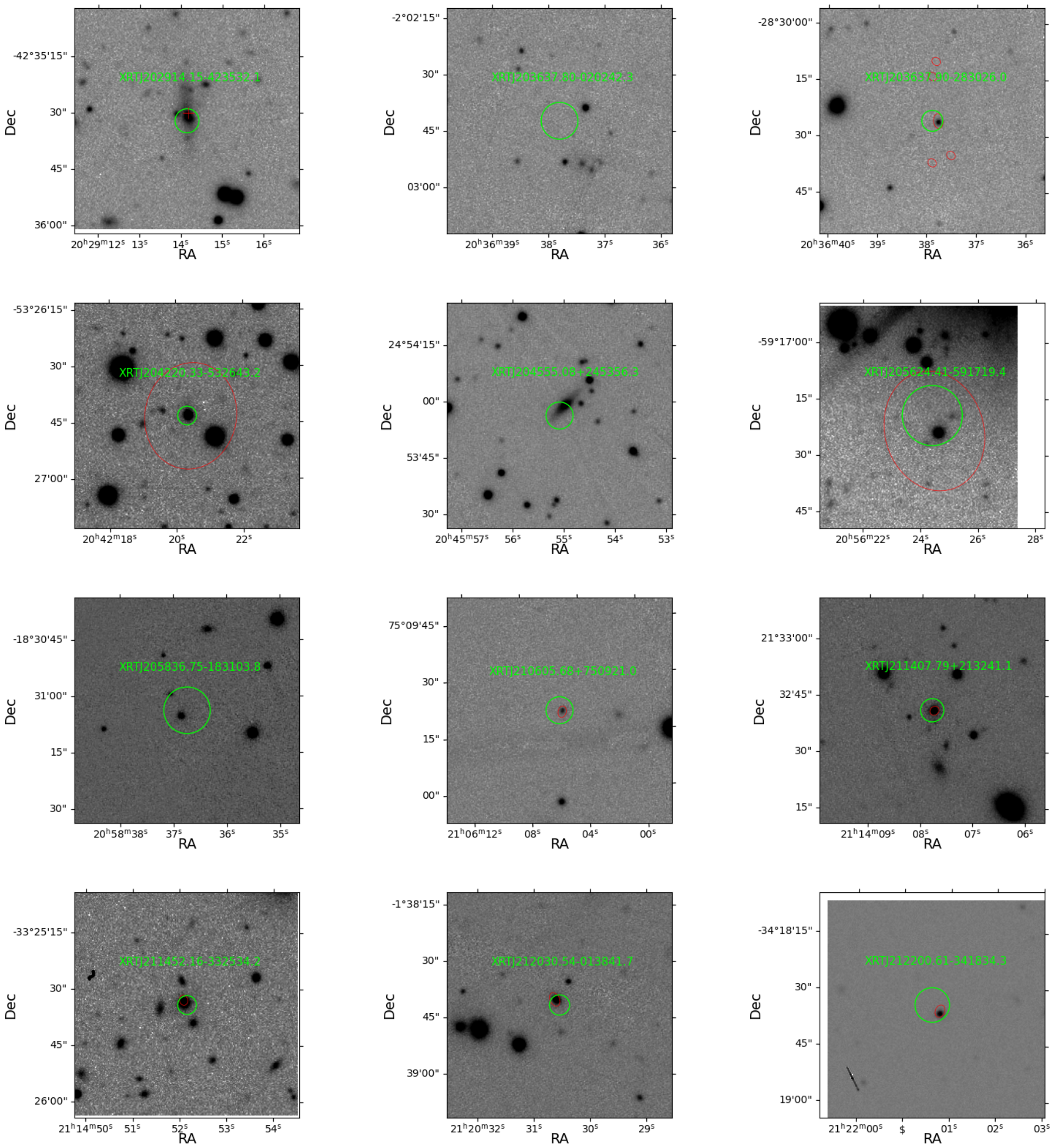

Figure A.2: Continued.

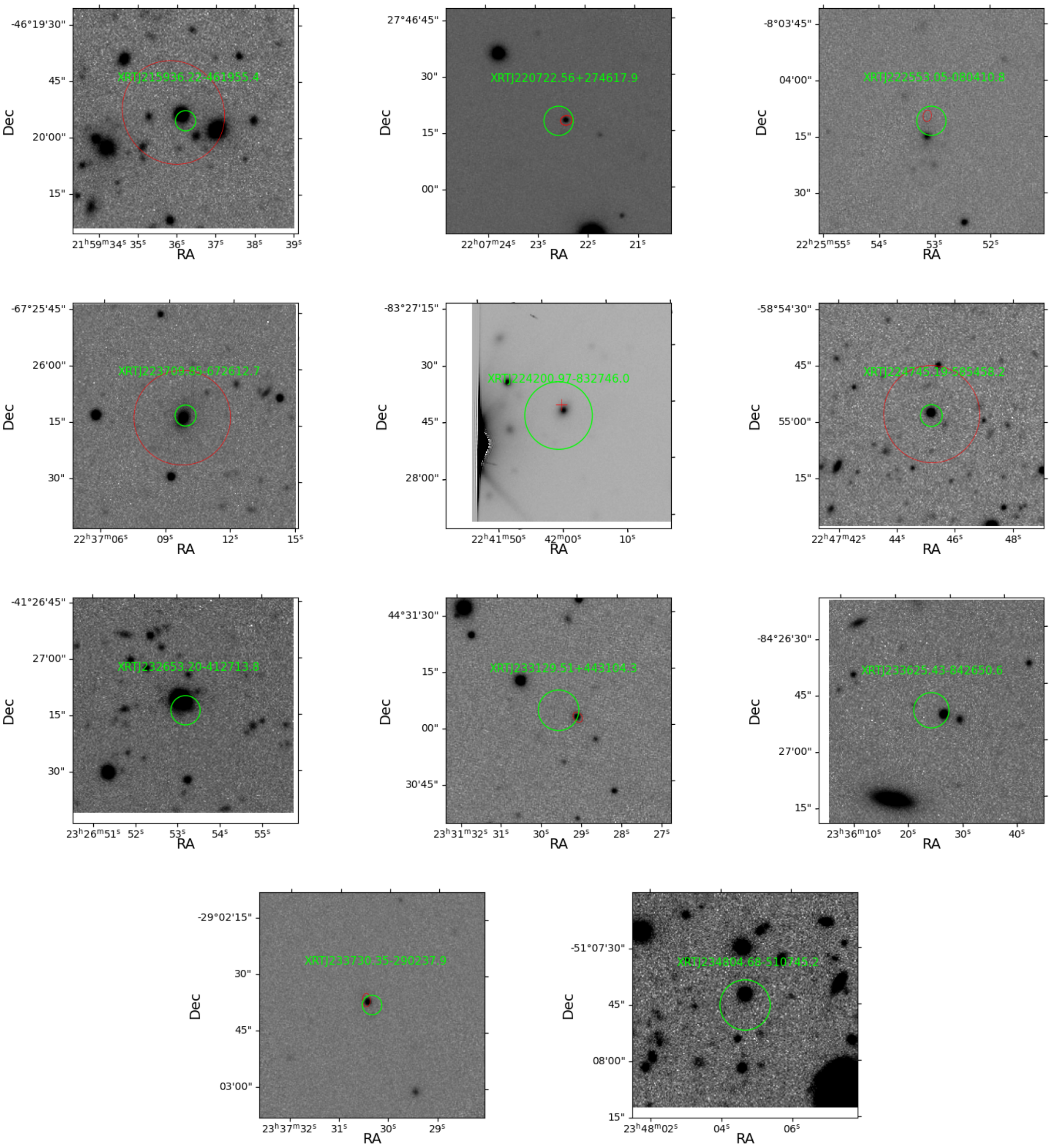

Figure A.2: Continued.

2FHL, 2BIGB, 4FGL-DR3, 2AGILE, FermiMeV, FMonLC.

A.6.0 Spectral energy distributions

Below are the Spectral Energy Distributions (SEDs) of the radio-loud objects analyzed in this paper. Black point are from VOU-Blazar, blue points from our analysis. The points with a triangle shape are upper limits. The red curve emulates the typical double-peaked shape of blazars, while the blue one is the template of a giant host galaxy at the object's redshift. At the top of each sub-figure, we provide the name of the UGS, the name of the proposed X-ray or optical counterpart, the classification given by optical spectroscopy, and the redshifts (red- shifts marked with a "*" are photometric, while the others are spectroscopic). BLL stands for BLL, FSRQ for Flat Spectrum Radio Quasar, BLG for BLL galaxy dominated, FR 1 for Fanaroff-Reley 1, radio galaxies exhibiting an extended jet structure, with the emission from the core dominating over that of the lobes.

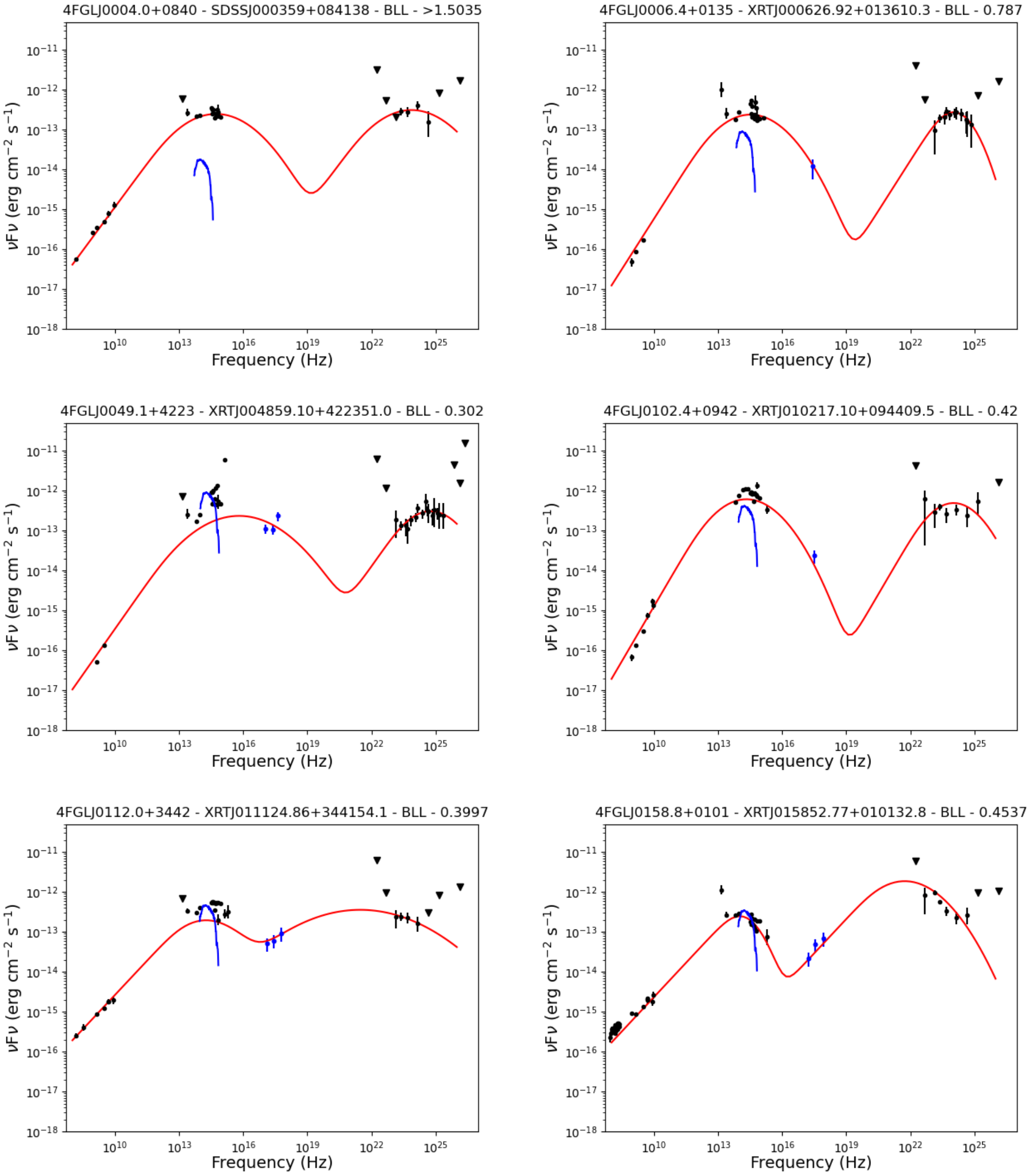

Figure A.3: SED of 6 UGSs analysed in this paper. Black point are from VOU-Blazar, blue points from our analysis. The points with a triangle shape are upper limits. The red curve emulates the typical double-peaked shape of blazars, while the blue one is the template of a giant host galaxy at the object's redshift. At the top of each sub-figure, we provide the name of the UGS, the name of the proposed X-ray or optical counterpart, the classification given by optical spectroscopy, and the redshifts (redshifts marked with a "*" are photometric, while the others are spectroscopic).

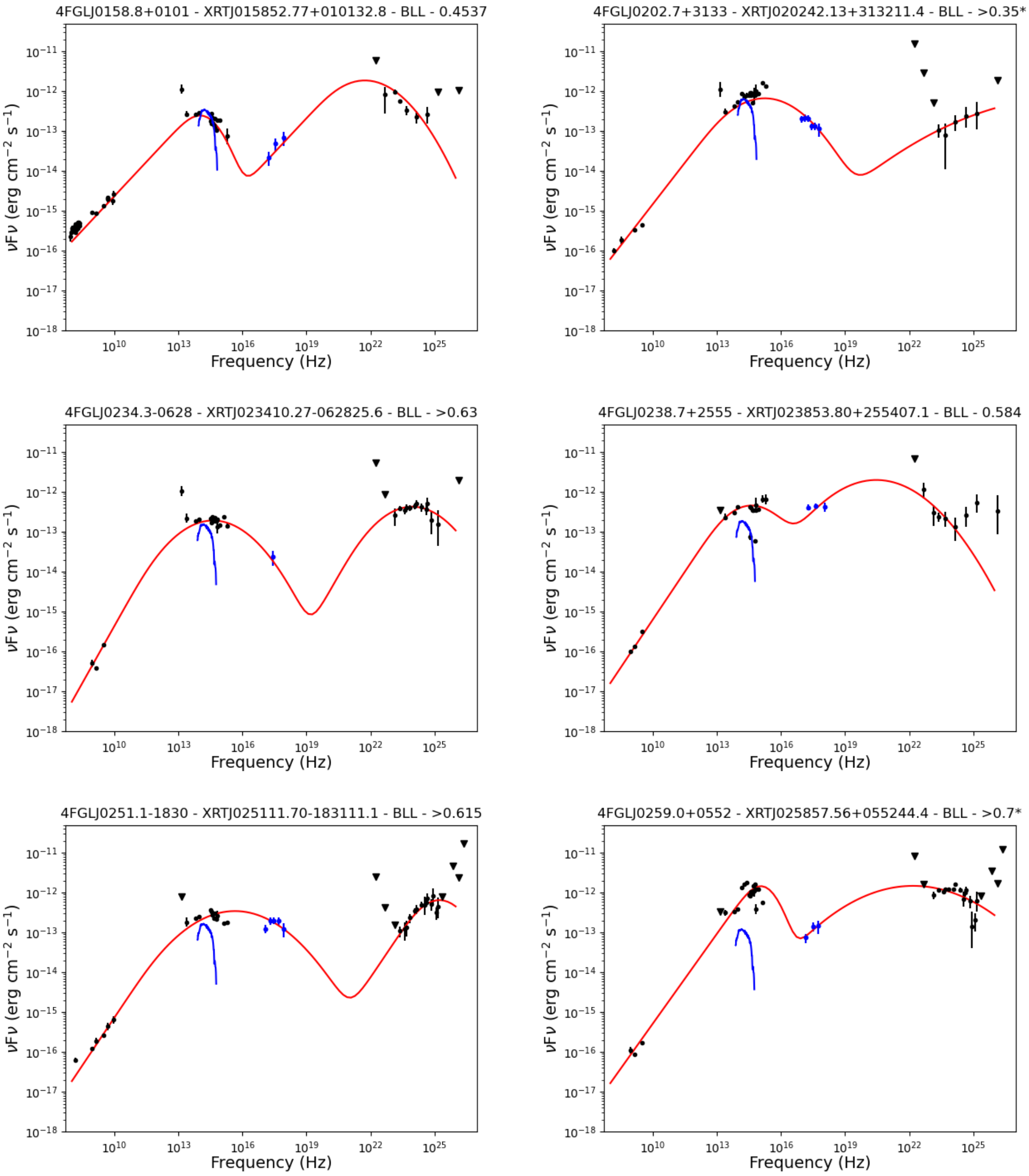
4FGLJ0158.8+0101 - XRTJ015852.77+010132.8 - BLL - 0.4537

4FGLJ0202.7+3133 - XRTJ020242.13+313211.4 - BLL - >0.35*

4FGLJ0234.3-0628 - XRTJ023410.27-062825.6 - BLL - >0.63

4FGLJ0238.7+2555 - XRTJ023853.80+255407.1 - BLL - 0.584

4FGLJ0251.1-1830 - XRTJ025111.70-183111.1 - BLL - >0.615

4FGLJ0259.0+0552 - XRTJ025857.56+055244.4 - BLL - >0.7*

Figure A.3: Continued.

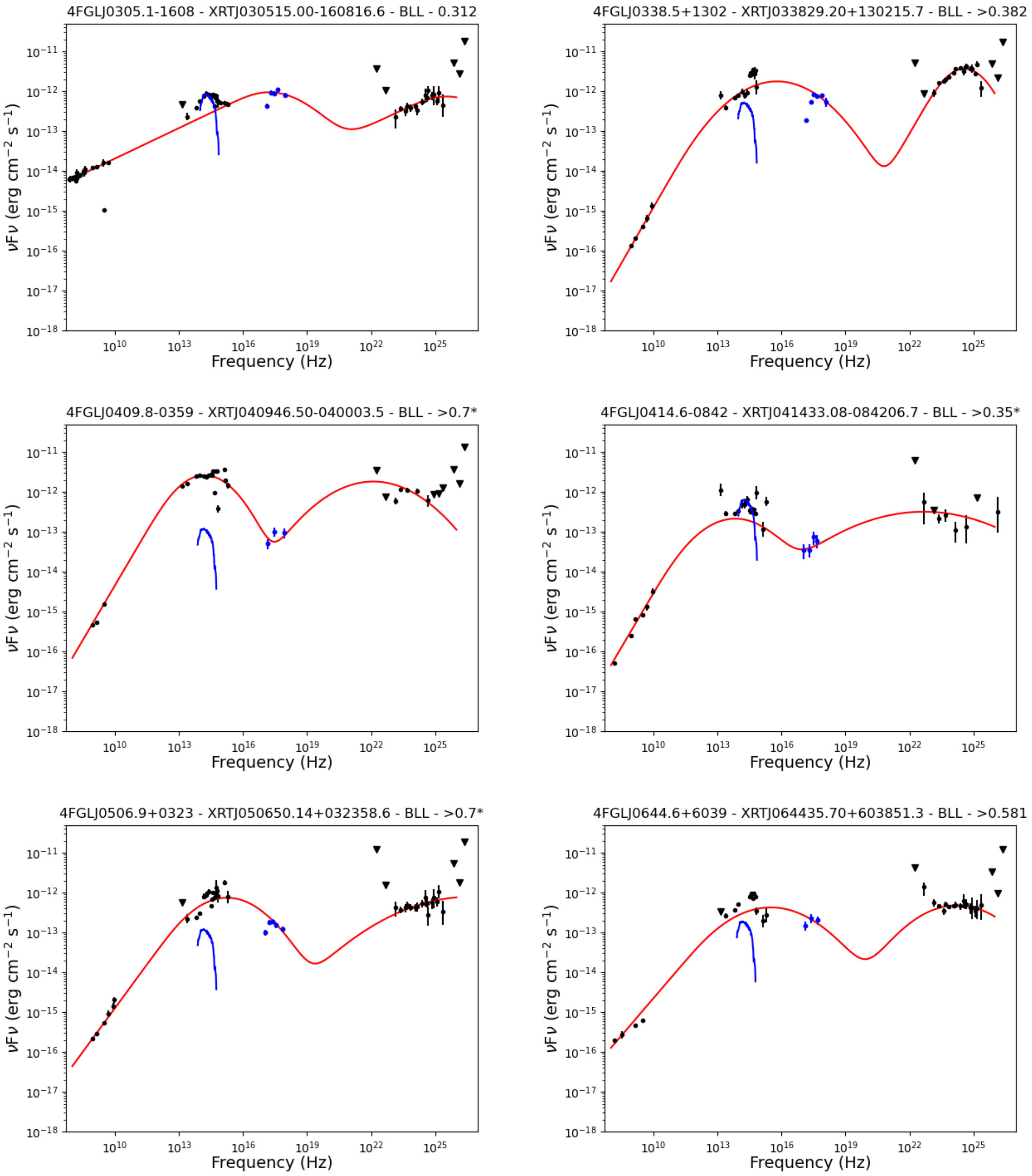

4FGLJ0305.1-1608 - XRTJ030515.00-160816.6 - BLL - 0.312

4FGLJ0338.5+1302 - XRTJ033829.20+130215.7 - BLL - >0.382

4FGLJ0409.8-0359 - XRTJ040946.50-040003.5 - BLL - >0.7*

4FGLJ0414.6-0842 - XRTJ041433.08-084206.7 - BLL - >0.35*

4FGLJ0506.9+0323 - XRTJ050650.14+032358.6 - BLL - >0.7*

4FGLJ0644.6+6039 - XRTJ064435.70+603851.3 - BLL - >0.581

Figure A.3: Continued.

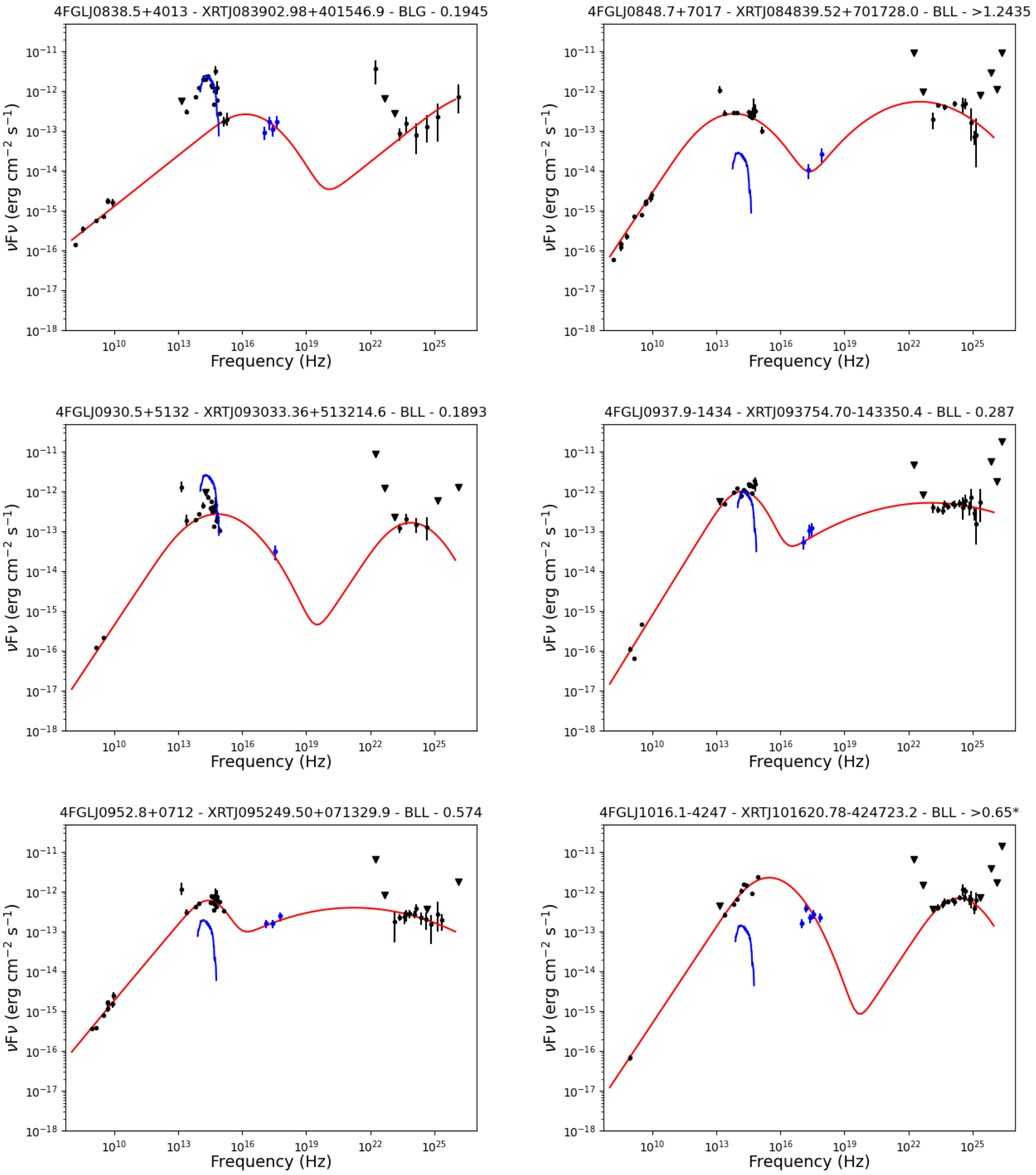

Figure A.3: Continued.

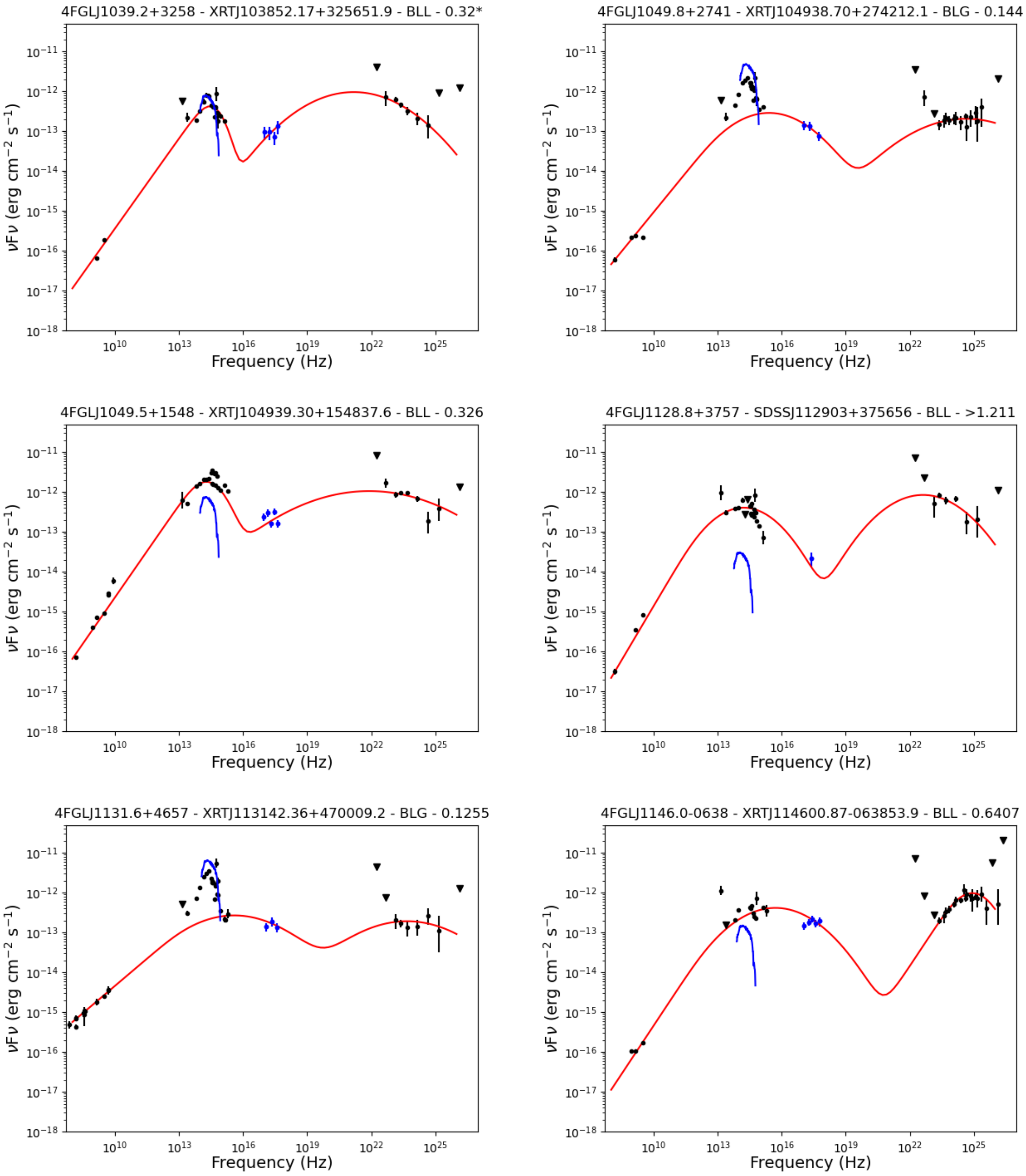

Figure A.3: Continued.

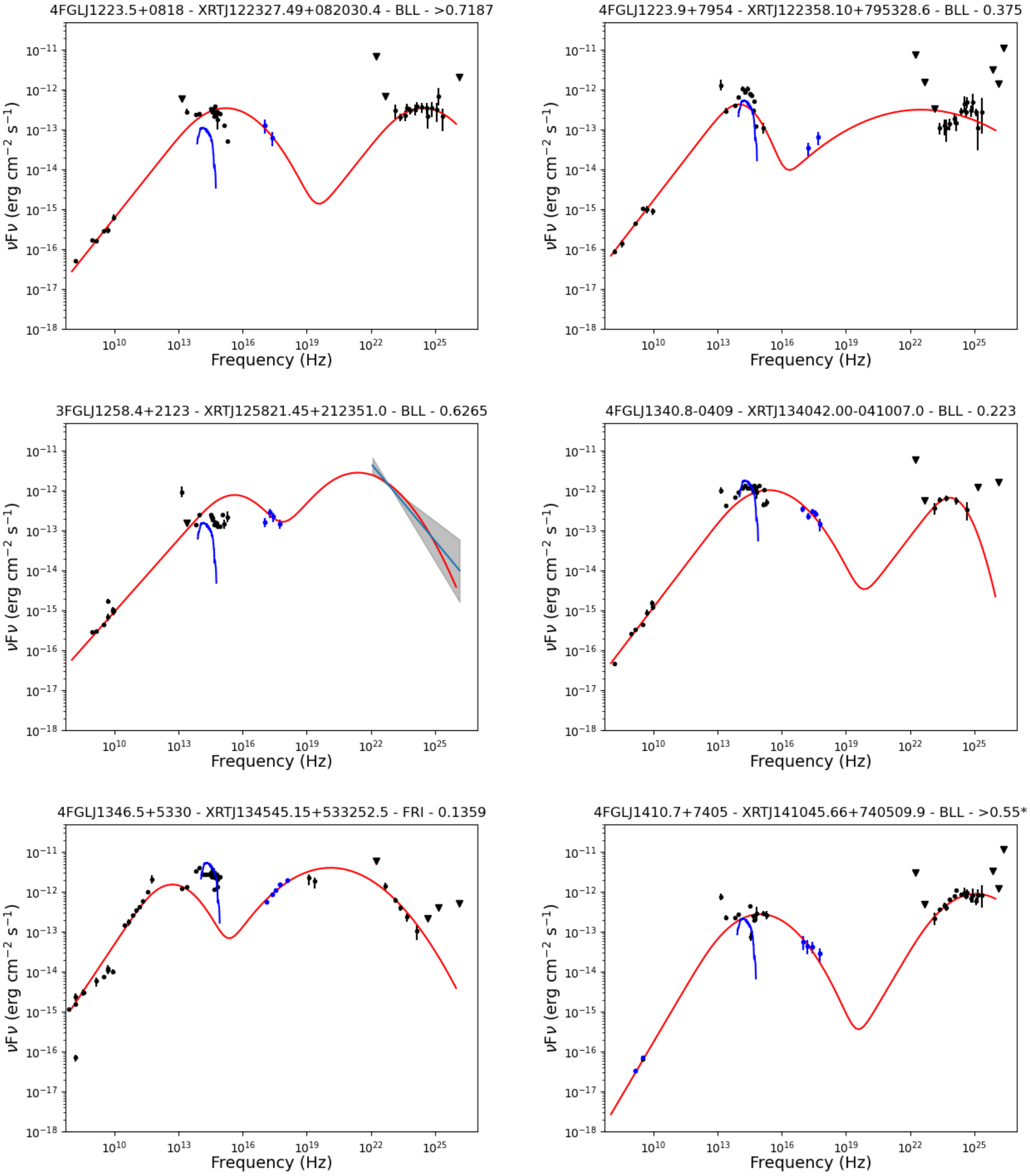

Figure A.3: Continued. It is worth to note that the γ-ray emitter 3FGLJ1258.4+213, is not listed in the fourth *Fermi* catalog. For this reason we plot the best-fit curve (blue line), and its associated uncertainty (grey shadow), of the γ-ray emission, using the fitting parameters reported in the 3FGL catalog.

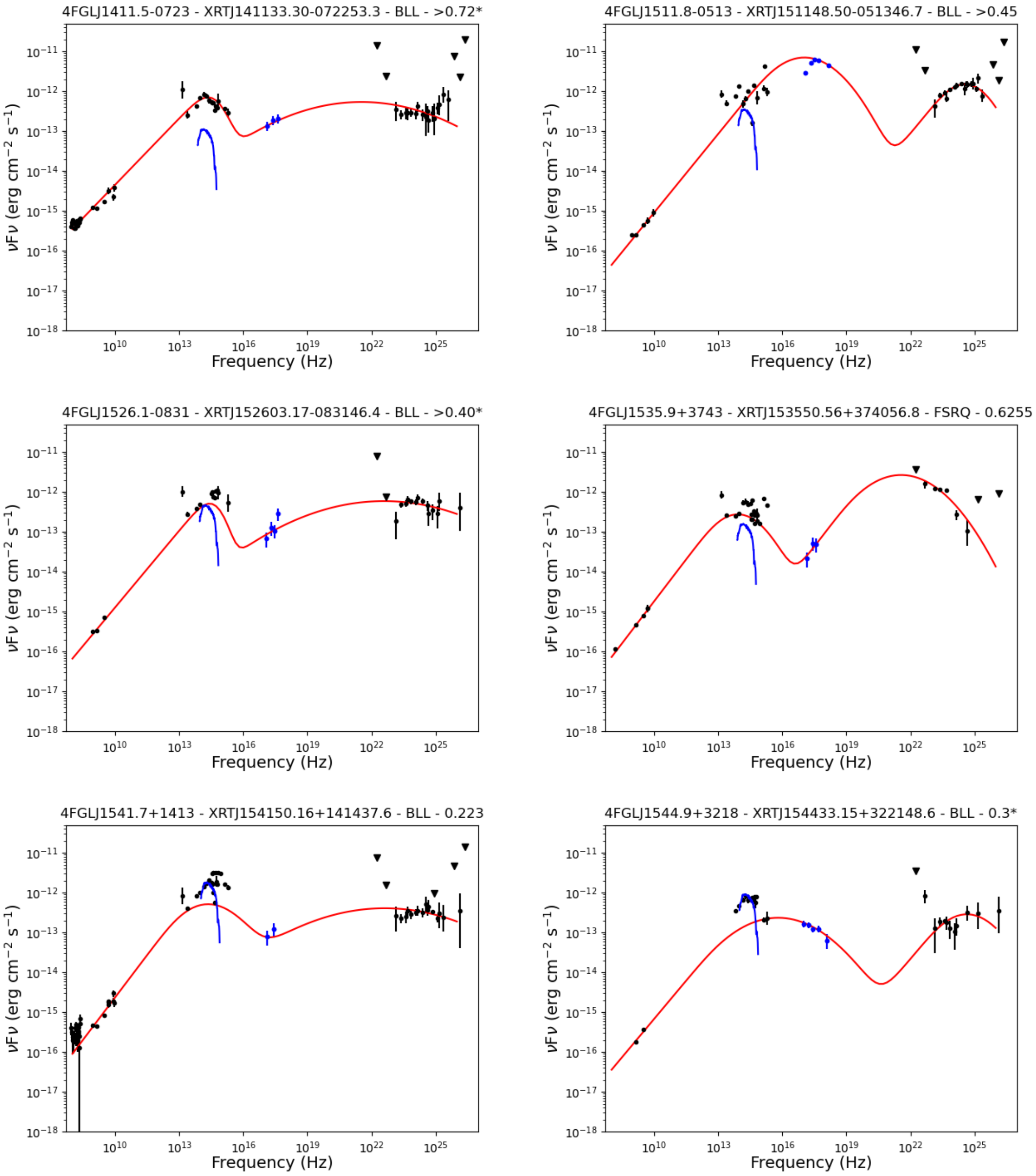
4FGLJ1411.5-0723 - XRTJ141133.30-072253.3 - BLL - >0.72*

4FGLJ1511.8-0513 - XRTJ151148.50-051346.7 - BLL - >0.45

4FGLJ1526.1-0831 - XRTJ152603.17-083146.4 - BLL - >0.40*

4FGLJ1535.9+3743 - XRTJ153550.56+374056.8 - FSRQ - 0.6255

4FGLJ1541.7+1413 - XRTJ154150.16+141437.6 - BLL - 0.223

4FGLJ1544.9+3218 - XRTJ154433.15+322148.6 - BLL - 0.3*

Figure A.3: Continued.

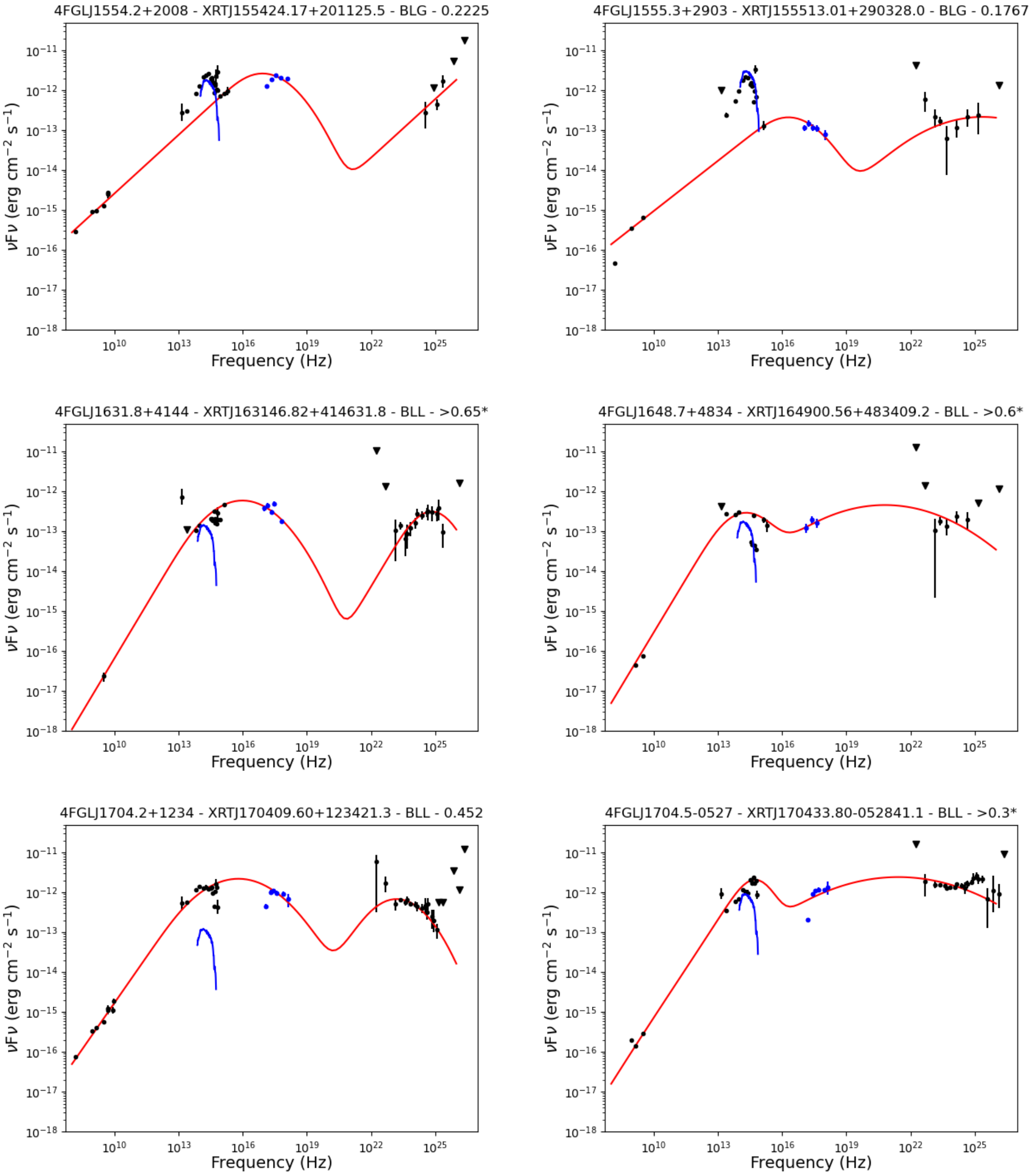

Figure A.3: Continued.

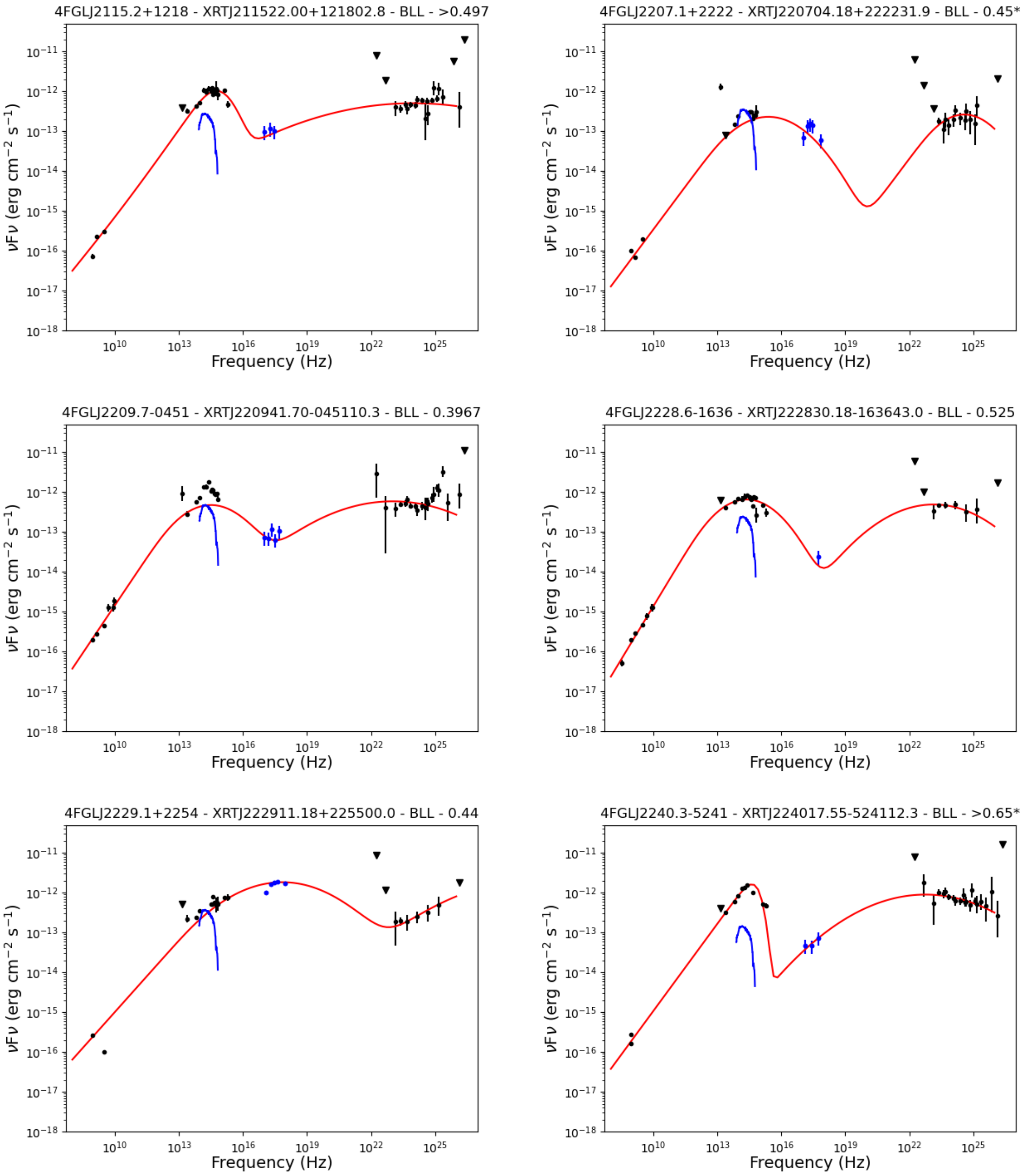

Figure A.3: Continued.

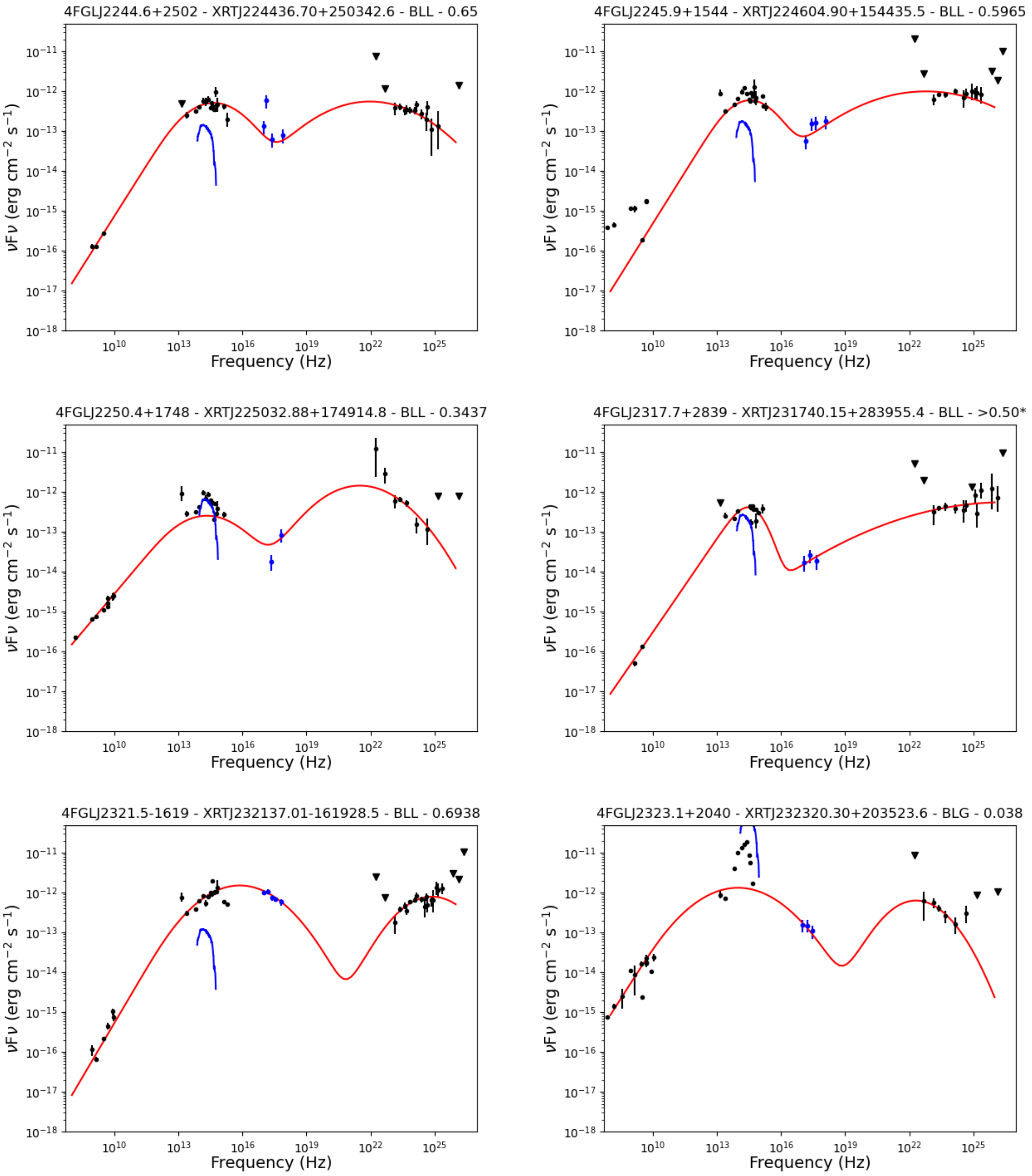
4FGLJ2244.6+2502 - XRTJ224436.70+250342.6 - BLL - 0.65

4FGLJ2245.9+1544 - XRTJ224604.90+154435.5 - BLL - 0.5965

4FGLJ2250.4+1748 - XRTJ225032.88+174914.8 - BLL - 0.3437

4FGLJ2317.7+2839 - XRTJ231740.15+283955.4 - BLL - >0.50*

4FGLJ2321.5-1619 - XRTJ232137.01-161928.5 - BLL - 0.6938

4FGLJ2323.1+2040 - XRTJ232320.30+203523.6 - BLG - 0.038

Figure A.3: Continued.

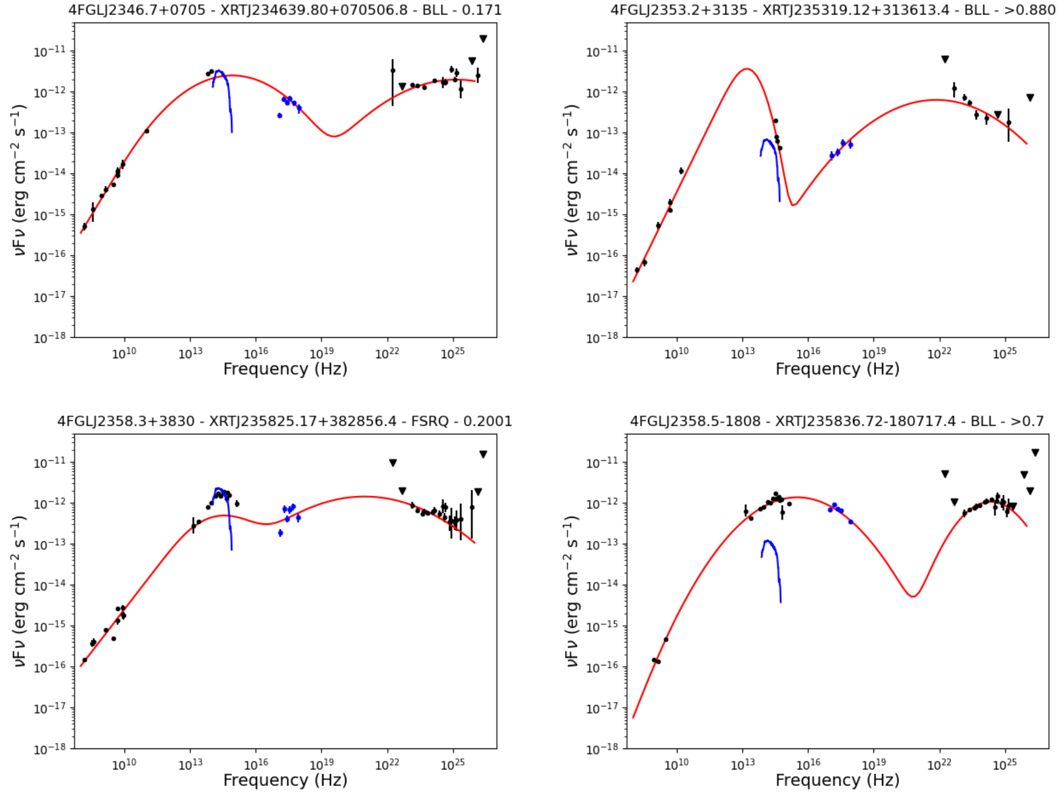

Figure A.3: Continued.

Bibliography

1998, Molecular symmetry and spectroscopy

Abbott, T. M. C., Adamów, M., Aguena, M., et al. 2021, The Astrophysical Journal Supplement, 255, 20

Abdo, A. A., Ackermann, M., Agudo, I., et al. 2010a, The Astrophysical Journal, 716, 30

Abdo, A. A., Ackermann, M., Ajello, M., et al. 2010b, Science, 328, 725

Abdo, A. A., Ajello, M., Allafort, A., et al. 2013, The Astrophysical Journal Supplement, 208, 17

Abdollahi, S., Acero, F., Ackermann, M., et al. 2020, The Astrophysical Journal Supplement, 247, 33

Abdollahi, S., Acero, F., Baldini, L., et al. 2022, The Astrophysical Journal Supplement, 260, 53

Acero, F., Ackermann, M., Ajello, M., et al. 2015, The Astrophysical Journal Supplement, 218, 23

Acero, F., Donato, D., Ojha, R., et al. 2013, The Astrophysical Journal, 779, 133

Ackermann, M., Ajello, M., Albert, A., et al. 2012a, The Astrophysical Journal Supplement, 203, 4

Ackermann, M., Ajello, M., Allafort, A., et al. 2011, The Astrophysical Journal, 741, 30

Ackermann, M., Ajello, M., Allafort, A., et al. 2012b, The Astrophysical Journal, 753, 83

Ackermann, M., Ajello, M., Atwood, W. B., et al. 2012c, The Astrophysical Journal, 761, 91

Ahumada, R., Allende Prieto, C., Almeida, A., et al. 2020, The Astrophysical Journal Supplement, 249, 3

Ajello, M., Angioni, R., Axelsson, M., et al. 2020, The Astrophysical Journal, 892, 105

Ajello, M., Atwood, W. B., Axelsson, M., et al. 2021, The Astrophysical Journal Supplement, 256, 12

Ajello, M., Baldini, L., Ballet, J., et al. 2022, The Astrophysical Journal Supplement, 263, 24

Ajello, M., Romani, R. W., Gasparrini, D., et al. 2014, The Astrophysical Journal, 780, 73

Alloin, D. 2006, Physics of Active Galactic Nuclei at all Scales, Vol. 693

Almeida, A., Anderson, S. F., Argudo-Fernández, M., et al. 2023, The Astrophysical Journal Supplement, 267, 44

Álvarez Crespo, N., Masetti, N., Ricci, F., et al. 2016a, The Astronomical Journal, 151, 32

Álvarez Crespo, N., Massaro, F., Milisavljevic, D., et al. 2016b, The Astronomical Journal, 151, 95

Anders, E. & Grevesse, N. 1989, , 53, 197

Angioni, R., Grandi, P., Torresi, E., Vignali, C., & Knödlseder, J. 2017, in American Institute of Physics Conference Series, Vol. 1792, 6th International Symposium on High Energy Gamma-Ray Astronomy, 050006

Arnaud, K. 2022, in AAS/High Energy Astrophysics Division, Vol. 54, AAS/High Energy Astrophysics Division, 203.02

Arnaud, K. A. 1996, in Astronomical Society of the Pacific Conference Series, Vol. 101, Astronomical Data Analysis Software and Systems V, ed. G. H. Jacoby & J. Barnes, 17

Atwood, W., Albert, A., Baldini, L., et al. 2013, arXiv e-prints, arXiv:1303.3514

Atwood, W. B., Abdo, A. A., Ackermann, M., et al. 2009, The Astrophysical Journal, 697, 1071

Baghel, J., Kharb, P., Hovatta, T., et al. 2024, Monthly Notices of the Royal Astronomical Society, 527, 672

Ballet, J., Bruel, P., Burnett, T. H., Lott, B., & The Fermi-LAT collaboration. 2023, arXiv e-prints, arXiv:2307.12546

Barthelmy, S. D. 2000, in Society of Photo-Optical Instrumentation Engineers (SPIE) Conference Series, Vol. 4140, X-Ray and Gamma-Ray Instrumentation for Astronomy XI, ed. K. A. Flanagan & O. H. Siegmund, 50–63

Barthelmy, S. D., Barbier, L. M., Cummings, J. R., et al. 2005, Space Science Reviews, 120, 143

Beckmann, V. & Shrader, C. R. 2012, Active Galactic Nuclei

Begelman, M. C., Fabian, A. C., & Rees, M. J. 2008, Monthly Notices of the Royal Astronomical Society, 384, L19

Berezinskii, V. S., Bulanov, S. V., Dogiel, V. A., & Ptuskin, V. S. 1990, Astrophysics of cosmic rays

Blandford, R. D. & Königl, A. 1979, The Astrophysical Journal, 232, 34

Blandford, R. D. & Payne, D. G. 1982, Monthly Notices of the Royal Astronomical Society, 199, 883

Boissay, R., Ricci, C., & Paltani, S. 2016, Astronomy and Astrophysics, 588, A70

Böttcher, M. 2019, Galaxies, 7, 20

Böttcher, M., Reimer, A., Sweeney, K., & Prakash, A. 2013, The Astrophysical Journal, 768, 54

Brightman, M., Bachetti, M., Earnshaw, H. P., et al. 2019, , 51, 352

Bruel, P., Burnett, T. H., Digel, S. W., et al. 2018, arXiv e-prints, arXiv:1810.11394

Bruni, G., Bassani, L., Persic, M., et al. 2022, Monthly Notices of the Royal Astronomical Society, 513, 886

Bruzewski, S., Schinzel, F. K., Taylor, G. B., & Petrov, L. 2021, The Astrophysical Journal, 914, 42

Bruzewski, S., Schinzel, F. K., Taylor, G. B., & Petrov, L. 2022, VizieR Online Data Catalog, J/ApJ/914/42

Burrows, D. N., Hill, J. E., Nousek, J. A., et al. 2005, Space Science Reviews, 120, 165

Buttiglione, S., Capetti, A., Celotti, A., et al. 2010, Astronomy and Astrophysics, 509, A6

Cardelli, J. A., Clayton, G. C., & Mathis, J. S. 1989, The Astrophysical Journal, 345, 245

CASA Team, Bean, B., Bhatnagar, S., et al. 2022, , 134, 114501

Cerruti, M. 2020, in Journal of Physics Conference Series, Vol. 1468, Journal of Physics Conference Series, 012094

Cerruti, M., Zech, A., Boisson, C., & Inoue, S. 2011, in SF2A-2011: Proceedings of the Annual meeting of the French Society of Astronomy and Astrophysics, ed. G. Alecian, K. Belkacem, R. Samadi, & D. Valls-Gabaud, 555–558

Chambers, K. C., Magnier, E. A., Metcalfe, N., et al. 2016, arXiv e-prints, arXiv:1612.05560

Chang, Y. L., Arsioli, B., Giommi, P., Padovani, P., & Brandt, C. H. 2019, Astronomy and Astrophysics, 632, A77

Chang, Y. L., Brandt, C. H., & Giommi, P. 2020, Astronomy and Computing, 30, 100350

Cheung, C. C., Donato, D., Gehrels, N., Sokolovsky, K. V., & Giroletti, M. 2012, The Astrophysical Journal, 756, 33

Cheung, C. C. & Fermi LAT Collaboration. 2010, in AAS/High Energy Astrophysics Division, Vol. 11, AAS/High Energy Astrophysics Division #11, 30.07

Coleman, G. D., Wu, C. C., & Weedman, D. W. 1980, The Astrophysical Journal Supplement, 43, 393

Cooray, A. 2016, Royal Society Open Science, 3, 150555

Coronado-Blázquez, J., Sánchez-Conde, M. A., Domínguez, A., et al. 2019, , 2019, 020

Costamante, L. 2020, in Multifrequency Behaviour of High Energy Cosmic Sources - XIII. 3-8 June 2019. Palermo, 35

Costamante, L., Cutini, S., Tosti, G., Antolini, E., & Tramacere, A. 2018, Monthly Notices of the Royal Astronomical Society, 477, 4749

Coziol, R., Andernach, H., Torres-Papaqui, J. P., Ortega-Minakata, R. A., & Moreno del Rio, F. 2017, Monthly Notices of the Royal Astronomical Society, 466, 921

D'Abrusco, R., Massaro, F., Paggi, A., et al. 2013, The Astrophysical Journal Supplement, 206, 12

de Angelis, A. 2001, in New worlds in astroparticle physics, ed. A. M. Mourao, M. Pimenta, P. M. Sa, & J. M. Velhinho, 140

de Menezes, R., Peña-Herazo, H. A., Marchesini, E. J., et al. 2019, Astronomy and Astrophysics, 630, A55

DeBoer, D. R., Gough, R. G., Bunton, J. D., et al. 2009, IEEE Proceedings, 97, 1507

Dermer, C. D. & Menon, G. 2009, High Energy Radiation from Black Holes: Gamma Rays, Cosmic Rays, and Neutrinos

Desai, A., Marchesi, S., Rajagopal, M., & Ajello, M. 2019, The Astrophysical Journal Supplement, 241, 5

Doert, M. & Errando, M. 2014, The Astrophysical Journal, 782, 41

Dole, H., Lagache, G., Puget, J. L., et al. 2006, Astronomy and Astrophysics, 451, 417

Done, C., Davis, S. W., Jin, C., Blaes, O., & Ward, M. 2012, Monthly Notices of the Royal Astronomical Society, 420, 1848

Elvis, M., Wilkes, B. J., McDowell, J. C., et al. 1994, The Astrophysical Journal Supplement, 95, 1

Evans, P. A., Beardmore, A. P., Page, K. L., et al. 2009, Monthly Notices of the Royal Astronomical Society, 397, 1177

Evans, P. A., Page, K. L., Osborne, J. P., et al. 2020, The Astrophysical Journal Supplement, 247, 54

Falcone, A., Stroh, M., Ferrara, E., et al. 2011, in AAS/High Energy Astrophysics Division, Vol. 12, AAS/High Energy Astrophysics Division #12, 4.03

Falcone, A., Stroh, M., & Pryal, M. 2014, in American Astronomical Society Meeting Abstracts, Vol. 223, American Astronomical Society Meeting Abstracts #223, 301.05

Falomo, R., Pian, E., & Treves, A. 2014, Astronomy and Astrophysics Review, 22, 73

Fanaroff, B. L. & Riley, J. M. 1974, Monthly Notices of the Royal Astronomical Society, 167, 31P

Fang, K. & Murase, K. 2018, Nature Physics, 14, 396

Frank, J., King, A., & Raine, D. J. 2002, Accretion Power in Astrophysics: Third Edition

Frater, R. H., Brooks, J. W., & Whiteoak, J. B. 1992, Journal of Electrical and Electronics Engineering Australia, 12, 103

Fronte, L., Mazzon, B., Metruccio, F., et al. 2023, in Journal of Physics Conference Series, Vol. 2429, Journal of Physics Conference Series, 012045

Fukugita, M., Ichikawa, T., Gunn, J. E., et al. 1996, The Astronomical Journal, 111, 1748

Gaisser, T. K. 1990, Cosmic rays and particle physics.

Gao, S., Fedynitch, A., Winter, W., & Pohl, M. 2019, Nature Astronomy, 3, 88

Garofalo, D., Singh, C. B., Walsh, D. T., et al. 2019, Research in Astronomy and Astrophysics, 19, 013

Gehrels, N., Chincarini, G., Giommi, P., et al. 2004, The Astrophysical Journal, 611, 1005

Ghisellini, G., Maraschi, L., & Treves, A. 1985, Astronomy and Astrophysics, 146, 204

Ghisellini, G., Righi, C., Costamante, L., & Tavecchio, F. 2017, Monthly Notices of the Royal Astronomical Society, 469, 255

Ghisellini, G. & Tavecchio, F. 2008, Monthly Notices of the Royal Astronomical Society, 387, 1669

Ghisellini, G., Tavecchio, F., Foschini, L., & Ghirlanda, G. 2011, Monthly Notices of the Royal Astronomical Society, 414, 2674

Ghisellini, G., Tavecchio, F., Maraschi, L., Celotti, A., & Sbarrato, T. 2014, Nature, 515, 376

Giommi, P., Glauch, T., Padovani, P., et al. 2020, Monthly Notices of the Royal Astronomical Society, 497, 865

Giommi, P., Padovani, P., & Polenta, G. 2013, Monthly Notices of the Royal Astronomical Society, 431, 1914

Giommi, P., Padovani, P., Polenta, G., et al. 2012a, Monthly Notices of the Royal Astronomical Society, 420, 2899

Giommi, P., Polenta, G., Lähteenmäki, A., et al. 2012b, Astronomy and Astrophysics, 541, A160

Giroletti, M., Massaro, F., D'Abrusco, R., et al. 2016, Astronomy and Astrophysics, 588, A141

Glauch, T., Kerscher, T., & Giommi, P. 2022, Astronomy and Computing, 41, 100646

Goad, M. R., Osborne, J. P., Beardmore, A. P., & Evans, P. A. 2007, GRB Coordinates Network, 7133, 1

Gordon, Y. A., Boyce, M. M., O'Dea, C. P., et al. 2021, The Astrophysical Journal Supplement, 255, 30

Grandi, P. 2012, in International Journal of Modern Physics Conference Series, Vol. 8, International Journal of Modern Physics Conference Series, 25–30

Grandi, P., Torresi, E., & Stanghellini, C. 2012, The Astrophysical Journal Letters, 751, L3

Grove, J. E. & Johnson, W. N. 2010, in Society of Photo-Optical Instrumentation Engineers (SPIE) Conference Series, Vol. 7732, Space Telescopes and Instrumentation 2010: Ultraviolet to Gamma Ray, ed. M. Arnaud, S. S. Murray, & T. Takahashi, 77320J

Guépin, C. 2020, Astronomy and Astrophysics, 641, A29

Guépin, C. & Kotera, K. 2017, in SF2A-2017: Proceedings of the Annual meeting of the French Society of Astronomy and Astrophysics, ed. C. Reylé, P. Di Matteo, F. Herpin, E. Lagadec, A. Lançon, Z. Meliani, & F. Royer, Di

Gunn, J. E., Siegmund, W. A., Mannery, E. J., et al. 2006, The Astronomical Journal, 131, 2332

Gürkan, G., Hardcastle, M. J., Best, P. N., et al. 2019, Astronomy and Astrophysics, 622, A11

Hale, C. L., McConnell, D., Thomson, A. J. M., et al. 2021, , 38, e058

Hambly, N., Read, M., Mann, R., et al. 2004, in Astronomical Society of the Pacific Conference Series, Vol. 314, Astronomical Data Analysis Software and Systems (ADASS) XIII, ed. F. Ochsenbein, M. G. Allen, & D. Egret, 137

Hambly, N. C., MacGillivray, H. T., Read, M. A., et al. 2001, Monthly Notices of the Royal Astronomical Society, 326, 1279

Hariharan, P. 2007, Basics of Interferometry, Second Edition

Harrison, C. M. 2016, Observational Constraints on the Influence of Active Galactic Nuclei on the Evolution of Galaxies

HI4PI Collaboration, Ben Bekhti, N., Flöer, L., et al. 2016, Astronomy and Astrophysics, 594, A116

Hotan, A. W., Bunton, J. D., Chippendale, A. P., et al. 2021, , 38, e009

Hovatta, T., Aller, M. F., Aller, H. D., et al. 2014, The Astronomical Journal, 147, 143

Hovatta, T., Lister, M. L., Aller, M. F., et al. 2012, The Astronomical Journal, 144, 105

IceCube Collaboration, Aartsen, M. G., Ackermann, M., et al. 2018, Science, 361, eaat1378

Järvelä, E., Berton, M., & Crepaldi, L. 2021, Frontiers in Astronomy and Space Sciences, 8, 147

Joffre, S., Silver, R., Rajagopal, M., et al. 2022, The Astrophysical Journal, 940, 139

Johnson, H. L. & Morgan, W. W. 1953, The Astrophysical Journal, 117, 313

Johnston, S., Bailes, M., Bartel, N., et al. 2007, , 24, 174

Johnston, S., Taylor, R., Bailes, M., et al. 2008, Experimental Astronomy, 22, 151

Jones, D. H., Read, M. A., Saunders, W., et al. 2009, Monthly Notices of the Royal Astronomical Society, 399, 683

Kaiser, N., Aussel, H., Burke, B. E., et al. 2002, in Society of Photo-Optical Instrumentation Engineers (SPIE) Conference Series, Vol. 4836, Survey and Other Telescope Technologies and Discoveries, ed. J. A. Tyson & S. Wolff, 154–164

Kaiser, N., Burgett, W., Chambers, K., et al. 2010, in Society of Photo-Optical Instrumentation Engineers (SPIE) Conference Series, Vol. 7733, Ground-based and Airborne Telescopes III, ed. L. M. Stepp, R. Gilmozzi, & H. J. Hall, 77330E

Kalfountzou, E., Jarvis, M. J., Bonfield, D. G., & Hardcastle, M. J. 2012, Monthly Notices of the Royal Astronomical Society, 427, 2401

Kataoka, J., Yatsu, Y., Kawai, N., et al. 2012, The Astrophysical Journal, 757, 176

Kaur, A., Falcone, A. D., & Stroh, M. 2019a, in AAS/High Energy Astrophysics Division, Vol. 17, AAS/High Energy Astrophysics Division, 106.09

Kaur, A., Falcone, A. D., Stroh, M. D., Kennea, J. A., & Ferrara, E. C. 2019b, The Astrophysical Journal, 887, 18

Kaur, A., Kerby, S., & Falcone, A. D. 2023, The Astrophysical Journal, 943, 167

Kellermann, K. I., Sramek, R., Schmidt, M., Shaffer, D. B., & Green, R. 1989, The Astronomical Journal, 98, 1195

Kembhavi, A. & Narlikar, J. 1999, Quasars and Active Galactic Nuclei: An Introduction, Quasars and Active Galactic Nuclei: An Introduction (Cambridge University Press)

Kerby, S., Kaur, A., Falcone, A. D., et al. 2021, The Astrophysical Journal, 923, 75

King, H. C. 1955, The History of the Telescope

Kollmeier, J. A., Zasowski, G., Rix, H.-W., et al. 2017, arXiv e-prints, arXiv:1711.03234

Komossa, S. 2008, in Revista Mexicana de Astronomia y Astrofisica Conference Series, Vol. 32, Revista Mexicana de Astronomia y Astrofisica Conference Series, 86–92

Kormendy, J. & Ho, L. C. 2013, Annual Review of Astronomy and Astrophysics, 51, 511

Kormendy, J. & Richstone, D. 1995, Annual Review of Astronomy and Astrophysics, 33, 581

Kovalev, Y. Y. 2009, The Astrophysical Journal Letters, 707, L56

Kun, E., Bartos, I., Tjus, J. B., et al. 2021, The Astrophysical Journal Letters, 911, L18

Lacy, M., Baum, S. A., Chandler, C. J., et al. 2020, , 132, 035001

Landi, R., Bassani, L., Stephen, J. B., et al. 2015, Astronomy and Astrophysics, 581, A57

Landoni, M., Paiano, S., Falomo, R., Scarpa, R., & Treves, A. 2018, The Astrophysical Journal, 861, 130

Landt, H., Padovani, P., & Giommi, P. 2002, Monthly Notices of the Royal Astronomical Society, 336, 945

Li, K.-L., Hou, X., Strader, J., et al. 2018, The Astrophysical Journal, 863, 194

Longair, M. S. 2011, High Energy Astrophysics

López-Caniego, M., González-Nuevo, J., Massardi, M., et al. 2013, Monthly Notices of the Royal Astronomical Society, 430, 1566

Maeda, K., Kataoka, J., Nakamori, T., et al. 2011, The Astrophysical Journal, 729, 103

Maini, A., Prandoni, I., Norris, R. P., Giovannini, G., & Spitler, L. R. 2016, Astronomy and Astrophysics, 589, L3

Malizia, A., Bassani, L., Bazzano, A., et al. 2012, Monthly Notices of the Royal Astronomical Society, 426, 1750

Mao, Z. & Yu, Y.-W. 2013, Research in Astronomy and Astrophysics, 13, 952

Marcha, M. J. M., Browne, I. W. A., Impey, C. D., & Smith, P. S. 1996, Monthly Notices of the Royal Astronomical Society, 281, 425

Marchesi, S., Kaur, A., & Ajello, M. 2018, The Astronomical Journal, 156, 212

Marchesini, E. J., Paggi, A., Massaro, F., et al. 2020, Astronomy and Astrophysics, 638, A128

Marchesini, E. J., Peña-Herazo, H. A., Álvarez Crespo, N., et al. 2019, Astronomy and Astrophysics, Supplement, 364, 5

Marchesini, E. J., Reynaldi, V., Vieyro, F., et al. 2023a, Astronomy and Astrophysics, 670, A91

Marchesini, E. J., Reynaldi, V., Vieyro, F., et al. 2023b, Astronomy and Astrophysics, 670, A91

Marr, J. M., Snell, R. L., & Kurtz, S. E. 2015, Fundamentals of Radio Astronomy: Observational Methods (Series in Astronomy and Astrophysics)

Marscher, A. P. & Gear, W. K. 1985, The Astrophysical Journal, 298, 114

Massaro, F., Álvarez Crespo, N., D'Abrusco, R., et al. 2016, Astronomy and Astrophysics, Supplement, 361, 337

Massaro, F., D'Abrusco, R., Giroletti, M., et al. 2013, The Astrophysical Journal Supplement, 207, 4

Massaro, F., D'Abrusco, R., Landoni, M., et al. 2015a, The Astrophysical Journal Supplement, 217, 2

Massaro, F., Landoni, M., D'Abrusco, R., et al. 2015b, Astronomy and Astrophysics, 575, A124

Massaro, F., Marchesini, E. J., D'Abrusco, R., et al. 2017, The Astrophysical Journal, 834, 113

Matsuoka, M., Kawasaki, K., Ueno, S., et al. 2009, Publications of the Astronomical Society of Japan, 61, 999

Mattox, J. R., Bertsch, D. L., Chiang, J., et al. 1996, The Astrophysical Journal, 461, 396

McConnell, D., Hale, C. L., Lenc, E., et al. 2020, , 37, e048

Meegan, C., Lichti, G., Bhat, P. N., et al. 2009, The Astrophysical Journal, 702, 791

Merloni, A., Predehl, P., Becker, W., et al. 2012, arXiv e-prints, arXiv:1209.3114

Mirabal, N., Frías-Martinez, V., Hassan, T., & Frías-Martinez, E. 2012, Monthly Notices of the Royal Astronomical Society, 424, L64

Monet, D. G., Levine, S. E., Canzian, B., et al. 2003, The Astronomical Journal, 125, 984

Monroe, T. R., Prochaska, J. X., Tejos, N., et al. 2016, The Astronomical Journal, 152, 25

Nasa High Energy Astrophysics Science Archive Research Center (Heasarc). 2014, HEAsoft: Unified Release of FTOOLS and XANADU, Astrophysics Source Code Library, record ascl:1408.004

Nemmen, R. S., Georganopoulos, M., Guiriec, S., et al. 2012, Science, 338, 1445

Netzer, H. 2013, The Physics and Evolution of Active Galactic Nuclei

Nolan, P. L., Abdo, A. A., Ackermann, M., et al. 2012, The Astrophysical Journal Supplement, 199, 31

Nori, M., Giroletti, M., Massaro, F., et al. 2014, The Astrophysical Journal Supplement, 212, 3

Osterbrock, D. E. 1980, in Ninth Texas Symposium on Relativistic Astrophysics, Vol. 336, 22–38

Osterbrock, D. E. & Pogge, R. W. 1985, The Astrophysical Journal, 297, 166

Padovani, P. 1999, in Vulcano Workshop 1998: Frontier Objects in Astrophysics and Particle Physics, ed. F. Giovannelli & G. Mannocchi, Vol. 65, 159

Padovani, P. 2017, Frontiers in Astronomy and Space Sciences, 4, 35

Padovani, P., Alexander, D. M., Assef, R. J., et al. 2017, Astronomy and Astrophysics Review, 25, 2

Padovani, P., Boccardi, B., Falomo, R., & Giommi, P. 2022, Monthly Notices of the Royal Astronomical Society, 511, 4697

Padovani, P. & Giommi, P. 1995, The Astrophysical Journal, 444, 567

Padovani, P., Oikonomou, F., Petropoulou, M., Giommi, P., & Resconi, E. 2019, Monthly Notices of the Royal Astronomical Society, 484, L104

Paiano, S., Falomo, R., Franceschini, A., Treves, A., & Scarpa, R. 2017a, The Astrophysical Journal, 851, 135

Paiano, S., Falomo, R., Treves, A., Franceschini, A., & Scarpa, R. 2019, The Astrophysical Journal, 871, 162

Paiano, S., Falomo, R., Treves, A., et al. 2021, Monthly Notices of the Royal Astronomical Society, 504, 3338

Paiano, S., Falomo, R., Treves, A., et al. 2023, Monthly Notices of the Royal Astronomical Society, 521, 2270

Paiano, S., Falomo, R., Treves, A., & Scarpa, R. 2020, Monthly Notices of the Royal Astronomical Society, 497, 94

Paiano, S., Franceschini, A., & Stamerra, A. 2017b, Monthly Notices of the Royal Astronomical Society, 468, 4902

Paiano, S., Landoni, M., Falomo, R., Treves, A., & Scarpa, R. 2017c, The Astrophysical Journal, 844, 120

Paiano, S., Landoni, M., Falomo, R., et al. 2017d, The Astrophysical Journal, 837, 144

Pajdosz-Śmierciak, U., Śmierciak, B., & Jamrozy, M. 2022, Monthly Notices of the Royal Astronomical Society, 514, 2122

Paliya, V. S., Domínguez, A., Ajello, M., Olmo-García, A., & Hartmann, D. 2021, The Astrophysical Journal Supplement, 253, 46

Paliya, V. S., Stalin, C. S., & Ravikumar, C. D. 2015, The Astronomical Journal, 149, 41

Panessa, F., Baldi, R. D., Laor, A., et al. 2019, Nature Astronomy, 3, 387

Peña-Herazo, H. A., Marchesini, E. J., Álvarez Crespo, N., et al. 2017, Astronomy and Astrophysics, Supplement, 362, 228

Peng, F.-K., Zhang, H.-M., Wang, X.-Y., Wang, J.-F., & Zhi, Q.-J. 2019, The Astrophysical Journal, 884, 91

Perryman, M. A. C. 2005, in ESA Special Publication, Vol. 576, The Three-Dimensional Universe with Gaia, ed. C. Turon, K. S. O'Flaherty, & M. A. C. Perryman, 15

Peterson, B. M. 1997, An Introduction to Active Galactic Nuclei

Petrov, L., Mahony, E. K., Edwards, P. G., et al. 2013, Monthly Notices of the Royal Astronomical Society, 432, 1294

Petrov, L., Phillips, C., Bertarini, A., Murphy, T., & Sadler, E. M. 2011, Monthly Notices of the Royal Astronomical Society, 414, 2528

Poppett, C. 2024, The NOIRLab Mirror, 7, 23

Potter, W. J. & Cotter, G. 2013, Monthly Notices of the Royal Astronomical Society, 436, 304

Prandini, E. & Ghisellini, G. 2022, Galaxies, 10, 35

Pringle, J. E. 1981, Annual Review of Astronomy and Astrophysics, 19, 137

Punsly, B. & Zhang, S. 2011, Monthly Notices of the Royal Astronomical Society, 412, L123

Rajagopal, M., Marcotulli, L., Labrie, K., Marchesi, S., & Ajello, M. 2023, The Astronomical Journal, 165, 42

Rakshit, S., Stalin, C. S., Chand, H., & Zhang, X.-G. 2017, The Astrophysical Journal Supplement, 229, 39

Rakshit, S., Stalin, C. S., Chand, H., & Zhang, X.-G. 2018, Bulletin de la Societe Royale des Sciences de Liege, 87, 379

Rando, R. 2022, The Fermi Large Area Telescope, ed. C. Bambi & A. Santangelo (Singapore: Springer Nature Singapore), 1–29

Ransom, S. M., Ray, P. S., Camilo, F., et al. 2011, The Astrophysical Journal Letters, 727, L16

Ricci, F., Massaro, F., Landoni, M., et al. 2015, The Astronomical Journal, 149, 160

Rieger, F. M. 2017, in American Institute of Physics Conference Series, Vol. 1792, 6th International Symposium on High Energy Gamma-Ray Astronomy, 020008

Righi, C. & Tavecchio, F. 2020, PoS, MULTIF2019, 036

Rodrigues, X., Gao, S., Fedynitch, A., Palladino, A., & Winter, W. 2019, The Astrophysical Journal Letters, 874, L29

Rusinek-Abarca, K. & Sikora, M. 2021, The Astrophysical Journal, 922, 202

Rybicki, G. B. & Lightman, A. P. 1979, Radiative processes in astrophysics

Ryle, M. & Hewish, A. 1960, Monthly Notices of the Royal Astronomical Society, 120, 220

Ryle, M., Hewish, A., & Shakeshaft, J. 1959, IEEE Transactions on Antennas and Propagation, 7, 120

Salvetti, D., Chiaro, G., La Mura, G., & Thompson, D. J. 2017a, Monthly Notices of the Royal Astronomical Society, 470, 1291

Salvetti, D., Mignani, R. P., De Luca, A., et al. 2017b, Monthly Notices of the Royal Astronomical Society, 470, 466

Saz Parkinson, P. M., Dormody, M., Ziegler, M., et al. 2010, The Astrophysical Journal, 725, 571

Sbarrato, T., Padovani, P., & Ghisellini, G. 2015, in Extragalactic Jets from Every Angle, ed. F. Massaro, C. C. Cheung, E. Lopez, & A. Siemiginowska, Vol. 313, 48–52

Sbarufatti, B., Treves, A., & Falomo, R. 2005, The Astrophysical Journal, 635, 173

Sbarufatti, B., Treves, A., Falomo, R., et al. 2006, The Astronomical Journal, 132, 1

Schinzel, F. K., Petrov, L., Taylor, G. B., & Edwards, P. G. 2017, The Astrophysical Journal, 838, 139

Schinzel, F. K., Petrov, L., Taylor, G. B., et al. 2015, The Astrophysical Journal Supplement, 217, 4

Schroller, M., Becker-Tjus, J., Reichherzer, P., et al. 2022, in 37th International Cosmic Ray Conference, 992

Seabroke, G. M., Fabricius, C., Teyssier, D., et al. 2021, Astronomy and Astrophysics, 653, A160

Seehars, S., Grandis, S., Amara, A., & Refregier, A. 2016, , 93, 103507

Seyfert, C. K. 1943, The Astrophysical Journal, 97, 28

Shakura, N. I. & Sunyaev, R. A. 1973, Astronomy and Astrophysics, 24, 337

Shaw, M. S., Filippenko, A. V., Romani, R. W., Cenko, S. B., & Li, W. 2013a, The Astronomical Journal, 146, 127

Shaw, M. S., Romani, R. W., Cotter, G., et al. 2012, The Astrophysical Journal, 748, 49

Shaw, M. S., Romani, R. W., Cotter, G., et al. 2013b, The Astrophysical Journal, 764, 135

Shaw, M. S., Romani, R. W., Cotter, G., et al. 2013c, The Astrophysical Journal, 764, 135

Shimwell, T. W., Hardcastle, M. J., Tasse, C., et al. 2022, Astronomy and Astrophysics, 659, A1

Stroh, M. C. & Falcone, A. D. 2013, The Astrophysical Journal Supplement, 207, 28

Summerer, L. & Purcell, O. 2009

Takahashi, Y., Kataoka, J., Nakamori, T., et al. 2012, The Astrophysical Journal, 747, 64

Takeuchi, Y., Kataoka, J., Maeda, K., et al. 2013, The Astrophysical Journal Supplement, 208, 25

The Dark Energy Survey Collaboration. 2005, arXiv e-prints, astro

Thompson, A. R., Clark, B. G., Wade, C. M., & Napier, P. J. 1980, The Astrophysical Journal Supplement, 44, 151

Tolamatti, A., Singh, K. K., & Yadav, K. K. 2023, Monthly Notices of the Royal Astronomical Society, 523, 5341

Tripathi, D., Giommi, P., Di Giovanni, A., et al. 2024, The Astronomical Journal, 167, 116

Ulgiati, A., Paiano, S., Treves, A., et al. 2024, Monthly Notices of the Royal Astronomical Society, 530, 4626

Urry, C. M. & Padovani, P. 1995, , 107, 803

Urry, C. M., Scarpa, R., O'Dowd, M., et al. 2000, The Astrophysical Journal, 532, 816

Uslenghi, M. & Falomo, R. 2011, in Society of Photo-Optical Instrumentation Engineers (SPIE) Conference Series, Vol. 8135, Applications of Digital Image Processing XXXIV, ed. A. G. Tescher, 813524

Véron-Cetty, M. P. & Véron, P. 2006, Astronomy and Astrophysics, 455, 773

Wang, D.-L., Wang, J.-G., & Dong, X.-B. 2009, Research in Astronomy and Astrophysics, 9, 1078

Watson, F. 2004, Stargazer : the life and times of the telescope

Webb, N. A., Coriat, M., Traulsen, I., et al. 2020, Astronomy and Astrophysics, 641, A136

Wester, W. & Dark Energy Survey Collaboration. 2005, in Astronomical Society of the Pacific Conference Series, Vol. 339, Observing Dark Energy, ed. S. C. Wolff & T. R. Lauer, 152

Wilms, J., Allen, A., & McCray, R. 2000, The Astrophysical Journal, 542, 914

Wilson, A. S. & Colbert, E. J. M. 1995, The Astrophysical Journal, 438, 62

Wilson, J. C., Hearty, F. R., Skrutskie, M. F., et al. 2019, , 131, 055001

Wright, E. L., Eisenhardt, P. R. M., Mainzer, A. K., et al. 2010, The Astronomical Journal, 140, 1868

Wu, H. K. J. 2018, PhD thesis, Rheinische Friedrich Wilhelms University of Bonn, Germany

Ye, X.-H., Zeng, X.-T., Huang, D.-Y., et al. 2023, , 135, 014101

York, D. G., Adelman, J., Anderson, John E., J., et al. 2000, The Astronomical Journal, 120, 1579